Scott Arthur
Masato Saitoh
Sudip Kumar Pal *Editors*

Advances in Civil Engineering

Select Proceedings of ICACE 2020

Springer

Lecture Notes in Civil Engineering

Volume 184

Lecture Notes in Civil Engineering (LNCE) publishes the latest developments in Civil Engineering - quickly, informally and in top quality. Though original research reported in proceedings and post-proceedings represents the core of LNCE, edited volumes of exceptionally high quality and interest may also be considered for publication. Volumes published in LNCE embrace all aspects and subfields of, as well as new challenges in, Civil Engineering. Topics in the series include:

- Construction and Structural Mechanics
- Building Materials
- Concrete, Steel and Timber Structures
- Geotechnical Engineering
- Earthquake Engineering
- Coastal Engineering
- Ocean and Offshore Engineering; Ships and Floating Structures
- Hydraulics, Hydrology and Water Resources Engineering
- Environmental Engineering and Sustainability
- Structural Health and Monitoring
- Surveying and Geographical Information Systems
- Indoor Environments
- Transportation and Traffic
- Risk Analysis
- Safety and Security

To submit a proposal or request further information, please contact the appropriate Springer Editor:

- Pierpaolo Riva at pierpaolo.riva@springer.com (Europe and Americas);
- Swati Meherishi at swati.meherishi@springer.com (Asia - except China, and Australia, New Zealand);
- Wayne Hu at wayne.hu@springer.com (China).

All books in the series now indexed by Scopus and EI Compendex database!

More information about this series at http://www.springer.com/series/15087

Scott Arthur · Masato Saitoh · Sudip Kumar Pal
Editors

Advances in Civil Engineering

Select Proceedings of ICACE 2020

Springer

Editors
Scott Arthur
School of Energy
Geoscience, Infrastructure and Society
Herriot Watt University
Edinburgh, UK

Masato Saitoh
Department of Civil and Environmental
Engineering
Saitama University
Saitama, Japan

Sudip Kumar Pal
Department of Civil Engineering
Chittagong University of Engineering
and Technology
Chattogram, Bangladesh

Contents

Contents

About the Editors

Dr. Scott Arthur is currently a professor at the Institute for Infrastructure and Environment, Heriot-Watt University, UK. He began his research career in 1992 working under the supervision of Prof. Richard Ashley on a high profile EPSRC funded project investigating sediment and pollutant transport within combined sewer networks. Following this work in Dundee, in 1996, he moved to a Post-Doctoral Research Associate position at Heriot-Watt University (Building Department with Prof John Snwaffield) and subsequently (August 2000) appointed within Heriot-Watt University to a lecturing position. Since that time, his research has been supported by EPSRC, the European Union, the Scottish Government, the Royal Academy of Engineering, SNIFFER, and CREW. Prof. Arthur research comprises work on all aspects of urban drainage systems from roof systems to urban watercourse and large sewer networks. He has published 57 international papers in indexed journals and has been involved in several research projects funded by Scottish Government and European Union.

Dr. Masato Saitoh is currently a professor at the Graduate School of Science and Engineering, Saitama University, Japan. After obtaining a Doctor of Engineering (D.Engg.) from Saitama University in 2001, Dr. Saitoh has moved to academia as an assistant professor at Saitama University. Earlier, he was working as a researcher at the Railway Technical Research Institute (RTRI) in Japan. His primary research interests include the dynamic response of the soil-pile system, foundation engineering. He has published 28 international papers in top-notch journals along with 13 national journals. Prof. Saitoh also holds 13 patents including international PCT subsidized by the Japan Science and Technology Agency (JST) on his developed research works and lead a significant number of research projects funded by the Japanese Government (JSPS). In 2017, Prof. Saitoh received best lecturer award from Saitama University for his outstanding teaching contribution. He also received the best paper award from the Japanese Geotechnical Society in 2003 and best speaker award of JSCE conference in 1997 and 1999. At present, he is an editorial board member of JSCE Journal H-division and reviewer of several reputed journals.

Dr. Sudip Kumar Pal is currently a professor and the head at the Department of Civil Engineering, Chittagong University of Engineering and Technology (CUET) in Bangladesh. He earned his Ph.D. from Heriot-Watt University in 2012. He has 20 years of experience at leading Bangladeshi academic institution and abroad through research activities and teaching students from various social and cultural backgrounds. His primary research interest focuses on sustainable urban drainage system, water and wastewater treatment, atmospheric pollution, and water harvesting technologies. Prof. Sudip has published 15 international journals, 3 national journals, and more than 20 conference proceedings both in Bangladesh and abroad. He has been involved in few research projects, e.g., textile effluent treatment under higher education in sustainable textile funded by DAAD, Germany, and rain water harvesting and hydropower generation using solar panel for indigenous people in Bangladesh funded by Innovate UK with national and international collaboration. He is a member of many professional organizations like ASCE, BHS, IEB. In addition, he serves the academic community as a reviewer of distinguished journals.

Changes in Quality of Supplied Drinking Water from Sources to Households in Dhaka City

Ahnaf Shahriyar, Naushin Tabassum, and Sheikh Mokhlesur Rahman

1 Introduction

Consumption of contaminated water causes about 80% of all diseases and over one-third of deaths in developing countries [1]. Thus, the availability of safe drinking water is one of the most important public health requirements, especially in developing countries. In Bangladesh, most of the urban population (99.1%) uses improved drinking water sources (tube well: 70.1%, piped water: 28.7%) [2]. According to the World Health Organization (WHO), improved drinking water sources are termed as those sources adequately protecting the water from outside contamination (predominantly fecal coliform) and include water from piped connection, public tap or standpipe, protected borehole or dug well, spring, and/or rainwater collection [3]. Due to the frequent contamination in piped supplies, source water from piped distribution and public tap is more likely to be contaminated in urban areas (55%) [2]. Water contamination occurs between the source and point of use, either in distribution pipe and/or different points in household storage reservoirs [4, 5].

Dhaka, the capital city of Bangladesh, has a water demand of about 2580 million liters per day [6]. The water supply authority, Dhaka Water Supply and Sewerage Authority (DWASA), mostly relies on groundwater (78%) to supply drinking water in the city of Dhaka and its surroundings, and the rest 22% of total water demand is met with surface water sources [7]. DWASA is divided into 11 'Maintenance, Operation, and Distribution System' (MODS) zones, of which ten zones are under Dhaka city and one under Narayanganj city [7]. DWASA has implemented a chlorination system at the sources for disinfection purposes and also to remove some pollutants from water [7]. Although regular monitoring of source groundwater and surface water

<hr>

A. Shahriyar and N. Tabassum has equal contribution

<hr>

A. Shahriyar · N. Tabassum · S. M. Rahman (✉)
Department of Civil Engineering, BUET, Dhaka, Bangladesh
e-mail: smrahman@ce.buet.ac.bd

is regulated by DWASA with a satisfactory result of the source water quality [7], 51.5% and 41.4% out of 2768 service recipients reported that the water supplied by WASA was dirty and had a bad smell, respectively [6]. Furthermore, contamination of harmful bacteria in DWASA-supplied water has been detected according to a report of the Local Government and Rural Development (LGRD) Ministry [8]. Studies have demonstrated that the bacteriological quality of WASA source water is superior to pipeline and house tap water, so water contamination might have taken place in the distribution system and/or domestic tanks or reservoirs [9]. Another study based on a quantitative analysis of 25 drinking water samples from different areas of Dhaka metropolis found that the overall quality of the samples was not satisfactory to be considered potable [10].

Some previous studies include a household drinking water quality assessment in Kisii town, Kenya [11], and a seasonal cohort study on household practices and post-collection contamination of water in Malawi [12]. Furthermore, a sanitary survey was carried out to detect *E. coli* contamination in water samples from different reservoirs in the rural areas in northern Jordan [13]. In Linden, Guyana, a health survey was performed for the development a water safety plan involving household storage reservoirs [5]. Previously a study conducted in Bangladesh, observed the microbial quality of Dhaka WASA drinking water with samples collected from source pump, pipeline, roadside tap, and different house tap [9]. Most of the previous studies were mainly focused on *E. coli* and residual chlorine, and hardly, any studies have been conducted addressing the assessment of water quality changes within different storage points of a household distribution system.

The current study explores the change in water quality supplied by Dhaka WASA compared to a ground water source and different points of households on an individual level and identifies the correlation between different parameters contributing to this variation. Besides, in this study, water quality was observed for multiple physical, chemical, and microbial parameters for both source and various points of households in Dhaka. Furthermore, the household's water uses and treatment practices, hygiene, user satisfaction, and perceptions of water quality by consumers were taken into consideration on an individual level.

To investigate the quality of DWASA-supplied drinking water of source and different points of household, two (MODS zones 2 and 3) out of eleven zones were selected. The change in water quality and intrusion of pathogenic microorganisms at various locations of the selected zones, the influence of socioeconomic conditions, and the individual household practices were observed. Drinking water samples were collected from three points (i.e., underground water reservoir—UGWR, overhead water tank—OHWT, and tap) of eight different households, and tests for different parameters were conducted. After the sample collection from the household, a short questionnaire survey was performed with the assistance of the household owner. Finally, statistical data analysis (Principal Component Analysis-PCA) was performed with the data extracted from laboratory testing.
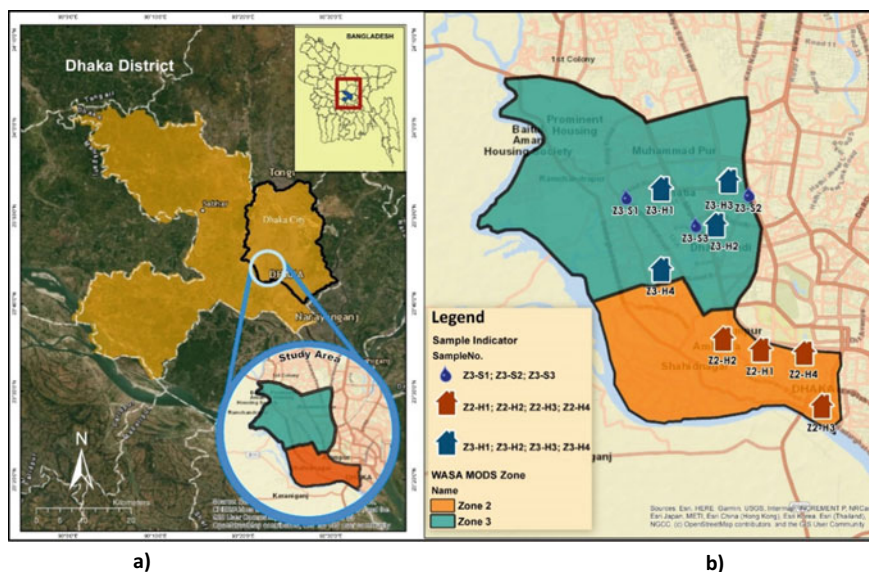
Fig. 1 a Map of the study area. **b** Sampling location

2 Materials and Methods

2.1 Study Area

The selected study area was MODS zone 2 and 3 due to the diversified inter-zonal and intra-zonal socioeconomic status. Zone 2 comprises West side of Nababpur Road, Hazaribag, Nababganj, Nilkhet, Azimpur to Buriganga. At the same time, zone 3 consists of the East side of Kazi Nazrul Islam Avenue, North side of Agargaon Road, Shyamoli, South side Nilkhet, and West side Beribadh. The majority of the inhabitants in the two zones have access to piped water supplied by DWASA; for few people, water sources may vary (e.g., pond, well, river, etc.) (Fig. 1).

2.2 Sample Collection

Four households from each zone and three nearby groundwater extraction pumps from zone 3 were selected as a sample collection point. For the groundwater samples of zone 2, data from the surface water treatment plant was used. The sampling points were named as follows: Zone 2 households (four samples)—'Z2-H1', 'Z2-H2', 'Z2-H3', 'Z2-H4'; Zone 3 households (four samples)—'Z3-H1', 'Z3-H2', 'Z3-H3', 'Z3-H4'; Zone 2 GW source (three samples)—'Z3-S1', Z3-S2', Z3-S3'. From

each household, three points (UGWR, OHWT, and Tap) were selected for identifying the probable source of contamination and observing the variation of different parameters along inside the household network.

2.3 Questionnaire Survey

Subsequent to the sample collection from the household, a short questionnaire survey was performed with the assistance of the household owner, comprising questions on the household details, occupants, education, income status, pipe connection status, cleaning frequency, zonal water logging history, and personal preferences and other comments.

2.4 Laboratory Tests

Tests for physical, chemical, and pathogenic parameters were done in the Environmental Engineering Laboratory of the Department of Civil Engineering, BUET. This study included tests of color, pH, electrical conductivity (EC), turbidity, total coliform (TC), fecal coliform (FC), iron (Fe), manganese (Mn), aluminum (Al), ammonia (NH_3), arsenic (As), lead (Pb), and residual chlorine (R-Cl_2). These parameters were selected based on the WASA Microbiology and Chemical Division's (DWASA Central Laboratory) standard testing framework. WHO guidelines for drinking water quality standards were adopted as the framework for comparing the test results [14].

2.5 Statistical Analysis

Principal component analysis (PCA) is a dimensionality-reduction method [11]. It decomposes a large dataset of correlated variables into a new set of variables (principal components or PCs), which explain as much of the total variation in the original dataset as possible [15]. In this study, the original dataset contained a 24 × 12 matrix, where the rows denote the samples, and the columns represent the testing parameters. PCA was performed by decomposing this multivariate dataset into two principal components, PC1 and PC2, to visualize the overall water quality change among the samples and the correlation between different parameters contributing to this variation.

3 Result and Discussion

3.1 Socioeconomic Conditions of the Selected Households

The questionnaire survey introduced several constructive insights on the overall study, including socioeconomic status, apartment and resident details, user perception and practices, cleaning frequency, satisfaction, and issues of the individual household. Figure 2 illustrates the key findings of the survey. The figure shows a notable monthly household income difference between the households of two zones, where zone 2 households lie in the 25,000–100,000 BDT range, and zone 3 households are in 50,000 higher than 100,000 range. All of the households from zone 2 experience waterlogging issues in recent years and none from zone 3. Two (Z2-H1 and Z2-H4) out of four perceive foul smell in the water, while the rest of the households observe no smell. One household from zone 2 (Z2-H1) and three households from zone 3 (Z3-H1, Z3-H3, Z3-H4) boil water before consumption, and all of the eight households use a water filter. Z2-H1, Z2-H2 households residents use ultrafiltration filter, Z2-H4 uses activated carbon filter, and the rest of the households use reverse
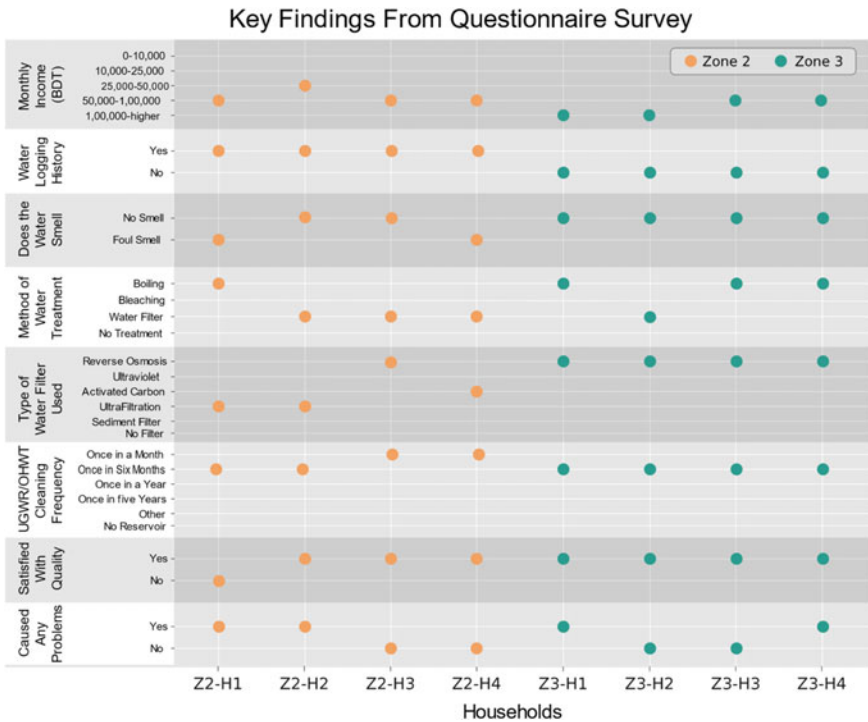
Fig. 2 Key findings from household questionnaire survey of zone 2 and zone 3; circular markings denoting the response of individual household

osmosis filter for water purification. The cleaning frequency of the households is mainly divided into two main categories: once a month and once in six months. Z2-H3 and Z2-H4 households clean their UGWR and OHWT once a month, and the rest of the households' cleaning frequency is once in six months. Except for one household from zone 2 (Z2-H1), the rest of the seven households' occupants are satisfied with the supplied water quality. Householders of Z2-H1, Z2-H2, Z3-H1, and Z3-H4 encountered problems, e.g., hair fall, allergic issues, rash, or other skin problems using the household tap water for showering purposes; in contrast, the other households did not experience such issues. Other survey questions show that all of the household owners are well educated with the minimum highest educational background of bachelor's degree.

Furthermore, the studied households are multistoried buildings with minimum and maximum occupants of 18 and 150, respectively. As the source of drinking water, every household uses a piped water supply. The connection of all households was under WASA supervision, and the average age of connection for the eight households is approximately 20 years. Lastly, no household occupants observed color, clarity, or taste issues.

3.2 Water Quality at Different Points in Household Water Distribution System

Figure 3a–h shows the variation of different water quality parameters among the different points of the eight households (zones 2 and 3) and the three groundwater sources (from zone 3 only). The standard levels of these parameters in drinking water are represented by the dashed horizontal lines in the plots.

In the case of color (Fig. 3a), household and source water samples from zone 3 got a significantly higher amount of color than the WHO (1993) standard for drinking water (15 Pt–Co). In contrast, the color was absent or found only in a minimal amount (<15 Pt–Co) in the zone 2 samples. Iron concentration from Fig. 3e does not precisely explain this difference though it is considered to be one of the primary reasons for water coloration [16]. Other reasons could be higher Mn concentration [17] and/or higher organic decomposition in the water supplied to zone 3. From Fig. 3b, for most of the households from both zones (five out of eight), turbidity was greater in the tap water samples than in the UGWT samples. Overall, samples from zone 2 were found to contain a higher amount of turbidity than zone 3 samples, which might be attributable to the occurrence of waterlogging in the previous years in zone 2 that contrasts with the zone 3 responses of waterlogging history (Fig. 2). If turbidity is caused by sewage matter, it will pose a serious threat to the consumer's health. Moreover, turbidity-causing particles could shield pathogenic organisms, and thus, the action of the disinfectant is hampered [18].

The residual chlorine (Fig. 3c) was less than the standard level of 0.2 mg/L for all the samples. It could be due to insufficient chlorination or a higher amount of

ammonia and/or microbial community present in water. For effective disinfection, residual chlorine should be present in the treated water at least at a concentration of 0.1–0.3 mg/L after 30 min of contact [18]. Figure 3d shows that the NH_3 concentration increased from UGWR to tap mostly in zone 3 households (three out of four). If drinking water having an ammonia concentration of more than 0.2 mg/L is chlorinated, taste and odor problems may occur [17]. However, all the tap water samples had NH_3 concentrations below the standard limit of 0.5 mg/L [14]. A higher amount of ammonia indicates insufficient chlorination and/or algal growth within the pipes.

Iron concentration (Fig. 3e) was higher than the WHO standard limit [14] in the samples from two out of four households from zone 3 and one out of four households from zone 2. Iron contamination might occur due to the use of cast iron, steel, or galvanized pipes in the water supply system. If this ferric iron concentration rises
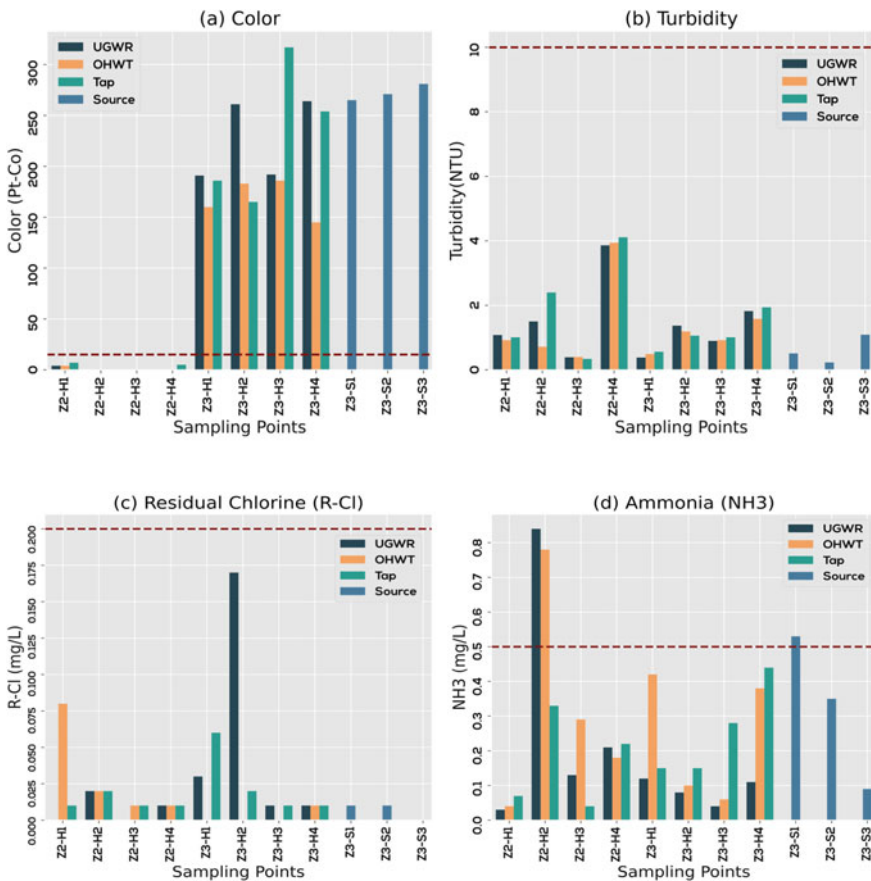
Fig. 3 Variation of **a** Color. **b** Turbidity. **c** Residual chlorine. **d** Ammonia. **e** Iron. **f** Lead. **g** Total coliform. **h** Fecal coliform in different points of household (UGWR, OHWT, Tap) and sources of zone 3; WHO water quality standard (dashed red line)
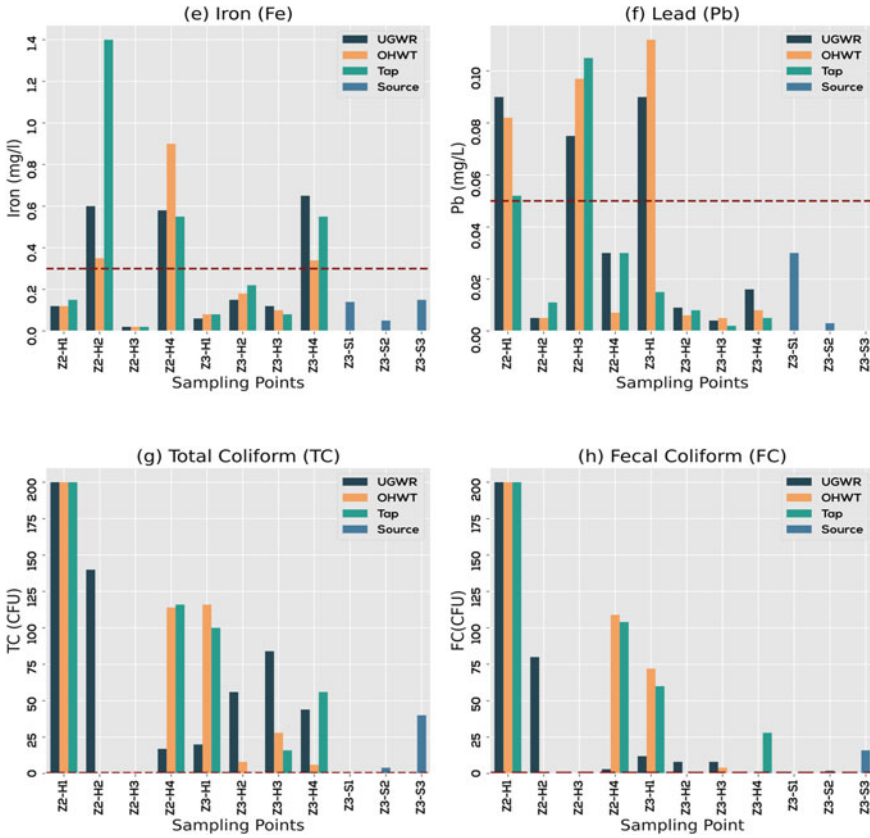
Fig. 3 (continued)

above 0.3 mg/L of water, it will stain laundry and sanitary ware [17]. Lead has been recognized to damage the functions of the brain and kidney [19]. In Dhaka city, lead has been found in an excessive concentration in the Dhanmondi lake water, possibly due to industrial effluent discharge containing lead compounds and atmospheric lead pollution existing in central Dhaka [20]. Lead concentration (Fig. 3f) in the tap water exceeded in two out of four households in zone 2 and was found to be within the USEPA standard (0.05 mg/L) in household water samples from zone 3. Overall, the lead concentration in zone 2 samples is higher than that of the zone 3 samples. Samples from three out of four zone 2 households showed an increase in the Pb concentration from OHWT to tap water, which may be attributable to lead contamination from age-old lead pipelines. Samples from the rest of the households showed a decrease in lead concentration from UGWR to tap water. It might be due to the reaction between lead and chlorine in the supplied water that forms an oxide which gets deposited on the inner wall of the pipes reducing the lead concentration in water.

The presence of coliform bacteria in treated water suggests inadequate treatment or post-treatment contamination in the distribution system [17]. Samples from three out of four households from zone 3 showed decreased TC count from UGWR to OHWT (Fig. 3g). For the rest of the households from both zones, either TC was absent or increased from UGWR to OHWT, indicating bacterial contamination within the household water supply system. From Fig. 3h, samples from two out of four households, from both zones, did not show any presence of FC in the tap water samples, and among these four households, three had FC contamination either in the UGWR or both in UGWR and OHWT. This indicates the effectiveness of the cleaning process of the OHWT of these households. The rest of the households were found to have more FC counts in the tap water than in the UGWR. This indicates fecal contamination of the water after it had been supplied to those households due to insufficient chlorination, as indicated by Fig. 3c.

3.3 Principal Component Analysis of Water Quality Data

Figure 4 shows the principal component analysis (PCA) biplot for the household and source water quality data. The analysis resulted in five principal components (PCs) with eigenvalues greater than 1, explaining 84.6% of the total variability. Among them, the first two principal components have been used to visualize the result.
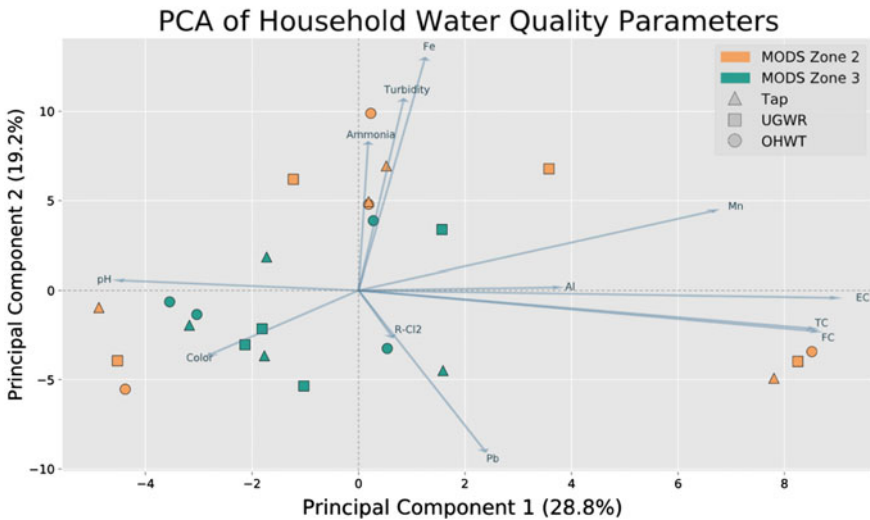
Fig. 4 Principal component analysis (PCA) biplot of zone 2 and zone 3 household water quality parameters of tap (triangle), UGWR (square), OHWT (circle), where PC1 and PC2 explain 28.8% and 19.2% of the total variation; corresponding eigenvectors of testing parameters (translucent blue arrow line)

PC1 explains 28.8% variability, and its major contributors are fecal coliform (TC), total coliform (FC), electric conductivity (EC), and manganese (Mn). On the other hand, iron (Fe), turbidity, and lead (Pb) are the main contributors in PC2 (19.2% variance). The plot illustrates the contribution of these components to each of the sampling sources. For example, zone 2 samples have a relatively higher contribution from both PC1 and PC2 than zone 3 samples. This makes the zone 2 samples more scattered in the space than the zone 3 samples. This indicates that the variability of quality in samples from zone 2 is higher than the variability of the samples from in zone 3, and also zone 3 water quality is more consistent across the different households. The loadings of the parameters are also shown in the plot using lines passing through the origin, which is defined as eigenvectors. The correlation between different parameters can be visualized from these lines. The closer the angle between two lines, the corresponding parameters are more likely to be positively correlated [21], e.g., TC and FC. If the lines are at a right angle, there is no correlation between them, and the more they diverge further from 90°, the more they are likely to be negatively correlated, e.g., pH and residual chlorine.

3.4   Implications

Generally, Dhaka WASA is held responsible for any deterioration in the quality of supplied water. The quality of source water most often satisfies the drinking water requirements set by the Environment Conservation Rules (ECR) [22]. However, water quality may get deteriorated even when the water flows through the distribution network in the city as well as within a household. From Fig. 3, it can be observed that in several cases, the water quality problem increased after it had been supplied to the UGWT. It indicates that consumers' practices also need to be improved to ensure better drinking water quality. From the PCA score-plot (Fig. 4), the zone 2 household samples are observed to be more scattered than zone 3 samples, which may be influenced by the variation of the economic status between these two zones as suggested by the survey report (Fig. 2). The impact of monthly income on the household water quality variation at different points has the scope for further investigation.

   As the samples were collected during February–March, the laboratory test results represent the quality of water at that time only. If it were possible to examine the water quality throughout the various seasons of the year, it would be more indicative of the overall scenario of the water quality throughout the year. Besides, samples were not collected from the distribution system, which could be helpful to identify issues within the distribution system. As for the effects of socioeconomic status on the water quality variation, more households will be needed to compare the income effect. Since only eight households of nearly similar income ranges were evaluated in this study, the aforementioned effects could not be assessed.

4 Conclusion

This study was mainly focused on the variation of water quality from groundwater sources to different points of households. The investigation shows that the individual hygiene practice and the storage cleaning frequency play a major role in the user end quality of supplied water, and contamination in water can occur in both distribution line and household reservoirs. Besides, the high amount of color in the zone 3 samples needs to be addressed with much concern as color-causing substances may react with the chlorine (added for disinfection) and form trihalomethanes (THMs) as byproducts which could be a potential threat to public health [18].

References

1. UNCED (1992) Protection of the quality and supply of freshwater resources: application of integrated approaches to the development, management and use of water resources, Chapter 18, Agenda 21. Rio de Janeiro, 1992. Available: https://sedac.ciesin.columbia.edu/entri/texts/a21/a21-18-freshwater.html
2. BBS and B. UNICEF (2013) Bangladesh MICS 2012–2013 water quality thematic report-final. Bangladesh Bureau of Statistics, Bangladesh. Available: https://washdata.org/file/633/download
3. WHO and UNICEF (2006) Meeting the MDG drinking water and sanitation target: the urban and rural challenge of the decade. World Health Organization (2006). Available: https://www.who.int/water_sanitation_health/monitoring/jmpfinal.pdf
4. Wright J, Gundry S, Conroy R (2004) Household drinking water in developing countries: a systematic review of microbiological contamination between source and point-of-use. Trop Med Int Health 9(1):106–117. https://doi.org/10.1046/j.1365-3156.2003.01160.x
5. U.S. Centers for Disease Control and Prevention (CDC) (2007) Household Water Use and Health Survey for the Water Safety Plan Linden, Guyana Dec. 2007. Available: https://www.cdc.gov/nceh/ehs/gwash/publications/household_water_use_health_survey_for_water_safety_plan_guyana_2007.pdf
6. Shahnur Rahman Md., Sahidul Islam Md. (2019) Dhaka WASA: governance challenges and way forward. https://doi.org/10.13140/RG.2.2.11501.95202
7. DWASA (2019) Annual report 2018 -2019: Dhaka water supply and sewerage authority. Available: http://dwasa.portal.gov.bd/sites/default/files/files/dwasa.portal.gov.bd/annual_reports/743e1a3c_035c_4f66_a5a7_6827f39f4c68/2020-11-08-13-12-fe46dfae2ee91e0cb90b9ec2fa149f5b.pdf
8. Harmful bacteria in Wasa water. (2019, July 8). *The Daily Star*. Available: https://www.thedailystar.net/frontpage/news/dhaka-wasa-water-contaminated-4-out-10-zones-1768156
9. Mahbub KR, Nahar A, Ahmed MM, Chakraborty A (2011) Quality analysis of Dhaka WASA drinking water: detection and biochemical characterization of the isolates. J Env Sci 9. https://doi.org/10.3329/jesnr.v4i2.10133

10. Ahmed T, Acharjee M, Rahman S, Jamal J, Munshi SK, Noor R (2013) Microbiological study of drinking water: qualitative and quantitative approach. Asian Jr Microbiol Biotech Env Sc 15(4):23–30

11. Ondieki JK, Akunga DN, Warutere PN, Kenyanya O (2021) Bacteriological and physico-chemical quality of household drinking water in Kisii Town, Kisii County, Kenya. Heliyon 7(5): e06937 https://doi.org/10.1016/j.heliyon.2021.e06937

12. Cassivi A, Tilley E, Waygood EOD, Dorea C (2021) Household practices in accessing drinking water and post collection contamination: a seasonal cohort study in Malawi. Water Res 189:116607. https://doi.org/10.1016/j.watres.2020.116607

13. Rabi AZ, Abo-shehada MN (1995) Sanitary survey of private drinking water reservoirs in Northern Jordan. Int J Environ Health Res 5(3):255–261. https://doi.org/10.1080/096031295 09356855

14. WHO (2011) Guidelines for drinking-water quality, 4th ed. World Health Organization, Geneva. Available: https://www.who.int/publications/i/item/9789241549950

15. Jolliffe IT (2005) Principal component analysis, 2nd edn. Springer. https://doi.org/10.1002/ 0470013192.bsa501

16. Sarin P et al (2004) Iron release from corroded iron pipes in drinking water distribution systems: effect of dissolved oxygen. Water Res 38(5):1259–1269. https://doi.org/10.1016/j.watres.2003. 11.022

17. WHO (ed) (1993) Health criteria and other supporting information, 2nd ed, vol 2, 4 vols. World Health Organization, Geneva. Available: https://www.who.int/water_sanitation_health/ dwq/2edaddvol2a.pdf

18. EPA (2001) Parameters of water quality: interpretation and standards.pdf. Environmental Protection Agency, Ireland

19. Sawyer CN, McCarty PL, Parkin GF (1994) Chemistry for environmental engineering. McGraw-Hill Inc., New York.

20. Ali A, Ahsanuzzaman ANM, Badruzzaman ABM, Rahman M (1998) Lead pollution of Dhanmondi Lake in Dhaka. Pol J Env Stud 47(5):289–296. https://doi.org/10.2166/aqua.199 8.35

21. Ngo L (2018) How to read PCA biplots and scree plots. BioTuring's Blog. https://blog.biotur ing.com/2018/06/18/how-to-read-pca-biplots-and-scree-plots/

22. The Environment Conservation Rules. Bangladesh: Bangladesh Gazette, 1997. Available: https://www.elaw.org/system/files/Bangladesh+--+Environmental+Conservation+Rules,+ 1997.pdf

Low-Cost Iron Removal Technology from Groundwater Using Locally Available Materials

M. Biswas and **M. S. Islam**

1 Introduction

Water is a tasteless, odorless, translucent, and almost colorless chemical substance that is the main component of the Earth's lakes, streams, oceans, and most living organism's fluids. 71% of the surface of the earth is covered with water. It is a crucial component for almost all life forms. 96.5% of this water is present in oceans and seas, 1.7% in glaciers, 1.7% in groundwater and Greenland and Antarctica ice caps, a small amount of which is also present in other water bodies, 0.01% in the air, such as clouds, vapor, and precipitation. In Bangladesh, the groundwater source is used mainly for drinking water. But, in the southern part of Bangladesh, the presence of an excess of As, Fe, Mn, and salinity is found in groundwater source. Iron is a non-hazardous element that can be a nuisance in the water supply. Excess quantities of iron can also discolor water and can cause stains on clothes, appliances, hair, and fixtures. If iron deposits build up in pressure tanks, water heaters, filters, and pipes, this can lead to reduced water pressure, decreased performance, and costly repairs. It can also cause water to have a taste of the metallic form and the odor issue can occur. The allowable limit for iron in water according to WHO is 0.3 mg/L [1], and Bangladesh standard is 0.3–1.0 mg/L [2].

Generally, in the systems of public water supply, the most common method that is used for iron removal from groundwater is separation and aeration. But at the domestic level, usually, this kind of method is not used. Various methods for iron removal had been studied earlier such as the method of ion exchange [3], oxidation method with oxidizing agents like potassium permanganate and chlorine [4], different

M. Biswas (✉)
Department of Civil Engineering, North Western University, Khulna 9100, Bangladesh

M. S. Islam
Department of Civil Engineering, Khulna University of Engineering & Technology, Khulna 9203, Bangladesh

filtering materials like activated carbon [5], bio-remediation [6], extraction of super-critical fluid [7], limestone treatment method [8], ash [9], granular aerated filter [10], and adsorption [11]. The method of iron removal from groundwater mainly involves three basic processes that are oxidation, settling, and filtration. But most of these iron removal methods suffer from some drawbacks like high capital, operational and maintenance cost, and poor people from rural and urban areas can hardly afford this type of costly method of iron removal. This has led to a search for cheaper and efficient substituents. The consumption of locally available resources as a natural biofilm provision media for the removal of iron is of increasing attention due to its low cost and low technology. Granular activated carbon (GAC) prepared using various local materials such as charcoal, rice husk, neem leaves, banana rind, stem or peels, and sugarcane baggage as the base material has been identified, investigated, and found capable of achieving a substantial iron removal from groundwater sources. Ash or charcoal makes water alkaline which facilitates the removal of iron in the water. It precipitates iron as ferrihydrite or goethite [12, 13].

Studies have been carried out about iron removal from water using the ash produced from banana residue. Ashes were produced by controlled combustion from various materials such as dry rice husk, pseudo-stem, banana leaf, bamboo, and rind. Due to subsequent potassium hydroxide formation, potassium is present in bananas. For this, the removal mechanism includes iron oxidation at alkaline media or high pH. An analysis of the effectiveness of chemical composition of the produced ash from banana in removing iron from the prefabricated water was also included in the study. It was later used in a low-cost water filtration model of the household type, in which the water was filtered using a cloth of cotton and then used the water for drinking after treatment with ash [14].

In 2012, Chaturvedi also studied iron removal methods from water for drinking. He studied different methods, such as electrocoagulation, media of BIRM, filtration by oxidation, lime softening, ion exchange, process of activated carbon adsorption, anthracite, mixture of sand, pebble, and green sand, and ultrafiltration. [15]. Carbonaceous shale and coal are also effective when used as filter media in the adsorptive filtration process of iron removal from groundwater by direct filtration [16]. When traditional methods of water purification are used, it cannot sufficiently remove the micro-contaminants present in water. So, the use of activated carbon is one of the most effective methods for removing these contaminants [17, 18]. Here, in this research, the filtration procedure was used to remove iron from groundwater, and the filter media were prepared using activated carbon from different local materials.

2 Methodology

In this experiment, mainly adsorption phenomena had been used for the removal of iron. Adsorption is a water treatment process that is widely used for removing organic substances. To remove iron from groundwater, this adsorptive filtration is

operated under anoxic conditions. In this experiment, aerobic conditions had been used in some locally collected adsorptive media for iron removal.

2.1 Materials Used

The total investigation had been done with five different filter media. Different adsorption media were used in the filter for iron removals such as activated carbon produced from sugarcane baggage, neem leaves, rice husk, banana peels, and banana pseudo-stem. These materials were collected locally at a very low cost. After that, activated carbon was prepared from these materials and used for iron removal by oxidation followed by precipitation. In every case, activated carbon made from one of the above five materials, coarse sand, and fine sand was used as the filter media for preparing the filter model.

2.1.1 Coarse Sand

Sylhet sand has been used here as coarse sand for increasing the rate of filtration. The fineness modulus of the coarse sand was determined as 2.23. Firstly, the specific coarse sand was cleaned in distilled water, and then, it was oven dried for 4 h. The sand was used in the filtration model, after being cooled to room temperature.

2.1.2 Fine Sand

Fine sands are deposits of glaciers that are found naturally, have high silica content and low soluble compounds of magnesium, calcium, and iron, and are very effective for removing sedimentation. But here, the media were used to remove the iron from raw water. Larger suspended particles settle in the top coarse sand layer, and smaller particles are consumed by sticking microscopic organisms in the layers of slime that form around the particles of fine sand. Kustia sand has been used here as fine sand, and fineness modulus of the sand was determined as 1.9.

2.1.3 Activated Carbon

Five types of activated carbons were used in the filters prepared from five local materials like sugarcane baggage, neem leaves, rice husk, banana peel, and banana pseudo-stem.

2.2 Preparation of Activated Carbon

Activated carbon from sugarcane baggage, neem leaves, rice husk, banana peels, and banana pseudo-stems had been used here as filter media for the removal of iron. Firstly, these materials were collected and sun-dried until they were fully moisture-free. Then, they were burnt in the gas oven in a closed clayey pot at a temperature of about 400–450 °C in the absence of oxygen for about 30–45 min. After that, they were crushed or grounded up and were used as filter media in the filter model for the removal of iron from water.

2.3 Development of Laboratory Standard Filter Model

A simple laboratory standard cylindrical-shaped filtration tube had been developed. The upper portion of the cylindrical tube was kept open for pouring the sample raw water. The base of the cylindrical tube was covered with a clean piece of cloth. A holding stand was kept for holding the cylindrical tube. From the base, a rubber tube of smaller diameter was extended to collect the treated water in a beaker. The schematic diagram of the filter model developed in the laboratory has been shown in Fig. 1. Following specifications of cylindrical tube were used in the laboratory filter model: (Table 1).
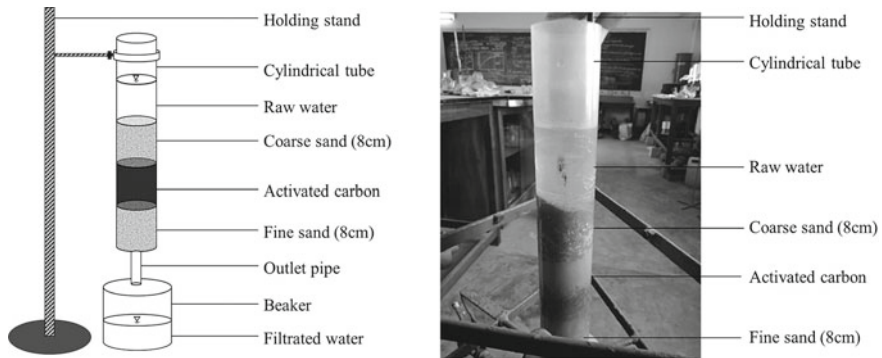
Fig. 1 Schematic and experimental representations of filter model

Tabel 1 Specifications of cylindrical tube

Cylindrical tube	Dimension (cm)
Length	35
Inner diameter	5
Outer diameter	5.5

Tabel 2 Different filter models prepared in the laboratory

Filter model	Upper layer (8 cm thickness)	The middle layer (Activated carbon) (6 cm, 8 cm, & 10 cm thickness, respectively)	Bottom layer (8 cm thickness)
Filter model 1	Coarse sand	Banana peels	Fine sand
Filter model 2		Rice husk	
Filter model 3		Neem leaves	
Filter model 4		Sugarcane baggage	
Filter model 5		Banana pseudo-stem	

2.4   Setup of Filter Media

Several filter models were prepared in the laboratory using five different activated carbon. For each activated carbon, three different filter models were prepared to increase the thickness of the activated carbon layer only keeping the thickness of other layers the same. In every filter model, three layers of filter media were used as shown in Table 2.

2.5   Filtration Procedure

The total procedure of this research had been done in some stages. Firstly, water contaminated with iron was collected from tube-well. Then, a laboratory-scale physical model of the filter was developed using coarse sand, fine sand, and activated carbon prepared from various local materials such as sugarcane baggage, neem leaves, rice husk, banana peels, and banana pseudo-stem. Initially, the selected parameters (pH, color, turbidity, iron, chloride, and hardness) of the collected raw water were measured in the laboratory. This raw iron water was filtrated (1000 ml of raw iron water for each filter model) through the prepared filter media and collected in a beaker. The filtration rate was measured at 240 ml/min. After that, the selected parameters of the treated water were measured.

3   Results and Discussions

The results were obtained from different tests of collected raw water and filtrated water from the laboratory analysis to evaluate characteristics and to obtain the performance of different filter media. The obtained results of the parameters are the average of three filter models for the same activated carbon of similar depths.

Fig. 2 Variation of iron
(before and after filtration)
with different filter media at
varying depth
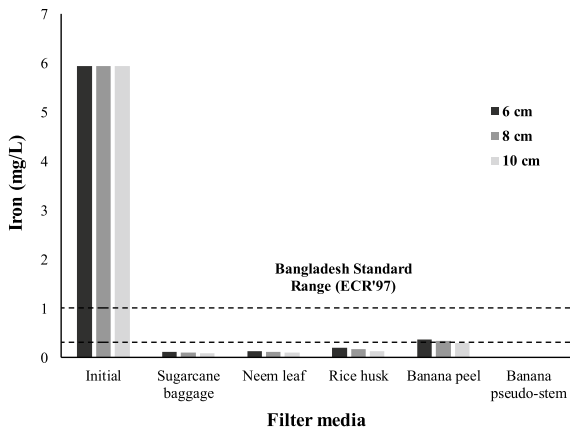
3.1 Iron Removal by Using Activated Carbon of Sugarcane Baggage as Filter Media

Collected raw water was filtrated through the developed filter media of coarse sand (8 cm), activated carbon from sugarcane baggage, and fine sand (8 cm). Increasing the thickness of the activated carbon layer (6, 8, and 10 cm, respectively), three different filter models were prepared, and the tests were performed. The raw water used for this research contains 5.94 mg/L of iron. Along with this, other parameters were also tested and found that it contains a pH value of 7.22, color of 318.27 Pt/Co unit, turbidity of 143.56 NTU, chloride of 1638.20 mg/L, and hardness of 834.92 mg/L. From Fig. 2, it can be seen that after filtration, iron concentration had been reduced to 0.11 mg/L, 0.09 mg/L, and 0.08 mg/L for the three filters (6, 8, and 10 cm depth of activated carbon, respectively), which indicate about 98.4% removal of iron and also within the allowable limit. Other parameters such as color, turbidity, chloride, and hardness of water had been reduced by 85.2%, 94.37%, 54.11%, and 64.13%, respectively. Although the increased pH value after filtration is within the allowable limit, the presence of a small fraction of alkali in the activated carbon attributed to the higher value of pH. Usually, pH value does not have any direct impact on the consumers, and any guideline value was not proposed for pH based on health.

3.2 Iron Removal by Using Activated Carbon of Neem Leaves as Filter Media

The same raw water was filtrated through a filter model prepared from coarse sand (8 cm), activated carbon from neem leaves, and fine sand (8 cm). From the graph of iron versus filter media in Fig. 2, it can be seen that the iron concentration has been reduced to 0.12 mg/L, 0.11 mg/L, and 0.09 mg/L, respectively, for three filters

from an initial value of 5.94 mg/L which indicates about 98.2% removal efficiency. Again the pH value had been increased but within the allowable limit of 6.5 to 8.5. Also, color, turbidity, chloride, and hardness of water had been reduced by 44.85%, 97.1%, 55.6%, and 57.46%, respectively.

3.3 Iron Removal by Using Activated Carbon of Rice Husk as Filter Media

Rice husk had been proved as an effective, natural, and cheap filter media for removal of odor, color, taste, and so on. Activated carbon prepared from rice husk is a source of amorphous reactive silica, and it can be used as a suitable filter media. Also in this research, rice husk activated carbon removed 97.2% of iron. It had been proved to be best for the removal of other related water quality parameters (color 98.42%, turbidity 98%, chloride 74.2%, and hardness 39.32%) except the increasing value of pH within the acceptable limit.

3.4 Iron Removal by Using Activated Carbon of Banana Peel as Filter Media

Iron removal by ash produced from banana had been reported previously, and the initial concentrations were 5.2 mg/L and 2.2 mg/L [9]. Here, the raw water had an iron concentration of 5.94 mg/L. Banana peel activated carbon filter media removed 94.5% of iron from the raw water. But other parameters such as color, turbidity, chloride, and hardness of water had been reduced by 50.17%, 20.69%, 54.64%, and 28.39%, respectively, which is a comparatively lower percentage of removal than other activated carbon filter media.

3.5 Iron Removal by Using Activated Carbon of Banana Pseudo-Stem as Filter Media

Iron removal using banana pseudo-stem ash had been studied earlier and proved to be best [9]. Also in this research, an activated carbon filter model using banana pseudo-stem removed 100% of iron from an initial concentration of 5.94–0 mg/L. Other parameter's removal efficiency was also good (color 91.16%, turbidity 97.81%, chloride 57.5%, and hardness 33.62%).

Fig. 3 Variation of color
(before and after filtration)
with different filter media at
varying depth
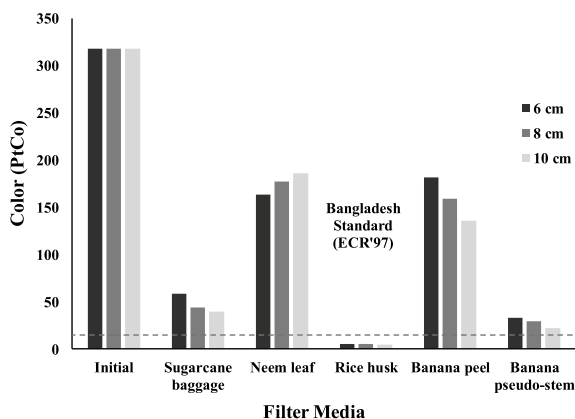
3.6 Evaluation of Better Performance Among the Activated Carbon Materials

From Fig. 2, it can be seen that banana pseudo-stem, sugarcane baggage, and neem leaves are the most potent materials for iron ion concentration removal compared to the other two materials. Among these materials, the banana pseudo-stem is the best material for iron removal from groundwater (100% removal efficiency). These materials are also locally available. Better removal of iron was observed with the increase in depth of activated carbon.

The pH values were found to be increasing with an increasing amount of activated carbon in the order like rice husk < banana pseudo-stem < banana peel < sugarcane baggage < neem leaves (Fig. 7). The pH values were above 8 for neem leaf and banana peel when the thickness of activated carbon was used 10 cm for the developed filter model. But all the values of pH were within the acceptable limit (6.5–8.5) according to WHO guidelines [1].

Other selected parameters of water before filtration and after filtration were executed, and the values of the parameters after filtration have been shown in Fig. 3 (color), Fig. 4 (turbidity), Fig. 5 (chloride), and Fig. 6 (hardness) for three different depths of the same activated carbon filter. From the graphs, it can be seen that the rice husk activated carbon filter has been proved best among the materials for color, turbidity, and chloride removal. For hardness removal, sugarcane baggage activated carbon showed better performance than others (Fig. 6).

3.7 Cost Analysis

The expenditure of all the adsorbent media used for the experiment excluding the cost of labor, cost of filter tube, maintenance cost, and cost of energy had been calculated.

Fig. 4 Variation of turbidity (before and after filtration) with different filter media at varying depth
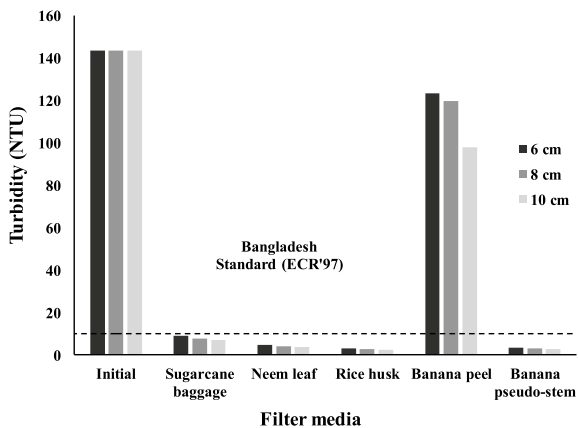
Fig. 5 Variation of chloride (before and after filtration) with different filter media at varying depth
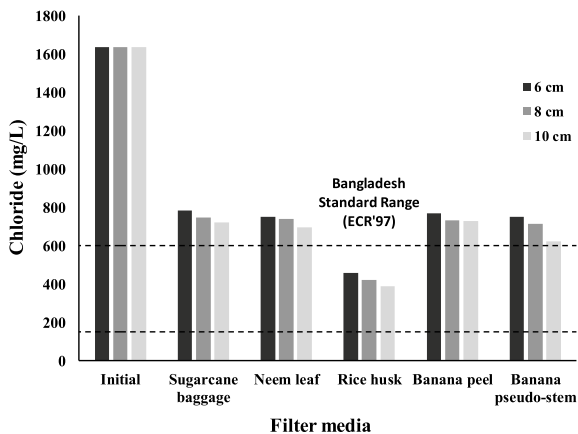
Fig. 6 Variation of hardness (before and after filtration) with different filter media at varying depth
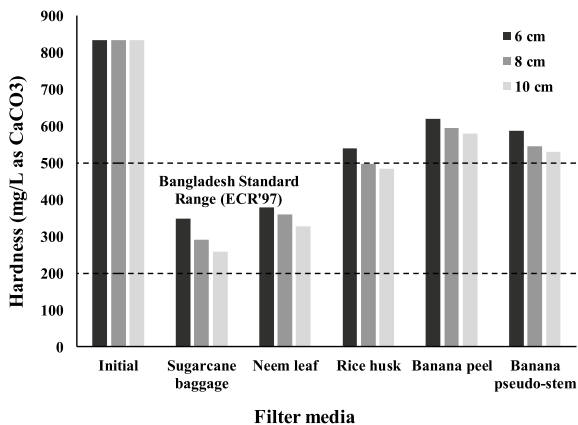
Fig. 7 Variation of pH
(before and after filtration)
with different filter media at
varying depth
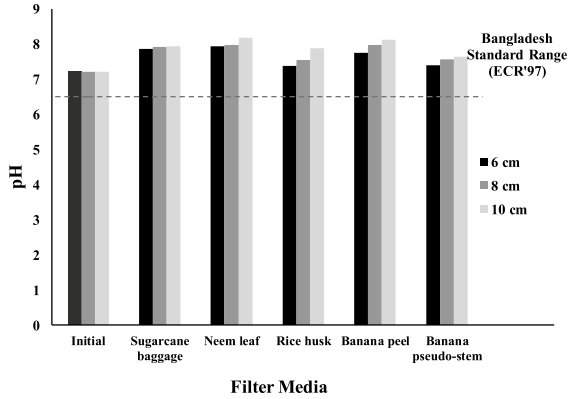
Coarse sand was collected 40 takas/ft^3, fine sand 30 takas/ft^3, and the local materials such as banana peel, banana pseudo-stem, and neem leaves were collected locally from the tree that is free of cost, rice husk 25 takas/kg, and sugarcane baggage 10 takas/kg. Activated carbon used in the filter model was 0.00041 kg/cm^3 of the filter volume. So, the total cost of the materials for one filter model was about 1 taka to 2.5 takas per cm^3 of the filter volume.

4 Conclusions

The traditional filtration method using activated carbon from locally available materials for iron removal can remove iron along with other related parameters to the desired level without increasing the values of pH beyond the allowable limit. Among these plant activated carbons used, banana pseudo-stem activated carbon has been proved to be best for iron removal (from 5.94 mg/L of iron before filtration to 0.00 mg/L of iron after filtration) from groundwater. But, if all other parameters are also taken into consideration, then better performance can be seen in the case of rice husk activated carbon filter (iron 97.2%, color 98.42%, turbidity 98%, chloride 74.2%, and hardness 39.32%). The designed activated carbon filter can be further modified for household use. For groundwater with higher iron concentrations, the amount of activated carbon can be increased. The use of this traditional filter has also some advantages like efficiency in removal, no electricity requirement, easily available materials, low cost for manufacturing, almost nil maintenance cost, and simplicity in application and use.

References

1. World Health Organization (2011) Guidelines for drinking-water quality, 4th edn
2. Rules EC (1997) Bangladesh Gazette (SRO No. 197-Law/97). Ministry of Environment and Forest, Government of Bangladesh
3. Vaaramaa K, Lehto J (2003) Removal of metals and anions from drinking water by ion exchange. Desalination 155:157–170. https://doi.org/10.1016/S0011-9164(03)00293-5
4. Ellis D, Bouchard C, Lantagne G (2000) Removal of iron and manganese from groundwater by oxidation and microfiltration. Desalination 130:255–264. https://doi.org/10.1016/S0011-9164(00)00090-4
5. Munter R, Ojaste H, Sutt J (2005) Complexed iron removal from groundwater. J Environ Eng 131:1014–1020. https://doi.org/10.1061/(ASCE)0733-9372(2005)131:7(1014)
6. Berbenni P, Pollice A, Canziani R, Stabile L, Nobili F (2000) Removal of iron and manganese from hydrocarbon-contaminated groundwaters. Bioresour Technol 74:109–114. https://doi.org/10.1016/S0960-8524(00)00003-1
7. Andersen WC, Bruno TJ (2003) Application of a gas–liquid entraining rotor to supercritical fluid extraction. Anal Chim Acta 485:1–8. https://doi.org/10.1016/S0003-2670(03)00400-8
8. Aziz HA, Yusoff MS, Adlan MN, Adnan NH, Alias S (2004) Physico-chemical removal of iron from semi-aerobic landfill leachate by limestone filter. Waste Manag 24:353–358. https://doi.org/10.1016/j.wasman.2003.10.006
9. Das B, Hazarika P, Saikia G, Kalita H, Goswami D, Das H, Dube S, Dutta R (2007) Removal of iron from groundwater by ash: a systematic study of a traditional method. J Hazard Mater 141:834–841. https://doi.org/10.1016/j.jhazmat.2006.07.052
10. Cho B-Y (2005) Iron removal using an aerated granular filter. Process Biochem 40:3314–3320. https://doi.org/10.1016/j.procbio.2005.03.031
11. Tahir SS, Rauf N (2004) Removal of Fe(II) from the wastewater of a galvanized pipe manufacturing industry by adsorption onto bentonite clay. J Environ Manage 73:285–292. https://doi.org/10.1016/j.jenvman.2004.06.009
12. Houben GJ (2003) Iron oxide incrustations in wells. Part 1: genesis, mineralogy and geochemistry. Appl Geochem 18:927–939. https://doi.org/10.1016/S0883-2927(02)00242-1
13. Komnitsas K, Bartzas G, Paspaliaris I (2004) Efficiency of limestone and red mud barriers: laboratory column studies. Miner Eng 17:183–194. https://doi.org/10.1016/j.mineng.2003.11.006
14. Bordoloi S, Nath SK, Dutta RK (2011) Iron ion removal from groundwater using banana ash, carbonates and bicarbonates of Na and K, and their mixtures. Desalination 281:190–198. https://doi.org/10.1016/j.desal.2011.07.057
15. Chaturvedi S, Dave PN (2012) Removal of iron for safe drinking water. Desalination 303:1–11. https://doi.org/10.1016/j.desal.2012.07.003
16. Chaudhuri M, Sapari NB, Mohak SFB (2008) Removal of iron from groundwater by direct filtration through coal and carbonaceous shale
17. Okoniewska E, Lach J, Kacprzak M, Neczaj E (2007) The removal of manganese, iron and ammonium nitrogen on impregnated activated carbon. Desalination 206:251–258. https://doi.org/10.1016/j.desal.2006.04.055
18. Savova D, Petrov N, Yardim M, Ekinci E, Budinova T, Razvigorova M, Minkova V (2003) The influence of the texture and surface properties of carbon adsorbents obtained from biomass products on the adsorption of manganese ions from aqueous solution. Carbon N Y 41:1897–1903. https://doi.org/10.1016/S0008-6223(03)00179-9

Spatial Variability of Metal Elements in Soils of a Waste Disposal Site in Khulna: A Geostatistical Study

H. Nath and I. M. Rafizul

1 Introduction

Today, thousands of processes are constantly contaminating soils on a daily basis. Accumulation of heavy metals and metalloids due to pollution from rapidly developing industrial areas, mine littering, disposal of high metal wastes, excess of lead in gasoline and paints, application of compost to grounds, animal compost, sewage sludge, pesticides, wastewater irrigation, leftovers from coal combustion, petrochemicals spilling and atmospheric deposition, etc., can be some of the major examples [1]. Heavy metals comprise some ill-defined groups of inorganic chemical hazards in the contaminated sites. The most hazardous and toxic heavy metals found in these groups are lead (Pb), chromium (Cr), arsenic (As), zinc (Zn), cadmium (Cd), copper (Cu), mercury (Hg), nickel (Ni), etc. In the soil, the concentration of these metals holds for a very long time and puts on a substantial threat to human health and the ecological system. Soil samples are taken from various points of the site to determine the concentration of heavy metals in a contaminated site, and several geostatistical approaches can provide precise predictions at the unsampled locations.

Spatial prediction, usually referred to as spatial interpolation, is a widely used analytical technique for estimating an unknown spatial value using known values observed at a range of sample locations [2]. The techniques of interpolation are based on the principles of spatial autocorrelation, which assumes that the points closer to each other are more similar than the farther ones [3]. There are several space interpolation methods, each according to different estimation criteria that are considered to produce a good prediction. This research focuses on four of the most commonly used methods for spatial interpolation: inverse distance weighting (IDW), ordinary kriging (OK), universal kriging (UK), and empirical Bayesian kriging (EBK). Such methods approximate values at unsampled locations with certain allocated weights

H. Nath (✉) · I. M. Rafizul
Department of Civil Engineering, Khulna University of Engineering and Technology, Khulna, Bangladesh

for each measurement based on the measurements at surrounding locations. Till now, there have been many comparisons made by many researchers between the results found from these methods.

Shiode and Shiode [2] reported ordinary kriging to be providing more accurate results than the other methods of interpolation for street-level spatial interpolation. In a study of soil texture, variance structure and soil-chemical properties ordinary kriging showed more accurate results than the other counterparts [4]. Again, IDW interpolation showed the best result while mapping organic matter contents for several fields [5]. According to Luo et al. [6], for offshore estimations, where site investigation is expensive, ordinary kriging is not suitable as this method requires a large number of in the interested area. Bayesian kriging method in this case can tackle the scarcity of data in the site of interest by making use of prior information from similar sites. Besides, some researchers found the results to be mixed between the kriging methods [7, 8].

This research focuses mainly on the evaluation and comparison of the results coming up relatively from inverse distance weighting (IDW), ordinary kriging (OK), universal kriging (UK), and empirical Bayesian kriging (EBK) and to come up with some map quality of soil contamination indicators in Rajbandh Waste Disposal Site, Khulna.

2 Materials and Methodology Adopted

2.1 Study Area

Khulna, which lies in the so-called transition area of the southwest tidal flood plain of the Ganges–Brahmaputra Delta, is the third-largest city in Bangladesh after Dhaka and Chittagong. This district occupies an area of 4394.96 km^2. Khulna is situated to the east of Satkhira, west of Bagerhat, south of Jessore and Narail, and north of the Bay of Bengal. Khulna's bounding coordinates are 22°47′16″ to 22°52′0″ north latitude and 89°31′36″ to 89°34′35″ east longitude. In 2020, the metropolitan area of Khulna had a projected population of 1.7 million roughly. The only official dumping site in the Khulna region is the Rajbandh waste disposal site (Fig. 1). The disposal site is situated 10 km west of the city. A total of 420–520 tons of MSW/day waste that is generated daily in Khulna City is disposed of directly at this 25-acre waste disposal site. A total of 60 soil samples from the various points at a depth of 0–30 cm of the disposal site are collected, and the locations of the sampling points were recorded using GPS (Fig. 1). The concentrations of the 21 metal elements like Al, As, Ba, Ca, Cd, Cr, Co, Cu, Fe, Hg, K, Mn, Na, Ni, Pb, Sb, Sc, Sr, Ti, V, and Zn in soils of the contaminated site were measured in the laboratory for further study using normal laboratory procedure.
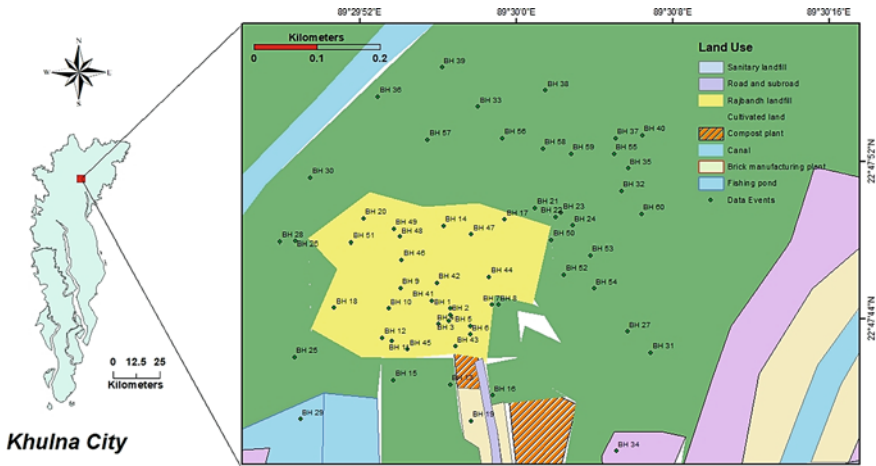
Fig. 1 Map of the study area with soil sampling locations

2.2 Laboratory Investigations

In the laboratory, the concentrations of metal elements in soil were measured through standard procedure. The acid digestion and atomic absorption spectrophotometer (AAS) analysis are described in the following articles.

2.2.1 Acid Digestion

To measure the concentration of metal elements in soil, laboratory work was done through the standard test method. In laboratory investigation, at first, 10 g of each soil sample was taken into a 100 ml conical flask. Already, the flask had been washed with deionized water prepared by adding 6 mL $HNO_3/HClO_4$ acid in ratio 2:1 and left overnight. Each sample was kept at 150 °C temperature for about 90 min. Later, the temperature was raised to 230 °C for 30 min. Subsequently, HCl solution was added in ratio 1:1 to the digested sample and re-digested again for another 30 min. The digested sample was washed into a 100 ml volumetric flask, and the mixture obtained was cooled down to room temperature.

2.2.2 Analysis of Metal Elements with AAS

After performing the digestion procedure, metal elements in this digested solution were determined using AAS in the laboratory, and the amount of each metal element was deduced from the calibration graph. The relevant concentrations of Al, Fe, Mn, Cr, Cu, Pb, Zn, Ni, Cd, As, Co, Sb, Sc, and Hg in mg/kg were measured.

2.3 Inverse Distance Weighting

Inverse distance weighting (IDW) is a sort of deterministic approach with a defined scattered set of points for multivariate interpolation. It is a localized and precise method that approximates an unknown spatial value at a target location using observed values at the neighboring sampling points in a straight line distance and applies a weight inversely proportional to the straight line distance from the corresponding sampling point [2]. The idea that points closer one to another have more similarities and correlations than ones farther away was used to establish all the interpolation approaches. Also in IDW, the rate of similarities and correlations between the neighboring sampling points is considerably assumed to be proportionate to the space between the points [9]. The accuracy of the IDW interpolations is greatly influenced by power parameters p. In this study, IDW on the heavy metals was performed for power 1–5 using the following Eq. (1).

$$Z_0 = \frac{\sum_{i=1}^{N} z_i d_i^{-n}}{\sum_{i=1}^{n} d_i^{-n}} \tag{1}$$

- Z_0 = estimated value of z variable in point I
- Z_i = sample value in point I
- d_i = distance between the sample point and estimated point
- N = a weigh coefficient based on distance
- n = prediction number per validation case.

2.4 Ordinary Kriging

Among all, ordinary kriging (OK) is the most commonly known and used kriging technique. This geostatistical technique uses data from the neighboring sampling points to predict the value of the desired sampling points that have defined variograms. Ordinary kriging is the most versatile kriging method since it acts on the assumption that the mean u is an unknown constant, and thus, random errors are unknown at data locations. Ordinary kriging is most suitable for data with a spatial trend and, besides that, this process can easily be adapted to limit (average) approximation from point estimation. The approximation of weighted average approximation provided by the ordinary kriging estimator at an unsampled location $Z(s_0)$ is represented by the following Eq. (2).

$$(s_0) = \sum_{i=1}^{n} \lambda_i z(s_i) \tag{2}$$

Here, λ is the weight of each sample observed.

2.5 Universal Kriging

Universal kriging (UK) is an ordinary kriging (OK)-type kriging technique. This technique working with either semivariograms or covariances is kriging with a local trend. This local trend is a previously defined deterministic function of coordinates which is an incessant and gradually varying trend surface on top of which the interpolated variation is imposed. With each output pixel, the local trend is recalculated. At an unsampled location u_0, the universal kriging estimator can be expressed by the following Eq. (3).

$$Z_k^*(u_0) = A + \sum_{s=1}^{n} \lambda_k(u_k).z(u_s) \tag{3}$$

Here, A is a constant shift parameter and the $\lambda_K(u_k)$'s are the kriging weights assigned to the n surrounding $z(u_s)$ sample data.

2.6 Empirical Bayesian Kriging

The empirical Bayesian kriging (EBK) technique is an incredibly simple, effective, and reliable solution, both for automated and collaborative data interpolation. It can be used to interpolate large data sets of up to hundreds of millions of data points [10]. EBK comprises of two models of geostatistics: a linear mixed model and an intrinsic random kriging model. Both models have been set in a single computational model represented by the following Eq. (4) [11].

$$z_i = y(s_i) + \epsilon_i, \quad i = \overline{1 \ldots K} \tag{4}$$

- $z_i =$ measured value at observed location
- $s_i =$ observed location
- $y(s) =$ studied Gaussian process
- $\epsilon_i =$ measurement error
- $K =$ number of measurements

In general, traditional kriging methods in the geostatistical analyst require manual adjustment of parameters, but empirical Bayesian technique automatically allows the adjustments through subsets and simulations [12]. Thus, the most challenging part of the construction of a valid kriging model is automated by this method. This approach differs from classical kriging techniques for the error made of the semivariogram model calculation. The data is first used for the semivariogram estimation. A new data set is considered using a semivariogram, and then, the proper values are obtained through continuous simulation at the input locations.

2.7 Assigning of Search Neighborhood

It is very important in a GIS analysis to assign the neighborhood criteria appropriately. When the measured points of data sets are situated at greater distances from the location of prediction, they are less autocorrelated to one another spatially. In this study, the measurement spheroid was divided into four sectors in which the minimum and maximum neighbor numbers were limited to 1 and 10, respectively, for all the methods. For inverse distance weighting, ordinary kriging, and universal kriging, the neighborhood type was "Standard." In the universal kriging method, "Gaussian" was used as the kernel function. For the empirical Bayesian kriging method, "Standard Circular" was selected as the neighborhood type.

2.8 Cross-Validation

The predictive accuracy of a linear regression equation is often evaluated by a cross-validation method. This is one of many common approaches for determining whether a statistical analysis is extended in an independent data set. In practice, it is primarily used when the goal is to determine the exactness in the action of a predictive model [13]. Initially, the points are split randomly into two data sets, one for the training phase and one for validation. Each element must validate in successive rounds with training and validation sets to minimize variability [14]. The precision of the interpolation methods was determined by estimating mean average prediction error (MAPE), root mean square prediction error (RMSPE), and standardized root mean square prediction error (SRMSPE). Yasrebi et al. [9] stated, in the case of MAPE, the lower its value, the lower the error of the method. According to them, a successful model should calculate MAPE values near zero to prove predictions are accurate or centered on the locations measured. The RMSPE and SRMSPE are also two methods to check the properness of a model. Jakubek and Forsythe [15] mentioned that low RMSPE and SRMSPE values indicate that predictions of a method are close to their original values. In this study, all the methods were assessed for MAPE values at first. Then, the best-fitted model was determined based on the accuracy of RMSPE values first and then SRMSPE.

3 Results and Discussions

3.1 Distribution of Metal Elements in Soils

Spatial distribution of metal concentrations is a helpful tool for visually classifying metal production sources as well as exposure hotspots with high metal content. The map created from different techniques of interpolation of metal elements provides

a clear idea of on-the-ground pollution measures of the soil by metal elements in the disposal site. In this study, predicted distribution maps were created for all metal elements (Al, As, Ba, Ca, Cd, Cr, Co, Cu, Fe, Hg, K, Mn, Na, Ni, Pb, Sb, Sc, Sr, Ti, V, and Zn) using four types of interpolation methods (IDW, OK, UK, and EBK). As all the metals were showing almost same type of distribution across the site, among these, the distribution maps for iron (Fe) and cadmium (Cd) are represented in Fig. 2. The findings showed that the pattern of distribution of the metals were both
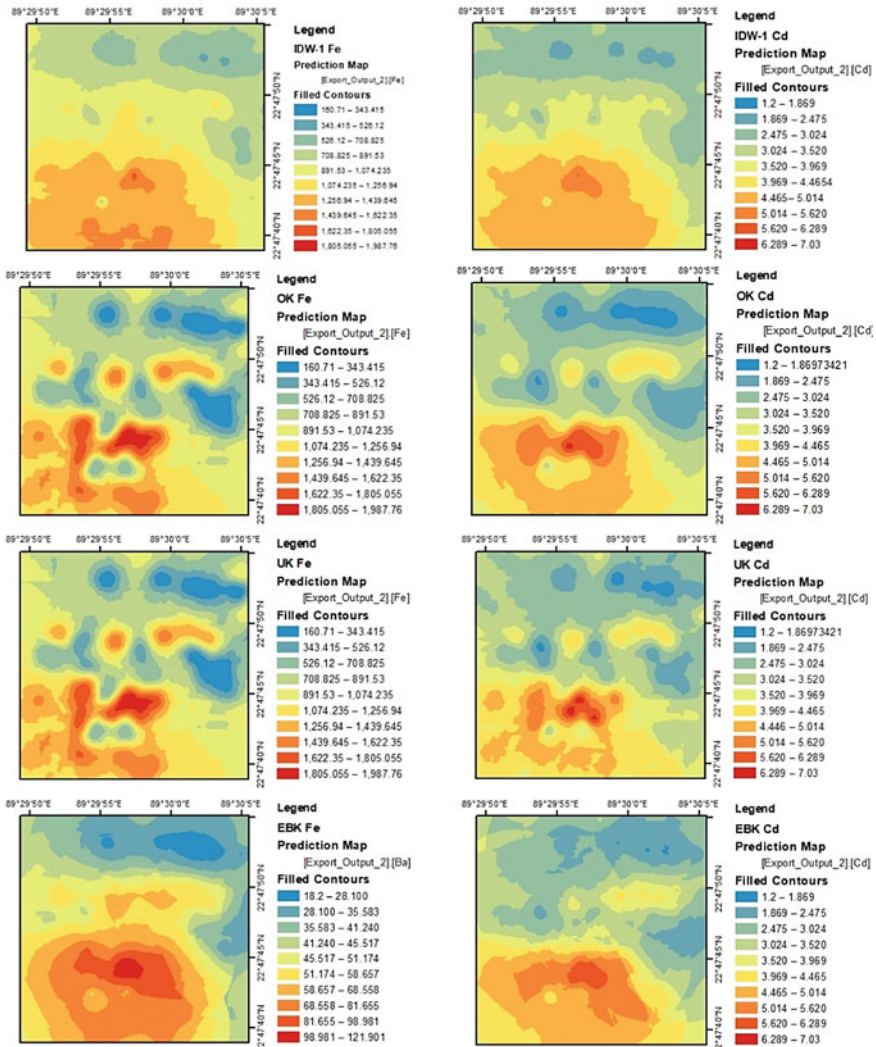
Fig. 2 Spatial distribution of Fe and Cd using inverse distance weighting, ordinary kriging, universal kriging, and empirical Bayesian kriging

zonal and concentrated. The maximum concentrations of all metals were between the disposal site's center and the southwest region where almost all the waste products were dumped initially. The concentration of the metals gradually decreased from the southeast to the northeast zone of the disposal site where the cultivated lands were situated away from the dumping point.

3.2 Interpolation and Cross-Validation of Results

IDW, OK, UK, and EBK techniques were used to interpolate the spatial variation of heavy metals and to find out the best model to predict the variability of them in the soil. In terms of MAPE results, Table 1 shows that the geostatistical kriging methods were performing better and providing less error in prediction than the deterministic IDW methods. In the analysis of almost all the metals, the geostatistical kriging

Table 1 MAPE values from various geostatistical methods

Metal elements	IDW-1	IDW-2	IDW-3	IDW-4	IDW-5	OK	UK	EBK
Aluminum (Al)	23.40	34.21	35.20	33.01	31.01	12.71	12.03	13.17
Arsenic (As)	0.22	0.33	0.33	0.31	0.28	0.11	0.13	0.13
Barium (Ba)	3.12	4.11	3.93	3.43	3.00	0.26	−0.25	1.47
Calcium (Ca)	7.81	11.36	11.67	10.81	9.97	6.39	−0.08	4.06
Cadmium (Cd)	0.11	0.18	0.19	0.17	0.15	0.05	0.05	0.08
Chromium (Cr)	0.06	0.14	0.15	0.13	0.12	0.02	0.04	0.14
Cobalt (Co)	0.31	0.37	0.34	0.28	0.25	0.05	0.01	0.03
Copper (Cu)	0.40	0.63	0.63	0.58	0.52	0.16	−0.04	0.25
Iron (Fe)	33.00	63.00	71.59	69.83	66.73	38.68	36.82	17.56
Mercury (Hg)	0.26	0.43	0.46	0.45	0.43	0.22	0.15	0.19
Potassium (K)	10.71	16.31	16.84	15.71	14.69	5.51	7.33	6.37
Manganese (Mn)	0.33	0.65	0.66	0.57	0.51	0.14	−0.10	0.28
Sodium (Na)	2.74	3.86	4.09	3.99	3.84	0.69	2.23	1.61
Nickel (Ni)	0.19	0.27	0.27	0.25	0.23	0.11	0.08	0.11
Lead (Pb)	1.37	2.09	1.94	1.69	1.49	0.08	−0.18	1.09
Antimony (Sb)	0.27	0.36	0.35	0.30	0.26	0.02	0.00	0.14
Scandium (Sc)	0.40	0.56	0.56	0.49	0.44	0.05	−0.06	0.22
Strontium (Sr)	1.02	1.45	1.43	1.28	1.16	0.21	−0.02	0.57
Titanium (Ti)	48.98	66.73	66.16	60.07	54.59	12.18	28.48	26.14
Vanadium (V)	1.72	2.64	2.71	2.49	2.27	0.84	0.33	1.02
Zinc (Zn)	0.71	1.36	1.45	1.33	1.19	0.66	0.55	0.41

MAPE = Mean average prediction error

Table 2 RMSPE values from various geostatistical kriging

	AL	As	Ba	Ca	Cd	Cr	Co	Cu	Fe	Hg	K
OK	118.29	1.33	14.85	38.91	1.22	1.98	1.31	2.13	450.57	1.68	79.21
UK	114.03	1.28	14.31	43.24	1.17	1.97	2.11	3.35	447.69	1.49	75.45
EBK	119.58	1.35	12.43	40.63	1.22	1.97	1.14	2.20	465.06	1.60	75.71

	Mn	Na	Ni	Pb	Sb	Sc	Sr	Ti	V	Zn
OK	5.43	23.93	1.22	12.08	1.54	2.43	5.78	273.19	10.11	7.58
UK	6.41	22.84	1.16	14.19	2.02	2.41	7.87	248.14	10.41	7.55
EBK	5.58	22.15	1.19	12.13	1.28	2.15	5.31	247.65	10.35	8.17

RMSPE = Root mean square prediction error

methods were showing lesser MAPE values than the deterministic IDW methods conducted from power 1 to 5.

Again, the RMSPE values for all the geostatistical methods are given in Table 2. OK's summary result showed the lowest RMSPE values of 38.91, 2.13, 450.57, 5.43, 1.54, and 10.11, respectively, for Ca, Cu, Fe, Mn, Sb, and V. UK showed the lowest RMSPE values for Al (114.03), As (1.28), Cd (1.17), Hg (1.49), Ni (1.16), and Zn (7.55). EBK showed the smallest RMSPE results for Ba (12.43), Co (1.14), K (75.71), Sc (2.15), Sr (5.31), and Ti (247.65).

Table 3 represents the SRMSPE values for the three types of kriging methods. Performed results show that these values were ranging around 0.89–0.95 for EBK, 1.09–5.68 for UK, and 0.75–1.16 for OK. So, though ordinary kriging sometimes shows better performance, in terms of cross-validation results, empirical Bayesian kriging is the interpolation method with the best performance here.

Table 3 SRMSPE values from various geostatistical kriging

	Al	As	Ba	Ca	Cd	Cr	Co	Cu	Fe	Hg	K
OK	0.75	0.78	0.87	0.90	0.90	0.93	1.16	0.67	0.89	1.10	0.90
UK	2.14	1.15	4.09	4.23	1.24	1.25	5.68	2.49	1.25	1.33	1.60
EBK	0.91	0.93	0.89	0.92	0.95	0.94	0.93	0.90	0.95	0.95	0.93

	Mn	Na	Ni	Pb	Sb	Sc	Sr	Ti	V	Zn
OK	0.87	0.99	0.91	0.73	0.87	0.93	0.82	0.92	0.76	0.82
UK	2.41	1.30	1.22	6.95	18.42	2.30	3.92	2.09	1.93	1.09
EBK	0.98	0.94	0.95	0.94	0.90	0.93	0.91	0.92	0.92	0.95

Table 4 Summary of semivariogram models for the metal elements

Metal elements	Nugget (C_0)	Sill $(C + C_0)$	$\frac{C_0}{C+C_0}$	Metal elements	Nugget (C_0)	Sill $(C + C_0)$	$\frac{C_0}{C+C_0}$
AL	0	41,991	0	Mn	0	50.26	0.00
As	0.59	4.79	0.12	Na	422.15	970.28	0.44
Ba	237.72	580.12	0.41	Ni	0	3.11	0.00
Ca	0	3527.4	0	Pb	128.26	158.92	0.81
Cd	0	2.76	0	Sb	2.64	4.85	0.54
Cr	0	6.4	0	Sc	5.37	12.64	0.42
Co	0	9.23	0	Sr	37.07	65.10	0.57
Cu	0.9	15.66	0.06	Ti	481.99	209,570.00	0.00
Fe	0	332,640	0	V	0	274.80	0.00
Hg	0	5.39	0	Zn	0	123.19	0.00
K	0	18,353	0				

3.3 Evaluation of Semivariogram Parameters

Table 4 shortens the parameters from the semivariogram models of the metal elements. The data from the semivariograms indicated the reality of different spatial dependence for the collected field soil properties. The nugget-to-sill ratio states the spatial autocorrelation. In Fig. 3, the semivariogram diagrams of barium, iron, and lead found from ordinary kriging are shown. The $C_0/(C + C_0)$ value measured for arsenic and copper was 12% and 6% indicating that the metals were distributed strongly spatially. The metals barium, sodium, antimony, scandium, and strontium were distributed at moderate levels as for $C_0/(C + C_0)$ values of 42%, 44%, 54%, 42%, and 57%, respectively. $C_0/(C + C_0)$ value equaling 81% depicted lead was weakly distributed in the study zone. Contrarily, calcium, cadmium, chromium, cobalt, iron, mercury, potassium, nickel, titanium, vanadium, and zinc were non-spatially correlated as their $C_0/(C + C_0)$ values were zero.

4 Conclusions

This study was conducted to find out the appropriate geostatistical approach to generate a proper spatial distribution map for metal elements in the soil. It was inferred from the prediction maps that all types of metal elements were showing the highest concentration in soil from the nearest point of the selected waste disposal site. The most surprising finding along these lines was that the three kriging methods like ordinary kriging, universal kriging, and empirical Bayesian kriging consistently and significantly outperformed the inverse distance weighting approach over all other factors. Again, among all three kriging methods, the empirical Bayesian kriging
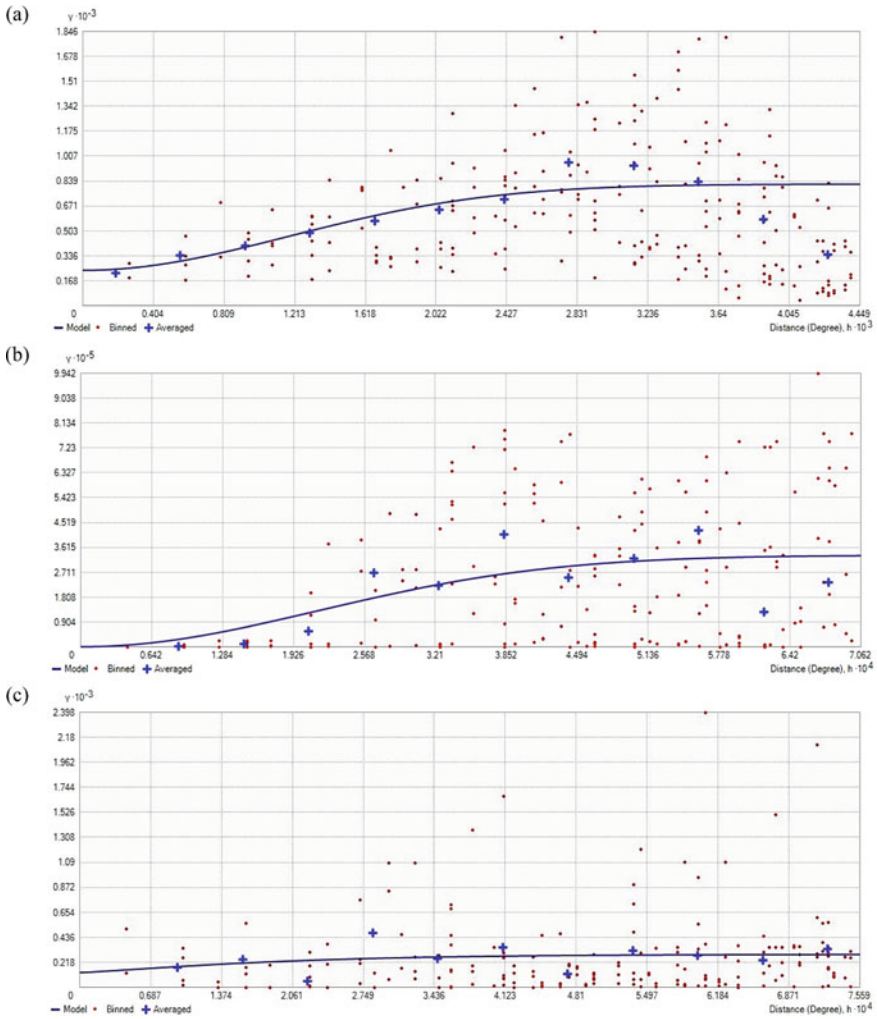
Fig. 3 Semivariogram models of (**a**) Ba, (**b**) Fe, and (**c**) Pb

method was superior to the other two approaches (like ordinary kriging and universal kriging). From the study, it can be concluded that the EBK method was the best to generate the prediction maps and generate spatial variability of metal elements in the soil.

References

1. Wuana RA, Okieimen FE (2011) Heavy metals in contaminated soils: a review of sources, chemistry, risks and best available strategies for remediation. ISRN Ecol 2011:1–20. https://doi.org/10.5402/2011/402647

2. Shiode N, Shiode S (2011) Street-level spatial interpolation using network-based IDW and ordinary kriging. Trans GIS 15:457–477. https://doi.org/10.1111/j.1467-9671.2011.01278.x

3. Arun PV (2013) A comparative analysis of different DEM interpolation methods. Egypt J Remote Sens Sp Sci 16:133–139. https://doi.org/10.1016/j.ejrs.2013.09.001

4. Yasrebi J, Saffari M, Fathi H, Karimian N, Emadi M, Baghernejad M (2008) Spatial variability of soil fertility properties for precision agriculture in Southern Iran. J Appl Sci 8:1642–1650

5. Gotway CA, Ferguson RB, Hergert GW, Peterson TA (1996) Comparison of kriging and inverse-distance methods for mapping soil parameters. Soil Sci Soc Am J 60:1237–1247. https://doi.org/10.2136/sssaj1996.03615995006000040040x

6. Luo W, Xuan T, Li J (2017) Estimating anisotropic soil properties using Bayesian Kriging. Geotech Spec Publ 370–381. https://doi.org/10.1061/9780784480717.035

7. Lapen DR, Hayhoe HN (2003) Spatial analysis of seasonal and annual temperature and precipitation normals in Southern Ontario, Canada. J Great Lakes Res 29:529–544. https://doi.org/10.1016/S0380-1330(03)70457-2

8. Schloeder CA, Zimmerman NE, Jacobs MJ (2001) Division S-8 - nutrient management & soil & plant analysis: comparison of methods for interpolating soil properties using limited data. Soil Sci Soc Am J 65:470–479. https://doi.org/10.2136/sssaj2001.652470x

9. Yasrebi J, Saffari M, Fathi H, Karimian N (2009) Evaluation and comparison of ordinary Kriging and IDW methods. Res J Biol Sci 4:93–102

10. Gribov A, Krivoruchko K (2020) Empirical Bayesian kriging implementation and usage. Sci Total Environ 722:137290. https://doi.org/10.1016/j.scitotenv.2020.137290

11. Krivoruchko K, Gribov A (2019) Evaluation of empirical Bayesian kriging. Spat Stat 32:100368 https://doi.org/10.1016/j.spasta.2019.100368

12. Sağir Ç, Kurtuluş B (2017) Hydraulic head and groundwater 111cd content interpolations using empirical Bayesian kriging (Ebk) and geo-adaptive neuro-fuzzy inference system (geo-ANFIS). Water SA 43:509–519. https://doi.org/10.4314/wsa.v43i3.16

13. Mosier CI (1951) The need and means of cross validation. I. Problems and designs of cross-validation. Educ Psychol Meas 11:5–11. https://doi.org/10.1177/001316445101100101

14. Bhunia GS, Shit PK, Maiti R (2018) Comparison of GIS-based interpolation methods for spatial distribution of soil organic carbon (SOC). J Saudi Soc Agric Sci 17:114–126. https://doi.org/10.1016/j.jssas.2016.02.001

15. Jakubek DJ, Forsythe KW (2004) A GIS-based kriging approach for assessing Lake Ontario sediment contamination. Gt Lakes Geogr 11:1–14

Low-Cost Salinity Treatment for Drinking Purpose Using Indigenous Materials

T. Chowdhury, J. Miah, and B. K. Banik

1 Introduction

There are various impacts of climate change. The most critical impacts are on the world's freshwater resources. Since 1948, river salinity has increased by 45% in the southern districts of Patuakhali, Pirojpur, Barguna, Satkhira, Bagerhat, and Khulna [1]. The varying degrees of salinity in drinking water collected from different natural sources affect approximately 20 million people living along the coast (Ministry of Environment and Forestry (MOEF) 2006). So, it is very much important to reduce salinity from water. From the literature review, it is seen that sodium ion (Na^+) and chloride ion (Cl^-) are mainly responsible for the salty taste of drinking water in Bangladesh [2]. Laterite soil has an important geotechnical property like adsorption capacity. Laterite-based soil filter has been used for improving the drinking water quality [3]. This laterite-based filter has reduced Na^+ 67%, Mg^{2+} 90% and other chemical components of water in a significant amount. The flow rate was 10 ml/min. Indian laterite soil is enriched with iron oxide, while in other continents, laterite soil is enriched with aluminum oxide [4]. Iron oxide has an adsorption capacity, and it was used for the removal of contaminants from water [5, 6]. Laterite soil is available in tropical and subtropical climate like Bangladesh, Srilanka, India, Thailand, etc. In Bangladesh, laterite soil is mainly available in Madhupur Tract or Red Soil Tract. Laterite soil is also available in Chattogram. Laterite soil has been used for removal of heavy metal [7]. Arsenic, cadmium, copper, lead, chromium and zinc have been removed by laterite soil [8, 9]. Rice husk ash (RHA) has been used for saline water treatment [10]. From the experiment, it has been seen that rice husk ash (RHA) is a

T. Chowdhury (✉) · J. Miah · B. K. Banik
Department of Civil and Environmental Engineering, Shahjalal University of Science and Technology, Sylhet, Bangladesh

B. K. Banik
e-mail: bijit-cee@sust.edu

good adsorbent for salinity removal. Rice husk ash has a higher percentage of sodium chloride adsorption of 27.83% [11].

The objective of the study was to develop a low-cost technique for salinity treatment of drinking water using indigenous materials. The specific objectives are to analyze the capacity of laterite soil (LS) and rice husk ash (RHA) to adsorb Cl^- ion with different mix ratio and the effects of thickness of mold on adsorption.

2 Materials and Methods

The research work was conducted in various steps. Firstly, the raw materials were collected and processed. The raw materials include laterite soil (LS), rice husk (RH), saw dust, coco peat, charcoal, betel nut husk and sand. The processing steps of LS involved air drying, hammering and sieving. Rice husk ash (RHA) was found through the burning of rice husk (RH). The processing of other materials incorporated meshing, washing and drying. Then, the primary setup of the plastic bottle was prepared to get the best two adsorbents (which will be used to make filter media) and the effective concentration of saline water. The primary setup was conducted by column method of filtration. Each adsorbent was filled in the plastic bottle up to a height of 20 with 2.5 cm coarse sand at the bottom and 2.5 cm fine sand at the top. Saline water was filled in column up to adsorbent height and kept in contact with an adsorbent for 15 min. Treated water was filtered through Whatman filter paper. Thereafter, the existence of chloride concentration in each sample was measured. The effective salinity concentration was 900 mg/l because in this concentration salinity removal efficiency was better than the other two concentrations (500, 700 mg/l). After that, the final setup was made to measure the salinity removal efficiency from drinking water. The method of the study is shown in Fig. 1.

2.1 Final Setup Preparation

The final filter media was prepared by the combination of LS and RHA with four different ratios and three different thicknesses. The combinations of LS and RHA are shown in Table 1.

Water was added periodically to make the mixer cohesive enough to bind LS and RHA. After that, the filter media were prepared with three different thicknesses by using a PVC pipe frame. The dimension of the mold and final setup is shown in Fig. 2.
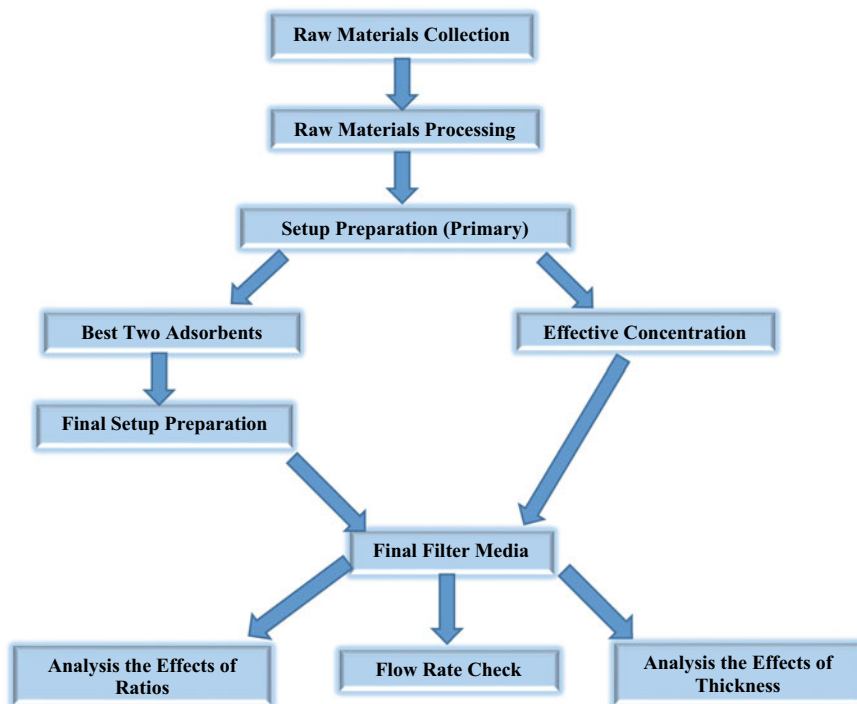
Fig. 1 Method of the study

Table 1 Percentage of LS and RHA for the filter media

No.	The thickness of filter media (in)	LS (%)	RHA (%)	Reference name[a]
01	1	100	0	1-LS100-RHA0
02		75	25	1-LS75-RHA25
03		65	35	1-LS65-RHA35
04		55	45	1-LS55-RHA45
05	1.5	100	0	1.5-LS100-RHA0
06		75	25	1.5-LS75-RHA25
07		65	35	1.5-LS65-RHA35
08		55	45	1.5-LS55-RHA45
09	2	100	0	2-LS100-RHA0
10		75	25	2-LS75-RHA25
11		65	35	2-LS65-RHA35
12		55	45	2-LS55-RHA 45

[a]Reference name indicates how the filter media referred to
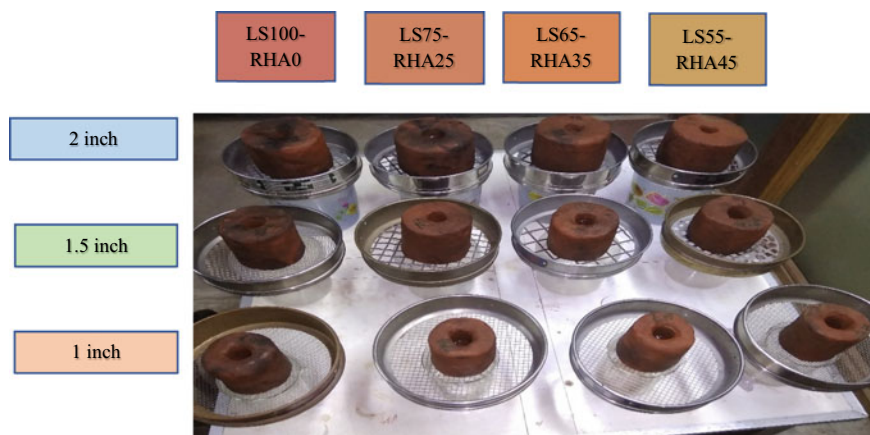
Fig. 2 Final setup

2.2 Measurements

Saline solution was prepared synthetically in the lab by adding sodium chloride (NaCl) in the tap water. Salinity was measured with respect to chloride concentration and electric conductivity. Electric conductivity was measured by the EC meter of the HANNA instrument. Chloride concentration was calculated by the Mohr method.

The relation between chloride concentration and salinity is given by

$$\text{Salinity} * \left[\text{mg/l}\right] = \left[0.03 + 1.805 \times \text{Chloride concentration(mg/l)}\right]$$

*Approved by Standard Methods Committee, 1985.

After preparing the final setup and saline solution, water was poured into the filter at 9:30 am. The data was taken from the respective filters twice a day. The first data was taken at 3:30 pm, and the second data was taken at 9:30 pm. The process was continued up to ten days with 6 h of the interval.

The flow rate was measured by weighting filtrate water within 1 h. Then, the results were converted to L/day.

$$\text{Flow Rate}(L/\text{Day}) = \left[\text{Filtrate water(kg/h)} \times 24\,\text{h/day} \times 1\,\text{L/kg}\right]$$

3   Results and Discussions

In this study, the locally available adsorbents were used for salinity removal. The soil samples were collected from 16 different places of Narsingdi district which is shown
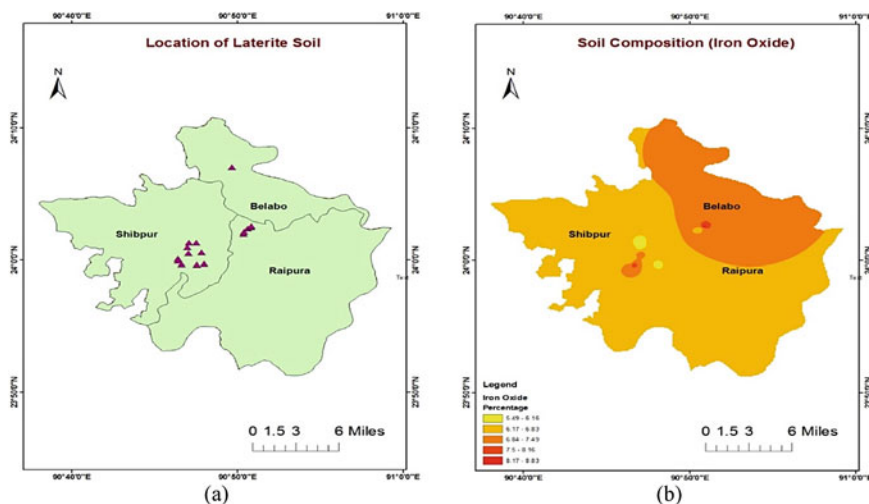
Fig. 3 **a** Soil location. **b** Iron oxide content (%)

in Fig. 3. Before using it as an adsorbent, the selection of laterite soil containing a high percentage of iron oxide was required. Thus, collected samples were processed for testing of soil composition and were examined by the XRF machine. The percentage of iron oxide is shown in [Fig. 3], and the sample containing a high percentage of iron oxide (8.85%) was chosen for the effective removal of salinity. The composition of selected soil sample was SiO_2 (60%), Al_2O_3(16.99%), Fe_2O_3 (8.85%), CaO (0.09%), MgO (0.36%), SO_3 (0.02%) and others (13.69%). The location of the selected soil sample is in Narsingdi district with latitude 24.04245 and longitude 90.847849.

Primary results were analyzed to check the efficiency of salinity removal of locally available materials. The salinity removal efficiency of indigenous adsorbents was analyzed for up to three days. The average results are shown in Table 2, and it is seen that rice husk ash (RHA) has the highest salinity removal efficiency among all

Table 2 Primary selection of local materials

Materials	Salinity removal efficiency (%)	Comment
RH	20.51	Slight brownish color filtrate
RHA	21.01	Clear filtrate
Saw dust	9.23	High brownish color filtrate
Coco peat	8.19	Not satisfactory
Charcoal	5.56	Color
Betel nut husk	7.69	Not satisfactory
Sand	1.08	Low removal

other local materials. Laterite soil (LS) and rice husk ash (RHA) were selected as the best two adsorbents for making filter media. The effective salinity concentration was 900 mg/l because in this concentration salinity removal efficiency was better than the other two concentrations (500, 700 mg/l).

Finally, it is seen that the highest value of average removal efficiency and peak removal efficiency was, respectively, 26.61% and 42.86% Figs. 4 and 5. All the highest values were found for the combination of LS100-RHA0 with 1 inch thickness. The highest average flow rate for this combination was 5.23 L/day. Removal efficiency decreased with the increment of thickness. The development of pore spaces may be the reason for such results. These pore spaces develop due to the sudden shrinkage of molds resulting from the firing process. The number of pores increases with thickness. Thus, it is seen that high thickness was not as effective as a thin one. Finally, it can be said that for the potential removal of a high percentage of saline
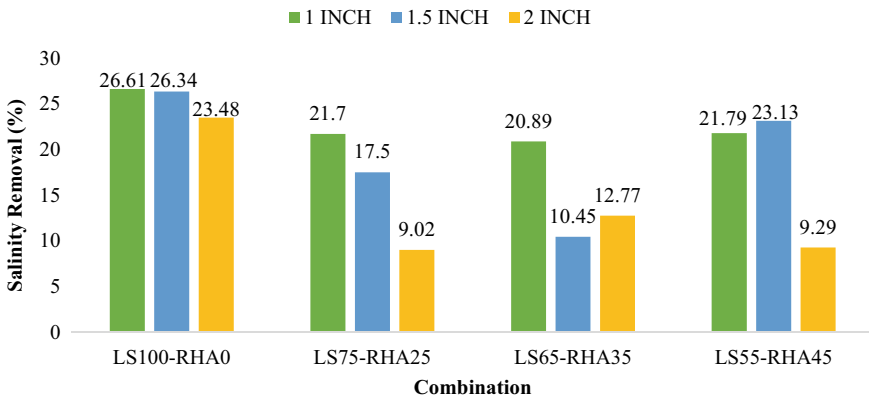
Fig. 4 Average salinity removal
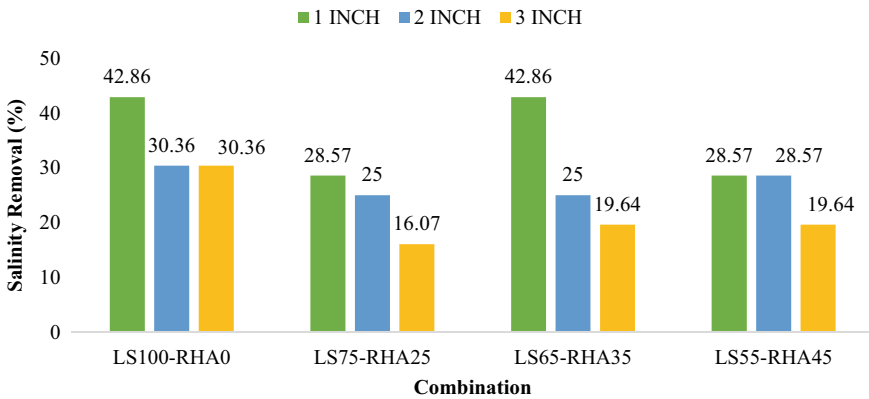
Fig. 5 Peak salinity removal

water the filter media with a combination of LS100-RHA0 and 1 inch thickness are suitable.

Finally, the drinking water quality parameters were analyzed to check the removal efficiency of selected filter media (LS100-RHA0 with 1 inch thickness).

4 Conclusions and Recommendations

The salinity removal efficiency for different indigenous materials was examined. The work was divided into two steps, namely primary and final. The primary setup was conducted for the query of the best local adsorbents. Rice husk ash (RHA) and laterite soil (LS) were found as the best two adsorbents. The effective concentration was 900 mg/l.

Thereafter, twelve filter media having three different thicknesses and four different combinations of RHA and LS were prepared. These filter media were checked for ten days. Each day two data were taken having continuous feed water supply with an interval of six hours. The highest removal efficiency was 42.86%, while the average removal efficiency was 26.61%. It was obtained from the combination of a hundred percent laterite soil (LS100-RHA0) and 1 inch thickness of filter media. The highest flow rate for LS100-RHA0 was 5.23 L/day.

However, in this study, real saline water could not be used because of high transportation costs, and water head pressure was not considered. The synthetic saline solution could be prepared by using distilled water instead of tap water. For better results, laterite soil enriched with high iron oxide content can be used.

References

1. Khan AE, Ireson A, Kovats S, Mojumder SK, Khusru A, Rahman A, Vineis P (2011) Drinking water salinity and maternal health in coastal Bangladesh: implications of climate change. Environ Health Perspect 119:1328–1332
2. Datta DK, Ghosh PK (2015) Groundwater of the municipalities of southwestern coastal Bangladesh. Surf Sub-Surf Water Asia Issues Perspect 120–145. https://doi.org/10.3233/978-1-61499-540-1-120
3. Paper C, Jayewardenepura S (2015) Improvement of drinking water quality using laterite based soil filter
4. Gidigasu M (2012) Laterite soil engineering: pedogenesis and engineering principles. Elsevier
5. Oliveira LCA, Rios RVRA, Fabris JD, Sapag K, Garg VK, Lago RM (2003) Clay–iron oxide magnetic composites for the adsorption of contaminants in water. Appl Clay Sci 22:169–177
6. Sizirici B, Yildiz I (2017) Adsorption capacity of iron oxide-coated gravel for landfill leachate: simultaneous study. Int J Environ Sci Technol 14:1027–1036
7. Pham TD, Nguyen HH, Nguyen NV, Vu TT, Pham TNM, Doan THY, Nguyen MH, Ngo TMV (2017) Adsorptive removal of copper by using surfactant modified laterite soil. J Chem https://doi.org/10.1155/2017/1986071
8. Aminah LN, Izaat MNMK (2011) Efficiency of lateritic soil for the removal of zinc from wastewater

9. Syama I, Thalla A, Manu D (2015) Performance of laterite soil grains as adsorbent in the removal of chromium. Curr World Environ 10:270–280. https://doi.org/10.12944/cwe.10.1.33

10. Province U, Lertsirivorakul R, Teasuwatseth M (2016) Saline water treatment using rice husk ash at a salt-making area. Ban Dung 2–5

11. Singh P, Garg S, Satpute S, Singh A (2017) Use of rice husk ash to lower the sodium adsorption ratio of saline water. Int J Curr Microbiol Appl Sci 6:448–458. https://doi.org/10.20546/ijcmas.2017.606.052

Development and Characterization of Novel Mn–Fe–Sn Ternary Nanoparticle by Sol–Gel Technique

M. N. Uddin [iD]**, G. C. Saha, M. A. Hasanath** [iD]**, M. T. Rahman, and M. M. Rashid**

1 Introduction

Industrial effluent frequently contains significant quantities of metals, which, when released unless appropriate treatment, will potentially harm individuals, animals, and vegetation together with the water environment. These effluents combine with toxic heavy metals, mostly cadmium (Cd), copper (Cu), zinc (Zn), chromium (Cr), lead (Pb), nickel (Ni), mercury (Hg), and arsenic (As) [1]. Since heavy metals have a relatively low water solubility, they cannot be degraded, so that they appear to accumulate [2]. Once they are ingested, they can accumulate in a living organism at low concentrations, potentially causing adverse effects like nervous system damage, cancer, and kidney failure [3, 4]. Due to heavy metals' toxicity, effluents need prior handling to discharge to surface water or be transported to a municipal wastewater treatment facility.

Different techniques like oxidation, ion exchange, chemical precipitation, electrochemical treatment, ultrafiltration, and membrane process have extensively been employed to extract heavy metals from effluent [5]. However, they have some limitations (i.e., poor performance, huge costs, and operating challenges) remained where modern and successful remediation procedures need to be developed [6]. In this case, the adsorptive method is usually chosen for removing these contaminants because of their simplicity of use and higher efficiency in extraction [7]. As a result, a wide variety of adsorbents is synthesized with various compositions [8], for instance, activated carbon [9], agricultural waste [10], and chitosan [11].

Nanotechnology has become an exciting arena in recent years. Nanoparticles are being used immensely due to their physical properties, tiny size, initiation, which are well known to affect the functioning of any other materials that come into

M. N. Uddin (✉) · G. C. Saha · M. A. Hasanath · M. T. Rahman · M. M. Rashid
Department of Civil Engineering, DUET, Gazipur, Bangladesh

G. C. Saha
e-mail: ganesh@duet.ac.bd

interaction with these small elements. Incorporating different techniques can easily prepare these particles. The researcher has recently developed a wide range of nano-adsorbents to remove organic and inorganic contaminants from wastewater/water [12]; such as a stannous-based nanoparticle [13], rGO aerogel [14], iron nanoparticle [15, 16], magnetic chitosan-iron hydrogel [17], mesoporous magnetic iron adsorbent [18], facile and scalable synthesis of α-Fe$_2$O$_3$/γ-Fe$_2$O$_3$/Fe/C nanocomposite [19], manganese-based nanoparticle [20], and polypyrrole decorated reduced graphene oxide-Fe$_3$O$_4$ magnetic composite [21].

Numerous approaches to nanoparticle synthesis are well-documented including co-precipitation [22], ion beam deposition [23], sol–gel [24], microemulsion [25], colloidal method [26], spray pyrolysis [27], template synthesis [28], laser pulse removal [29], high energy ball milling [30], spark discharge [31], biological synthesis [32], physical vapor deposition [33], and chemical vapor deposition [34]. But the sol–gel technique for the synthesis of metal oxides has various benefits over other processes [35]. Despite being a relatively old method, it has extensively used to prepare different materials because sol–gel synthesis is one of the easiest, quickest, and cheapest methods and has its specific benefits, such as the uniformity of the product formed, low processing temperature, reproducibility, and the creation of complex structures and composite materials. The development of nanoparticles utilizing the sol–gel technics offers beneficial optical attributes. The sol–gel technique can be utilized to developed various sorts of materials for instance ceramics, thin-film coating, nanoparticles, microparticles, aerogel, xerogel, and fibers; advancing a wide kind of uses [36].

Previously, synthesized iron oxide nanoparticles had been reported by various researchers [36–40]. Besides this, tin oxide nanoparticles were developed [41–44], whereas Mn-based nanoparticles were synthesized employing the sol–gel technique [45–49]. Scientists have already established Fe, Mn, and Sn as prominent adsorbents to remove pollutants from water/wastewater. However, ternary nanoparticles were previously not developed to the best of our knowledge, together with iron, stannous, and manganese. In this study, an attempt has made to develop a novel ternary nanoparticle comprising Mn, Fe, and Sn keep focusing on three objectives: (i) to synthesize Mn–Fe–Sn nanocomposite via a facile method; (ii) to characterize as-synthesis nanocomposite; and (iii) later on use as an adsorbent to evaluate its performance to the removal of heavy metals from aqueous media.

2 Methodology

2.1 Synthesis of Mn–Fe–Sn Nanoparticles

In this study, the sol–gel technique [50] has been applied to develop the nanostructure of Mn–Fe–Sn ternary oxides. The ternary oxide adsorbent of Sn–Mn–Fe has produced with the following process: potassium permanganate (KMnO$_4$) and iron

(II) chloride (FeCl$_2$) were dissolved in 100 mL of DI water, respectively. The KMnO$_4$ solution has gradually applied to the FeCl$_2$ solution with vigorous magnetic stirring, and at the same time, 2M NaOH solution was added to the mixed solutions to develop gels of manganese and iron hydroxide, maintaining a solution pH at 3–4. The stirring continued for the next 30 min following addition. Likewise, the hydroxide gel of tin and manganese also made. The hydroxide gel of tin and manganese was then added to the gel of iron and manganese dropwise with magnetic stirring for 1 h. The developed gel-like precipitate of hydroxide was allowed to mature for 24 h in the mother liquor. The precipitate was filtered and rinsed to remove chloride entirely with de-ionized water, and then, it was oven-dried at 105 °C. The dried material was crushed into powder, followed by calcination at 650 °C for 3 h.

2.2 Characterization

Electron microscope (FESEM) model: JSM 7600F, JEOL-Japan, was employed to inspect the topography by scanning its surface, which can create high-resolution images of a sample surface, and the forms of elemental components were revealed by the energy-dispersive X-ray spectroscopy (EDX) attached with (FESEM) model: JSM 7600F, JEOL-Japan. Besides this, X-ray diffraction (XRD) using the model: Empyrean, PANalytical-Netherlands, was employed to determine whether Mn–Fe–Sn nanomaterials are crystalline or non-crystalline. Furthermore, a Fourier transform infrared spectroscopy (FTIR) from SHIMADZU Corp. Kyoto, Japan (model IR Prestige-21) was used to observe functional clusters of Mn–Fe–Sn.

3 Results and Discussions

A methodical characterization of Mn–Fe–Sn nanoparticles has performed using SEM, EDX, FTIR, and XRD studies. The surface topography of the Mn–Fe–Sn nanoparticles was analyzed by SEM analysis.

Figure 1 illustrates the micrograph images of Mn–Fe–Sn nanoparticles. Mn–Fe–Sn adsorbent demonstrates that the substance has made up of many aggregated small and large particles [51], nanowires [52], heterogeneous, irregular, rough [53], and porous surfaces [54]. Also, the surface of particles seems to possess porous surfaces that specify a higher surface area, having many pores [55] present in Mn–Fe–Sn nanoparticles. Likewise, it indicates numerous binding sites and the porous nature of particles with huge internal spaces where metal ions can be entrapped and adsorbed.

The elements of the Sn–Mn–Fe nanoparticles were analyzed by EDX Fig. 2, which confirmed O, Sn, Mn, and Fe in the prepared nanoparticle. The peaks in the position of 0.52 keV, 5.9 keV, 6.40 keV, and 3.44 keV corresponded to the conditional energy of Mn, Fe, Sn, and O, respectively. In EDX analysis (Fig. 2), Mn, Fe, Sn,
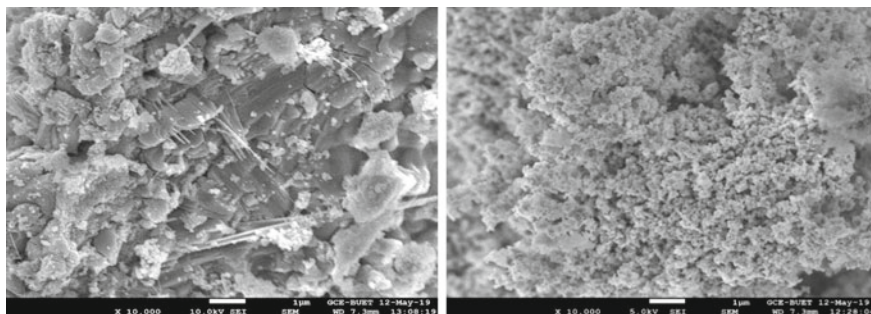
Fig. 1 SEM micrograph image of Mn–Fe–Sn nanoparticle
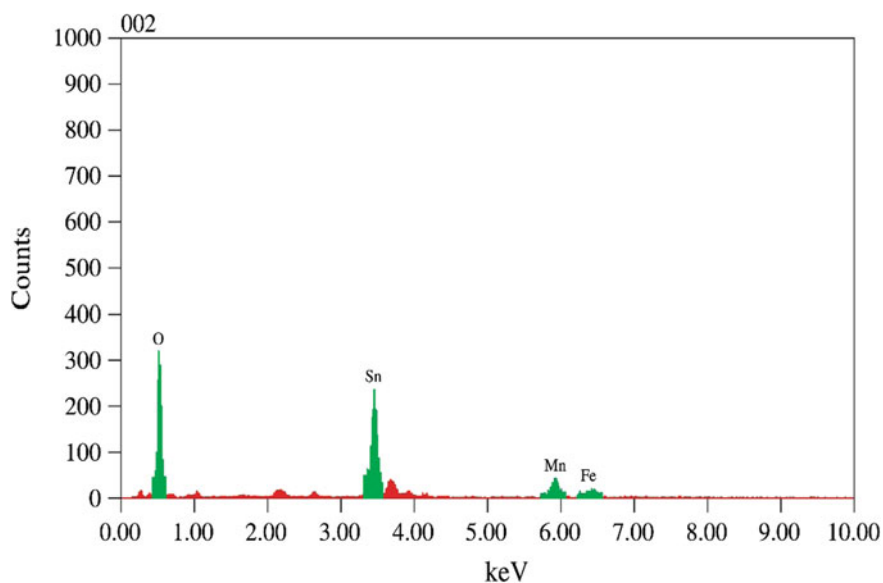
Fig. 2 Energy-dispersive spectroscopy spectrum of Mn–Fe–Sn ternary nanoparticles

and O are the significant components of Mn–Fe–Sn–O's entire surface with weight percentages of 5.24%, 2.97%, 3.04%, and 88.75%, respectively, as given in Table 1.

Table 1 Elemental composition of Mn–Fe–Sn ternary oxide nanoparticle

Elements	Weight%	Atom%
O	88.75	63.54
Mn	5.24	12.87
Fe	2.97	7.43
Sn	3.04	16.16
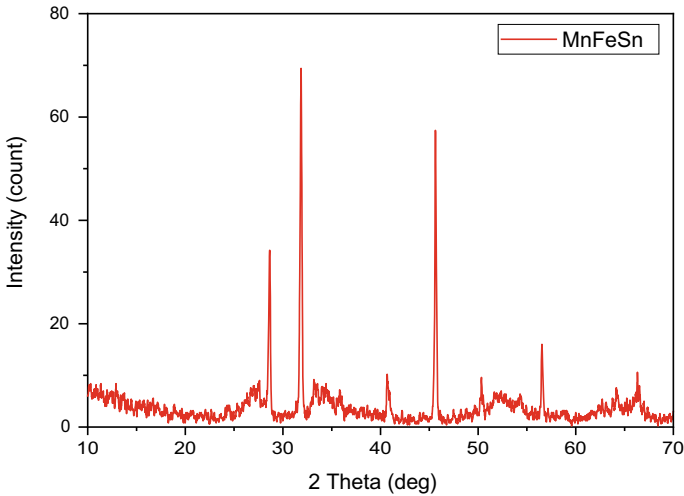
Fig. 3 XRD pattern of Mn–Fe–Sn oxide nanoparticle

The frequency obtained by the XRD analysis is displayed on a graph that shows intensity versus the angle 2θ Fig. 3. The sample has evaluated, and the location of the most remarkable peak had calculated, $2\theta = 45.6766°$, together with half the average width of this highest point, FWHM $= 0.304999° = 0.00532323676$ radians, and the spacing for the highly intense peak have determined in the XRD pattern as $d = 0.2656$ nm. Particle size (D) evaluated from X-ray diffraction records using the Scherer formula, Eq. (1):

$$D = \frac{K\lambda}{\text{FWHM} \cos\theta} \tag{1}$$

$K =$ constant Scherer, FWHM $=$ full width with half the reflection peak having higher intensity in the diffraction pattern, $\lambda =$ X-rays wavelength, and $\theta =$ X-ray diffraction angle.

In the formula, the Scherer constant (K) is responsible for the molecular shape, and it is typically having a value of 0.9 [56]. Using data from XRD pattern: $K = 0.9$, $\lambda = 0.154252$ nm, $2\theta = 45.6766° = 0.398603531$ radians, FWHM $= 0.304999° = 0.00532323676$ radians, and substituting these values into the Scherer formula, the nanoparticle was found to range between 15.83 and 48.29 nm.

The Fourier transform infrared (FTIR) spectrum in the variety of 300–4000 cm^{-1} is applied to assess the functional groups present in the synthesized Mn–Sn–Fe ternary nanoparticle shown in Fig. 4. This FTIR spectrum revealed the presence of a variety of functional groups on the Mn–Fe–Sn nanoparticle surface.

The absorbance peaks in the fingerprint region are below the wavelength of 1000 cm^{-1} which are derived from generally interatomic vibrations, which generally arise due to hydroxides and oxides of nanoparticles. The dominant and sharp peak at
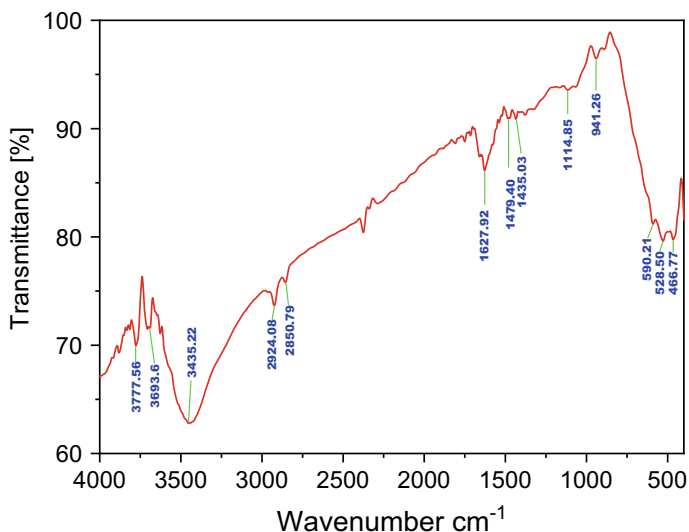
Fig. 4 FTIR spectrum of Mn–Fe–Sn nanoparticle

590 cm^{-1} is due to the Sn–O form of vibration in SnO_2 [20, 22]. The spectrum also exhibits a peak at 528 cm^{-1}, which belongs to the magnetite-related Fe–O vibration [57, 58]. The peak detected at 466 cm^{-1} is refer to the O–Mn–O bond [59, 60]. Moreover, the picks positioned at 1627 cm^{-1} and 3452 cm^{-1} result from the bending vibration of absorbed water and O–H stretching, respectively. The observed FTIR results confirmed that the synthesized nanoparticles are Mn–Fe–Sn oxides without any significant impurity.

4   Conclusion

The sol–gel technique has developed nanoparticles of Mn–Fe–Sn. The developed materials were then analyzed by SEM, XRD, EDX, and FTIR spectroscopy. The SEM was used to observe the topography of the prepared material, which showed that it has a rough, irregular, heterogeneous, and porous surface that is typical of a promising adsorbent for metal ions in the aqueous or liquid medium. EDX also investigated it and confirmed the presence of the oxides of Mn–Fe–Sn. Besides, the FTIR spectrum of the materials clearly shows the Mn–Fe–Sn–O absorption bands around 600–450 cm^{-1}. The XRD findings indicated that the size of nanoparticles is in the range of 15.83–48.29 nm. Studies on the potential use of the developed nanomaterials as an adsorbent are well underway.

of Civil Engineering, Dhaka University of Engineering & Technology, Gazipur, Gazipur-1700, Bangladesh, Department of Glass and Ceramic Engineering, Bangladesh University of Engineering and Technology (BUET), Dhaka-1000, Bangladesh, and Centre for Advanced Research in Sciences (CARS), University of Dhaka, Dhaka-1000, Bangladesh.

References

1. Boddu VM, Abburi K, Talbott JL, Smith ED (2003) Removal of hexavalent chromium from wastewater using a new composite chitosan biosorbent. Environ Sci Technol 37:4449–4456. https://doi.org/10.1021/es021013a
2. Ayub S, Siddique AA, Khursheed MS, Zarei A, Alam I, Asgari E, Changani F (2020) Removal of heavy metals (Cr, Cu and Zn) from electroplating wastewater by electrocoagulation and adsorption processes. Desalin WATER Treat 179:263–271. https://doi.org/10.5004/dwt.2020.25010
3. Shin K-Y, Hong J-Y, Jang J (2011) Heavy metal ion adsorption behavior in nitrogen-doped magnetic carbon nanoparticles: isotherms and kinetic study. J Hazard Mater 190:36–44. https://doi.org/10.1016/j.jhazmat.2010.12.102
4. Al-Saydeh SA, El-Naas MH, Zaidi SJ (2017) Copper removal from industrial wastewater: a comprehensive review. J Ind Eng Chem 56:35–44. https://doi.org/10.1016/j.jiec.2017.07.026
5. Sumaila A, Ndamitso MM, Iyaka YA, Abdulkareem AS, Tijani JO, Idris MO (2020) Extraction and characterization of chitosan from crab shells: kinetic and thermodynamic studies of arsenic and copper adsorption from electroplating wastewater. Iraqi J Sci 61:2156–2171. https://doi.org/10.24996/ijs.2020.61.9.2
6. Mohan D, Pittman CU Jr (2006) Activated carbons and low cost adsorbents for remediation of tri- and hexavalent chromium from water. J Hazard Mater 137:762–811. https://doi.org/10.1016/j.jhazmat.2006.06.060
7. Iram M, Guo C, Guan Y, Ishfaq A, Liu H (2010) Adsorption and magnetic removal of neutral red dye from aqueous solution using Fe_3O_4 hollow nanospheres. J Hazard Mater 181:1039–1050. https://doi.org/10.1016/j.jhazmat.2010.05.119
8. Gupta VK, Jain R, Malathi S, Nayak A (2010) Adsorption–desorption studies of indigocarmine from industrial effluents by using deoiled mustard and its comparison with charcoal. J Colloid Interface Sci 348:628–633. https://doi.org/10.1016/j.jcis.2010.04.085
9. Huang X, Yu J, Shi B, Hao H, Wang C, Jia Z, Wang Q (2020) Rapid prediction of the activated carbon adsorption ratio by a regression model. Chemosphere 245:125675. https://doi.org/10.1016/j.chemosphere.2019.125675
10. Tsade H, Murthy HCA, Muniswamy D (2020) Bio-sorbents from agricultural wastes for eradication of heavy metals: a review. J Mater Environ Sci 11:1719–1735
11. Vakili M, Deng S, Cagnetta G, Wang W, Meng P, Liu D, Yu G (2019) Regeneration of chitosan-based adsorbents used in heavy metal adsorption: a review. Sep Purif Technol 224:373–387. https://doi.org/10.1016/j.seppur.2019.05.040
12. Choi Y-L, Choi J-S, Lingamdinne LP, Chang Y-Y, Koduru JR, Ha J-H, Yang J-K (2019) Removal of U(VI) by sugar-based magnetic pseudo–graphene oxide and its application to authentic groundwater using electromagnetic system. Environ Sci Pollut Res 26:22323–22337. https://doi.org/10.1007/s11356-019-05260-5
13. Zhang M, Li Y, Uchaker E, Candelaria S, Shen L, Wang T, Cao G (2013) Homogenous incorporation of SnO_2 nanoparticles in carbon cryogels via the thermal decomposition of stannous sulfate and their enhanced lithium-ion intercalation properties. Nano Energy 2:769–778. https://doi.org/10.1016/j.nanoen.2013.01.009
14. Liu W, Cai J, Li Z (2015) Self-assembly of semiconductor nanoparticles/reduced graphene oxide (RGO) composite aerogels for enhanced photocatalytic performance and facile recycling

in aqueous photocatalysis. ACS Sustain Chem Eng 3:277–282. https://doi.org/10.1021/sc5006473

15. Alidokht L, Khataee AR, Reyhanitabar A, Oustan S (2011) Reductive removal of Cr(VI) by starch-stabilized Fe0 nanoparticles in aqueous solution. Desalination 270:105–110. https://doi.org/10.1016/j.desal.2010.11.028

16. Zhang YC, Li J, Zhang M, Dionysiou DD (2011) Size-tunable hydrothermal synthesis of SnS_2 nanocrystals with high performance in visible light-driven photocatalytic reduction of aqueous Cr(VI). Environ Sci Technol 45:9324–9331. https://doi.org/10.1021/es202012b

17. Yu Z, Zhang X, Huang Y (2013) Magnetic Chitosan–Iron(III) hydrogel as a fast and reusable adsorbent for Chromium(VI) removal. Ind Eng Chem Res 52:11956–11966. https://doi.org/10.1021/ie400781n

18. Wang P, Lo IMC (2009) Synthesis of mesoporous magnetic γ-Fe_2O_3 and its application to Cr(VI) removal from contaminated water. Water Res 43:3727–3734. https://doi.org/10.1016/j.watres.2009.05.041

19. Yin L, Pan Y, Li M, Zhao Y, Luo S (2020) Facile and scalable synthesis of α-Fe2O3/γ-Fe_2O_3/Fe/C nanocomposite as advanced anode materials for lithium/sodium ion batteries. Nanotechnology 31:155402. https://doi.org/10.1088/1361-6528/ab647f

20. Gheju M, Balcu I, Vancea C (2016) An investigation of Cr(VI) removal with metallic iron in the co-presence of sand and/or MnO_2. J Environ Manage 170:145–151. https://doi.org/10.1016/j.jenvman.2016.01.013

21. Wang H, Yuan X, Wu Y, Chen X, Leng L, Wang H, Li H, Zeng G (2015) Facile synthesis of polypyrrole decorated reduced graphene oxide–Fe_3O_4 magnetic composites and its application for the Cr(VI) removal. Chem Eng J 262:597–606. https://doi.org/10.1016/j.cej.2014.10.020

22. de Mello LB, Varanda LC, Sigoli FA, Mazali IO (2019) Co-precipitation synthesis of (Zn-Mn)-Co-doped magnetite nanoparticles and their application in magnetic hyperthermia. J Alloys Compd 779:698–705. https://doi.org/10.1016/j.jallcom.2018.11.280

23. Semenova AA, Semenov AP, Goodilin EA, Semenova IA (2019) Synthesis of plasmonic photonic crystal SiO_2–Ag nanostructures by ion beam deposition of silver clusters onto silica microspheres. Bull Russ Acad Sci Phys 83:1415–1418. https://doi.org/10.3103/S1062873819110200

24. Amir M, Gungunes H, Baykal A, Almessiere MA, Sözeri H, Ercan I, Sertkol M, Asiri S, Manikandan A (2018) Effect of annealing temperature on magnetic and Mössbauer properties of $ZnFe_2O_4$ nanoparticles by Sol-gel approach. J Supercond Nov Magn 31:3347–3356. https://doi.org/10.1007/s10948-018-4610-2

25. Wu H, Luo B, Gao C, Wang L, Wang Y, Zhang Q (2019) Synthesis and size control of monodisperse magnesium hydroxide nanoparticles by microemulsion method. J Dispers Sci Technol 1–7. https://doi.org/10.1080/01932691.2019.1594887

26. Chang C, He Y, Pan C (2020) Aqueous methods for the synthesis of colloidal metal oxide nanoparticles at ambient pressure. In: Colloidal metal oxide nanoparticles. Elsevier, pp 41–66

27. Lim HR, Jung SJ, Hwang TY, Lee J, Kim KH, Cho H, baek, Choa YH, (2019) Electromagnetic wave absorption properties of Fe/MgO composites synthesized by a simple ultrasonic spray pyrolysis method. Appl Surf Sci 473:1009–1013. https://doi.org/10.1016/j.apsusc.2018.12.222

28. Chen G, Liu P, Liao Z, Sun F, He Y, Zhong H, Zhang T, Zschech E, Chen M, Wu G, Zhang J, Feng X (2020) Zinc-mediated template synthesis of Fe-N-C electrocatalysts with densely accessible Fe-Nx active sites for efficient oxygen reduction. Adv Mater 1907399:1–7. https://doi.org/10.1002/adma.201907399

29. Franzel L, Bertino MF, Huba ZJ, Carpenter EE (2012) Synthesis of magnetic nanoparticles by pulsed laser ablation. Appl Surf Sci 261:332–336. https://doi.org/10.1016/j.apsusc.2012.08.010

30. De Carvalho JF, De Medeiros SN, Morales MA, Dantas AL, Carriço AS (2013) Synthesis of magnetite nanoparticles by high energy ball milling. Appl Surf Sci 275:84–87. https://doi.org/10.1016/j.apsusc.2013.01.118

31. Gao X, Xu C, Yin H, Chen P, Wang X, Song Q, Liu J (2020) Synthesis of nano titanium oxide with controlled oxygen content using pulsed discharge in water. Adv Powder Technol 31:986–992. https://doi.org/10.1016/j.apt.2019.12.021

32. Chokriwa A, Sharma MM, Singh A (2014) Biological synthesis of nanoparticles using bacteria and their applications. Am J Pharmtech Res 4:38–61

33. Pandey PA, Bell GR, Rourke JP, Sanchez AM, Elkin MD, Hickey BJ, Wilson NR (2011) Physical vapor deposition of metal nanoparticles on chemically modified graphene: observations on metal-graphene interactions. Small 7:3202–3210. https://doi.org/10.1002/smll.201101430

34. Hasanzadeh I, Jafari Eskandari M (2020) Direct growth of multiwall carbon nanotube on metal catalyst by chemical vapor deposition: In situ nucleation. Surf Coatings Technol 381:125109. https://doi.org/10.1016/j.surfcoat.2019.125109

35. Xu J, Yang H, Fu W, Du K, Sui Y, Chen J, Zeng Y, Li M, Zou G (2007) Preparation and magnetic properties of magnetite nanoparticles by sol-gel method. J Magn Magn Mater 309:307–311. https://doi.org/10.1016/j.jmmm.2006.07.037

36. Kumar A, Yadav N, Bhatt M, Mishra NK, Chaudhary P, Singh R (2015) Sol-gel derived nanomaterials and it's applications: a review. Res J Chem Sci 5(12):98–105

37. Kayani ZN, Arshad S, Riaz S, Naseem S (2014) Synthesis of iron oxide nanoparticles by sol-gel technique and their characterization. IEEE Trans Magn 50:1–4. https://doi.org/10.1109/TMAG.2014.2313763

38. Lu Y, Yin Y, Mayers BT, Xia Y (2002) Modifying the surface properties of superparamagnetic iron oxide nanoparticles through a sol−gel approach. Nano Lett 2:183–186. https://doi.org/10.1021/nl015681q

39. Jitianu A, Crisan M, Meghea A, Rau I, Zaharescu M (2002) Influence of the silica based matrix on the formation of iron oxide nanoparticles in the Fe_2O_3–SiO_2 system, obtained by sol–gel method. J Mater Chem 12:1401–1407. https://doi.org/10.1039/b110652j

40. Dong W, Zhu C (2002) Use of ethylene oxide in the sol–gel synthesis of α-Fe_2O_3 nanoparticles from Fe(iii) salts. J Mater Chem 12:1676–1683. https://doi.org/10.1039/b200773h

41. Gu F, Fen Wang S, Feng Song C, Kai Lü M, Xin Qi Y, Jun Zhou G, Xu D, Rong Yuan D (2003) Synthesis and luminescence properties of SnO_2 nanoparticles. Chem Phys Lett 372:451–454. https://doi.org/10.1016/S0009-2614(03)00440-8

42. Zhang J, Gao L (2004) Synthesis and characterization of nanocrystalline tin oxide by sol–gel method. J Solid State Chem 177:1425–1430. https://doi.org/10.1016/j.jssc.2003.11.024

43. Aziz M, Saber Abbas S, Wan Baharom WR (2013) Size-controlled synthesis of SnO_2 nanoparticles by sol-gel method. Mater Lett 91:31–34. https://doi.org/10.1016/j.matlet.2012.09.079

44. Köse H, Karaal Ş, Aydin AO, Akbulut H (2015) Structural properties of size-controlled SnO_2 nanopowders produced by sol–gel method. Mater Sci Semicond Process 38:404–412. https://doi.org/10.1016/j.mssp.2015.03.028

45. Almamoun O, Ma S (2017) Effect of Mn doping on the structural, morphological and optical properties of SnO_2 nanoparticles prepared by Sol-gel method. Mater Lett 199:172–175. https://doi.org/10.1016/j.matlet.2017.04.075

46. Samoila P, Sacarescu L, Borhan AI, Timpu D, Grigoras M, Lupu N, Zaltariov M, Harabagiu V (2015) Magnetic properties of nanosized Gd doped Ni–Mn–Cr ferrites prepared using the sol–gel autocombustion technique. J Magn Magn Mater 378:92–97. https://doi.org/10.1016/j.jmmm.2014.10.174

47. Ibrahim I, Ali IO, Salama TM, Bahgat AA, Mohamed MM (2016) Synthesis of magnetically recyclable spinel ferrite (MFe_2O_4, M = Zn Co, Mn) nanocrystals engineered by sol gel-hydrothermal technology: high catalytic performances for nitroarenes reduction. Appl Catal B Environ 181:389–402. https://doi.org/10.1016/j.apcatb.2015.08.005

48. Bayappagari B, Shaik K, Chakraborty D, Kunapalli CK (2021) Structural, optical and magnetic properties of vacuum annealed Fe, Mn doped NiO nanoparticles. Appl Phys A 127:49. https://doi.org/10.1007/s00339-020-04161-6

49. Jasrotia R, Puri P, Singh VP, Kumar R (2021) Sol–gel synthesized Mg–Ag–Mn nanoferrites for power applications. J Sol-Gel Sci Technol 97:205–212. https://doi.org/10.1007/s10971-020-05428-3

50. Peña-Garcia R, Guerra Y, Milani R, Oliveira DM, Rodrigues AR, Padrón-Hernández E (2020) The role of Y on the structural, magnetic and optical properties of Fe-doped ZnO nanoparticles

synthesized by sol gel method. J Magn Magn Mater 498:166085. https://doi.org/10.1016/j.jmmm.2019.166085

51. Zhang G, Qu J, Liu H, Liu R, Wu R (2007) Preparation and evaluation of a novel Fe-Mn binary oxide adsorbent for effective arsenite removal. Water Res 41:1921–1928. https://doi.org/10.1016/j.watres.2007.02.009

52. Zhu J, Wei S, Chen X, Karki AB, Rutman D, Young DP, Guo Z (2010) Electrospun polyimide nanocomposite fibers reinforced with core-shell Fe-FeO nanoparticles. J Phys Chem C 114:8844–8850. https://doi.org/10.1021/jp1020033

53. Rastghalam ZS, Yan C, Shang J, Cheng T (2020) The role of Fe oxyhydroxide coating, illite clay, and peat moss in nanoscale titanium dioxide (nTiO$_2$) retention and transport in geochemically heterogeneous media. Environ Pollut 257:113625. https://doi.org/10.1016/j.envpol.2019.113625

54. Liang R, Liang Z, Chen F, Xie D, Wu Y, Wang X, Yan G, Wu L (2020) Sodium dodecyl sulfate-decorated MOF-derived porous Fe$_2$O$_3$ nanoparticles: high performance, recyclable photocatalysts for fuel denitrification. Chin J Catal 41:188–199. https://doi.org/10.1016/S1872-2067(19)63402-9

55. Tazikeh S, Akbari A, Talebi A, Talebi E (2014) Synthesis and characterization of tin oxide nanoparticles via the Co-precipitation method. Mater Sci Pol 32:98–101. https://doi.org/10.2478/s13536-013-0164-y

56. Gorer S, Kodes G, Sorek Y, Reisfeld R (1997) Crystal phase transformation in sol-gel films of nanocrystalline CdSe and CdS. Mater Lett 31:209–214. https://doi.org/10.1016/S0167-577X(96)00272-8

57. Mahdavi M, Bin AM, Haron MJ, Namvar F, Nadi B, Ab Rahman MZ, Amin J (2013) Synthesis, surface modification and characterisation of biocompatible magnetic iron oxide nanoparticles for biomedical applications. Molecules 18:7533–7548. https://doi.org/10.3390/molecules18077533

58. Paul HL, Antunes APM, Covington AD, Evans P, Phillips PS (2013) Bangladeshi leather industry: an overview of recent sustainable developments. SLTC J 97:25–32. https://doi.org/10.1016/S0011-9164(04)00193-6

59. Asfaram A, Ghaedi M, Hajati S, Goudarzi A (2015) Ternary dye adsorption onto MnO$_2$ nanoparticle-loaded activated carbon: derivative spectrophotometry and modelling. RSC Adv 5:72300–72320. https://doi.org/10.1039/c5ra10815b

60. Gupta K, Bhattacharya S, Chattopadhyay D, Mukhopadhyay A, Biswas H, Dutta J, Ray NR, Ghosh UC (2011) Ceria associated manganese oxide nanoparticles: synthesis, characterization and arsenic(V) sorption behavior. Chem Eng J 172:219–229. https://doi.org/10.1016/j.cej.2011.05.092

Potential Utilization of Textile Dyeing Sludge, Pet Granules, and Fly Ash in Lightweight Concrete Block

M. T. Rahman ⓘ **, G. C. Saha, M. A. Hasanath** ⓘ **, and M. N. Uddin** ⓘ

1 Introduction

The textile and garments industry plays significant roles in the economic growth of Bangladesh. Textile is one of the largest industrial segment in Bangladesh [1]. Effluent treatment plants (ETPs) are being operated to treat the wastewater produced by industry. The treatments lead to the accumulation of sludge in both primary and secondary clarifiers. This sludge has several detrimental effects which can lead environmental pollution [2]. There are many dyeing industries in Bangladesh, mainly located in Gazipur and Narayanganj areas [3].

On the other hand, about 1.3 million cft of fly ash are being generated and dumped from coal-fired power plants alone per annual in Bangladesh, and it was predicted to reach an alarming level of 9.5 million cft by 2018 [4]. Several more similar power plants are scheduled to be in full operation soon, making this disposal problem even worse [5]. Air pollution due to direct emissions of noxious gases from the power plants and airborne fly ash (also known as pulverized fuel ash) from disposal sites may result in contamination of both surface water and soil along with its loss of fertility. Another waste material is plastic bottles, which are being produced large amounts and increasing day by day. PET is widely being used in food industries as bottles and containers for a long time [6], which creates a substantial amount of waste that poses an environmental problem non-biodegradable in nature, whereas healthy and sustainable reuse of plastic offers a host of advantages [7].

Textile dyeing sludge, fly ash, and PET granules are already used individually in concrete blocks in several studies, and results were found in quite variant. Textile dyeing sludge was used as fine aggregate in concrete in a study by Dwivedi and Kulkarni, Thomas and Nair used fly ash as fine aggregate in concrete blocks, whereas

M. T. Rahman (✉) · G. C. Saha · M. A. Hasanath · M. N. Uddin
Department of Civil Engineering, DUET, Gazipur, Bangladesh

G. C. Saha
e-mail: ganesh@duet.ac.bd

concrete with PET granules was investigated in other research [8–10]. Due to the technological development and mitigation of environment and health-related problems associated with brick manufacturing, people are being interested in using the concrete block, which may lighter in weight than brick (less than clay-fired brick of specific gravity 2.4) [11].

With this background, this study is mainly concerned about the prospects of eco-friendly block-making practices in Bangladesh by partially replacing the sand and stone chips by dyeing sludge, PET granules, and fly ash, which will also impart lightness in weight compared with ordinary concrete block.

2   Materials and Methods

2.1   Material Collection

Two types of materials were used for block fabrication. The first one is construction materials, e.g., cement, sand, and stone chips, and the second one is waste materials, e.g., textile dyeing sludge, PET granules, and fly ash. PCC cement (Holcim brand), stone chips (0.5 in. downgraded), and fine sand were collected from the local market. Dry sludge has been collected from a textile dyeing factory named Unimax Textile Mill Ltd., located in Gazipur, Bangladesh. Fly ash was collected from Barapukuria Thermal Power Plant, Dinajpur, Bangladesh. The PET has collected from the local market, which was available in granules in the market. All materials were collected and protected to avoid any constitutional damage.

2.2   Material Preparation

Dyeing sludge was prepared for block making, and other materials (cement, sand, stone chips, fly ash, and PET granules) were used directly. As it contained moisture, it was oven-dried at 105 °C for 24 h. Then the sludge was pulverized manually. After grinding, sludge was sieved by BS #4 sieve (4.75 mm opening) for eliminating coarse particles.

2.3   Material Characterization

Atomic absorption spectrophotometer (AAS) was used to determine heavy metals in the textile dyeing sludge after digesting by aqua regia. The oxide composition of fly ash and dyeing sludge was investigated by XRF (model- Shimadzu XRF-1800). pH and EC were measured by a digital device (Hach HQ40d Multi) after dilution,

whereas FM and specific gravity of sand and stone chips were calculated according to ASTM C136-01 and ASTM C97, respectively. The specific gravity of sludge and fly ash was computed according to ASTM D854-14. The fineness test of cement was conducted by following the ASTM C184 method. The compressive strength of the block was tested according to a standard method of ASTM (ASTM C67-14). Moisture absorption and the specific gravity of block were tested following ASTM D570 and ASTM C 127- 07.

2.4   Experimental Design and Procedure

Cement, stone chips, sand, and waste materials, i.e., textile dyeing sludge, fly ash, and PET granules used in different combinations. Two types of combinations have experimented; block, where the sand was partially replaced by waste materials Table 1 and another, was a replacement of coarse aggregate or stone chips with PET granules Table 2. Each combination has three replications, and the mixing ratio was 1:2:4 (cement: sand: stone chips). Steel form was used for block making, and the size of the form was $9.5'' \times 4.5'' \times 2.75''$.

The steel form was kept on the bare steel sheet to avoid any water leak from mixed concrete. The blocks were kept in the form for 24 h for hardening after casting. Then it was kept in a plastic water bucket for 28 days of curing. The final phase was the measure of properties by tests of the block. After 28 days of curing, the block's test, e.g., compressive strength, water absorption, and specific gravity, was performed. Leaching tests have been carried out in two stages: one was in 7 days, 14 days, 21 days, and 28 days of the curing period and another was after 28 days of cured

Table 1 Material combinations for block making

Combination ID	Volumetric percentage of materials (Sand replaced by waste materials, i.e., textile dyeing sludge, fly ash, and PET granules)					
	Cement (%)	Stone chips (%)	Sand (%)	Dyeing sludge (%)	Fly ash (%)	PET granules (%)
$A_{100}S_{100}W_0$ (control)	100	100	100	0	0	0
$A_{100}S_{85}W_5$	100	100	85	5	5	5
$A_{100}S_{70}W_{10}$	100	100	70	10	10	10
$A_{100}S_{55}W_{15}$	100	100	55	15	15	15
$A_{100}S_{40}W_{20}$	100	100	40	20	20	20
$A_{100}S_{25}W_{25}$	100	100	25	25	25	25
$A_{100}S_{10}W_{30}$	100	100	10	30	30	30

Note Here, A = coarse aggregate
S = sand, and
W = Waste materials (textile dyeing sludge, fly ash, and PET granules)

Table 2 Combination of materials for block making where stone chips replaced by PET granules

Combination ID	Volumetric percentage of materials (Stone chips replaced by PET granules)			
	Cement	Sand	Stone chips	PET granules
$S_{100}A_{100}P_0$ (control)	100	100	100	0
$S_{100}A_{95}P_5$	100	100	95	5
$S_{100}A_{90}P_{10}$	100	100	90	10
$S_{100}A_{85}P_{15}$	100	100	85	15
$S_{100}A_{80}P_{20}$	100	100	80	20
$S_{100}A_{75}P_{25}$	100	100	75	25
$S_{100}A_{70}P_{30}$	100	100	70	30

Note Here, A = coarse aggregate, S = sand, and P = PET granules

blocks. The water–cement ratio was kept 0.55 for all replication. For the proper mixing of materials, a concrete mixture machine and a mini vibrator were used to ensure the proper compaction.

3 Results and Discussions

3.1 Characteristics of Materials

In this study, two types of the experiment have conducted: replacement of sand by textile dyeing sludge, PET granules, fly ash, and another was a replacement of stone chips by PET granules. pH, EC, specific gravity of used materials are obtainable in Table 3.

pH of textile dying sludge and fly ash was found 6.70 and 6.30, respectively. In previous studies, pH of dying sludge was found in a range from 6.46 to 7.35 [3, 10, 12]. EC of dyeing sludge and fly ash was measured to be 2.54 mscm^{-1} and 0.49 mscm^{-1}, respectively. Specific gravity of dyeing sludge, fly ash, and PET granules were found 1.64, 2.27, and 1.33, respectively. The specific gravity of dyeing sludge, fly ash, and

Table 3 Characteristics of materials

Parameters	Construction materials		Waste materials		
	Cement	Sand	Dyeing sludge	Fly ash	PET granules
pH	–	–	6.70	6.30	–
EC (mscm^{-1})	–	–	2.54	0.49	–
Specific gravity	3	2.73	1.64	2.27	1.33
FM	–	2.63	2.78	1.07	2.33

Table 4 Oxide compositions of fly ash and textile dyeing sludge

Oxide	Fly ash (%)	Sludge (%)
Al_2O_3	22.69	23.3712
Fe_2O_3	4.76	20.5220
SiO_2	64.19	19.2084
SO_3	0.89	14.7977
CaO	1.08	9.8955
P_2O_5	0.67	2.8250
MgO	0.26	2.7304
TiO_2	3.70	2.4789
Na_2O	0.15	1.8301
Cl	–	0.8164
K_2O	1.28	0.5027
ZnO	0.01	0.3562
CuO	–	0.2930
MnO	0.03	0.1972
NiO	0.01	0.0948
Cr_2O_3	0.04	0.0806

PET granule is lower than sand and stone chips. So, there is a possibility to have a lightweight block. Usually, the specific gravity of dyeing sludge ranges from 1.1 to 2.54 [10, 13, 14]. FM of sand, sludge, and PET granules are 2.63, 2.78, and 2.33, respectively, and these are almost similar. The fineness of cement used in this study was found 99%. According to ASTM, a suitable cement fineness should be higher than 90%.

Heavy metals, i.e., Zn. Cu. Cr. Pb and Ni, were found 133, 239, 1.0, 1.8, and 8.5 $mgkg^{-1}$, respectively. The source of these metals is probably because of the type of dyes the industry used. Many metal pigments are being used to the dying units of the textile industry [15]. In the present analysis, Zn and Cu levels were 133 and 239 $mgkg^{-1}$, respectively, while Salma and Iqbal reported 328 and 265 $mg\ kg^{-1}$ [16]. From oxide composition analysis, 23% Al_2O_3, 20% Fe_2O_3 in sludge, and 64% SiO_2 in fly ash have been found by XRF Table 4.

22.69% and 23.37% alumina (Al_2O_3) were found in fly ash and dyeing sludge, respectively. It is well-documented that alumina acts as a cementing material in block or brick. The excess amount of alumina in brick makes it too hard and brittle [17]. Good quality brick or block contains 50–60% silica. Silica prevents raw bricks from cracking, shrinking, and warping. Iron oxide acts as a flux like lime, while iron also increases the blocks' durability and impermeability [18]. Silica measured 64.14% and 19.21% in fly ash and textile dyeing sludge in this study.

3.2 Properties of Block

Different combinations with three replication of stone chips, cement, sand, and waste materials have been used to fabricate the block. Two categories of the block were manufactured, i.e., sand replaced by waste materials (textile dyeing sludge, fly ash, and PET granules) with different percentages, and another category was a partial replacement of stone chips by PET granules in a varied proportion.

It is observed that compressive strength increases with the increase in waste materials up to 45% (15% sludge, 15% fly ash, and 15% PET granules) with a concurrent decrease in specific gravity Fig. 1. The compressive strength of $A_{100}S_{85}W_5$ (15% sand replaced by 5% dyeing sludge, 5% fly ash, and 5% PET granules) was found at 2.54 kg/mm^2.

Compressive strength decreased chronologically with the increase of waste materials from 20 to 30% Fig. 1. The specific gravity of fabricated blocks was reduced from 2.21 ($A_{100}S_{100}W_0$) to 1.79 ($A_{100}S_{10}W_{30}$) with the increase of waste materials. It means the lightness in the weight of the block compared to the control. Parallelly, water absorption capacity increased with the increase of waste materials (Fig. 2). Maximum water absorption capacity (20.50%) has been noticed after 28 days of curing at the $A_{100}S_{10}W_{30}$ combination. The specific gravity and water absorption capacity illustrate the pores of the block.
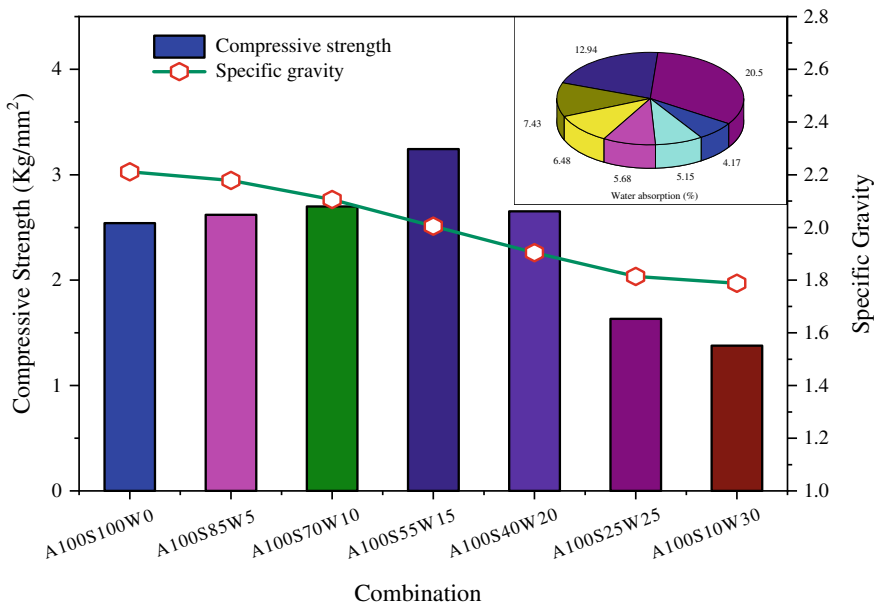
Fig. 1 Compressive strength, specific gravity, and water absorption capacity of the block where sand replaced by textile dyeing sludge, fly ash, and PET granules
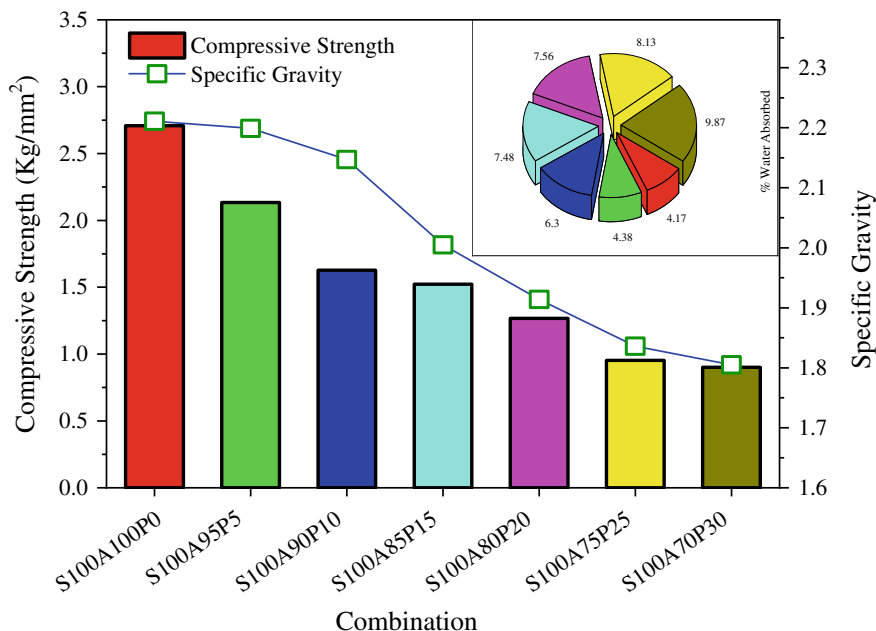
Fig. 2 Compressive strength, specific gravity, and water absorption capacity of the block where stone chips replaced by PET granules

A chronological decrease of compressive strength and specific gravity has been observed in the combination of stone chips replacement by PET granules Fig. 2. The highest compressive strength gained 2.71 kg/mm^2 at control treatment and reduced to 0.90 kg/mm^2 at $S_{100}A_{70}P_{30}$. This reduction in strength may be due to the frictional and bond strength differences between stone chips and PET granules.

Water absorption capacity also decreased sequentially, only 4.17% water absorbed by control where 30% stone chips replacement block by PET granules absorbed 9.87%. The blocks of stone chips replacement by PET granules are significantly useful compared to the control specimen.

Dyeing sludge contaminated by heavy metals and leaching curing water test at 7th, 14th, 21st, and 28th days performed from to trace the heavy metals. Leaching tests were carried out for the maximum waste material used specimen ($A_{100}S_{10}W_{30}$). From Table 5, it is observed that the possibility of extraction of heavy metal from the block is hardly expectable.

4   Conclusion

The maximum compressive strength, specific gravity for the first category (sand replaced by waste materials) were found 3.24 kg/mm^2 and 2.01, respectively, where

Table 5 Availability of heavy metal from curing water

Combination ID	Heavy metal	Unit	7 days	14 days	21 days	28 days
$A_{100}S_{10}W_{30}$	Zn	$mgkg^{-1}$	ND	ND	ND	ND
	Pb		ND	ND	ND	ND
	Ni		ND	ND	ND	ND
	Cr		ND	ND	ND	ND
	Cu		ND	ND	0.0043	0.0081

45% sand was replaced by waste materials (textile dyeing sludge, fly ash, and PET granules). Fabricated concrete block is lighter in weight than the control sample, and ordinary clay-fired brick. The negligible levels of heavy metal leaching were found from this block. Strength and specific gravity were found 2.134 kg/mm^2 and 2.20, respectively, for the second category (stone chips replaced by PET granules in different volumetric percentages) where 5% stone chips were replaced by PET granules, which is lower than the controlled sample and unadoptable. Considering the results, it can be summarized that the textile dyeing sludge, fly ash, and PET granules could be a potential source of raw materials to be used for lightweight block manufacturing, which may present an eco-friendly solution for the dumping problem associated with these waste materials.

References

1. Rasel MS, Das D, Khan MR (2020) Current scenario of textile sector in Bangladesh (2019); a comprehensive revie. Int J Innov Stud Sci Eng Technol 6:55
2. Bin AT, Behrose B, Ahmed S (2018) Utilization of textile sludge and public health risk assessment in Bangladesh. Sustain Environ Res 28:228–233. https://doi.org/10.1016/j.serj.2018.04.003
3. Islam MM, Mahmud K, Faruk O, Billah S (2011) Assessment of environmetal impacts for textile dyeing industries in Bangladesh. Int J Environ Sci Dev 2:428–436. https://doi.org/10.1109/GTEC.2011.6167665
4. Tamim M, Dhar A, Hossain S (2013) Fly ash in Bangladesh- an overview. Int J Sci Eng Res 4:4
5. Rasel AR Coal-based power projects still a distant dream. Dhaka Trib
6. Moghaddam TB, Karim MR, Soltani M (2013) Utilization of waste plastic bottles in asphalt mixture 2. Lab Invest 8:264–271
7. Subramani T, Pugal VK (2015) Experimental study on plastic waste as a coarse aggregate for structural concrete. Int J Appl Innov Eng Manag 4:144–152
8. Thomas RV, Nair DG (2015) Fly ash as a fine aggregate replacement in concrete building blocks. Int J Eng Adv Res Technol 1:47–51
9. Fataniya R, Maaze R, Kapadiya K, Pipalia PVF (2015) Experimental investigation of concrete masonry units with plastic bottle cores and PET fibers. Int J Sci Res Dev 3:705–708
10. Kulkarni GJ, Dwivedi AK (2012) Textile mill sludge as fine aggregate. Glob J Res Eng Ind Eng 12:21–25
11. Toolbox TE (2003) Solids and metals—specific gravities. In: Eng. ToolBox. https://www.engineeringtoolbox.com/specific-gravity-solids-metals-d_293.html. Accessed 29 Sep 2020

12. Nessa B, Rahman MM, Shammi M, Rahman MA, Chowdhury TR, Ahmad M, Uddin MK (2016) Impact of textile sludge on the growth of red amaranth (*Amaranthus gangeticus*). Int J Recycl Org Waste Agric 5:163–172. https://doi.org/10.1007/s40093-016-0126-6
13. Baskar R, Begum K, Sundaram S (2006) Characterization and reuse of textile effluent treatment plant waste sludge in clay bricks. J Univ Chem Technol Metall 41:473–478
14. Jahagirdar SS, Shrihari S, Manu B (2015) Reuse of incinerated textile mill sludge as adsorbent for dye removal. KSCE J Civ Eng 7:1982–1986. https://doi.org/10.1007/s12205-015-0731-3
15. Halimoon N, Yin RGS (2010) Removal of heavy metals from textile wastewater using zeolite Environment Asia. Environ 3(special issue) 3:124–130. https://doi.org/10.14456/ea.2010.51
16. Iqbal SA, Mahmud I Quader (2014) Textile sludge management by incineration technique. Procedia Eng 90:686–691. https://doi.org/10.1016/j.proeng.2014.11.795
17. Maaze R, Kumar V, Mishra SK (2016) Influence of marble and aluminium waste powder on the performance of bricks. Int J Eng Dev Res 4:907–912
18. Aziz DMA, A text book of engineering materials, BUET. Hafiz Book Center, Dhaka

Assessment of Hazardous and Precious Metal Content in E-Waste

T. T. Meem, M. S. Khan, M. M. Hassan, and R. Mamtaz

1 Introduction

E-waste is common terminology for an amalgam of electrical and electronic equipment (EEE) that has become obsolete to its users. It includes various devices like computers, computer peripherals, cellular phones as well as home appliances like refrigerators, air-conditioners, and washing machines. With an advancement of technology and shorter lifespans of electronic devices, e-waste is expected to grow to 52.2 MT in 2021 globally, with an annual growth of 3–4% [1]. In recent years with increasing economic growth, the electronic market has also escalated in Bangladesh. As a result, it is expected that the amount of generated e-wastes in Bangladesh will reach up to 4.62 MT by 2035, with a growth rate of 20% [2].

Electrical components contain various types of heavy metals, of which some are hazardous (lead, cadmium, chromium, etc.) and some are valuable (gold, silver, copper, etc.). Once turned the EEE into wastes, these toxic metals pose a serious risk to the environment and human health and, on the other hand, offer economic benefit if these valuable metals can be recovered successfully.

T. T. Meem (✉)
Department of Civil Engineering, Presidency University, Dhaka, Bangladesh

M. S. Khan
Institute of Water Modelling, Dhaka, Bangladesh

M. M. Hassan
International Training Network, Bangladesh University of Engineering and Technology, Dhaka, Bangladesh

R. Mamtaz
Department of Civil Engineering, Bangladesh University of Engineering and Technology, Dhaka, Bangladesh

In Bangladesh, most of the e-wastes are landed on the landfill along with other wastes and only a small fraction of e-waste is recycled. There are two types of recyclers in Bangladesh: registered recyclers and the informal sector. Registered recyclers who are very few in numbers, mainly dismantle, and separate the components from the collected e-wastes and then recycle some parts such as steel and copper in the local market. The other components which are rich in valuable metals are exported to foreign countries where value metal recovery has to be done [3]. The informal recyclers, known as Bhangari Businessmen, also sell some parts directly in the market. They also recover some value metals by open burning or following some crude methods without adopting any health or safety measures. Therefore, the establishment of an environment-friendly recovery process is the crying need of the present time to facilitate the economic benefit from e-wastes as well as to protect the environment and human health.

In the present-day world, two major contributors of e-wastes are computers and cellphones. The printed circuit board (PCB) of computer and cell phone contains a considerable amount of heavy metals compared to other components present in these two types of equipment. Usually, PCB contains various types of precious and toxic metals like gold, palladium, silver, copper, iron, tin, nickel, and lead[4]. There are some tested methods of recovering these metals from e-wastes such as pyrometallurgy, hydrometallurgy, and bio-hydrometallurgy [3]. Hydrometallurgical methods have some advantages over the pyro- metallurgical process like lower toxic residues and higher energy efficiency [5]. In hydrometallurgical processes, the aqueous solution is used to extract metals from e-wastes. After the solution is separated from the solids, it is often subjected to various processes of purification and concentration before the valuable metal is recovered, either in its metallic state or as a chemical compound. The hydrometallurgical recovery process usually involves oxidative leaching for the extraction of metals followed by separation and purification procedures [6].

The main objective of this study was to assess the content of valuable metals such as gold and silver in selected e-wastes. The present research adopted a simple modified hydrometallurgical process [7] to determine the contents of gold (Au) and silver (Ag) from RAM and PCB of computers and mobile phones. The study also assessed the removal potential of harmful metal lead (Pb) from these components.

2 Methodology

2.1 Sample Collection

In this study, three types of e-waste samples were used, such as PCBs of discarded computers and cell phones of different brands and RAMs of waste computers (Fig. 1). These samples were collected from the informal e-waste recyclers' shops (Bhangari Shops) located in Chankharphul and Elephant Road, Dhaka.

(a)   (b)

(c)
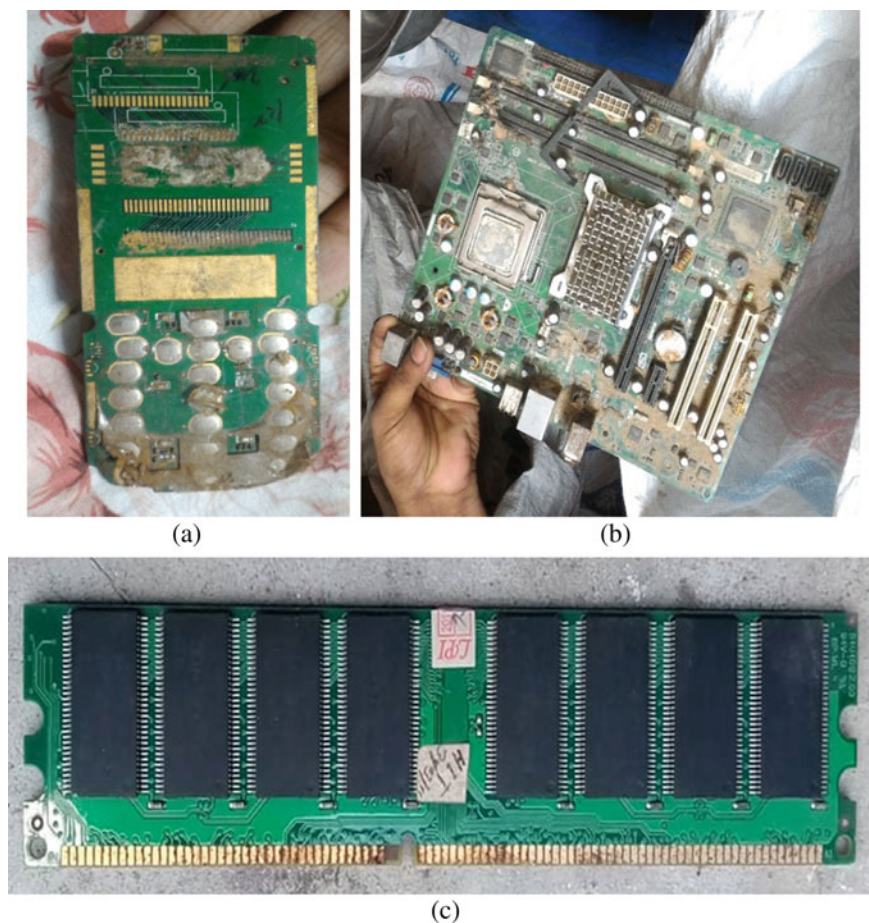
Fig. 1 **a** Mobile phone's PCB. **b** Computer's PCB and **c** RAM of a computer

2.2 Sample Preparation

After the collection of samples, the external components attached to PCBs and RAMs were removed, cut into small pieces, and cleaned off dust carefully. Before the experimentation, the samples were further crushed using a hammer into granular size for better reaction with acid. The increased surface area increases the reactivity and speeds up the chemical reactions. Such prepared RAM samples of about 1 gm and PCBs of 4 gm were used in the experimental procedures.

2.3 Experimental Process

The experimental process was carried out in three stages (Fig. 2) in Environmental Engineering Laboratory, BUET, following Dehchenari et al. [7]. Two sets of samples from each of the three items (PCB of mobile, PCB of computer, RAM of computer) were prepared to measure the metal concentration at two different stages. Each sample was decanted into five test tubes for five separate reading, and later the mean of the five readings was taken and standard deviation was calculated for increasing data reliability and accuracy. RAM samples of 0.53 gm and PCBs of 2 gm were used for each set. At stage 1, concentrated nitric acid (around 2.5 ml) was added to the ground RAM and PCB items and allowed for 1 h to complete the reaction. Then 4 ml aqua regia ($HCl + HNO_3$) was added to the samples to dissolve gold (stage 2). At this stage, brown NO_2 gas was released after adding aqua regia (Fig. 3a). The solution was then decanted, and the pieces were washed with 10 ml concentrated HCl acid so that all gold content was fed into the solution. Now H_2SO_4 was added to the solution for complete removal of HNO_3 (Fig. 3b) and sedimentation of lead sulfate (Stage 3). The time required for complete removal is around 45 min. At this stage, the solution's color was greenish-yellow. There was some emulsification observed due to silver chloride, a portion of which was separated through filtration.

The concentrations of heavy metals such as gold, silver, and lead of the prepared solutions were analyzed following the first and third stages of leaching. Each sample was diluted to 50 ml by adding distilled water, and thus, five samples of each item were prepared for analysis. The heavy metal concentration was measured using flame atomic absorption spectrophotometer (AAS) following the standard method (SM3111) [8].

Fig. 2 Flow diagram of the research methodology

Fig. 3 Experimental process. **a** Brown NO_2 gas formed at stage 2. **b** Final solution for analysis

3   Results and Discussion

The concentration of gold, lead, and silver in the prepared three samples of each PCB and RAM items at first stage leaching and final stage (stage 3) leaching has been measured using AAS and average concentration with standard deviation is presented in Table 1. Table 1 shows that only a very small number of metals (Au, Ag, and Pb) have been dissolved due to nitric acid addition at the first stage. Most of the gold has been detected at the final stage of reaction with aqua regia forming tetrachloroaurate (III) anions in solution.

After analyzing the concentration of gold, silver, and lead in prepared e-waste samples, the potential of the recovery of these metals has been determined based on the total amount of RAM and PCBs considered in this study and are presented in Figs. 4, 5, and 6, respectively.

From Fig. 4, it has been observed that the recovery potential of gold was found highest in computer's RAMs (3911 mg/Kg) among the three tested samples at the final stage of reaction as gold dissolves only in aqua regia. It also shows that computer

Table 1   Average concentration of gold, silver, and lead in e-wastes samples

Specimen	Stage	Gold (Au) concentration, mg/l (Mean $\pm$ SD)	Silver (Ag) concentration, mg/l (Mean $\pm$ SD)	Lead (Pb) concentration, mg/l (Mean $\pm$ SD)
RAM of computer	Stage 1	0.34 ± 0.11	0.00	2.37 ± 0.85
	Final stage	41.65 ± 9.43	0.03 ± 0.009	0.95 ± 0.31
PCBs of computer	Stage 1	0.46 ± 0.21	<MDL (0.01)	272.6 ± 86.9
	Final stage	5.88 ± 1.83	<MDL (0.01)	23.54 ± 4.89
PCBs of mobile	Stage 1	0.01 ± 0.005	0.04 ± 0.012	3.48 ± 1.54
	Final stage	1.24 ± 0.26	0.70 ± 0.25	4.28 ± 1.75
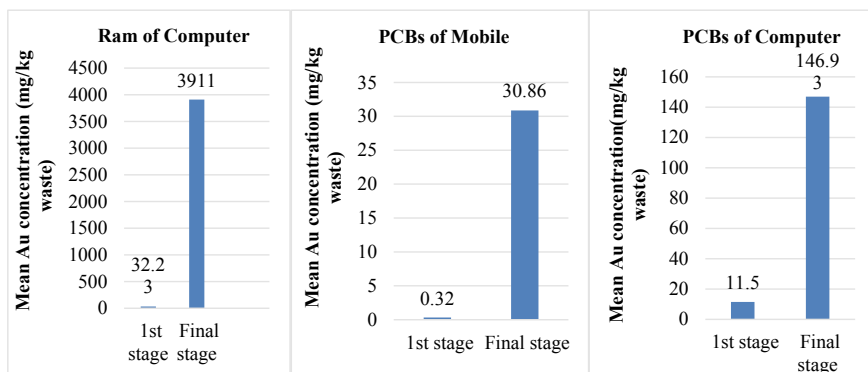
Fig. 4   Gold (Au) content in computer's RAM and PCBs of mobile phones and computer
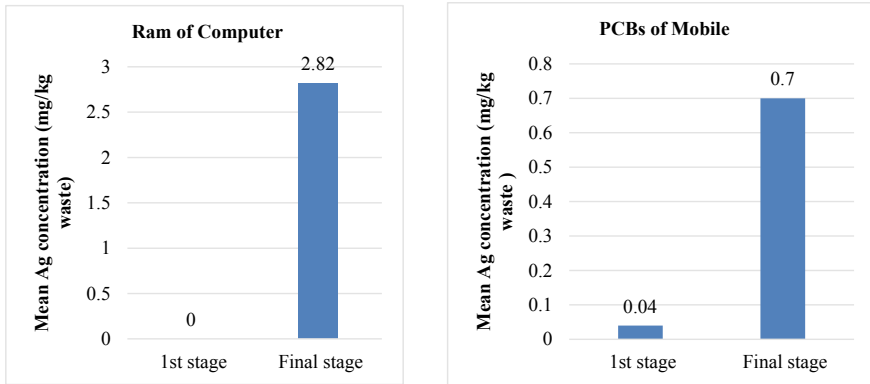
Fig. 5 Silver (Ag) content in RAM of computer and PCBs of mobile phones
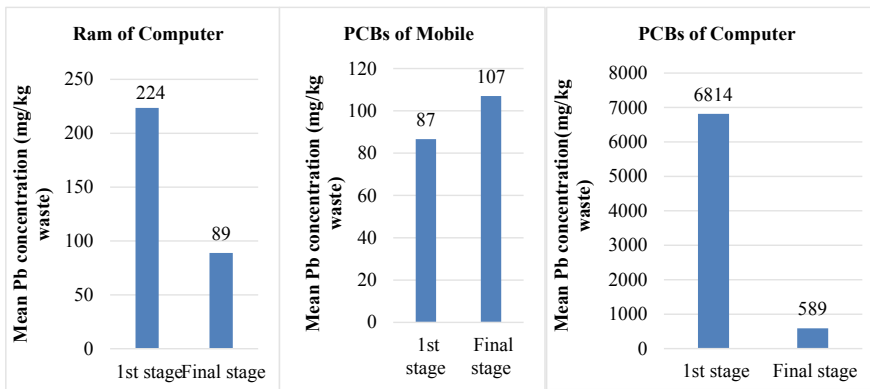
Fig. 6 Lead (Pb) content in computer's RAM, and mobile phone and computer's PCB

PCB contains a higher amount of gold (146.93 mg/kg) than the mobile phone's PCB (30.86 mg/kg).

Figure 5 shows that the amount of silver in mobile phone PCB and computer RAM is not much. However, silver content in computer's RAM is higher (2.82 mg/kg) than that of the mobile phone's PCB (0.7 mg/kg). From Table 1, it is also found that silver content in computer PCBs is undetectable because of a very small amount.

Regarding the concentration of lead in the e-waste samples, a higher concentration was observed in RAM and computer PCB in the first stage of leaching as soluble lead nitrate was formed in this stage (Fig. 6). At the final stage, after adding H_2SO_4, lead sulfate was formed which is insoluble and precipitated; thus, it showed the reduced lead concentration in the solution at the final stage. Figure 6 shows that the highest reduction (91%) of lead was found for computer's PCB. In contrast, it was 60% for computer's RAM. However, higher lead content was found in mobile phones PCB

at the final stage and the reason for this increase could not be explained and needs further investigation.

Dehchenari et al. [7] found the average amount of gold in CPU boards as 0.138 mg/L after the first stage reaction, whereas the amount of gold for RAM, computer, and mobile PCBs were found as 0.34 mg/L, 0.46 mg/L, and 0.013 mg/L, respectively, in the present study. The concentration of gold found by Dehchenari et al. [7] at the final stage of leaching is similar to this study. However, the amount of silver found in the present research is much lower than that of Dehchenari et al. [7]. Petter et al. [9] characterized mobile PCBs using three different types of reagents. Characterization using aqua regia shown gold and silver concentration as 95.09 and 136.52 mg/kg waste, respectively. 123.48 (mg/kg) Au and 28.8 (mg/kg) Ag were found through leaching by the commercial cyanide-based reagent. Thiosulfate (sodium, ammonium)-based leaching concentrations were lowest which were 9.94 (mg/kg) Au and 37.34 (mg/kg) Ag. Compared with these methods, the results of this paper found significantly less silver content in all the samples. Maksym et al. [10] separated all metallic and nonmetallic components of RAM by using chemical treatment and subsequent leaching processes to liberate gold from gold-plated components. Their result showed that more than 2204 mg/kg RAM could be recovered through this process, whereas the result of this paper found that the recovery potential of gold in RAM is 3911 mg/kg. Reviewing and comparing these research findings, it can be said that RAM and PCB of computer and mobile phones contain a considerable amount of gold and silver.

4 Conclusions

E-waste is often called 'Urban Mines' as it contains valuable and precious metals. The present research shows that PCB and RAM contain a significant amount of gold. Computers RAM is enriched with more gold than computer's PCB. Therefore, there exists good potential for recovery of this precious metal if the hydrometallurgical method can be applied safely. However, the silver content in RAM and PCB is insignificant. The content of hazardous metal (lead) in computer's PCB is higher than that of RAM. Recovery of these metals can reduce the dependency on natural minerals as well as decrease the risk of environmental pollution.

References

1. Baldé CP, Wang F, Kuehr R, Huisman J (2015) The global e-waste Monitor 2014. United Nations University, IAS-SCYCLE, Bonn
2. Mamtaz R, Ahmed S, Noor I, Rahman S, Shams P, Gulshan F (2019) Generation of E-waste and its future trend in Bangladesh. In: Proceedings of international research conference (IRC 2019), June 11–12, Copenhagen, Denmark, pp 655–660
3. CERM (2018) Assessment of generation of E-waste, it's impact on environment and resource recovery potential in Bangladesh. Research Project Report of Centre for Environmental and Resource Management (CERM), BUET, Dhaka Bangladesh
4. Chatterjee S (2012) Sustainable electronic waste management and recycling process. Am J Environ Eng 2:23–33. https://doi.org/10.5923/j.ajee.20120201.05
5. Tuncuk A, Akcil A, Yazici EY, Devici H (2012) Aqueous metal recovery techniques from e scrap: hydrometallurgy in recycling. Miner Eng 25:28–37. https://doi.org/10.1007/s11356-016-8313-6
6. Schlesinger ME, King MJ, Sole KC, Davenport WG (2011) Extractive metallurgy of copper, 5th ed. Elsevier Ltd. https://doi.org/10.1016/C2010-0-64841-3
7. Dehchenari M, Hosseinpoor S, Aali R, Iran NS, Mehdipour M (2017) Simple method for extracting gold from electrical and electronic wastes using hydrometallurgical process. Environ Health Eng Manage J 4(41):55–58. https://doi.org/10.15171/EHEM.2017.08
8. SM 3111(2017) Metals by flame atomic absorption spectrometry. Standard methods for the examination of water and wastewater. http://www.standardmethods.org. Accessed 20 June 2018
9. Petter PMH, Veit HM, Bernardes AM (2015) Leaching of gold and silver from printed circuit board of mobile phones. Rem Rev Escola de Minas 68(1):61–68. https://doi.org/10.1590/0370-44672015680152
10. Tatariants M, Yousef S, Denafas G, Tichonovas M, Bendikiene R (2017) Recovery of gold, other metallic and non-metallic components of full-size waste random access memory. J Clean Prod. https://doi.org/10.1016/j.jclepro.2017.11.132

Numerical Modelling of the Rate-Dependent Characteristics of Laterally Loaded Single Pile in Dry Sand

A. K. Saha, M. Saitoh, N. R. Shrestha, and C. S. Goit

1 Introduction

Pile foundations are subjected to significant amount of lateral load in coastal and offshore areas due to wind, earthquake, waves and water pressure. These lateral loads come in the form of pseudo-static and cyclic load with a wide range of amplitudes and rates (velocities) at different time events. A number of experimental investigations have been carried out in the past considering the maximum applied load, amplitude and the number of cycles of loading [1–5]. However, to the best of the authors' knowledge, the loading rate effects on the lateral pseudo-static and cyclic loads have been neglected in most of the experimental and numerical investigations. For a safe, efficient and cost-effective design of soil pile systems, experimental and numerical investigations are required to predict the response of laterally loaded piles under different loading rates.

This paper presents the finite element (FE) analysis for simulating the rate-dependent characteristics of a laterally loaded single pile foundation system. A scaled model single pile embedded in dry sand subjected to different rates of lateral pseudo-static and cyclic loadings is considered for the numerical modelling. Numerical analysis is carried out using nonlinear finite element software PLAXIS 3D. Effects of loading rate on the failure pattern of the soil near the pile are analysed in terms of bearing capacity of the pile based on the load–deflection curve at the pile head, bending moment distributions and pile deflections profile along the pile depth, and soil surface deformation pattern.

A. K. Saha (✉)
Bangladesh Atomic Energy Commission, Dhaka, Bangladesh

M. Saitoh · N. R. Shrestha · C. S. Goit
Department of Civil and Environmental Engineering, Saitama University, Saitama, Japan
e-mail: saity@mail.saitama-u.ac.jp

C. S. Goit
e-mail: chandra@mail.saitama-u.ac.jp

2 Numerical Modelling

The numerical model developed in this research is based on the reduced scale experimental model investigations on shaking table carried out at Saitama University, Japan [6, 7]. The scaling law derived by Kokusho and Iwatate [8] incorporating the effect of low confining pressure of soil under 1 g condition is used in this study. Similar experimental studies on the soil–pile foundation system were carried out in the past [9, 10]. A solid cylindrical pile made of polyoxymethylene homopolymer (POM-H) with a diameter $(d) = 40$ mm and length $(L) = 900$ mm rigidly connected to a solid pile head (125 mm × 125 mm × 125 mm) and embedded in dry Gifu sand is modelled.

Soil is modelled using ten-nodded tetrahedral elements. The nonlinear behaviour of soil is modelled using Mohr–Coulomb failure criteria (linear elastic perfectly plastic) with non-associated flow rule. To capture the behaviour of pile adjacent to soil under considered loadings (discussed later), pile is modelled using solid elements with linear elastic properties (Fig. 1).

Discretization is done according to Kramer (1996) and Kuhlmeyer and Lysmer (1973), and the average element dimension (AES) that is representative for refinement degree of the mesh should be limited to 1/8 to 1/5 of the shortest wavelength considered in the analysis [11]. A total of 27,415 elements with average element size 0.35 m are used to model the soil–pile system. In order to simplify the model, pile cap is not modelled. A vertical gap of 35 mm between the top surface of sand and pile head is provided to eliminate the resistance of the pile head under the applied different rate pseudo-static and cyclic loadings. The Young's modulus of soil for the model is same as the equivalent low-strain Young's modulus obtained from the free field response analysis of Gifu sand [12], and the distribution profile is considered
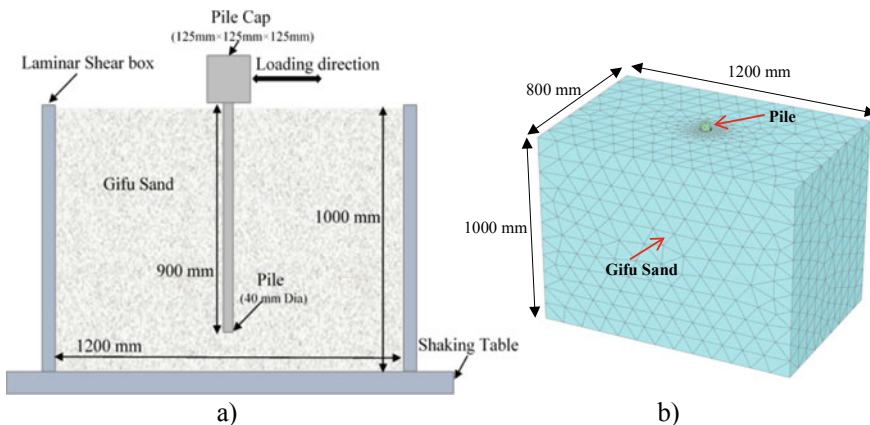
Fig. 1 **a**) Schematic layout of the experimental setup [6, 7] and **b**) 3D FE model geometry of the single pile–soil system

Table 1 Material properties of the FEM

Parameter	Symbol	Sand	Pile
Young's modulus of soil (kN/m²)	E	38,820	2.8×10^6
Poisson's ratio	ν	0.45	–
Cohesion (kN/m²)	c	2	–
Friction angle (°)	ϕ	40.7	–
Dilatancy angle (°)	ψ	16	–

to be linearly increasing with the depth (inhomogeneous considerations). Material properties for the model are given in Table 1.

Due to lateral dynamic loading, gapping and slippage occur at the pile–soil interface, which is a major source of stiffness degradation of the pile–soil foundation system. In this study, the pile–soil interface is modelled with six-nodded triangular elements connecting both sides of pile elements to soil elements. Interface nonlinearity is simulated as surfaces with frictional slip elements having a strength reduction factor R_{inter}, considered as 0.85 equivalent to 85% of adjacent Gifu sand shear strength. Prescribed boundary displacements are introduced at the boundaries of model for equal experimental condition. Fixed deformation boundary conditions are imposed on the edges of the model, while free field is imposed in horizontal loading direction allowing soil to move in horizontal shear as a free field. The pile head is fixed in all directions but free in horizontal direction with prescribed surface displacement (displacement control) to simulate the experimental conditions. In pseudo-static case, a prescribed lateral displacement (pull and push) of 20% of the pile diameter, i.e. 8 mm, is applied at the top of the pile with three different loading rates: 0.01, 10 and 500 mm/s, i.e. very low to high. For cyclic case, on the other hand, four different prescribed displacement amplitudes of 5% of d (2 mm), 10% of d (4 mm), 15% of d (6 mm) and 20% of d (8 mm) with three different loading rates of 0.01, 10 and 500 mm/s are applied for three consecutive cycles. Loading rates are defined by adding dynamic displacement multiplier in horizontal direction with time (Fig. 2). Analyses comprise of three consecutive steps: (a) generation of initial stresses, (b) activate pile in the model and (c) apply loads (pseudo-static and cyclic actions). A
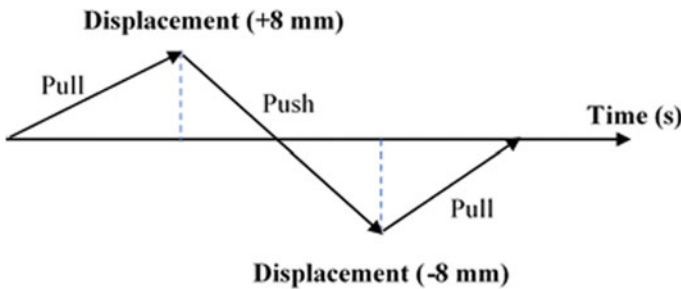
Fig. 2 Displacement multiplier in terms of loading rate in FEM

constant dynamic time step, $\Delta t = 0.001s$ is considered. Newmark implicit time integration scheme is employed for iteration [11, 13]. Validation of the numerical result is carried out with the experimental result from Shrestha et al. [6, 7].

3   Results and Discussions

Lateral resistances are measured for 8 mm pile head deflection under very low loading rate (0.01 mm/s), high loading rate (10 mm/s) and very high loading rate (500 mm/s) and are presented in Fig. 3a. The result shows that the lateral load capacity of pile increases with the increase in the loading rate for both pull and push directions. The initial stiffness increases, while the residual displacement decreases with the increasing loading rate. It is also found that the load deflection behaviour is nonlinear and loading rate effects is visible in loading part of the load deflection curves. In the unloading part, however, there is no significant change. In contrast to the effects of loading rate on pile capacity, the magnitude of bending moment and pile deflection along the pile length is unaffected even for large range of loading rate considered in the numerical investigation, as shown in Fig. 3b, c. This suggests that the failure pattern of soil near the pile is consistent regardless of different loading rates.

In the case of cyclic loading, three cycles of ±2 mm, ± 4 mm, ±6 mm and ±8 mm displacements with loading rates of 0.01, 10 and 500 mm/s are applied. Results presented in Fig. 4 show a similar trend of rate-dependent characteristics. With the
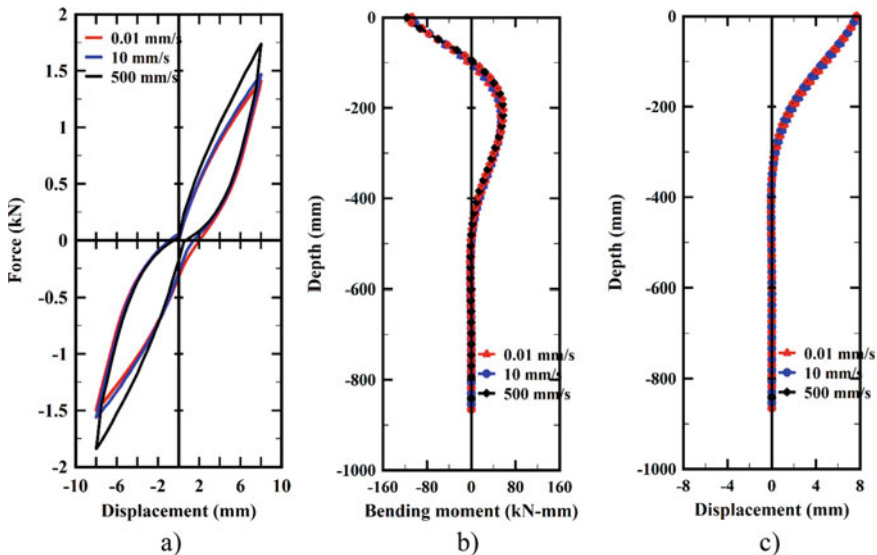
Fig. 3 **a**) Force–displacement relationship **b**) Bending moment distribution along the pile length and **c**) Lateral deflection of pile
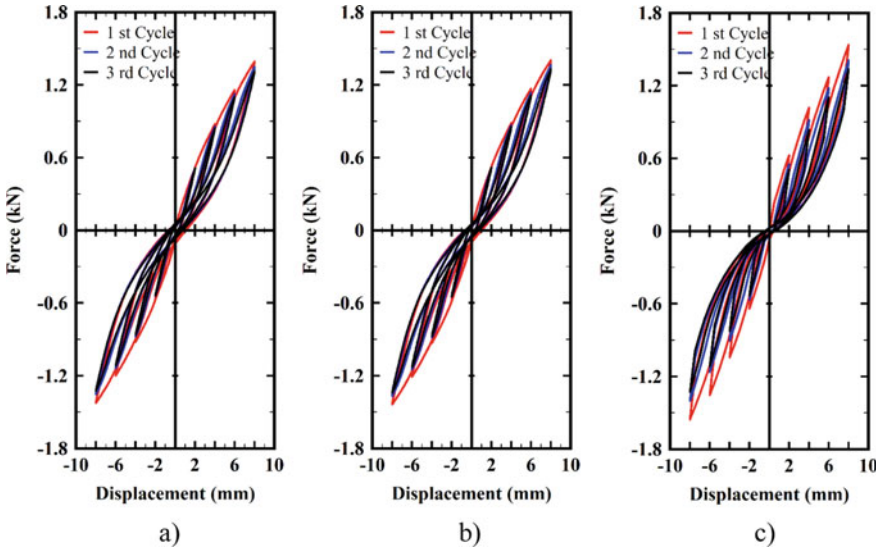
Fig. 4 Force–displacement relationship for cyclic loading: **a**) 0.01 mm/s. **b**) 10 mm/s and **c**) 500 mm/s

increase in loading rate, the bearing capacity of pile increases. It is also observed that due to the increase in the number of loading cycle, the bearing capacity of pile decreases while the residual displacement (accumulated displacement) increases.

To find out the reason behind this rate-dependent characteristics of soil–pile system, soil surface deformation pattern are investigated. From obtained results, a noteworthy change is found in soil surface displacement contours for 8 mm displacement with different loading cases (0.01, 10 and 500 mm/s). Figures 5 and 6 show a discernible decrease in the displacement of soil near the pile in both horizontal loading (x) and vertical (z) direction appear when a very high velocity of 500 mm/s
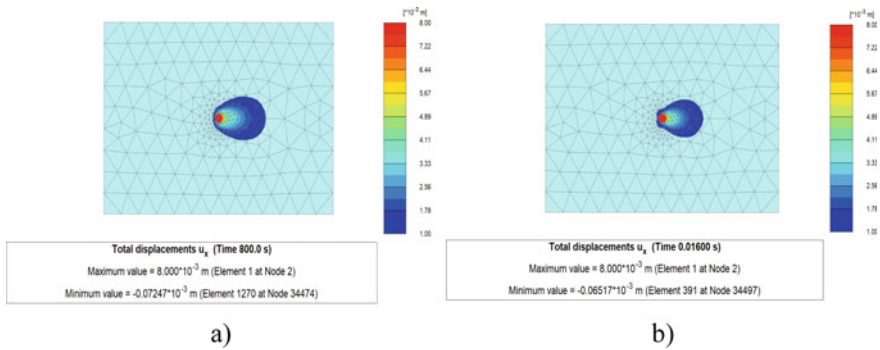
Fig. 5. Soil surface deformation near the pile in loading direction. **a**) 0.01 mm/s and **b**) 500 mm/s
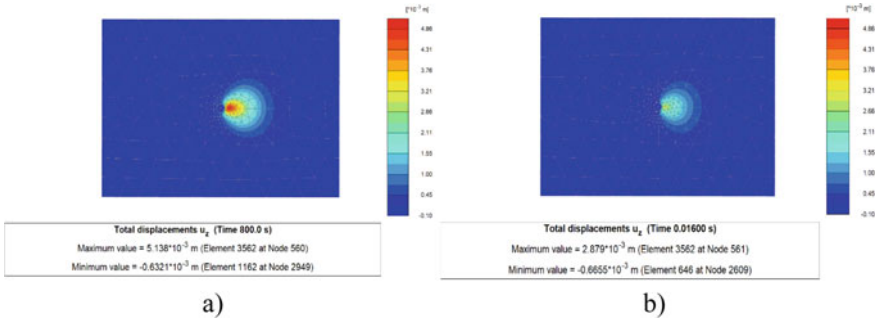
Fig. 6. Soil surface deformation near the pile in vertical direction. **a)** 0.01 mm/s and **b)** 500 mm/s
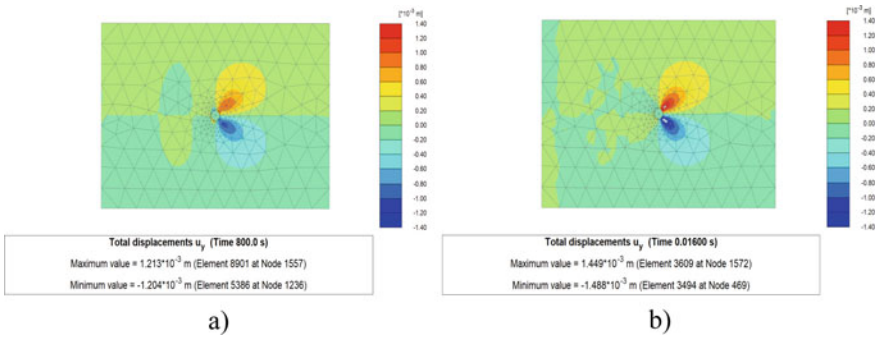
Fig. 7. Soil surface deformation near the pile in perpendicular to loading direction. **a)** 0.01 mm/s and **b)** 500 mm/s

loading is applied. Figure 7 shows an increase in the displacement of soil near the pile in perpendicular to loading direction (y) at 500 mm/s.

Kimura et al. [14] proposed a relation between soil viscosity and inertial force with pile resistance force (statnamic loading) for an axially loaded pile.

$$F_{\text{static}} = F_{\text{max}} - \text{CV} - \text{Ma} \tag{1}$$

where F_{max}= maximum reaction force, F_{static}= initial static reaction force, M= mass of the soil–pile system, a= acceleration, C= damping coefficient and V= rate of loading. Equation (1) was derived through a simple vibration theory based on an assumption that a vertical vibrating pile generates a simple single degree of freedom system. In reality, however, CV terms may consist of not only the effect of viscosity of soil; but also an inertia effect of soil mass near the pile: the mass of soil is accelerated during rapid pile moving even with a constant pile head velocity. So, CV is a conceptional representative of such complicated behaviour of neighbouring soil and details should be investigated. So far, it could be inferred that the bearing capacity increases due to such CV effects during rapid loadings.

   This inference may be deduced from the numerical result shown in Figs. 5 and 6 which shows a notable decrease in the displacement of soil near the pile for high velocity 500 mm/s loading. This may be attributed to the resistance due to CV effects including the soil mass inertia. Meanwhile, the displacement of soil in perpendicular to loading direction (y) tends to increase (Fig. 7): this increase could be an alternative moving of soil mass, which is disturbed in the moving to loading and vertical directions.

4   Conclusions

This paper presents a finite element (FE) analysis for a scaled model single pile embedded in dry sand subjected to different rates of lateral pseudo-static and cyclic loadings. Obtained results show that the lateral load bearing capacity of the pile increases significantly with the increase in the loading rate. The bending moment and lateral deflection along the pile are independent of rate-dependent behaviour, suggesting similar failure mode for different loading velocity. The soil surface deformation near the pile may be attributed to the resistance of soil due to the combined effects of soil viscosity and inertia of soil mass near the pile. These findings provide a valuable understanding to engineers in evaluating the performance of pile foundations under lateral loading more precisely.

References

1. Zhang C, White D, Randolph M (2011) Centrifuge modeling of the cyclic lateral response of a rigid pile in soft clay. J Geotech Geoenviron Eng 137(7):717–729
2. Harry PG (1982) Single pile response to cyclic lateral load. J Geotech Eng Div 108(3):355–375
3. Seed HB, Lundgren R (1954) Investigation of the effect of transient loadings on the strength and deformation characteristics of saturated sands. ASTM 54:1288–1306
4. Nguyen QH (2008) Rapid load testing of piles in sand, effects of loading rate and excess pore pressure. Master thesis, Hanoi University of Civil Engineering, Vietnam
5. Suits LD, Sheahan TC, Kong L, Zhang L (2007) Rate-controlled lateral-load pile tests using a robotic manipulator in centrifuge. Geotech Test J 30:13138. https://doi.org/10.1520/GTJ13138
6. Naba RS, Saitoh M, Saha AK, Goit CS (2020) Frequency- and intensity-dependent impedance functions of laterally loaded single piles in cohesionless soil. Soils Found. https://doi.org/10.1016/j.sandf.2020.11.004
7. Naba RS, Saitoh M, Saha AK, Goit CS (2020) Rate –dependent cyclic lateral load test on a single pile in sand. In: Proceedings of the 5th international conference on civil structural and transportation engineering (ICCSTE'20), Paper no. 231. https://doi.org/10.11159/iccste20.231
8. Kokusho T, Iwatate T (1979) Scaled model tests and numerical analyses on nonlinear dynamic response of soft grounds. Proc Jpn Soc Civ Eng 1979(285):57–67

9. Goit CS, Saitoh M (2013) Model tests and numerical analyses on horizontal impedance functions of inclined single piles embedded in cohesionless soil. Earthq Eng Eng Vib 12:143–154. https://doi.org/10.1007/s11803-013-0158-0

10. Ullah MS, Kajiwara K, Goit CS, Saitoh M (2019) Frequency and intensity dependent dynamic responses of soil-steel pipe sheet pile (SPSP) foundation-superstructure system. Soil Dyn Earthq Eng 125:105730. https://doi.org/10.1016/J.SOILDYN.2019.105730

11. Brinkgreve R, Egin E, Swolfs W (2017) User's manual for plaxis 3D.Delft University of Technology & Plaxis bv, The Netherlands

12. Goit CS, Saitoh M (2014) Model tests on horizontal impedance functions of fixed-head inclined pile groups under soil nonlinearity. J Geotech Geoenviron Eng 140:4014023. https://doi.org/10.1061/(ASCE)GT.1943-5606.0001127

13. Taha AEI, Naggar MH, Turan A (2015) Numerical modelling of the dynamic lateral behavior of geosynthetics-reinforced pile foundation system. Soil Dyn Earthq Eng 77(2015):254–266

14. Kimura M, Hasegawa M (1969) Statnamic load tests on model pile group and piled raft in sand: JSCE, 2004. In: Lee KL, Seed HB, Dunlop P (eds) Effect of transient loading on the strength of sand. 7th international conference soil mechanical found engineering 1:239–247

Macro- and Micro-mechanical Responses of Granular Materials Under Different Stress Paths Using DEM

M. M. Sazzad, M. S. Azad, and A. Ghosh

1 Introduction

Stress path is very important in geotechnical engineering which represents the successive states of stress in granular materials such as sand during loading or unloading while carrying out the laboratory tests on test specimens. Due to the variation of the stress states, granular materials also respond differently. The study of stress paths is important for formulating different constitute equations. The stress paths usually studied in geotechnical engineering include conventional triaxial compression, triaxial compression, axial extension, plane strain compression, mean stress compression, reduced triaxial compression, reduced triaxial extension, and hydrostatic compression. Being a very important part of geotechnical engineering studies, numerous experimental studies were carried out and reported in the literature considering stress paths [1–3]. The experimental results are then used to develop constitutive equations to predict the complex behavior of granular materials under different loading conditions. Since the constitutive modeling of granular materials under different loading conditions mainly depends on the boundary behavior obtained from the laboratory tests without considering the inherent particulate behavior, the geotechnical engineers often rely on the experiences and judgments. To develop a constitutive model based on the inherent micro-mechanics, the evolution of the microstructures and their characteristics must be incorporated into the constitutive

M. M. Sazzad (✉)
Department of Civil Engineering, Rajshahi University of Engineering & Technology, Rajshahi, Bangladesh

M. S. Azad
Department of Civil and Environmental Engineering, Konkuk University, Seoul, Republic of Korea
e-mail: samdaniazad@konkuk.ac.kr

A. Ghosh
Department of Civil Engineering, Port City International University, Chittagong, Bangladesh

laws. Few studies in the literature have attempted to understand the complex inherent microstructures that evolve under complex loading conditions. Among others, Ng [4] studied six different stress paths and indicated that simulated behavior is very similar to the laboratory results under different loading conditions for sands. It was also reported that the difference between the triaxial compression and plane strain compression is very similar to that observed for sands. A comparison between the conventional triaxial compression and plane strain compression was also reported by Sazzad and Suzuki [5], and a strong correlation between the evolution of the stress–strain and the fabric ratio–strain was established under these loading conditions. Their study observed a unique macro–micro-relationship regardless of the stress paths and loading conditions. Similar other studies in the literatures [6–11] reported the influence of stress paths on the macro-scale (behavior at the boundary) and the micro-scale (behavior at the particle level). In this paper, a comprehensive study is attempted to explore both the macro- and micro-mechanical behaviors of granular materials under four different stress paths namely triaxial compression, plane strain compression, axial extension, and mean stress compression. To carry out the simulation, a numerical sample consisting of spheres was prepared. In this study, spheres were used to reduce the computational costs of the simulation. The isotropically compressed sample was subjected to four different stress paths. Same isotropically compressed sample was used for each simulation to eliminate the biasness of the initial fabric prior to shear of the sample under different stress paths. The simulated data were investigated comprehensively, and the results were reported.

2 Discrete Element Method

The discrete element method (DEM) is a very popular method nowadays to study the microstructural behavior of a granulate system. It is introduced by Cundall and Strack [12]. It is widely used in different branches of science and engineering particularly in geotechnical engineering [4, 6, 9]. The basic structures and equations involved in DEM are very simple, yet its computer programming is complicated and requires huge time to run. Newton's second law of motion is used to obtain the displacement by double integrations for a very small time step. Force–displacement law is used to compute the force using the incremental displacement. The equations involved are as follows:

$$m\ddot{x}_i = \sum F_i, \quad i = 1 - 3 \tag{1}$$

$$I\ddot{\theta} = \sum M \tag{2}$$

where F_i, M, m, I, $\ddot{x}_i$, and $\ddot{\theta}$ are the force components, moment, mass of particle, moment of inertia, translational acceleration components, and rotational acceleration, respectively.

3 Computer Program

In this study, the computer program OVAL is used [13, 14]. The code is written in FORTRAN language and can run both on Windows and Linux platforms. OVAL was used in many simulations earlier, and its efficacy has been established through several publications [13–17]. A linear contact model is used in the present study. In the linear contact model, three linear springs are used. One linear spring is used in the normal direction, and the others are used in the tangential directions to compute normal and shear forces, respectively. Friction sliders have also been used to facilitate the control of slippage between particles and to incorporate the effect of friction angle. The viscosity coefficients (translation and rotational body damping) in OVAL are a fraction of the critical damping.

4 Sample Generation and Preparation

A numerical sample is generated in a cubical frame. The particles were idealized as spheres to reduce the computational cost of simulation. Consideration of complex particle shapes and a huge number of particles would otherwise require a huge computation time. The spheres were placed in the cube shape sample with the variation of the particle diameters randomly. A representative sample was used, and the number of particles of the representative sample was 8000. The initially generated sample was subjected to isotropic compression step by step by using the periodic boundary, a boundary condition in which a particle that straddled a periodic boundary has a numerical image at the opposite boundary, till the isotropic stress reached 100 kPa. When the isotropic stress reached 100 kPa, the void ratio of the sample became 0.57. It should be noted that the interparticle friction at the stage of the isotropic compression was intentionally turned off to ensure the formation of the densest sample. Later, the desired interparticle friction angle is introduced before the start of the simulation.

5 Simulation Conditions

Simulation of triaxial compression, axial extension, plane strain compression, and mean stress compression was conducted. In the case of the triaxial compression test, the vertical height along x_1—direction decreased with a very small strain increment of 0.00002%, while the stresses in the other two directions (x_2—direction and x_3—direction) remained constant (100 kPa). In the case of the axial extension test, the vertical height along x_1—direction increased with a very small strain increment of 0.00002%, while the stresses in the other two directions (x_2—direction and x_3—direction) remained constant (100 kPa). In the case of the plane strain compression

Table 1 DEM parameters used in the simulations

DEM parameters	Values
Normal contact stiffness, k_n (N/m)	1×10^6
Shear contact stiffness, k_s (N/m)	1×10^6
Mass density (kg/m^3)	2650
Increment of time step (s)	1×10^{-6}
Interparticle friction coefficient (μ)	0–0.50
Damping coefficients	0.05

test, the vertical height along x_1—direction decreased with a very small strain increment of 0.00002%, while the stress in x_3—direction remained constant (100 kPa) and the increment of strain in x_2—remained is zero. In the case of the mean stress compression, the vertical height along x_1—direction decreased with a very small strain increment of 0.00002%, while the mean stress remained constant by adjusting the movement of the other two boundaries along x_2—direction and x_3—direction. The DEM parameters and their corresponding values are presented in Table 1. The simulated conditions are depicted in Fig. 1 as well. It should be noted that the same isotropically compressed sample was used in the simulation, so that no bias of the simulated results was noticed due to the variation of the initial fabric of the sample.

6 Macro-mechanical Behavior

The macro-mechanical behavior is discussed in this section. The relationship between the deviatoric stress and mean stress is depicted in Fig. 2. Here, the deviatoric stress is defined as $q = \sigma_1 - \sigma_3$, and mean stress is defined as $p = (\sigma_1 + \sigma_2 + \sigma_3)/3$, where σ_1, σ_2, and σ_3 are the stresses along x_1, x_2, and x_3 directions, respectively. Figure 3a depicts the evolution of deviatoric stress with axial strain ε_1. The simulated behavior of the present study is very similar to that observed in the experimental and numerical investigation [4, 5, 10, 11, 18]. The highest deviatoric stress is obtained for plane strain compression (PSC). This is also in accordance with similar other studies in the literature [4, 9]. The deviatoric stress is the minimum for mean stress compression (MSC) as expected. This is due to the continuous rearrangement of the contact fabric during MSC to maintain the target mean stress [4]. Triaxial compression (TC) and axial extension (AE) depict the intermediate behavior where the deviatoric stress in AE is greater than TC [4]. This behavior is consistent with that observed in the sand. The evolution of the volumetric strain defined as $\varepsilon_v = \varepsilon_1 + \varepsilon_2 + \varepsilon_3$ with axial strain ε_1 is depicted in Fig. 3b. The positive sign of ε_v indicates compression, while the negative sign indicates dilation. The compressive behavior is followed by huge dilative behavior regardless of the stress path applied. Such tendency is usual in dense sand. The huge dilation observed in this study particularly in AE is related to the excessive dense soil (void ratio = 0.57) as compared to the other studies in the literature [4, 8, 10].
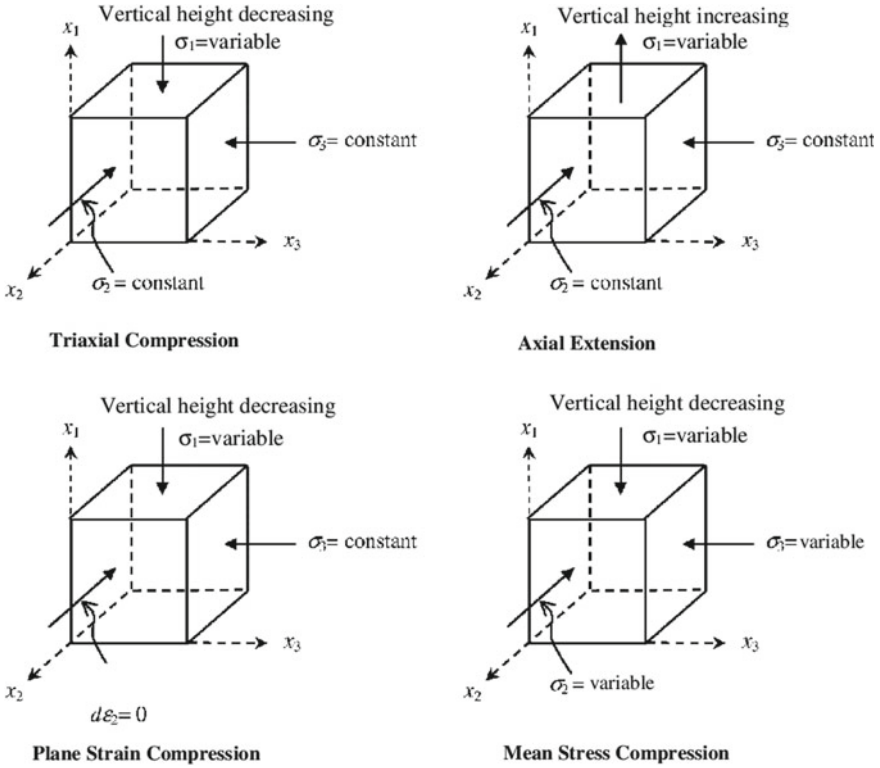
Fig. 1 Graphical representation of the simulation conditions for different stress paths

Fig. 2 Relationship between the q and p for different stress paths
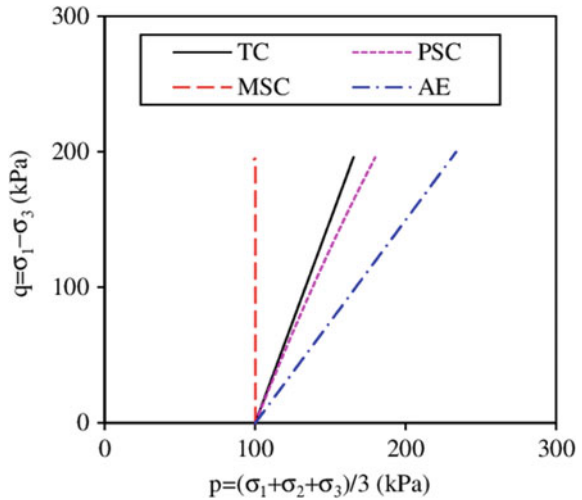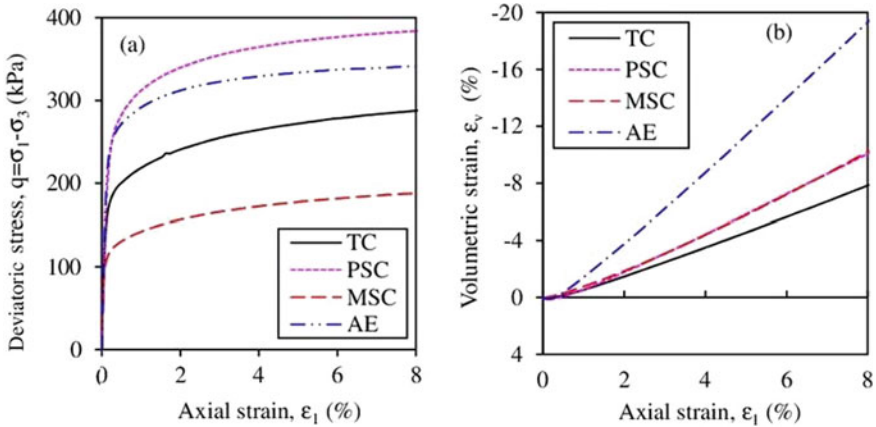
Fig. 3 **a** Relationship between **a** q and ε_1, **b** ε_v and ε_1 for different stress paths

7 Macro-mechanical Behavior

The evolution of different micro-mechanical quantities is discussed in this section. The evolution of the average coordination number defined as twice the total number of contacts divided by the total number of particles considered in the simulation with axial strain is depicted in Fig. 4a. A sharp decrease of average coordination number at the beginning of shear is noticed regardless of the stress path applied. This is because of the disintegration of contacts between particles at the beginning of shear and the fabric of the sample becomes anisotropic from the isotropic state. Although the isotropic condition is the same, a huge loss of average coordination number is
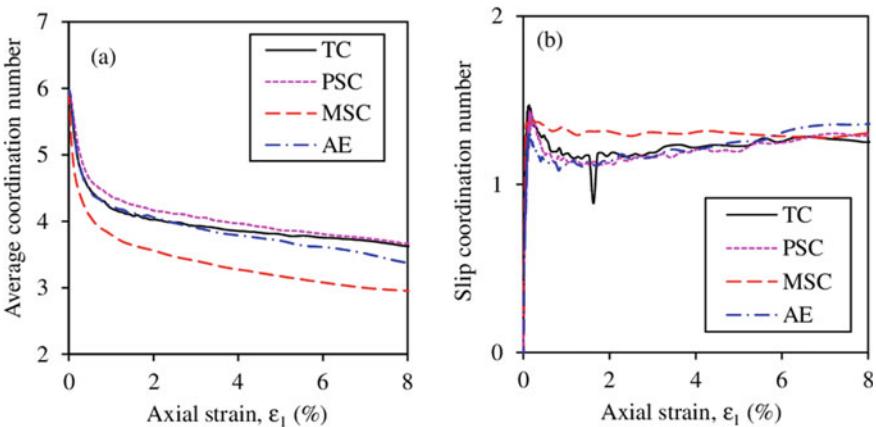
Fig. 4 Evolution of coordination number with axial strain. **a** Average coordination number. **b** Slip coordination number

observed for MSC compared to the other stress paths like TC, PSC, and AE. In the case of MSC, the boundaries of the sample need to move to adjust the target mean stress, and consequently, more contact disintegration takes place resulting in the decrease of average coordination number. On the contrary, the evolution of slip coordination number defined as twice the total number of slip contacts divided by the total number of particles with axial strain is depicted in Fig. 4b. Slip coordination number is sharply picked at a very small strain level, and as the loading continues, it reduces and depicts almost similar behavior regardless of the stress path applied except MSC.

The evolution of deviatoric contact fabric quantified by a fabric tensor considering all and strong contacts between particles is depicted in Fig. 5, while the evolution of contact fabric ratio considering all and strong contacts between particles is depicted in Fig. 6. The fabric tensors considering all and strong contacts are defined as follows [19, 20]:
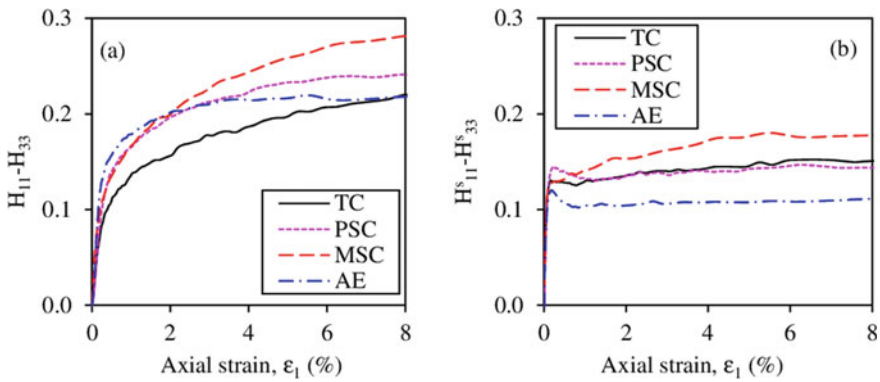
Fig. 5 Evolution of deviatoric contact fabric with axial strain. **a** Considering all contacts. **b** Considering strong contacts only
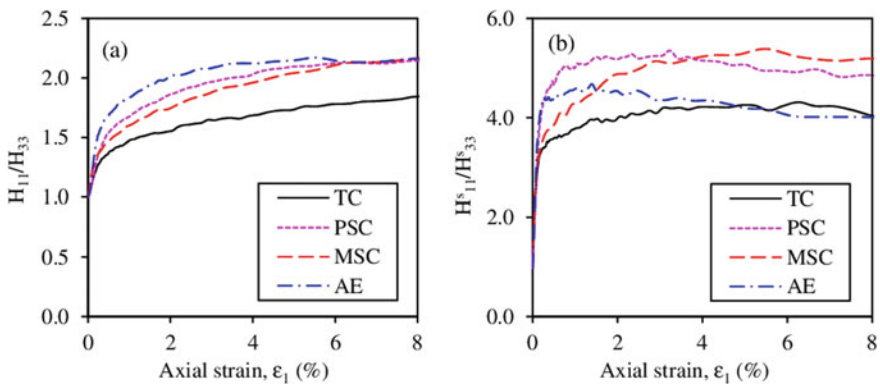
Fig. 6 Evolution of contact fabric ratio with axial strain. **a** Considering all contacts. **b** Considering strong contacts

$$H_{ij} = \frac{1}{N_c} \sum_{c=1}^{N_c} n_i^c n_j^c \qquad i, j = 1 - 3 \tag{3}$$

$$H_{ij}^s = \frac{1}{N_c} \sum_{s=1}^{N_c^s} n_i^s n_j^s \qquad i, j = 1 - 3 \tag{4}$$

Here, n_i^c is the contact normal vector at the i-th contact, and n_i^s is the contact normal vector at the i-th strong contact. N_c and N_c^s are the number of total contacts and number of strong contacts, respectively. A contact is considered to be strong if the normal force between particles during contacts is greater than the average normal force of all contacts. The evolution of deviatoric fabric $H_{11} - H_{33}$ considering all contacts with axial strain is depicted in Fig. 5a, whereas the evolution of deviatoric fabric $H_{11}^s - H_{33}^s$ considering strong contacts with axial strain is depicted in Fig. 5b. A qualitative similarity between the pattern of the evolution of $H_{11} - H_{33}$ with ε_1 and $q = \sigma_1 - \sigma_3$ with ε_1 is noticed. Nevertheless, the quantitative pattern is not similar. For example, q is highest for PSC, whereas $H_{11} - H_{33}$ is highest for MSC. Similar behavior is noticed in Fig. 5b. On the other hand, if the ratio of fabric is considered in contrast to the deviatoric fabric and its evaluation is depicted in Fig. 6, a quantitative similarity between the evolution of stress ratio and fabric ratio with strain is noticed for all other stress paths (TC, PSC, AE) except MSC when strong contacts are considered [compare Fig. 6b with Fig. 3a].

A relationship between fabric ratio considering strong contact and stress ratio is also developed and shown in Fig. 7. A unique behavior is noticed regardless of the stress paths only at a very small strain range (up to 1% of axial strain).

Fig. 7 Relationship between fabric ratio (strong contacts only) and stress ratio for different stress paths
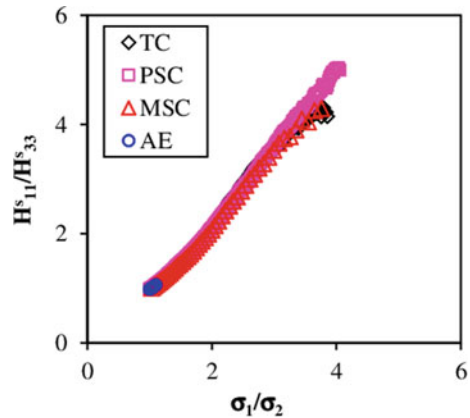
8   Conclusions

A numerical study is conducted using the DEM to explore the micro-mechanical characteristics of a granulate system such as sand for different stress paths. The macro-mechanical behavior is also presented. For this, a numerical sample consisting of 8000 spheres was prepared and compressed isotropically to 100 kPa. The numerical sample was subjected to shear under different stress paths. The same sample prior to shear was used to eliminate the biasness of the initial fabric of the test samples as usually occurred in experimental studies. The simulated macro-mechanical results of the present study were compared with the experimental and numerical results of the earlier published studies and found excellent qualitative agreements among them. Average coordination number and slip coordination number evolve differently with axial strain. A huge loss of average coordination number is observed for mean stress compression compared to other stress paths considered in this study. Slip coordination number sharply picked at a very small strain level and depicts almost similar behavior at the higher strain except mean stress compression. The fabric ratio rather than the deviatoric fabric matches well with the stress ratio rather than the deviatoric stress with strain. The relationship between stress ratio and fabric ratio considering only strong contacts is almost linear and unique regardless of the stress paths only at a very small strain level.

References

1. Tatsuoka F, Sakamoto M, Kawamura F (1986) Strength and deformation characteristics of sand in plane strain compression. Soils Found 26(1):65–84. https://doi.org/org/10.3208/sandf1972.26.65
2. Wang Q, Lade PV (2001) Shear banding in true triaxial tests and its effect on failure in sand. J Eng Mech 127(8):754–761. https://doi.org/org/10.1061/(ASCE)0733-9399(2001)127:8(754)
3. Shapiro S, Yamamuro JA (2003) Effects of silt on three-dimensional stress–strain behavior of loose sand. J Geotech Geoenvir Eng 129(1):1–11. https://doi.org/10.1061/(ASCE)1090-0241(2003)129:1(1)
4. Ng T-T (2005) Behavior of gravity deposited granular material under different stress paths. Can Geotech J 42(6):1644–1655
5. Sazzad MM, Suzuki K (2012) A comparison between conventional triaxial and plane-strain compression on a particulate system using 3D DEM. Acta Geotechnica Slovenica 9(2):17–23
6. Thornton C (2000) Numerical simulations of deviatoric shear deformation of granular media. Geotechnique 50(1):43–53
7. Ng T-T (2004) Macro- and micro-behaviors of granular materials under different sample preparation methods and stress paths. Int J solids Struct 41(21):5871–5884. https://doi.org/10.1016/j.ijsolstr.2004.05.050
8. Sazzad MM, Modaressi-Farahmand-Razavi SK, A, (2012) Macro-micro responses of granular materials under different b values using DEM. Int J Geomech 12(3):220–228. https://doi.org/10.1061/(ASCE)GM.1943-5622.0000133
9. Sazzad MM, Suzuki K (2013) Density dependent macro-micro behavior of granular materials in general triaxial loading for varying intermediate principal stress using DEM. Granular Matter 15(5):583–593. https://doi.org/10.1007/s10035-013-0422-z

10. Sazzad MM, Shaha RK, Islam MS, Kawsari S (2015) Macro and micro responses of granular materials under plane strain compression by 3D DEM. Int J Adv Structs Geotech Eng 4(2):114–119

11. Sazzad MM (2019) Effect of intermediate principal stress on the behavior of granular materials at a low mean stress by DEM. Geotech Geol Eng 37(5):4539–4550. https://doi.org/10.1007/s10706-019-00929-7

12. Cundall PA, Strack ODL (1979) A discrete numerical model for granular assemblies. Geotechnique 29(1):47–65. https://doi.org/10.1680/geot.1979.29.1.47

13. Kuhn MR (1999) Structured deformation in granular materials. Mech Mater 31(6):407–429. https://doi.org/10.1016/S0167-6636(99)00010-1

14. Kuhn MR (2003) Smooth convex three-dimensional particle for the discrete element method. J Eng Mech 129(5):539–547. https://doi.org/10.1061/(ASCE)0733-9399(2003)129:5(539)

15. Kuhn MR, Renken HE, Mixsell AD, Kramer SL (2014) Investigation of cyclic liquefaction with discrete element simulations. J. Geotech Geoenviron Eng 140(12):1–13. https://doi.org/10.1061/(ASCE)GT.1943-5606.0001181

16. Sazzad MM, Suzuki K (2010) Micromechanical behavior of granular materials with inherent anisotropy under cyclic loading using 2D DEM. Granular Matter 12(6):597–605. https://doi.org/10.1007/s10035-010-0200-0

17. Sazzad MM (2016) Micro-scale responses of granular materials at different confining pressures using DEM. Acta Geotech. Slovenica 13(1):26–36

18. Cornforth DH (1964) Some experiments on the influence of strain conditions on the strength of sand. Geotechnique 14(2):143–167

19. Satake M (1982) Fabric tensor in granular materials. In: Vermeer PA, Luger HJ (eds) Proceeding of IUTAM Symposium on Deform Fail of Granular Materials. Balkema, Delft, pp 63–68

20. Sazzad MM (2014) Micro-scale behavior of granular materials during cyclic loading. Particuology 16:132–141. https://doi.org/10.1016/j.partic.2013.12.005

Suitability Number, Fineness Modulus, Density, and Strength Parameter Relations of Sandy Soil

K. F. Ahmed, T. Sultana, M. Z. Abedin, and K. A. Farzana

1 Introduction

As a construction material, sandy soil has the multipurpose use in various capacities such as backfill material in retaining structures, sand compaction pile and vibro-compaction subsoil improvement procedures, embankment and earth-dams fills, and other similar works. Backfill material is naturally used to fill up any excavation to stabilize the soil and resist the structural failure. Generally, the sandy soil while used as a construction material is judged by two empirical parameters based on mass grain properties namely fineness modulus (FM) and suitability number (S_N). Fineness modulus is perhaps the most widely known especially in determining the properties of artificially prepared civil engineering materials where sandy soil acts as a component. Brown [1] introduced another empirical parameter, termed as suitability number, of sandy soil in order to examine its suitability as backfill material. He defined the suitability number, S_N as given by Eq. (1).

$$S_N = 1.7 \sqrt{\frac{3}{D_{50}^2} + \frac{1}{D_{20}^2} + \frac{1}{D_{10}^2}} \tag{1}$$

where D_{50}, D_{20}, and D_{10} are the diameters corresponding to percent fineness of, respectively, 50, 20, and 10, respectively. He also proposed a backfill rating scheme as per stability number given in Table 1.

Relative density is another important indicator of mass of soil aggregates that determine the shear strength of soil and its parameters. Ahsan et al. [2] observe that

K. F. Ahmed (✉) · T. Sultana · M. Z. Abedin · K. A. Farzana
Department of Civil Engineering, MIST, Dhaka, Bangladesh
e-mail: fariha@ce.mist.ac.bd

M. Z. Abedin
e-mail: zabedin@ce.mist.ac.bd

Table 1 Backfill rating as proposed by Brown (1977)

Range of suitability number (S_N)	Rating as backfill
0–10	Excellent
10–20	Good
20–30	Fair
30–40	Poor
>50	Unsuitable

a strong linear increasing correlation exists between angle of internal friction and relative density. Likewise, the shear strength and density might differ according to the gradation and interlocking of sandy soil.

Arinze et al. [3] performed examined the suitability of Umuahia sands from Nigeria as backfill materials for vibroflotation compaction of cohesionless soils. According to them, the samples with higher average particle sizes had a better suitability number rating compared to lower effective sizes. Pogu et al. [4] carried out a research on suitability of sands from different locations of Nigeria as backfill material for vibroflotation. They found that strong correlations exist between suitability number, S_N, and various gradation parameters of sandy soil. Ground improvement involving sand aggregate as fill material should be carefully examined for its suitability. There exist various methods that determine the suitability of fill materials; namely suitability number S_N, fineness modulus FM, gradation parameters, density, and so on. Significant works have been done on these aspects, but relationships between two important parameters like fineness modulus and suitability number are still apparently unexplored. This paper presents the relationship among suitability number, fineness modulus, density and shear strength parameter of sandy soil, so that it can be suitable in the practicing field.

2 Materials and Methods

The present study was mainly concerned with the relationships of fineness modulus, density, and strength parameter with the suitability number (S_N) of coarse-grained soil. Random data were generated using Excel program for various soil gradation and suitability number, S_N. Besides, corresponding fineness modulus, FM were estimated using those data. Sand samples were prepared, and density and direct shear tests were carried out on the sampled soil.

Samples of both categories like randomly selected where all standard sieve particles were considered and uniformly gradated (100% passing through No. 8 sieve and retained on No. 16 sieve) were considered for preparation of samples. One hundred of such data were generated, and experiments were, however, carried only on samples of two backfill criteria (stability number 0–10, and 20–30) suggested by Brown [1].

For preparing the sample, naturally available cohesionless soil (Sylhet sand) was sieved, and particles retained on 4.75, 2.38, 1.19, 0.60, 0.297, 0.148, 0.075 mm and

Fig. 1 Preparation of sand samples

pan were separated and collected in separate containers. Having the same weight ratio as used in Excel program, sand samples were prepared with particles of varying coarseness. Total eight samples were prepared, where five samples having suitability number between 0 and 10 and three samples between 20 and 30. Following similar procedures, four more samples of uniform size gradation were prepared. Sand samples with preparation tools are shown in Fig. 1.

For the purpose of present investigation, maximum and minimum densities and direct shear tests were also done. The maximum dry densities of the sand samples were determined as per the respective standard procedures of ASTM [5, 6]. A standard CBR mold having a volume of 0.00278 m^3 was used for this purpose.

In order to determine the shear strength parameter of sand samples (angle of internal friction, φ), direct shear test was carried out following the standard test procedures of ASTM [7]. The test was performed by shearing a specimen at a controlled strain rate.

3 Results and Discussions

In this study, relationship among suitability number, fineness modulus, density, and angle of internal friction of sandy soil were investigated. The test results are analyzed and presented in the following sections.

3.1 Suitability Number and Fineness Modulus

Fineness modulus and suitability numbers as obtained from randomly generated data using Excel program were plotted in Fig. 2 where the trend line indicated a general trend of decreasing fineness modulus (FM) with increasing suitability number (S_N).

$$FM = -0.061S_N + 3.448$$
$$R^2 = 0.613$$
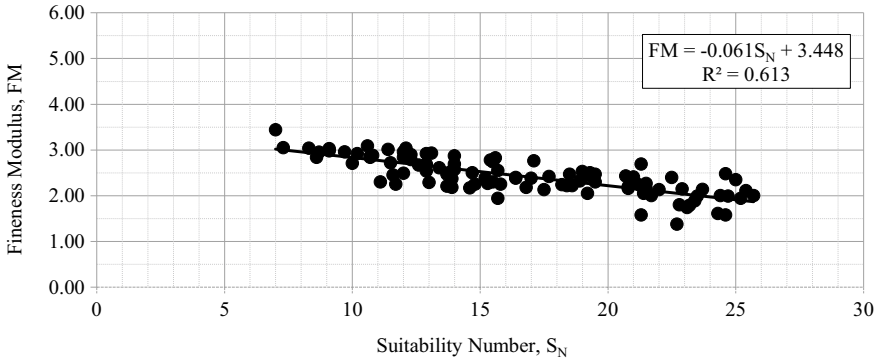
Fig. 2 Relationship between fineness modulus and suitability number for randomly generated data

$$FM = -0.059S_N + 3.471$$
$$R^2 = 0.933$$
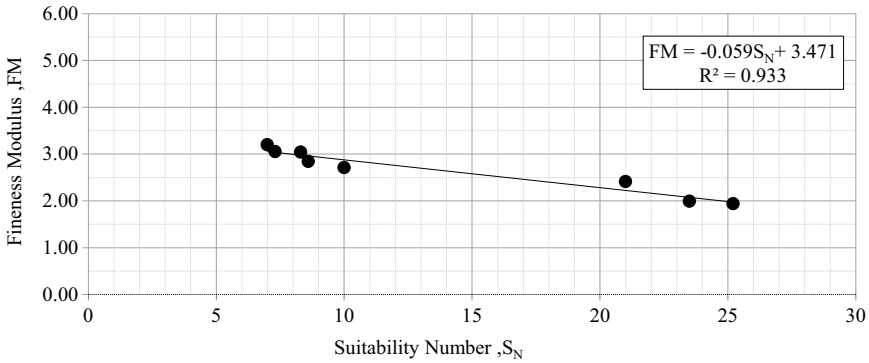
Fig. 3 Fineness modulus and suitability number for selected sand samples

However, only 61% (Regression Coefficient $R^2 = 0.613$) of the variability of FM can be explained by the independent variable, S_N.

For the selected prepared sample, relations between suitability number and fineness modulus were observed only for the S_N value between 0 and 10, and between 20 and 30. A strong relationship ($R^2 = 0.933$) was observed as that can be seen from Fig. 3. Besides, Fig. 4 shows the relationship between suitability number and fineness modulus for the uniform gradation of sand. A nonlinear relationship can be found with a good correlation coefficient of 0.9583.

3.2 Density and Direct Shear Test Results

From 100 generated samples, five samples having suitability number between 0 and 10 ($S1$, $S2$, $S3$, $S4$, and $S5$) and three samples for suitability number between 20

$$FM = 0.0138S_N^2 - 0.4874S_N + 5.3026$$
$$R^2 = 0.9583$$
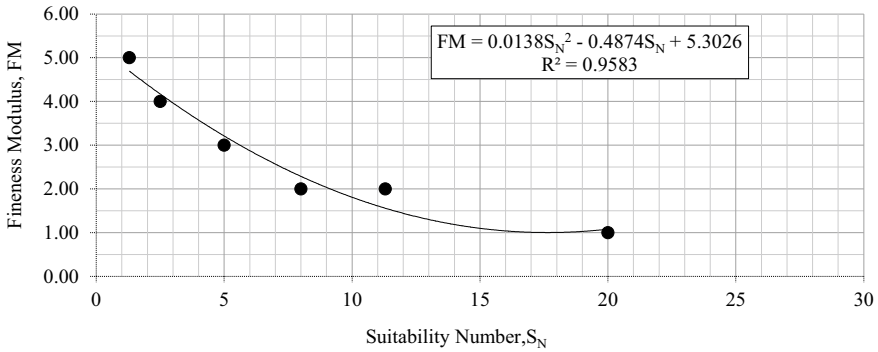
Fig. 4 Fineness modulus and suitability number for uniformly graded sand

Table 2 Results of density and angle of internal friction for sand samples

Sample designation	Suitability number (S_N)	Minimum dry density (kN/m^3)	Maximum dry density (kN/m^3)	Angle of internal friction (°)
S1	7.0	16.17	17.41	43.9
S2	7.3	15.42	16.79	43.2
S3	8.3	15.58	17.15	42.2
S4	8.6	15.36	16.91	42.0
S5	10.0	14.94	16.42	41.0
S6	21.0	15.92	17.41	42.8
S7	23.5	15.47	17.01	35.3
S8	25.2	15.68	16.88	38.9

and 30 (S6, S7, and S8) were taken to find their density and direct shear strength parameter, φ. Scattered relationship was observed between density and angle of internal friction. From the results, it can be observed that minimum or maximum dry density ranges from 14 to 17 kN/m^3 and the angle of internal friction is between 39 and 44°. The results are reported in Table 2.

3.3 Suitability Number and Angle of Internal Friction

Figures 5 and 6 show the relationship between suitability number and angle of internal friction for randomly generated sand samples. In Fig. 5, the regression coefficient (R^2) value of 0.523 does not suggest a strong correlation between them. Figure 6, however, shows strong correlations between angle of internal friction and suitability number within selected range between 0 and 10, with a correlation coefficient of 0.965.
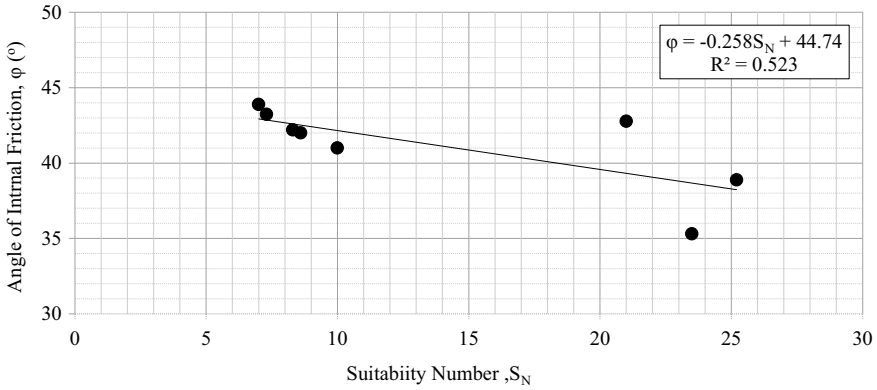
Fig. 5 Relationship between suitability number and angle of internal friction (randomly generated sand samples)
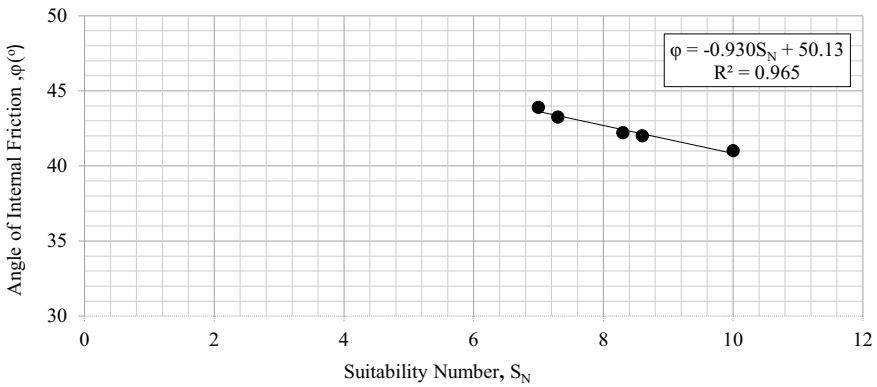
Fig. 6 Relationship of suitability number and angle of internal friction (S_N between 0 and 10)

3.4   Suitability Number and Gradation Parameters Relation

Statistical analysis of the data of gradation parameters and suitability number yields good correlations ($R^2 = 0.903$–0.905) between suitability number and gradation parameters for randomly generated sand samples.

$$S_N = 30.46 - 29.67 D_{10} - 30.62 D_{20} - 7.93 D_{30}; \; R^2 = 0.905 \qquad (2)$$

$$S_N = 30.09 - 27.477 D_{10} - 37.852 D_{20} - 1.50 D_{50}; \; R^2 = 0.903 \qquad (3)$$

The following equations were obtained to represent similar relations considering uniform gradations of sand samples.

$$S_N = 24.10 - 1149.5 D_{20} + 1151.4 D_{30} - 77.04 D_{50}; \; R^2 = 0.957 \qquad (4)$$

$$S_N = 23.38 + 97.94 D_{10} - 1106.6 D_{20} + 937.8 D_{30}; \; R^2 = 0.951 \qquad (5)$$

The findings suggest that strong correlations exist between suitability number, S_N, and various gradation parameters of sandy soil. This agrees with the findings of Pogu et al. [3].

3.5 Fineness Modulus and Gradation Parameters Relations

Analysis of the limited number of data of fineness modulus and gradation parameters yielded the following equations for the relationship between fineness modulus and gradation parameter for uniform gradation of sand samples. The correlation coefficient (R^2) of higher than 0.998 suggests that strong correlations exist between fineness modulus, FM, and various gradation parameters for uniform gradation of sand samples. However, no significant relationship was found to exist between fineness modulus, FM, and gradation parameters for the randomly generated sand samples.

$$\mathrm{FM} = 0.33 + 142.49 D_{20} - 155.18 D_{30} + 20.92 D_{50}; \quad R^2 = 0.999 \qquad (6)$$

$$\mathrm{FM} = 0.26 + 144.57 D_{20} - 150.77 D_{30} + 14.40 D_{60}; \quad R^2 = 0.998 \qquad (7)$$

4 Conclusion

The following conclusions can be drawn from the observations of the present study:

1. The suitability number, S_N, of sandy soils is dependent on various combinations of gradation parameters like D_{10}, D_{20}, D_{30}, D_{50}, and D_{60}.
2. Fineness modulus, FM, of uniformly graded sand samples is dependent on combined gradation parameters D_{10}, D_{20}, D_{30}, D_{50}, and D_{60}. However, for other gradations, the relationship cannot be defined.
3. There exists inverse correlation between fineness modulus and suitability number.
4. Within the suitability number rated as excellent (0–10), there is a decreasing trend of angle of internal friction, φ, for a higher value of suitability number, S_N.

5. Equations are proposed to correlate suitability number with fineness modulus
   and other parameters that can be used to estimate the gradation and other parame-
   ters. However, their generalization would require further extensive studies using
   samples from various locations and sources.

References

1. Brown RE (1977) Vibroflotationcompaction of cohesionlesssoils. ASCE J GeotechEngDiv
   103(12):1437–1451
2. Ahsan Z, Chik Z, Abedin Z (2014) Therelationship of particle gradation and relative density
   with soil shear strength parameters from direct shear tests. Aust J Basic Appl Sci 8(19) Special
   2014:271–275
3. Arinze EE, Egbuna IC (2014) Suitability of Umuahiasands as backfill materials for vibroflota-
   tioncompaction of cohesionlesssoils. Electron J Geotech Eng 19(Y):8977–8982
4. Pogu JH, Okafor CC, Ezeokonkwo JC, Suitability of sands from different locations ofNsukka as
   backfill material for vibroflotation. Niger J Technol 37(4):867. https://doi.org/10.4314/njt.v37
   i4.2
5. ASTM D 4253, Standard test methods for maximum index density and unit weight of soils using
   a vibratory table. ASTM international, West Conshohocken, PA, 1–15. https://doi.org/10.1520/
   D4253-14
6. ASTM D 4254, Standard test methods for minimum index density and unit weight of soils and
   calculation of relative density. ASTM Standards. https://doi.org/10.1520/D4253-16E01
7. ASTM D3080, Standard test method for direct shear test of soils under consolidated drained
   conditions. ASTM international, 1–9. https://doi.org/10.1520/D3080

Shear Strengthening of RC Beam Using Jute Fibre-Reinforced Polymer Laminate

M. A. Alam and M. M. Rahman

1 Introduction

Nowadays, shear strengthening of reinforced concrete beam is very common and popular to retrofit deficient existing structures. Shear failure is disastrous and happens usually without advance warning. It is always desirable to fail the beam in flexure rather than in shear for ensuring sufficient ductility. Many existing reinforced concrete (RC) members are found to be imperfect in shear strength and need to be repaired. Shear strengthening of RC beam using externally bonded steel plates, carbon fibre-reinforced polymer laminate (CFRP) and glass fibre sheets are commonly used nowadays [1, 2]. However, CFRP is more expensive, and steel plate has corrosion property. Also, CFRP is very dangerous for human health and environment because of releasing airborne carbon dust during their production and usage [3, 4]. Moreover, CFRP laminate is less effective for shear strengthening of RC beam due to debonding failure.

Premature debonding failures of externally bonded synthetic fibre-based composite plates are very much common in shear strengthening of RC beams because of stiffer linear elastic nature of the materials. Since natural fibres (jute and kenaf) are soft in nature having low modulus of elasticity as compared to synthetic fibre (carbon and glass), natural fibre-based composite plates could be the alternatives of synthetic fibre-based plates for shear strengthening of RC beam to eliminate debonding of laminate. Significant research works have been conducted to develop and fabricate composite plates using jute, kenaf, bamboo, sisal and banana fibres [5–7]. However, the tensile strength of the fabricated natural fibre-based composites plates of existing research is very low and thus may not be effective to use in structural application. The fabrication process proposed by Alam [8] could enhance the tensile strength

M. A. Alam (✉) · M. M. Rahman
Department of Civil Engineering, University of Asia Pacific, Dhaka 1215, Bangladesh
e-mail: dr.ashraful@uap-bd.edu

of jute fibre composite plate as well. It had been recommended that the increased amount of fibres in plate could enhance tensile strength of composite plate.

Furthermore, debonding of externally bonded plates could be reduced using appropriate anchor systems. Various anchor systems such as bolts, feng, spoke and embedded connector have been proposed by researchers. Embedded connector would be more appropriate for uni-directional fibre-based composite plate. Although kenaf with high fibre content had shown high tensile strength [8], research on high-strength JFRP laminate for shear strengthening of reinforced concrete is limited. Moreover, investigation on anchor system would have substantial importance for effective shear strengthening of RC beam using JFRP laminate. The main aim of the research work is to fabricate high-strength jute fibre composite plate for effective shear strengthening of reinforced concrete beams using embedded connector anchor system.

2   Experimental Program

2.1   Details of Beam Specimens

In the experimental program, total of three full scale (1300 mm × 250 mm × 150 mm) reinforced concrete beam specimens were prepared. The beams were shear reinforced using 8 mm steel bar with the spacing of 55 mm. The shear reinforcement had been provided at one shear span of beam, while other shear span was left without shear reinforcement to ensure shear failure of beam from that side. One beam was left as un-strengthened condition, one was shear strengthened using jute fibre-reinforced polymer (JFRP) laminate without anchor system, and the last one was shear strengthened using JFRP laminate with double connector anchor system (JPDC). The details of specimens are shown in Table 1.

Table 1   Details of beam specimens

Beam specimens			JFRP plate			Anchor system	
Specimen ID	Shear reinforcement		Spacing (mm)	Width (mm)	Thickness (mm)	Types	Diameter (mm)
	On plate side	Other side					
CB	No	8 mm @55 mm c/c	–	–	–	–	–
JP0	No	8 mm @55 mm c/c	250	25	7.1	–	–
JPDC	No	8 mm @55 mm c/c	250	25	7.1	Double connector	16

8mm diameter @ 55 mm c/c

2-16mm diameter

2-10mm diameter

P

250mm

250mm

150mm

100mm 550mm 550mm 100mm
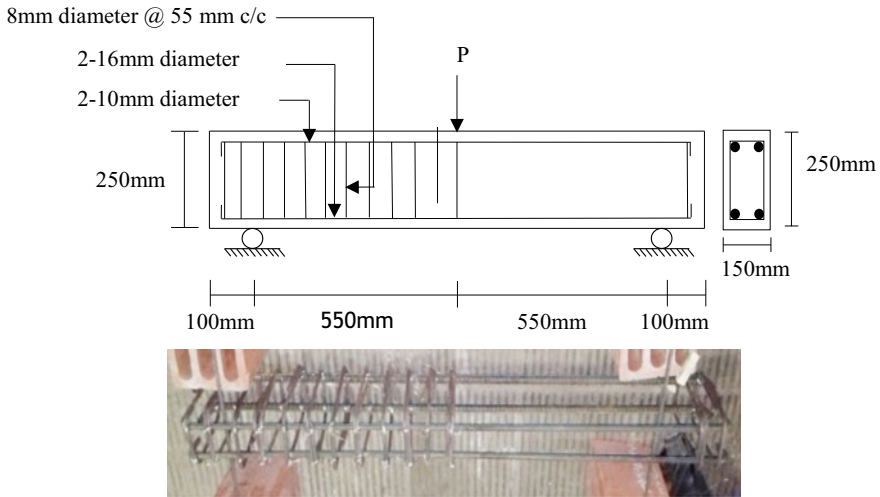
Fig. 1 Details of under shear reinforced beam

2.2 Preparation of Beam Specimens

2.2.1 Fabrication of Beam and JFRP Laminate

The reinforcement details of beam specimens are shown in Fig. 1. The beams having 2–16 mm diameter flexural reinforcement at bottom of the beam, 2–10 mm diameter bar at top as hanger bar. The shear reinforcement of 8 mm bar was used at one shear span of beam with the spacing of 55 mm, while another shear span was left without shear reinforcement as shown in Fig. 1. It is expected that the beam would fail by shear from un-reinforced shear span of beam. The shear reinforcement spacing of beam (55 mm) was based on theoretical predictions of shear and flexural capacities of strengthened beams. The JFRP laminate had been fabricated using un-treated jute fibre and epoxy. The epoxy consisted of resin and hardener, and the well-mixed epoxy was applied on straight jute fibre which was laid on steel casting mould. Once the epoxy became semi-solid, the epoxy-soaked jute fibre was compressed and was left for 24 h curing.

2.2.2 Properties of Materials

The yield and tensile strength of flexural reinforcement (16 mm bar) was 515 MPa and 665 MPa, respectively, and the shear reinforcement had 363 MPa and 400 MPa yield and tensile strength, respectively. All beams were cast using 30 MPa concrete. The concrete was produced using drum mixture with the cement, fine aggregate

and coarse aggregate ratio of 1:3.53:5.53. The water–cement ratio of concrete mix was 0.67. The density and tensile strength of JFRP laminate were 1.352 g/cm^3 and 162 MPa, respectively.

2.2.3 Strengthening of Beam Specimen

The loose particle on bonding surfaces of beams was removed. The surface was prepared to fix JFRP laminate with the spacing of 100 mm centre to centre at the shear span where no shear reinforcement was provided. The JFRP plate having the dimension of 7.1 mm × 25 mm × 250 mm was fabricated for shear strengthening of RC beam. The beams were drilled using drill head to insert 20 mm embedded connector. The maximum depth of the connector was 25 which was within the cover of concrete. The strengthening process should not disturb the core part of the concrete, and thus, the connector was placed within cover part of concrete. The prepared bonding face of concrete and connector was shown in Figs. 2 and 3, respectively.

The beam surface was then cleaned with compressed air and a dry rag cloth. Finally, the beam surface and bonding face of JFRP laminate were cleaned with thinner. The connector was prepared with two 20 mm diameter holes with 25 mm in depth, and 16 mm diameter steel bar was inserted in both adhesive filled holes before bonding of shear strips as shown in Fig. 4. The laminates were then bonded on the surface of the concrete beams using Sikadur 31 CF adhesive. The thickness of adhesive was approximately 3 mm as per instruction of manufacturer. Excessive thickness of adhesive may cause failure of laminate due to failure of adhesive rather

Fig. 2 Surface preparation for JP0

Fig. 3 Surface preparation for JPDC
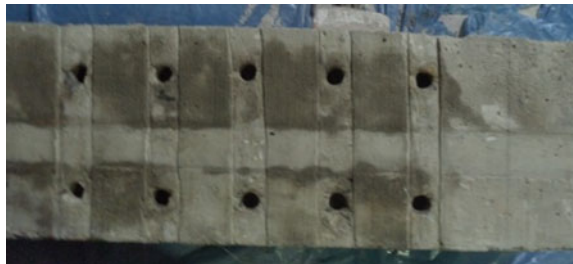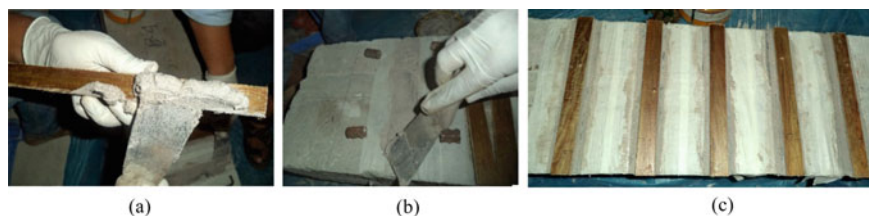
Fig. 4 **a** Epoxy adding on the JFRP, **b** fixing double connector, **c** fixing JFRP plates with epoxy
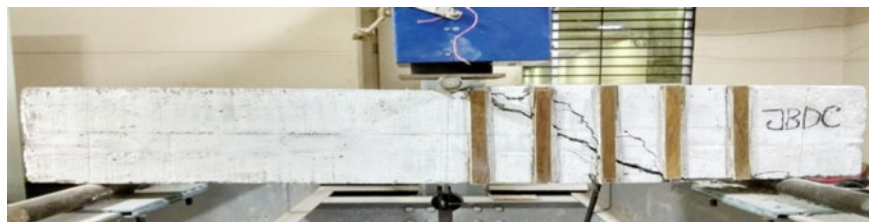
Fig. 5 Test set-up and testing of beam

than fracture of laminate or fracture of concrete. The laminates were only placed on shear span (550 mm) of the beams with 100 mm spacing as shown in Figs. 2 and 4. The details of strengthening process are shown in Fig. 4.

2.3   Test Set-up and Testing of Beam Specimens

All specimens were instrumented properly before testing of beams as shown in Fig. 5. Dial gauge was placed at bottom–middle of beam to record mid-span deflection. All beam specimens were tested under single-point loading as shown in Fig. 5. The beams were tested over a clear span of 1100 mm with shear span of 550 mm.

Loads were applied by hydraulic jack and measured by a load cell. At each load stage, cracks were noted, and developing crack pattern was marked on the surface of beams. The final failure mode was carefully observed and recorded.

3   Result and Discussions

3.1   Mode of Failure

The experimental results of all beam specimens are summarized in Table 2. The control beam which was not strengthened failed due to shear failure, and the failure

Table 2 Experimental results of strengthened beams

ID	Concrete strength (MPa)	Shear crack load (kN)	Increased shear crack load by JFRP laminate (%)	Failure load (kN)	Increased failure load (%)	Mode of failure
CB	28.1	52.4	–	63.53		Shear
JP-0	28.1	80.2	53	126	98	Laminate debonding and shear
JPDC	28.1	80.2	53	128.32	102	Flexural and anchor failure

occurred at the side of the beam where no shear reinforcement was provided, as shown in Fig. 6(i). The strengthened beam with JFRP laminate without anchor (JP-0) was failed due to debonding of laminate followed by shear. The shear failure happened due to crushing of concrete at compression strut of shear span as shown in Fig. 6(ii). Whereas, JFRP laminate strengthened beam with anchor system (JPDC) failed by flexure and cover separation of flexural bar. Because of anchor system, laminate did not show any debonding failure. Thus, beam JPDC failed due to flexure followed by crushing of concrete. It was also noticed that anchor of JPDC failed due to crushing of concrete. The shear crack inclination of CB and JP0 was almost 45 degree. In general, the JFRP laminate strengthened beams had shown ductile nature of failure and showed higher deflection before failure of beam (Fig. 7). Since, JFRP laminate is soft in nature, would be able to absorb more energy, thus showed higher deflection before failure. Results also showed that JFRP laminate reduced deflection as compared to un-strengthened control beam (Fig. 7).

i: Control beam

ii: JFRP beam without connector

iii: JFRP beam with connector
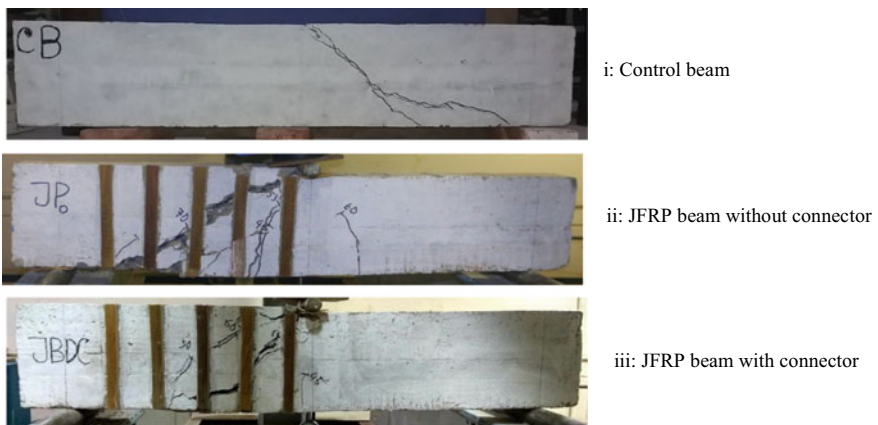
Fig. 6 Failure modes of strengthened beams

Fig. 7 Load–deflection of beam specimens
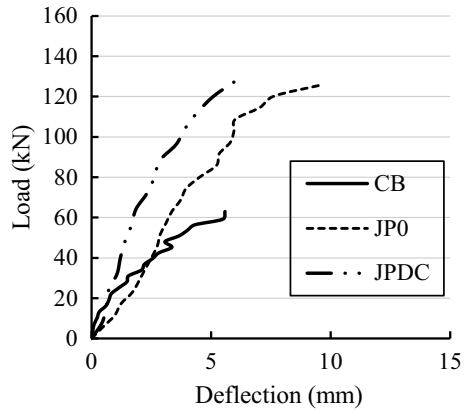
Fig. 8 Failure load of beam specimens
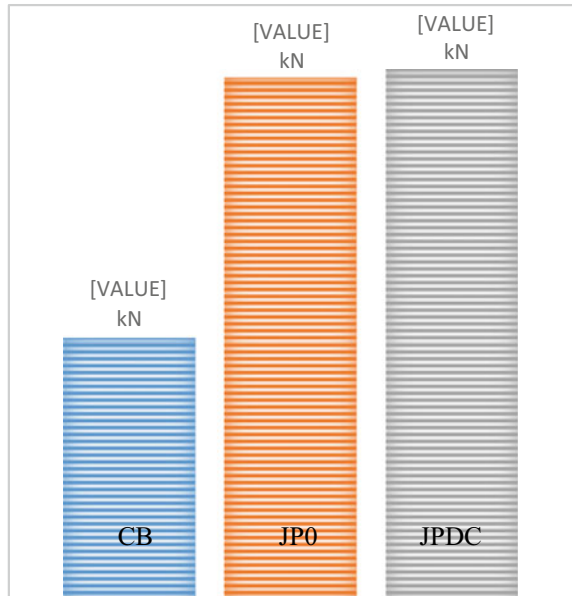
3.2   Strength Enhancement

Results showed that JFRP laminate enhanced shear cracking and failure loads of shear-strengthened beams significantly as compared to un-strengthened control beam shown in Table 2. The shear crack load of control beam was almost close with failure load. Since there was no shear reinforcement on failure side of beam, the beam had failed immediately after shear cracking of concrete. Both JFRP laminate strengthened beams had shown almost 53% higher shear crack load than control beam. Results also showed that JFRP laminate strengthened beams JP0 and JPDC had 98% and

102% higher shear capacity as compared to control beam, respectively. Strengthened beam with anchor system had shown highest shear capacity than others. Since anchor prevented debonding of JFRP laminate, it had shown higher failure load.

4   Conclusion

In this research, jute fibre-reinforced polymer laminates had been used for shear strengthening of RC beam. Results showed that jute fibre-reinforced polymer (JFRP) laminate significantly increased shear capacities of reinforced concrete beams. The JFRP laminate had almost increased 98 and 102% shear capacities of beam as compared to un-strengthened control beam. Strengthened beam with anchor system had shown highest shear capacity. JFRP had excellent nature to delay debonding of laminate, strengthened beam without anchor system failed by fracture of laminate followed by debonding and finally failed by shear. Whereas, strengthened beam with anchor system failed by flexure and crushing of concrete along with failure of connector. JFRP laminate reduced deflection of beam and would enhance ductile nature of beam.

References

1. Banjara, N.K., Ramanjaneyulu, K.: Investigations on behaviour of flexural deficient and CFRP strengthened reinforced concrete beams under static and fatigue loading. Constr. Build. Mater. **201**, 746–762 (2019). https://doi.org/10.1016/j.conbuildmat.2019.01.010
2. Kim, Y., Ghannoum, W.M., Jirsa, J.O.: Shear behavior of full-scale reinforced concrete T-beams strengthened with CFRP strips and anchors. Constr. Build. Mater. **94**, 1–9 (2015). https://doi.org/10.1016/j.conbuildmat.2015.06.005
3. Baan, R.A., Grosse, Y.: Man-made mineral (vitreous) fibres: evaluations of cancer hazards by the IARC monographs programme. Mutat. Res. **553**(1–2), 43–58 (2004). https://doi.org/10.1016/j.mrfmmm.2004.06.019
4. National Aeronautics and Space Administration: Carbon Structure Hazard Control, WSTF-RD-1219-001-15 (2015)
5. Codispoti, R., Oliveira, D.V., Olivito, R.S., Lourenço, P.B., Fangueiro, R.: Mechanical performance of natural fiber-reinforced composites for the strengthening of masonry. Compos. B Eng. **77**, 74–83 (2015). https://doi.org/10.1016/j.compositesb.2015.03.021
6. Sen, T., Jagannatha Reddy, H.N.: Strengthening of RC beams in flexure using natural jute fibre textile reinforced composite system and its comparative study with CFRP and GFRP strengthening systems. Int. J. Sustain. Built Environ. **2**, 41–45 (2013). https://doi.org/10.1016/j.ijsbe.2013.11.001

7. Carvalho Bello, C.B., Boem, I., Cecchi, A., Gattesco, N., Oliveira, D.V.: Experimental tests for the characterization of sisal fiber reinforced cementitious matrix for strengthening masonry structures. Constr. Build. Mater. **219**, 44–45 (2019). https://doi.org/10.1016/j.conbuildmat.2019.05.168
8. Alam, M.A., Riyami, K.A.: Shear strengthening of reinforced concrete beam using natural fibre reinforced polymer laminates. Constr. Build. Mater. **162**, 683–696 (2018). https://doi.org/10.1016/j.conbuildmat.2017.12.011

Concrete Core Strength of RC Beam Under Different Stress Conditions

G. Biswas, M. K. Hasan, and S. S. Ali

1 Introduction

Micro-cracks can be present if the core is drilled from a region of a structure that has been subjected to stress resulting from either applied loads or restraint of imposed deformations. Rough handling may cause micro-cracks in concrete core specimens. Micro-cracks in a core reduce the strength [1]. The core strength decreases with the reduction of the diameter of cores, the increase in core moisture content, the drilling at the right angle to the casting direction, and the reduction in concrete strength [2]. The core strength is lower than the cylinder strength due to damage that occurred during drilling and the presence of a small amount of coarse aggregate. So, the strength correction factor is required to evaluate the core strength [3]. If the reinforcements are present in the core, then the core strength does not mean the compressive strength of concrete in the structure from which the core was extracted [4]. Chkheiwer and Kadim showed that the depth factor of the bottom to top zone strength in vertical cast direction is (1.110) and (1.066) for traditional concrete and the superplasticizer concrete, respectively, while the location factor of the center zone in vertical cast direction corresponding to (1.088) and (1.103) [5].

The rate of applied load is controlled by machine operators at the time of the compressive strength test. The applied load might be at a rate of movement that will create a stress rate of 35 ± 7 psi/s on the specimen. The size of the specimen, the elastic modulus of the test sample, and the stiffness of the testing machine are some

G. Biswas (✉)
Bangladesh Railway, Rajbari, Bangladesh

M. K. Hasan
Bangladesh Water Development Board, Dhaka, Bangladesh

S. S. Ali
Department of Civil Engineering, BUET, Dhaka, Bangladesh
e-mail: skali@ce.buet.ac.bd

of the variables on which the rate of the movement is dependent [6]. Few machine operators need to use to get precise test results.

In numerous circumstances, it is troublesome to drill a core from a structural member without cutting reinforcements. Therefore, a guideline is vital if reinforcement is cut during the drilling of the concrete core. ACI 214 suggests trimming the core to remove the reinforcement as long as the desired length-to-diameter ratio (L/D) is maintained. ASTM C42 suggests that if a core contains reinforcement, it is prohibited to determine splitting tensile strength, compressive strength, or flexural strength [6, 7]. However, if there is no possibility to extract a core that does not contain embedded reinforcement perpendicular to the coring direction, at that point, testing a sample is permitted under ASTM C42.

It is an arguable topic whether reinforcements will exist or not in the concrete cores. Experts give a different opinion to clarify the behavior of concrete core specimens. A few think that it increases the strength of the concrete specimens. While others consider that presence of reinforcement decreases the compressive strength of the concrete cores. On the other side, a few specialists accept that it has exceptionally little influence on concrete core strength. Numerous standards do not consider the influence of existing reinforcement within the concrete cores. Thus, they did not make any adjustments for the presence of reinforcement in concrete cores. But, British standard and concrete society made corrections for embedded reinforcement.

Some studies give guidance on the effects of embedded reinforcement in concrete test specimens. Loo et al. conducted a study with 174 cylinders and 24 cores including steel reinforcement ranging from #3 to #6 and concluded that the influence of steel reinforcement on the concrete core strength varied greatly with the L/D ratio of the core [8]. The core strengths decreased with the inclusion of steel reinforcement at L/D ratio of 2, and the effect of the embedded reinforcement decreases as the L/D ratio decreases to 1.0, at which point there are no significant effects on the cylinder strength.

If cores contain reinforcement, it will weaken the strength of the existing structure and concrete quality. It also decreases the strength of the concrete cores. To eradicate this problem, technicians need to cut concrete core without having reinforcement by scanning through magnate. Bartlett and MacGregor proposed corrections for concrete core strength if cores contain reinforcement [9]. The corrections are shown in Table 1. Bartlett and Macgregor adjustments are for the reinforcement which runs at right angles to the direction of drilling. This guidance does not incorporate how much reinforcement exists within the concrete cores. It also does not incorporate the size of the reinforcement. Thus, there are no guidelines on the amount of reinforcement and the size of the reinforcement.

Table 1 Correction factors for embedded reinforcement in core specimen

Number of embedded reinforcement	Strength correction factor
1	1.08
2	1.13

Depending on loading, the concrete at different locations of a beam experiences different stress conditions. Thus, the location of reinforced concrete members from where the cores are taken should be given importance for finding the respective representative compressive strength. Therefore, this study concentrated on the effect of different stress conditions on the concrete core strength of the reinforced concrete beam.

2 Materials and Methods

The experimental work was conducted in the Bangladesh University of Engineering and Technology concrete laboratory in order to evaluate the effects of stress conditions on the concrete core strength of the RC beam. In this experiment, six simply supported beams (three beams with stone chips and three beams with brick chips) were cast using three mix ratios (1:1.25:2.5, 1:1.5:3, and 1:2:4). The core samples were drilled from the reinforced beam after two-point loading test (Fig. 1). The beams were tested up to the first cracking load.

Steel reinforcement was provided within the beams basically to assure the safety of the beams during carrying the beams. Beams were carried to the materials laboratory utilizing two overhead cranes and trolley. Therefore, minimum reinforcement was provided to prevent shrinkage and temperature cracks. Figure 2 provides the reinforcement layout for the beam. The hoisting system was arranged to carry the beam from one place to another place in the laboratory. Figure 2 shows the location of each hoist anchor.

After the compression test of standard cylinders (4 in. × 8 in.), the beam's micro-cracked load was calculated. All beams front surface were lime painted for the easy
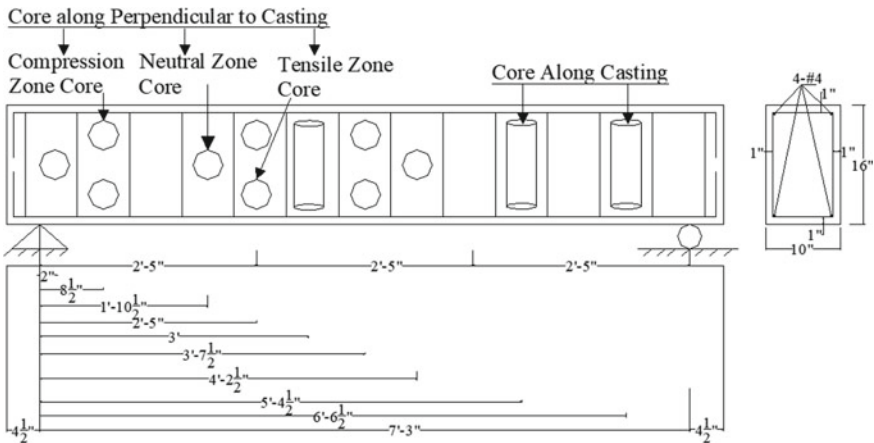
Fig. 1 RC beam and its core drilling plan after two-point loading test
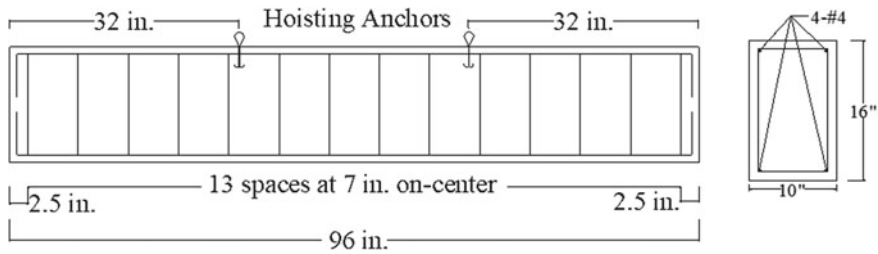
Fig. 2 Hoisting arrangement and reinforcement layout of RC beam

inspection of micro-cracks. Two-point loading test was performed in the BUET strength of materials laboratory using a universal testing machine. The load was increased gradually, and the deflection was measured with the help of a deflection gauge. The propagation of any micro-crack was inspected carefully. The load was stopped when the load reached the calculated cracking load.

Only 4 in. diameter core was drilled from beams in order to study the effect of various stress conditions on core strength. Three cores were drilled from the compression zone, three cores were drilled from the neutral zone, and three cores were drilled from the tension zone. The drilling direction was perpendicular to the casting direction for the cores of those three zones. Another three cores were drilled along the direction of concrete casting compaction. A total of 72 numbers 4 in. diameter cores were drilled from six beams after two-point load test.

3   Results and Discussion

Different stress conditions may have some effects on the core strength of concrete. To study this effect, six beams (size: 96 in. × 16 in. × 10 in.) were cast and tested by two-point loading. The load was applied gradually up to the first cracking load, which may be different from the theoretical first cracking load. The calculated first cracking loads are shown in Fig. 3.

Fig. 3 Calculated cracking load of RC beam during two-point load test
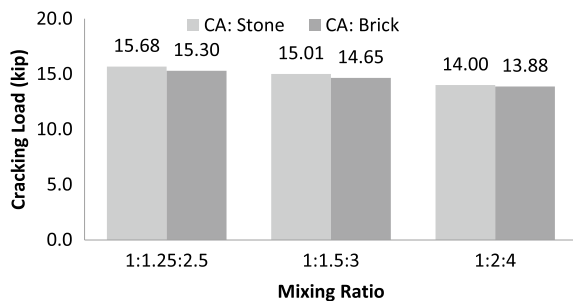
Figure 4 shows the deflection of the reinforced concrete beam for gradually applied load up to the first cracking load during the two-point load test. As expected, the load vs. deflection curve is a straight line up to the first cracking load during the two-point loading. It also indicates that the beam with brick aggregate deflects more than that of the beam with stone aggregate.

Figure 5 shows the comparisons of the strength of concrete core at different locations of RC beam after bending test. In this case, six RC beams with stone aggregate and six RC beams with brick aggregate are considered for the two-point loading test. From Fig. 5, it is clear that the ratio of concrete core strength to standard cylinder strength is always less than one. Moreover, as the mix ratios of concrete decreased, the related strength ratio also decreased. For high-strength concrete, the variation is low, but for the low strength concrete, the variation is high. It is observed
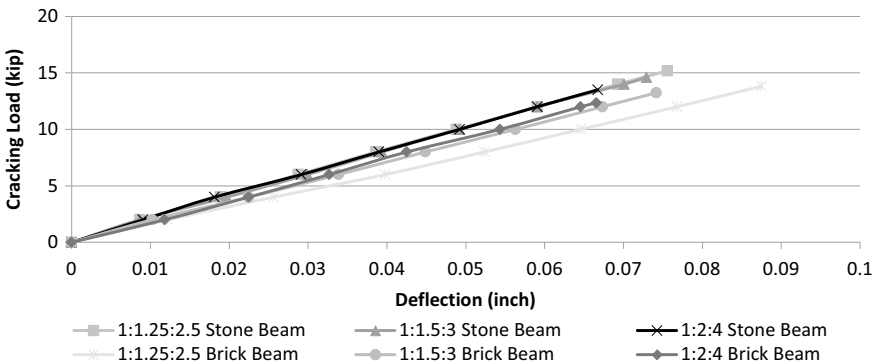
Fig. 4 Deflection of RC beam for gradually applied load up to first cracking loading
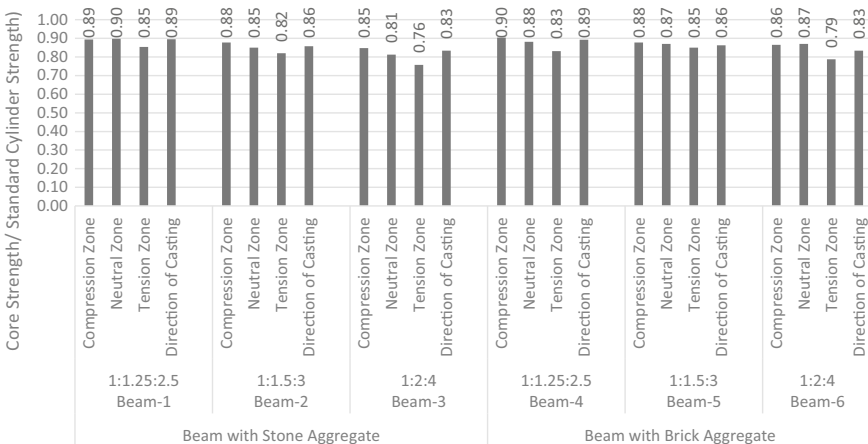
Fig. 5 Concrete core strength at different location of beam after two-point loading test

that the standard cylinder compressive strength is always higher than that of concrete core strength. It also represents that the cores in the compression zone experienced higher strength than the core in the neutral zone, and the cores in the neutral zone experienced higher strength than the core in the tension zone.

From the previous figures and discussion, it is observed that the cores in the compression zone experienced higher strength than the core in the neutral zone, and the cores in the neutral zone experienced higher strength than the core in the tension zone. One of the rationales of this phenomenon is that micro-cracks usually occurred in the tension zone. As a result, the strength is low in the tension zone.

4   Conclusion

Based on this experimental study on concrete core strength, the following conclusion can be drawn:

1. The concrete cores drilled from different locations of reinforced concrete beam experience variations in compressive strength.
2. The compressive strength of cores drilled from the tension zone, compression zone, and neutral zone of the reinforced concrete beam has been found lower than the corresponding cylinder strength.
3. The cores in the compression zone experience higher strength than the core in the neutral zone and tension zone, and the cores in the neutral zone experience higher strength than the core in the tension zone.

References

1. Szypula, A., Grossman, J.S.: Cylinder versus core strength. Concr. Int. **12**, 55–61 (1990)
2. Khoury, S., Aliabdo, A.A.H., Ghazy, A.: Reliability of core test—critical assessment and proposed new approach. Alex. Eng. J. **53**, 169–184 (2014). https://doi.org/10.1016/j.aej.2013.12.005
3. Ju, M., Park, K., Oh, H.: Estimation of compressive strength of high strength concrete using non-destructive technique and concrete core strength. J. Appl. Sci. **7**, 1–16 (2017). https://doi.org/10.3390/app7121249
4. Lessly, S.H., Senthil, R., Krishnakumar, B.: A study on the effect of reinforcement on the strength of concrete core. Mater. Today: Proc. (2020)
5. Chkheiwer, A., Kadim, J.: Evaluation of effecting factors of traditional and super plasticizer concrete core strength. Kufa J. Eng. **09**, 220–233 (2018). https://doi.org/10.30572/2018/kje/090415

6. AASHTO T 24M/T 24-15: Standard method of test for obtaining and testing drilled cores and sawed beams of concrete. In: Standard Specifications for Transportation Materials and Methods of Sampling and Testing, vol. 23, pp. 2841–2852 (2018)
7. ACI 214.4R-03: Guide for obtaining cores and interpreting compressive strength results. ACI Committee Rep. **10**, 1–16 (2003)
8. Loo, Y.H., Tan, C.W., CTT: Effects of embedded reinforcement on measured strength of concrete cylinders. Mag. Concr. Res. **41**, 11–18 (1989). https://doi.org/10.1680/macr.1989.41.146.11
9. Michael Bartlett, F., MacGregor, J.G.: Equivalent specified concrete strength from core test data. Concr. Int. **17**, 52–58 (1995)

Post-Fire Residual Capacity of Reinforced Concrete Beam

M. H. Bhuiyan and S. Ahmed

1 Introduction

Over the last few years, the fire hazard is a common scenario in developing countries due to lake of proper planning. In these regions, reinforced concrete (RC) is the main construction material due to its availability and low price. Low thermal conductivity coupled with high heat capacity gives RC structure good fire-resisting property [1, 2]. However, RC members lose their strength and stiffness under fire exposure condition comparing to that of ambient conditions [3]. This degradation of strength and stiffness of RC members under fire exposure condition depends on the temperature and duration of the fire exposure and material properties of concrete and reinforcing steel at elevated temperature.

The assessment of the post-fire residual capacity of the structure is critical for the rehabilitation of a fire-affected structure. Previous studies showed that there are different approaches to evaluate the residual capacity of RC structures. Some of the individuals used laboratory environment to examine the residual capacity [1, 4–7]. They noticed that duration of fire and rebar peak temperature had significant effect on the residual capacity of RC members. Some other researchers [8–10] used simplified cross-sectional or finite element analysis method to determine the residual capacity of RC beams. Hsu and Lin [8] divided critical section into number of strips and calculate the temperature of each strip, then used strength–temperature relation of concrete and steel reinforcement to evaluate the residual capacity which was very cumbersome. In the other hand, Kodur et al. [10] used residual strength of rebar at

M. H. Bhuiyan
Department of Civil Engineering, Daffodil International University, Dhaka, Bangladesh
e-mail: mehedihassanbhuiyan.ce@diu.edu.bd

S. Ahmed (✉)
Department of Civil Engineering, Bangladesh University of Engineering and Technology, Dhaka, Bangladesh
e-mail: shameemahmed@ce.buet.ac.bd

the peak temperature and design equations of ambient temperature [11] to compute the post-fire residual capacity of RC beams. In this method, reduction of concrete strength due to the exposure to fire was ignored. Ožbolt et al. [12] proposed detailed transient 3D thermo structural FE analysis to evaluate post-fire capacity of RC beams.

The aim of this study was to examine the post-fire residual capacity of the RC beam using FE model. For this purpose, FE model of RC beams with different span lengths and cross sections was developed to determine their residual capacities when exposed to fire for 30–240 min. In addition, the clear cover of the RC beams was varied to observe the effect of clear cover on the residual capacity. Finally, the residual capacity determined by FE analysis was compared with the computed residual capacity using simplified method.

2   Finite Element Model

The post-fire capacity of RC beam was determined by using FE software package ABAQUS [13]. The full analysis was conducted in two steps: thermal analysis and structural analysis. At first, concrete beam with steel reinforcement was modeled where reinforcements were tied with concrete for proper transfer of heat and force. In thermal analysis, ASTM E119 [14] fire curve was applied as a fire temperature on the bottom and sides of the RC beam. Top of the beam and top 150 mm of both sides of the RC beam were considered unexposed to fire due to the presence of slab. The convective heat transfer coefficients were taken as 25 and 9 W/(m^2 K) for fire exposed and unexposed surfaces of RC beam, respectively, in accordance with Eurocode 2 [3]. While considering radiative heat transfer, the emissivity constant of 0.8 was considered for fire exposed concrete surface [3]. In the FE thermal analysis, eight node continuum element DC3D8 and two node link element DC1D2 were used for concrete and steel reinforcement, respectively [13].

In the second step, temperature of different elements from thermal analysis was assigned as the initial condition for the structural analysis from FE model using predefined field. In the FE model for structural analysis, the mesh distribution remained same as the thermal model. However, DC3D8 and DC1D2 elements were replaced with C3D8R element for concrete and T3D2 element for reinforcement, respectively [13]. To achieve sufficiently accurate result within optimal computation time, a tolerance limit of 0.02 was used in Newton–Raphson solution technique, and line search control was activated for rapid convergence [2, 15–19].

3   Material Property for FEA

In this study, the compressive strength of concrete (f_c') at room temperature was considered 27.6 MPa, and the tensile strength was taken as 10% of f_c' [20]. The yield strength of the steel reinforcement f_y at room temperature was 420 MPa. Previous
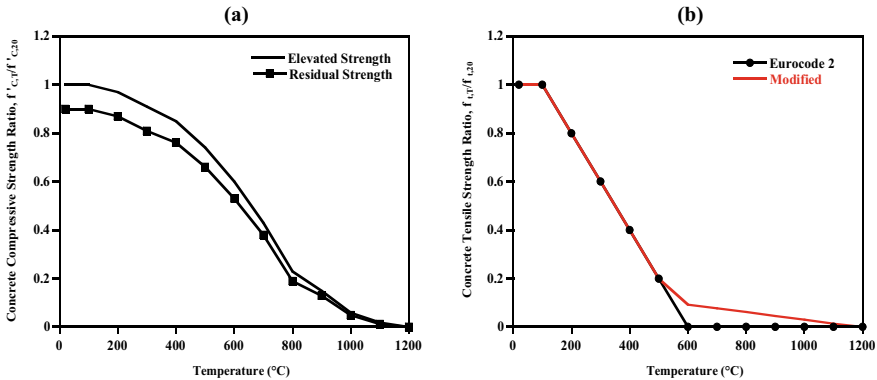
Fig. 1 Variation of concrete **a** compressive and **b** tensile strength ratio with temperature

studies reported that the compressive and tensile strength of concrete decrease at elevated temperature due to fire exposure and these strengths further decrease after a cool down period, commonly known as residual strength [2, 21]. Figure 1a shows the variation of compressive strength of concrete at elevated temperature according to Eurocode 2 [3] and residual strength of concrete according to [2, 21]. The residual strength of concrete thus found was used in the structural analysis model to determine the residual capacity of RC beam after fire exposure. Figure 1b shows that at 600 °C the tensile strength capacity of concrete becomes zero as per Eurocode 2 and an increase of this temperature makes convergency problem in FE model. To solve this problem, Dwaikat and Kodur [22] modified the tensile strength capacity of concrete above 600 °C temperature. The modified tensile strength relationship of concrete with temperature was used in this study.

The stress–strain relationship of concrete generally divides into three parts, namely linear elastic, hardening and softening. The first part is linear elastic up to 30 to 50% of compressive strength of concrete [2, 20, 23]. So, in this study, linear elastic part was assumed 33% of f_c'. The hardening portion of this curve tends to parabolic [3, 20, 21, 23], and softening part may be linearly descending [3, 24, 25] or parabolic [24, 26]. For both hardening and softening parts, parabolic stress–strain relationship was considered. Moreover, the dilation angle of concrete was taken as 35° [27, 28]. The yield strength of reinforcing steel at elevated temperature and their residual yield strength after cool down is presented in Fig. 2 [2]. The temperature-dependent properties, e.g., conductivity, specific heat and density of concrete and steel were used according to Eurocode 2 for this analysis [3].
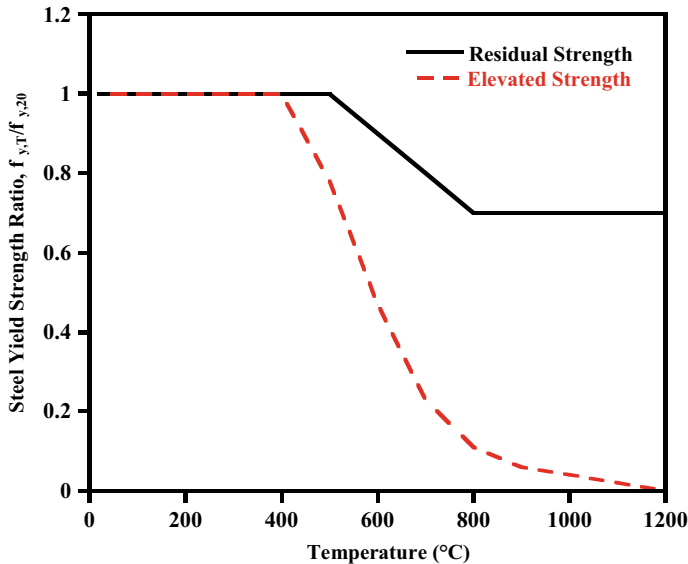
Fig. 2 Variation of yield strength of steel with temperature

4 Validation of the FE Model

The FE model was validated against the test performed by Dwaikat and Kodur [1]. They tested a 3960 mm long simply supported beam with 406×254 mm rectangular cross section. Middle 2440 mm of the beam was exposed to ASTM E119 fire [14]. The beam had $3\phi 19$ mm tension bars at the bottom and $2\phi 13$ mm compression bars at the top. As shear reinforcement, $\phi 6$ mm was provided with a spacing of 150 mm over the beam length. The compressive strength on test day and 28-day tensile strength were measured as 58.2 ± 3.1 MPa and 3.7 ± 0.5 MPa, respectively. The yield strength of longitudinal bars and transverse bars was 420 MPa and 280 MPa, respectively.

Authors applied 50 KN load at 610 mm apart from center of the beam for 30 min before the beam was exposed to fire. In the laboratory, structural fire test chamber was designed specially so that load could be maintained constantly throughout the duration of the fire. Following the procedure discussed in the previous section, the beam was modeled, and the results obtained from FE analysis were compared with test results. Figure 3a shows the near overlapping experimental and modeling results in case of temperature variation with respect to time at three specific points (i.e., at mid depth, at quarter depth, and at bottom rebar) of the beam mid-section. Both experimental and modeling results show that the mid-span deflection increased with time until the beam failed after 180 min of fire exposure due to diminished strength and stiffness (Fig. 3b).
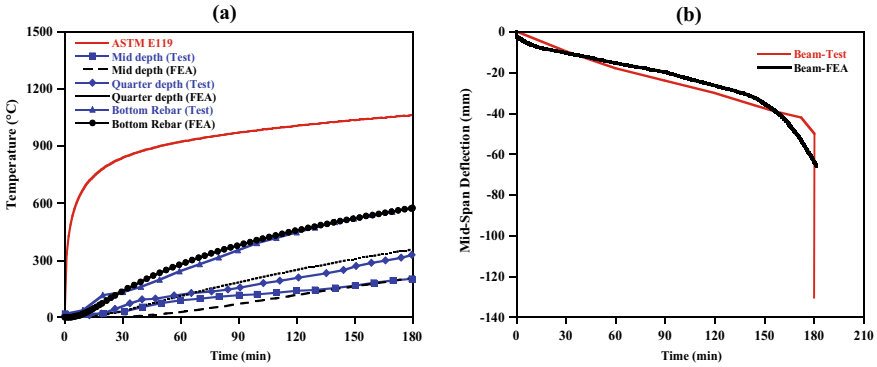
Fig. 3 Comparison of the RC beam tested by Dawaikat [1]: **a** test and FE computed temperature at various location **b** test and FE computed mid-span deflection of simply supported beam

5 Parametric Study

The validated FE approach was used to determine the residual capacity of 4 (four) RC beams after exposure to fire. The length (L) and support to support distance (L_s) of B1 and B2 beams were 6000 mm and 5600 mm, respectively. The cross section and reinforcement of beam B1 and B2 were same as shown in Fig. 4, albeit clear covers of B1 and B2 were 38 mm and 50 mm, respectively. For B3 and B4 beams pair, L and L_s were 4500 mm and 4200 mm, respectively. The cross section and reinforcement of B3 and B4 were same, albeit clear cover of B3 and B4 was 38 mm and 50 mm, respectively.

The RC beams were designed as per ACI Code 318–08 [11] for 4 kip/ft uniformly distributed load considering f'_c as 27.6 MPa and f_y as 420 MPa as discussed in Sect. 3. Fire was applied on three sides of the beam as depicted in Fig. 4. The capacity of all four RC beams were determined in ambient conditions and after 30, 60, 120, 180 and 240 min exposure to standard ASTM E119 fire [14]. A total of 24 models were thus analyzed for different fire scenarios.
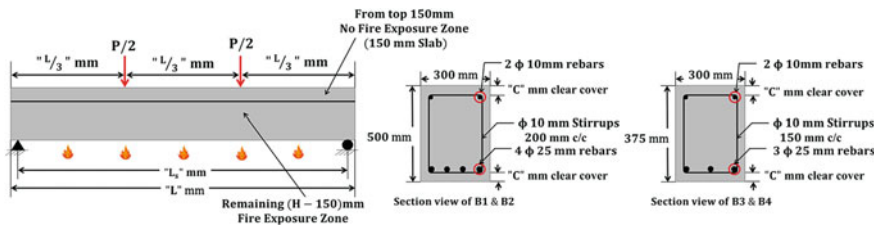
Fig. 4 Beam sectional profile detail of typical RC beams selected for parametric study

6   Results and Discussions

The post-fire residual capacity and stiffness of all four beams (i.e., B1, B2, B3 and B4) decrease with longer fire exposure time. These contribute to the higher deflections at ultimate loads for longer period (i.e., 240 min) and shown in Figs. 5 and 6 for beams B1 and B2, and B3 and B4, respectively. Beams B1 and B2 had the same cross section and span length with different clear cover. However, up to 120 min of fire exposure, the residual capacity of B1 and B2 did not differ significantly. After that, the residual capacities of B2 were slightly higher than B1. Both B1 and B2 beams showed ductile post failure behavior up to 120 min of fire exposure. After 180 min and 240 min of exposure, failure of both B1 and B2 beams was brittle in nature as failure occurred due to the crushing of concrete. From Fig. 6, similar behavior was found for B3 and B4 beams. For B3 and B4 beams, brittle failure was observed after 240 min of exposure.

In Fig. 7, the ratio of post-fire residual moment capacity to the ambient moment capacity of all the four RC beams was shown for different exposure times. The residual moment capacity of B1 and B2 beam pair decreases slower than B3 and B4 beam pair up to 120 min of fire exposure which was reversed after 120 min of fire exposure. In addition, it is observed that up to 120 min of fire exposure, clear cover of the beam does not play any important role in the residual moment capacity. But for exposure longer than 120 min, the residual moment capacity of the beams with 50 mm clear cover (i.e., B2 and B4 beams) was 3–5% higher than the residual capacity of the beams with 38 mm clear cover (i.e., B1 and B3 beams).

The post-fire residual capacity of the studied RC beams with their peak temperature at bottom reinforcement after different fire exposure times is presented in Table 1. The residual capacities determined by FE analysis were also compared with the residual moment capacity computed using simplified method proposed by Kodur
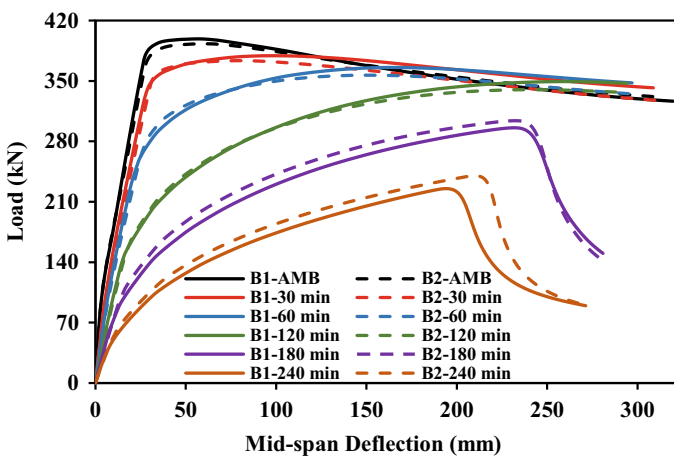
Fig. 5 Post-fire load–displacement behavior of B1 and B2 after different fire exposure time
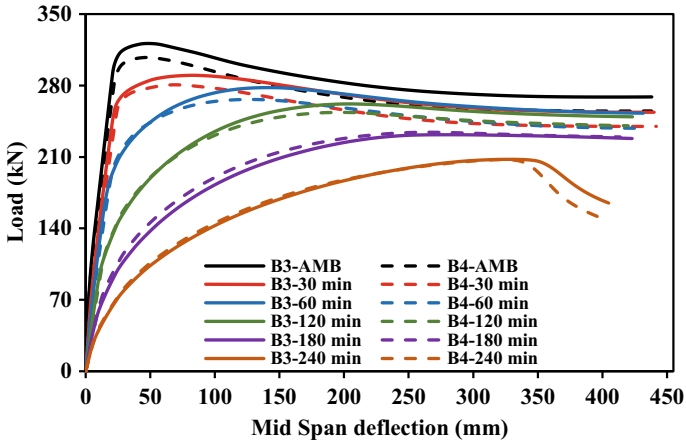
Fig. 6 Post-fire load–displacement behavior of B3 and B4 after different fire exposure time
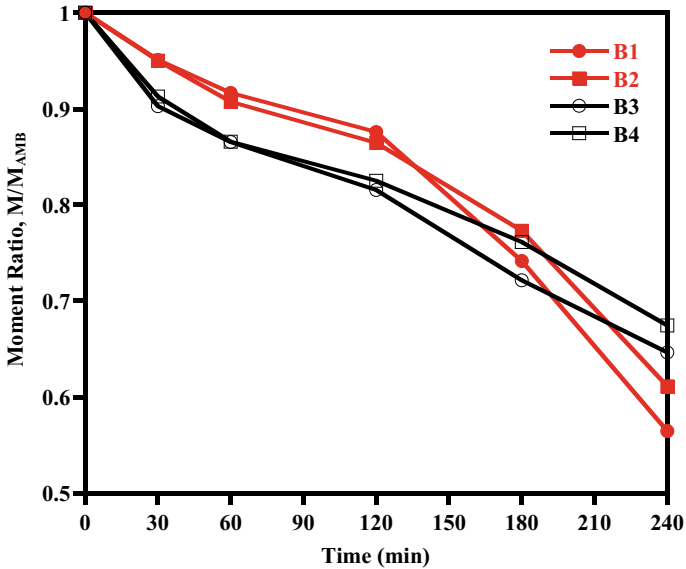
Fig. 7 Variation of the ratio of post-fire residual moment capacity to the ambient moment capacity with fire exposure time

et al. [10]. In the simplified method, the post-fire residual moment capacity depends on the residual strength of steel reinforcement. As shown in Fig. 2, residual yield stress of reinforcement is equal to the yield stress at ambient temperature up to 500 °C. This explains the fact that when peak rebar temperature is less than 500 °C, RC beam's residual capacity remains same as ambient condition. From Table 1, it is

Table 1 Post-fire residual moment capacity of RC beam for different exposure time

Specimen ID	Rebar temperature (°C)	Residual capacity (kN)	
		FEA	Simplified approach [10]
B1-AMB	20	398.8	352.0
B1-30 min	163	379.3	352.0
B1-60 min	336	365.6	352.0
B1-120 min	551	349.3	336.5
B1-180 min	681	295.7	296.0
B1-240 min	740	225.2	277.0
B2-AMB	20	393.1	341.1
B2-30 min	128	373.6	341.1
B2-60 min	281	356.7	341.1
B2-120 min	486	339.9	341.1
B2-180 min	621	303.9	305.4
B2-240 min	713	240.3	277.2
B3-AMB	20	321.2	265.0
B3-30 min	188	290.0	265.0
B3-60 min	370	277.9	265.0
B3-120 min	589	261.9	245.0
B3-180 min	713	231.8	215.8
B3-240 min	764	207.7	203.5
B4-AMB	20	307.5	253.6
B4-30 min	147	280.7	253.6
B4-60 min	309	266.3	253.6
B4-120 min	520	253.7	249.4
B4-180 min	654	234.2	220.2
B4-240 min	732	207.5	202.5

observed that for B3 and B4 beams, simplified method conservatively predicts the post-fire residual capacity. However, for B1 and B2 beams, simplified method seems nonconservative when beams exposed in fire for longer period. In FE analysis, both residual strength of concrete and steel was considered for determining the residual capacity. On the other hand, in simplified method, only residual strength of steel was used assuming that failure would be initiated by the yielding of reinforcement. If a beam fails due to the crushing of concrete, then the simplified method overestimates the residual capacity of that beam. For example, when B1 and B2 beams were exposed for 180 and 240 min in fire, they showed brittle failure due to crushing of concrete. This contributes to overestimation of residual moment, i.e., 277 kN against 225.2 kN for B1 beam under 240 min exposure time.

7 Conclusion

In this present study, a parametric study was performed to compute the post-fire residual capacity of RC beam using FE analysis. Before parametric studying, FE model was verified against experimental results. A total of 24 models were analyzed for two different span length and four beam sections with 38 and 50 mm clear covers. From the analysis, it was observed that with the increase of exposure time, the post-fire residual capacity decreased. After 120 min of exposure, the residual moment capacity became 80% of its ambient capacity. After that point, residual capacity reduced more quickly. After 240 min of exposure, the residual capacity became around 55% of its ambient capacity. It was observed that, after longer period of fire exposure, failure of RC beam may become brittle in nature. In this study, it was found that clear cover of RC beams has no significant effect on the post residual capacity of the RC beams. The FE model results were also compared with the calculated residual capacity using simplified method. Comparison showed that simplified method can be nonconservative when the RC beam failed due to the crushing of concrete.

References

1. Dwaikat, M.B., Kodur, V.K.R.: Response of restrained concrete beams under design fire exposure. J. Struct. Eng. **135**, 1408–1417 (2009). https://doi.org/10.1061/(ASCE)ST.1943-541X.0000058
2. Kodur, V.K.R., Agrawal, A.: An approach for evaluating residual capacity of reinforced concrete beams exposed to fire. Eng. Struct. **110**, 293–306 (2016). https://doi.org/10.1016/j.engstruct.2015.11.047
3. EN 1992-1-1: Eurocode 2: Design of Concrete Structures—Part 1-1: General Rules and Rules for Buildings (2004)
4. Kumar, A, Kumar, V.: Behaviour of RCC beams after exposure to elevated temperatures. J.—Inst. Eng. India Part CV Civ. Eng. Div. **84**, 165–170 (2003)
5. Choi, E.G., Shin, Y.-S., Kim, H.S.: Structural damage evaluation of reinforced concrete beams exposed to high temperatures. J. Fire Prot. Eng. **23**, 135–151 (2013). https://doi.org/10.1177/1042391512474666
6. Xu, Y., Wu, B., Jiang, M., Huang, X.: Experimental study on residual flexural behavior of reinforced concrete beams after exposure to fire. In: Advanced Materials Research, pp. 183–187. Trans Tech Publications Ltd.(2012)
7. El-Hawary, M.M., Ragab, A.M., El-Azim, A.A., Elibiari, S.: Effect of fire on flexural behaviour of RC beams. Constr. Build. Mater. **10**, 147–150 (1996). https://doi.org/10.1016/0950-0618(95)00041-0
8. Hsu, J.-H., Lin, C.-S.: Effect of fire on the residual mechanical properties and structural performance of reinforced concrete beams. J. Fire Prot. Eng. **18**, 245–274 (2008). https://doi.org/10.1177/1042391507077171
9. Bai, L., Wang, Z.: Residual bearing capacity of reinforced concrete member after exposure to high temperature. In: Advanced Materials Research, pp. 577–581. Trans Tech Publications Ltd. (2012)
10. Kodur, V.K.R., Dwaikat, M.B., Fike, R.S.: An approach for evaluating the residual strength of fire-exposed RC beams. Mag. Concr. Res. **62**, 479–488 (2010). https://doi.org/10.1680/macr.2010.62.7.479

11. American Concrete Institute (ACI 318-99): Building Code Requirements for Structural Concrete (1999)
12. Ožbolt, J., Bošnjak, J., Periškić, G., Sharma, A.: 3D Numerical analysis of reinforced concrete beams exposed to elevated temperature. Eng. Struct. **58**, 166 (2014). https://doi.org/10.1016/j.engstruct.2012.11.030
13. Abaqus 6.14 Documentation
14. ASTM E119: Standard Test Methods for Fire Tests of Building Construction and Materials, ASTM International, West Conshohocken, PA. ASTM Int West Conshohocken, PA 552 (2016). https://doi.org/10.1520/E0119-14
15. Wu, B., Lu, J.Z.: A numerical study of the behaviour of restrained RC beams at elevated temperatures. Fire Saf. J. **44**, 522–531 (2009). https://doi.org/10.1016/j.firesaf.2008.10.006
16. Rafi, M.M., Nadjai, A., Ali, F.: Finite element modeling of carbon fiber-reinforced polymer reinforced concrete beams under elevated temperatures. ACI Struct. J. (2016)
17. Schweizerhof, K.: Consistent concept for line search algorithms in combination with arc-length constraints. Commun. Numer. Methods Eng. **9**, 773–784 (1993). https://doi.org/10.1002/cnm.1640090908
18. Crisfield, M.A.: Accelerated solution techniques and concrete cracking. Comput. Methods Appl. Mech. Eng. **33**, 585–607 (1982). https://doi.org/10.1016/0045-7825(82)90124-4
19. Gao, W.Y., Dai, J.G., Teng, J.G., Chen, G.M.: Finite element modeling of reinforced concrete beams exposed to fire. Eng. Struct. **52**, 488–501 (2013). https://doi.org/10.1016/j.engstruct.2013.03.017
20. Hafezolghorani, M., Hejazi, F., Vaghei, R., Bin, J.M.S., Karimzade, K.: Simplified damage plasticity model for concrete. Struct. Eng. Int. **27**, 68–78 (2017). https://doi.org/10.2749/101686616X1081
21. Europeenne, N.: EUROPEAN STANDARD Eurocode 4: Design of composite steel and concrete structures-Part 1-1: General rules and rules for buildings (2004)
22. Dwaikat, M.B., Kodur, V.K.R.: Hydrothermal model for predicting fire-induced spalling in concrete structural systems. Fire Saf. J. **44**, 425–434 (2009). https://doi.org/10.1016/j.firesaf.2008.09.001
23. Najafgholipour, M.A., Dehghan, S.M., Dooshabi, A., Niroomandi, A.: Finite element analysis of reinforced concrete beam-column connections with governing joint shear failure mode. Lat. Am. J. Solids Struct. **14**, 1200–1225 (2017). https://doi.org/10.1590/1679-78253682
24. Youssef, M.A., Moftah, M.: General stress-strain relationship for concrete at elevated temperatures. Eng. Struct. **29**, 2618–2634 (2007). https://doi.org/10.1016/j.engstruct.2007.01.002
25. Hajiloo, H., Green, M.F.: GFRP reinforced concrete slabs in fire: finite element modelling. Eng. Struct. **183**, 1109–1120 (2019). https://doi.org/10.1016/j.engstruct.2019.01.028
26. Wahalathantri, B., Thambiratnam, D., Chan, T., Fawzia, S.: A Material Model for Flexural Crack Simulation in Reinforced Concrete Elements Using ABAQUS (2011)
27. Wosatko, A., Winnicki, A., Polak, M.A., Pamin, J.: Role of dilatancy angle in plasticity-based models of concrete. Arch. Civ. Mech. Eng. **19**, 1268–1283 (2019). https://doi.org/10.1016/j.acme.2019.07.003
28. Díaz, R., Wang, H., Mang, H., Yuan, Y., Pichler, B.: Numerical analysis of a moderate fire inside a segment of a subway station. Appl. Sci. **8** (2018). https://doi.org/10.3390/app8112116

Influence of Inorganic and Natural Fibers on Low-Strength Concrete Properties

R. Sabrin, A. Islam, and N. S. Rahat

1 Introduction

For both engineered and non-engineered structures, practical application of low-cost, low-strength concrete (LSC) is not limited, especially in a developing country like Bangladesh. Increased deficiency of good quality of aggregates, poor design and construction practices cause high susceptibility of concrete strength, leading to brittle failure under lateral loads. Wide range of LSC, compressive strength varying from 4 to 20 MPa was found from the data analysis of the existing structure of developing countries [1, 2]. Nevertheless, LSC has been performing as compacted fill materials, conventional lean-mix floors or bases, flow-able backfills, etc. [3, 4].

In structural applications, there is a high significance of material brittleness. Unfortunately, brittleness and low tensile strength are the innate flaws of plain concrete, whereas brittleness, a mechanical property of a specific material, is not precisely defined by any author. However, higher brittleness of a material can be detected by lower values of elongation, the formation of cracks in an indentation, higher resilience, fracture failure, higher angle of internal friction, the formation of fines, higher compressive-to-tensile strength ratio [5]. Another definition of brittleness is lack of ductility [6]. Determining how brittle a material is basically an empirical measure. It can be signified the relative susceptibility of a specific material to two opposing mechanical responses [7].

With the growing interest in introducing fiber into the fresh normal to ultra-high-strength concrete as strengthening materials, mechanical properties specially the tensile strength were witnessed to increase by many researchers [8–16]. Considering

R. Sabrin (✉)
Department of Civil Engineering, Military Institute of Science and Technology, Dhaka, Bangladesh

A. Islam · N. S. Rahat
Department of Civil Engineering, Ahsanullah University of Science and Technology, Dhaka, Bangladesh

availability and cost-effectiveness, inorganic waste: glass fiber (GF) or agricultural surplus: jute fiber (JF) can be utilized as reinforcing material. Therefore, it is reasonable to observe the mechanical behavior of fiber-reinforced low-strength concrete (FR-LSC).

The present research aimed to investigate the individual influence of various reinforcing parameters, fiber types (natural JF, inorganic GF), content (constant volumetric fraction of 0.5%), lengths (20, 30 mm) and aspect ratios on the basic mechanical properties in terms of compressive strength and tensile strength of FR-LSC specimens. Furthermore, this study also provides a comparative assessment of the brittleness nature of FR-LSC over the LSC.

2 Experimental Program

2.1 Materials

In this experiment, the constituent materials of concrete included stone chips (max size of 19 mm) as coarse aggregate (CA), natural river sand as fine aggregate (FA), GF or JF as reinforcing material, ordinary Portland cement (C) and freshwater (W). Used cement had a specific gravity of 3.12. Materials were collected from a local source. The particle size distribution of FA presented in Table 1 indicates that gradation did not fall within the specified limits. After the investigations of aggregates following standard procedure, the bulk specific gravity (SSD), water absorption and unit weight of CA were found to be 2.56, 2.48% and 1550 kg/m^3 respectively. For FA, those physical properties were observed to be 2.34, 1.05% and 1635 kg/m^3 respectively. Two different fibers, e-glass fiber and raw jute fiber having two variable lengths of 20 and 30 mm, were chosen for the test (Fig. 1). Both e-glass and jute fibers were

Table 1 Grain size distribution of fine aggregate

Particle size (mm)	4.75	2.36	1.18	0.6	0.3	0.15	0.075	Fineness modulus (FM) = 1.34
% passing	100	100	96.67	84.97	59.50	24.91	0	
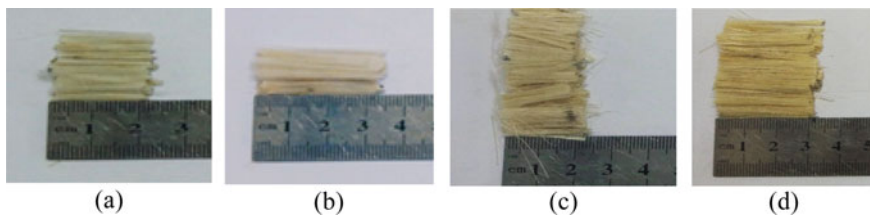
Fig. 1 Fibers with variable lengths: **a** GF (20 mm); **b** GF (30 mm); **c** JF (20 mm); **d** JF (30 mm)

Table 2 Properties of GF and JF used

Fiber type		Color	Diameter, d_f (μm)	Length, l_f (mm)	Aspect ratio (l_f/d_f)	Density (g/cm^3)	Tensile strength (MPa)
G20	Glass fiber	Whitish	1.5	20	133.33	2.58	3445
G30				30	200		
J20	Jute Fiber	Brown	2.0	20	100	1.45	300–700
J30				30	150		

Table 3 Constituent materials of LSC mixtures (for 1 m^3 of concrete)

Concrete mix (symbol)	Fiber type and content			CA (kg)	FA (kg)	C (kg)	W (kg)
	Type	V_f (%)	(kg)				
LSC-F0	–	–	–	1302	686.7	201.6	100.8
LSC-G20	G20	0.50	1806				
LSC-G30	G30	0.50	1806				
LSC-J20	J20	0.50	1015				
LSC-J30	J30	0.50	1015				

bought from the local market. E-glass fiber was supplied from India and the local price of the product ranges from 350 to 550 BDT/kg. Compared to glass fiber, jute fiber is inexpensive (approximately 75 BDT/kg) and available agricultural product of Bangladesh. Properties of GF and JF are shown in Table 2; data of density and tensile strength were collected from the manufacturer.

2.2 Concrete Mixing Proportions

There is no standard mix design method for LSC. Therefore, traditional and local procedure, a volumetric mix proportion of 1:3:6 represents C: FA: CA was adopted for the cementitious composite. Five concrete mixes were prepared with water-to-cement ratio (by weight) of 0.50. For fiber-reinforced LSC specimens, fiber volume fraction (V_f) of 0.50% was maintained. Accordingly, the proportions of constituent materials for LSC mixes investigated are shown in Table 3.

2.3 Sample Preparation and Test Procedure

For five trial mixes, a total of 60 cylinder concrete specimens of size 100 mm × 200 mm were prepared to evaluate compressive and tensile strength at two curing ages: 7 and 28 days. Two different types of raw fiber, JF and GF, were collected
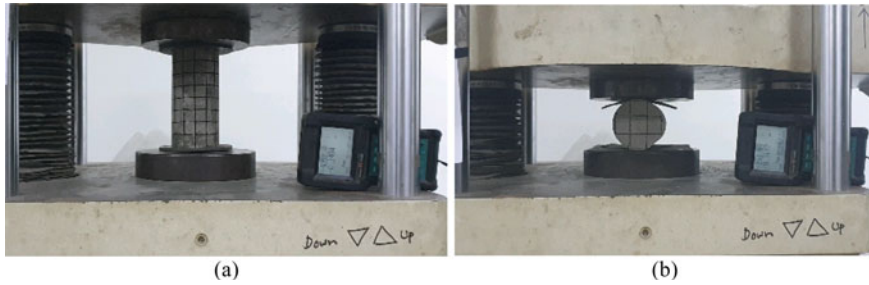
Fig. 2 Experimental test setup: **a** compressive strength test and **b** split tensile strength test

and cut into two variable lengths 20 mm and 30 mm with the hand scissors. The fiber quantity of 0.5% of the total volume of the concrete was kept constant. To ensure the proper distribution of fiber, fibers were added gradually during concrete mixing in the mixture machine. Concrete workability was measured by a slump cone test before placing the mixture into the cylindrical steel molds. Slump values for all LSC specimens studied were found to be 130 ± 10 mm which confirmed a flowable concrete. Cylindrical specimens were demolded after 24 h of casting and afterward submerged in the freshwater for curing. Following 7 and 28 days of curing, samples were collected from the curing tank and then specimens became ready for the strength test.

To investigate the effect of fiber type and fiber length on the load carrying capacity of the LSC, specimens were tested by using a universal testing machine (UTM). Gradually, the load was applied with a constant deformation rate of 1 mm/min until the failure of the specimen. Testing of uniaxial compressive strength [17] and split tensile strength [18] of the cylinder samples were performed. Both of the test setups for conducted experiments are shown in Fig. 2.

3 Experimental Results and Discussion

3.1 Effect of Fiber on Compressive and Tensile Strength of LSC

Experimental results of uniaxial compressive strength and split tensile strength for all concrete mixes studied are presented in Table 4. Figure 3a, b clarify the ranges of the compressive and tensile strength, respectively, found at 28 days of curing of the concrete specimens.

From the test results, it is found that concrete having JF enhanced both the compressive and tensile strength of the LSC than concrete with GF. However, for both cases, it is evident that adding shorter fiber (20 mm) is better in terms of strength

Table 4 Compressive strength and split tensile strength test result

Concrete mix	Compressive strength, C (MPa)					Split tensile strength, T (MPa)				
	7 days	28 days				7 days	28 days			
	avg	avg	SD	CoV	% SI	avg	avg	SD	CoV	% SI
LSC-F0	6.3	8.1	0.70	8.65	-	1.2	1.7	0.23	13.85	-
LSC-G30	6.5	8.2	0.27	3.33	1.7	1.2	1.8	0.07	4.21	6.6
LSC-J30	6.6	8.3	0.65	7.88	2.6	1.3	1.8	0.14	7.91	9.6
LSC-G20	7.1	9.8	1.19	12.17	20.9	1.5	2.2	0.10	4.78	33
LSC-J20	7.8	11.3	1.55	13.72	39.9	1.6	2.7	0.15	5.51	62

avg—average; SD—standard deviation; CoV—coefficient of variance; % SI—strength increment (%) = [(strength of FRC − strength of LSC-F0)/strength of LSC-F0] × 100%
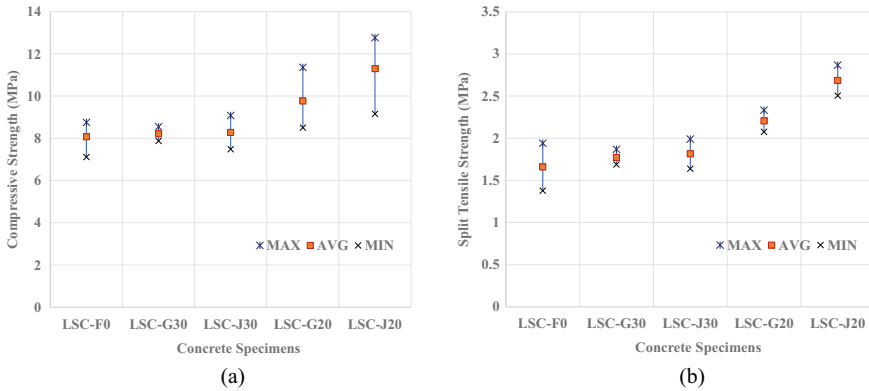
Fig. 3 Effect of GF and JF on 28 days of strength of LSC **a** compressive strength, **b** tensile strength

than the inclusion of longer fiber (30 mm). Among all five concrete mixes investigated in this study, the strength enhancement of LSC-J20 specimens is noteworthy. For LSC-J20, 28 days of cylinder compressive strength varied from 9.2 to 12.8 MPa, with an average of 39.9% strength improvement and split tensile strength ranged from 2.5 to 2.9 MPa, with an average 62% strength increment was noticed over the reference mix, LSC-F0.

3.2 Influence of Introducing Fiber on the Strength Gain with the Ages of LSC

The influence of the type and length of fiber on the development of the LSC compressive and tensile strength for early (7 days) and extended curing ages (28 days) are illustrated in Fig. 4. It was observed that compared to plain LSC, incorporating GF or JF is beneficial in terms of attaining compressive and tensile strength for 7 and 28 days of curing. With the ages, enhancement in tensile strength, presented in Fig. 4c, d was found to be more remarkable than the improvement in compressive strength, shown in Fig. 4a, b. Nevertheless, introducing a longer length of fiber can cause discontinuation of constituent distribution or improper dispersion in concrete matrix leading to an insignificant increment in strength. Concrete with the 30 mm fiber cut showed lower compressive strength gaining rate in 28 days rather than early stages. However, test results revealed that with 0.5% volume fraction, LSC-J20 exhibited the highest mechanical strength properties from early to matured curing ages (from 7 to 28 days) of concrete compared to other concrete mixes.
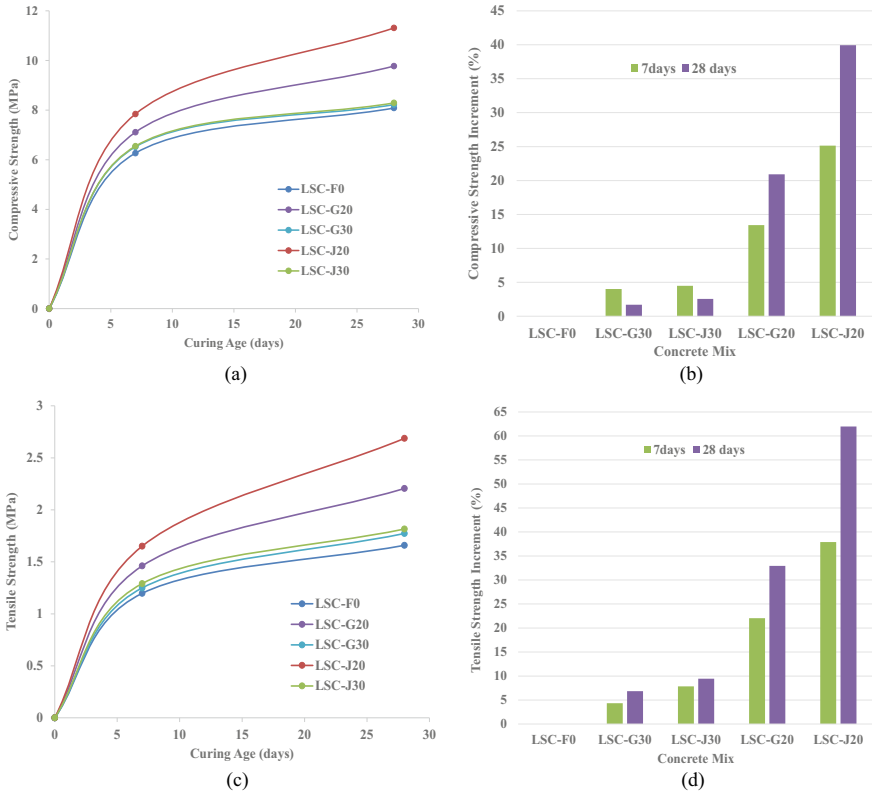
Fig. 4 Effect of fiber on the strength gain of different concrete mixes with curing ages **a** compressive strength, **b** increment of compressive strength, **c** tensile strength, **d** increment of tensile strength

3.3 Role of Fiber on Brittleness of LSC

Different methods or empirical equations can be followed to compute the brittleness index (BI) of a material. Zheng et al. [19] suggested stress–strain hysteresis loops to calculate the BI of concrete. To measure BI of rock, Hucka and Das [5] proposed Eq. (1) and researchers [7, 20] also used Eqs. (2)–(4). In this study, Eqs. (1–4) were used to assess the brittleness of the concrete (Table 5).

$$BI_1 = \frac{C - T}{C + T} \quad \dots \tag{1}$$

$$BI_2 = \frac{C}{T} \quad \dots \tag{2}$$

$$BI_3 = \frac{C \times T}{2} \quad \dots \tag{3}$$

Table 5 Brittleness of concrete

Concrete mix	Aspect ratio of fiber	Brittleness index, 28 days				T/C, 28 days	Reduction in brittleness of LSC (%)
		BI_1	BI_2	BI_3	BI_4		
LSC-F0	–	0.659	4.867	6.706	2.590	0.205	–
LSC-G30	200	0.646	4.644	7.275	2.697	0.215	4.81
LSC-J30	150	0.640	4.555	7.544	2.747	0.220	6.86
LSC-G20	133.33	0.631	4.421	10.796	3.286	0.226	10.10
LSC-J20	100	0.615	4.194	15.233	3.903	0.238	16.04

$$BI_4 = \sqrt{\frac{C \times T}{2}} \quad \ldots \tag{4}$$

Here, Brittleness Index, BI_1, and BI_2, are unitless parameters, BI_3 and BI_4 are in $(MPa)^2$ and MPa, respectively. The lower BI_1 and BI_2 and higher BI_3 and BI_4 indicate lower brittleness of the material. Alternative simplified form, the tension-to-compression ratio (T/C), can directly represent the brittleness behavior of concrete [21]. The greater the value of T/C, the lower the brittleness, which indirectly infers improved ductility and toughness [22]. Comparative brittleness nature of fiber added LSC for 28 days is presented in Table 5.

Figure 5a, b illustrate the T/C ratio and reduction of the brittleness of different concrete mix, respectively. It was found that for both the curing ages (7 and 28 days), the brittleness of LSC was decreased by introducing fiber in fresh concrete. A good percentage of reduction in brittleness was found for both LSC with GF or JF of 20 mm length (lower aspect ratio). LSC-J20 showed comparatively better performance in
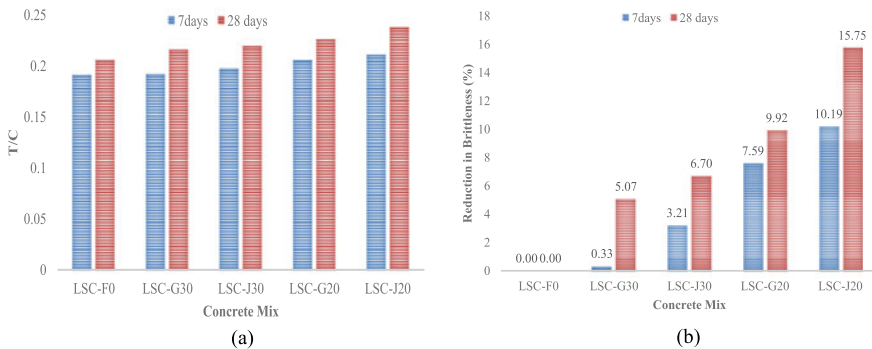
Fig. 5 Brittleness parameters of LSC mixes **a** variation in tensile-to-compressive strength ratio, **b** comparison in reduction of brittleness

terms of brittleness, in other words, more ductile than other studied concrete specimens. More specifically, for 7 and 28 days, the brittleness of LSC-J20 was abated 9.96% and 16.04% of LSC-F0, respectively.

It is more likely that when the crack initiates, fiber performs as a bridging material to prevent the further opening or propagation of cracks. Therefore, it can be said that the crack arresting mechanism of LSC with JF having an aspect ratio of 100 suppress over LSC with fiber having a lower aspect ratio. Interestingly, neglecting the effect of fiber type, the brittleness of LSC gradually reduced with the diminution of the aspect ratio of fiber. Further investigations are necessary to comprehend this phenomena.

4 Conclusion

Based on the assessment and earlier discussion, the following conclusions can be drawn:

- In general, both compressive and tensile strength of LSC were improved with the addition of 0.5% JF or GF. Evaluating the performance, JF can be a better choice over GF to include in the fresh concrete.
- A lower length, in other words, a lower aspect ratio of fiber incorporated LSC exhibited better results in terms of compressive strength, split tensile strength and brittleness than LSC with a higher aspect ratio of fiber at both 7 and 28 days of curing ages.
- With the inclusion of jute fiber having 20 mm length (aspect ratio 100), approximately 39.9% enhancement in compressive strength and drastically increment in split tensile strength (62%) with respect to the plain LSC can be achieved for 28 days of curing. Moreover, 28 days of brittleness of this concrete mix potentially reduced to approximately 16% compared to the plain concrete.

References

1. Darmawan, M.S., Bayuaji, R., Husin, N.A., Chomaedhi, S.I.: A case study of low compressive strength of concrete containing fly ash in East Java Indonesia. Procedia Eng. **125**, 579–586 (2015). https://doi.org/10.1016/j.proeng.2015.11.064
2. Ahmad, S., Pilakoutas, K., Khan, Q.uz.Z., Neocleous, K.: Stress–strain model for low-strength concrete in uni-axial compression. Arab. J. Sci. Eng. **40**, 313–328. https://doi.org/10.1007/s13369-014-1411-1

3. Ten, K.W., Wang, H.Y., Shu, C.Y., Su, D.S.: Engineering properties of controlled low-strength materials containing waste oyster shells. Constr. Build. Mater. **46**, 128–133 (2013). https://doi.org/10.1016/j.conbuildmat.2013.04.020

4. Bangladesh Water Development Board: Standard Schedule of Rates Manual, vol. 1, June 2019. Bangladesh Water Development Board, Dhaka (2019)

5. Hucka, V., Das, B.: Brittleness determination of rocks by different methods. Int. J. Rock Mech. Min. Sci. **11**, 389–392 (1974). https://doi.org/10.1016/0148-9062(74)91109-7

6. Hetényi, M.I.: Handbook of Experimental Stress Analysis. Wiley (1966)

7. Altindag, R.: Assessment of some brittleness indexes in rock-drilling efficiency. Rock Mech. Rock Eng. **43**, 361–370 (2010). https://doi.org/10.1007/s00603-009-0057-x

8. Mansur, M.A., Aziz, M.A.: A study of jute fibre reinforced cement composites. Int. J. Cem. Compos. Light Concr. **4**, 75–82 (1982). https://doi.org/10.1016/0262-5075(82)90011-2

9. Song, P.S., Hwang, S., Sheu, B.C.: Strength properties of nylon- and polypropylene-fiber-reinforced concretes. Cem. Concr. Res. **35**, 1546–1550 (2005). https://doi.org/10.1016/j.cemconres.2004.06.033

10. Sivakumar, A., Santhanam, M.: Mechanical properties of high strength concrete reinforced with metallic and non-metallic fibres. Cem. Concr. Compos. **29**, 603–608 (2007). https://doi.org/10.1016/j.cemconcomp.2007.03.006

11. Sadiqul Islam, G.M., Das, GS.: Evaluating plastic shrinkage and permeability of polypropylene fiber reinforced concrete. Int. J. Sustain. Built. Environ. **5**, 345–354 (2016). https://doi.org/10.1016/j.ijsbe.2016.05.007

12. Dayananda, N., Keerthi Gowda, B.S., Easwara Prasad, G.L.: A study on compressive strength attributes of jute fiber reinforced cement concrete composites. IOP Conf. Ser. Mater. Sci. Eng. **376** (2018). https://doi.org/10.1088/1757-899X/376/1/012069

13. Algburi, A.H.M., Sheikh, M.N., Hadi, M.N.S.: Mechanical properties of steel, glass, and hybrid fiber reinforced reactive powder concrete. Front. Struct. Civ. Eng. **13**, 998–1006 (2019). https://doi.org/10.1007/s11709-019-0533-7

14. Wang, J., Dai, Q., Si, R., Guo, S.: Mechanical, durability, and microstructural properties of macro synthetic polypropylene (PP) fiber-reinforced rubber concrete. J Clean Prod. **234**, 1351–1364 (2019). https://doi.org/10.1016/j.jclepro.2019.06.272

15. Shaikh, F.U.A., Luhar, S., Arel, H,Ş., Luhar, I.: Performance evaluation of Ultrahigh performance fibre reinforced concrete—a review. Constr. Build. Mater. **232** (2020). https://doi.org/10.1016/j.conbuildmat.2019.117152

16. Khan, M., Rehman, A., Ali, M.: Efficiency of silica-fume content in plain and natural fiber reinforced concrete for concrete road. Constr. Build. Mater. **244**, 118382 (2020). https://doi.org/10.1016/j.conbuildmat.2020.118382

17. ASTM C39/C39M-20: Standard Test Method for Compressive Strength of Cylindrical Concrete Specimens. ASTM International, West Conshohocken, PA (2020)

18. ASTM C496/C496M-17: Standard Test Method for Splitting Tensile Strength of Cylindrical Concrete Specimens. ASTM International, West Conshohocken, PA (2017)

19. Zheng, C., Lou, C., Du, G., Li, X., Liu, Z., Li, L.: Mechanical properties of recycled concrete with demolished waste concrete aggregate and clay brick aggregate. Results Phys. **9**, 1317–1322 (2018). https://doi.org/10.1016/j.rinp.2018.04.061

20. Jiang, J., Wang, D., Han, X., Di, S.: Relationship between brittleness index and crack initiation stress ratio for different rock types. Adv. Civ. Eng. (2020). https://doi.org/10.1155/2020/8091895

21. Li, R., Zhang, X.H., Meng, Y.F.: Study of performance on reduce fragility and increase the toughness of fly ash ceramsite concrete. Adv. Mater. Res. **977**, 120–123 (2014). https://doi.org/10.4028/www.scientific.net/AMR.977.120

22. Li, W., Huang, Z., Wang, X.C., Zhang, J.P.: Study on tension and compression ratio and discount ratio of rubber modified silica fume concrete. Appl. Mech. Mater. **670–671**, 396–400 (2014). https://doi.org/10.4028/www.scientific.net/AMM.670-671.396

Seismic Evaluation of Stainless Steel-Reinforced Concrete Bridge Pier Using Performance-Based Damage States

K. A. Farzana and K. S. Ahmed

1 Introduction

Bridges are an important means of transportation system everywhere in the world. For the sustainability of bridges in an earthquake event, collapse or damage assessments are essential criteria to consider in the structural assessment. So in recent years, increased interest has been grown among researchers to define performance objectives for structures. In performance-based design procedure, a structure is designed to attain specific performance levels under seismic excitation and an annual probability of exceedance of each level [1]. The post-earthquake functionality of bridge is predicted by limiting its damage and reducing residual deformation in PBD approach [1]. The structure is designed to behave more ductile by dissipating energy during seismic excitation and thus minimizing the repairing as well as maintenance cost substantially. Previously, performance-based seismic assessment of reinforced concrete bridge was conducted depending on the level of importance of bridge, and also the repairing techniques were mentioned for different performance levels [2–5]. An experimental program on a 1/3 scale bridge pier was conducted at BUET-JIDPUS laboratory, Dhaka under cyclic loading [6]. The damage of bridges causes economic and life loss during the earthquake. Therefore, the main focus of this research is to limit the damage of bridge to full operational level after a certain seismic excitation. The collapse vulnerability of the steel fiber-reinforced bridge pier was assessed previously by [7].

In order to enhance the resilience of structures against earthquake, the huge number of research work has been carried out using passive control such as isolators

K. A. Farzana (✉) · K. S. Ahmed
Department of Civil Engineering, Military Institute of Science and Technology, Dhaka,
Bangladesh
e-mail: afia@ce.mist.ac.bd

K. S. Ahmed
e-mail: drksa@ce.mist.ac.bd

or dampers [8–10]. For existing structure, seismic performance of structural column can be improved by concrete jacketing [11]. The stainless steel shows high ductility and corrosion resistivity than conventional carbon steel. It is known from the literature that stainless steel shows higher yield point, ultimate strength and higher strain hardening property than carbon steel [12, 13]. Under same seismic excitation, stainless steel-reinforced column shows less severe damage than reinforced with carbon steel by dissipating more energy due to its hysteretic behavior [14]. Stainless steel and carbon steel differ both in mechanical and chemical properties. Several studies have been done to enumerate the capacity of stainless steel to satisfy structural demand in seismic excitation. Stainless steel contains more than 10.5% chromium and less than 1.5% carbon which makes it corrosion resistive. Again 8–10% nickel makes this material more ductile than mild steel [15]. Numerous studies proved the efficiency of SS-reinforced structure in seismic region. Zhang [16] focused on the impact of lateral loading on SS-reinforced bridge pier and found that stainless steel can resist the impact by dissipating energy under impact loading. A recent study conducted on local SS rebars shows that the bonding strength of SS is significantly good in concrete for both smooth and sand-coated steel [17]. The outcome of the study boosts the confidence of engineering community in using SS as rebar in concrete structures.

The chemical composition of the local SS rebar is presented in Table 1. The chemical composition of the stainless steel reflects that such properties and proportions of ingredients lie in 200 series SS (grade 201). Figure 1 shows the typical stress–strain curve for stainless steel and carbon steel. The carbon steel shows a defined sharp yield point, but stainless steel does not show any sharp yield point [18]. In order to investigate the mechanical properties of this local stainless steel rebars, tensile strength tests are conducted for few samples using Instron 8805,1000 kN hydraulic testing machine as shown in Fig. 2. Based on the tensile strength test data, the mechanical properties of SS rebar are presented in Fig. 3. The results show that the yield strength at 0.2% strength is 517 MPa with an ultimate strength of 728 MPa, whereas the strain at ultimate strength of the SS rebar is 18%. This data has been further used in the numerical analysis of the bridge pier conducted in this study.

Table 1 Composition of the local stainless steel	Name of the alloy	Percentage (weight)
	Carbon (C)	0.075
	Silicon (Si)	0.292
	Manganese (Mn)	10.22
	Phosphorus (P)	0.026
	Sulfur (S)	0.002
	Nickel (Ni)	1.13
	Chromium (Cr)	13.8
	Copper (Cu)	0.820
	Iron (Fe)	Balance
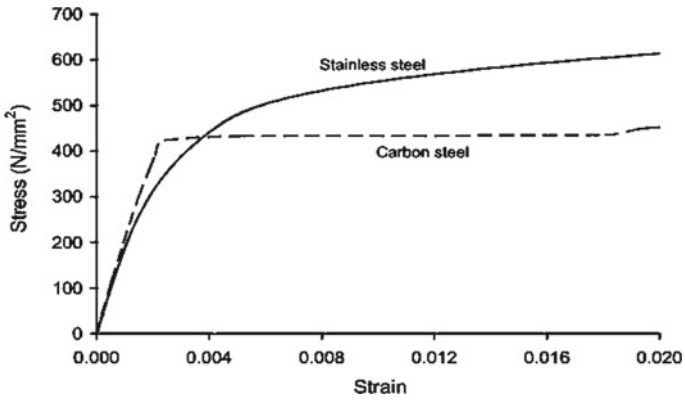
Fig. 1 Typical mechanical properties of carbon steel and stainless steel

Fig. 2 Test setups and failure modes of the samples [19]
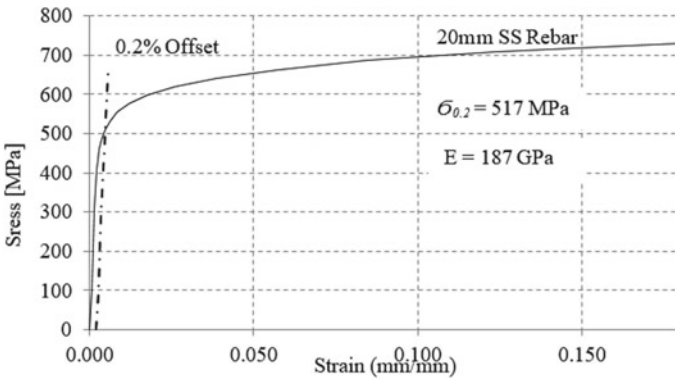
Fig. 3 Mechanical properties of the stainless steel grade 201

Previously, stainless steel was used because of its corrosion resistance. But nowadays for application in seismic region, it is becoming popular because of its remarkable ductile capacity. This paper assessed the comparative seismic performance of SS-reinforced bridge pier and carbon steel-reinforced bridge pier by performing nonlinear pushover analysis (NSPA). Different damage states are also developed according to code to understand the bridge piers functionality after an earthquake event.

2 Methodology

This section includes the geometric properties of the bridge pier, finite element modeling approach and performance-based bridge design and damage states under certain limit states. A standard bridge pier is selected for this study from existing literature [3] using AASHTO guideline [20]. The geometric features of the pier are presented below.

2.1 Geometry of Bridge Pier

In this section, the geometry of a bridge pier is described. For longitudinal and transverse reinforcement, stainless steel was used. This bridge needs to satisfy the purpose of a lifeline bridge to all traffic after an earthquake event with return period of 475 years. The studied bridge pier was designed considering a constant diameter of 1.6 m, the column was reinforced with 42 longitudinal stainless steel bars of 28 mm diameter with a reinforcement ratio of 1.4%, and 16 mm diameter stainless steel bars were used at 76 mm pitch. Aspect ratio 5 was selected which lead the height of the pier to be 8 m. The elevation and cross-sectional view of SS-reinforced bridge

Fig. 4 Cross section and elevation of SS-reinforced concrete bridge pier
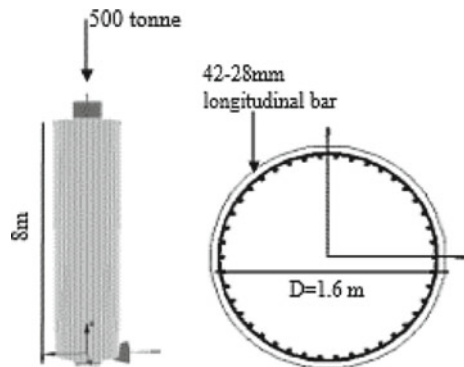
Table 2 Material properties

Material	Property	Values
Concrete	Compressive strength (MPa)	28
	Elastic modulus (GPa)	20.8
	Tensile strength (MPa)	2.2
	Strain	0.002
Stainless steel	Elastic modulus (GPa)	187
	Yield stress (MPa)	517
	Ultimate stress (MPa)	728
	Ultimate strain	0.18
Carbon steel	Elastic modulus (GPa)	207
	Yield stress (MPa)	550
	Ultimate stress (MPa)	621

is shown in Fig. 4. The other properties used in this study such as elastic modulus, yield stress and strain are given in Table 2.

Plastic hinge length for the pier was calculated by the equation prescribed by Paulay and Priestley [21] as shown in Eq. (1)

$$L_{\mathrm{p}} = 0.08L + 0.022d_{\mathrm{b}}f_{y} \tag{1}$$

where L = length of the member in mm; d_{b} = bar diameter in mm and f_{y} = yield strength of rebar in MPa.

For parametric study bridge pier of different yield strength, compressive strength and the longitudinal ratio were considered, and for every pier plastic hinge length was calculated with this equation.

2.2 Finite Element Modeling

The SS-reinforced bridge pier was modeled in finite element software SeismoStruct 2020. NSPA has been conducted to develop performance damage states of the bridge pier. This software is capable of predicting large displacement under both static and dynamic loads considering both geometric nonlinearities and material inelasticity. The Menegotto-Pinto steel model with Monti-Nuti (1992) post elastic buckling was used for stainless steel reinforcement. The Menegotto-Pinto (1973) model was used for conventional steel reinforcement for modeling a mild steel-reinforced bridge pier. For confined and unconfined concrete, the Mander et al. (1988) concrete model was used. From the above consideration, a bridge pier was reinforced with conventional steel reinforcement, and other one was modeled with ductile stainless steel. The moment–curvature relationship for both the bridge piers is determined as shown in Fig. 5 and found to be comparable.
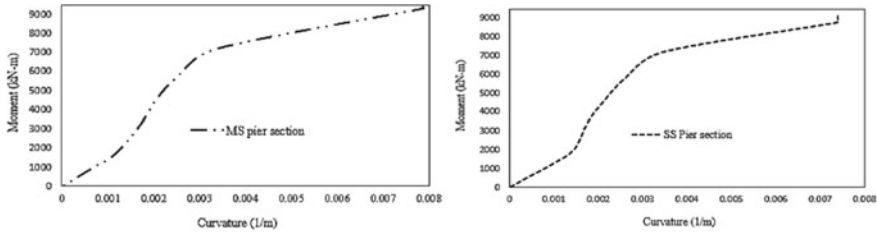
Fig. 5 Moment–curvature relationship of MS-RC and SS-RC bridge pier section

3   Performance-Based Damage States Criterion

Performance-based seismic design largely depends on the correlation between seismic performance levels and engineering damage states parameters. Among several damage states suggested by the researchers, three of them are commonly used, i.e., serviceability, damage control and life safety damages states [22]. Serviceability limit states say under seismic excitation, no damage repair is required and operation of the structure will not be hampered. Damage control indicates damage is repairable and operation is suspended while repairing. For life safety limit state, the structure will not collapse, but post-earthquake repairing is not possible. The performance objective depends on qualitative and quantitative parameters such as strain limits and drift. Depending on strain values of concrete and steel, four performance criteria have been considered here, the rebar concrete hairline cracking, yielding, concrete cover spalling and core concrete crushing. Under the serviceability limit, the structure is repairable, but reinforcing steel strain is limited to 0.015 for concrete structure [22]. For SS-reinforced bridge pier, the performance limits were considered based on the proposed damage states by [23]. Table 3 shows the damage states with their associated functional level.

Table 3 Performance criteria

Damage parameter	Damage state	Service	Performance description	Damage classification	Socioeconomic description
Cracking	DS-I	Immediate	Onset of hairline cracks	Minimal damage	Fully operational
Yielding	DS-II	Limited	Theoretical first rebar yield of longitudinal rebar	Repairable damage	Operational
Spalling	DS-III	Service disruption	Concrete spalling	Extensive damage	Life safety
Core crushing	DS-IV	Life safety	Crushing of core concrete	Probable replacement	Near collapse

The yielding of longitudinal SS rebar took place at tensile strain of steel which can be calculated as the ratio of yielding force and elastic modulus. Priestly (1996) recommended spalling strain of concrete to be 0.004. According to Kowalsky [24], crushing strain of confined concrete ranges between 0.015 and 0.05. For this paper, crushing strain of SS-RC bridge pier is calculated using the following Eq. (2) proposed by [24]

$$\varepsilon_{cu} = 0.004 + 1.4 \rho_s f_{yh} \varepsilon_{su}/f'_c \tag{2}$$

where ε_{cu} = ultimate compression strain; ε_{su} = steel strain at maximum tensile stress; f'_c = concrete compressive strength in MPa; f_{yh} = yield strength of transverse steel in MPa and ρ_s = volumetric ratio of confining steel.

Nonlinear pushover analysis was conducted to investigate the effect of flexural limit state on SS-RC bridge pier of different parameters. The pier will fail by concrete failure if the strain of concrete core reaches the ultimate strain (ε_{cu}). Failure will occur due to steel failure if the strain in steel rebar reaches to ultimate strain (ε_{su}).

4 Results and Discussions

4.1 Nonlinear Pushover Analysis

To understand the seismic vulnerability and inelastic behavior of the pier, nonlinear pushover analysis (NSPA) is an important step. In NSPA, the pier was subjected to incremental lateral load 1 m in form of displacement along with the axial load 500 tone in pier. From Fig. 6, it is observed that the SS-RC bridge pier shows ductile behavior [23]. At point A, the pier reaches the operation level of limit states, where damage is minimal and the seismicity has a probability of exceedance of 10% in 50 years with a return period of 475 years. Near collapse, state is reached at point B where extensive damage has been occurred under 2% probability of exceedance in 50 years with a return period of 2475 years according to Eurocode-8 [19]. In Fig. 7, it is found that both the OL and NC damage states are reached at an early stage in
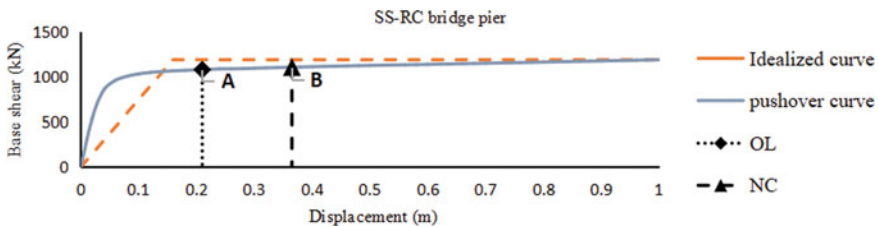
Fig. 6 Base shear versus target displacement for SS-RC bridge pier
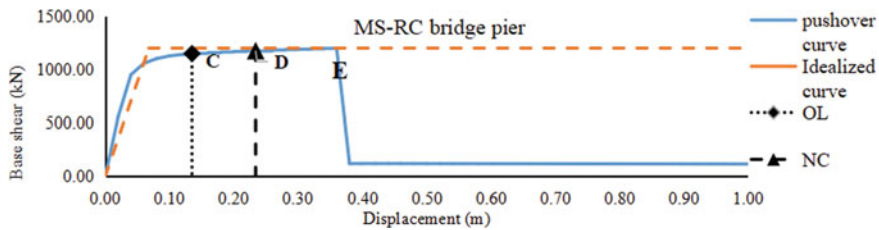
Fig. 7 Base shear versus target displacement for MS-RC bridge pier

case of MS-RC bridge pier. The pier could not sustain the lateral load increment and collapsed at point E with 0.36 m displacement.

4.2 Comparison of Performance Damage States Between MS-RC and SS-RC Bridge Pier

Behavior mode assessment is important to observe the seismic response of a structure. Depending on lateral deformation, structure can be classified as brittle, strength degradation and ductile [23]. For defining serviceability, damage control states of bridge pier displacement evaluation are important rather than forces. Therefore, Priestley [25] has also given emphasize on displacement-based design approach for seismic response evaluation in their researches. According to Federal Emergency Management Agency (FEMA) [26], two performance ranges are defined in Figs. 8 and 9. The damage control stage covers elastic range of structure, where the damage is low and repairing cost is also minimum. In Fig. 8, it can be seen that MS-RC bridge pier shows brittle behavior, and damage control state is limited to yielding and cracking stage.

SS-RC bridge pier in Fig. 9 is showing more ductile behavior than MS-RC bridge pier, and damage control state ranges up to spalling stage with larger lateral deformation. Among four limit states, cracking occurs at same displacement for both pier,
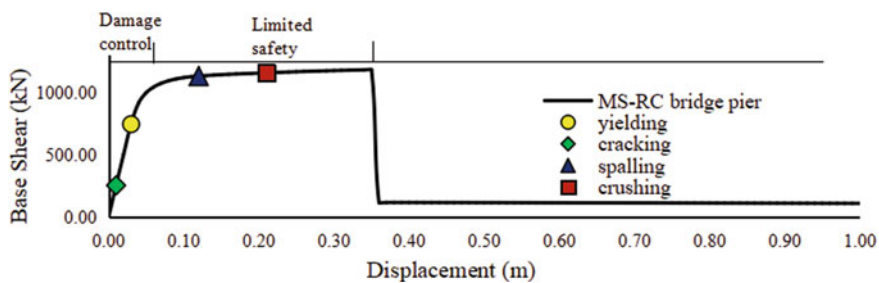
Fig. 8 Pushover curve showing damage states for MS-RC bridge pier
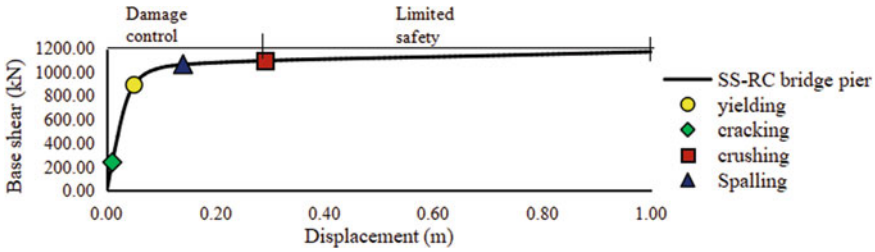
Fig. 9 Pushover curve showing damage states for SS-RC bridge pier

yielding has increased displacement up to 40%, spalling and crushing have displacements of 14.3 and 27.6%, but the base shear decreases to 6.5, 5.4 and 5% in case of cracking, spalling and crushing, whereas 16.5% base shear increases for yielding in case of SS-RC bridge pier. In limited safety range, large deformation and damage may occur which causes significant risk of life and economic losses. Stainless steel enhances the ductile capacity of the pier by allowing the pier to achieve higher yielding, and therefore by dissipating more energy, it can reduce the probability of failure.

4.3 Parametric Study

The performance of the bridge pier can be estimated in terms of different limit states by defining corresponding strain limits. In order to observe the effect of different parameters of SS-RC bridge pier, four performance criteria have been considered: the cracking, yielding, spalling and crushing of concrete and longitudinal steel as stated in the previous section. In Table 4, three parameters are selected to conduct the NSPA to see the influence of variable parameters on the pier. Table 5 shows the different pier properties used in the analysis.

All the parameters affect the flexural performance of the pier substantially. The higher value of the parameters increase the capacity of the piers. In Fig. 10, it is observed that for 42.4 MPa concrete strength yielding and cracking occur at higher values of base shear 17.6% and 16.5%, respectively, while the base shear of spalling and crushing increases by 5 and 4.2% compared to 28 MPa. Compressive strength

Table 4 Details of variable parameters used in the study

Variable parameter	Value		Unit
	Level-1	Level-2	
Compressive strength of concrete, f_c'	28	42.4	MPa
Yield strength of steel, f_y	517	748	MPa
Longitudinal steel reinforcement ratio, ρ_L	1.4	1.7	%

Table 5 Details of SS-RC bridge pier

Variable	Pier-ID	f_c'(MPa)	f_y (MPa)	$\rho_L(\%)$
Compressive strength of concrete, f_c'	P-1–28	28	748	1.7
	P-1–42.4	42.4	748	1.7
Yield strength of steel, f_y	P-2–517	42.4	517	1.4
	P-2–748	42.4	748	1.4
Longitudinal steel reinforcement ratio, ρ_L	P-3–1.4	28	517	1.4
	P-3–1.7	28	517	1.7
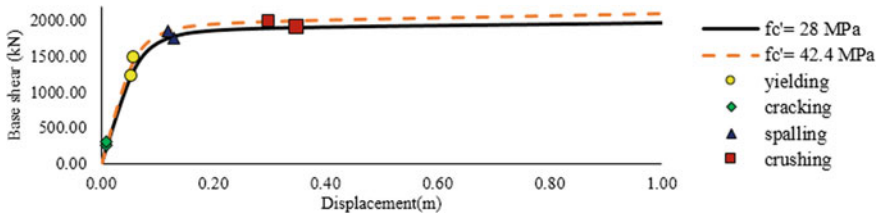
Fig. 10 Pushover curve considering variable compressive strength of concrete

28 MPa decreases displacement at yield state by 16% while cracking occurs at same displacement, but in spalling and crushing states, the displacement increases by 7.7 and 14.2%. Low compressive strength has low modulus of elasticity which lead the pier to achieve more deformability and causes higher displacement. The pier exhibits lower stiffness at low compressive strength and thus shows more effectiveness than high strength concrete.

Figure 11 shows how the variable yield strength affects the flexural capacity of bridge pier. It is seen that the higher yield strength (748 MPa) increases value of base shear significantly. Four limit states cracking, yielding, spalling and crushing have base shear increment of 1.7%, 24.3%, 20.5% and 27.6%, and larger displacement by 16.7%, 6.7% and 3.2% for yielding, spalling and crushing, respectively, but displacement in concrete cracking is found similar compared to lower yield strength of steel 517 MPa.
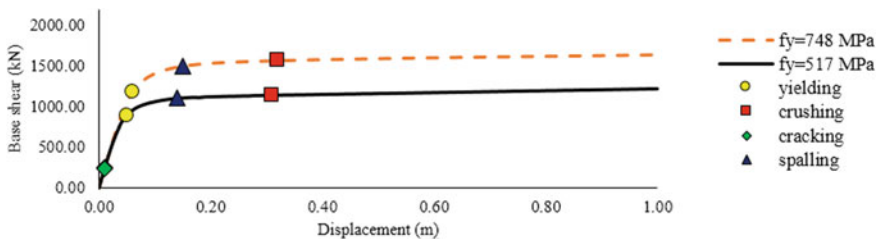
Fig. 11 Pushover curve considering variable yield strength of steel
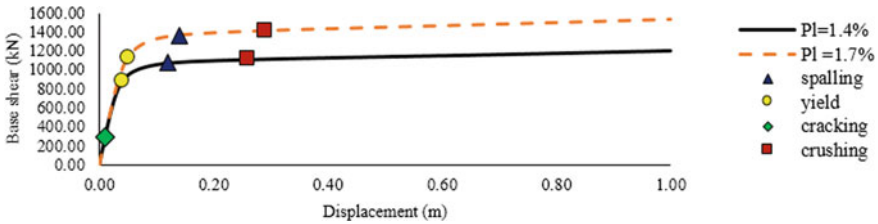
Fig. 12 Pushover curve considering variable steel reinforcement ratio

In Fig. 12, it is observed that longitudinal reinforcement ratio influences the base shear capacity of pier substantially. For cracking, yielding, spalling and crushing, the base shear is improved by 1.5, 22, 20.5 and 21.3% for 1.7% reinforcement ratio. The displacement is increased by 20% for yielding, 14.2% for spalling and 10.3% for crushing states compared to 1.4% steel ratio. Higher steel ratio influences the pier stiffness considerably.

5   Conclusion

In order to develop performance-based seismic design, it is important to define flexural limit states in a structure. Nonlinear pushover analysis is performed on the actual bridge pier to evaluate the damage states in terms of base shear and displacement. From the study, it is seen that the SS-RC bridge pier can sustain seismic excitation effectively by ductile structural behavior and higher energy absorption capacity. Though the pier shows more lateral displacement, it provides better performance under lateral load and resists the structure from brittle failure. Post-earthquake loss of life and structural damage are lesser in case of the SS-RC bridge pier. SS-RC pier controls the damage up to near collapse limit state for its ductile mode of behavior. The pier remains operational, and less repair is required under this damage control state.

In case of MS-RC bridge pier, it is found that at a lower drift value, the structure behaves more brittle and collapses under lateral load increment. This phenomenon is not desirable for any designer to build structure in seismic zone. Moreover, the yielding of longitudinal reinforcement occurs at an early stage in case of carbon steel which may not be the true representative of ductile behavior. In this regard, stainless steel shows more resilient characteristics by yielding in higher displacement and lower base shear. From the parametric study, it is observed that a higher value of different parameters can increase the SS-RC bridge pier capacity considerably. As an example, with a compressive strength of 42.4 MPa, the base shear increases at yielding, cracking, spalling and crushing limit states by 17.6%, 16.5%, 5% and 4.2%, respectively. A higher value yield strength (748 MPa) results higher base shear for

all four limit states by 24.3, 1.7, 20.5 and 27.6%. High steel ratio (1.7%) improves the base shear capacity by 22, 1.5, 20.5 and 21.3% compared to that of 1.4% steel.

It can be concluded from the investigation that stainless steel can be used as rebar in concrete structure as it is more preferable for application in the seismic region for its exceptional ductile behavior and inherent corrosion resistivity. Using stainless steel in bridge pier can reduce the long-term maintenance cost and economic loss under strong ground motion. Moreover, its energy dissipation capacity is higher than conventional carbon steel which will certainly make it more popular to build a sustainable structure. To obtain the desired damage state and to keep the bridge operational after an earthquake event, stainless steel rebars can make a difference.

References

1. Priestley, M.J.N.: Performance based seismic design. Bull. N. Z. Soc. Earthq. Eng. **33**(3), 325–346 (2000). https://doi.org/10.5459/bnzsee.33.3.325-346
2. Sheikh, M.N., Légeron, F.: A checking method for multiple seismic performance objectives of bridge piers designed according to code provisions. J. Earthq. Eng. **20**(7), 1148–1168 (2016). https://doi.org/10.1080/13632469.2015.1118709
3. Muntasir Billah, A.H.M., Shahria Alam, M.: Performance-based seismic design of shape memory alloy-reinforced concrete bridge piers. I: development of performance-based damage states. J. Struct. Eng. (United States), **142**(12) (2016). https://doi.org/10.1061/(ASCE)ST.1943-541X.0001458
4. Cassese, P., De Risi, M.T., Verderame, G.M.: Seismic assessment of existing hollow circular reinforced concrete bridge piers. J. Earthq. Eng., 1–36 (2018). https://doi.org/10.1080/13632469.2018.1471430
5. Parghi, A.M.: Seismic performance evaluation of circular reinforced concrete bridge piers retrofitted with fiber reinforced polymer. Researchgate.net (2016). https://doi.org/10.14288/1.0308726
6. Al-Hussaini, T.M., et al.: New dynamic testing facility at BUET-JIDPUS: cyclic loading of 1/3 scale damaged RC column retrofitted with externally wrapped CFRP sheets. In: 15th International Conference on Structural and Geotechnical Engineering. Egypt
7. Pang, Y., Li, L.: Seismic collapse assessment of bridge piers constructed with steel fibers reinforced concrete. PLoS ONE **13**(7) (2018). https://doi.org/10.1371/journal.pone.0200072
8. Farzana, K., Ahmed, K.: Performance based seismic analysis of stainless steel reinforced concrete bridge pier using damping ductility relationship. In: Adavnce in Bridge Engineering IABSE.
9. Tabassum, T., Ahmed, K.S.: Improving lateral load bearing capacity of RC buildings using non-linear dampers. Int. J. Sci. Technol. **46**(1), 31–40 (2018)
10. Ahmed, K.S., et al.: Seismic performance investigation of base isolation system for typical residential building in Bangladesh. Adv. Civ. Infrastruct. Constr. Mater. **4**(1) (2016)
11. Mahmud, R., Ahmed, K.S.: Interface dependency of reinforced concrete jacketing for column strengthening. Struct. Build. **173**(1), 31–41 (2020). https://doi.org/10.1680/jstbu.17.00124
12. Melo, J., Afshan, S., Rossetto, T., Varum, H.: Experimental investigation of cyclic response of stainless-steel reinforced concrete columns. In: Proceedings of the SECED 2019 Conference: Earthquake Risk and Engineering towards a Resilient World. SECED: London, UK., (September), pp. 1–9 (2019)
13. Zhou, Y., Ou, Y.-C., Lee, G.C., O'connor, J.S.: A pilot experimental study on the low cycle fatigue behavior of stainless steel rebars for warthquake engineering applications. Masters Abstr. Int. **47**(1) (2008)

14. Franchi, A., Crespi, P., Bennani, A., Farinet, M.: Stainless steel rebar for seismic applications. Solid Mech. Its Appl. **140**, 255–264 (2006). https://doi.org/10.1007/1-4020-4891-2_21
15. Gardner, L.: The use of stainless steel in structures. Prog. Struct. Eng. Mater. (2005) https://doi.org/10.1002/pse.190
16. Zhang, G., Xu, S., Xie, H., Zhou, X., Wang, Y.: Behavior of stainless steel-reinforced concrete piers under lateral impact loading. Adv. Mech. Eng. **9**(5) (2017). https://doi.org/10.1177/1687814017709936
17. Islam, K., et al.: Exploratory study on bond behavior of plain and sand coated stainless steel rebars in concrete. Structures. **27**, 2365–2378 (2020). DOI: https://doi.org/10.1016/j.istruc.2020.07.039
18. Liao, F.-Y., Han, L.-H., Tao, Z., Rasmussen, K.J.R.: Experimental behavior of concrete-filled stainless steel tubular columns under cyclic lateral loading. J. Struct. Eng. **143**(4), 04016219 (2017). https://doi.org/10.1061/(asce)st.1943-541x.0001705
19. Ahmed, K.S., Habib, M.A., Asef, M.F.: Flexural response of stainless steel reinforced concrete beam. Structures **34**, 589–603. https://doi.org/10.1016/j.istruc.2021.08.019 (2021)
20. Officials, T.: AASHTO guide specifications for LRFD seismic bridge design. In: Transportation, (May), 1 v. (loose-leaf) (2011). https://doi.org/10.2337/dc12-1714
21. Paulay,T., Priestley, M.N.J.: Seismic Design of Reinforced Concrete and Masonry Buildings. Willey, NewYork (1992)
22. Kowalsky, M.J.: Deformation limit states for circular reinforced concrete bridge columns. J. Struct. Eng. New York, N.Y. **126**(8), 869–878 (2000). https://doi.org/10.1061/(ASCE)0733-9445(2000)126:8(869)
23. Hose, Y., Silva, P., Seible, F.: Development of a performance evaluation database for concrete bridge components and systems under simulated seismic loads. Earthq. Spectra. **16**(2), 413–442 (2000). https://doi.org/10.1193/1.1586119
24. Kowalsky, M.J., Priestley, M.J.N., MacRae, G.A.: Displacement-based design of RC bridge columns in seismic regions. Earthqu. Eng. Struct. Dynam. **24**(12), 1623–1643 (1995). https://doi.org/10.1002/eqe.4290241206
25. Priestley, M.J.N., Calvi, G.M., Kowalsky, M.J.: Displacement-based seismic design of bridges. In: Bridge Engineering Handbook: Seismic Design, 2nd edn, pp. 201–236. CRC Press (2014). https://doi.org/10.1201/b15663
26. FEMA 356: FEMA 356—Prestandard and Commentary for the Seismic Rehabilitation of Buildings, Federal Emergency Management Agency. Report FEMA-356, Washington, DC (2000). Retrieved from http://scholar.google.com/scholar?hl=en&btnG=Search&q=intitle:Prestandard+and+commentary+for+the+seismic+rehabilitation+of+buildings#0
27. Kolias, B.: Eurocode 8—part 2. Seismic design of bridges. In: Eurocodes: Background and Applications, p. 20. Brussels (2008). Retrieved from http://eurocodes.jrc.ec.europa.eu/showpage.php?id=332

Investigation on Progressive Damage of CFRP Strengthening Tubular Stainless Steel Member Under Concentrated Loading

S. M. Z. Islam, B. Ahmed, J. D. Roy, S. S. Shamim, H. I. Tusher, S. Alam, and Md. R. Hasan

1 Introduction

Stainless steel is beneficial in terms of strength capacity and corrosion resistance for the civil engineering construction works. The advanced use of stainless steel is urging day by day for its better structural performance and outstanding features of aesthetics and long-term durability. Under concentrated loading, stainless steel experiences web crippling if stiffeners have not been used. It is very often to observe the web crippling for the steel tubular members subjected to concentrated loading. This web crippling and buckling can be improved significantly by applying CFRP strengthening technique [1–4]. In the previous study, failure of CFRP-strengthened steel sections had been occurred due to debonding of CFRP plate from the steel substrate. Currently, fiber-reinforced polymer (FRP)-to-concrete bonded joints had been performed by different authors to identify the debonding and interfacial stresses [5–8]. Recently, CFRP strengthening technique for carbon tubular steel had been studied and the bond behavior, different types of adhesive bonded failures and interfacial shear stress were noticed. The different failure modes including interfacial failure and interfacial shear stress-slip in CFRP-strengthened carbon tubular steel are shown in Figs. 1 and 2 [9, 10]. Likewise, the other authors, Fernando [10] also performed tests and FEA to comprehend the failure mechanisms and to develop reliable numerical models in CFRP-strengthened sections. From this study, it can be concluded that externally adhesive bonding was influenced by physical, chemical, and interlocking mechanical connections.

S. M. Z. Islam (✉) · B. Ahmed · J. D. Roy · S. S. Shamim · H. I. Tusher · S. Alam
Department of Civil Engineering, Rajshahi University of Engineering and Technology, Rajshahi 6204, Bangladesh

Md. R. Hasan
Department of Civil Engineering, Bangladesh Army University of Engineering and Technology, Natore, Bangladesh
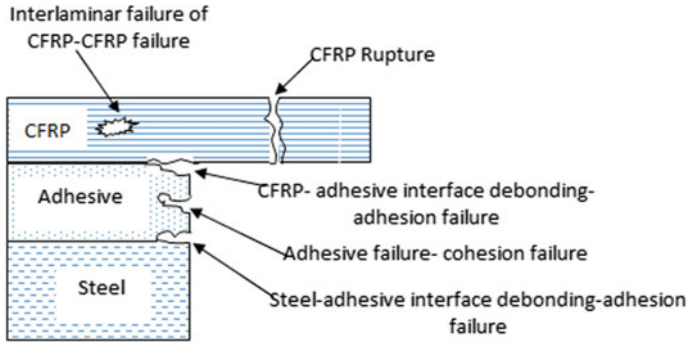
Fig. 1 Observed failure modes in CFRP-strengthened steel sections

Fig. 2 $\sigma_s - \delta$ curves for steel sections
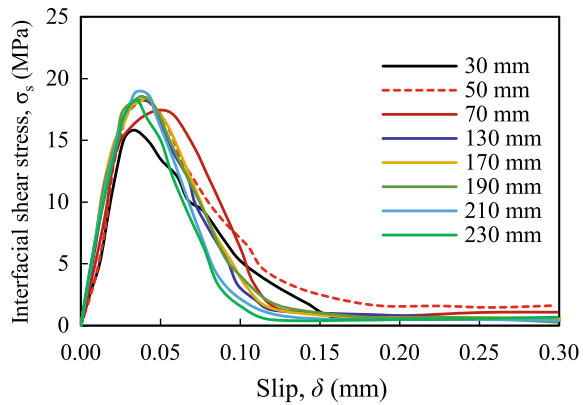
The debonding mechanism between steel surface and epoxy resin was explained by traction–separation law using cohesive element [11–17]. The cohesive elements available in ABAQUS [11] can be used to simulate progressive damage analysis of the test results. Cohesive COH3D8 elements were considered to determine the initiation of damage the adhesive material. Fracture was initiated from end and extended to mid of the section. At the same time, separation of CFRP and steel tube also started due to incremental loading. The damage initiation in the structures can be modeled by progressive damage modeling [11]. The potential failure mechanisms can be severely reducing the complexity of the progressive failure analyses. The mechanism includes adhesive failure, cohesion failure, interlaminar CFRP failure, CFRP rupture failure, fiber fracture, delamination, and their interactions.

In this research, ABAQUS [11] had been used to predict the progressive damage of the test results including material and geometrical nonlinearity. Cohesive Zone Model (CZM) was applied to notice the progressive damage failure that is explained the debonding failure of CFRP-strengthened steel sections. The test results and the simulated results of CFRP-strengthened steel sections were compared to check the

applicability of the proposed CZM. The simulated results were verified by the test results. Good agreement had been found between the FE results and the tested epoxy damage started and progressive collapse types of CFRP-strengthened steel sections. Structural integrity and progressive failure behavior of the adhesive bonded CFRP-strengthened steel sections were predicted by the CZM.

2 Material Properties

The material properties for steel, the adhesive materials and CFRP were measured by the tensile coupon tests, and the detailed procedure is explained by Islam and Young [2]. In this study, six different types of FRP and three different adhesives materials were used, and the designation of the materials was described in the previous study [2]. The stress–strain (σ–ε) diagram for the materials obtained from the tensile coupon tests is presented in Figs. 3 and 4.

Fig. 3 $\sigma - \varepsilon$ diagram of stainless steel and FRP
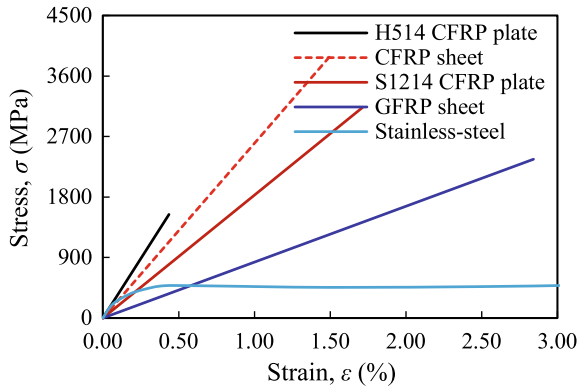
Fig. 4 $\sigma - \varepsilon$ diagram of different adhesives materials
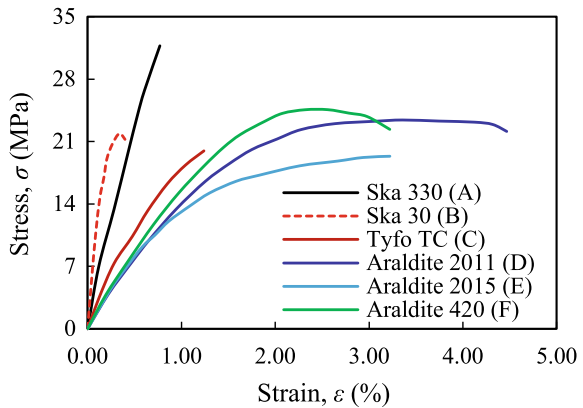
3   Test Program and Results

In this section, an extensive test program on CFRP-strengthened steel sections
subjected to concentrated loading has been presented. In this study, both rectan-
gular hollow section (RHS) and square hollow section (SHS) were considered for
the testing program. The specimens were designated by $b \times d \times t$, where b is the
flange width; d is the depth of web; and t is the thickness of web. Two different thick-
ness 1.5 and 2.5 mm were selected for both RHS and SHS. The specimen dimensions
were taken as $30 \times 50 \times 2.5$; $50 \times 50 \times 2.5$; $50 \times 50 \times 1.5$; $100 \times 50 \times 2.5$ and $150
\times 50 \times 2.5$. These five sections were chosen based on availability of material as well
as considered as wide range of slenderness ratio (minimum to maximum slender-
ness ratio). The sections dimensions of both RHS and SHS are presented in Fig. 5.
Extensive tests (a total of 53) were conducted in this study, and Islam and Young
[2] described the testing procedure in detail in the previous research. The surface
preparation of the steel section is crucial to find the better strength. In this study, the
procedure applied by Fawzia et al. [9] was adopted for better results. In Fig. 6, the
surface treatment was performed by electric grinder (G) for all CFRP-strengthened
specimens. According to ASCE specification [18], the specimens were tested under
concentrated loading for four different loading conditions (ETF, ITF, EOF and IOF),
where ETF, ITF, EOF and IOF refer to End-Two-Flange; Interior-Two-Flange; End-
One-Flange and Interior-One-Flange loading. For example, the experimental setup
for ETF loading condition and the failure mode are shown in Figs. 7 and 8.

   In this study, adhesion failure, interlaminar FRP failure and combination of adhe-
sion and interlaminar FRP failure were experienced. The adhesion failure modes
were found in between the adhesive and the adherents' surface. Due to the strong
localize adhesive bonding, interlaminar CFRP failure had been occurred between
the CFRP and steel surfaces. In this failure mode, the adhesive cannot mobilize the
stress distribution. The CFRP layer participates in the stress transfer mechanism in the
adhesive layer and the steel surface. The ultimate capacity of the members depends
on the failure of adhesive and CFRP layer. Initial crack initiated at the end of the
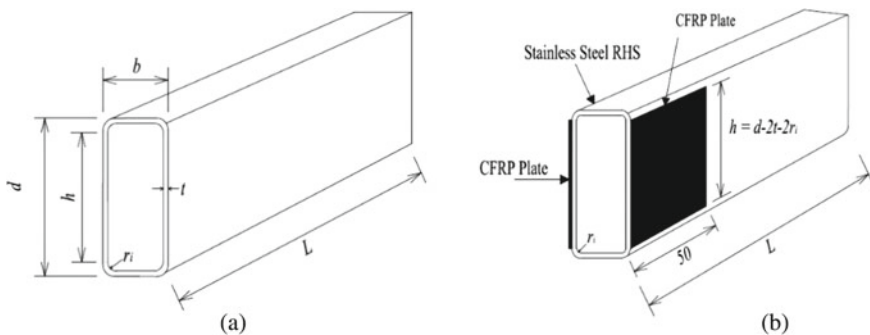
Fig. 5 Section dimensions for **a** RHS and **b** FRP RHS

(a) Electric grinder   (b) Surface treated by electric grinder
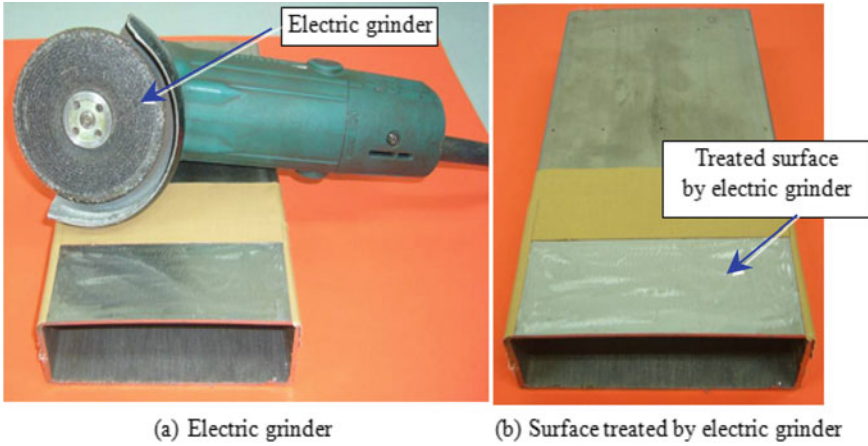
Fig. 6 Surface treatment done by electric grinder

Fig. 7 Specimen and testing setup in ETF condition
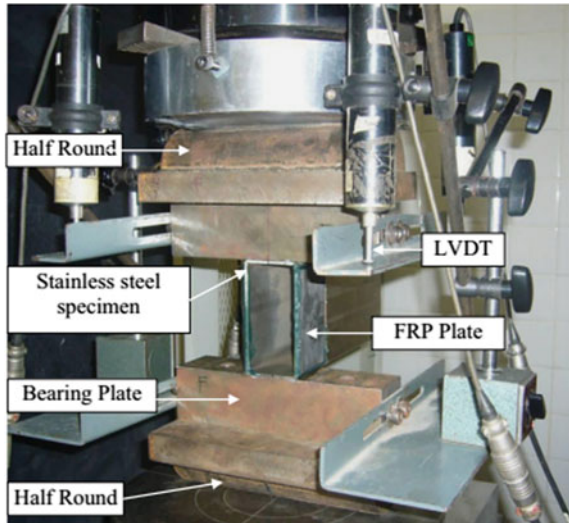
CFRP plate, and high interfacial stress had been found at that region. Debonding extended gradually toward the mid-section of the web after initiation of first crack at the plate end. Crack was propagated gradually and reached at a certain limit where CFRP-strengthened steel section cannot resist the additional load. Further applied load was carried by the externally bonded CFRP plate. The failure modes for different sections are shown in Fig. 9 under the ETF loading condition.

From the test, the ultimate capacity had been reported for different sections with CFRP treated and without CFRP, where P_u denotes the web crippling load with CFRP-strengthened sections and P_{u0} is the ultimate capacity of normal steel section.

Fig. 8 Failure mode in ETF condition
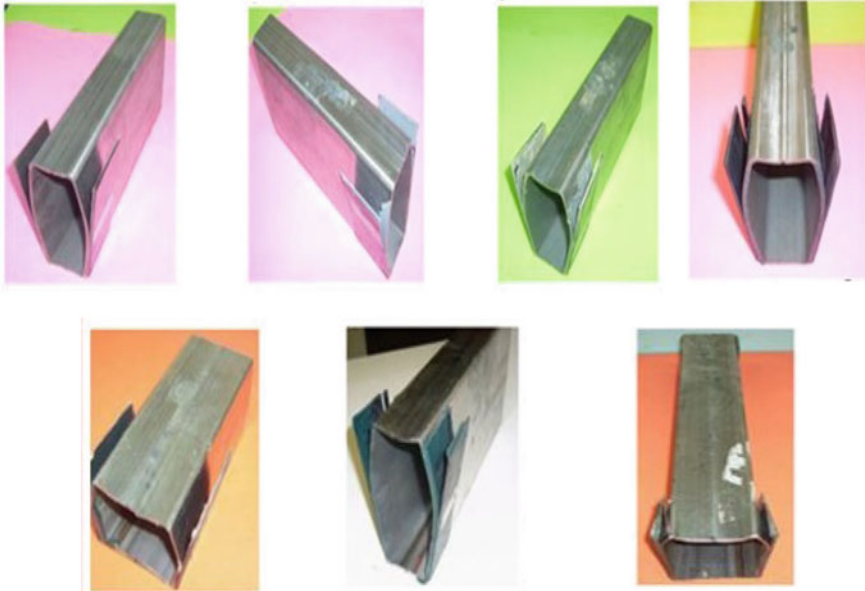
Fig. 9 Failure modes appearance in CFRP-strengthened steel sections

Fig. 10 Ultimate capacity
with respect to *h/t* ratios and
different failure modes
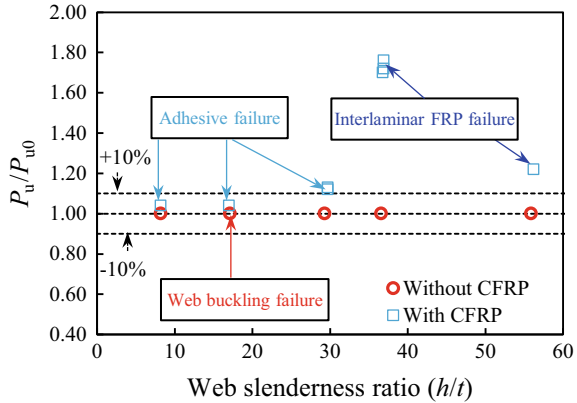
In Fig. 10, the ratio of $\frac{P_u}{P_{u0}}$ varies with the web slenderness ratio (h/t) for RHS and SHS stainless steel sections. From the figure, it was found that the $\frac{P_u}{P_{u0}}$ values increase with the increase of (h/t) ratios. Based on test results, without CFRP strengthen specimen were failed by web buckling, where, as CFRP strengthen specimen were failed by either adhesive failure or Interlaminar FRP failure. The web crippling load enhancement was found to be 4%, 4%, 13%, 76% and 22%, for measured web slenderness ratio 8.2, 17.0, 29.7, 36.9 and 56.2, respectively, subjected to ETF loading as shown in Fig. 10. No load carrying enhancement was found without FRP strengthen specimen, whereas FRP strengthen specimen load carrying capacity enhanced up to around 76%. In graphical presentation, ±10% dotted line indicated, those specimens which have enhanced load carrying capacity above 10% due to FRP strengthening. More than 10% improvement of load carrying capacity was found which has slenderness ratio above around 30.

4 Finite Element Analysis (FEA)

The simulation results were verified with the test results. In this study, commercially available numerical software ABAQUS version 6.9-1 was used to simulate the test data. The adhesion response was performed by the traction separation law in ABAQUS. In the 3D model, mesh sensitivity analysis was performed and proper mesh size (10 mm × 10 mm) was selected to minimize the computational time and accurate results. In the corner region, dense meshing was used. The mesh details for steel section and corner region are shown in Fig. 11a. The cross section of composite layers for CFRP-strengthened web section is shown in Fig. 11b which is illustrated and magnified view of layer of interface of steel-adhesive-CFRP. Figure 11b presents position and arrangement of steel-adhesive-CFRP layer with different color and thickness and interface between steel-adhesive and adhesive-CFRP. Compressive load *P* is applied on the top flange of the section. The compressive load *P* will be

(a) Meshing

(b) Cross section of composite web thickness
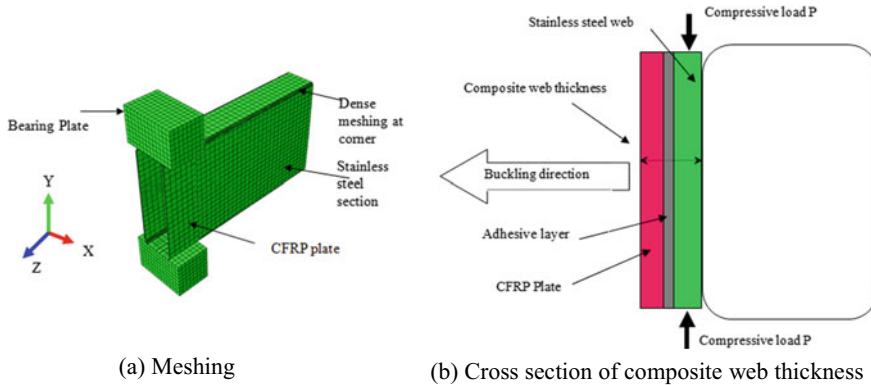
Fig. 11 Meshing of stainless steel section and composite web thickness

distributed along the web of the section as shown in Fig. 11b. To consider the adhesive response, COH3D8, 8-node three-dimensional cohesive elements were selected in the 3D model. To capture the initial damage, traction separation law was applied for the elements. The controlling parameters were included to consider the adhesive response. The material model for tensile stress for adhesive materials was used input parameter. Due to the tensile strain debonding had been happened during entire failure. Failure in epoxy resin was defined by strength criteria.

5 Verification of FEA

A total of 32 test results were simulated by 3D FEA model. The failure modes for CFRP-strengthened section obtained from test and simulated results showed good agreement as shown in Fig. 12a, b. The progressive damage modes from both test and simulation were also verified. The ultimate capacity-deformation curves were also compared by FEA. An excellent agreement had been found for load-deformation curve as shown in Fig. 12c.

6 Progressive Damage Mechanism Analysis

In the adhesively bonded joints, cohesive elements in the FEA can be described the traction–separation law, cohesive zone behavior, crack propagation in adhesive layer. Crack was initiated at the adhesive layer, and the adhesive fracture energy was also generated. This energy through the adhesive layer was determined, using the following equations. Equation (1) is used for computing adhesively bonded joint fracture energy and crack propagation.

(a) Test (b) FEA

(c) Comparison between test and FEA results
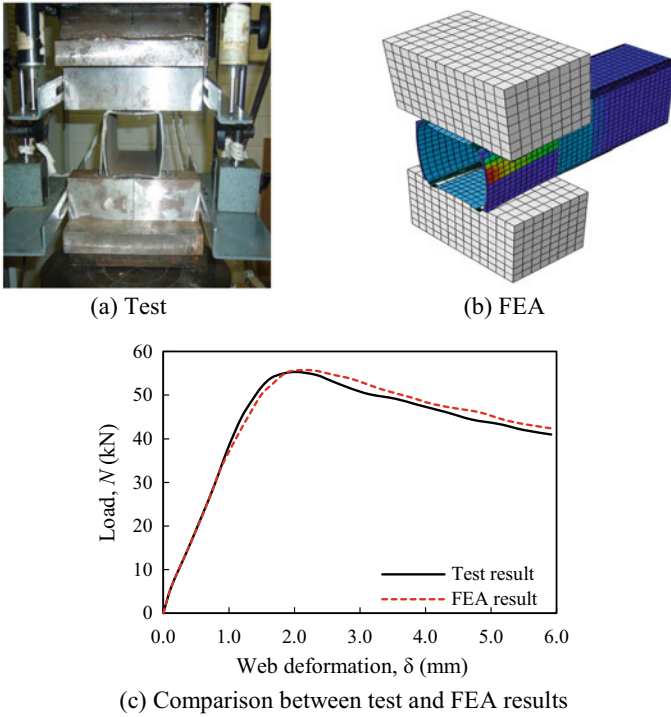
Fig. 12 Failure modes and load-deformation curve for both test and FEA

$$G_c = \left(\frac{P}{b}\right)^2 \left(\frac{4m}{E}\right)\left(1 + \frac{2\Delta}{3a}\right) \qquad (1)$$

where G_c = adhesive fracture energy, P = load, b = width, and a = crack length. E = modulus of elasticity, $m = \frac{3a^2}{h^2}$. Δ = length correction factor. The crack length was corrected by this factor, and the local deformation beyond the crack tip was determined. Due to the traction properties of the materials, the relative displacement of adhesive materials was controlled by the cohesive traction properties law. Generally, the cohesive traction properties' law refers to either equivalent displacement or strain. The debonding or decohesion had been propagated in damage zone in FEA under incremental concentric loading. The facture mode and stress concentration on adhesive layer under gradual increment of loading which are shown in Figs. 13 and 14. In Fig. 12, it was shown that the load gradually increases with increases of deflection up to peak load. Initial loading and intermediate loading indicate 5–10% of peak loading and 60–70 of peak loading, respectively. After the peak, load was decreased, and deformation was increased due to progressive debonding initiated. Final loading indicates the stage of loading, where FRP was debonded from steel surface; usually, it was final stage of loading at 90–100% of total deformation. From the FEA results,

(a) Initial loading   (b) Intermediate loading   (c) Final loading
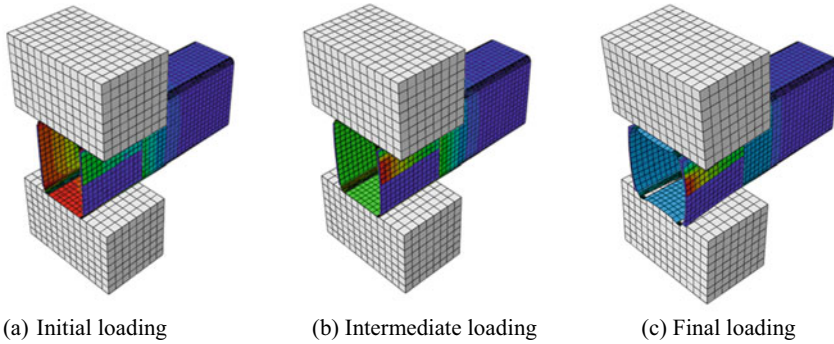
Fig. 13 Different stage failure mode of stainless steel section

(a) Initial loading   (b) Intermediate loading   (c) Final loading
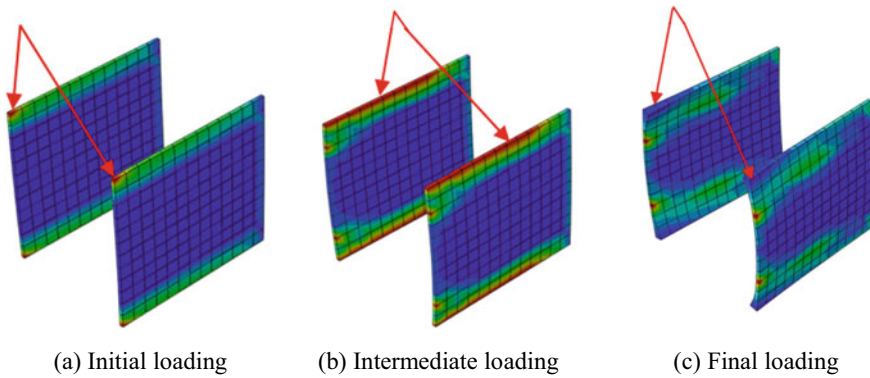
Fig. 14 Stress concentration on adhesive layer at different stage of loading

it is worth noting that the stress concentration at the top and bottom corner edge of adhesive layer is higher at early stage of loading (see Figs. 13a and 14a). The highest stress concentration had been found at the end edge of adhesive layer which is shown in Figs. 13c and 14c. After a certain limit of stress concentration, it was started to fail and deboned. In the FEA, the initiation of damage of adhesive layer is shown in Fig. 13c.

The failure mechanism of adhesive materials depends on the loading application and the von Mises stress. Von Mises stress had been found maximum at corner region when the load application is at initial stage. The value of this maximum stress is shown with red color in the corner edge of epoxy layer as shown in Fig. 14a. The peak von Mises stress is depicted at the upper and lower edges of epoxy layer due to the incremental loading. When the von Mises stress reaches at peak, the debonding at epoxy layer starts initiated. On the other hand, adhesive layer starts to fail when maximum von Mises stress due to high level of loading.
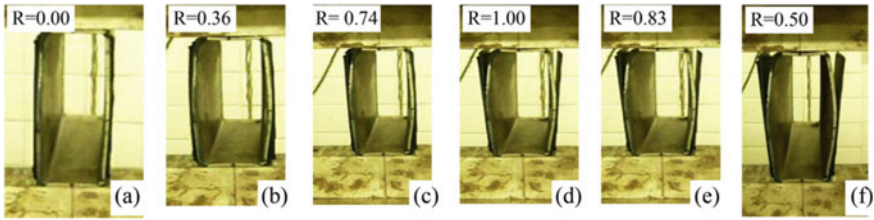
Fig. 15 Tested progressive failure of adhesive bonded CFRP-strengthened steel sections
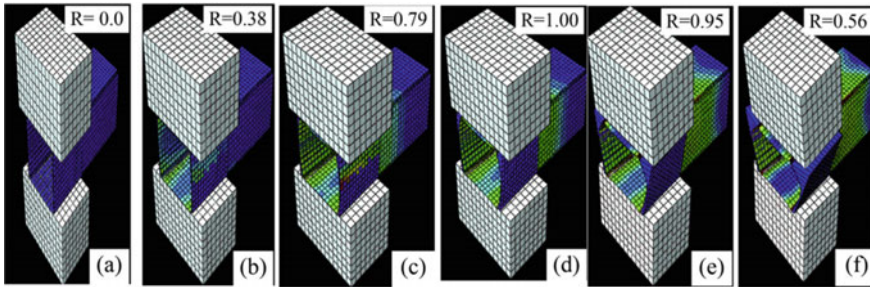
Fig. 16 FEA progressive failure of adhesive bonded CFRP-strengthened steel sections

In FEA, similar progressive damage in the epoxy layer due to the peak von Mises stress had been noticed. The progressive damage modes noticed at the adhesive layer in both test and FEA are shown in Figs. 15 and 16. The progressive collapse can be explained by the load ratio R. The load ratio (R) is defined as the ratio of applied load at particular stage and the ultimate load (peak/maximum load) from either test or FEA. The values of R are presented in Figs. 15 and 16. It is worth noting that progressive collapse noticed in test and FEA have excellent agreement. At the beginning of load application, the R value is zero and it increases due to gradual load application and debonding starts gradually from either top or bottom boundary to mid-portion of web. The results from test and FEA showed that the progressive collapse types can be verified accurately by FEA.

7 Conclusion

In this study, progressive damage of CFRP-strengthened steel section was analyzed by developed CZM. Experimentally, the progressive collapse and the fracture mechanism of CFRP-strengthened steel section under axial loading are complicated jobs. Therefore, reliable and accurate nonlinear finite element analysis is crucial to predict the progressive damage and final failure of CFRP-strengthened steel section. To predict the progressive failure behavior of CFRP-strengthened steel section, the CZM

was proposed and implemented. Laboratory test was performed, and the test results were simulated by the FEA, and good agreement had been found between them in terms of failure mechanisms and the load-deformation curves. The structural integrity also can be evaluated by CZM. The simulation results showed that this model can be used to proclaim the progressive damage mechanism of CFRP-strengthened steel section subjected to concentrated loading.

References

1. Islam, S.M.Z., Young, B.: Ferritic stainless-steel tubular members strengthened with high modulus CFRP plate subjected to web crippling. J. Constr. Steel Res. **77**, 107–118 (2012)
2. Islam, S.M.Z., Young, B.: FRP strengthening of lean duplex stainless steel hollow sections subjected to web crippling. Thin-Walled Struct. **85**, 183–200 (2014)
3. Islam, S.M.Z.: Strengthening of Aluminium and Stainless-Steel Tubular Sections with Fibre-Reinforced Polymer. Ph.D. Thesis, Department of Civil Engineering, The University of Hong Kong. Hong Kong, China (2012)
4. Islam, S.M.Z., Cai, Y., Young, B.: Design of CFRP-strengthened stainless steel tubular sections subjected to web crippling. J. Constr. Steel Res. **159**, 442–458 (2019)
5. Lu, X.Z., Jiang, J.J., Teng, J.G., Ye, L.P.: Finite element simulation of debonding in FRP-to-concrete bonded joints. Constr. Build. Mater. **20**, 412–424 (2006)
6. Smith, S.T., Teng, J.G.: FRP-strengthened RC beams. II: assessment of debonding strength models. Eng. Struct. **24**, 397–417 (2002)
7. Smith, S.T., Teng, J.G.: Interfacial stresses in plated beams. Eng. Struct. **23**, 857–871 (2001)
8. Zhang, L.F., Teng, J.G.: Finite element prediction of interfacial stresses in structural members bonded with a thin plate. Eng. Struct. **32**(2), 459–471 (2009)
9. Fawzia, S.: Bond Characteristics Between Steel and Carbon Fibre Reinforced Polymer (CFRP) Composites. Civil Engineering Department, Monash University, Melbourne Australia (2007)
10. Fernando, N.D.: Bond Behaviour and Debonding Failures in CFRP Strengthened Steel. Department of Civil and Structural Engineering, The Hong Kong Polytechnic University, Hong Kong (2010)
11. ABAQUS Analysis User's Manual: version 6.9-1. ABAQUS Inc. (2009)
12. Leone Jr. F.A., Girolamo, D., Dávila C.G.: Progressive Damage Analysis of Bonded Composite Joints. NASA Scientific and Technical Report, NASA Center for Aero Space Information, NASA/TM, 2012-217790 (2012)
13. Liu, W., Chang, X., Zhang, X., Zhang, Y.: Progressive damage analysis of carbon/epoxy laminates under couple laser and mechanical loading. Results Phys. **7**, 995–1005 (2017)
14. Im, J., Kang, S., Shin, K., Hwang, T.: Prediction of onset and propagation of damage in the adhesive joining of a dome-separated composite pressure vessel including temperature effects. Int. J. Precis. Eng. Manuf. **18**(12), 1795–1804 (2017)
15. Blackman, B.R.K., Hadavinia, H., Kinloch, A.J., Williams, J.G.: The use of a cohesive zone model to study the fracture of fibre composites and adhesively bonded joints. Int. J. Fract. **119**, 25–46 (2003)

16. Georgiou, I., Hadavinia, H., Ivankovic, A., Kinloch, A.J., Tropsa, V., Williams, J.G.: Cohesive zone models and the plastically deforming peel test. J. Adhes. **79**(3), 239–265 (2003)
17. Diehl, T.: Using ABAQUS Cohesive Elements to Model Peeling of an Epoxy-Bonded Aluminum Strip: A Benchmark Study for Inelastic Peel Arms. ABAQUS User Conference, Stockholm, Sweden (2006)
18. ASCE: Specification for the Design of Cold-Formed Stainless Steel Structural Members. SEI/ASCE 8-02. Reston, VA: American Society of Civil Engineers (2002)

Slag and Silica Fume-Based Geopolymer Mortar Using Locally Available Waste Filler Materials

Md. Nasimuzzaman, M. S. Ayon, and G. M. Sadiqul Islam

1 Introduction

Public attitudes toward conserving natural resources and reducing environmental degradation have led people to focus on habitual construction material substitutes in recent years. The current cement consumption is four billion tons/year, increasing by 4% every year. At this moment, ordinary Portland cement is the worlds' top binding material for concrete [1]. Portland cement manufacturing annihilates energy; notably, the process releases at least 0.7 ton of CO_2 into the atmosphere from one-ton cement production. In addition, various greenhouse gases, including nitrogen oxides and sulfur oxides, are being released [2]. Industrial wastes, including fly ash, ground granulated blast furnace slag (GGBS), mine waste, and red mud, have become a matter of concern as it requires land to fill and requires careful management. The urgency to explore practically usable alternative and eco-friendly substitutes to standard cementitious concrete has paved the way to develop new materials for the construction sector.

Geopolymer is an eco-friendly alternative to the traditional OPC-based concrete that can decrease 8% of greenhouse gas. In addition, industrial waste materials could be reused in its production [3]. The mineral binder is made by amalgamating aluminosilicate materials with a highly concentrated alkali solution. The dissolved alumina and silica species go through polymerization to form a three-dimensional amorphous structure providing comparable strength to the OPC-based concrete [4]. Better compressive strength and fire resistance, lower thermal conductivity, shrinkage and setting times, rapid hardening, excellent durability, and acid resistance have made geopolymer materials a better choice than ordinary Portland cement [5, 6]. The

Md. Nasimuzzaman (✉) · M. S. Ayon · G. M. S. Islam
Department of Civil Engineering, Chittagong University of Engineering & Technology, Chattogram 4349, Bangladesh

G. M. S. Islam
e-mail: gmsislam@cuet.ac.bd

alkaline activator solutions comprise sodium or potassium-based soluble alkalis. It is often used to originate geopolymer concrete in the fusion of sodium hydroxide (NaOH) and sodium silicate (Na_2SiO_3) [7]. The study indicated NaOH significantly impacts the structure and the compressive strength of geopolymers while used a concentration of 2–16 M [8]. The strength of mixes increased with NaOH concentration. However, flowability and setting time reduced. The polymerization reaction generally occurs at elevated temperatures or ambient temperatures [9]. For producing high-strength geopolymers, commonly, 12 M of NaOH solution is used, maintaining a low liquid-to-binder ratio of about 0.4 and curing temperature around 70 °C for at least 24 h. The binders mixed react more efficiently when the sodium-silicate-to-sodium-hydroxide mass ratio is between 2.0 and 2.5 [10]. Before testing compressive strength, all the specimens were cured in an oven for 18 h at 65 °C and placed at room temperature (about 26–29 °C) [11]. Geopolymers are connected to the group of strong and durable cementitious materials that harden at less than 100 °C [5, 12].

GGBS is a by-product of the steel industry. Its both pozzolanic and cementitious properties suggest this as a mineral admixture in concrete production. High-strength concrete can be produced from an alkali-activated GGBS binder. For every ton of steel, about half a ton of blast furnace slag is expected to be produced. Disposing of the slag as waste would have a negative impact on the environment. The early strength gain of GGBS in geopolymer concrete can reduce the construction cost and its disposal difficulties. Silica fume is a by-product generated from silicon-based elemental silicon or alloys in electric arc furnaces. This is an artificial, ultrafine, and amorphous glassy solid containing silicon dioxide spheres with high surface area and water demand [13]. Both GGBS and silica fume could be used as a binder in geopolymer mortar. Sand is an essential component in concrete construction and is generally used as filler. Natural sand is becoming a scarce commodity in the recent past. Natural sand extraction affects the amount of soil moisture that causes groundwater depletion to have an enormous and constant environmental influence [14]. Excavation of sand provokes the collapse of adjacent lands and causes to execute fluctuation of ecology [15]. To secure the remaining sand and gravel, unsheathing is excessively taxed or else prohibited in the various zone of the world [16]. Hence, the construction industries need to discover replacements to meet the propagated requirements for fine aggregates. Waste materials like brick dust, fly ash, and waste glass could replace sand. Using these waste materials as a filler replacement can be reduced environmental pollution, and it is also an alternative solution to the disposal challenge of these industrial wastes. This research, therefore, studied the performance of filler replacement by industrial wastes in GGBS and silica fume based geopolymers to conserve the environment and explore eco-friendly option for concrete filler.

2 Materials and Methods

2.1 Materials

Waste materials including GGBS and silica fume were used as a binder in geopolymer mortar. Brick dust, waste glass, fly ash, and EN sand are used to replace fine aggregate. NaOH (6 M) and sodium silicate were used as an alkali activator solution. GGBS was obtained from a cement industry sourced earlier from Japan. The material is off-white color mainly composed of calcium oxide, silica, and alumina (around 90%). The specific gravity of GGBS was found to be 2.56. Silica fume was obtained from Elkem production supplied by Consol Limited, Bangladesh. The particle size of silica fume ranges from 0.1 to 0.3 μm which is spherically shaped. It is a highly reactive pozzolana that contains silicon dioxide (around 90%). Specific gravity was found to be 2.48.

Fly ash was obtained from a Barapukuria Thermal Power plant in Bangladesh. The material is enriched with silica and alumina. Brick dust was obtained from a construction site of CUET. Also, the red color of the material may provide an attractive visual appearance. The waste glass was collected from a hotel in front of CUET. Waste glass is enriched with silica and calcium. EN standard [17] sand is natural sand imported from France. It is free from impurity and circular. It has isometric particles and generally is well graded.

Coarse-grained fine aggregate was obtained from the northeast region of Bangladesh. The gradation was matched with EN standard [17] requirements to compare performance between them. The particle size distribution of sand is given in Table 1. The maximum particle size of all filler materials is shown in Table 2.

Table 1 Particle size distributions of sand

Sieve No.	Sieve opening (mm)	% pass
8	2.36	100
16	1.19	75
30	0.6	25
50	0.3	18
Pan	–	0

Table 2 Maximum particle size of filler materials

Sample name	Passing through ASTM sieve	Max. particle size, mm
Standard sand	#100	2.36
EN Standard sand	–	2.00
Waste glass	#30	25
Brick dust	#50	18
Fly ash	#200	0.075

Initially, the required quantity of sodium hydroxide (NaOH) was placed in the beaker to prepare a 6 M solution. Next, a calculated amount of water was added and prepared for the suspension. Sodium silicate (Na_2SiO_3) was then mixed with the prepared 6 M NaOH suspension. The mixture of NaOH and Na_2SiO_3 solutions was prepared for not more than one hour before mixing the mortar for polymerization. In the alkaline solution, Na_2SiO_3/NaOH ratio was 2.5.

2.2 Sample Preparation

GGBS (80%) and silica fume (20%) were used as binders throughout the study. Fine aggregate in the mixture was partially (5–20%) replaced by waste glass, fly ash, brick dust, and EN standard sand. The detailed mix proportion is given in Table 3. In all these geopolymer mortars, a sand/binder ratio of 2.75 and an activator/binder ratio of 0.45 were used. The amount of excess water was determined from the flow test. A flow value of 185 ± 5 mm was taken as control water content. For uniformity, 22.5% (of binder content) excess water was added with the mixture to make the mortar workable.

Mix proportion of mortar (kg/m^3)

Table 3 Proportions of fine aggregates (sand and industrial waste) in geopolymer mortar

Mix	Sand	Brick dust	Fly ash	Waste glass	EN sand
Control	100	–	–	–	–
B5	95	5	–	–	–
B10	90	10	–	–	–
B15	85	15	–	–	–
B20	80	20	–	–	–
F5	95	–	5	–	–
F10	90	–	10	–	–
F15	85	–	15	–	–
F20	80	–	20	–	–
G5	95	–	–	5	–
G10	90	–	–	10	–
G15	85	–	–	15	–
G20	80	–	–	20	–
E5	95	–	–	–	5
E10	90	–	–	–	10
E15	85	–	–	–	15
E20	80	–	–	–	20

Mix ID	Fine aggregate		Binder		Alkaline solution		Water
	Natural sand	Industrial by-products	GGBS	Silica fume	NaOH	Na$_2$SiO$_3$	
Control	1365	0	400	100	64	160	112
B5	1300	70					
B10	1230	135					
B15	1160	205					
B20	1095	275					

2.3 Mixing and Curing

An automatic machine was used to mix the mortar as per EN 196-1 [18]. At first, graded sand was poured into a sand container. Next, sand replacement (5, 10, 15, and 20%) material (brick dust, fly ash, waste glass, and EN sand) was placed on top of the graded sand. Full binders are then placed inside the mixing bowl, and after that, a previously prepared and measured quantity of activator solution with the required water was poured one by one. Once the mortar mixing machine started, it mixes the binder and liquid first and then automatically intake the inert part and mixes it at a low speed. After an interval, the machine started automatically at high speed. Mixing was done at standard room temperature within a total of 4 min [18]. After finishing the mixing process, mortars were placed and compacted into a 40 × 40 × 160 mm rectangular mold as instructed in the standard [18]. Then the mortar was compacted using a jolting machine for 2 min. The samples were then kept at room temperature for 24 h. These were then demolded and kept in an oven at 60^0C for 18 h. After that, the samples were again placed at room temperature for the remaining period before testing at 3 and 7 days.

2.4 Compressive Strength Test

Compressive strength was tested at the age of 3 and 7 days as per BDS EN 196-1 [17]. The reported result was the average of six samples. The compression testing machine had a loading rate of 2400 ± 200 N/s. A standard jig had placed between the compression machine's platters to transmit the load to the compression surfaces of the mortar prism specimen. The test was carried out on halves of the prism broken by using suitable means which do not subject the halves to significant stresses. Each prism half was tested by loading its side faces using the compression testing machine. The compressive strength σ was calculated in MPa by dividing the maximum load at fracture (N) by 1600 (the area of the platens 40 mm × 40 mm) in square millimeters.

3 Result and Discussion

3.1 Workability

The variation in workability (measured through flow test) of mortars was evaluated by partially replacing various filler material. An additional water/binder ratio of 0.225 was maintained for preparing these mortar samples. A typical flow test is shown in Fig. 1. Different combinations of partially replaced filler materials gave mixed results. Control flow value (185 ± 5) mm without filler replacement was taken as standard. As shown in Fig. 2, the flow value varied depending on the replacement material type. A sudden increase in flow value was observed while the waste glass replaced 10% filler; this was similar for 15% replacement. At 20% replacement level, flow value decreased from the previous replacement level. Waste glass is composed of mainly silica, a relatively cleaner type of filler, therefore increasing the workability of

Fig. 1 **a** Mortar sample in brass mold and **b** Sample shape turned into a pancake shape
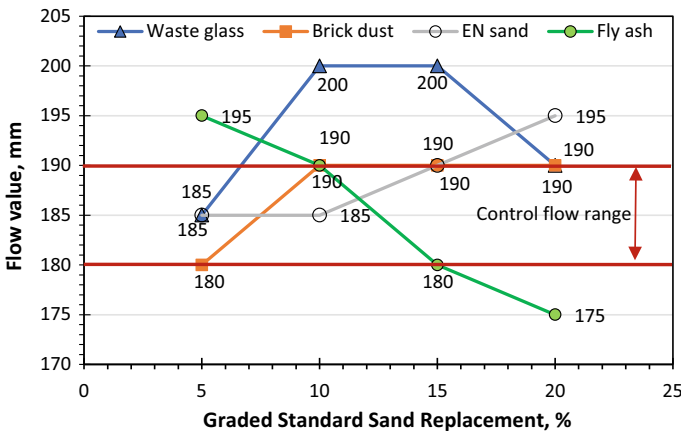
Fig. 2 Geopolymer mortar flow value

mortar. The study [19] found an increase in flow value by partially replacing cement with ground glass powder up to 25%. The waste glass used in this study was passed through the #30 (600 μm) ASTM sieve, which is smaller than the original filler (sand) that was replaced. Therefore, it gave a higher flow up to 15% replacement for being a relatively cleaner material. However, it is a smaller particle size than the original sand; its flow performance was slightly downgraded at a 20% replacement level in geopolymer mortars.

The brick dust was smaller than waste glass passing through #50 (300 μm) ASTM sieve. Change in flow value with brick dust was not significant. A 5% replacement gave lower flow, and all other replacement level gave a slightly higher value than control flow constantly. However, all the flow value with filler replacement by brick dust was within the range of control flow. The effect of impurities in filler sand used in Bangladesh was noted by replacing this with EN standard sand. Both of these materials were similar in particle size. The flow value was increased from control flow by replacing more local sand with EN standard cleaner sand. This is expected to improve significantly if a higher amount of EN sand is used. The use of fly ash as filler gave the opposite trend in flow value than other materials.

An increase in fly ash replacement level gave gradually decreased the flow value of mortar. With 15 and 20%, replacement gave a lower flow than the control flow. A study [20] with cement replaced by fly ash in concrete showed an increase in workability. This study worked with geopolymer mortars where the amount of water was limited to wet the constituent material. The finer segment of fly ash was obtained by passing them through the #200 (75 μm) ASTM standard sieve. Therefore, the surface area of the materials was much higher than the original filler sand. Thus, the available water could not thoroughly wet the enormous surface area of the finer fly ash, and the expected ball/bearing effect [21] of finer fly ash could not be started. Therefore, it is not recommended to replace more than 15% graded sand with fine fly ash in geopolymer mortars.

3.2 Compressive Strength

The compressive strength of geopolymer mortar was evaluated by replacing the filler material using a different possible alternative. The 3- and 7-days compressive strengths of geopolymer mortar are given in Table 4 and graphically represented in Figs. 3, 4, 5, and 6. The maximum compressive strength of geopolymer mortars was obtained with a 15% replacement of filler with brick dust. Sample B15 gave more than 200% compressive strength (at three days 45.8 MPa and seven days 46.6 MPa) than control strength of 3 days and 7 days (Fig. 3). A study [22] found significant improvement in the compressive strength of mortars by replacing cement with similar size brick dust with water-reducing admixtures. The performance of fly ash as filler replacement was not that impressive. No significant change in compressive strength was noted with the sand replacement by fly ash. Fly ash is expected to participate in

Table 4 Development of compressive strength (MPa) at different ages

Label	Control	B5	B10	B15	B20	F5	F10	F15	F20
3-day	19.6	16.4	37.8	45.8	44	15.7	13.9	14.5	15.4
7-day	21.5	17.8	44	46.6	44.7	16.3	16.2	15.3	15.5
Label	**E5**	**E10**	**E15**	**E20**	**G5**	**G10**	**G15**	**G20**	
3-day	17.5	14.6	18.4	39.6	9.9	14.7	20.4	19.9	
7 day	29.6	26.5	30	41.6	10.3	17.3	20.6	25.8	

Fig. 3 Compressive strength of brick dust mortar
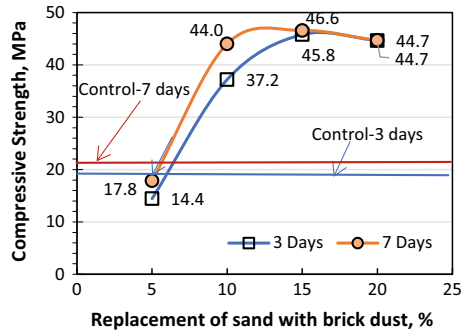
Fig. 4 Compressive strength of fly ash mortar
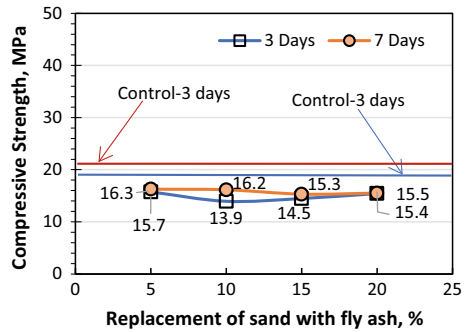
Fig. 5 Compressive strength of EN sand mortar
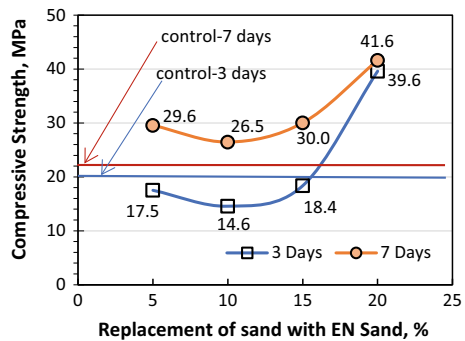
Fig. 6 Compressive strength of waste glass mortar
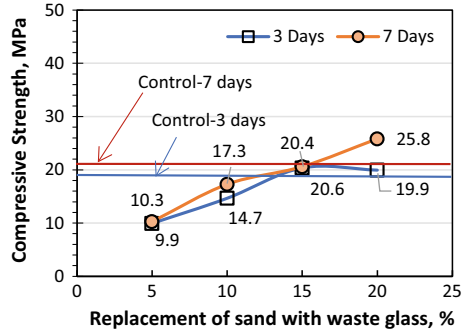
geopolymerization [23]; however, the compressive strength interfered by the workability (shown in Fig. 2). The compressive strength improvement of Portland–fly ash cement paste with silica fume was found higher than the blends without silica fume (for the same fly ash content) [20]. At both 3 days and 7 days, all fly ash mortar gave less strength than the control mixture (Fig. 4).

EN sand also gave a gradual improvement of geopolymer mortar compressive strength. The improvement mainly was noted for 7 days of curing (Fig. 5). In both three and 7-days curing, 20% replacement gave maximum compressive strength (Fig. 5). The improvement of strength with 20% sand replacement (sample E20) by EN standard sand was around 200%, reflecting the effect of possible impurities present in filler materials. Although the grading of locally obtained sand and EN standard sand was similar, the EN sand gave a better fresh performance of geopolymer mortars which was also reflected in its compressive strength results. A gradual increase in compressive strength was found by replacing the graded sand with waste glass powder (Fig. 6). With 15% (G15) replacement of filler sand, the compressive strength was comparable with the control mortar. The 7-days compressive strength of 20% waste glass sample was highest among the tested geopolymer mortars made by replacing the filler with waste glass. However, the improvement in flow value with glass did not reflect in their compressive strength test results. This requires further research to draw any definite conclusion in this regard.

3.3 Failure Pattern Under Compressive Load

The mortar sample under compressive loading should follow a good pattern to confirm the interface was built satisfactorily. The mortar sample's fracture pattern was examined visually to determine whether it is satisfactory. The failure area of the mortar ascertains those failure patterns. According to [24], both satisfactory and unsatisfactory failure was observed in the samples tested (Fig. 7). Brick dust and EN sand samples provide acceptable failure, and waste glass provides both satisfactory
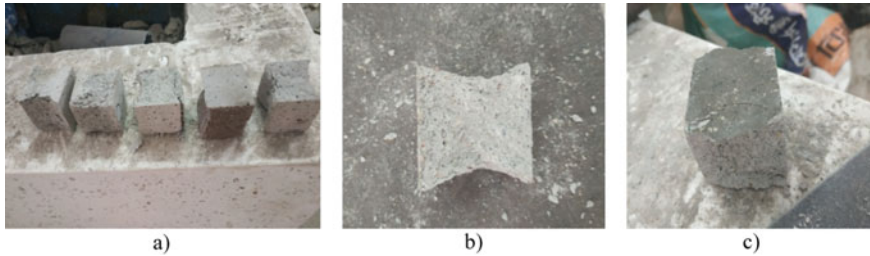
Fig. 7 **a** Geopolymer mortar after the compression test, **b** Satisfactory failure, and **c** Unsatisfactory failure

and unsatisfactory failure. In the case of fly ash, maximum test samples display unsatisfactory failure. This failure occurs not because of the fault in the testing machine or insufficient attention to the testing procedure especially positioning of the specimen as stated by BS EN 12390-3 [25]. This indicates the influence of compaction. The samples gave satisfactory failure, had a better flow, and significantly improved their compressive strength.

3.4 Environmental and Economic Considerations

The study indicates that there is a considerable possibility of using industrial by-products in the construction sector. Geopolymer is an eco-friendly alternative binder. Almost one ton of carbon dioxide (CO_2) emits into the ambience from the production of one-ton cement [21]. Fly ash, waste glass, and brick dust are not easily biodegradable. Therefore, without disposing of these waste materials in the construction industry, the betterment of the environment is done by saving the landfill area, conserving the virgin materials, and reducing greenhouse gas production. Among the used filler replacement, 20% brick dust gave the best promising results in geopolymer mortars. In addition, a 20% replacement of filler with waste glass could also be a better way of using this in a cementitious system.

In the local market of Bangladesh, sand costs 45 BDT/cft while brick dust, waste glass, and fly ash costs roughly 5–10 BDT/cft (transport cost only), 100 BDT/cft [19], and 20–25 BDT/cft (transport cost mainly). Therefore, considering a 20% replacement of sand by brick dust can reduce the geopolymer mortar production cost by 30–35%. As the strength improvement was found more than 200%, this was also contending in the estimation. Brick dust is generally found in construction sites after grinding brick to prepare brick chips. Fly ash is a by-product of coal, GGBS is a by-product of the steel industry, and silica fume is a by-product of silicon and ferrosilicon alloy. As an imported material, the price of silica fume in Bangladesh is higher than cement. However, the geopolymer mortar production cost with this binding material (a combination of silica fume, GGBS, and alkaline solution) will be

20–30% lower than cement, comparing the recent price of cement is 480 BDT/50 kg bag in the local market of Bangladesh [19].

4 Conclusion

This research focused on the performance of different filler materials in GGBS and silica fume-based geopolymer mortars. In general, the workability of geopolymer mortars was increased with the amount of filler replacement by various materials. However, fly ash gave the opposite trend due to high surface area and water demand. In most cases, the compressive strengths of geopolymer mortars were improved with time (3 days to 7 days). The strength was generally enhanced with an increase in filler replacement level. Brick dust was found to be efficient filler material. The workability was similar to the control mix until 20% replacement of filler sand by brick dust. Compressive strength improvement of more than 200% was very promising and therefore marked as an eco-friendly material for geopolymer production. Due to the high surface area, the replacement of filler by fly ash did not give better performance than the control mortar. From an economic and environmental perspective, both waste glass and brick dust could be an excellent option for a filler in concrete construction.

References

1. Jaskula, B.B.W.: Mineral Commodity Summary 2014—Gallium. US Geol. Surv. (2014)
2. Gartner, E.: Industrially interesting approaches to 'low-CO$_2$' cements. Cem. Concr. Res. **34**(9), 1489–1498 (2004)
3. Komljenović, M., Baščarević, Z., Bradić, V.: Mechanical and microstructural properties of alkali-activated fly ash geopolymers. J. Hazard. Mater. **181**(1–3), 35–42 (2010)
4. Part, W.K., Ramli, M., Cheah, C.B.: An overview on the influence of various factors on the properties of geopolymer concrete derived from industrial by-products. Constr. Build. Mater. **77**, 370–395 (2015)
5. Lyon, R.E., Balaguru, P.N., Foden, A., Sorathia, U., Davidovits, J., Davidovics, M.: Fire-resistant aluminosilicate composites. Fire Mater. **21**(2), 67–73 (1997)
6. Lee, N.K., Jang, J.G., Lee, H.K.: Shrinkage characteristics of alkali-activated fly ash/slag paste and mortar at early ages. Cem. Concr. Compos. **53**, 239–248 (2014)
7. Kong, D.L.Y., Sanjayan, J.G.: Damage behavior of geopolymer composites exposed to elevated temperatures. Cem. Concr. Compos. **30**(10), 986–991 (2008)
8. Huseien, G.F., Mirza, J., Ismail, M., Ghoshal, S.K., Ariffin, M.A.M.: Effect of metakaolin replaced granulated blast furnace slag on fresh and early strength properties of geopolymer mortar. Ain Shams Eng. J. **9**(4), 1557–1566 (2018)

9. Verdolotti, L., Lannace, S., Lavorgna, M., Lamanna, R.: Geopolymerization reaction to consolidate incoherent pozzolanic soil. J. Mater. Sci. **43**(3), 865–873 (2008)
10. Ng, C., Alengaram, U.J., Wong, L.S., Mo, K.H., Jumaat, M.Z., Ramesh, S.: A review on microstructural study and compressive strength of geopolymer mortar, paste and concrete. Constr. Build. Mater. **186**, 550–576 (2018)
11. Islam, A., Alengaram, U.J., Jumaat, M.Z., Bashar, I.I.: The development of compressive strength of ground granulated blast furnace slag-palm oil fuel ash-fly ash based geopolymer mortar. Mater. Des. **56**, 833–841 (2014)
12. Davidovits, J.: Geopolymers. J. Therm. Anal. **37**(8), 1633–1656 (1991)
13. Erdoğdu, P.T.K.: Effects of fly ash particle size on strength of Portland. **28**(9), 1217–1222 (1998)
14. Andrew, S., William, K.: Lightweight Concrete, 3rd ed. Applied Science Library (1978)
15. Ashraf, M.A., Maah, M.J., Yusoff, I., Wajid, A., Mahmood, K.: Sand mining effects, causes and concerns: a case study from bestari jaya, Selangor, Peninsular Malaysia. Sci. Res. Essays **6**(6), 1216–1231 (2011)
16. Sreenivasa, G.: Use of manufactured sand in concrete and construction an alternate to river sand. India, 2012
17. BDS EN: EN 196–1, Determination of strength. Methods Test. Cem. (2016)
18. BS EN 196–1: Methods of testing cement. Determination of strength. British Standards Institution-BSI and CEN European Committee for Standardization (2005)
19. Islam, G.M.S., Rahman, M.H., Kazi, N.: Waste glass powder as partial replacement of cement for sustainable concrete practice. Int. J. Sustain. Built. Environ. **6**(1), 37–44 (2017)
20. Nochaiya, T., Wongkeo, W., Chaipanich, A.: Utilization of fly ash with silica fume and properties of Portland cement-fly ash-silica fume concrete. Fuel **89**(3), 768–774 (2010)
21. Islam, G.M.S., Islam, M.M., Akter, A., Islam, M.S.: Green construction materials—Bangladesh perspective. In: International Conference on Mechanical Engineering and Renewable Energy (ICMERE2011), 2011
22. Li, L.G., Lin, Z.H., Chen, G.M., Kwan, A.K.H.: Reutilizing clay brick dust as paste substitution to produce environment-friendly durable mortar. J. Clean. Prod. **274**, 122787 (2020)
23. Al-Majidi, M.H., Lampropoulos, A., Cundy, A., Meikle, S.: Development of geopolymer mortar under ambient temperature for in situ applications. Constr. Build. Mater. **120**, 198–211 (2016)
24. Muhamad, K., Hamiruddin, N.A., Razak, R. A.: Effect of steel fibre contents with high strength fibre reinforced concrete. Int. J. Adv. Sci. Res. Eng. (2018)
25. BS EN: 12390-3. Testing Hardened Concrete—Compressive Strength of Test Specimens. British Standards Institution, London, UK (2019)

Ternary Combination of Industrial Wasts for Sustainable Geopolymer Mortars

T. Faria, J. Ferdous, and G. M. Sadiqul Islam

1 Introduction

The civil engineering practice has always welcomed effective new material/methods to meet up the growing requirements of future construction systems. In the middle of the eighteenth century, Portland cement was developed by Joseph Aspdin [1]. Later, it was improved in all forms for a better outcome. Despite its most significant consumption as a binding material, its high environmental burden also started to affect the world. Portland cement is being produced using the technology of 'two grinding and one calcinating' principally using limestone and clay as raw materials. For the calcination process, a temperature in the range of 1450 °C is applied. A Chinese study [2] revealed that the country's consumption of limestone, clay, iron powder, coal and electricity was one billion tons, 180 million tons, 50 million tons, 100 million tons and 60 billion kW/h per year in the production of cement. Every ton of cement production approximately emits 1 kg sulfur dioxide (SO_2), 2 kg oxides of nitrogen (NO_x), and 10 kg dust. Each year about 4 billion tons and 7% emissions of CO_2 have been reported to produce because of the production of cement all over the world [2].

Following this, the impetus to explore the alternative of Portland cement concrete and mortar has become one of the gripping fields for research. To minimize the emission from the cement industry as well as conservation of energy while managing the waste material for environmental protection, researchers started to develop new types

T. Faria · J. Ferdous (✉) · G. M. S. Islam
Department of Civil Engineering, Chittagong University of Engineering & Technology,
Chattogram - 4349, Bangladesh
e-mail: u1501116@student.cuet.ac.bd

T. Faria
e-mail: u1501033@student.cuet.ac.bd

G. M. S. Islam
e-mail: gmsislam@cuet.ac.bd

of mortar and concrete [3]. Among all these new materials, geopolymeric material is found to be the most effective binder which could replace the traditional cement either totally or partially. In 1979, Davidoits first introduced geopolymer, alkali-activated base materials consisting of aluminum and silicon with a three-dimensional net-like structure to serve as a binder [2]. The aluminosilicate powder could generally be an industrial by-product such as fly ash, ground granulated blast furnace slag (GGBS), ladle furnace slag (LS), silica fume (SF) and thermally activated clays (e.g., metakaolin) or a combination of these, activated by alkaline solution (NaOH or KOH with sodium silicate) to produce alkali-aluminosilicate gel [4]. The LS is a by-product of iron purifying and the production industry could be a potential material in geopolymer application that gained less attention [3]. To maximize the utilization of industrial waste a full replacement of cement by pozzolanic material is recommended. Therefore, geopolymer mortar without using cement clinker could be a greener construction material for sustainable construction practice [2]. Compared to Portland cement, geopolymer has technical advantages, including high early strength development, better durability, lower permeability and shrinkage and more excellent resistance to acid and fire with the ability to immobilize hazardous atoms [5]. Almost no greenhouse gas is generated in the process of geopolymerization, and the raw material has embodied carbon [2]. The geopolymerization process increases the pH of the mixture and accelerates the reaction rate between solids [6].

In geopolymer mortar, heat curing plays a vital role in enhancing chemical reaction and improving compressive strength. Heat curing accelerates the initial improvement of compressive strength [7]. The study used coal fly ash [4], a combination of rice husk ash and spent diatomaceous earth [8] as a binary combination for geopolymer production. However, a minimal study could be found with a ternary mixture of binders. Kumar et al. [9] studied a ternary combination of GGBS, fly ash and SF geopolymer. This study, therefore, combined GGBS, LS and SF for the production of geopolymer mortars. The main aim was to obtain the optimum material combination for geopolymer mortar including different GGBS, LS and SF under varying curing conditions while keeping the sodium silicate-to-sodium hydroxide ratio and activator to binder ratio constant. The activator concentration was 4, 6 and 8 M. The workability of geopolymer mortar was evaluated to obtain optimum activator concentration. The compressive strengths of GGBS, LS and SF combined geopolymer mortars were evaluated concerning the effect of different alkaline activator concentrations and curing conditions (age and temperature).

2 Materials and Methods

2.1 Materials

Geopolymer mortar was prepared using industrial by-products GGBS, LS and SF as binder. In addition, EN standard sand, alkaline activator and water were used.

Table 1 Chemical composition of binder materials

Chemical composition	GGBS (%)	Ladle slag (%)	Silica fume (%)
SiO_2	33.4	25.0	89.0
Al_2O_3	14.3	12.3	0.5
Na_2O	0.2	0.4	0.2
K_2O	0.3	0.4	1.1
CaO	41.1	46.4	0.9
MgO	3.9	4.3	1.6
TiO_2	0.6	0.2	–
P_2O_5	0.1	2.7	–
SO_3	2.6	–	0.4
FeO	–	1.5	–
Fe_2O_3	0.6	–	1.5
Cr_2O_3	–	0.7	–
Loss on Ignition	0.1	1.1	2.9

Table 2 Grading of EN standard sand

Sieve size	Weight, g	Cumulative weight, g	% cumulative weight
#16	97	97	22.1
#30	131	228	52.1
#50	137	365	83.3
#100	73	438	100
#200	62	500	–

Finely ground GGBS powder was used in the range of 50–70% of the binder. LS was used as 20 and 30% of the total binder. SF, a highly reactive pozzolana has a physical effect as filler was used in the range of 10–20% of the binder. GGBS and LS were obtained from the local cement and iron production industry, respectively. In addition, Elkem micro-silica was obtained through a local supplier. The chemical properties of GGBS, LS and SF are given in Table 1.

A combination of sodium silicate and NaOH was used as the alkaline activator. The chemical composition of sodium silicate is $SiO_2 = 30\%$, $Na_2O = 14\%$ and $H_2O = 56\%$ in its liquid form. The NaOH solution is prepared by dissolving the required quantity (40 g/L for 1 M) of its flakes (98% purity) into distilled water to obtain the desired concentration. The concentrations of NaOH solution were 4, 6 and 8 M. EN Standard sand [10] imported from France origin through a local supplier was used as fine aggregate. Required quantity 1350 ± 5 g for a single test in the desired gradation was packed in a plastic bag. The grading of EN standard sand is given in

Table 2. This sand was found with minimum moisture content (0.02%) in a sealed plastic bag. The fineness modulus of the sand was found to be 2.57.

In preparation of geopolymer mortar samples, a combination of GGBS, LS, and SF and the alkaline activator was used as a binder. Additional distilled water (13, 15 and 17% for 4 M, 6 M and 8 M, respectively) was used for improving the flow of the geopolymer mortar. Trial mixes were conducted to obtain the optimum combination/condition for the desired properties of mortar samples.

2.2 Mixing, Casting and Curing

Initially, the alkaline activator solution comprised of NaOH and sodium silicate was prepared. 40 g of NaOH flakes were required to be dissolved in 1L distilled water to prepare a 1 M solution. The required quantity of NaOH flakes was dissolved in 1L water to produce 4, 6 and 8 M solutions. After preparation, the solution was kept for 2 h and allowed to cool down before use. After preparing the solution, sodium silicate was added, maintaining SS/SH ratio of 2.5. The dry combined binder (GGBS, LS and SF) was placed inside the mixing bowl, and the alkaline activator solution was added. After initial mixing at low speed, the EN standard sand was added gradually from the hopper automatically while the mixing continues. In addition to the activator solution excess, 13–17% water was added based on the molarity of NaOH to maintain a balanced liquid proportion in the mortar samples. Finally, all the materials were mixed in the mixture for about 3 min with 180 rotations of the paddle. Immediately after mixing, the workability test was carried out using a flow table. After the flow test, the mixture was hand mixed and placed in the 3-gang (40 × 40 × 160 mm) iron mold in 2 equal layers. The mortar samples were compacted using a jolting machine for proper compaction in steps. Each layer received 60 jolts. Figure 1 gives different steps followed to prepare/test geopolymer mortars.

After finishing compaction, the mold was covered with transparent plastic sheets to confine the moisture contents of the mortar specimens and kept at room temperature for a few hours. Then the sample, including mold was placed in an oven for 24 h at 60 and 80 °C. One set of the sample was cured at ambient temperature (25–30 °C).

(a)   (b)   (c)   (d)
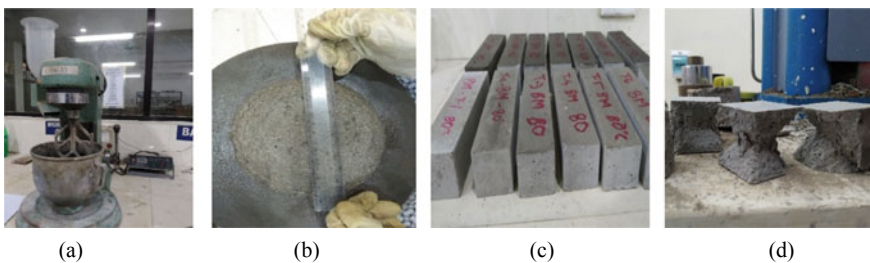
Fig. 1 **a** Mortar mixer machine, **b** flow test, **c** demolded sample after heat curing, **d** crushed sample

After 24 h of heat curing, the specimen was taken out of the oven and allowed to cool at room temperature. Then, the sample was removed from the mold and kept at ambient temperature for the rest period until the test. The samples were tested for compressive strength after 3 and 7 days. A total number of 216 mortar samples were prepared using different combinations.

3 Results and Discussions

3.1 Workability

The workability of a mix is classified based on the flow diameter. The minimum flow diameter of 150 ± 5 mm is considered convenient for placing and compacting the mixture in molds [11]. Flow test results are given in Fig. 2. In the mortar preparation process, 13, 15 and 17% excess water was added for 4, 6 and 8 M samples. In general, the flow diameter was found to be within 130–155 mm. The samples having workability within this range is defined as moderately stiff [11]. With the increase in activator strength (4–8 M), the change in flow value was not significant but was found within the expected range. On the other hand, the binder components used in the sample have a considerable influence on workability. A study [12] indicated increasing slag content in geopolymer mortar can reduce the flow. A higher quantity of LS (G50L30S20) in the combination could also impair the flow. The optimum flow was obtained with 60% GGBS, 20% LS and 20% SF samples. As the amount of excess water applied was increased with the concentration of the activator, the flow value seemed to be in a reasonable range. In general, the use of slag within a limited range and silica fume within 15–20% gives a better result.
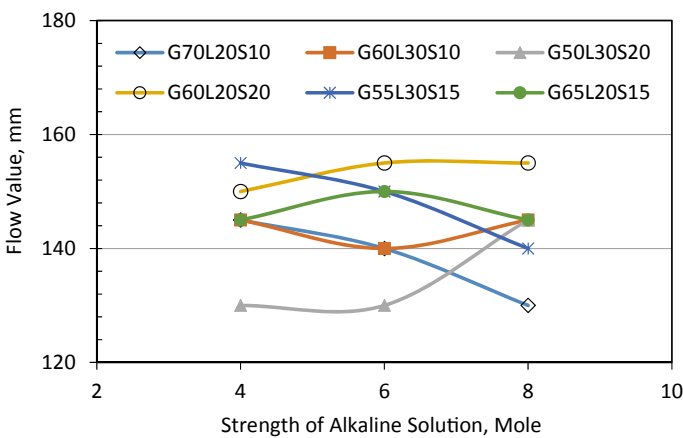
Fig. 2 Variation of flow with strength of the alkaline solution

3.2 Compressive Strength

In geopolymer mortar, the strength of the binder and activator has a significant effect on its performance. The following section gives the correlation between the compressive strength with a variation of binder combination, the strength of the alkaline solution, Si/Al ratio, curing temperature and age.

3.3 Effect of Curing Temperature

Figure 3 gives the variation in compressive strength of different binder combination with variation in curing temperature for different strength of the alkaline solution. In this study, all the samples were cured in the oven at 60 and 80 °C for 22–24 h, few hours after casting to compare with those cured without elevated heat (25–30 °C). Although curing at high temperatures provides high early strength [12], heat curing may not be available for cast in situ construction. Nevertheless, the same mixture
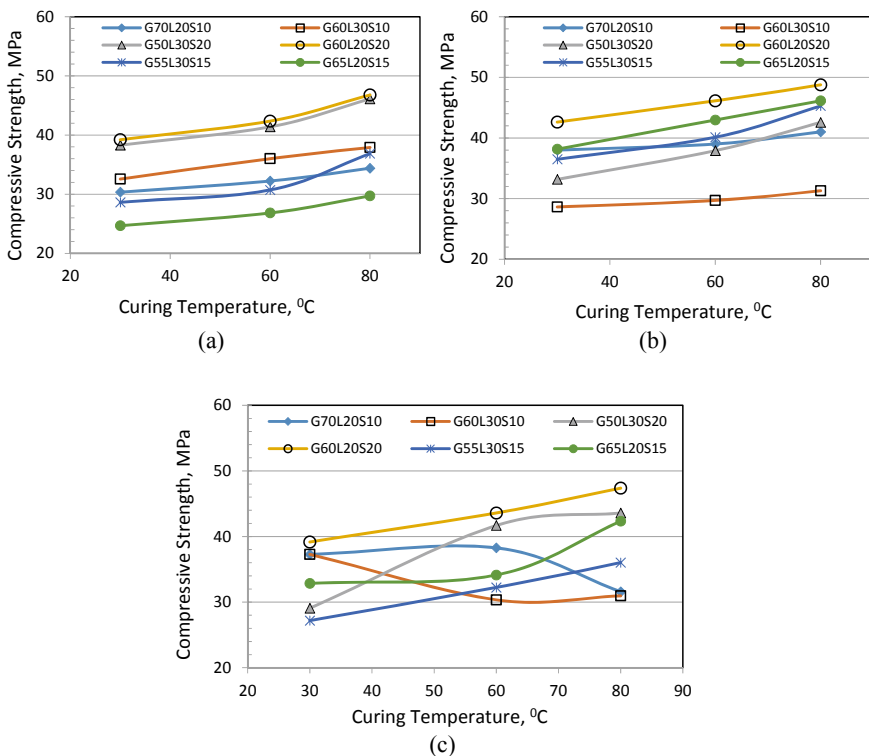
Fig. 3 Strength versus curing temperature **a** 4 M NaOH, **b** 6 M NaOH and **c** 8 M NaOH

can be cured at ambient temperature to achieve reasonable strength gradually over age. With a little exception, all the samples' compressive strength was influenced by curing temperature. In general, a positive trend was noted with the temperature rise. However, the strength increase rate was more for 60 °C heat curing compared to 80 °C. Sample G60L20S20 gave the highest compressive strength (46.8, 48.8 and 47.4 MPa) with curing at 80 °C regardless of activator strength.

In this case, the compressive strength of samples with 4, 6 and 8 M was very similar, indicating the effect of temperature curing on silica fume and GGBS is significant. In contrast, the samples with 10% SF and 30% LS gave relatively much lower compressive strength. They again supported the earlier conclusion that the effect of temperature on GGBS and SF is significant. As the amount of GGBS increases in the binder, the compressive strength decrease for both 20 and 30% LS using 4, 6 and 8 M alkaline solution. In the case of LS content, better results are found at 30% LS for each percentage of GGBS using a 4 M alkaline solution. At the same time, samples with 6 M and 8 M activator gave an increase in compressive strength at 20% LS. The variation of compressive strength is similar for each curing temperature.

3.4 Effect of Strength of Activator

The strength of the alkaline solution is an essential parameter in the evaluation of the strength of the mortar. In this study, the alkaline activator is a combination of NaOH and sodium silicate solution. Keeping the amount of sodium silicate fixed, 4, 6 and 8 M molarity of sodium hydroxide was used to observe the influence of the activator on compressive strength. As shown in Fig. 4, compressive strength increases around 25% as the strength of the alkaline solution increases from 4 to 6 M. However, in some cases, the strength decreased (12% in the extreme case) further while the activator concentration increased from 6 to 8 M. Therefore, a 6 M alkaline solution was found to be optimum for these ternary combined geopolymers.

In the case of 4 M alkaline solution, as the percentage of LS increases from 20 to 30% for the samples with 10 and 15% silica fume, strength increases; however, while the share of silica fume reaches 20%, strength reduces slightly. For samples using 6 and 8 M alkaline solution, when ladle slag increases from 20 to 30%, compressive strength decrease for all samples. However, an increase in silica fume up to 20% gives the highest compressive strength for each concentration of the alkaline solution.

With the 4 M alkaline Solution, an increase in GGBS content from 50 to 60% for 20% SF samples increased the compressive strength. However, with a further rise in GGBS content from 60 to 70% for 10–15% silica fume samples, a gradual strength reduction was observed. For both 6 and 8 M alkaline solutions, an increase in GGBS content from 50 to 70% increased the compressive strength with all three different percentages (10, 15, and 20%) of SF. A maximum of 20% SF yields the highest compressive strength for each molarity of the alkaline solution and curing condition.
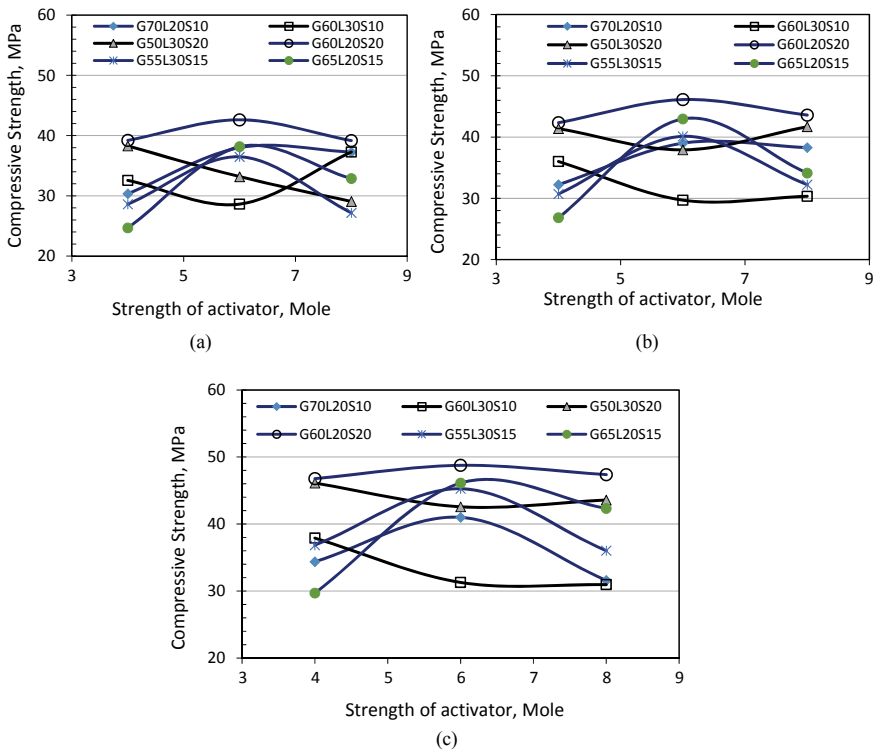
Fig. 4 Compressive strength versus activator concentration at **a** ambient, **b** 60 °C and **c** 80 °C curing

Therefore, the results can be summarized as an increase in alkaline solution strength helps GGBS to perform effectively as a binder component.

3.5 Effect of Curing Age

The effect of curing age (3–7 days) on the strength development of geopolymer mortar is given in Fig. 5. Tests were performed on three sets of specimens cured at ambient, 60 and 80 °C temperature. After 24 h heat curing in the oven at 60 and 80 °C temperature, the ambient temperature was maintained for the remaining period until the compression test. The increment in compressive strength with time was found to be ranged between 4.8 and 21.3%.

For the set initially cured for 3 days, almost 92–96% of the ultimate strength (7 days) gain was found. The heat curing influenced mortar samples with all binder combinations for gaining high compressive strength at an early age. The increase in strength further continued up to 7 days. On average, a 10% increment was
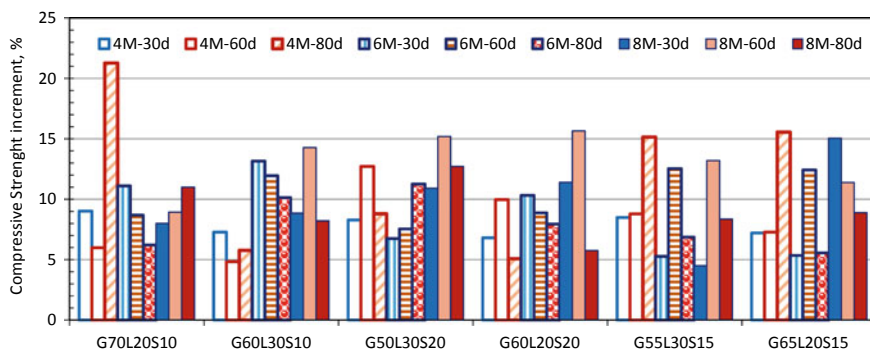
Fig. 5 Compressive strength increment of mortar samples from 3 to 7 days

found between 3 and 7 days. A study [13] indicated high temperatures significantly influence the compressive strength of geopolymer mortars.

3.6 Effect of Silica Alumina Ratio

The silica/alumina ratio has a significant influence on the strength of geopolymer mortar. A study [14] indicated compressive strength generally increases with Si content, although the increment is not linear. Theoretically, the bond between Si–O–Si is stronger than the Si–O–Al and Al–O–Al, which means that the strength increases with increasing Si/Al ratio [14]. The lower compressive strength occurs due to the delay of geopolymerization process for low Si/Al. Figure 6 gives the Si/Al ratio with compressive strength. In general, the compressive strength was increased with Si/Al ratio for varying curing conditions and alkaline concentration.

4 Conclusion

Industrial wastes were used in the preparation of geopolymer mortar. The effect of alkaline concentration, curing temperature and age on the compressive strength of the prepared binder samples was studied. The optimum compressive strength was found to be 48.8 MPa using 60%, 20% and 20% GGBS, LS and SF, respectively, with a 6 M alkaline solution and 80 °C temperature. A high concentration of alkaline media can interfere with the workability of geopolymer mortars. Therefore, excess water would be required to maintain workability. High temperatures and prolonged curing can improve strength. The activator concentration has a significant influence. Although the 8 M activators gave higher compressive strength, a 6 M activator would be optimum for these ternary combined geopolymer binders considering other
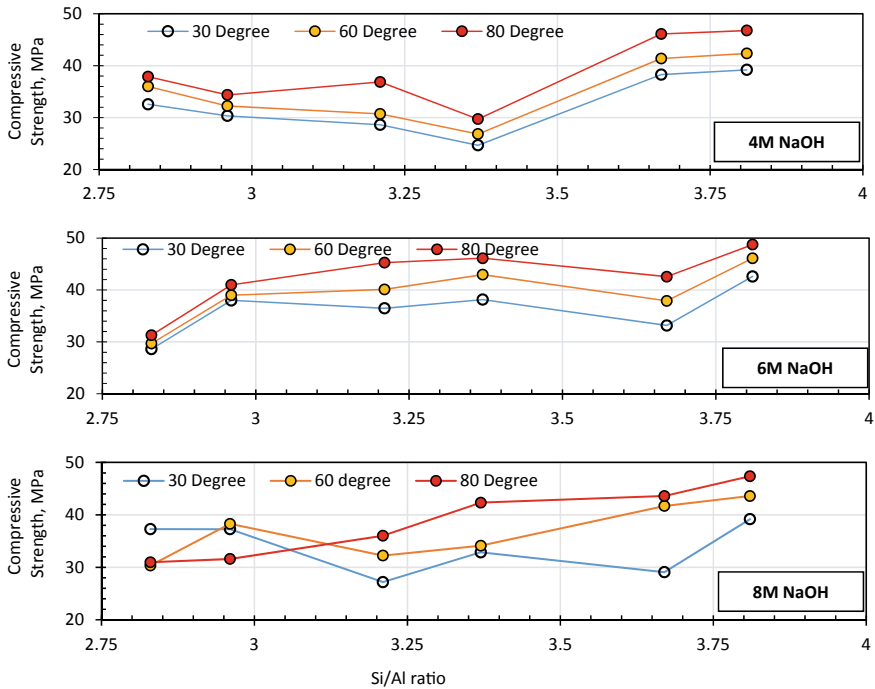
Fig. 6 Variation in compressive strength with Si/Al ratio

parameters. The compressive strength was increased with Si/Al content, generally. Therefore, the proposed ternary blended industrial by-product-based binders could be sustainable construction materials through safe industrial waste management.

References

1. Black, L., Purnell, P.: Promoting Access to White Rose Research Papers Universities of Leeds, Sheffield and York. May (2010). https://doi.org/10.1179/174367510X12714358363805
2. Zhang, P., Zheng, Y., Wang, K., Zhang, J.: A review on properties of fresh and hardened geopolymer mortar. Compos. Part B Eng. **152**, 79–95 (2018). https://doi.org/10.1016/j.compos itesb.2018.06.031
3. Sarker, S., Islam, G.M.S., Sadique, M., Shubbar, A.A.: Non-fired building block using industrial wastes (2020)

4. Andini, S., Cioffi, R., Colangelo, F., Grieco, T., Montagnaro, F., Santoro, L.: Coal fly ash as raw material for the manufacture of geopolymer-based products. Waste Manag. **28**(2), 416–423 (2008). https://doi.org/10.1016/j.wasman.2007.02.001

5. De Pereira, D.S.T., et al.: Comparative analysis between properties and microstructures of geopolymeric concrete and Portland concrete. J. Mater. Res. Technol. **7**(4), 606–611 (2018). https://doi.org/10.1016/j.jmrt.2018.08.008

6. Wardhono, A.: The effect of sodium hydroxide molarity on strength development of non-cement class C fly ash geopolymer mortar. J. Phys. Conf. Ser. **947**(1) (2018). https://doi.org/10.1088/1742-6596/947/1/012001.

7. Khale, D., Chaudhary, R.: Mechanism of geopolymerization and factors influencing its development: a review. J. Mater. Sci. **42**(3), 729–746 (2007). https://doi.org/10.1007/s10853-006-0401-4

8. Mejía, J.M., Mejía De Gutiérrez, R., Montes, C.: Rice husk ash and spent diatomaceous earth as a source of silica to fabricate a geopolymeric binary binder. J. Clean. Prod. **118**, 133–139 (2016). https://doi.org/10.1016/j.jclepro.2016.01.057

9. Ravi Kumar, P., Bhandari, A., Ravi, T.D., Rooby, J., Sundararajan, T.: Strength of geopolymer paste using a ternary blend of fly ash GGBFS and silica fume under ambient conditions. Int. J. Innov. Technol. Explor. Eng. **8**(11), 3784–3790 (2019). https://doi.org/10.35940/ijitee.K2156.0981119.

10. BS EN 196–1: Methods of Testing Cement. Determination of Strength. British Standards Institution-BSI and CEN European Committee for Standardization (2005)

11. Mermerdaş, K., Manguri, S., Nassani, D.E., Oleiwi, S.M.: Effect of aggregate properties on the mechanical and absorption characteristics of geopolymer mortar. Eng. Sci. Technol. an Int. J. **20**(6), 1642–1652 (2017). https://doi.org/10.1016/j.jestch.2017.11.009

12. Nath, P., Sarker, P.K.: Effect of GGBFS on setting, workability and early strength properties of fly ash geopolymer concrete cured in ambient condition. Constr. Build. Mater. **66**, 163–171 (2014). https://doi.org/10.1016/j.conbuildmat.2014.05.080

13. Kuri, J.C., Khan, M.N.N., Sarker, P.K.: Workability, strength and microstructural properties of ground ferronickel slag blended fly ash geopolymer mortar. J. Sustain. Cem. Mater., pp. 1–18 (2020). https://doi.org/10.1080/21650373.2020.1823905

14. He, P., Wang, M., Fu, S., Jia, D., Yan, S., Yuan, J.: Effects of Si/Al ratio on the structure and properties of metakaolin based geopolymer. Ceram. Int. **42**(13), 14416–14422 (2016). https://doi.org/10.1016/j.ceramint.2016.06.033

Effect of Compaction Pressure on the Properties of Eco-Friendly Building Block Produced from Industrial By-Products

Ezaz Ahmed, Syed Maruf-Ul Hassan, and G. M. Sadiqul Islam

1 Introduction

In order to provide adequate housing to meet the alarming increase in population, enormous number of brick kiln were established in Bangladesh without maintaining any kind of guidelines. The relevant authority has been struggling to guide these uncontrolled kilns to follow regulations. In consequence, the uncontrolled emission of different toxic gases from these kilns has led to the deterioration of the ecosystem with unpredictable long-term effects. Therefore, the Government of Bangladesh (GoB) has banned the use of clay bricks for government construction work after 2024. The construction industry has never been fully sustainable and therefore requires a great effort to conserve virgin material for future generations. To achieve sustainability in the construction sector the GoB gave impetus for an alternative way to produce bricks, especially by using the waste materials. It creates a value of the waste products as well as saves the environment from pollutions [1].

The traditional red brick (clay formed and burnt) is one of the prime materials, responsible for making the construction industry unsustainable in Bangladesh. This requires the upper fertile top clayey soil (150–600 mm) from the agricultural field. The production of 25 billion bricks per year consumes 100 million tons of virgin agricultural clay [2]. If such damage continues, national food security might face huge strife to satisfy the demand for food of the next generation. The brick kiln owners have long been consuming the hills in Khagrachari remote areas especially

E. Ahmed (✉) · S. M.-U. Hassan · G. M. S. Islam
Department of Civil Engineering, Chittagong University of Engineering & Technology, Chattogram 4349, Bangladesh
e-mail: u1501041@student.cuet.ac.bd

S. M.-U. Hassan
e-mail: u1501054@student.cuet.ac.bd

G. M. S. Islam
e-mail: gmsislam@cuet.ac.bd

in winter for the production of bricks. This hill cutting triggers the land sliding by heavy rainfall during the winter season. The Brick Manufacturing and Brick Kilns Establishment (control) Act 2013 prohibits the use of soil collected from agricultural land or hills as a raw material in brick manufacturing [3]. Not only this agricultural land but also the environment is in threat from the clay burning process [3]. The Brick Manufacturing and Brick Kilns Establishment (control) Act prohibits the use of wood as fuel in brick kilns. Manufacturers can only use standard coal as fuel; however, this also releases large amounts of CO_2 into the atmosphere.

The latest 2018 Department of Environment (DoE) data reported 7,707 brick kilns in Bangladesh including 366, 1529, 356, 2295, 873, and 1176 in Barisal, Chattogram, Sylhet, Dhaka, Khulna, and Rajshahi division, respectively [4]. In 2015, DoE reported 1,957 brick kilns (total 6895) did not have proper permission to run. Those enormous illegal number of brick kilns were responsible for half of the air pollution of Dhaka city in 2017–18 fiscal year [4]. According to the World Health Organization (WHO), Dhaka came out as the second-worst city in air pollution behind Delhi and Cairo in 2018 [5]. The United Nations (UN) health entity estimated 37,000 deaths per year in Bangladesh due to air pollution. Unfortunately, the average age of the victims is 38 years [4]. According to a report of WHO, around 7 million die from exposure to fine particles in polluted air every year [5]. Ninety percent of the deaths were in low- and middle-income countries, mainly in Asia and Africa. It caused stroke, heart disease, lung cancer, chronic obstructive, pulmonary disease, and respiratory infections. In Bangladesh, the hospital treats about 100 outdoor patients every day and most of them come with respiratory problems. GoB has already taken the initiative to shut down all harmful brick kilns by 2024 [1].

Fly ash is a by-product produced from the combustion of coal (both bituminous and lignite) [6]. The only coal-based power plant in Barapukuria, Bangladesh, is generating 525 MW power with approximately 1,09,200 Metric tons fly ash as a by-product every year [7]. The government is planning to open 13 coal power plants in the upcoming years. Among these, Matarbari power plant (1200 MW), Payra thermal power plant (1320 MW), and Rampal power plant (1320 MW) are going to be opened before 2024 [8]. According to the data available, ash produced is approximately 10% by mass of the coal burnt [9]. Out of this ash, 80% is estimated to be fly ash and the rest is bottom ash. Once the ongoing construction of coal-based power plants will be completed the production of fly ash is projected to 865,000 MT per annum from 2024 onward [1]. This will create enormous storage, disposal, and management crisis for the producers. It is generally insoluble in water, but the insignificant amount of heavy metal present in fly ash may come from leeching. Due to the presence of alumino-silicate compounds fly ash is capable of carrying a pozzolanic reaction with free lime [10]. Induction furnace slag (IFS) is a by-product of the steel purification and making process. This material is slightly pours with high hardness [1].

Using cement as a binder for making non-fired brick could be an option to reduce pollution from the brick industry. However, high cement content could lead to the same environmental damage indirectly as cement production also leads to higher emission [11]. In addition, ordinary cement-based block requires a higher curing

period which may increase the cost of production due to space and time requirement [12]. In addition to participating in reaction with a binding material, generally, water is required in concrete to wet the surface of the aggregate to make a plastic mixture of the various ingredients provide workability of concrete. Adding more water than that required for hydration to the mix leaves behind pores that cause the high water absorption of concrete when get matured. The water molecule at the microscopic level becomes availed by the hydration reaction which generally evaporates with time. Hyper-pressing is a technology for the production of chemically bonded building blocks without heat application. This technology compacts the ingredients with extremely high pressure. Therefore, high pressure can reduce the water demand significantly (minimum requirement for hydration). Low water/cement ratio is expected to provide higher strength, durability and less permeability. Thus, hyper-pressing ensures the mix economical. This research, therefore, studied the effect of compaction pressure on the strength and other properties (water absorption, efflorescence, hardness, and microstructure) of building blocks. Induction furnace slag (IFS) was used as replacement of fine aggregate (local sand), and locally available fly ash was used as a filler material. Combinations of CEM I and lime were used as a binding material. The aim is to improve properties of building block alternative to clay burnt brick using industrial by-products and compaction pressure keeping the cement content as low as possible.

2　Materials and Methods

Combination of CEM I of 52.5 N grade [13] and building lime was used as a binder. Fine aggregate (locally available river sand) was replaced by IFS of 10 mm maximum particle size. Locally available fly ash was used as filler material. The chemical compositions of the constituent materials are shown in Table 1. The particle size distribution of IFS and sand is given in Fig. 1. The IFS, lime, and fly ash samples were obtained from the BSRM industry. Sand and cement were collected from the local market. Mixing of the material was completed following the undermentioned mixture proportion of Table 2.

A different stage of the building block preparation is sequentially presented in Fig. 2. All the ingredient materials except water were mixed thoroughly for 25 min

Table 1 Chemical composition of materials used in this study

Materials	CaO %	SiO_2%	Al_2O_3%	Fe_2O_3%	MgO %	Na_2O %	K_2O %	TiO_2%	MnO %
IFS	5.2	47.1	5.9	16.8	2.9	1.4	0.3	1.9	5.5
FA	1.1	54.2	16.3	2.2	0.4	0.3	0.6	2.3	–
Lime	94.1	1.1	0.6	0.7	0.8	1.9	0.1	0.1	1.0
Cement	64.4	23.4	5.3	3.8	1.8	1.1	0.6	0.5	–
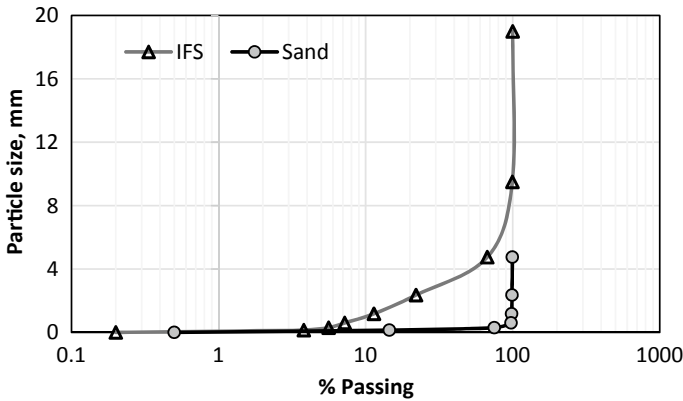
Fig. 1 Particle size distribution of sand and IFS

Table 2 Mix proportion of the building blocks (by weight %)

Batch name	Ingredients, mass % of the total mix					
	Fly ash	Sand	IFS	Lime	Cement	Water
I45L5C10	40	0	45	5	10	10.5
I45L7.5C7.5	40	0	45	7.5	7.5	10.3
I45L10C5	40	0	45	10	5	11
I30L7.5C7.5	40	15	30	7.5	7.5	10.7
I15L7.5C7.5	40	30	15	7.5	7.5	10.5
I0L7.5C7.5	40	45	0	7.5	7.5	10.3
I35L5C5	40	15	35	5	5	10.1

using a mixture machine at 22 rev/minute. Then water is added until the surface of the mixture is wet. The water content was varied between 10 and 12% of the full mixture weight. The wetted mixture is again been thoroughly mixed for 10 min using the mixture machine. The size of the building block was 230 × 100 × 75 mm. After mixing homogeneously, the material was poured into the mold and then pressurized by an automatic machine to minimize void. The amount of water was optimized between 10 and 12% of the total weight of the mixture to be compacted with sufficient workability at high pressure, viz. 10.3 and 20.7 MPa.

A total of 120 building blocks were made of which 84 were tested for compressive strength. The remaining 36 were used for other tests. Compaction pressure of 10.3 MPa was used to cast half of the building blocks, while the rest of them experienced 20.7 MPa. Around 3.5 kg mixture was required to fill up the mold to maintain a constant volume during casting. The pressure was applied to the building block in three rounds. Each of them continued for 3 s. After setting the binders, underwater curing was followed until testing the building blocks. The testing procedure was done according to BDS 208 [14]. After compaction, the surface was not required to finish
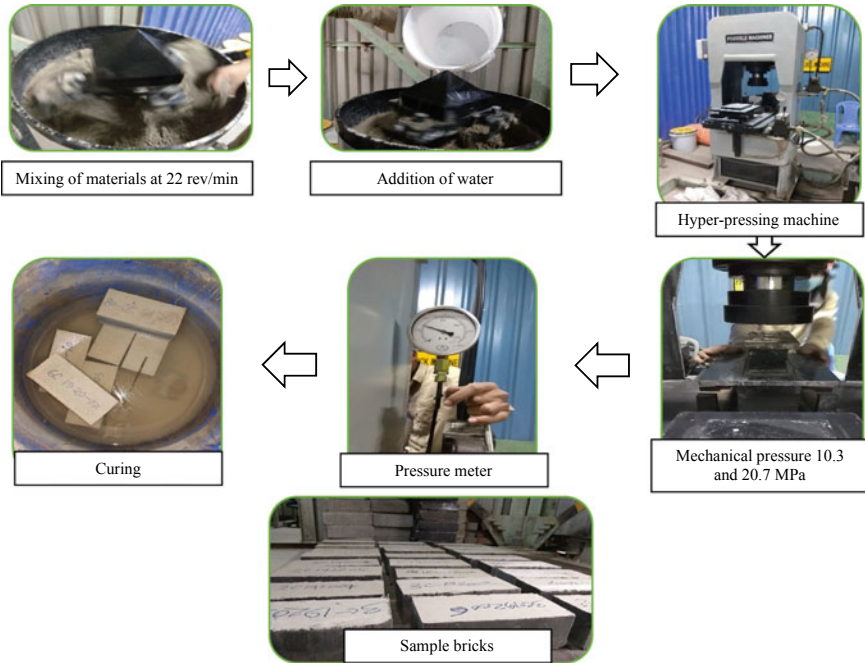
Fig. 2 Different stages of the preparation of building blocks

further. Therefore, no additional measure was taken to level the loading surfaces for the crushing strength test. Compressive strength was tested at 28 days.

3 Results and Discussions

3.1 Compressive Strength

The major part of this experiment was concerned with the crushing strength of the building block samples. Generally, the crushing strength of hyper-press building block is a function of w/c ratio, compaction pressure, cement type, aggregate type, test procedure, specimen shape, size, age, and curing. Figure 3 shows the effect of compaction pressure on the compressive strength test results. By increasing the compaction pressure from 10.3 to 20.7 MPa, significant improvements (37–55%) in compressive strength were noted. Especially the effect on the lower compressive strength batches was improved one half of its basic strength at 10.3 MPa compaction pressure. Therefore, keeping other parameters the same just improving the compaction pressure can improve the situation significantly and also requires
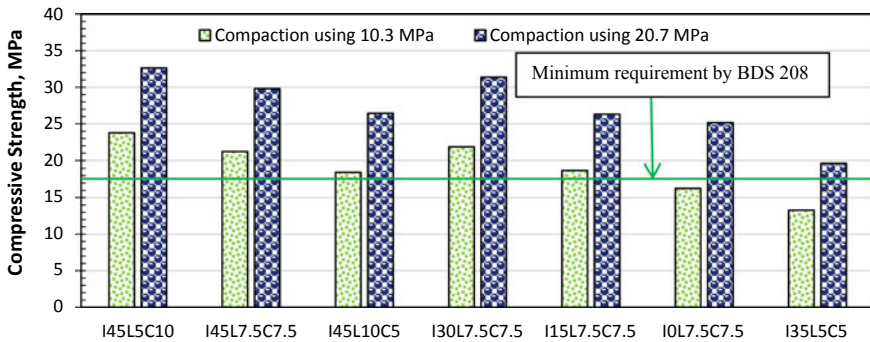
Fig. 3 Compressive strength of building blocks

almost no additional material but a small amount of electric energy [15]. All building blocks prepared with higher compaction pressure met the strength (17.2 MPa) conforming criteria specified by BDS 208 [14]. With 10.3 MPa compaction pressure, the last two batches which have comparatively less amount of IFS did not achieve the requirement of first-class brick specified by BDS. In addition, I35L5C5 is composed of a 10% binder which is less than 5% from other mixtures. With the improved compaction pressure, this mixture also achieved the minimum strength requirements specified by BDS.

3.2 Water Absorption

Water absorption is an important criterion of the building block to be considered for its intended use. Empirically, water absorption of building block is a function of the type of aggregates, void, testing procedure, time, and weather. The water absorption by weight should not exceed 10%, 15%, and 20% for bricks of S, A, and B grades classified according to BDS 208, respectively [14]. The water absorption test of results of building blocks compacted with 20.7 MPa at 28 days is given in Fig. 4. The improvement of microstructural integrity and density using high pressure is reflected in the absorption of water. All the test result complied with BDS 208 and was well below the maximum range of 10–20%.

3.3 Efflorescence, Hardness, and Microstructure

Efflorescence, hardness, and microstructure were also examined to ensure the long-term performance of building block. The efflorescence test result indicates the presence of any soluble salt in the building block. This test is conducted according to
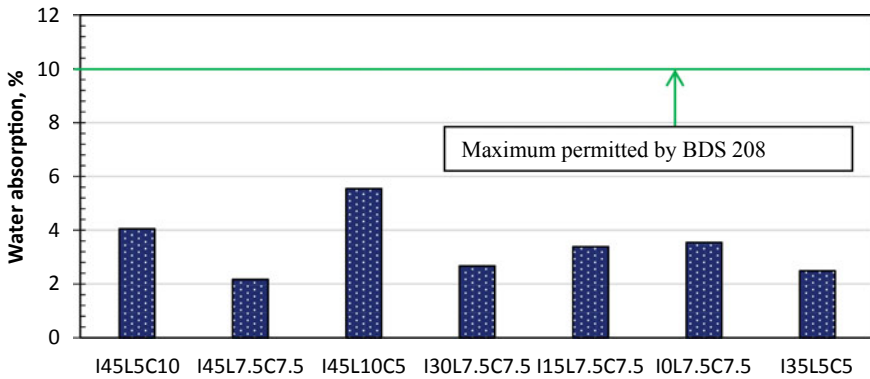
Fig. 4 Water absorption of building blocks

Table 3 Efflorescence, hardness, and microstructure test results of the building blocks

Name of the test	Result
Efflorescence	Nil
Hardness	No impression
Structural microstructure	Homogeneous and compact

the BDS 208 [14]. The hardness test indicates the surface resistance of the building block. The microstructure of the building blocks was observed after crushing strength to evaluate the relative amount of void in the structural part of the building block. Table 3 gives a summary of the test results and observations. In general, the clay burnt bricks produced in the south zone of Bangladesh suffers from efflorescence. The produced building blocks were found free from this adverse effect. The surface hardness was found sufficient to withstand. The dense microstructure indicates the overall improved property of the building block through higher compaction pressure.

3.4 Effect of IFS Content

The American Society for Testing and Materials (ASTM) defines steel slag as a nonmetallic product, consisting essentially of calcium silicates and ferrites combined with fused oxides of iron, aluminum, manganese, calcium, and magnesium that are developed simultaneously with steel in basic oxygen, electric arc, or open-hearth furnaces. This nonmetallic product makes a good bonding with fine aggregate and filler. The rough surface creates a better interlocking with sand. Sand also fills the internal void of IFS. Therefore, to achieve optimum property, a certain amount of sand is required.

In this study, sand is consecutively replaced by IFS. As shown in Fig. 5, introducing IFS in the place of sand increased the strength for both 10.3 and 20.7 MPa compaction
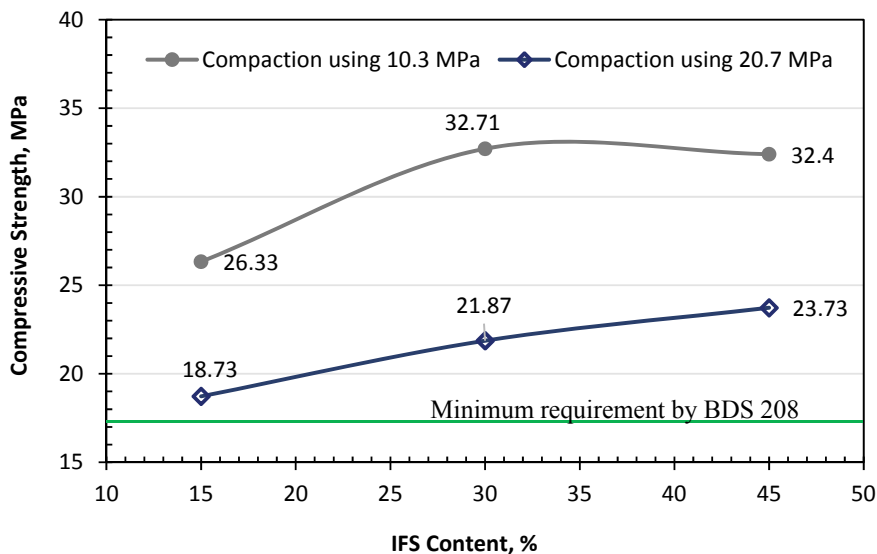
Fig. 5 Effect of IFS content on the compressive strength of building blocks

pressures. However, the absence of sand gave lower strength of building blocks. This might cause due to poor interlocking. This result is supported by the water absorption test results shown in Fig. 4. With 15% sand and 30% IFS content, the water absorption was found to be less than 3% by weight. It is, therefore, recommended to use optimum quantity (15% of the total mix by weight) of sand for the best strength results.

3.5 Cost Analysis

This study aimed to use the maximum possible amount of IFS in the place of sand to maximize the use of this by-product. This will impact the sustainable use of the material and the cost-effectiveness of the finally produced building block. Figure 6 gives a cost analysis of the individual materials/process to produce 100 building blocks. These totals 670 Bangladeshi Taka (BDT) including marketing of the product. The Public Works Department (PWD) rate schedule for first-class brick is 870 BDT/100 clay burnt bricks.

For proper interlocking of the materials, compaction is mandatory. Water assists to lubricate the material for proper compaction however to increase the w/c ratio. Increasing w/c affects the building block strength adversely. It is, therefore, would be necessary to increase the amount of binding material to ensure the quality of the building block. This is expected to result in cost ineffectiveness. Strength improvement (thereby cost) with compaction pressure of the binding materials could be reduced by up to 50%. The electricity cost to improve the compaction pressure
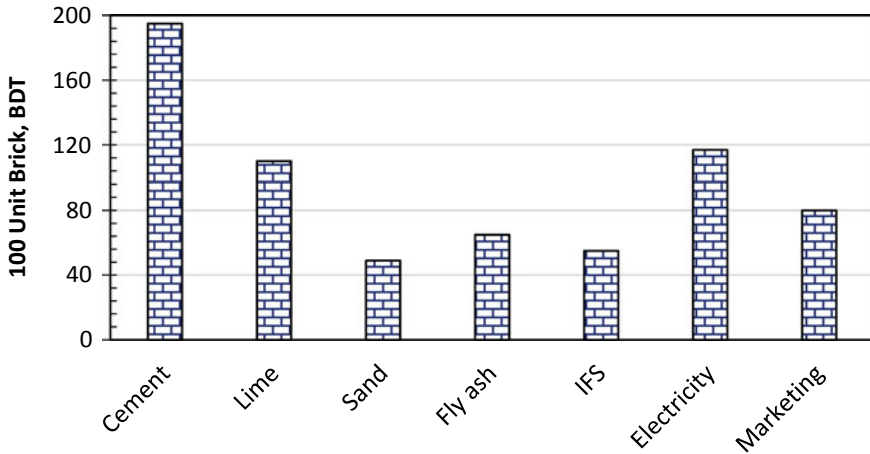
Fig. 6 Cost analysis of building blocks

from 10.3 to 20.7 MPa is much less than the cost of saved binding materials. The high pressure also ensures better microstructural property and low water absorption of the block. The above analysis indicates the cost-effectiveness of the building block produced by the hyper-pressing technique with waste materials. Moreover, the produced material gives better property than that specified by BDS and PWD rate schedule. The technique will therefore be considered as a cost-effective and sustainable method for building block production.

4 Conclusion

This study aimed to produce a building block of traditional size and shape used in Bangladesh using industrial by-products and hyper-pressing technology. The experimental investigation gives the following conclusion:

a. Replacement of sand by IFS increases the properties of the building block. However, a minimum amount of sand is required to produce better interlocking between ingredients. With 35% IFS, combining with 10% sand and hyper-pressing with 20.7 MPa pressure provides the optimum result.

b. Replacing cement with lime reduces the strength of the building block. However, to produce a cost-effective building block up to 7.5% lime could be permitted in the mixture.

c. An increase in compacting pressure improves strength. However, this will also increase the cost of the electric bill. Overall, 20.7 MPa compacting pressure will balance between the cost of binding material and electricity bill to optimize the overall cost of building block production.

d. Cost analysis indicates that the produced building block is cost-efficient than the usual clay burnt brick.

References

1. Sarker, S., Islam, G. M. S., Sadique, M., Shubbar, A.A.: Non-fired building block using industrial wastes. In: Proceedings of the 5th International Conference on Civil Engineering for Sustainable Development (ICCESD 2020), 7–9 February 2020, KUET, Khulna, Bangladesh, 2020
2. Correspondent, S.: Shun Burnt Bricks to Save Topsoil. The Daily Star, Dhaka, Bangladesh, p. Back page (2018)
3. Bangladesh National Parliament: Brick Manufacturing and Brick Kilns Establishment (Control) Act, p. 11. Dhaka, Bangladesh (2013)
4. Alam, H.: Brick kilns top polluter. The Daily Star, Dhaka, Bangladesh, p. Front Page (2019)
5. Griffiths, J.: Most polluted cities in the world: 22 of the top 30 are in India—CNN. CNN Health, Hong Kong (2019)
6. Islam, G.M.S., Islam, M.M., Akter, A., Islam, M.S.: Green construction materials—Bangladesh perspective. In: International Conference on Mechanical Engineering and Renewable Energy (ICMERE2011), 2011
7. Tamim, M.M., Dhar, A., Hossain, M.S.: Fly ash in Bangladesh-an overview. Int. J. Sci. Eng. Res. **4**(4) (2013)
8. BPDB: Bangladesh Power Development Board 2020. [Online]. Available: www.bpdb.gov.bd/bpdb_new/index.php/site/page/5a3f-2fdb-e75f-3cab-e66b-f70d-5408-cbc9-f489-c31c (Accessed: 28-Nov-2020)
9. BCMCL: Barapukuria Coal Mining Company Limited (BCMCL). (2020). [Online]. Available: www.bcmcl.org.bd/
10. McCarthy, M.J., Sadiqul Islam, G.M., Csetenyi, L.J., Jones, M.R.: Colorimetric evaluation of admixture adsorption by fly ash for use in air-entrained concrete. Mater. Struct. Constr. (2012)
11. Surul, O., Bilir, T., Gholampour, A., Sutcu, M., Ozbakkaloglu, T., Gencel, O.: Recycle of ground granulated blast furnace slag and fly ash on eco-friendly brick production. Eur. J. Environ. Civ. Eng. (2019)
12. Gupta, V., Siddique, S., Chaudhary, S.: Optimum mixing sequence and moisture content for hydrated lime fly ash bricks. J. Clean. Prod., p. 124859 (2020)
13. BDS: EN 197–1, Composition, specifications and conformity criteria for common cements. Cement (2011)
14. BSTI: BDS 208: Specification for Common Building Clay Bricks (3rd revision). Dhaka, Bangladesh (2009)
15. Danso, H.: Influence of compacting rate on the properties of compressed Earth blocks. Adv. Mater. Sci. Eng. **2016** (2016)

Smart Monitoring of Pavement Condition Utilizing Vehicle Vibration and Smartphone Sensor

Asaduzzaman and S. Rana

1 Introduction

A good road network is of paramount importance for economic development of a country. As the cost associated with pavement monitoring and maintaining is very high and require specialized instruments, it is almost impossible for a developing country like Bangladesh to ensure proper monitoring and maintaining of the country's road network. In the case of Bangladesh, the construction, maintenance and rehabilitation of main road network is under the control of Roads and Highway Department (RHD). For the year 2018–19 to 2022–23, the maintenance cost of the road network under RHD has been estimated to be 263,190.15 million Taka [1]. A large portion of this money will be used for monitoring of the road network. The use of smartphone sensors along with conventional vehicles for pavement monitoring can greatly reduce the cost, required time and complexity of pavement monitoring and maintenance. For a developing country like Bangladesh, use of smartphone sensors and conventional vehicle can ensure large scale monitoring of all the road network regularly even including local road network also.

For development of cost-effective and easily implementable road monitoring system, researches are now being conducted all over the world. Gonzalez et al. [2] used data obtained from accelerometers to estimate power spectral density (PSD) of the roads for approximation of the road roughness condition. This method requires a transfer function to establish relation between PSD of vertical accelerations of the vehicle and PSD of road profile. Allaire and Hanson [3] studied the use of smartphones for measurement of changes in IRI values of pavements. The changes in IRI values can be used for imposing vehicle weight restrictions or performing

Asaduzzaman (✉) · S. Rana
Department of Civil Engineering, Bangladesh University of Engineering & Technology, Dhaka, Bangladesh

S. Rana
e-mail: shohel@ce.buet.ac.bd

pavement strength test. In this research, TotalPave Inc. was used for processing of the obtained data. Yousefzadeh et al. [4] studied the possibility of using artificial neural networks for estimation of road profiles in terms of road roughness and power spectral density. However, for using artificial neural networks, the behavior of the vehicle under each ISO road profile has to be properly used during the training phase of the neural network. Forslof and Jones [5] took part in the development of Roadroid Android application for continuous pavement condition monitoring using smartphones. Several studies have been performed using Roadroid application for pavement condition monitoring [6–8] using correlation based method with actual IRI. Also, there are several smartphone-based apps such as TotalPave, RoadLab Pro, etc., for pavement monitoring through smartphones. However, the obtained results from these apps can deviate from the actual condition of the pavement if calibration of the particular vehicle used is not performed properly.

In this paper, a new method of pavement monitoring is proposed using smartphone sensors and vehicle dynamics. The proposed method consists of two steps. The vehicle through which measurements are to be taken is modeled as a Quarter-car (QC) model. In the first step, calibration of the vehicle is performed by estimating vehicle suspension damping parameter using a system identification technique. In the second step, estimation of pavement profile is performed using an inverse mathematical formulation of the calibrated vehicle model.

Pavement profiles are representation of the vertical aspects of the pavement, including crest and sag curves, and the straight grade lines connecting them. For the purpose of monitoring pavement condition, the roughness of the pavement is expressed in terms of several indexes, among which International Roughness Index (IRI) is most commonly used. The IRI is a good pavement condition indicator as it is reproducible, stable with time and summarizes roughness properties of the pavement which impact vehicle response traveling over it. The IRI of the pavement can be calculated as shown in Eq. (1).

$$\text{IRI} = \frac{1}{L} \int_{0}^{t} \left| \dot{Y}_s - \dot{Y}_{us} \right| \mathrm{d}t \tag{1}$$

where L is the length of the road, t is travel time, $\dot{Y}_s$ and $\dot{Y}_{us}$ are sprung and un-sprung mass vertical accelerations, respectively.

2 Mathematical Model

The Quarter-car model is a model of one corner (a quarter) of a car consisting of five components as shown in Fig. 1. QC model is a simplified suspension system. In Fig. 1, schematic diagram of a Quarter-car model with its components is shown. Here, M_s is one-fourth of the sprung vehicle mass, which includes the mass of all
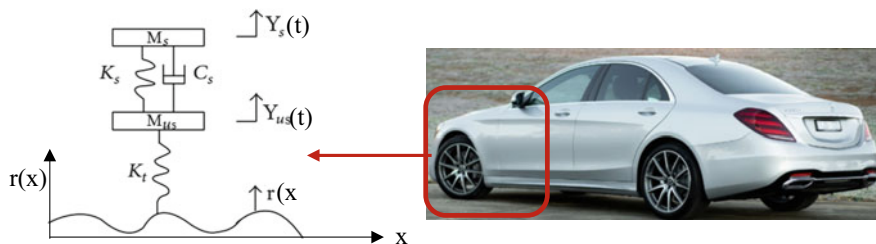
Fig. 1 Quarter-car model

the elements supported by the suspension (frame, internal components, etc.), and its displacement is represented by $Y_s(t)$. K_s represents the stiffness of suspension spring, and C_s represents the damping coefficient of the suspension system. M_{us} is the un-sprung mass which includes mass of wheels, brakes, axles and so forth and $Y_{us}(t)$ represents its displacement. At last, K_t is the stiffness of tire spring and $r(x)$ is the pavement profile.

The equation of motion of the QC dynamic system shown in Fig. 1 is shown in Eq. (2) in matrix form.

$$[M]\ddot{Y}(t) + [C]\dot{Y}(t) + [K]Y(t) = Pr(x) \tag{2}$$

where M, C and K are the system mass, damping and stiffness matrices, respectively; $\ddot{Y}$, $\dot{Y}$ and Y are acceleration, velocity, and displacement matrices, respectively; P is the matrix prescribing the force; $r(x)$ represents pavement profile.

$$[M] = \begin{bmatrix} M_s & 0 \\ 0 & M_{us} \end{bmatrix} \quad [K] = \begin{bmatrix} K_s & -K_s \\ -K_s & K_s + K_t \end{bmatrix} \quad [C] = \begin{bmatrix} C_s & -C_s \\ -C_s & C_s \end{bmatrix}$$

$$P = \begin{bmatrix} 0 \\ K_t \end{bmatrix} \quad \ddot{Y}(t) = \begin{bmatrix} \ddot{Y}_s(t) \\ \ddot{Y}_{us}(t) \end{bmatrix} \quad \dot{Y}(t) = \begin{bmatrix} \dot{Y}_s(t) \\ \dot{Y}_{us}(t) \end{bmatrix} \quad Y(t) = \begin{bmatrix} Y_s(t) \\ Y_{us}(t) \end{bmatrix}$$

The dynamic system described by Eq. (2) can alternatively be represented by state-space model. State-space model or representation is a mathematical model of a physical system as a set of input, output and state variables related by differential equations of first order. The state variables are the smallest possible subset of system variables having the capability of representing the entire state of the system at any given time. Considering $\ddot{Y}_s$ and $\ddot{Y}_{us}$ are first-order differentials of the $\dot{Y}_s$ and $\dot{Y}_{us}$ respectively, Eq. (2), in form of general state-space representation, can be written as Eqs. (3) and (4). Both sprung mass and un-sprung mass vertical accelerations, $\ddot{Y}_s$ and $\ddot{Y}_{us}$, can be obtained through Eq. (4).

$$\dot{x}(t) = [A_c]x(t) + [B_c]r(x) \tag{3}$$

$$y(t) = \begin{bmatrix} \ddot{Y}_s(t) \\ \ddot{Y}_{us}(t) \end{bmatrix} = [C_c]x(t) + [D_c]r(x) \tag{4}$$

where

$$[A_c] = \begin{bmatrix} 0 & I \\ -M^{-1}K & -M^{-1}C \end{bmatrix} \quad [B_c] = \begin{bmatrix} 0 \\ -M^{-1}P \end{bmatrix}$$

$$[C_c] = \begin{bmatrix} -\mathbf{M}^{-1}\mathbf{K} & -\mathbf{M}^{-1}\mathbf{C} \end{bmatrix} \quad [D_C] = [\mathbf{M}^{-1}\mathbf{P}]$$

$$\dot{x}(t) = \begin{bmatrix} \dot{Y}_s(t) \\ \dot{Y}_{us}(t) \\ \ddot{Y}_s(t) \\ \ddot{Y}_{us}(t) \end{bmatrix} \quad x(t) = \begin{bmatrix} Y_s(t) \\ Y_u(t) \\ \dot{Y}_s(t) \\ \dot{Y}_{us}(t) \end{bmatrix}$$

where $\mathbf{x(t)}$ is the $2\,N \times 1$ state vector, $\mathbf{A_c}$ is the $2\,N \times 2\,N$ matrix for system dynamics, $\mathbf{B_c}$ is the $N \times m$ continuous time input-state matrix, $\mathbf{C_c}$ is the $p \times 2\,N$ state-output matrix, and $\mathbf{D_c}$ is the $p \times m$ feedthrough matrix, where $2\,N$ is the order of the states to equivalently represent the second-order system and m is the number of input and p is the number of output of the system. $r(x)$ is the external excitation as in Eq. (3) and $\mathbf{B_c}$ is a matrix which relates the locations of the input to the internal variables of the realization. Similarly, $\mathbf{y}$(t) are sensor measurements such as acceleration, and $\mathbf{C_c}$ is a matrix which constructs these physical quantities from the internal state variables $\mathbf{x}$(t).

3 Pavement Profile Estimation Procedure

Vehicle vertical un-sprung mass acceleration ($\ddot{Y}_{us}$) can be obtained from Eq. (4) as shown in Eq. (5). From Eq. (5), rearranging for $r(x)$, we have Eq. (6).

$$\ddot{Y}_{us}(t) = [C_c]x(t) + [D_c]r(x) \tag{5}$$

$$r(x) = -\frac{[C_c]}{[D_c]}x(t) + \frac{1}{[D_c]}\ddot{Y}_{us}(t) \tag{6}$$

In Eq. (3), substituting $r(x)$, we have

$$\dot{x}(t) = \left([A_c] - \frac{[B_c][C_c]}{[D_c]}\right)x(t) + \frac{[B_c]}{[D_c]}\ddot{Y}_{us}(t) \tag{7}$$

Equations (6) and (7) can be considered to be the inverse formulation of the state-space model represented by Eqs. (3) and (4). Considering a state-space model by Eqs. (6) and (7), the pavement profile, $r(x)$, can be estimated as the output from Eq. (6) by solving Eq. (7) using a numerical integration technique. The un-sprung mass vertical acceleration $\ddot{Y}_{us}$ will be taken as the input into the vehicle dynamic system. Note that this vertical acceleration will be collected using smartphone sensor in practical situation by using a smartphone application.

4 Numerical Simulation and Analysis

In this study, numerical simulation and analysis included the generation of road profiles, the simulations of vehicle movements over the generated pavements, the collection of vehicle acceleration data, the generation of algorithm for estimation of unknown vehicle suspension damping parameter using a system identification technique and estimation pavement profile, the determination of IRI of the pavement.

4.1 Unknown Vehicle Parameter Estimation

Vehicles: In this study, simulation of a vehicle, golden car, is performed, and the dynamic parameters of which are given in Table 1. Four vehicle speeds are used ranging from 5 to 20 km/h. **Pavement Profile**: A known pavement profile (speed bump) (Fig. 2) with 0.15 m in height and 0.61 m in length is generated based on Eq. (8) for unknown vehicle parameter estimation.

$$H(x_{b}) = \frac{H}{2} * \left\{ 1 - \cos\left(\frac{2\pi x_{b}}{L}\right) \right\} \tag{8}$$

where L = Length of the speed bump; H = Height of the speed bump; x_{b} = Horizontal coordinates along the length of the speed bump.

At first, the acceleration data is collected by simulated movement of the vehicle with all the parameter known as in Table 1 over pavement profile (speed bump)

Table 1 Vehicle dynamic parameters

Vehicle name	Sprung mass (M_s) Kg	Un-sprung mass (M_{us}) Kg	Suspension spring constant (K_s) N/m	Suspension system damping coefficient (C_s) N s/m	Tire spring constant (K_t) N/m
Golden car	250	37.5	15,825	1,500	163,250
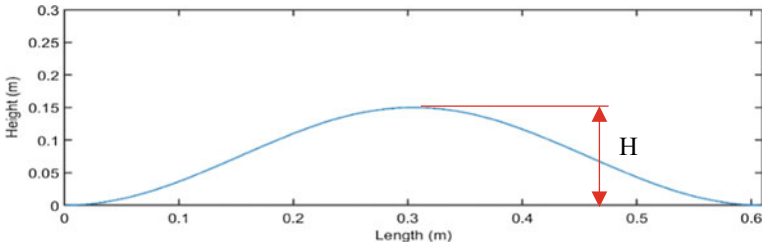
Fig. 2 Simulated speed bump

at different speeds by solving the state-space formulations (Eqs. 3 and 4) using a numerical integration scheme such as fourth-order Runge–Kutta method. For acceleration data collection, sampling frequency of 200 Hz is used. A typical acceleration response is shown in Fig. 3.

Next, for unknown parameter estimation, except for suspension system damping coefficient (C_s), the other four parameters are considered to be known. Suspension system damping coefficient (C_s) is considered to be unknown as vehicle mass data are readily available for most vehicles. From the vehicle mass data, other parameters of the vehicle, such as, K_s, K_t can be estimated using ratios of golden car parameters [9]. The parameter estimation technique is represented in step-1 of Fig. 4. A mathematical structure of the vehicle system with the unknown parameter subjected to speed bump profile excitation is formulated following Eq. (3). The sprung mass acceleration as the output data of the dynamics system and speed bump excitation as input are passed through the system identification technique, continuous time linear and nonlinear grey-box modeling algorithm, and the unknown parameter, C_s is estimated as shown in Fig. 5. From Fig. 5, it can be seen that the estimated values of the parameters are fairly close to the actual value. Also, the differences between the values estimated by using linear and nonlinear grey-box models are reasonably small.
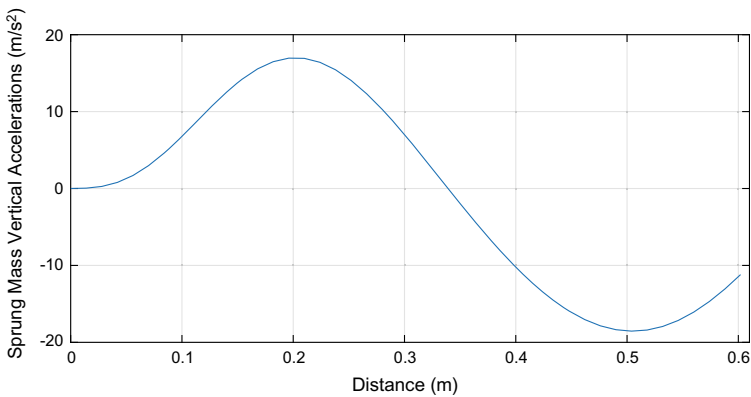
Fig. 3 Golden car sprung mass accelerations at 10 km/h
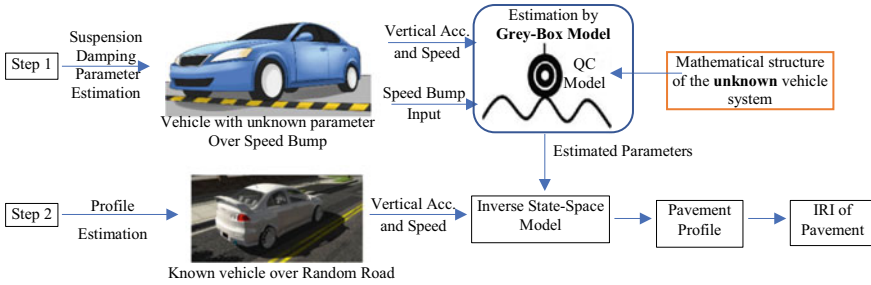
Fig. 4 Schematic diagram of the proposed method

Fig. 5 Golden car C_s estimation
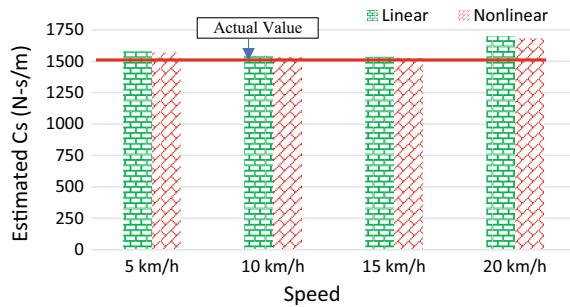
4.2 Pavement Profile Estimation

For pavement profile estimation, a Class A-B pavement based on ISO 8608 road roughness classification is generated [10]. The profile is generated based on Eq. (9) [11] and is of 250 m in length.

$$h(x) = \sum_{i=0}^{N} \sqrt{\Delta n} . 2^k . 10^{-3} . \left(\frac{n_0}{i.\Delta n} \right) . \cos(2\pi.i.\Delta n.x + \varphi_i) \tag{9}$$

Here, x is the abscissa variable from 0 to L; the length of the road profile is L and B is the sampling interval, $\Delta n = 1/L$; $N = L/B$; k is a constant value depending on ISO road profile classification. k assumes integers increasing from 3 to 9, corresponding to the road roughness profiles from class A–B to class G–H. Also, $n_0 = 0.1$ cycles/m; φ_i is random phase angle following a uniform probabilistic distribution within the 0–2π range.

For pavement profile estimation, four vehicle speeds are used ranging from 10 to 40 km/h. The un-sprung mass acceleration data obtained by simulated movement of the calibrated vehicle over pavement profile whose profile is to be estimated and is used as the input of the inverse state-space representation of the QC dynamic system as in Eq. (7), and the pavement profile is estimated from Eq. (6) by solving Eq. (7)
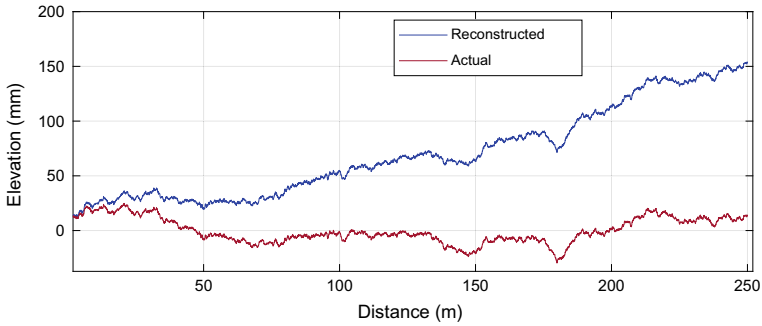
Fig. 6 Actual and reconstructed profiles

using numerical integration scheme, fourth-order Runge–Kutta method as before (see step 2 of Fig. 4). After the reconstruction of the pavement profile, it is compared with the actual pavement profile as shown in Fig. 6.

From the comparison between actual and reconstructed pavement profiles, it is seen that drifting has occurred. In order to remove the drifting, Butterworth high-pass filter is used with a cutoff wavelength of 30.48 m. The cutoff wavelength is selected to be 30.48 m as it is the longest wavelength by which IRI measurement is generally affected [9]. After filtering, the estimated or reconstructed pavement match reasonably well with each other as shown in Fig. 7. Finally, the IRIs of the estimated pavement at various speed are calculated as per Eq. (1) and shown in Fig. 8. It can be seen that the IRI values of the estimated pavements at different speeds are very close to each other. The estimated value of IRI is also nearly close (within 3.5%) with the actual value of Class A-B pavement roughness.
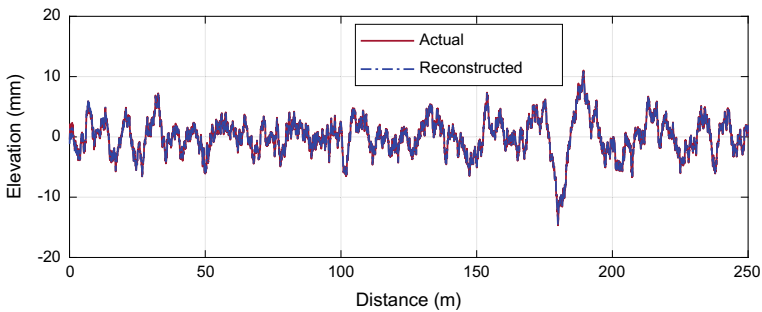
Fig. 7 Actual and reconstructed profiles after filtering

Fig. 8 IRI of estimated profiles at various vehicle speeds
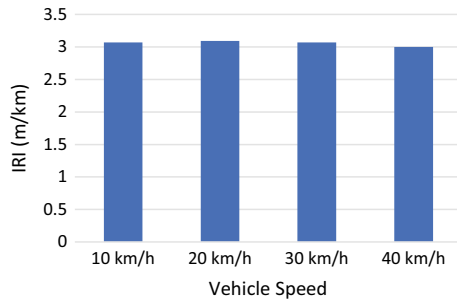
4.3 Influence of Measurement Error

During practical measurement, there may be two sources of measurement error. The first one is the ability of smartphone sensor to sense the acceleration response, and the second one is the noise in the measured response. However, the applicability of smartphone as accelerometer sensor has been investigated using the response collected from a practical model and comparing it with the analytical results. The investigation yielded a reliable result which is available in the Ref. [12]. Secondly, the effect of noise is evaluated herein. The noisy measured response is determined as

$$\ddot{Y}_m = \ddot{Y} + \frac{n}{100}\Omega_{noise}\sigma\left(\ddot{Y}\right) \tag{10}$$

where $\ddot{Y}_m$ = noisy response; $\ddot{Y}$ = response without noise; n = the noise percentage; Ω_{noise} = Gaussian noise with a standard normal distribution, $\sigma\left(\ddot{Y}\right)$ is the standard deviation of the "measured" response.

5% measurement noise has been considered in this study. Next, the pavement profile reconstruction procedure with 5% noisy response is repeated for the above pavement. The actual and reconstructed profiles of the pavement are shown in Fig. 9. It can be observed that, due to noise in the response, the reconstructed pavement profile deviates from the actual profile. However, the profiles match reasonably well though the vehicle response is contaminated by noise. The difference between the actual and the reconstructed profiles determined from noisy vehicle response is objectively determined in terms of IRI. The IRI of the actual and reconstructed pavement profiles are calculated as 3.11 m/km and 3.19 m/km, respectively. The error is 2.6% of the actual value which may be considered as not too much significant.
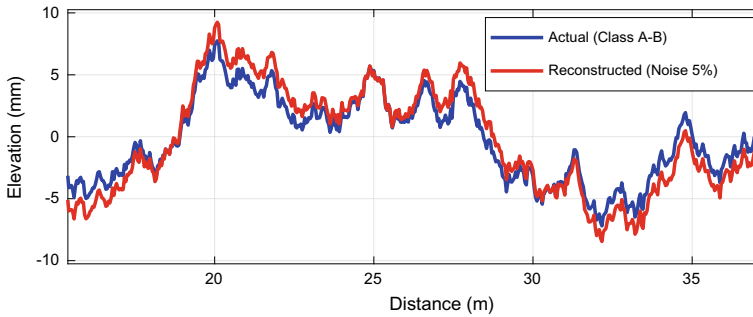
Fig. 9 Reconstructed profiles with noise

5   Conclusion

In this paper, a new method for pavement monitoring is developed in which vehicle calibration is performed in the first stage and using the calibrated vehicle, the estimation of the pavement profile is performed in the second stage. In the numerical simulation stage, the proposed method is found to be capable of estimating unknown vehicle parameter with reasonable accuracy. Also, the actual and estimated pavement profiles are found to match each other reasonably well. The IRI of the pavements is estimated with acceptable accuracy, and vehicle speed in practical range is found to have little impact on the estimation method. The method is expected to be cost efficient, rapid and capable of monitoring all the road network regularly as the ordinary vehicles and smartphones are readily available to all. Experiments based on the proposed method of pavement monitoring are necessary to be performed in real life with actual vehicles, smartphones and pavements to observe the performance and to carry out necessary modifications for easier and more accurate pavement monitoring.

References

1. Roads and Highways Department: Maintenance and Rehabilitation Needs Report of 2018–2019 for RHD Paved Roads. Government of the People's Republic of Bangladesh, Ministry of Road Transport and Bridges, Dhaka (2018)
2. Gonzalez, A., O'Brien, E.J., Li, Y., Cashell, K.: The use of vehicle acceleration measurements to estimate road roughness. Veh. Syst. Dyn.: Int. J. Veh. Mech. Mobility **46**(6), 483–499 (2008)
3. Allaire, F., Hanson, T.: Potential of road roughness data from smartphone as an input to spring weight restriction decision-making. Paper presented at the Conference of the Transportation Association of Canada, St. John's, NL, 2017 (2017)
4. Yousefzadeh, M., Azadi, S., Soltani, A.: Road profile estimation using neural network algorithm. J. Mech. Sci. Technol. **24**(3), 743–754 (2010)
5. Forslof, L., Jones, H.: Roadroid: continuous road condition monitoring with smart phones. J. Civ. Eng. Architect. **9**, 485–496 (2015)
6. Schlotjes, M.R., Visser, A., Bennett, C.: Evaluation of a smartphone roughness meter. In: Proceedings of the 33rd Southern African Transport Conference, pp. 141–153 (2014)

7. Aydin, M.M., Yildirim, M.S., Forslof, L.: The use of smart phones to estimate road roughness: a case study in Turkey. Eng. Sci. (NWSAENS) **13**(3), 247–257 (2018)
8. Naji, M.S.: Using smartphone and GIS to measure IRI in Gaza Road network. M. Engg. Thesis, Faculty of Engineering—Civil Engineering, Islamic University of Gaza (2017)
9. Sayers, M.W., Karamihas, S.M.: The Little Book of Profiling. University of Michigan (1998)
10. International Standards Organisation: ISO 8608: Mechanical Vibration-Road Surface Profiles-Reporting of Measured Data (1995)
11. Agostinacchio, M., Ciampa, D., Olita, S.: The vibrations Induced by surface irregularities in road pavements—a Matlab® approach. Eur. Transp. Res. Rev. **6**, 267–275 (2014)
12. Blum, N.C.: System Identification of Vehicle Dynamics and Road Conditions Using Wireless Sensors. Ph.D. Thesis, Department of Civil and Environmental Engineering, University of Illinois (2015)

Non-destructive Testing of Concrete Cubes Under Various Curing Conditions: The Inaccuracies and Flaws

A. Ghosh[ID]**, A. Das**[ID]**, and N. Apu**[ID]

1 Introduction

The non-destructive testing is used to ensure product integrity, manufacturing, in-service inspections and provides a quality level. However, the in situ concrete strength measurement is the main challenge in case of NDT [1]. Because, in the structural defects, material components strength deteriorating is due to improper mix ratios, poor quality material specifications, and inadequate supervision [2]. The strength of the concrete needs to be checked, and there are several methods of non-destructive testing that could determine the concrete strength. The ultrasonic pulse velocity and rebound hammer test offer a promising way among them to assess the concrete strength as it focuses on the elastic wave propagation and hardness of the concrete.

The concrete properties can be influenced by the atmosphere such as relative humidity, ambient temperature, and hot weather [3]. Several studies have been performed to determine the curing temperature effect on the concrete, and from these studies, the results indicated that curing period, type of the solidified sample, and environment and curing condition are the important parameter on concrete strength evaluation [4–6]. According to ACI 308R-01, minimum seven days curing is required to attain the compressive strength of concrete [7]. In these experiments, the idea is to find out the concrete strength under different curing periods along with different curing procedure by the RH testing and UPV and compared the result with the destructive compressive strength of concrete. The study also performs a specific test of ultrasonic pulse velocity on a larger concrete block with a comparatively larger void to find out the specific knowledge gap since the velocity determination by ultrasonic pulse velocity has a flaw in case the void is smaller in size.

A. Ghosh (✉) · A. Das · N. Apu
Department of Civil Engineering, Indian Institute of Technology Bombay, Mumbai, India
e-mail: avishek.ghosh.c2018@iitbombay.org

2   Methods and Materials

Depending of the design and material properties, RH testing comprises of direct mechanical solution. The hardness of concrete on the close surface connects to the mechanical solution for the RH estimation. The hardness of the concrete materials again depends on the porosity of materials as the porosity decreases the hardness increases and provides a consistency in the strength assessment. Due to the minimal expense of the procedure, the RH test is considered as one of the straightforward and non-ruinous tests for concrete structures. Ernst Schmidt developed the relationship in between rebound number of RH and the compressive strength. However, the relationship was not unique and needs to be adjusted with the gradation of the concrete and the shape of the structure. Utilizing information from 1 to 40 years of age structures [8], it has found that, equivalent solid strength, RH values are almost 4 points higher than the destructive compressive strength of concrete block.

Numerous variables may influence to an alternate degree concrete strength and hammer number. Their impact has been brought up and measured by numerous authors [9–11] and concrete hardness/thickness, age/carbonation of surface and close surface condition. Voids have high impact where presents extreme size of aggregate, surface routineness, and rugosity.

In the UPV testing, the speed of pulse wave is higher in the first few days after solidifying starts of the concrete blocks. The reason for the higher pulse wave may be related with the Young's modulus, as the wave speed is higher in the elastic media, and in the initial stage the concrete shows more elastic properties which expand the value of wave velocity [12]. So, the UPV results can be related with the strength of the concrete. Though the variation of the wave velocity with time is the major concern in the UPV testing method, the velocity depends on the curing procedure and it generally decreases with time [13]. Other factors may also influence the wave velocity, as in general, it shows higher velocity in the first few days and shows lower value after 5, 6 days [14–16]. These factors may vary from the water–cement ratio, aggregate shapes which are the most influential and rebar condition, and ingredients of cement mixture has lower impact on the wave velocity.

2.1   Materials Characteristics

In this experiment, M25 concrete cube had been used. The M25 stands for the targeted concrete cube strength will be 25 MPa after 28 days [17]. To maintain the quality, the targeted strength was determined 31.6 Mpa and the cube was prepared by maintaining water–cement ratio 0.45. The mixing ratio of cement, sand, and aggregate was maintained properly to achieve the desired strength. 20 and 10 mm two types of coarse aggregate were used.

Table 1 Number of cubes and the curing period

Sample no.	Type	Age of concrete cubes
1,2,3	1	3 days MWC + 3 days NC = Total age 6 days (varied curing)
4,5,6	2	7 days MWC + 21 days NC = Total age 28 days (varied curing)
7,8,9	3	11 days MWC + 17 days NC = Total age 28 days (varied curing)
10,11,12	4	14 days MWC + 14 days NC = Total age 28 days (varied curing)
13,14,15	5	3 days MBC Only = Total age 6 days
16,17,18	6	7 days MBC Only = Total age 7 days
19,20,21	7	14 days MBC Only = Total age 14 days
22, 23, 24	8	28 days MBC Only = Total age 28 days

2.2 Preparation and Curing Period of the Specimen

In the laboratory, the concrete mixtures were prepared at a room temperature of 24°. A total of 24 no. of cubes was prepared, and the total amount of approximately 40 kg of cement, 22 L of water, 67 kg of 20 mm aggregate, 45 kg of 10 mm aggregate and 65 kg of sand were mixed altogether. The casting molds were kept for 24 h to settle down and after that the molds were removed. The samples were then divided into eight different groups (types) where four types of samples kept into water for various days which is referred here as moisture water curing (MWC) and another four types of samples kept under buried moist soil condition for various days which is referred here as moisture buried curing (MBC). Samples, which were kept without curing, is referred as non-curing (NC). Their curing period has been enlisted in the following table (Table 1).

In this works, a pit size of 2 × 1.5 × 1 m was excavated and buried curing performed by placing cubes in the trail pit. Finally, another 24 blocks were kept under water and soil in different days to check the compressive strength of concrete blocks.

2.3 Calibrating the NDT Instruments

One of the fundamental steps for assessing the better grade of concrete properties is NDT equipment calibration. NDT examination includes the estimation, assessment, and analyzing the strength and property of the concrete structures. This estimation has several deficiencies because of different components associated with the investigation interaction. The nature of measurement recorded relies upon the adjustment of the instrument before it is taken on the site. For instance, rebound hammer before utilized on the genuine design or structure, correlation diagram is given on the instrument that is aligned utilizing the laboratory data of concrete blocks [18]. The crushing strength (fc) is acquired from the chart given in the instrument manual or figuring

from model accessible from the literature. The quality as well as exactness of fc assessment depend on the accuracy of the calibration method and calibration information. Codes and norms additionally recommend calibration of rebound hammer instrument utilizing appropriate strategy and furthermore give calibration curves. The rebound hammer was calibrated in this investigation and correlated the Brinell hardness number of 5000 N/mm^2.

Accordingly, it is important to adjust the instrument accurately to include the uncertainties associated with the computation. Curve fitting along with regression analysis, artificial neural networks (ANN), and Bayesian methods has been used for the calibration purpose. The calibration charts and conversion models provide more accurateness in the measurement activity. The relationship in between UPV and water immersion and porosity provide a surface plot which help to find out the properties of the concrete materials [19] while the relationship of RN, UPV, and compressive strength of concrete cubes can be determined by 3D plots [20]. The European National code has been proposed for the calibration prior to the usage of the NDT equipment in each project [21]. Linear polarization resistance (LPR) based on Faraday's law and Flick's law has been developed for corrosion occurrence in the materials [22]. These different models suit to find out the real phenomena in the concrete materials, and with the help of this calibration, data known as model calibration determine the suitability of each model in various projects [23, 24].

2.4 Testing Procedure

The hardness and the strength in the cover of the concrete cube can be estimated by the RH test. A specific guideline has provided for the rebound hammer test [25]. The repetition of the RH test on the same cover and same side of the concrete block will decrease its acceptability rather than taking the correlation with the standard strength tests. For instance, if the N value changes in between 10 and 12 points, the results are obviously different.

When the rebound hammer was calibrated, for taking the readings purpose, the hammer was held at right angles to the surface of the concrete structure. The test then needs to be conducted horizontally on vertical surface along with vertically upward or downward on horizontal surfaces. The impact point was kept at least 20 mm away from edge on concrete surface to reduce the shape discontinuity effect on rebound hammer.

Later, UPV test is conducted on the concrete cube. The basic idea of this technique involves the wave propagation through the concrete material and measures the sound speed through transducers to predict the strength of the materials and evaluate the modulus of elasticity and find out the presence of internal damages such as voids, cracking which will affect the inner strength of the concrete and other damage due to the aging of the concrete materials. The main purpose of this method is in finding an areas of weak concrete and the changes in concrete condition of a sound structure.

a) Direct   b) Semi-direct   c) Indirect
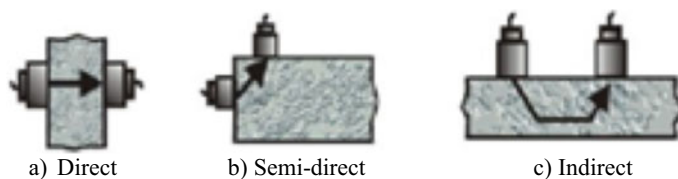
Fig. 1 Ultrasonic pulse velocity testing
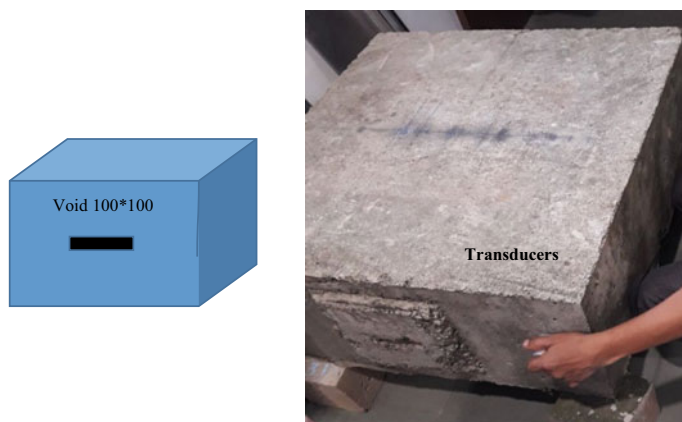
Fig. 2 UPV on a concrete slab

The test had been conducted in direct, indirect, and semi-direct method. In the direct method, it the sound measured by accessing direct contact of propagation and receiving on the transducers by placing it in the opposite direction of the concrete slab. In the semi-direct process, the sound path length was approximately equal to the distance of a third side of a triangle formed by the adjacent sides of a concrete floor (Fig. 1). In the indirect method, the testing requires access on the same surfaces, unless indirect (surface transmission) testing was done.

To compare the UPV which is the natural frequency of transducers (electroacoustical) being 55 kHz is being used in the test a larger concrete slab of 750(L) × 750(B) × 350(D) mm was used for the study [26]. Oscilloscope was used to study the change in wave effect. A center void on 100 mm width and 10 mm thick was present (Fig. 2).

3 Results and Discussion

In the rebound hammer test, the test result needs to be compared with the destructive compressive strength testing to get an idea of the testing accuracy.

The NDT testing is counted as a flawless testing; however, the prediction of concrete strength could be allowed ±25% of the actual compressive strength of the concrete. The accuracy is greatly increased if the core samples obtained from the structure and the rebound hammer test conducted on the specimen are made of same mix proportion and the same concrete materials.

In Fig. 3, the compressive strength for cube and hammer test had been gradually increased with curing period. In the x-axis, the sample type represents four types of varied curing for first figure and four types of moisture buried curing for second figure. Each type comprised of three cubes each in totalling of 24 cubes were tested both in cube and hammer test. The sample cubes of equivalent 14 days moisture curing and 14 days non-curing had showed the maximum compressive strength of approximately 32 MPa for both rebound hammer test and crushing cube test. At the same time, sample cubes of 14 days moisture buried curing (MBC) showed almost the maximum compressive strength compared to 28 days buried curing cubes. The compressive strength of cube decreased after 14 days in MBC. Due to non-uniformity in the materials and less voids detection at rebound hammer, the crushing cube test showed 16.6% more compressive strength than the hammer test in varied curing and 20% in MBC. As the hammer test is a non-destructive testing, the compressive strength is at reserve side compared to crushing strength. However, based on rebound number except the first set of samples (3 days curing and 3 days non-curing prior to the test), all the samples performed fair to good quality (Fig. 4).

In Fig. 5, the compressive strength also raised with curing period. The x-axis represents equivalent age of concrete for both figures. However, it is clearly visible that varied curing of concrete cube gives more strength than concrete cube under moisture buried curing.

In Fig. 6, the 24 samples were taken for ultrasonic pulse velocity test after 3, 7, 11, 14, and 28 days later. The sample type 1, type 2, type 3, and type 4 were kept completely under water for such days before testing. At the same time, the sample
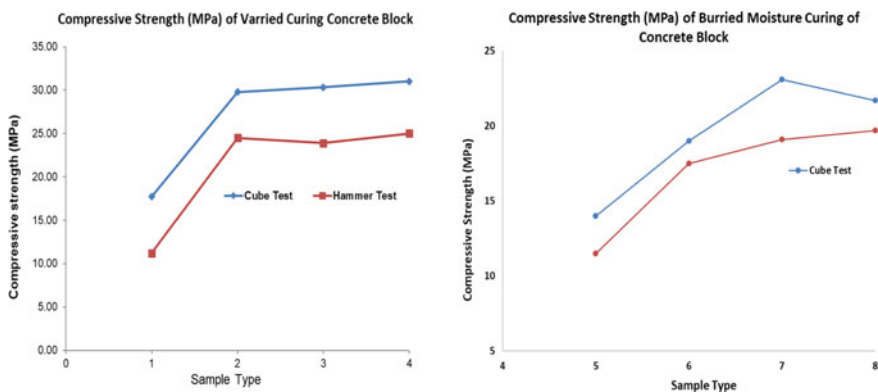
Fig. 3 Comparison of strength between compressive test and hammer test for varied curing (left) and moisture buried curing (right)
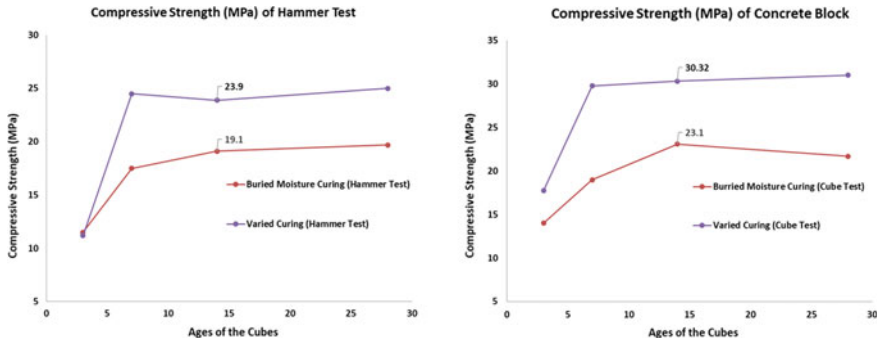
Fig. 4 Comparison between varied curing and moisture buried curing for hammer test (left) and compressive test (right)
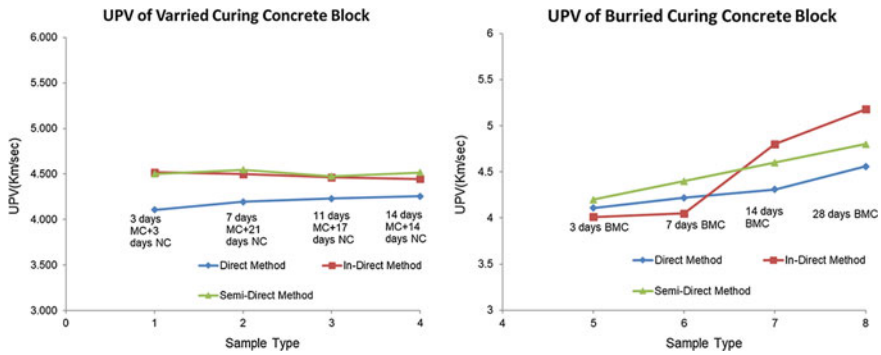
Fig. 5 UPV test value under various methods for varied curing (left) and moisture buried curing (right)

type 5, type 6, type 7, and type 8 were kept completely under moist soil for such days before testing. The compressive strength of such 12 samples was found similar compressive strength result as varied curing condition. However, the compressive strength of 12 samples under moisture buried curing condition slightly increased with the curing period. It has been clearly visible that, the direct method shows the lowest velocity of 8.8%, 6.9%, 5.7% compared to indirect and semi-direct method in case of varied curing condition. Though in the MBC spikes after 14 days of curing clearly indicate that, the cube gained its strength during this time period.

The probable reason for the variation in different direction is that, in direct method, the wave has to travel a shorter way compared to other methods and the defect in the other portion of the concrete could not be detected.

In Fig. 7, direct method is showing better result than indirect and semi-direct method. However, it showed discontinuities in MBC in semi-direct and indirect direction. The probable reason of the discontinuities was due to improper handling
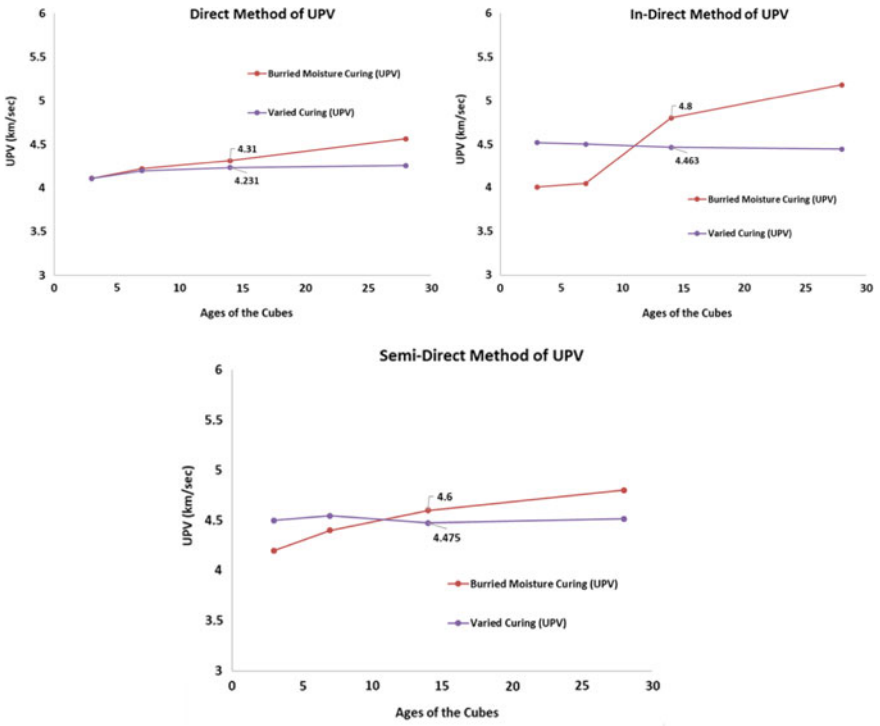
Fig. 6 Comparison of UPV results in between varied curing and moisture buried curing (direct, indirect, and semi-direct method, respectively, from left)

Fig. 7 UPV measurement in different direction
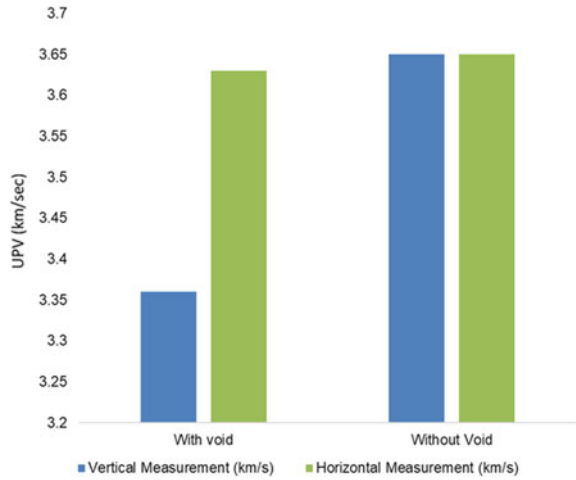
of the transducers in these direction, though further experiments need to continue to find out the animalities of the buried curing condition.

However, the elastic properties and the density of the medium do not fully depend on the curing as the wave velocity varies 3.6% in direct method from varied curing condition to 9% in MBC. The method also indicates that, due to the smaller cube size, the void in the sample could not be determined by UPV. The test later proceeded on the larger void to determine the effectivity of pulse velocity.

UPV is generally used for checking the quality of concreting done but, in this project, show that it can also be used to detect huge voids. While investigating the specimen in vertical direction, there is a significant change in UPV in the specimen whereas while investigating in horizontal direction there is negligible change in UPV.

This is because of the size and directionality of the void (100 mm x 10 mm). This shows that UPV method cannot detect very thin voids in the horizontal direction.

4   Conclusion

The results obtained from the RH tests came up with slight variations between the numbers of rebounds from the hammer and the compressive strength. The strength from the rebounds tested lower than the compressive strength test which is indicative of improper handling of hammer and instrumental error. However, the aged samples that were wet cured for 14 days and dry cured 14 days and samples cured under the earth for 14 days came back with the most promising results with almost highest compressive strength under RH testing for varied and standard curing methods.

The age of the concrete plays more of a significant role then the way it was cured as a defining parameter when it comes to UPV testing which shows that there was little to no changes in the wave velocity due to various curing times. When compared, the highest velocity was obtained from semi-direct and indirect UPV testing, whereas the direct method of measuring velocity came back with a lower value when compared to the other two methods. However, the results obtained from the direct method can be considered as satisfactory or "good" in terms of sensitivity and quality; based on the fact that the results obtained ranged from 3.5 to 4.5 km/s.

The void detection however could not be measured accurately as the compression wave travels for a short duration of time before becoming inaccurate. Therefore, the tests were carried out on samples with large voids on the vertical axis, where transducers were kept in a vertical direction; the result obtained showed 3.35 km/s. When measured in the horizontal axis, where transducers were placed in the horizontal direction, the result obtained showed 3.64 km/s which indicated that the voids were smaller when compared to testing being done in the vertical axis.

The results indicate that concrete can gain its estimated strength after 14 days of adequate curing. However, it also indicates that NDT is still not 100% accurate. Therefore, to obtain the most accurate results, it is recommended that non-destructive testing and destructive testing are carried out side by side when trying to attain a precise gauge on the strength of concrete.

References

1. Breysse D, Martínez-Fernández JL (2014) Assessing concrete strength with rebound hammer: review of key issues and ideas for more reliable conclusions. Mater Struct 47:1589–1604. https://doi.org/10.1617/s11527-013-0139-9
2. Wedatalla AMO, Jia Y, Ahmed AAM (2019) Curing Effects on High-Strength Concrete Properties. Adv Civ Eng 2019:1683292. https://doi.org/10.1155/2019/1683292
3. Weather FIPC on PCWG on C in H, Précontrainte FI de la, Construction FIPC on P (1986) Concrete construction in hot weather. Thomas Telford Publishing
4. Aldea C-M, Young F, Wang K, Shah SP (2000) Effects of curing conditions on properties of concrete using slag replacement. Cem Concr Res 30:465–472
5. Zeyad AM (2019) Effect of curing methods in hot weather on the properties of high-strength concretes. J King Saud Univ Sci 31:218–223
6. Mohamed HA (2011) Effect of fly ash and silica fume on compressive strength of self-compacting concrete under different curing conditions. Ain Shams Eng J 2:79–86
7. ACI Committee 305 (2007) ACI 305.1–06 Specification for hot weather concreting. ACI Man Concr Pract Part 2 Constr Pract Insp Pavements 305.1-1–305.1-8
8. Aydin F, Saribiyik M (2015) Correlation between Schmidt hammer and destructive compressions testing for concretes in existing buildings. Sci Res Essays 5:1644–1648
9. Pessiki SP (Chair) (2003) In-place methods to estimate concrete strengths. ACI 228.1R-03 report
10. Proverbio E, Venturi V (2005) Reliability of nondestructive tests for onsite concrete strength. 10 DBMC, Lyon
11. Szilagyi K, Borosnyoi A (2009) 50 years of experience with the Schmidt rebound hammer, concrete structures. Ann Tech J 10:46–56
12. Qaswari HY (2000) Concrete strength by combined nondestructive methods simply and reliably predicted. Cem Concr Res 30:739–746
13. Sturrup VR, Vecchio FJ, Caratin H (1984) Pulse velocity as a measure of concrete compressive strength. In: In situ/nondestructive testing of concrete, special publication SP–82. American Concrete Institute, Detroit; pp 201–228
14. Trtnik G, Kavcic F, Turk G (2009) Prediction of concrete strength using ultrasonic pulse velocity and artificial neural networks. Ultrasonics 49:53–60
15. Samarin A, Meynink P (1981) Use of combined ultrasonic and rebound hammer method for determining strength of concrete structural member. Concr Int 25–29
16. Mehta PK (1991) Durability of concrete–fifty years of progress? Spec Publ 126:1–32
17. Ploix M, Garnier V, Breysse D, Moysan J (2011) NDE data fusion to improve the evaluation of concrete structures. NDT E Int 44(5):442–448
18. Sbartaï Z, Breysse D, Larget M, Balayssac J (2012) Combining NDT techniques for improved evaluation of concrete properties. Cem Concr Compos 34(6):725–733
19. B. EN:13791 (2007) Assessment of in situ compressive strength in structures and precast concrete components
20. Lu C, Jin W, Liu R (2011) Reinforcement corrosion-induced cover cracking and its time prediction for reinforced concrete structures. Corros Sci 53(4):1337–1347
21. Muto M, Beck JL (2008) Bayesian updating and model class selection for hysteretic structural models using stochastic simulation. J Vib Control 14(1–2):7–34

22. Beck JL, Yuen K-V (2004) Model selection using response measurements: Bayesian probabilistic approach. J Eng Mech 130(2):192–203
23. IS 456 (2000) Concrete, plain and reinforced. Bur Indian Stand Delhi, pp 1–114
24. Bungey JH (1980) The validity of ultrasonic pulse velocity testing of in-place concrete for strength. NDT Int 13:296–300
25. IS 13311 (Part 1) (1992) IS 13311–1 (1992) Method of non-destructive testing of concrete, Part Ultrasonic pulse velocity. Bur Indian Standards 1–7
26. Helal J, Sofi M, Mendis P (2015) Non-destructive testing of concrete: a review of methods. Electron J Struct Eng 14:97–105

Evaluating the Properties of Demolished Aggregate Concrete with Non-destructive Assessment

M. H. R. Sobuz 📍, **S. D. Datta** 📍, and **M. Rahman** 📍

1 Introduction

DAC is a modern concrete development concept which had a huge concern in the construction industries to achieve the sustainability criteria for structure. In the modern world of civilization, the increasing tendency of inhabitants leads to a greater amount of urbanization and industrialization that leads to the fast consumption of natural sources whereas generates a huge amount of wastage material. As the industrialization and urbanization procedure increases day by day, there is a severe need to demolished the old structure and replaced the new one. From the evaluation of the demolished waste impact on the environment, it appears that around 3 billion tons of demolition and construction debris were produced yearly and increasing constantly [1]. Another construction debris is developed from the destructive testing of the standard concrete cylinders during concrete production and testing procedures [2]. According to Hamad and Dawi [2], the tested concrete cylindrical specimen represents a decent lot of the dumped construction waste. Therefore, the growth of such waste harms the environment if there is a lack of planning to dispose of, manage, and handle the wastage materials properly. Considering all of the facts, environmental degradation can be minimized by processing those constructions and demolishing waste into the recycled aggregate and NDT approaches to find out the material properties of the specimen.

Several investigations have marked their footstep on the zone base of fresh and hardened properties of DAC [3–6]. The fresh state behavior of DAC has an important impact on the hardened state nature of the concrete [7]. Therefore, there have

M. H. R. Sobuz (✉) · S. D. Datta · M. Rahman
Department of Building Engineering and Construction Management, Khulna University of Engineering and Technology, Khulna – 9203, Bangladesh
e-mail: habib@becm.kuet.ac.bd

M. Rahman
e-mail: mizan16@becm.kuet.ac.bd

been limited studies on the fresh behavior of the DAC [7–9]. The fresh properties have been transformed by the incorporation of DCA particles because of the surface roughness, angularity, and porosity of the DCA aggregate particles [10]. According to Ajdukiewicz and Kliszczewicz [11], the water content has to be revised for the incorporation of the DCA particles in the fresh concrete mix. Most of them exhibited that the amplified concentration of DCA was offensive to the compressive strength of concrete [3]. According to Zhang et al. [5] and Zaetang et al. [4], the strength and flow ability of concrete decrease with the incorporation of DCA particles. Consequently, Limbachiya et al. [12] concluded that the DCA surface and cement exhibited weaker cohesion force than the normal aggregates and cement matrix that moderate the strength with the percent increment of DCA. The compressive strength of DAC showed around 10–25% inferior to the traditional concrete produced with NCA [3, 13], whereas the splitting tensile strength of 25%, 50%, and 100% replacement of DCA showed 6%, 10%, and 40% smaller than NSC, respectively [14]. However, the evaluation of compressive strength and other parameters for both new and existing construction work is necessary during the quality assessment of the structural element and their service life for reasons of renovation or regular inspection [15]. The assessment can be obtained through destructive testing which leads to high cost, waste material, and timewasting process. Furthermore, Sunayana and Barai [16] developed a linkage between the compressive strength and the rebound number (RN). Therefore, the NDT assessment through rebound hammer can predict the fresh behavior, destructive compressive strength, splitting tensile strength, and DCA concrete layer quality.

From several investigations, it is prominent that there is an inadequate number of studies in the development of empirical relations of DAC through NDT. Considering this fact, this study elaborates on the effect of DCA particle replacement through fresh test (slump and compaction factor), hardened test, and NDT properties assessment. Furthermore, this investigation also detects the comparative relations between hardened properties such as cylindrical compressive and splitting tensile strength with NDT assessment of rebound hammer test for the different DCA replacement at 7 and 28 days. Therefore, the properties of DAC can be predicted through NDT assessment.

2 Materials and Experimental Methods

2.1 Materials

Ordinary Portland cement of CEM-1 was used which satisfied the ASTM C150 [17] for this experiment. Silica fume was used as a 10% substitution of cement. The nominal size of 20 mm stone chips was considered as natural coarse aggregate (NCA) having a fineness modulus (F.M) of 3.27 whereas the same size range of 5–19 mm DCA particles having a F.M of 3.44 was determined according to ASTM C33 [18]
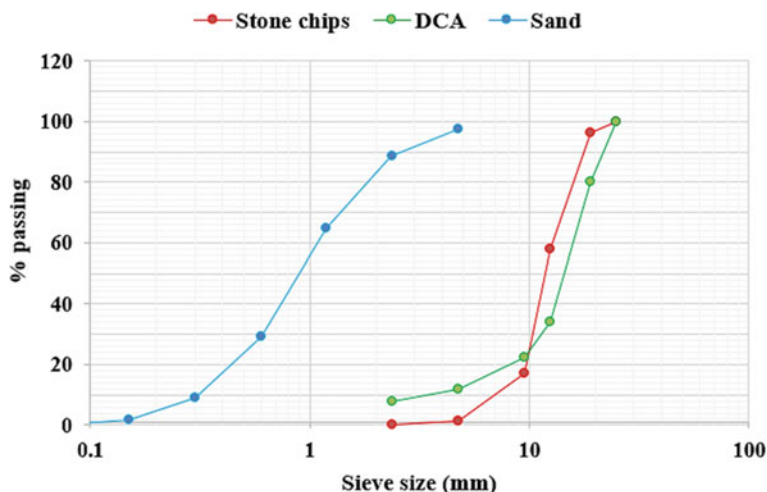
Fig. 1 Gradation curve for stone chips, DCA, and sand

as shown in Fig. 1. The demolished waste was obtained from the construction debris of the "New Academic Building" located at Khulna University of Engineering and Technology, Khulna, Bangladesh. Subsequently, DCA particles were detached from the demolished waste and broken down into the desired size and specification. The specific gravity of sand, stone chips, and DCA particles was obtained 2.34, 2.72, 2.58, respectively, following the ASTM C29/C29M [19]. Also, a high range water reducer was implemented as 1.3% of the binder (cement + silica fume) to minimize the water–cement ratio.

2.2 Mix Preparation, Batching, and Curing

The mixed preparation was conducted following the standard: ACI 363R [20]. A total of four concrete mixes was arranged to evaluate the properties of DAC. Several trials of the mixes were performed to adjust the w/c ratio and the percentage of superplasticizer. From the investigation, the water–binder ratio (w/b) was adjusted at 0.33 and the mix ratio of 1:1.54:2.41. The control mix is designated as NDCA-0% having 0% concentration of DCA particles and the rest of the mixes are designated as NDCA-15%, NDCA-30%, and NDCA-45% containing 15, 30, and 45% replacement of NCA by DCA as shown in Table 1. This mixing of the fresh DAC was conducted according to ASTM C685 [21]. After the fresh test, the concrete mix was poured in 252 nos. 100 × 200 mm cylindrical molds which were cured in water for 7 and 28 days as shown in Fig. 2a–c. Therefore, the prepared specimens were taken out a day before testing from the curing tank and kept in the open air.

Table 1 Mix proportion (kg/m^3)

Mix ID	Cement	Silica fume	NCA	DCA	Sand	Superplasticizer	Water
NDCA-0%	500	50	1172	–	772	1.30	0.33
NDCA-15%	500	50	997	176	772	1.30	0.33
NDCA-30%	500	50	820	352	772	1.30	0.33
NDCA-45%	500	50	645	527	772	1.30	0.33
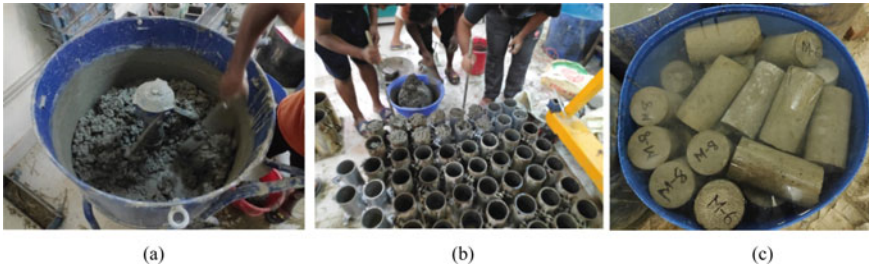
Fig. 2 **a** Mixing of concrete; **b** specimen preparation; **c** curing

2.3 Experimental Methods

The slump test was conducted by following ASTM C143 [22] standard to determine the workability of the concrete mix and the effect of DCA particles over the slump value as illustrated in Fig. 3a. In addition, following BS 1881 [23], a compaction factor test was conducted to find out the average compaction factor of the fresh concrete mix as shown in Fig. 3b. Furthermore, the compressive and splitting tensile strength tests were conducted based on the ASTM C39 [24] and ASTM C496 [25], respectively, after the 7 and 28 days curing of the cylindrical specimen. The compressive strength setup was presented in Fig. 3c. The NDT assessment of the concrete specimen was
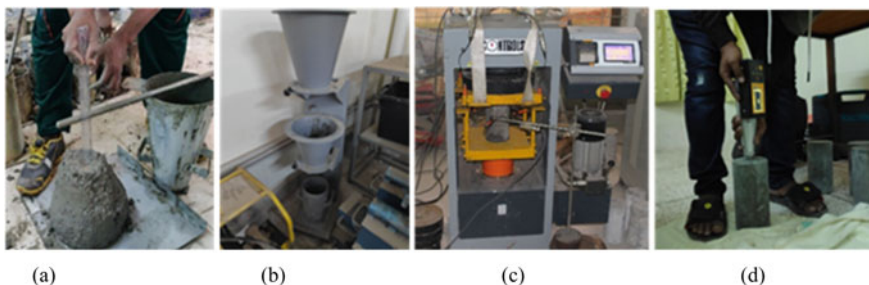
Fig. 3 Experimental investigation of **a** slump test; **b** compaction factor test; **c** compressive strength set up; and **d** rebound hammer test

conducted through the rebound hammer test by following the ASTM C805 [26] standard as shown in Fig. 3d.

3 Results and Discussions

3.1 Effect of DCA on the Slump and Compaction Factor

Figure 4 represents the slump (mm) value of DAC having various percentage replacement of DCA particles and the compaction factor of the concrete. The analysis represents a decreasing trend of slump value when the volume of DCA particles intensified in the mix. A similar kind of trend was observed for the compaction factor test of the freshly mixed DAC. In comparison with the NDCA-0% (control mix), the slump of the fresh concrete mix decreases 2.91, 6.98, and 12.79% for the 15, 30, and 45% replacement of coarse aggregate by DCA, respectively, whereas the compaction factor decreases 0.6, 1.03, and 2.25% for the same replacement with respect to NDCA-0%. As the DCA particles were set as saturated surface dry before mixing, the DCA absorbed little water at the mixing stage. In addition, the rough texture of DCA takes up the harshness of the concrete mixture and therefore reduced its slump value and compaction factor at a higher replacement level [27].
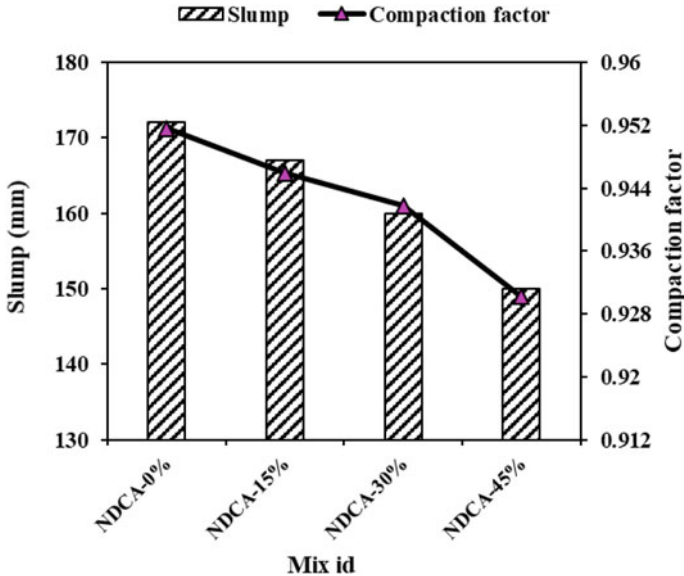
Fig. 4 Slump and compaction factor of DAC

3.2 Effect of DCA on Compressive and Splitting Tensile Strength

From Fig. 5, it was appeared that NDCA-15%, NDCA-30%, and NDCA-45% concrete mixes decrease 20.7, 26.24, and 30.13% of compressive strength, respectively, compared to NDCA-0% (control mix) at 7 days, whereas the 28 days compressive strength shows 16.21, 24.86, and 29.48% decrease of NDCA-15%, NDCA-30%, and NDCA-45% mixes, respectively, than the control mix. Due to the large number of voids created by DCA particles, the compressive strength declines with the concentration. Moreover, the DCA surface and cement paste produce weak cohesion force between them as a result this cohesion force cannot match with the cohesion force of NCA and cement matrix [28]. Furthermore, Tavakoli and Soroushian [29] concluded that the interfacial transition zone (ITZ) of DAC cannot touch the benchmark while it is compared to NAC. This kind of degradation in strength behavior represents the existence of the old adhered mortar in the parent concrete. On the other hand, inherent microcracks in ITZ leads to the upstream stress contraction at the crack order as the transmission of microcracks in the concrete affects compressive strength gradually when the replacement of DCA increases [30].

Figure 5 also represents the splitting tensile strength profile in the secondary axis at 7 days and 28 days, respectively. In comparison, the splitting tensile strength achieved around 9%–11% of the compressive strength of concrete specimens at the respective
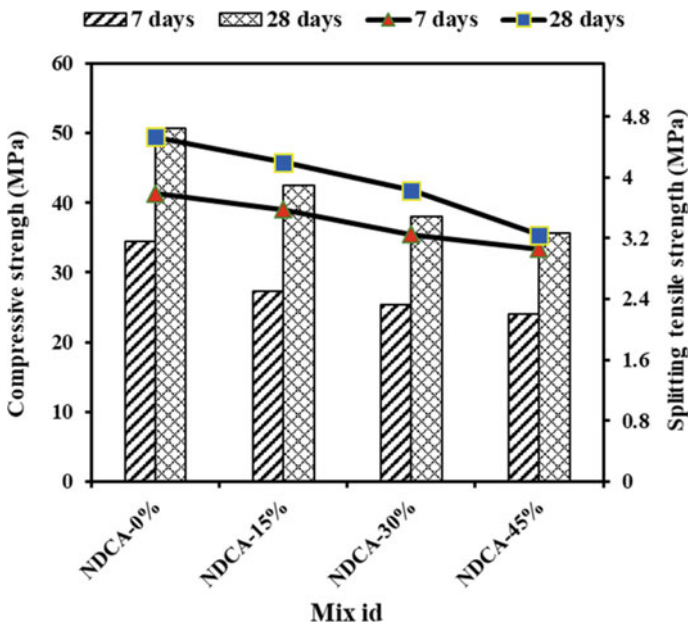
Fig. 5 Compressive and splitting tensile strength with different content of DACs

ages. From the evaluation of Fig. 5, NDCA-15%, NDCA-30%, and NDCA-45% concrete mixes show 5.54%, 14.28%, and 19.26% decrease in compressive strength, respectively, compared to NDCA-0% at 7 days whereas 28 days tensile strength show 7.28%, 15.45%, and 28.48% reduction with respect to control mix. The DCA surface and cement paste developed a lower bonding tendency due to weaker cohesion force between them and provide a decreasing trend in all tested ages. Therefore, the decreasing trend of splitting tensile strength relates to the previous findings of the researcher [11, 31, 32]. According to the experimental investigation by Silva, de Brito [31], the increased amount of porosity in DCA particles leads toward the greater strength loss of the DAC.

3.3 Effect of DCA on NDT Assessment

The rebound hammer test provides the rebound number (RN) of the cylindrical specimen to quantify the compressive strength of the concrete. Table 2 represents the RN value where the quality of mixes is obtained in a very good layer up to NDCA30% at 28 days whereas 45% replacement of DCA concrete shows "good layer" according to the concrete quality classification of Yahya [33]. As similar to the previous outcomes, the RN value decreases with the increment of DCA percentage due to the porous ITZ in the concrete. After the concrete mixing, more porous ITZ is created in the DAC as the evaporation of water continues to the concrete mixes [34]. As a result, the bond between DCA and cement matrix affected adversely which leads to the lower RN value of DAC.

The RN value can predict the compressive strength of the DAC as represented in the following Fig. 6. This investigation recommends a single variable linear regression equation for assessing the compressive strength of the concrete mix. The best-fitted curve is a straight line that contains the rebound number (N) from the NDT approach and the corresponding destructive compressive strength of concrete (f'_c). The correlation is represented as the following equation of $f'_c = 1.2436\,N - 9.7075$ where the R^2 value is obtained to be 96% which leads to a significant correlation.

Table 2 Rebound number specifications of DAC

Mix	Age (day)	Rebound number	Concrete quality
NDCA-0%	7	33.9	Good layer
	28	47.3	Very good layer
NDCA-15%	7	31.4	Good layer
	28	42.6	Very good layer
NDCA-30%	7	28.4	Fair
	28	40.7	Very good layer
NDCA-45%	7	26.5	Fair
	28	35.8	Good layer
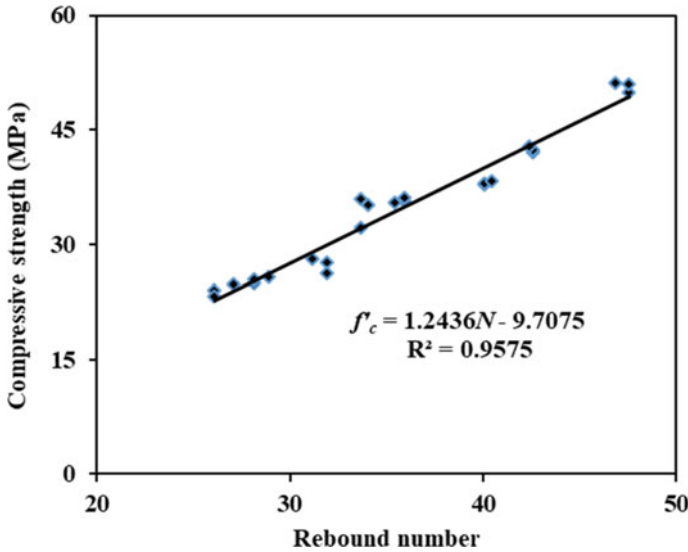
Fig. 6 Relationship between compressive strength and rebound number

The regression representation satisfied the previous investigation of Mahdi Shariati [35].

In addition, the rebound number can predict the splitting tensile behavior of concrete. The proportional relationship between the NDT and split-tensile strength represents a significant co-relation of $R^2 = 0.81$. The correlation is represented as the following equation of $f_{spt} = 0.0638\,N + 1.4015$. In the meantime, the RN value is measured of the surface hardness properties of concrete and is generally inclined to the mortar fraction of the specimen. As a result, the splitting tensile strength and rebound number complement each other and show a linear relationship like the following Fig. 7.

4 Conclusions

This paper presents the experimental investigation of fresh and hardened properties of concrete with varying densities of DCA by quantifying the destructive and non-destructive techniques. Therefore, the outcomes of this study are summarized below:

- The fresh and hardened properties showed decreasing fashion with increasing the demolished aggregate densities for the production of recycled low-cost concrete.
- The test results are also revealed that the prediction of the hardened properties through the rebound number exhibited well estimation with a good coefficient of regression through the experimental results for DCA.
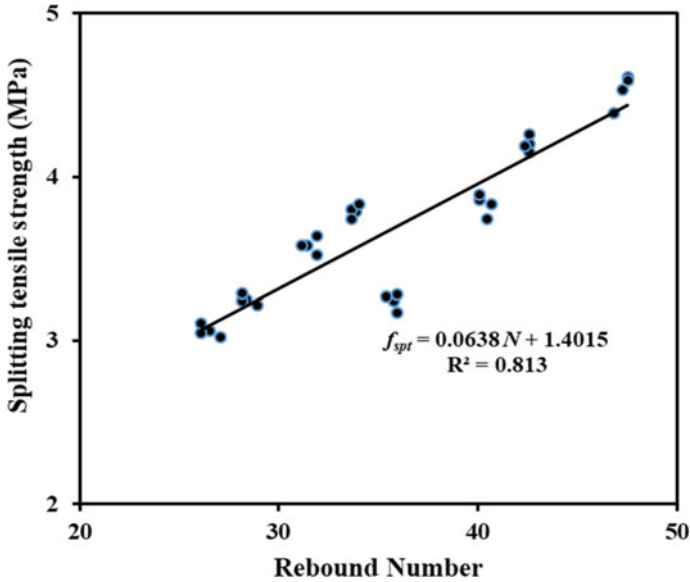
Fig. 7 Relationship between rebound number and splitting tensile strength

- The determination of concrete strength through NDT can assist in the practice regarding quality control of concrete work, and it needs the calibration with the experimental results.
- The NDT techniques applications in the real field may save time, labor, without using heavy machinery and cost of the construction industry. Hence, the utilization of building demolished debris in the structural concrete production provides great possibilities in the construction sector as it reduces the construction waste and adverse environmental impact.

References

1. Akhtar A, Sarmah A (2018) Construction and demolition waste generation and properties of recycled aggregate concrete: a global perspective. J Cleaner Prod 186.
2. Hamad BS, Dawi AH (2017) Sustainable normal and high strength recycled aggregate concretes using crushed tested cylinders as coarse aggregates. Case Stud Constr Mater 7:228–239
3. Bai GZ, Liu C, Liu BC (2020) An evaluation of the recycled aggregate characteristics and the recycled aggregate concrete mechanical properties. Constr Build Mater 240:117978

4. Zaetang Y, Sata V, Wongsa A, Chindaprasirt P (2016) Properties of pervious concrete containing recycled concrete block aggregate and recycled concrete aggregate. Constr Build Mater 111:15–21

5. Zhang et al (2015) Influence of carbonated recycled concrete aggregate on properties of cement mortar. Constr Build Mater 98:1–7

6. Mohammed TU (2007) Bangladesh–sustainable development of concrete technology. In: Proceedings of the CBM-CI–International workshop

7. Kurda RdB, Silvestre J, José D (2017) Influence of recycled aggregates and high contents of fly ash on concrete fresh properties. Cement Concr Compos 84:198–213

8. Limbachiya M, Seddik MS, Ouchagour Y (2012) Use of recycled concrete aggregate in fly-ash concrete. Constr Build Mater 27:439–449

9. Faleschini F, Jiménez, Barra M, Aponte D, Vázquez E, Pellegrino C (2014) Rheology of fresh concretes with recycled aggregates. Constr Build Mater 73:407-416

10. Safiuddin et al (2013) Use of recycled concrete aggregate in concrete: a review. J Civ Eng Manage 19:796–810

11. Ajdukiewicz A, Kliszczewicz A (2002) Influence of recycled aggregates on mechanical properties of HS/HPC. Cem Concr Compos 24(2):269–279

12. Limbachiya M, Meddah MS, Ouchagour Y Performance of Portland/Silica fume cement concrete produced with recycled concrete aggregate. ACI Mater J 109(1)

13. Tabsh SW, Abdelfatah AS (2009) Influence of recycled concrete aggregates on strength properties of concrete. Constr Build Mater 23:1163–1167

14. Bairagi NK, Ravande K, Pareek VK (1993) Behaviour of concrete with different proportions of natural and recycled aggregates. Resour Conserv Recycl 9(1):109–126

15. Pucinotti R (2013) Assessment of in situ characteristic concrete strength. Constr Build Mater 44:63–73

16. Sunayana S, Barai SV (2017) Recycled aggregate concrete incorporating fly ash: comparative study on particle packing and conventional method. Constr Build Mater 156:376–386

17. ASTM Standard specification for Portland cement, in ASTM C150/C150M-19a2019. West Conshohocken, PA

18. ASTM Standard specification for concrete aggregates, in C33/C33M-182018, ASTM International, West Conshohocken, PA

19. ASTM Standard test method for bulk density ("unit weight") and voids in aggregate, in C29/C29M2017. ASTM International, West Conshohocken, PA

20. ACI Committee High-strength concrete (ACI 363R). ACI Symposium Publication, p 228

21. ASTM (2017) Standard specification for concrete made by volumetric batching and continuous mixing. ASTM International, West Conshohocken, PA

22. ASTM Standard test method for slump of hydraulic-cement concrete, in C143/C143M-122012. ASTM International, West Conshohocken, PA

23. BS Method for determination of compacting factor in BS 1881: Part 1031993. British Standards Institution, London

24. ASTM Standard test method for compressive strength of cylindrical concrete specimens, in ASTM C39/C39M-182018. ASTM International, West Conshohocken, PA

25. ASTM (2017) Standard test method for splitting tensile strength of cylindrical concrete specimens, in ASTM C4962017. ASTM International, West Conshohocken, PA

26. ASTM Standard test method for rebound number of hardened concrete, in C805/C805M-182018. ASTM International, West Conshohocken, PA

27. Safiuddin et al (2011) Properties of high-workability concrete with recycled concrete aggregate. Mater Res 14:248–255

28. Limbachiya M, Meddah MS, Ouchagour Y (2012) Use of recycled concrete aggregate in fly-ash concrete. Constr Build Mater 27(1):439–449

29. Tavakoli M, Soroushian P (1996) Strengths of recycled aggregate concrete made using field-demolished concrete as aggregate. Mater J 93(2):178–181

30. González-Fonteboa B, Martínez-Abella F (2008) Concretes with aggregates from demolition waste and silica fume. Materials and mechanical properties. Build Environ 43(4):429–437

31. Silva RV, de Brito J, Dhir RK (2015) Tensile strength behaviour of recycled aggregate concrete. Constr Build Mater 83:108–118
32. Kim K, Shin M, Cha S (2013) Combined effects of recycled aggregate and fly ash towards concrete sustainability. Constr Build Mater 48:499–507
33. Yahya Z et al (2018) Influence of Kaolin in fly ash based geopolymer concrete. Destr Nondestr Testing 374(1):012068
34. Poon CS, Shui Z, Lam L (2004) Effect of microstructure of ITZ on compressive strength of concrete prepared with recycled aggregates. Constr Build Mater 18(6):461–468
35. Shariati M, Ramli-Sulong NH, Arabnejad MM, Shafigh P, Sinaei H (2011) Assessing the strength of reinforced concrete structures through ultrasonic pulse velocity and Schmidt rebound hammer tests. Sci Res Essays 6(1):213–230

Influence of Activator and Superplasticizer on Fly Ash-Based Geopolymer Paste and Mortar

S. M. Shahriar Sifat, E. Kabir, and G. M. Sadiqul Islam

1 Introduction

To achieve sustainable development goals (SDGs), new creative ideas are important to keep our environment safe and clean. Geopolymer is a modern eco-friendly construction material and an alternative to Portland cement concrete [1, 2]. The use of geopolymer materials is expected to reduce the demand for Portland cement which is responsible for high CO_2 emission. In the 1950s, Glukhovsky first discovered alkali-activated alumino-silicate. The name Geopolymer was pointed by a French Professor Davidovits in 1978 to illustrate a broad range of materials differentiated by a network of inorganic molecules. He proposed that an alkaline solution could be used to react with the silicon and aluminum in a source material of geopolymer origin or in a by-product such as fly ash, blast furnace slag, and rice husk ash to produce binders; through the chemical reaction by the polymerization process, he called the term geopolymer binders [3–5]. Most scientists preferred the name "geopolymer" to name all the siliceous-aluminous binders that were activated. The alkaline solution composed of NaOH and Sodium Silicate is known as activators. The chemical process involved in the formation of geopolymer binders is completely different from that of OPC paste. Here polymerization process takes over the hydration process of the OPC paste setting process. During the geopolymerization process, silicon (Si) and aluminum (Al) atoms react to form molecules that are chemically and structurally comparable to those binding natural rocks. High alkaline solutions are used

S. M. S. Sifat (✉) · E. Kabir · G. M. S. Islam
Department of Civil Engineering, Chittagong University of Engineering & Technology,
Chattogram-4349, Bangladesh
e-mail: u1401068@student.cuet.ac.bd

E. Kabir
e-mail: u1401073@student.cuet.ac.bd

G. M. S. Islam
e-mail: gmsislam@cuet.ac.bd

to induce the silicon and aluminum atoms in the source materials to dissolve and form the geopolymer paste. The chemical reaction period is fast, and the required curing period could be even less than 24 h [4]. Metakaolin and fly ash are the most preferred materials for geopolymer manufacturing among all the aluminosilicate products. Fly Ash's one-ton price is just a small fraction of a ton of cement's price. Studies estimated the cost of fly ash-based geopolymer concrete is 10–30% cheaper than that of Portland cement concrete [6]. If we consider the carbon credits, fly ash can be very profitable and earn monetary benefits through the carbon credit trade. It is to be mentioned that one carbon credit has a redemption value of more than 20 Euros. The low creep, small drying shrinkage, resistance to sulfate attack, and good acid resistance offered by the heat-cured fly ash-based geopolymer concrete can yield additional economic benefits [6]. In many cases, the activator makes the mixture stiff, and the workability of the mixture reduces significantly. Although owing to its low price and accessibility, fly ash seems to be more beneficial to current scientists. Studies [7, 8] developed a 100% fly ash binder in the mortar by activating it with alkali components including caustic alkalis, silicate salts, and weak acid non-silicate salts. Fly ash and highly alkaline solution together produce a new inorganic aluminosilicate polymer product forms yielding polymeric Si-O-Al-O. The response between them, through the polymerization phase, will create an inorganic binder. Another way to activate effectively low to mild alkali material containing mainly silicate and calcium will generate silicate hydrate gel (C–S–H) comparable to the bond created in common cement but with a reduced Ca/Si proportion.

To achieve significant compressive strength as well as feasible workability within short curing periods, the activation process of silica and alumina-rich pozzolanic material like fly ash is recommended to activate with alkaline elements at certain high temperatures [9]. Sarker and Rangan [6] emphasized more on the early strength gain property of geopolymer concrete with the application of heat. In addition to this, a high concentration of alkali activators generally interferes with the workability of the end product and therefore influences its compressive strength development. Research [10] was carried out on the rheological behavior of fly ash-based geopolymer using chemical admixture. This study, therefore, aimed to prepare a sufficiently workable mixture with help of superplasticizers. The initial heat curing improved early strength and the effect of activator concentration was evaluated.

2 Materials and Methodology

2.1 Fly Ash

Fly ash is a fine gray powder consisting mostly of spherical, glassy particles that are produced as a by-product in coal-fired power stations. There are two kinds of fly ash viz. class C and F. This study used class F fly ash which is produced by the combustion of bituminous coal and contains less than 5% of the CaO. It has

Table 1 Properties of fly ash

Description	Results
Physical appearance	Ash
Loss on ignition (%)	3.5
Fineness (cm^2/g)	2435
Free CaO (%)	0.74
CaO (%)	2.1
SiO_2 (%)	55.7
Moisture (%)	0.21

Fig. 1 Fly ash used in this study

pozzolanic properties. The fly ash was obtained from a local cement manufacturing industry. The properties and physical appearance of class F fly ash used in this study are given in Table 1 and Fig. 1, respectively.

2.2 Alkaline Activator

A study [11] indicated alkaline activators based on sodium are more efficient. Single activator types, either NaOH or silicate do not yield promising results. Therefore, a mixture of NaOH and sodium silicate was used to prepare fly ash-based geopolymer mortar. It has been noted that concrete or mortar's compressive strength is increased with the molarity of activators [6]. The activator materials were obtained from an authentic chemical supplier. NaOH and sodium silicate were obtained in the form of solid pellets and semisolid form with high density, respectively. Figures 2 and 3 show pellet form of NaOH and sodium silicate solution. The required quantity of NaOH pellets was dissolved into water to prepare specified concentrations (8–16 M) of sodium hydroxide solution. The mixing of NaOH and sodium silicate solution

Fig. 2 Dry Sodium
Hydroxide pallets
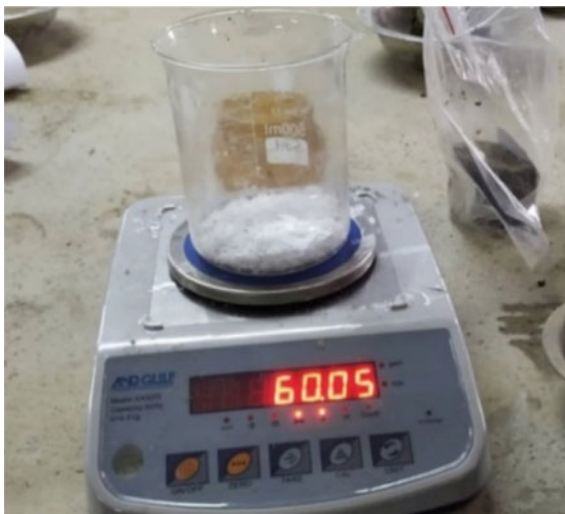
Fig. 3 Sodium Silicate
solution
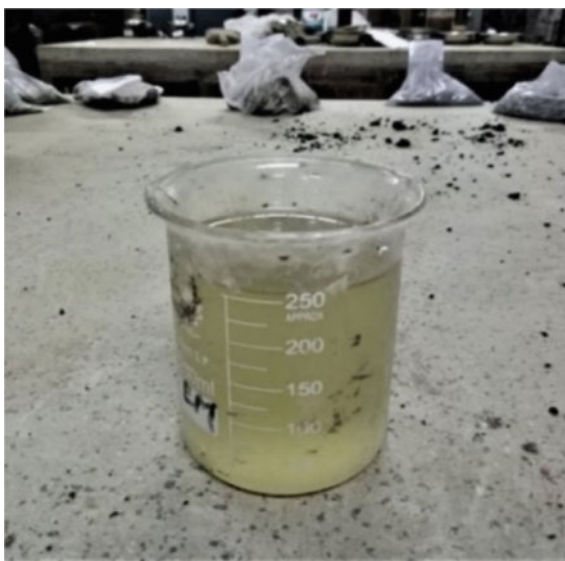
should be done in a proper way considering their uniformity. Safety measures were
maintained during the laboratory work.

2.3 Admixture

A water reduction admixture can be used up to 2% to maintain the workability and thereby to improve the strength properties of the cementitious system [12]. An earlier study found no adverse effect on the addition of the naphthalene-based superplasticizer for strength development up to a dosage of 2% [13]. The prepared combination of alkaline activators is a highly viscous fluid. To obtain the required workability in both paste and mortar, modified polycarboxylic ether-based superplasticizers were used. This carboxylic ether polymer with long side chains application was recently developed to use in high-performance concrete. At the beginning of the mixing process, it initiates the same electrostatic dispersion mechanism similar to traditional superplasticizers; however, the side chains linked to the polymer backbone generate a steric hindrance which greatly stabilizes the cement particles' ability to separate and disperse. The steric hindrance provides a physical barrier (alongside the electrostatic barrier) between the binder grains. In this way, water demand in cementitious media could be reduced significantly.

2.4 Mix Design

Three different concentrations of activator solution viz. 10, 12, and 14 M were considered in the mix designs. The alkaline solution to fly ash ratios were 0.45 and 0.5. The specimens were of two types. The mortar specimens had the sand to fly ash ratio of 2.75, and the pastes without sand were made completely with fly ash and alkaline activators. Different admixtures dosage viz. 0, 1, and 2% were applied to the above mixes. Temperature curing is necessary for the fly ash-based geopolymer for their initial setting. Heat curing was carried out for 24 h.

2.5 Preparation of Samples

ASTM standard sand [14] and fly ash were thoroughly mixed together in a closed box in dry condition. The aggregates are prepared in the SSD condition. Then activator solution was prepared and blended with superplasticizer (if applicable). The mixture of sodium hydroxide and sodium silicate should be prepared just before blending with fly ash; otherwise, sodium hydroxide pellets can accumulate as sediments. A study [15] indicated 7–20% excess water could be added to the mix if required. This study used 7% excess water in addition to the above liquid mixture. Then the alkaline liquid was mixed with the dry mixed materials. Mixing was continued for 4–5 min to get a uniform mixture. A total of 216 nos. $50 \times 50 \times 50$ mm cubes were prepared using different combinations. The compaction was done by 25 blows in each layer, finishing in 3 layers using a specified small wooden block. After compaction and

Fig. 4 Wrapped finished sample inside the molds before heat curing

surface finishing, the sample inside the iron mold was kept in an oven for 24 h at 75 °C controlled temperature for the advancement of the polymerization reaction. Special care was taken to trap the moisture inside the specimen. Thin transparent wrapping papers were used to cover the molds before placing them in the oven for heat curing. Figure 4 shows that the sample is ready to be kept inside the oven.

3 Result and Discussion

3.1 Workability of Mortar

The workability of geopolymer mortars was tested following ASTM C1437 [16]. The samples with the activator to fly ash ratio of 0.50 were tested. Figure 5 gives the flow value of geopolymer mortars using different activator concentrations and admixture content. The workability is decreased with an increase in activator concentration. Less water and a higher amount of solid were used to prepare high molar activators. This made the solution more viscous itself, and therefore, the workability was reduced with an increase in activator concentration. A positive change in workability was found using an increased dosage of admixture in the mixture. The sample with a 12 M activator had the maximum influence of admixture. With a 10 M concentration of alkaline activator, maximum flow of 153 mm was achieved.
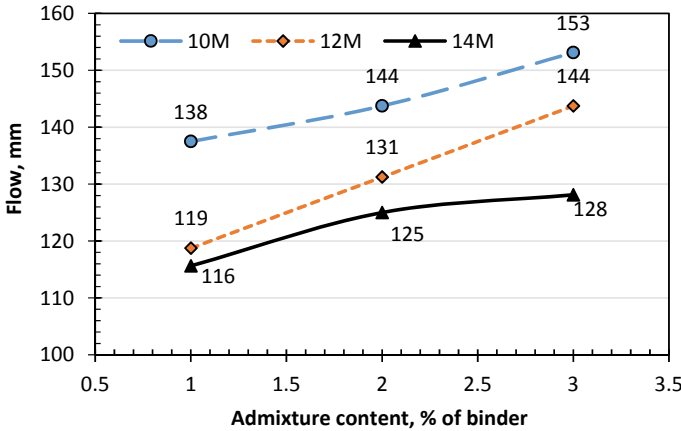
Fig. 5 Variation of workability of geopolymer mortar with admixture and activator concentration

Table 2 Weight variation of different specimens

Specimens	Weight* (gm)
Cement mortar	238
Geopolymer mortar	214
Geopolymer paste (without sand)	188

*Average weight of a $50 \times 50 \times 50$ mm block after curing for 28 days

3.2 Weight Variation

Geopolymer Mortars were found much lighter than the traditional mortars made of cement and sand (Table 2). Though the strength of the mortars made from geopolymers is almost similar to cement mortars. The paste samples were found to be almost 25% lighter than traditional cement mortars. The specific gravity of cement (3.15) is much higher than that of fly ash (~2.2) which made the prepared sample lighter. With this lightweight, fly ash geopolymer concrete would have less dead load than traditional cement concrete and expected to have a positive contribution in the section design.

3.3 Compressive Strength

The variation in compressive strength of paste and mortar samples with activator/binder ratio and admixture content for paste and mortar is given in Figs. 6 and 7, respectively. Wrappers were used to ensure no loss of moisture from the mold. However, increased moisture contents in the paste samples often led to swelling,
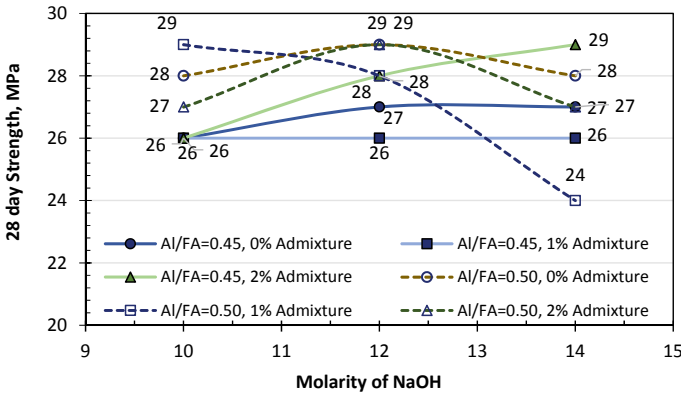
Fig. 6 Compressive strength of paste samples at 28 days
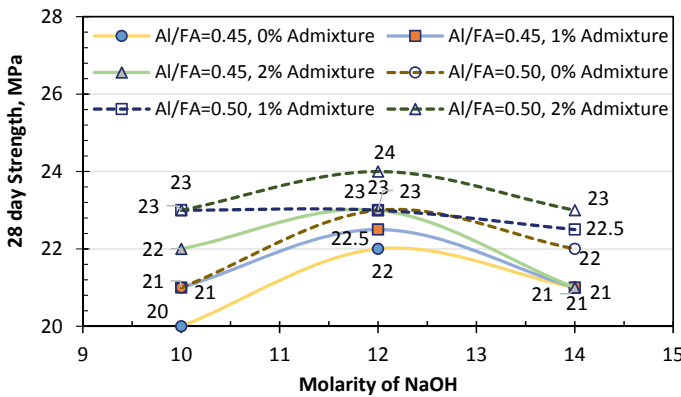
Fig. 7 Compressive strength of mortar samples at 28 days

and leak of moisture has resulted in cracking of the samples. Therefore, no extra water was used in the mixing of Geopolymer pastes. As the mortars are much more resistant to these adverse actions, the use of 7% excess water to the solid components provided better results in terms of both compressive strength and workability. During heat curing, the rate of rising in compressive strength is generally faster. Afterward, the rate of change is moderate.

As shown in Figs. 6 and 7, the compressive strength of paste and mortar was varied between 24–29 MPa and 20–24 MPa, respectively. With some exceptions, the 12 M strength activator gave optimum compressive strength in both media. For the paste samples with Al/FA = 0.45, the strength increased with a molarity of activators, however, keeping other conditions the same 14 M strength of activator gave the lowest strength for Al/FA = 0.5. With the Al/FA = 0.45, the effect of admixture was noticeable. Increasing the concentration of the activator made the sample more

viscous in general. The use of admixture with the high activator concentration helped to pack the sample better which influenced the compressive strength of the paste.

For mortar samples, generally maximum compressive strength was obtained with 12 M activator strength. Both 10 and 14 M samples gave lower strength. This might be due to a lack of available activators for reaction in 10 M samples and low workability for 14 M samples due to the high concentration and poor compaction. The admixture had a positive influence on the strength of mortar samples. The strength was increased gradually with the admixture dose. With 2% admixture content, highest compressive strength was noted for both Al/FA = 0.45 and Al/FA = 0.5.

Figures 8 and 9 show the effect of super plasticizing admixture on the compressive strength of paste and mortar samples, respectively. No definite correlation was noted
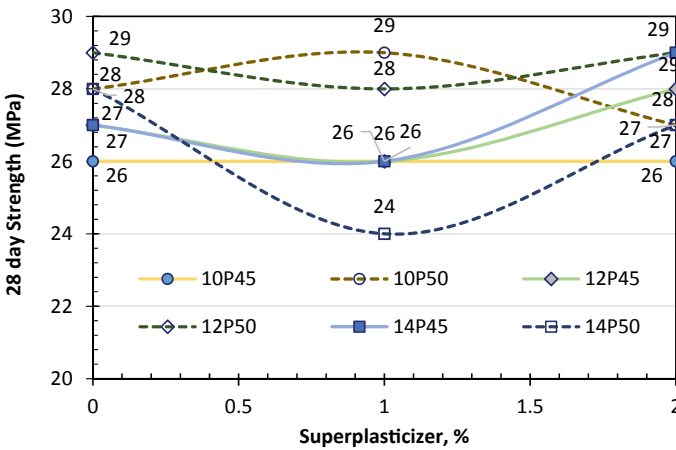
Fig. 8 Effect of admixture on paste
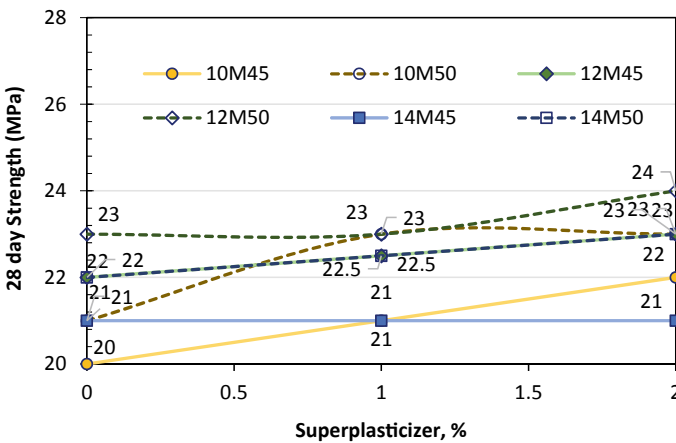
Fig. 9 Effect of admixture on mortar

with the admixture dose and compressive strength of the paste samples. The admixture influenced lower Al/FA ratio samples better than the samples with Al/FA = 0.5. The flow test results indicated a positive influence on the workability of mortars up to a dose of 2%. This trend was mostly satisfied with the compressive strength of the mortar samples. An admixture dose of up to 2% was found to be beneficial to increase the compressive strength up to 3 to 4%. This is because a very small amount of extra water was used throughout the study. The application of admixture reduced water demand. Better mixing and compaction were conducted with the help of a superplasticizer. The influence of admixture was noted higher for Al/FA = 0.5 samples.

4 Conclusion

Several combinations of geopolymer mix designs were evaluated throughout the study considering the variables including an alkaline solution to fly ash mass ratio, sand to fly ash ratio, the molarity of activator, and application of admixture. The following conclusions were made from the experimental study:

- Geopolymer mortars gave better dimensional stability than paste samples. The inert sand helped to retain its shape after heat curing.
- The weight of the geopolymer mortar is significantly lower than traditional cement-based mortars due to the lighter weight of the binder. This can further be used to prepare lightweight geopolymer blocks.
- The workability of geopolymers can greatly be enhanced by the use of PCE-based admixture.
- Activator concentration of 12 M was found to be optimum considering the workability and compressive strength using PCE-based admixture.
- In general, the PCE-based admixture dose (up to 2%) had a positive influence on the compressive strength. However, with higher activator concentration, this interfered and the strength reduced.
- Almost 90% of the ultimate strength (28 days) can be gained within 3 days of heat curing.

References

1. Pacheco-Torgal F (2015) Introduction to handbook of alkali-activated cements, mortars and concretes. In: Handbook of alkali-activated cements, mortars and concretes. Elsevier Inc., pp 1–16

2. Garcia-Lodeiro I, Palomo A, Fernández-Jiménez A (2015) An overview of the chemistry of alkali-activated cement-based binders. In: Handbook of alkali-activated cements, mortars and concretes. Elsevier Inc., pp 19–47
3. Davidovits J (1994) Properties of geopolymer cements. In: First international conference on alkaline and cement concrete
4. Davidovits J (1999) Chemistry of geopolymeric systems, terminology. In: Second international conference on geopolymer
5. Sarker PK (2016) Fly ash: sources, applications and potential environmental impacts. UK
6. Sarker PK, Rangan BV (2013) Geopolymer concrete using fly ash. In: Fly ash: sources, applications and potential environments impacts
7. Talling B, Brandstetr J (1989) Present state and future of alkali-activated slag concretes. In: Fly ash, Silica fume, Slag National Pozzolans Concrete Proceedings of Third International Conference. https://doi.org/10.14359/1873
8. Bakharev T, Sanjayan JG, Cheng YB (1999) Alkali activation of Australian slag cements. Cem Concr Res. https://doi.org/10.1016/S0008-8846(98)00170-7
9. Davidovits J (1991) Geopolymers—inorganic polymeric new materials. J Therm Anal 37:1633–1656. https://doi.org/10.1007/BF01912193
10. Montes C, Zang D, Allouche EN (2012) Rheological behavior of fly ash-based geopolymers with the addition of superplasticizers. J Sustain Cem Mater 1:179–185. https://doi.org/10.1080/21650373.2012.754568
11. Robayo-Salazar RA, Rivera JF, Mejía de Gutiérrez R (2017) Alkali-activated building materials made with recycled construction and demolition wastes. Constr Build Mater 149:130–138. https://doi.org/10.1016/j.conbuildmat.2017.05.122
12. Islam GMS, Raihan MT, Hasan MM, Rashadin M (2019) Effect of retarding superplasticizers on the properties of cement paste, mortar and concrete. Asian J Civ Eng 20:591–601. https://doi.org/10.1007/s42107-019-00128-y
13. Hardjito D, Rangan BV (2005) Development and properties of low-calcium fly ash-based geopolymer concrete
14. ASTM (2017) C778, Standard specification for standard sand. Annu B ASTM Stand 4.01
15. Patankar SV, Ghugal YM, Jamkar SS (2015) Mix design of fly ash based geopolymer concrete. In: Advances in structural engineering: materials, vol 3
16. ASTM (2015) C1437, Standard test method for flow of hydraulic cement mortar. Annu B ASTM Stand 04.01

Flexural Behaviour of Reinforced Concrete Beams Retrofitted with Ferrocement

M. Chanda, M. B. Zisan, and A. Dhar

1 Introduction

The reinforced concrete (RC) is a superior construction material widely used in bridges, buildings, tunnels, etc., because of the simple fabrication process and design philosophy. A reinforced concrete structure often exhibits distress or partial damage during its service period because of the improper design, overloading, change in the design code, material degradation, and corrosion that reduces the service demand. Under such conditions, a complete replacement or demolition of the entire structure might be uneconomical that impact the environment also. Therefore, strengthening or retrofitting a damaged component is a becoming way of restoring serviceability for reinforced concrete structures. A flexural member like beam undergoes cracking due to flexure or shear due to overloading, resulting in the collapse of connecting columns. Steel plate bonding, concrete jacketing, fiber-reinforced polymer, and FRP are mostly used for re-strengthening a partially or completely damaged beam. The cost and unavailability of FRP materials limit its application, especially within the developing countries. Under such restrictions, locally available ferrocement can be more advantageous for enhancing the flexural capacity of a beam element both at service and ultimate loads [1]. It is lightweight, can be employed easily, and performs superior performance against crack propagation [2]. A study shows that ferrocement jacketing of a beam reduces the crack width by about 36% [3].

Though the experiment method is the most accurate way to predict the response of a retrofitted beam, the incurred cost and manual work limit the experimental investigations [4]. The finite element analysis (FEA) is computationally efficient for modeling and analyzing retrofitted concrete beams comparable to practical tests [2].

M. Chanda (✉) · M. B. Zisan · A. Dhar
Department of Civil Engineering, Chittagong University of Engineering and Technology, Chattogram, Bangladesh

M. B. Zisan
e-mail: basirzisan@cuet.ac.bd

The nonlinear behavior and flexural characteristics of simple reinforced concrete and prestressed beams have been studied through the FE method [5, 6]. Another study described that the deflections and the crack propagation in a concrete beam could accurately be measured through FE analysis by ANSYS [7]. This powerful program is used to analyze a beam's behavior under different collapse mechanisms and to visualize the process of flexural crack generation [8]. Therefore, the objective of this study is to evaluate the response of a reinforced concrete beam and the same beam retrofitted with ferrocement using the finite element method. For this purpose, concrete beams modeled by ANSYS and verified with the past experimental results are analyzed. The performance of the beam is expressed in terms of vertical load–deflection relationship, in-service concrete stress, and cracking behavior.

2 Finite Element Modeling

Three types of beams described in Table 1 are considered in this study and analyzed by ANSYS 15. The control beam (CB) is a rectangular RC beam with a length of 1000 mm, a width of 225 mm, and a height of 150 mm. The span length of the beams is 0.9 m. The bottom and top reinforcement steel consist of two steel of diameter 12 mm and 10 mm, respectively, and the concrete cover is 25 mm. The shear reinforcement consists of an 8 mm bar spaced by 75 mm. Figure 1 shows the dimensions and the loading conditions of the control beam, CB. In CB-1, the shear reinforcement of the control beam (CB) is replaced by a 3.5 mm diameter wire mesh furnished with a 25 mm square opening. Similarly, in CB-2, the longitudinal and transverse steels are replaced by an equivalent amount of wire mesh of 4.7 mm diameter and

Table 1 Designation of different types of beams

Model	Definition
CB	Control beam
CB-1	Control beam with equivalent wire mesh (diameter 3.5 mm with opening size 25 mm) replacing only shear reinforcement
CB-2	Control beam with equivalent wire mesh (diameter 4.7 mm with opening size 25 mm) replacing the main and shear reinforcements

(a) Longitudinal section   (b) Transverse section
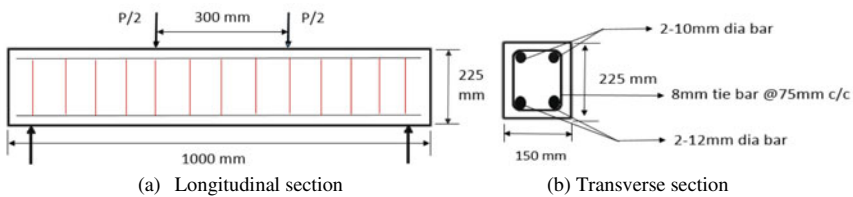
Fig. 1 Dimension and loading position in control beam (CB)

Table 2 Material properties

Material	E (GPa)	ν	$f_c{}'$ (MPa)	σ_y (MPa)	E_t (MPa)	Open shear transfer coef	Close shear transfer coef
Concrete	20	0.2	22.0	–	–	0.3	1.0
Support and loading plates	200	0.3	–	–	–	–	–
Reinforcement and wire mesh	200	0.3	–	414	20	–	–

E: Elastic modulus, ν: Poisson's ratio, $f_c{}'$: Concrete strength, σ_y: Yield strength and E_t: Tangent modulus

25 mm square openings. The material properties for concrete, reinforcing steel, and ferrocement are listed in Table 2. Both reinforcing cord and wire mesh are considered bilinear isotropic material. The experimental beam is designed with a compressive strength of 22.0 MPa. The Poisson's ratio for steel and concrete is assumed to be 0.2 and 0.3, respectively. The linear isotropic and multilinear isotropic material model is considered for concrete material [7]. The modulus of rupture for concrete is determined using Eq. (1), where $f'c$ is the compressive strength of concrete.

$$f_r = 0.7\sqrt{f_c'} \tag{1}$$

The open shear transfer and close shear transfer coefficients are assumed to be 0.3 and 1.0, respectively [8]. Shear transfer coefficients for open crack set greater than 0.20 to avoid the convergence problems. The following assumptions are made for modeling the RC beams:

1. Both concrete and steel are isotropic.
2. Enough bond strength exists at the reinforcement and concrete interface.

Both concrete and all supporting and loading steel plates are modeled with the Solid65 element. Solid65 is an 8-node three-dimensional element having three translational degrees of freedom at each node. All reinforcing steels and wire mesh are discretized with two Link8 element. Link8 has two nodes and three translation degrees of freedom at each node. Figure 2 shows the geometry of Solid65 and Link8 elements [9]. Figure 3a, b, and c show the FE model for longitudinal and transverse reinforcement in CB, CB-1, and CB-2, respectively. Figure 3d shows the boundary conditions and position of the vertical load on the beam. The bottom steel plate's support condition is considered a hinge at one end and roller at the opposite end that allows rotation. At the connection, both reinforcing steel and concrete share a common node. Total vertical loads are halved and applied at one-third and two-thirds points, as shown in Fig. 3d. The response of the analyzed beam is obtained through an incremental nonlinear static analysis.

(a) 3-D Solid65   (b) Link180

Fig. 2 Element geometry

(a) Longitudinal and shear reinforcement in CB   (b) Longitudinal and shear reinforcement in CB-1

(c) Longitudinal and shear reinforcement in CB-2   (d) Loading and boundary conditions
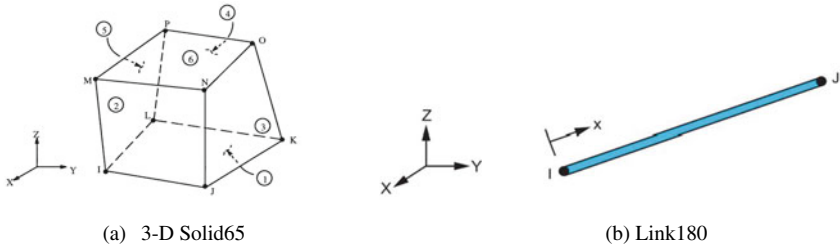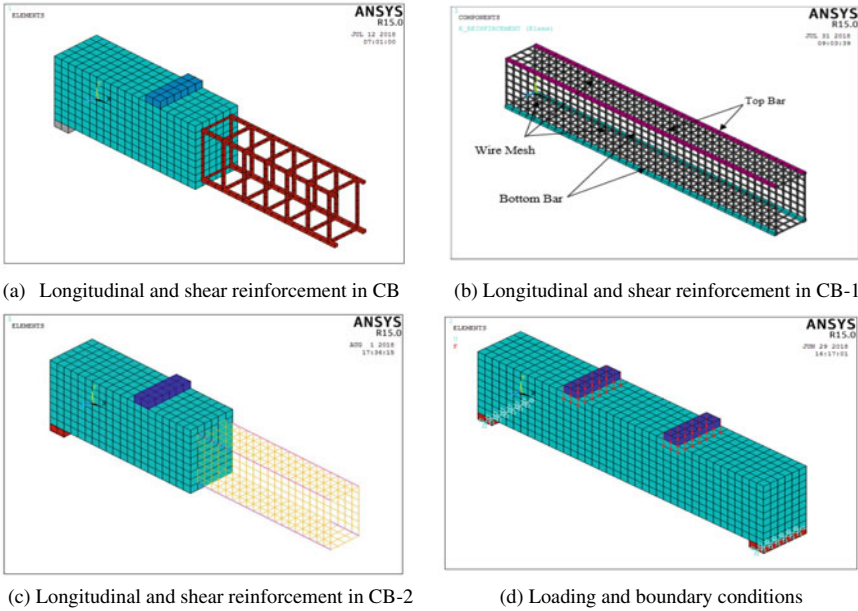
Fig. 3 FE models of analyzed beam

3 FE Model Verification

The FE models are verified with the past experimental results [10]. Two beams, one reinforced with longitudinal and shear reinforcement (CB) and another with longitudinal and shear reinforcement addition to ferrocement (FRB-1), are tested. Figure 4a shows the flexural test conducted using a universal testing machine of structural engineering laboratory, CUET. One deflection gauge at mid-span and the other two just below that third-point loading is used to estimate those respective points' deflection. For verification purposes, only mid-span deflection is considered. Figure 4b shows the deformed shape of the CB obtained from the FE analysis. The deformed shape of the tested beam is difficult to observe since displacement

(a) Flexural test [10] (b) Deflection from FE model
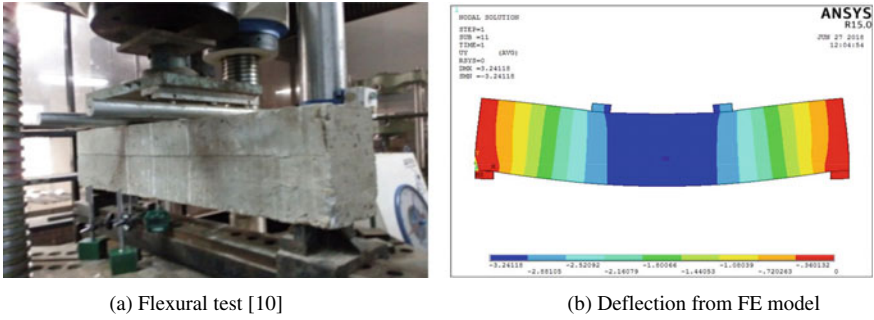
Fig. 4 Deflection from experiment and FE analysis

is minimal. Figure 5 shows a comparison of the load-deformation relation between tested beams [10] and FE analysis results. It shows that flexural failure anticipated in the experimented beam, CB at 120 kN with a mid-span deflection of 4.70 mm. The FRB-1 fails at 160 kN experiences a deflection of 4.60 mm. The corresponding values for the same beam obtained from the FE analysis are 130 kN and 3.4 mm for CB, 165 kN, and 3.25 mm for FRB-1. Therefore, the ultimate load obtained from FE analysis is 6.25% larger than that of the experimental result. Similarly, under the same vertical load level, the tested beams show 29.35% higher displacement than the FE analysis result. The fabrication, quality control, and testing facilities might be the possible reason for such a higher value. Therefore, the FE model is considered to be suitable for the prediction of flexural response.
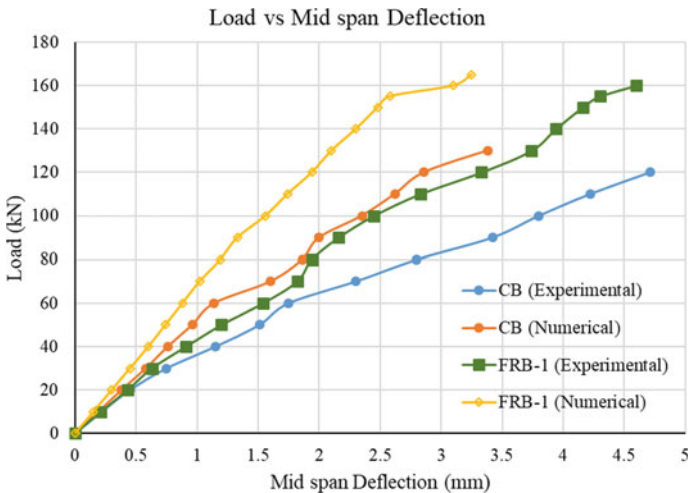
Fig. 5 Load-deflection relationships of verified beams
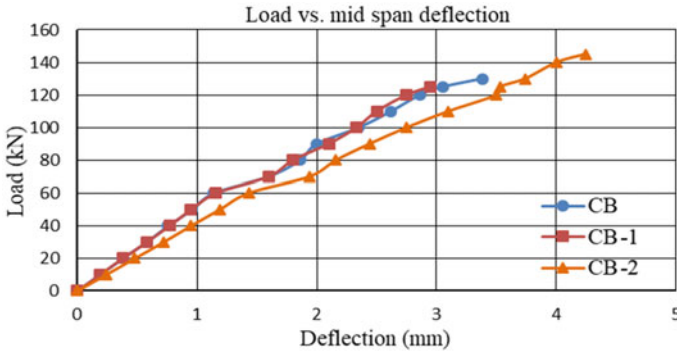
Fig. 6 Load–deflection relationships for different beam models

4 Result and Discussion

4.1 Load–Deflection Relationship

The load–deflection relationships obtained from the FE analysis for CB, CB-1, and CB-2 beams are shown in Fig. 6. Here, the displacement of the beams means the vertical displacement of the bottom surface at the mid-span location. It shows that both CB and CB-1 beams exhibit almost the same displacement under an equal magnitude of incremental vertical load. Both CB and CB-1 are reinforced with an equal amount of longitudinal reinforcement except for the shear reinforcement. An equivalent amount of ferrocement replaces shear reinforcement in CB-1. Both displacement and the ultimate load capacity of beam CB-2 are increased by 25 and 10% when an equivalent amount of ferrocement replaces main reinforcement and shear reinforcement. Therefore, a beam reinforced with ferrocement increases the ductility of the beam and performance under flexural load.

4.2 Concrete Stress

Figure 7 shows the in-service compressive stress at the mid-span and the top surface of the beams. Compressive stress shows a similar relationship to a load–displacement relationship. It shows that the induced compressive stress in CB and CB-1 is equal in magnitude, whereas CB-2 exhibits stress about two times of CB or CB-1. It was observed that both CB and CB-1 sustain 5.9 MPa compressions or 125 kN yield loads at the flexural failure level. Figure 8 represents the tensile stress at the mid-span bottom surface of the beams. It shows that the beam reinforced with ferrocement improves the tensile capacity. All beams remain elastic until the first crack generation, and the first crack develops at 60 kN vertical load. After the first crack initiation,
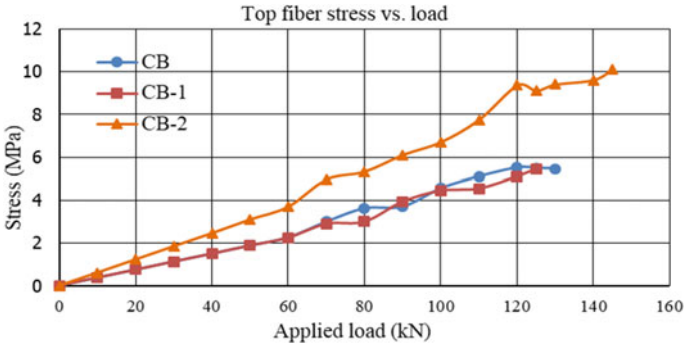
Fig. 7 Top fiber stress in different beams
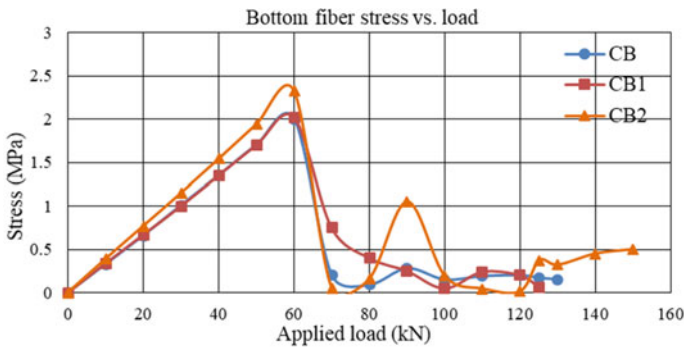
Fig. 8 Bottom fiber stress in different beams

tensile stress dropped significantly to zero, and for further increases in vertical load, there is no significant change in tensile stress.

5 Conclusions

The flexural behavior of concrete beams reinforced with conventional steel rebars is studied using the FE method. The same beam partially or fully reinforced with ferrocement is also studied to investigate its feasibility. For this purpose, the FE model is verified with past experimental results. The beams' flexural behaviors furnished with ferrocement are evaluated in terms of vertical load–displacement relationship and working stress in concrete. From the FE analysis result, the following conclusions can be drawn:

- The beam reinforced with ferrocement shows superior performance compared to the steel-reinforced concrete beam. The ultimate load capacity of a ferrocement beam is about 11.5% more than that of a steel-reinforced concrete beam.
- Both vertical displacement and working stress at anticipated failure are higher than that of the steel-reinforced concrete beam. The ferrocement beam shows higher ductility than the steel-reinforced concrete beam.
- The first crack initiating load is not affected by reinforcement type and generates at the same loading magnitude.

References

1. Andrews G, Sharma AK (1998) Repaired reinforced concrete beams. ACI Concr Int 47–50
2. Janney JR (1954) Nature of bond in pre-tensioned prestressed concrete. J ACI Proc 50(5):717–736
3. Kaushik SK, Dubey AK (1994) Performance evaluation of RC ferrocement composite beams. Proceedings of Fifth International Symposium, UMIST, International Journal of Engineering 2(1):240–256
4. Neha S, Malipatil M (2014) Parametric study on reinforced concrete beam using ANSYS. Civ Environ Res 6(8):88–94
5. Faherty KF (1972) An analysis of a reinforced and a prestressed concrete beam by finite element method. Doctorate's Thesis, University of Iowa, Iowa City
6. Sowmya E, Venkatasubramani R (2017) Numerical study of wire mesh orientation on retrofitted RC beams using ferrocement jacketing. Int Res J Eng Technol (IRJET) 4(11):1471–1475
7. Wolanski AJ (2004) Flexural behavior of reinforced and prestressed concrete beams using finite element analysis. Master's Thesis, Marquette University
8. Tjitradi D, Eliatun E, Taufik S (2017) 3D ANSYS numerical modeling of reinforced concrete beam behavior under different collapsed mechanisms. Int J Mech Appl 7(1):14–23. https://doi.org/10.5923/j.mechanics.20170701.02
9. ANSYS Inc (2013) Release 15.0 documentation, theory references
10. Niloy SH, Islam MM (2017) Flexural behavior of reinforced concrete beams retrofitted with ferrocement. Bachelor's Thesis, Chittagong University of Engineering and Technology, Chittagong, Bangladesh

Effect of Pre-curing on Strength Development of Brick Aggregate Concrete in Sea Water Environment

M. T. Alam, M. S. Islam, and M. M. Islam

1 Introduction

Concrete has been used as a construction material since past century and is becoming a vital issue for the scientists and technologists to evaluate its effective use in normal as well as aggressive environments [1]. The review of literature reveals that if designed properly, structural concrete made with cement as binding material and stone chips as coarse aggregates shows adequate durability characteristics even in aggressive environments including marine environment [1, 2].

In most of the developed countries, concrete is made from crushed stone chips of required size as coarse aggregate together with other component materials including cement and river sand. In developing countries like Bangladesh, broken brick bats known as khoa is generally used as coarse aggregate in concrete due to the higher cost or non-availability of stone chips. It has been found that concrete made with well burnt brick aggregate, it is possible, to achieve high strength concrete [3]. Research also showed that only 7% strength is reduced if crushed brick is used as coarse aggregate in concrete in place of natural aggregate [4].

Durability becomes an important factor for structural concrete exposed to marine environment [5]. Although in general sense, marine environment indicates the environment surrounded by the seawater, the complexities inherent in such an environment are not usually clear. It is not just over the sea, rather extent over the coast, the neighborhood of tidal cracks, back water and estuaries [6]. Inland RC structures exposed to seawater environment are often reported to be deteriorated due to either

M. T. Alam (✉) · M. S. Islam · M. M. Islam
Department of Civil Engineering, CUET, Chittagong, Bangladesh
e-mail: tareq@cuet.ac.bd

M. S. Islam
e-mail: msislam@cuet.ac.bd

M. M. Islam
e-mail: mislamq@cuet.ac.bd

degradation of concrete or corrosion of rebar or both effects [7]. Also, in coastal areas and other adjacent places, the ground water and soil contain an excess amount of aggressive chemicals such as chloride, sulfate, etc. So prior to the construction of any R.C Structure in such location, proper steps regarding the selection of construction material and techniques should be taken to reduce the risk of deterioration of structural concrete owing to the adverse effect of aggressive salt ions.

Most of the existing literatures cover laboratory as well as field investigation regarding the performance/durability of concrete made of crushed stone in different marine environment [8]. But, information of brick aggregate concrete exposed to similar environment is very rare. On the other hand, the physical and chemical characteristics of stone chips are not same as that of brick aggregates. Thus, it is very much essential to conduct in depth study regarding the performance of brick aggregate concrete in marine environment. The present study may be helpful to assess the suitability of locally available brick bats as a useful component of structural concrete for marine construction.

The purpose of this study is to investigate the compressive strength behavior of brick aggregate concrete in marine environment. However, the specific objectives are (i) to observe the strength developments and (ii) effect of pre-curing on strength behavior of brick aggregate in artificially created sea water of different concentration, simulating the marine environment condition.

2 Characteristic Features of Marine Environment

Concrete when placed in marine environment are always subjected to aggressive loading over their entire life. So, it is necessary to understand the characteristics of seas, the various aggressive agents, their nature, intensity of attack, its different detrimental zones, etc., in order to get satisfactory performance of marine structures. Apart from the influence of temperature and pressure, the density of seawater is governed primarily by its salinity [9]. Salinity of seawater for an open sea is generally found to be about 3.5% [10]. Different factors such as evaporation and precipitation, inflow of rivers, melting of polar ice are responsible for the variation of salinity over the ocean surface. [9].

All atmospheric gasses are found in the sea [11]. Among these gasses, Nitrogen, Oxygen, and Carbon dioxide are important in the life of marine plants and animals because of their physiological importance. Nitrogen, Oxygen, and Carbon dioxide vary from about 8 to 18 ml/l of water, 5 to 10 ml/l of water, and 35 to 60 ml/l of water, respectively. Besides its physiological action, Oxygen plays an important role in rebar corrosion process.

Deterioration of concrete in marine environment varies depending on the tidal range, nature, extent, and mechanism of deterioration process. Based on these factors, concrete exposed to a sea water environment can be subdivided into different zones, namely (i) atmospheric zone (ii) Spalsh Zone (iii) Tidal Zone, and (iv) Submerged zone. Of them Spalsh zone is the most critical for structural concrete due to continuous
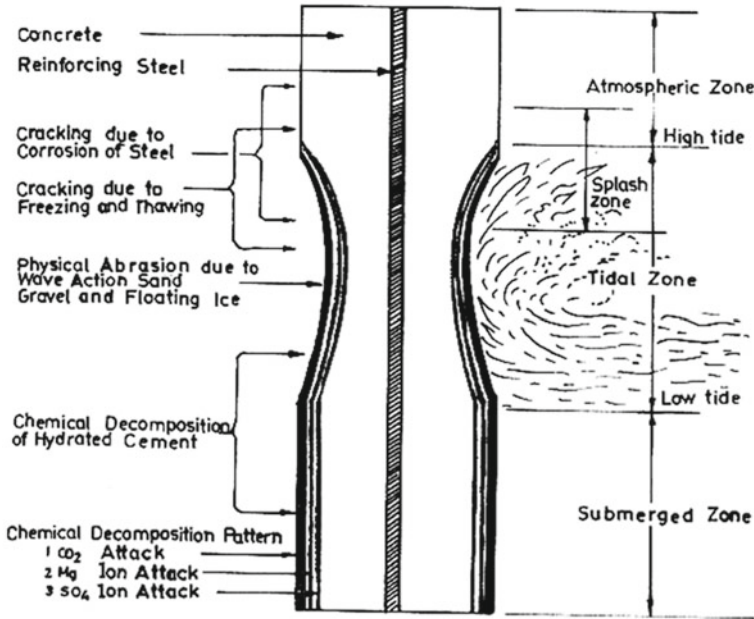
Fig. 1 Deterioration of brick aggregate in sea water environment

contact with highly aerated sea water, erosive effect of salt water spray, and wave action (Ross 1988). The second most critical zone is tidal zone where the structure experience alternate wetting–drying cycle in sea water that leads to buildup of salt ion in structural concrete causing structural distress. In atmospheric zone, ambient air is saturated with heavy moisture and contains substantial amounts of salts and gases [12], whereas submerged zone is considered as lowest corrosive one due to non-availability of harmful gases O_2, CO_2, etc., although large hydrostatic pressure causes rapid penetration of harmful salt solutions within concrete. Figure 1 explains the deterioration process of structural concrete in marine environment.

3   Sea Salt Action on Hardened Concrete

Chloride can be introduced inside the concrete in two ways (i) through the mixing as contaminates and (ii) as a result of post setting exposure to sea water, the compounds of chloride form the highest proportion, i.e., 88 to 89% of the total dissolved salts present in sea water. Regarding ionic composition, it provides about 55% of the total salt ion concentration, and Chloride ions may attack concrete in different forms. Mainly its form expansive product named Friedl's salt, Calcium chloroaluminate $3CaO.Al_2O_3.CaCl_2.10H_2O$, which initiates cracks in the concrete. Besides excessive formation of calcium chloride, which may leach out, results in formation of voids

in concrete. These voids increase permeability of concrete. The process of chloride attack on concrete may be explained by the following series of chemical reaction:

$$Ca(OH)_2 + NaCl \rightarrow CaCl_2 + 2NaOH$$

$$CaCl_2 + 3CaO.Al_2O_3 + 10.H_2O \rightarrow 3CaO.Al_2O_3.CaCl_2.10H_2O$$
(Calcium ChloroAlumnate or Friedls Salt)

$$Ca(OH)_2 + MgCl_2 \rightarrow CaCl_2 + Mg(OH)_2$$
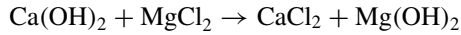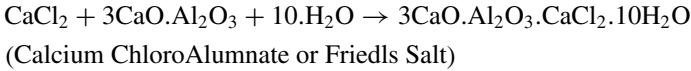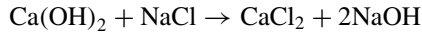
According to Mehta [5], $MgCl_2$ reacting with $Ca(OH)_2$ of hydrated cement paste form Calcium chloride, which being soluble gets leached out leading material loss and weakening.

Sulfate in the SW environment exist in various salts such as magnesium sulfate, calcium sulfate, and Potassium sulfate. The sulfate attack is generally attributed to formation of expansive Ettringite ($3CaO.Al_2O_3.3CaSO_4.31 H_2O$) (Calcium aluminate sulfate). Crystallization of both Ettringite and Gypsum induce stresses inside the concrete may result in the surface cracking known as softening type of attack.

The process of sulfate attack on concrete may be explained by the following series of chemical reactions:

$$2(3CaO.Al_2O_3.12H_2O) + 3(MgSO_4.7H_2O)$$
$$\rightarrow CaO.Al_2O_3.3CaSO_4.31H_2O + Al(OH)_3$$
$$+ 3Mg(OH)_2 + 8Mg(OH)_2$$
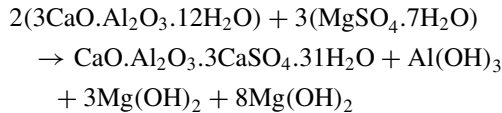
Magnesium sulfate also reacts with $Ca(OH)_2$ and yields $CaSO_4.2H_2O$ which is turn reacts with calcium aluminates hydrate to form additional calcium aluminates sulfate hydrate (Ettringite) as below:

$$Ca(OH)_2 + MgSO_4.7H_2O \rightarrow CaSO_4.2H_2O + Mg(OH)_2 + 2H_2O$$

$$2(3CaO.Al_2O_3.12H_2O) + 3CaSO_4.2H_2O + 13H_2O$$
$$\rightarrow CaO.Al_2O_3.3CaSO_4.31H_2O(Ettringite)$$
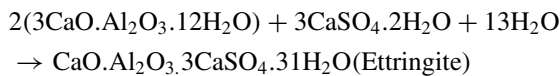
4 Experimental Program

The experimental program was carried out to study the effect of pre-curing on the compressive strength behavior of brick aggregate concrete both in plain water (PW) and artificial sea water (SW) of different concentration. The variable parameters studied and the materials involved were as follows:

Table 1 Physical properties of fine and coarse aggregate

	CA	FA
Specific Gravity	2.21	2.59
Unit Weight(kg/m^3)	1420	1540
Fineness Modulus	–	2.57
Absorption Capacity(%)	8.38	1.2

4.1 Materials

(a) **Cement:** Ordinary Portland Cement (OPC) Type-1, conforming to ASTM C-150 was used as binding material.
(b) **Aggregate**: Brick chips from crushed clay brick with a maximum nominal size of 20 mm was used as coarse aggregate. Natural sand passing through 4.75 mm sieve and retained on 0.075 mm sieve collected from local area was used as fine aggregate. The grading of the aggregates and its physical properties is given in Table 1.
(c) **Sea salt:** Laboratory grade chemicals/salts as per composition of seawater were collected for creating artificial marine environment.

4.2 Variable Studied

(a) **Curing environment:** Both plain water (PW) as well as artificially made sea water (SW) was used for curing the test specimen. Concentrations of artificially made sea water were 1 T, 3 T, and 5 T, respectively. 1 T sea water was made by mixing plane water with exact amount and proportion of principal salts found in natural sea water (Table 2). Thus, 3 T, 5 T will have salt concentration enhanced to 3 and 5 times as for normal sea water. The enhanced concentrations were used to study accelerated effects of marine environment.
(b) **Concrete Grade:** Three different grades of concrete, namely concrete M33, concrete M27, and concrete M21 were designed and cast as per standard code

Table 2 Specified salt contents of artificial seawater used in experimental program/lit

Salt	Amount (gm)
Sodium chloride	27.2
Magnesium chloride	3.8
Magnesium sulfate	1.7
Calcium sulfate	1.2
Potassium sulfate	0.9
Calcium carbonate	0.1
Magnesium bromide	0.1
Total	**35**

Table 3 Mix proportions of concrete

Constituent and properties	Concrete A (M34)	Concrete B (M27)	Concrete C (M21)
Cement (kg/m^3)	500	480	435
Water (kg/m^3)	220	226	220
Sand (kg/m^3)	520	530	545
Brick Chips (kg/m^3)	1120	1130	1150
water/cement Ratio	0.44	0.47	0.5
Slump (mm)	60	64	68

of practice. Table 3 shows the design mix proportion of different grades of concrete. M33 means concrete having 28 days average concrete strength of 33 MPa. Similarly, M27 and M21 concrete were designed to have strength 27 MPa and 21 MPa, respectively.

(c) **Exposure period/State:** Test specimens were tested periodically after the specified curing periods of 1, 3, 6, and 9 months in PW, 1 T, 3 T, and 5 T sea water environments under submerged (SUB) state of exposure.

(d) **Size of specimens:** 100 mm cubical specimens were designed and casted as per ASTM standard.

A total of 1152 no specimens were cast in the laboratory. After casting, the specimens were kept at 27^0C temperature and 90% relative humidity for 24 h. After demolding, all the specimens were pre-cured in PW for 0,7,14, and 28 days at room temperature. After pre-curing, the specimens were kept in tanks containing PW, 1, 3, and 5 T sea water under SUB state for different exposure periods. Figure 2 shows the curing arrangement of specimens in artificial seawater under SUB state of exposure.

Fig. 2 Submerged state curing arrangement in artificial sea water of different concentration

5 Results and Discussion

As stated in the experimental program, the test specimens after specific curing periods were tested for compressive strength. The average of the three test results was considered as representative value for each strength test case. However, all the test results are presented in Figs. 3, 4, 5, 6, 7, and 8. Figure 3 represents the compressive strength values of concrete A specimens pre-cured in PW water for different periods (1, 7, 14 & 28 days) and exposed to SUB state in SW of different concentrations (1 T, 3 T & 5 T) over the exposure periods of 1, 3, 6, and 9 months. Similarly, Figs. 4 and 5 represent the corresponding strength values for concrete B and concrete C, respectively. Moreover in each figure, the strength values are expressed as relative strengths (%) of PW cured specimens to get the clear idea about the strength development of specimens in PW as well as SW of different concentrations. Relative strength of all specimens has been calculated with respect to the corresponding strength of PW cured specimens and shown in Figs. 6, 7, and 8.

From the figures, it is seen that in PW environment, all the specimens show the continuous gain in strength with exposure times, and the rate of gain in strength is higher in early stages. With the increase in time, the strength gaining slows down. In SW environment, similar trend of strength gaining also observed but rate of strength gaining is lower. Particularly in case of lower grade concrete (concrete C) exposed to 5 T SW environment, strength deteriorations starts after 6 months of exposure. For higher grade concrete (concrete A), the strength gaining from 6 to 9 months is very marginal which indicates the sign of strength deterioration after longer curing

Fig. 3 Compressive strength of brick aggregate concrete **A** in SW environment
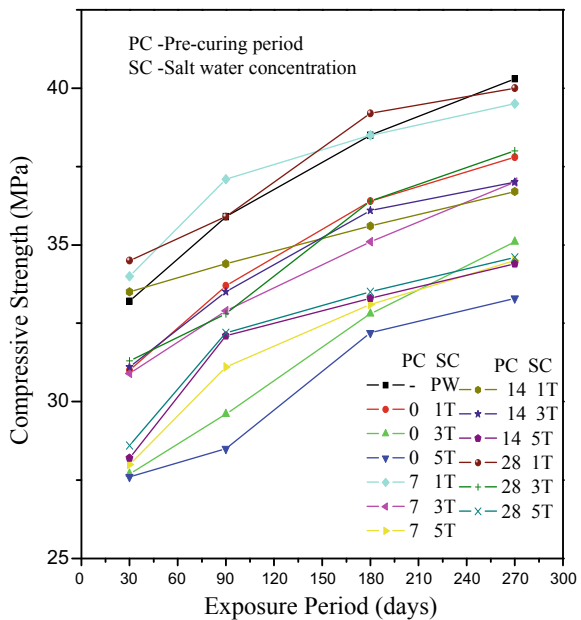
Fig. 4 Compressive strength
of brick aggregate concrete
B in SW environment
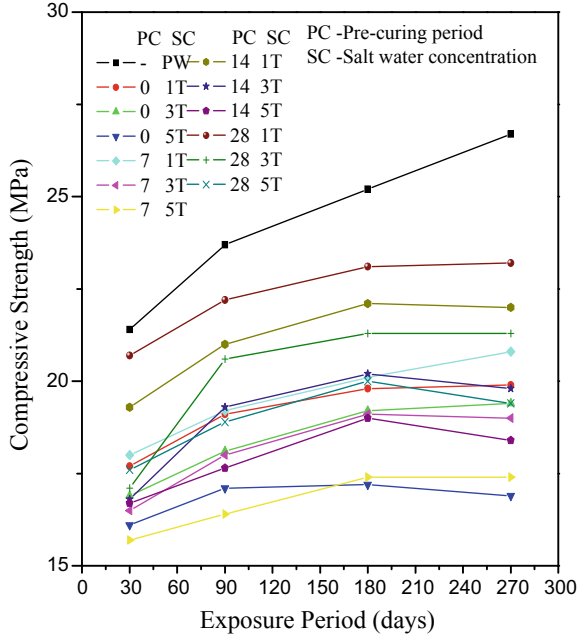
Fig. 5 Compressive strength
of brick aggregate concrete
C in SW environment
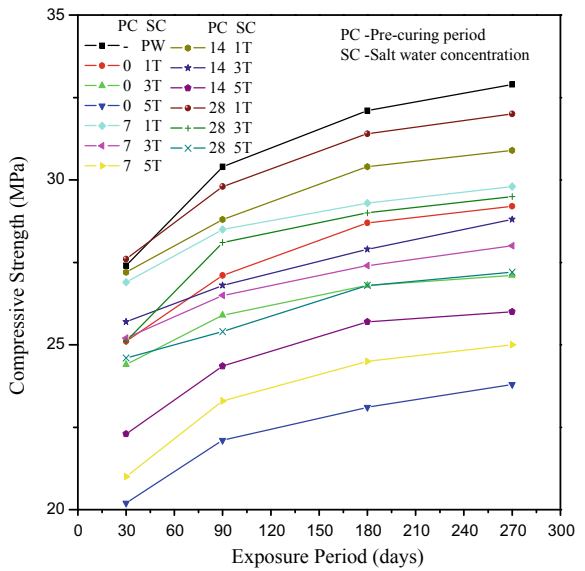
Fig. 6 Relative Strength of brick aggregate concrete **A** in SW environment
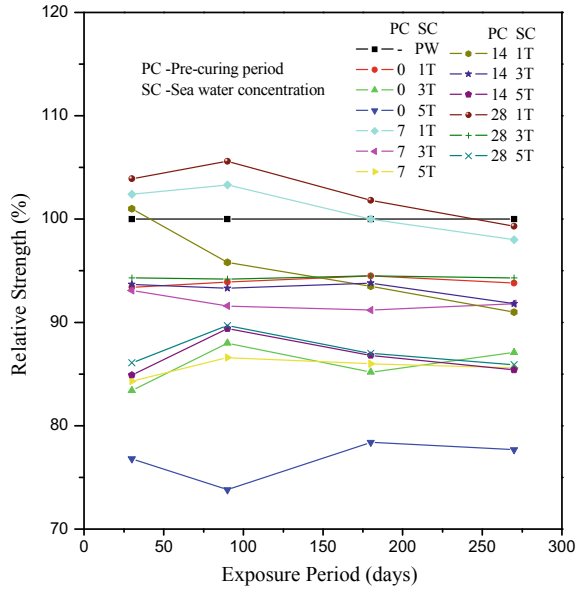
Fig. 7 Relative Strength of brick aggregate concrete **B** in SW environment
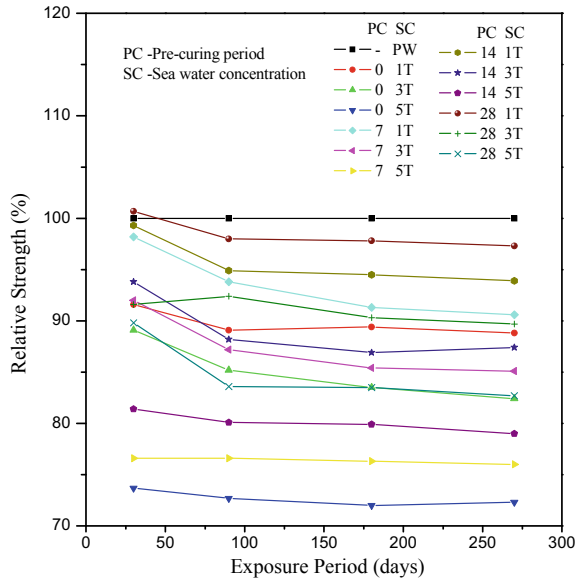
periods. However, as compared to PW environment, all the specimens suffer loss in strength in SW environment. As the concentrations of curing solution increases, the loss in strength also increases although not at proportional rate. From the figures, it is seen that, for concrete A in SUB state and 9mexposure period, the strength

deterioration of the specimen vary from 3.0 to 6.2%, 8.2 to 12.9%, and 14.1 to 20.0% in IT, 3 T, and 5 T SW environment, respectively. The corresponding value for concrete B varies from 5.8 to 13.7%, 10.3 to 17.6% and 17.3 to 27.73% and for concrete C from 13.1 to 25.5%, 21.1 to 27.3% and 23.3 to 43.7%, respectively.

From these figures, it is observed that as expected, the maximum strength deteriorations occur for lower grade concrete specimens (concrete C) and in enhanced SW environments (5 T, SW). In 1 T concentration, few specimens show higher strength than PW environment particularly for higher concrete A, under SUB condition. However, comparison of the strength data reveals that higher grade concrete shows around 22 to 50% lower strength deterioration than lower grade concrete B & C. Possible causes of strength reduction are the formation of expansive as well as leachable compounds when concrete specimens are cured in sea water. When concrete exposed to marine environment, sea water enters into concrete and reacts with hydrated cement product to form *Ettringite* and *Frields* salt. These salts which are expansive in nature induce stresses in the concrete and create micro-cracks inside the concrete. These cracks weaken the bond between hydrated products and aggregate. Besides concrete become porous gradually due to leaching action of the newly formed compounds. Thus, the concrete is deteriorated and loss in compressive strength of concrete occurs.

Pre-curing in PW before exposure to SW shows significant effect on strength development of concrete specimens. Four pre-curing periods of 0, 7, 14, and 28 days have been considered in the study. From the observed data, it is seen that with the increase of pre-curing period, the strength gaining of specimens increase, i.e., strength loss decreases. Particularly specimens without pre-curing in PW, suffer

maximum strength loss as compared to pre-cured specimens. Again after 14 days pre-curing in PW, the effect of pre-curing regarding strength deterioration is found to be insignificant. For example, after 9 months exposure in 5 T solutions, the strength deterioration values of non-pre-cured concrete specimens vary in the range of 17.0 to 25.0%, 28 to 35.0%, and 43.0 to 48.0%, respectively, for Concrete A, B & C respectively. Whereas the corresponding values for 7 to 28 days pre-cured specimens vary from 14 to 20% for concrete A, 21 to 31% for concrete B, and 27 to 43% for concrete C. From this discussion, it is seen that non-cured specimens suffer 18 to 30% higher strength deterioration than pre-cured specimens in SW environments.

6 Conclusions

The result of investigation conducted on different brick aggregate concrete specimens exposed to seawater of various concentrations for varying period up to 9 month have been presented in this paper. Conclusions drawn based on these results are summarized below. These results may provide some guidelines regarding the use of brick aggregate in marine concrete structure.

I. Concrete specimens lose its compressive strength with time when exposed to seawater environment as compared to the plain water environment. It increases with the increase of the salt concentration of curing environment although the rate of increase was not found to be proportional.

II. Gain in compressive strength of high grade concrete specimens exposed to sea water environment is observed to be higher in initial stages then become slower for longer expose period. Lower grade concrete specimens also show similar behavior in early stage but suffer reduction in gain in strength at later periods.

III. The effect of pre-curing of specimens with plain water is seen to play an important role in strength development of concrete in seawater. At least 14 days pre-curing in PW is found effective in marine environment. Concrete specimens directly exposed to sea water without pre-curing suffer 18 to 30% higher strength deterioration than pre-cured concrete specimens.

IV. Higher grade concrete A showed better strength performance than the lower grade concrete B and C. Concrete A specimens showed 22 to 50% lower strength deterioration than the concrete B & C specimens.

References

1. Mohammad TU, Yamaji T, Hamadi H (2002) Chloride diffusion, microstructure and mineralogy of concrete after 15 years of exposure in tidal environment, ACI Mater. J. 99(3):256–263
2. Mohammad TU, Yamaji T, Hamadi H (2003) Corrosion of steel bars in cracked concrete under marine environment. J Mater Civ Eng ASCE 15(5):460–469

3. Akhtaruzzaman AA, Hasnat A (1983) Properties of concrete using crushed brick as aggregate. ACI Concr Int Des Constr 5(2):58–63
4. Khaloo AR (1994) Properties of concrete using crushed clinker brick as coarse aggregate. ACI Mater J 91(2):401–407
5. Mehta PK (1980) Durability of concrete in marine environment—a review. In: Performance of concrete in marine environment, ACI Pub., SP-65, pp 1–20
6. Geymayr GW (1980) Repair of concrete in marine environment. In: Performance of concrete in marine environment, ACI Pub., SP-65, pp 527–556
7. Raina VK (1988) Deterioration and durability of concrte, chapter-3, Concrete for construction, facts and practice. Tata McGraw Hill Pub. Co.Ltd., New Delhi, pp 114–141
8. Bouzoubaa N, Zhang MH, Malhotra VM (2001) Mechanical properties and durability of concrete made with high volume fly ash blended cements using coarse fly ash. Cem Concr Res 31. 1993-1402
9. Marshall AL (1990) The marine environment. Marine Concrete, Van Nostrand Reinhold, New York, pp 8–51
10. Biczok I (1972) Concrete corrosion, concrete protection. Akademiai Kiado, Budapest
11. Patel MH (1989) The ocean environment. Dynamics of offshore structures, Butterworth & Co. Ltd., pp 38–73
12. Patil BT (1981) Investigation on corrosion of steel and deterioration of concrete structures under marine condition. INCOE81, Madras, pp V7-V11

Early Age and Long-term Mechanical Performance of Mortars Incorporating High-volume GGBS

A. A. Shubbar, M. S. Nasr, G. M. Sadiqul Islam, Z. S. Al-Khafaji, M. Sadique, K. Hashim, and L. N. Assi

1 Introduction

Environmental pollution as a result of greenhouse gas emissions from various industries has become an important issue that concerns scientists around the world in recent decades. What exacerbated these emissions is the increasing population growth and, thus, the increase in industrial requirements, including the construction sector. One of the most important elements of construction sector is concrete [1]. Concrete consists

A. A. Shubbar (✉) · M. Sadique · K. Hashim
Department of Civil Engineering, Liverpool John Moores University, Liverpool L3 2ET, UK
e-mail: a.a.shubbar@ljmu.ac.uk

M. Sadique
e-mail: M.M.Sadique@ljmu.ac.uk

K. Hashim
e-mail: K.S.Hashim@ljmu.ac.uk

M. S. Nasr
Technical Institute of Babylon, Al-Furat Al-Awsat Technical University (ATU), Babylon, Iraq
e-mail: mohammed.nasr@atu.edu.iq

G. M. S. Islam
Department of Civil Engineering, Chittagong University of Engineering & Technology (CUET), Chattogram 4349, Bangladesh
e-mail: gmsislam@cuet.ac.bd

Z. S. Al-Khafaji
Ministry of Oil, Al-Furrat Al-Awsat Distribution Foundation, Babylon, Iraq

Department of Building and Construction Technical Engineering, College of Technical Engineering, The Islamic University, 54001 Najaf, Iraq

L. N. Assi
Department of Civil and Environ. Engineering, University of South Carolina, 300 Main Street, Columbia, SC B12729208, USA
e-mail: lassi@email.sc.edu

of cement, aggregates, and water. Traditionally, cement is considered as prime binder in concrete. The annual world cement production in 2018 was 4.1 Giga tons, which resulted emission of considerable greenhouse gas into the atmosphere. The cement industry ranks third, after the road sector and power generation, in terms of greenhouse gas emissions [2, 3]. Cement industry is liable for 7% global annual carbon dioxide production [4, 5]. As a result, the concrete researchers gave impetus on the use of supplementary cementitious materials (SCM) as well as waste materials including silica fume [6], fly ash, metakaolin, rice husk ash [7], cement kiln dust, waste papers, and ground granulated blast furnace slag (GGBS) as one of the solutions to reduce this environmental impact. Recycling of solid waste/by-products from various industries has also become an issue worthy of attention for scientists due to their potential environmental damage [8, 9]. GGBS is a by-product of making iron or steel, which is extracted from the blast furnace in water or steam where it is dried and converted into granules and then into powder by grinding it in a ball mill [10].

GGBS was used in concrete as a partial substitute for cement due to its latent hydraulic properties. In addition, the pozzolanic reaction improves the fresh and durability properties of concrete [11]. Cakır and Akoz [12] reported that using GGBS in proportions of 30 and 60% as substitution of cement within the ages 7–180 days reduced the compressive strength compared to the control mix. However, the durability against the aggressive solutions and water of GGBS-based mixtures was enhanced as a result of decreasing the capillary and porosity. Shariq et al. [13] studied compressive strength development of concrete with and without GGBS for the period 3–180 days. It was found that 40% GGBS incorporation increased the compressive strength on 56 days and beyond, while the 60% GGBS strength was lower than that for 40% GGBS. Zhao et al. [14] replaced cement with 20, 30, and 40% GGBS in self-compacting concrete (SCC). The SCC was tested up to 90 days, and it was found that GGBS-based SCC reduced the mechanical properties at early age compared to the control SCC; however, the reduction rate became insignificant at later ages. Study investigated the performance of concrete incorporated recycled aggregate and GGBS in proportions of 0, 40, and 60% at the ages 28, 90, and 180 days. Results showed that the compressive strength at early and later ages was reduced, while the durability characteristics were improved with the increase of GGBS content [11].

According to the above, very limited studies addressed the high volume fraction of GGBS at ages beyond one year. Thus, this study aims to explore the performance of mortar made with GGBS up to 70% as replacement of cement at 1, 2, 3, 7, 14, 21, 28, 56, 90, and 550-day age.

2   Materials and Methods

Type CEM-II/A/LL 32.5-N cement, GGBS, and natural sand were used to prepare mortar mixtures for this study. Cement and GGBS were obtained from CEMEX Company ltd., Warwickshire, UK and Hanson Heidelberg Cement Group, UK,

Table 1 Chemical composition of cement and GGBS

Item	PC	GGBS
CaO (%)	65.2	42.5
SiO$_2$ (%)	24.6	41.1
Al$_2$O$_3$ (%)	1.7	5.1
Fe$_2$O$_3$ (%)	1.6	-
MgO (%)	1.3	4.3
Na$_2$O (%)	1.3	3.1
K$_2$O (%)	0.8	0.7
SO$_3$ (%)	2.6	1.3
TiO$_2$ (%)	-	1.0
LOI (%)	0.3	0.4
pH	12.7	11.02
Specific gravity	2.98	2.80

respectively. Shimadzu EDX-720 energy dispersive X-ray florescence spectrometer (EDXRF) was used to analyze the chemical composition of cement and GGBS as shown in Table 1. The specific surface area of the cement and GGBS was 29,561, and 39,671 cm^2/ml, respectively, which was obtained using a Quantasorb NOVA 2000 Brunauer, Emmett and Teller (BET) analyzer.

Four combinations were prepared for this study. The control mixture (cement only) and three other mixtures replaced cement with GGBS in the range of 30–70% (by weight). Fixed sand/binder (S/B) and water/binder (W/B) of 2.5 and 0.4, respectively, was used for all mixtures. The details of mortars are presented in Table 2. The performance of high volume fraction of GGBS in mortars was evaluated through laboratory tests including initial and final setting times, compressive strength, and ultrasonic pulse velocity test. Vicat apparatus was used to measure the setting time according to BS EN 196–3 [15]. The compressive strength of mortars was tested according to BS EN 196-1 [16]. Three 40 × 40 × 160 mm prisms were casted to test the compressive strength. These were broken into two halves under a three-point loading and then tested with specified standard compression jigs. Average of the six compressive strength test results was reported at each curing age. BS 1881-203 [17] was followed for conducting the UPV test using 100 × 100 × 100 mm cubes. An average of three specimens was reported as UPV. Both compressive strength and

Table 2 Mix proportions details

Mix	PC (%)	GGBS (%)	S/B	W/B
Control	100	0	2.5	0.4
G30	70	30	2.5	0.4
G50	50	50	2.5	0.4
G70	30	70	2.5	0.4
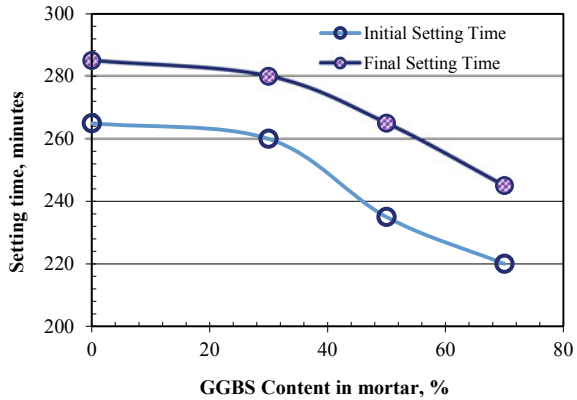
UPV tests were carried out after 1, 3, 7, 14, 21, 28, 56, 90, and 550 days of water curing.

3 Results and Discussions

3.1 Setting Time

The setting time in cement-based materials is influenced by factors including its chemical composition, the ambient temperature, the type and quantity of any admixture used as well as the binder to the water ratio [18]. The initial and final setting times of GGBS-based and control mortars are given in Fig. 1. In general, all mortar samples conformed to the setting time requirements of BS EN 197-1 and the time decreased with increase in GGBS content compared to that for the control mix. These decline rates were increased with the increase of GGBS content in the mixture. The lowest initial and final setting time values were recorded for G70 mixture, which was 220 and 245 min, respectively, compared to 265 and 285 min, for the control sample. This reduction in the setting time can be attributed to the reduction in the available free water content in the mix as a result of incorporating a material (GGBS) with a higher surface area than cement [19].

3.2 Compressive Strength

Improvement of compressive strength of mortars with time is shown in Fig. 2. GGBS incorporated mortars gave lower compressive strength compared to control concrete up to 21 days. With the increase in cement replacement level, the strength was decreased. The hydration rate of GGBS incorporated mortars is slower at early age

Fig. 2 Compressive strength of mortars at the ages 1–550 days
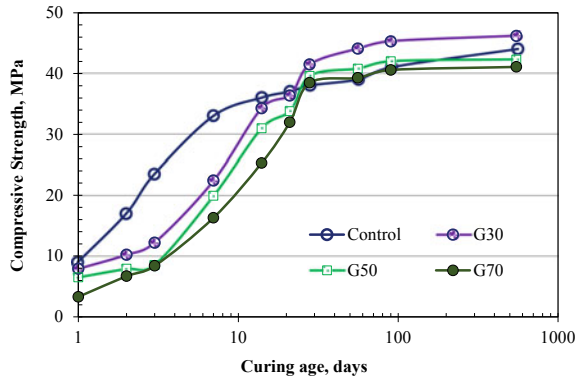
[20]. At and above 28 days, the compressive strength of all mortars was confirmed to the standard requirements (32.5 MPa) and the strength behavior depended on the GGBS content in the mix. The compressive strength of G30 mortar was found to be higher than that of the control mix throughout the ages 28 to 550 days. The improvements were 11, 13, 11, and 4% at 28, 56, 90, and 550 days, respectively. This enhancement is attributed to both the hydraulic and pozzolanic reactions of GGBS with calcium hydroxide, which leads to the formation of additional C-S–H gel, thereby densifying the microstructure by refining the pores within the matrix [21]. The G50 mortar gave improved compressive strength at the ages 28, 56, and 90 days then remains almost similar (4% less) at 550 days.

On the other hand, G70 mortar gave similar strength to control mortar at 28, 56, and 90 days. However, this mixture gave 7% less compressive strength than the control mortar at 550 days. Indeed, no significant improvement in compressive strength of G30, G50, and G70 mortars was obtained beyond 90 days. This may be due to the insufficient amount of $Ca(OH)_2$ available for the pozzolanic reaction of GGBS, or the alumino-silicate minerals of GGBS had been totally reacted with available $Ca(OH)_2$.

3.3 Ultrasonic Pulse Velocity (UPV)

UPV is a non-destructive technique used to predict the strength of a material or to calculate its low-strain modulus of elasticity. This also used to detect inside defects such as cracks, decay, and voids by measuring the velocity of waves traveling through that material [22]. The UPV results of the control and GGBS incorporated mortars are given in Fig. 3.

In general, the results indicated that the presence of GGBS led to a decrease in the UPV values compared to the GGBS-free mixture. Maximum diminishing in UPV results was recorded at one day curing with a shortening of 11, 23 and 36% at replacement proportions of 30%, 50%, and 70%, respectively, from the control

Fig. 3 UPV test results at
1–550 days curing age
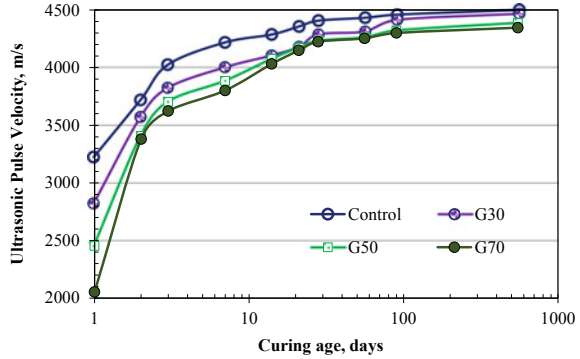
mortar. For the period from 1 to 28 days, it was found that the decrease in the velocity values declined with time.

At 28 days, the UPV values of GGBS incorporated mortar were found to be similar but less than the reference mixture. This behavior is expected because, with continuous curing, the porosity within the matrix will decrease as a result of the formation of hydration products through hydraulic and pozzolanic reactions of GGBS, which finally causes the microstructure to be densified. Furthermore, with increase in cement replacement with GGBS, the velocity generally found to be decreasing. As with the compressive strength test results beyond 28 days, the UPV for a particular mortar mix was found to be similar until 550 days. Figure 4 shows relationship between compressive strength and UPV of all mortars tested in this study. A power relationship was obtained with good correlation. Earlier study found similar correlation between concrete strength and UPV [23].

Fig. 4 Relationship between
UPV and compressive
strength of mortar

$y = 0.1903e^{0.0012x}$
$R^2 = 0.8675$
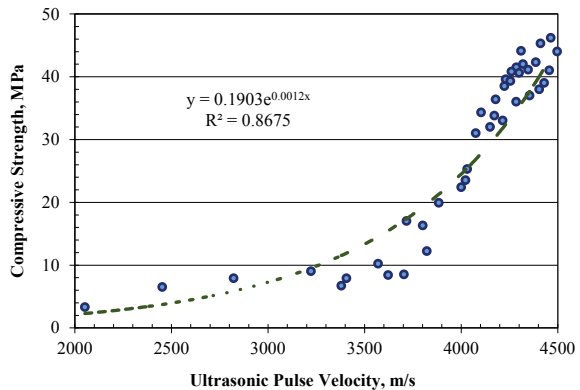
4 Conclusion

1. The substitution of cement with a high volume fraction of GGBS decreased the initial and final setting times. The fineness of composed materials could be a controlling factor.
2. At early ages (up to 21 days), GGBS incorporation reduced the compressive strength for all replacement levels. From 28 to 90 days, the compressive strengths of GGBS incorporated mortars were found to be similar to control mortar. With minor exception, the strength improvement with time for each mortar class was not significant from 90 to 550 days. All strength results conformed to the standard requirement.
3. The UPV values were diminished with GGBS content. As with compressive strength, this was not improved with time from 90 days and beyond.
4. A good power correlation was obtained between the compressive strength and UPV values.
5. In summary, from an environmental viewpoint and depending on the compressive strength and velocity results obtained, all GGBS ratios used can be considered satisfactory despite a slight reduction in strength at 50 and 70% GGBS at the age of 550 days. Thus, an eco-friendly mortar was produced.

References

1. Hasan ZA, Nasr MS, Abed MK (2019) Combined effect of Silica fume, and glass and ceramic waste on properties of high strength mortar reinforced with hybrid fibers. Int Rev Civ Eng 10:267–273. https://doi.org/10.15866/irece.v10i5.16960
2. Shubbar AA, Sadique M, Shanbara HK, Hashim K (2020) The development of a new low carbon binder for construction as an alternative to cement. In: Advances in sustainable construction materials and geotechnical engineering. Springer, pp 205–213
3. McCarthy MJ, Sadiqul Islam GM, Csetenyi LJ, Jones MR (2012) Colorimetric evaluation of admixture adsorption by fly ash for use in air-entrained concrete. Mater Struct Constr. https://doi.org/10.1617/s11527-012-9870-x
4. Shubbar AA, Sadique M, Kot P, Atherton W (2019) Future of clay-based construction materials—a review. Constr Build Mater 210:172–187. https://doi.org/10.1016/J.CONBUILDMAT.2019.03.206
5. Islam GMS, Rahman MH, Kazi N (2017) Waste glass powder as partial replacement of cement for sustainable concrete practice. Int J Sustain Built Environ 6:37–44
6. Abed M, Nasr M, Hasan Z (2018) Effect of silica fume/binder ratio on compressive strength development of reactive powder concrete under two curing systems. In: MATEC Web of conferences. EDP Sciences, p 02022
7. Nayel IH, Burhan SK, Nasr MS (2018) Characterisation of prepared rice husk ash and its effects on strength development in recycled aggregate concrete. In: IOP conference series: materials science and engineering. IOP Publishing, p 12009
8. Nayel IH, Nasr MS, Abdulridha SQ (2020) Impact of elevated temperature on the mechanical properties of cement mortar reinforced with rope waste fibres. In: IOP conference series: materials science and engineering. Institute of Physics Publishing

9. McCarthy MJ, Strompinis N, Csetenyi LJ, Islam GMS (2015) Influence of Portland cement characteristics on air-entrainment in fly ash concrete. Mag Concr Res 67. https://doi.org/10.1680/macr.14.00279

10. Shubbar AAF, Atherton W, Jafer HM, Dulaimi AF, Al-Faluji D (2017) The development of a new cementitious material produced from cement and GGBS. In: The 3rd BUiD doctoral research conference-faculty of engineering and IT. BUiD, pp 51–63

11. Majhi RK, Nayak AN (2019) Bond, durability and microstructural characteristics of ground granulated blast furnace slag based recycled aggregate concrete. Constr Build Mater 212:578–595

12. Çakır Ö, Aköz F (2008) Effect of curing conditions on the mortars with and without GGBFS. Constr Build Mater 22:308–314

13. Shariq M, Prasad J, Masood A (2010) Effect of GGBFS on time dependent compressive strength of concrete. Constr Build Mater 24:1469–1478

14. Zhao H, Sun W, Wu X, Gao B (2015) The properties of the self-compacting concrete with fly ash and ground granulated blast furnace slag mineral admixtures. J Clean Prod 95:66–74

15. BS EN 196-3 (2005) Methods of testing cement. Determination of setting times and soundness. British Standards Institution-BSI and CEN European Committee for Standardization

16. BS EN 196–1 (2005) Methods of testing cement. Determination of strength. British Standards Institution-BSI and CEN European Committee for Standardization

17. BS 1881: Part 203 (1983) Recommendations for measurement of velocity of ultrasonic pulses in concrete. British Standards Institution, UK

18. Chi M (2016) Synthesis and characterization of mortars with circulating fluidized bed combustion fly ash and ground granulated blast-furnace slag. Constr Build Mater 123:565–573

19. Shubbar AA, Al-Jumeily D, Aljaaf AJ, Alyafei M, Sadique M, Mustafina J (2019) Investigating the mechanical and durability performance of cement mortar incorporated modified fly ash and ground granulated blast furnace slag as cement replacement materials. In: 2019 12th International conference on developments in esystems engineering (DeSE). IEEE, pp 434–439

20. Shariq M, Prasad J, Ahuja AK (2008) Strength development of cement mortar and concrete incorporating GGBFS

21. Liu J, Guo R (2019) The microstructures of hardened composite binders containing steel slag and GGBS at 10 years. Constr Build Mater 225:1152–1159. https://doi.org/10.1016/j.conbuildmat.2019.08.026

22. Wang C-C, Wang H-Y (2017) Assessment of the compressive strength of recycled waste LCD glass concrete using the ultrasonic pulse velocity. Constr Build Mater 137:345–353

23. Trtnik G, Kavčič F, Turk G (2009) Prediction of concrete strength using ultrasonic pulse velocity and artificial neural networks. Ultrasonics 49:53–60. https://doi.org/10.1016/j.ultras.2008.05.001

Microbial Technology—A Sustainable Alternative to Improve Concrete Quality

S. N. Priyom, M. M. Islam, M. S. Islam, and W. Shumi

1 Introduction

Concrete is basically an artificial stone and has numerous comparable properties to natural stone. The advantages of concrete are high compressive quality, long assistance life, and great imperviousness to fire, etc. together with some other negative properties. Among them, the principle ones are lower tensile strength and formation of cracks. Experimental studies show that tensile strength of concrete is about eight to ten times lower than its compressive strength.

On the other hand, cracking is an unavoidable property of concrete and occurs due to its brittle nature. It is an indication that the tensile strength has locally been exceeded. Aggressive ions can penetrate through these cracks, corrode the steel reinforcement, and ultimately reduce the life span of structure. Hence, it is necessary to limit maximum crack width by using appropriate empirical formula [1, 2]. In particular, Eurocode 2 suggests that the maximum crack width should be up to 0.4 mm for mild and up to 0.2 mm for aggressive environments, to limit the danger of corrosion. Traditional repair practices could have the lack of compatibility between the repair and concrete substrate. Hence, it is necessary to look for new materials which could have autogenously crack-healing ability.

One of the most studied concepts in this regard is biogenic self-healing concrete. The biogenic self-healing agents, i.e., bacteria with nutrient, are incorporated in

S. N. Priyom (✉) · M. M. Islam · M. S. Islam · W. Shumi
Department of Civil Engineering, CUET, Chittagong, Bangladesh

M. M. Islam
e-mail: mislam@cuet.ac.bd

M. S. Islam
e-mail: msislam@cuet.ac.bd

W. Shumi
e-mail: shumi@cu.ac.bd

concrete during mixing. When water enters though cracks, these biological agents get activated and start depositing organic mineral. This bio-mineralization process is termed as "Microbiologically Induced Calcite Precipitation (MICP)" which ultimately fills the open cracks. Consequently, cracks are sealed and the structure becomes less susceptible to damages [3, 4].

In this form of study, the process of MICP technique is briefly analyzed. The aim of this research work is to evaluate variation of strength of concrete with different microbial groups and to establish an optimum concentration of bacterial culture in concrete.

2 Principles of MICP Technique

Concrete starts its life at a pH around 13. However, this study is concentrated on organisms which could be able to survive at high alkaline environment. It has been found that "alkaliphilic" types of bacteria could survive in this extreme condition. They have the ability to form calcite precipitation as extra cellular product.

Different metabolic pathways are involved in calcite precipitations. One method of accomplishing MICP is by "**enzymatic hydrolysis of urea.**" In this cycle, bacteria transform urea into ammonia and carbon dioxide. Development of ammonia gives rise to the value of pH from neutral to alkaline condition and at last outcomes in arrangements of carbonate minerals [5].

$$CO(NH_2)_2 + 2H_2O \xrightarrow{\text{Microbial urease}} NH_2COOH + NH_3$$

$$NH_2COOH + H_2O \xrightarrow{\text{Spontaneous}} NH_3 + H_2CO_3$$
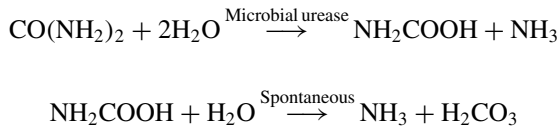
Four factors are associated with this mineral deposition: (a) concentration of calcium ions; (b) dissolved inorganic carbon ratio; (c) pH; and (d) presence of nucleation sites. But the forward one plays a great role for continuous mineral formation. The outer microbial cell walls are charged with negative groups. Divalent cations (Ca^{2+}, Mg^{2+}) are anchored with them at neutral pH and make them suitable nucleation sites for calcite deposition. At the point when water enters into the cracks, bacterial spores start to germinate and recover urea lysis activity. In this urease-mediated measure, the response of urea and water yields CO_2 and ammonia. On account of the high pK assessment of the NH_3/NH_4^+ framework (about 9.2), the response achieves a pH augmentation and move in the carbonate equilibrium (CO_2 to HCO_3^- and CO_3^{-2}) which brings about the precipitation of calcium carbonate when satisfactory measure of calcium particles (Ca^{2+}) is available. Schematic diagram of urea lysis precipitation can be found in Fig. 1 [6].

$$Ca^{2+} + Bacteria\,Cell \rightarrow Cell\,\text{-}\,Ca^{2+}$$
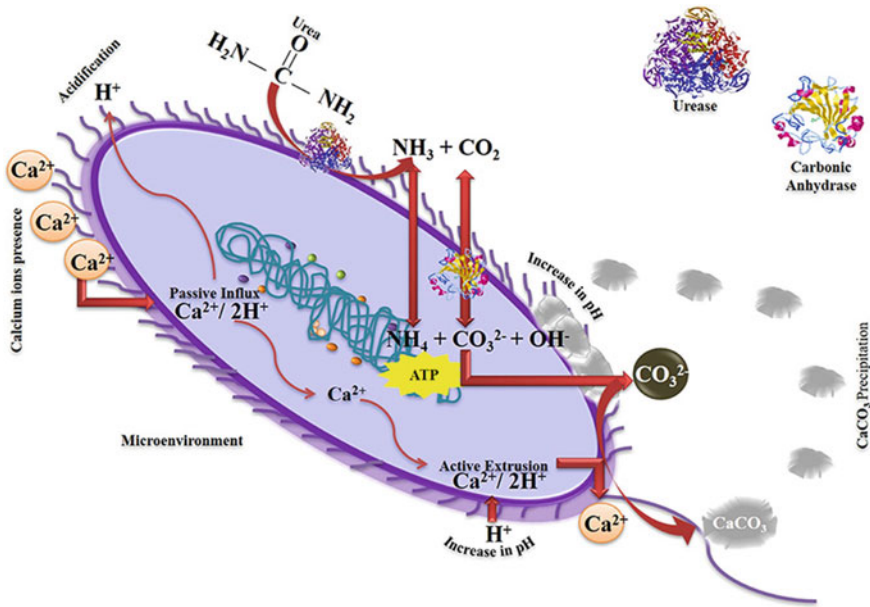
Fig. 1 Urea lysis carbonate precipitation occurring at the microbial cell wall [6]

$$\text{Cell - } Ca^{2+} + CO_3^{2-} \rightarrow \text{Cell - } CaCO_3$$
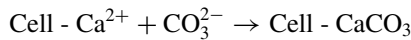
Another metallic pathway is "**oxidation of organic carbon.**" This pathway is practically like enzymatic hydrolysis of urea. But here in this pathway, precipitation of calcium carbonate is because of metabolic change of Ca-source according to the following reaction. This calcite deposition even goes on increasing when produced CO_2 reacts with $Ca(OH)_2$.

$$\text{Substrate}(Ca \text{ - source}) + O_2 \rightarrow CaCO_3 + CO_4 + H_2O$$

$$CO_2 + Ca(OH)_2 \rightarrow CaCO_3 + H_2O$$
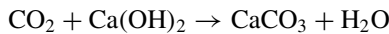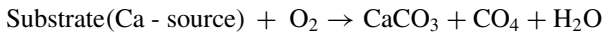
Both hydrolysis of urea and oxidation of organic compound need oxygen to begin and maintain metabolic activity of bacteria. "**Anoxic oxidation of organic carbon**" consumes nitrate and nitrite ions as electron acceptor. This process is known as "**denitrification.**" Under oxygen limited conditions, denitrification can be expected to dominate and generate carbonate and bicarbonate ions which are necessary for calcite formation. Although precipitation rates by hydrolysis of urea are 100–1000 times higher than through denitrification, denitrification could be more advantageous than urea hydrolysis as sufficient quantity of oxygen and nutrients cannot be ensured [7].

3 Selection of Appropriate Bio-Agents

As stated before, concrete creates a high alkaline environment which is unfavorable and harsh for living organisms. Hence, the microbes used in concrete should fit in following two special criterions.

1. Ability to withstand with high alkaline environment
2. Capability of spore germination at that condition

The organisms which can be isolated from soil sample and feces have the ability to produce spores, a torpid state which is characterized by no metabolism, high chemical and mechanical resistance. Spores are feasible for as long as hundred years, and they become active when the conditions are affable once more. Microbes can remain in a torpid state in the concrete mortar until cracking happens and water entering through the cracks carries the spores to dynamic state so the precipitation of $CaCO_3$ can occur. Studies showed that special genus of bacteria are capable of producing urease. This urease influences the mineral precipitation process by those four factors as stated earlier. Table 1 showed the types of bacteria used in concrete in various literatures.

In this study, microbial concrete was prepared incorporating two alkaliphiles, i.e., *Bacillus cereus* and *Escherichia coli*. Again incorporation of these bacterial strains in concrete can be done in following two ways.

1. By direct method
2. By encapsulation method.

In the direct application strategy, bacterial spores and calcium lactate is added into concrete legitimately when mixing of concrete is done. The utilization of this microbes and calcium lactate does not change the properties of cement. At the point when cracks are happened in the structure because of clear reasons, the microorganisms are presented to climatic changes. At the point when water interacts with

Table 1 Types of bacteria used in concrete

Bacteria	References
Bacillus sphaericus	Reddy et al. [8] Sahoo et al. [9]
Bacillus subtilis	Karimi et al. [10] Neeladharan et al. [11]
Escherichia coli	Ansari et al. [12] Vijay et al. [13]
Bacillus pasteurii	Metwally et al. [14] Yoosathaporn et al. [15]
Bacillus cohnii	Jena et al. [16] Tiwari et al. [17]
Bacillus flexus	Elumalai et al. [18] Priya et al. [19]
Bacillus cereus	Alshalif et al. [20] Mondol et al. [21]

these microbes, they germinate and feed on calcium lactate and create limestone. Henceforth, the cracks are fixed.

In case of encapsulation method, bacteria and calcium lactate are put inside treated clay pellets, and concrete is prepared. About 6% of the clay pellets are added for marking microbial concrete [6].

Among these two techniques, encapsulation method is generally utilized, despite the fact that it is costlier than direct application. But direct application method is exclusively used here in this study for microbial concrete preparation.

4 Materials and Experimental Details

"**Royal Cement**" conforming to ASTM C150 was used as binding material. The normal consistency of cement paste was 26%. The initial and final setting time were recorded as 150 and 230 min, respectively, while the specific gravity was found to be 3.15 following ASTM guidelines.

In this present study, "**crushed stone**" of maximum nominal size 12.5 mm was used as coarse aggregate. The specific gravity and water absorption capacity of crushed stone were found to be 2.74 and 2.33%, respectively. Locally available "**Sylhet sand**" having FM value 2.51 was used as fine aggregates for all concrete mixes. The specific gravity and water absorption capacity of fine aggregate were found to be 2.61 and 2.78%, respectively.

The present study considers potential stains of *Bacillus cereus* and *Escherichia coli* as isolates to be tested. Cultures of bio-agents were collected from University of Chittagong, Chattogram. A pre-fixed culture density was maintained for preparing different grades of concrete. Five different ratios of plain water to microbial culture were directly added to concrete matrix to investigate the effect of microbial percentages in concrete.

In this study, stains of *B. cereus* and *E. coli* with proper culture media were directly added to concrete matrix. Following four operations are involved in preparing desired culture media.

1. Preparation of Luria–Bertani (LB) Broth Media
2. Sterilization of medium
3. Inoculation and incubation of the organisms
4. Determination and adjustment of optical density.

Preparation of LB Broth Media: One of the generally utilized rich mediums called "Luria–Bertani broth" is well known with bacteriologists because it allows quick growth and good growth yields for many species. This media was utilized for the growth and maintenance of selected bacterial species. The recipe for Luria–Bertani broth is summarized in Table 2.

Table 2 Recipe for Luria–Bertani media [22]

Ingredients	Quantity (g/l)
Peptone	10
Yeast extract	5
NaCl	10

Fig. 2 **a** Ingredients taken in conical flask; **b** prepared Luria–Bertani media

Sterilization of medium: Required amount of peptone, yeast extract and NaCl were taken in a conical flask first. Then required amount water was added at room temperature. Finally, the solution was stirred slowly to prepare Luria–Bertani broth media. Figure 2 shows the preparation of Luria–Bertani media.

Autoclaving: It is commonly used to germ free the medium using high-pressure steam. At first, air was taken out from the autoclave chamber to set up a low-pressure atmosphere. Next, stream was pumped through the chamber at a higher pressure than normal atmospheric pressure so it would arrive at a temperature of about 121 °C. The specific time 15–20 min is required eliminate the all germs present in medium. The whole process needs two hours to accomplish.

Inoculation and incubation of the organisms: As soon as the media was sterilized approximately for two hours, the media was inoculated by the organisms (*B. cereus* and *E. coli*). One loop of bacteria was introduced here by a needle in prepared media. After inoculation, the conical flask was placed into incubator. This was the place where 35-40ºC temperature was maintained and let the bacteria to multiply through binary fission. Concentration of bacteria would depend on the growth phase of bacteria and germination time.

Determination and adjustment of optical density: Generally, bacteria grown in batch culture progress through four phases of growth: lag, exponential, stationary, and death. Optical density gives a moment guess of bacterial cell tally estimated utilizing

Table 3 Different microbial groups

Group	Plain water (%)	Microbial culture (%)	Remarks
A	100	0	Conventional concrete
B	75	25	Microbial concrete
C	50	50	
D	25	75	
E	0	100	

a spectrophotometer. The optical density of a culture was estimated according to a media blank. The ideal OD_{600} for the diverse bacterial strains by and large differs. Bacteria for preparation of competent cells would regularly be cultured to OD_{600} = 0.5 ± 0.1 [23]. Appropriate dilution factor was applied to get anticipated optical density.

5 Concrete Mix Design

Several trial mix ratios were obtained to arrive at final mix ratios. Final mix design was prepared following ACI 211 standards. The mix ratio for 20 MPa design strength on the 28th day was derived to be 1.0:2.67:2.70 for water cement ratio of 0.592, whereas the corresponding mix ratio for 30 MPa design strength was 1.0:1.74:2.03 for water cement ratio of 0.445. In case of 40 MPa design strength, the ratio was derived to be 1.0:1.33:1.73 and the water cement ratio was 0.380.

Five different ratios of plain water to microbial culture were used in this research work. 100 mm cubical concrete specimens were prepared following ASTM standards. Specimens were taken out periodically from curing conditions and subjected to compressive strength test. Table 3 summarizes different microbial groups.

6 Test Results and Discussion

The compressive strength was tested according to the guidelines of ASTM C39 standards. The compressive strength test results of 20, 30, and 40 MPa concrete with different culture content after 28, 60, and 90 days of curing are graphically represented in Figs. 3, 4, 5, 6, 7, and 8. The results depict that with increase in microbial content, the strength of concrete also increases. Similar observations are also found by other researchers [12, 20].

Figures 3, 4, 5, 6, 7, and 8 clearly demonstrate the variation in compressive strength with different microbial percentages for different curing periods. The compressive strengths of Group A were found to be 21.1, 31.3, and 41.5 MPa, respectively, for the
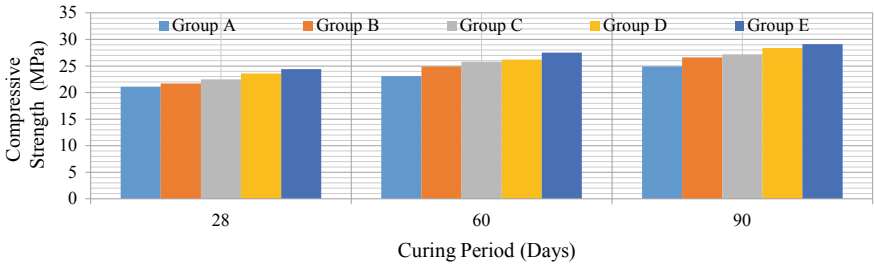
Fig. 3 Compressive strength of 20 MPa microbial concrete for different curing ages (*B. cereus*)
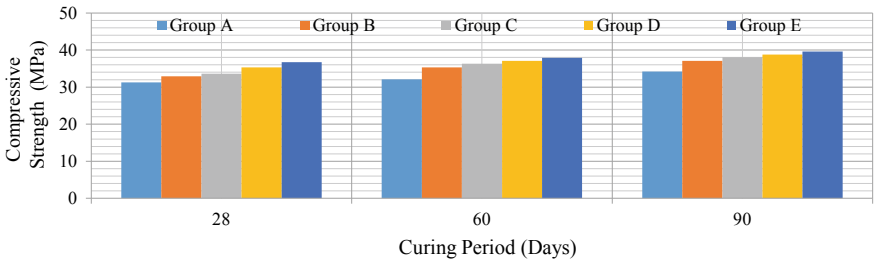
Fig. 4 Compressive strength of 30 MPa microbial concrete for different curing ages (*B. cereus*)
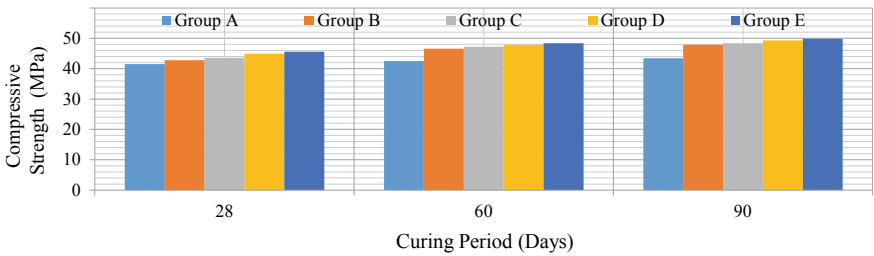
Fig. 5 Compressive strength of 40 MPa microbial concrete for different curing ages (*B. cereus*)
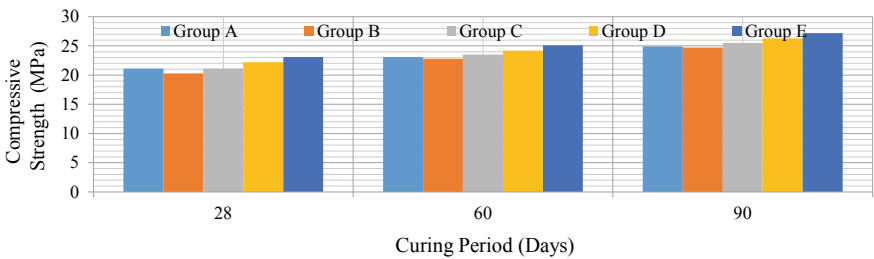
Fig. 6 Compressive strength of 20 MPa microbial concrete for different curing ages (*E. coli*)
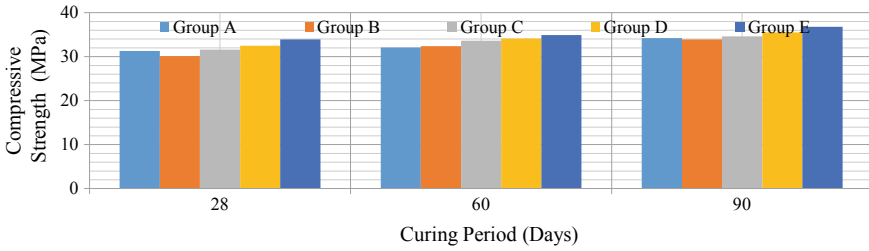
Fig. 7 Compressive strength of 30 MPa microbial concrete for different curing ages (*E. coli*)
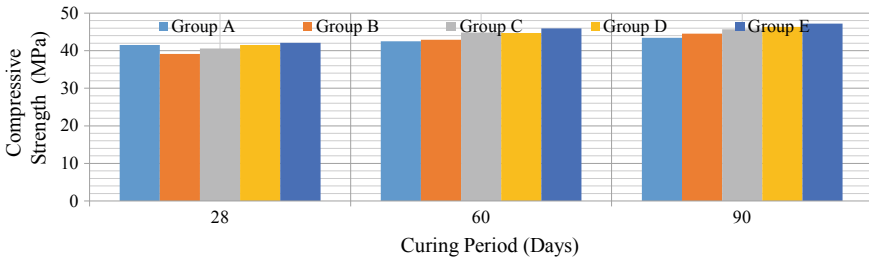
Fig. 8 Compressive strength of 40 MPa microbial concrete for different curing ages (*E. coli*)

design strengths at the age of 28 days whereas the maximum corresponding values (Group E) were 24.4, 36.7, and 45.6 for *B. cereus* induced concrete and 23.1, 33.9, and 42.1 MPa for *E. coli* induced concrete. Group E (0:100) was also found to be effective in increasing compressive strengths at 60 and 90 days of curing for both bacterial strains.

Table 4 shows the increment of compressive strength of microbial concrete at 28 days. It is seen that both *B. cereus* and *E. coli* show positive responses to increase compressive strength when culture percentages are increased. Among all microbial groups, Group E (0:100) shows maximum increment in compressive strength. This may be because of the development of more noteworthy mineral depositions in internal structures of concrete. While comparing the variation of mechanical strengths

Table 4 Increment in compressive strength (28 days) with respect to Group A

Group	20 MPa		30 MPa		40 MPa	
	B. cereus (%)	*E. coli* (%)	*B. cereus* (%)	*E. coli* (%)	*B. cereus* (%)	*E. coli* (%)
B	2.84	−3.79	5.11	−3.83	3.13	−5.78
C	6.64	0	7.35	0.96	5.06	−2.17
D	11.85	5.21	12.78	3.83	8.19	0
E	15.64	9.48	17.25	8.31	9.88	1.45

between *B. cereus* and *E. coli,* it has been observed that *B. cereus* is more likely to show better response to compressive strength for all design strengths of concrete.

7   Conclusions and Recommendations

The experimental program was planned to observe the performance of two different bacterial strains in concrete with regards to strength development. Three different grades of concrete, five ratios of water to microbial culture were used. However, based on the limited number of variables/ parameters studied and also the review of relevant literatures, the followings are the conclusions and recommendations therefore.

1. Summarizing the strength data, it has been observed that the concrete strength development using *B. cereus* strain is more than that of *Escherichia* strain. Hence, *B. cereus* bacteria may be chosen over *E. coli* for making Microbial Concrete.
2. While comparing different grades of concretes, it has been observed that strength increases more in case of lower grades of concrete for all curing days. Hence, MICP technique is found to be more effective in increasing density of lower grade of concrete.
3. The concentration of bacterial culture in concrete is observed to play a vital role in improving its quality. 0:100 ratio of plain water to microbial culture is found to provide maximum strength for all grades of concrete. The use of maximum bacterial culture increases the capability of bacterial strains for producing MICP that fills the cracks when appear and ultimately reduces the repair cost.
4. Group D (25:75) is also found to be effective in increasing compressive strength of concrete. As the initial cost of culture production is higher, Group D can also be chosen to minimize culture costing. Hence, among the five groups (plain water to microbial culture), the ratio 25:75 can be considered optimum with regards to strength development as well as economy point of view.
5. Bacterial growth is found to be maximum at an $OD_{600} = 0.5$ at different literature. Varying OD_{600} with a range of 0.4 to 0.6 and comparing their test results against OD_{600}, a complete study of microbial concrete may be established.
6. Growth of bacterial strains is highly dependent on temperature. The optimum growth temperature for *Bacillus cereus* and *Escherichia* varies from 30° to 40°C. Delay growth of strain might be observed in Nutrient Agar medium during winter season. Hence, a nutritionally rich medium named Luria–Bertani medium is proposed for maintaining $OD_{600} = 0.5 \pm 0.1$.

References

1. Schlangen E, Joseph C (2009) Self-healing processes in concrete. In: Verlag W-VCH (ed) Self-healing materials. GmbH & Co. KGaA, Weinheim, Germany, pp 141–182
2. Pacheco J, Šavija B, Schlangen E, Polder RB (2014) Assessment of cracks in reinforced concrete by means of electrical resistance and image analysis. Constr Build Mater 65:417–426
3. Jonkers Henk M, Thijssen A, Muyzer G, Copuroglu O, Schlangen E (2010) Application of bacteria as self-healing agent for the development of sustainable concrete. Ecol Eng 36:230–235
4. Ter Heide N (2005) Crack healing in hydrating concrete. MSc Thesis, Delft University of Technology, Delft
5. Wang J, Ersan YC, Boon N, De Belie N (2016) Application of microorganisms in concrete: a promising sustainable strategy to improve concrete durability. Appl Microbiol Biotechnol 100:2993–3007
6. Castro-Alonso MJ, Montañez-Hernandez LE, Sánchez-Muñoz MA, Franco MR, Narayanasamy R, Balagurusamy N (2019) Microbially induced calcium carbonate precipitation (MICP) and its potential in bioconcrete: microbiological and molecular concepts. Front Mater. https://doi.org/10.3389/fmats.2019.00126
7. Tziviloglou E (2009) Self-healing in ECC materials with low content of different microfibers and micro-particles. MSc Dissertation, Delft University of Technology, Delft
8. Reddy BM, Revathi D (2019) An experimental study on effect of Bacillus sphaericus bacteria in crack filling and strength enhancement of concrete. Mater Today Proc 19(2):803–809
9. Sahoo KK, Sathyan AK, Kumari C, Sarkar P, Davis R (2016) Investigation of cement mortar incorporating Bacillus sphaericus. Int J Smart Nano Mater 7(2):91–105
10. Karimi N, Mostofinejad D (2020) Bacillus subtilis bacteria used in fiber reinforced concrete and their effects on concrete penetrability. Constr Build Mater. https://doi.org/10.1016/j.conbuildmat.2019.117051
11. Neeladharan C et al (2018) Application of Bacillus subtilis bacteria for improving properties and healing of cracks in concrete. IJARTET 5(5):118–123
12. Ansari N, Joshi R (2019) A study on self-healing property of concrete using E. Coli as bacteria. IJRAR 6(2):61–66
13. Vijay GA, Tamilarasan R, Yashwanth C, Arun A, Arunachalam E (2019) Experimental investigation on self healing concrete using E.Coli bacteria. Int J Trend Res Dev (IJTRD) 6(2):155–161
14. Metwally GAM, Mahdy M, El-Raheem AHA (2020) Performance of bio concrete by using Bacillus Pasteurii bacteria. Civ Eng J 6(8):1443–1456
15. Yoosathaporn S, Tiangburanatham P, Bovonsombut S, Chaipanich A, Pathom-aree W (2016) A cost effective cultivation medium for bio-calcification of Bacillus pasteurii KCTC 3558 and its effect on cement cubes properties. Microbiol Res. https://doi.org/10.1016/j.micres.2016.03.010
16. Jena S, Basa B, Panda KC (2021) Effect of Bacillus Cohnii bacteria on the properties of concrete. In: Das B, Barbhuiya S, Gupta R, Saha P (eds) Recent developments in sustainable infrastructure. Lecture notes in civil engineering, vol 75. Springer, Singapore. https://doi.org/10.1007/978-981-15-4577-1_50
17. Tiwari S, Pal S, Puria R, Nain V, Pathak RP (2019) Mechanical and microstructure study of the self healing bacterial concrete. Mater Sci Forum 969:472–477. https://doi.org/10.4028/www.scientific.net/MSF.969.472
18. Mohan GG, Gurumurthy K, Elumalai A (2020) An experimental study on performance of Bacillus pumilus KC845305 and Bacillus flexus KC845306 in bacterial concrete. J Appl Sci Eng 23(1):1–8
19. Krishnapriya S, Venkatesh Babu DL, Arulraj GP (2015) Isolation and identification of bacteria to improve the strength of concrete. Microbiol Res 174. https://doi.org/10.1016/j.micres.2015.03.009

20. Alshalif AF, Juki MI, Othman N, Al-Gheethi AA, Khalid FS (2019) Improvement of mechanical properties of bio-concrete using Enterococcus faecalis and Bacillus cereus. Environ Eng Res 24:630–637. https://doi.org/10.4491/eer.2018.306
21. Mondal S, Ghosh A (2018) Investigation into the optimal bacterial concentration for compressive strength enhancement of microbial concrete. Constr Build Mater 183:69–75
22. MacWilliams MP, Liao M-K (2006) Luria Broth (LB) and Luria Agar (LA) media and their uses protocol. American Society for Microbiology, pp 1–4
23. Tu Z et al (2005) An improved system for competent cell preparation and high efficiency plasmid transformation using different Escherichia coli strains. Electron J Biotechnol 8(1):114–120

Assessment of Closure's Impact on Water Related Problems Around the Ononto Closure: An Integrated Approach for Solution

M. A. R. Islam, T. K. Shamma, J. J. Anika, and M. Hossain

1 Introduction

Ichamoti is an enormous river which once connected world's two largest basin Ganga and Jamuna but currently restricted by Ononto closure. Ichamoti River flows through Pabna town in 10-km area. Once mighty Ichamoti River has totally lost its flow and some part of it turned into a dumping site for garbage. Now, the river is nothing but the place of dirty water and garbage harmful for environment [1]. Ichamoti resuscitation project is an initiative to give life to river Ichamoti. BWDB took this project as a challenge. This study aims to evaluate the present condition of Ononto closure over Ichamoti River and future aspects after constructing a bridge in place of Ononto closure. Reasons behind establishment of Ononto closure, its effects on natural flow of Ichamoti River and the effect of constructing a bridge in place of the closure are the major research questions of this study. Ononto closure's effects on livelihood, land use pattern and ecosystem of surrounding area has to be explored. After exploring all of this, sustainability of Ononto closure can be realized. Water resources management is one part of the overall management of the environment and the preservation of ecosystems which is a prerequisite for sustainable development. Water resources management therefore needs to be coordinated with other disciplines and sectors that affect the water resources or are affected by how well the water is managed [2]. This research aims to determine what changes should be made to improve current scenario based on findings and general people recommendations. The whole study is based on primary raw data. Not that much reliable data could be gathered from KII with professional personnel. Pabna district is located almost at the middle of

M. A. R. Islam (✉) · J. J. Anika · M. Hossain
Institute of Water and Flood Management, Bangladesh University of Engineering and Technology, Dhaka, Bangladesh

T. K. Shamma
Institute of Water and Flood Management, UKRI GCRF Living Deltas Hub Project, Bangladesh University of Engineering and Technology, Dhaka, Bangladesh

Fig. 1 Study area

Bangladesh. It is surrounded by the river Jamuna on the east, Natore district on the west, Sirajganj district on the north, Kushtia and Rajbari districts on the south. Our study area, Ononto closure is situated at the Dogachhi union of Pabna sadar upazila. Basically, Ononto closure is a road that was built for transportation purposes, while obstructing the flow path. Now, a bazaar has been established on that. We divided the area into two zones: upstream and downstream. East side of the closure that is later connected through Varara khal is the downstream zone, and west side waterlogged area is the upstream zone (Fig. 1).

2 Materials and Methods

2.1 Methods for Social Analysis

This study has identified the social and environmental impacts are by meeting with the stakeholders. A brief questionnaire and checklist were prepared to conduct KII and FGD, respectively. This study identified primary and secondary stakeholders include all those who affect and are being affected by policies, decisions or actions for this particular issue and consulted with them. The primary stakeholders are the grass-root stakeholders, such as project affected persons and general public including women and people with physical disabilities residing in the project area. This study consulted with both benefitted and non-benefitted stakeholders. The secondary stakeholders are the people, department, institutions, organizations who has influenced the project and

its design including Bangladesh Water Development Board, DoE, local administration officials, elite persons. During the consultations, socio-economic, water related issues, fisheries and agriculture issues were discussed in detail, including potential impacts of the interventions on the environmental and social parameters. Institutional issues were also discussed where the participants provided their opinions and suggestions freely (Fig. 2).

During the consultations, some stakeholders expressed proposal for opening the road and making a bridge, most of the stakeholders highly supported this idea and positive attitude toward this very idea and demanded its rapid implementation for the purpose of maintaining flow of the river. The communities expect the project to provide to them employment opportunities. In this discussion, stakeholders provided their feedback on some issues: (1) Rainy season inundation problem will reduce after via ducting, (2) Water qualities will improve, (3) Fisherman community feels optimistic about water flows and fish diversities. (4) Opportunity for farmers to use river water for irrigation (Fig. 3).

Fig. 2 FGD with local stakeholder and KII with BWDB
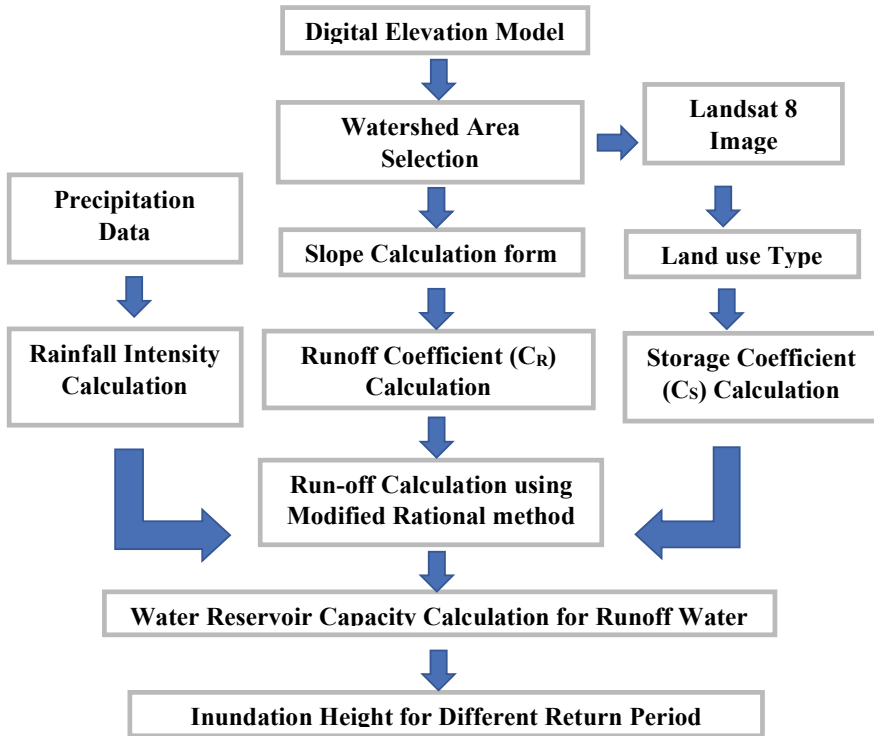
Fig. 3 Methodological framework

2.2 Methodology for Hydrological Analysis

This study has calculated total runoff volume generated after precipitation for different return period and reservoir capacity and inundation height changes before and after via ducting. Digital elevation model (DEM) & contour map have been prepared using elevation data has been collected from ASTER 30 m data using inverse distance weighting (IDW) for interpolation technique. Watershed area around reservoir has been selected after identifying the slopes from DEM and contour Map (Fig. 4).

Rational method has been used to calculate runoff as this simplest and most commonly used technique [3] using precipitation data from BMD. Equation used for this:

$$QP = CSCRIA/3600 \tag{1}$$

Here, in Eq. (1), QP = Peak runoff (m³/s), A = Area, CS = Storage coefficient, CR = Runoff coefficient, I = Rainfall intensity (mm/h).
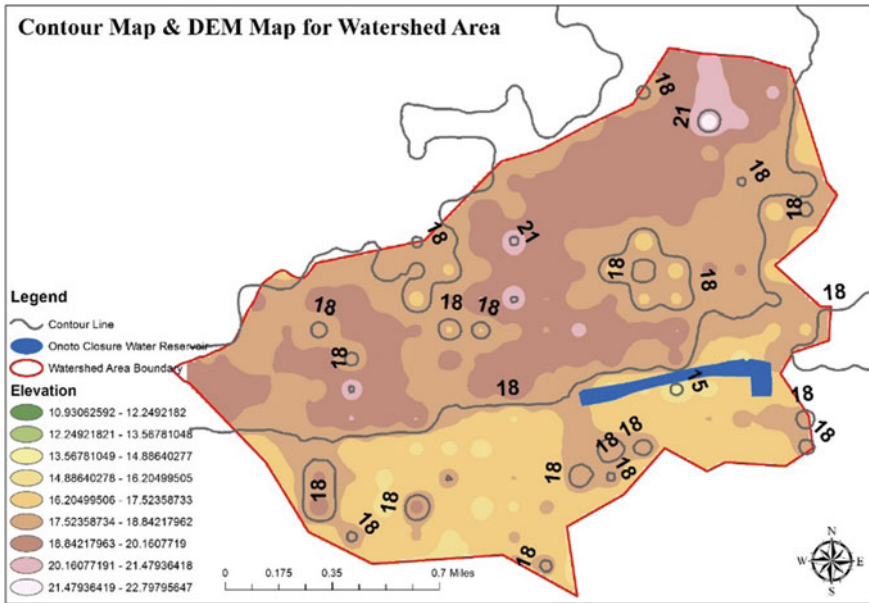
Fig. 4 DEM and contour map

For rainfall intensity, short duration rainfall data is required which is unavailable for Pabna, but available for Dhaka. Khan [4, 5] showed that it is possible to calculate short duration rainfall data for different project area from short duration rainfall of Dhaka by multiplying a conversion factor. This study only calculated conversion factor for Pabna using daily 24 h. Rainfall data of Pabna and Dhaka for 20 year (1995–2014) and multiplied it with previously calculated short duration rainfall data for Dhaka by Khan [4, 5] (Table 1). Equation used for rainfall intensity:

$$I = a/(Tb + c) \qquad (2)$$

Here, in Eq. (2), I = Rainfall intensity (mm/h), T = Duration (h), a, b, c = Constant.

Table 1 Short duration rainfall data for Dhaka

Return period (Y)	T (h)	0.25	0.5	1	2	3	6	12
2	I	92.40	78.60	56.20	36.70	27.00	15.40	9.40
5	I	109.70	95.70	71.40	50.10	39.00	23.00	14.10
10	I	121.10	107.00	81.40	58.90	46.90	28.00	17.30
25	I	135.60	121.30	94.10	70.10	56.90	34.30	21.20
50	I	146.30	132.00	103.50	75.40	64.30	39.00	24.10

Table 2 Short duration rainfall data for Pabna

Return Period (Y)	T (h)	0.25	0.5	1	2	3	6	12
2	I	123.15	104.76	74.90	48.91	35.99	20.53	12.53
5	I	146.21	127.55	95.16	66.77	51.98	30.65	18.79
10	I	161.41	142.61	108.49	78.50	62.51	37.32	23.06
25	I	180.73	161.67	125.42	93.43	75.84	45.72	28.26
50	I	194.99	175.93	137.95	100.49	85.70	51.98	32.12

This study follows below equations for conversion factor calculation, showed in (Khan 2015).

$$R1 = \text{Average } A/\text{Average } C = 2.1620 \tag{3}$$

$$R2 = \text{Average } B/\text{Average } A = 0.6154 \tag{4}$$

$$\text{Conversion Factor for Pabna } = R1 * R2 = 1.33 \tag{5}$$

Here, in Eqs. (3) and (4), Average $A = $ Long term (20 Years) mean annual maximum daily rainfall for 139.8 mm Average $B = $ and calculate the mean annual maximum daily rainfall using annual maximum daily rainfall data from rain gauge station nearest to Ononto closure. Average $C = $ mean annual maximum daily rainfall of Dhaka for the same period of record in above. In Eq. (5), $R1 = $ Ratio between Dhaka long term mean annual maximum daily rainfall and Dhaka shorter period rainfall. $R2 = $ Ratio between the Pabna mean annual maximum daily rainfall and Dhaka mean annual rainfall on that same period.

From Eq. (5), the final calculated conversion factor of 1.33 has been multiplied to previous table to calculate short duration rainfall data for Pabna (Table 2).

Calculating runoff co-efficient (CR) land use map require to prepare as it varies with land use types. Pavement, urban areas have low-infiltration value and high-co-efficient value, while agricultural land, open space behave opposite [6]. This study prepared land use map of watershed area using Landsat 8 (OLI) Green, RED and NIR bands applying supervised classification technique. This study takes co-efficient value 0.6, 0.6 and 0.8 for building & paved area, parks/open space and agricultural field, respectively. Multiplying with the land use percentage, we have reached to 0.5912 as runoff co-efficient value (Fig. 5).

For storage co-efficient (Cs), this study calculated average ground slope from contour map produced from DEM. Pabna has a very flat topology and rain water moves slowly in flat topography [4, 5]. Cs also varies with different land use type for runoff co-efficient. This study used 0.9, 0.7 and 0.4 for residential urban building & paved area, parks and open space and agricultural field, respectively [7]. Multiplying with the land use percentage, we have reached to 0.8483 as storage co-efficient value.
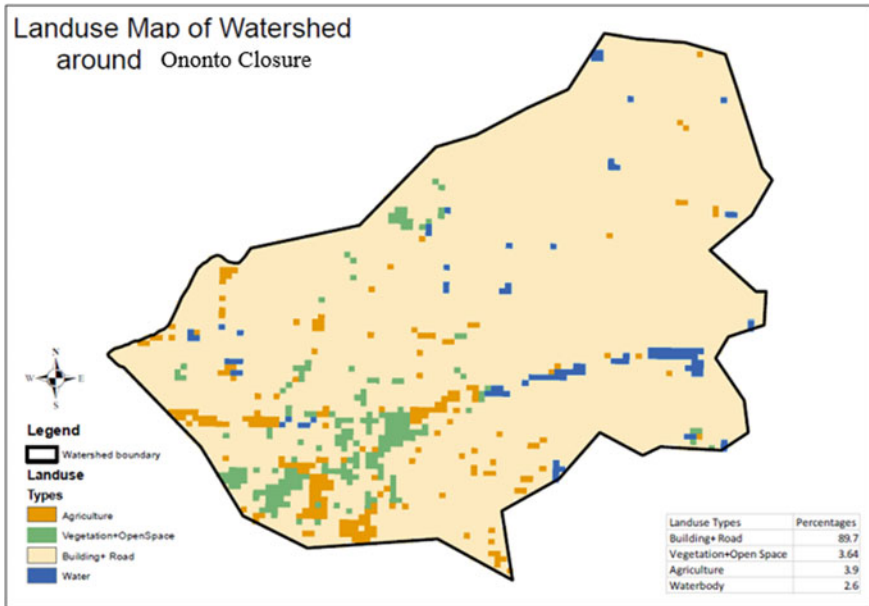
Fig. 5 Landuse map of watershed area

Final step is inundation height calculation. This research aimed to look for capacity of water reservoir of Ononto closure after precipitation in two scenarios for comparison. Scenario 1 is with Ononto closure when no water can pass. Scenario 2 is water can pass via Ononto Closure and flow toward Hazipara reservoir.

3 Results and Discussions

3.1 Socio-physical Findings

We divided our study area into two zones for analysis purpose. These two zones are upstream and downstream of Ononto closure. The area directly receiving flow of Padma through Ramchandrapur regulator is delineated as upstream of Ononto closure. The area from Ononto closure to Hazirhat which moves toward Varara canal is downstream area. Information was collected mostly from local people through field observations, FGD, semi-structure interview and KII.

Fig. 6 Municipal Waste dumpped in the water bodies lead to a Water quality issue in upstream

3.1.1   Water Quality

Water quality is better in downstream despite having lesser flow, although there are some point sources for pollution close to industry and pharmaceutical company. Upstream water is highly polluted for fish to survive; it also has a strong odor. Although the water from upstream is used by locals for cooking, people believe that this water is the reason for skin disease among them (Figs. 6 and 7).

3.1.2   Water Flow

Water flow observed through transect walk with a local man named MD. Razzak Mia revealed that stagnant water was the main reason for pollution in the upstream which often resulted in waterlogging during heavy rainfall. In the downstream from Ononto bazar to Hazirhat, the river is uneven in width, in some places, there are fish cultivation ponds obstructing natural flow (Figs. 8 and 9).

Fig. 7 Eutrophication leads to Water pollution in downstream side

3.1.3 Landuse Pattern

Transect walk with Md. Razzak Mia was helpful getting the general landuse idea. Most of the land in upstream are households, some previously used agricultural land is now barren. The main point Ononto closure is now known as Ononto bazar, a commercial area. In the downstream, most area is dedicated to fishing except for two industries. There are some lands occupied by local people who used it for agricultural and residential purposes.

3.1.4 Water Logging

According to our semi-structure interviews, it was found that 200–300 household in upstream of Ononto closure gets flooded for at least 2–3 months during monsoon period every year at the upstream. During extreme events, they take shelter nearby primary school when the inundation depth is 3–3.5 feet. Maximum local people said that poor drainage system and Ononto closure that disturbed the natural water flow are responsible for waterlogging whereas some claimed that water flow during opening time of Ramchandrapur regulator also contributes to this phenomenon. Downstream shows no such water logging issues except for natural flooding during heavy rainfall.

Fig. 8 Snapshot of water body at Hazirhat gher area

Fig. 9 Local people showing inundation height during flood event during site visit

3.1.5   Waste Dumping

Semi-structure interview also revealed that whole Pabna city's solid waste and waste water are dumped in the upstream section of Ononto closure without any regulation. Downstream area had industrial pollution sourced from one food processing industry and one pharmaceutical company. People who lease land for fish cultivation are facing financial losses because of this.

3.1.6   Livelihood of Residents

People who live in this zone are hardly dependent on the water flow of this closure. Degrading water quality encouraged people to take jobs in the city or at the bazaar, especially who used to be fishermen before. Rickshaw puller, construction worker, shopkeeper, carpenter, house maid, job holder, etc., various types of occupation are observed among the people living in the upstream zone. At the downstream of the Ononto closure, there are farming lands as well as fisheries opportunity. People grow rice in some lands alongside the river using the surface water from the river. As the flow is connected with the Ganges, it has a good quality water for culture fisheries.

3.1.7   Land Ownership

Semi-structure interview was conducted to gather information regarding land ownership. According to peoples claim, houses are being built since last 40 years. People living here are either land owners or tenants; however, there is a field in the middle abandoner due to territorial issue. Upstream people living closer to the Ononto closure faces the worst situation during inundation period. Except for some factories, land ownership scenario in downstream is similar to upstream.

3.2   *Inundation Scenario Comparison*

For Scenario 1, the present condition, while water is not allowed to pass via Ononto closure. The reservoir area calculated is 78,550 m^2 with available water capacity of 95,045.5 m^3. While in scenario 2, when water will be allowed to pass via Ononto closure total reservoir area becomes 234,350 m^2 with available water capacity of 484,545.5 m^3. This research calculated inundation height for 1-h precipitation of 2, 5, 10, 25 and 50 years of return period and finds completely two contradictory inundation condition of two different scenario. This study calculated inundation height calculation for two different scenarios (Table 3).

Table 3 Inundation calculation process

		1 h of precipitation of 2 years of return period
Runoff Volume calculation	Rainfall intensity, mm	74.9
	Storage coefficient, C_S	0.84838
	Runoff coefficient, C_R	0.59124
	Watershed area (Ha)	1268.764
	Runoff volume (m^3/h)	192,919.6635
Scenario 1	Reservoir area (sqm)	78,550
	Reservoir height from top of water (m)	1.21
	Current reservoir capacity (volume)	95,045.5
	Inundation height (m)	1.25
	Scenario	*Inundation*
Scenario 2	New reservoir area (m^2)	155,800
	New reservoir height (m)	2.5
	New reservoir capacity (volume)	389,500
	Total capacity (volume)	484,545.5
	Inundation height (m)	-1.24440
	Scenario	*No Inundation*

3.2.1 Inundation Comparison for Scenario 1 and Scenario 2

For scenario 1, in every magnitude of Rainfall, there is some height of inundation which validates the information collected from physical interviews. For scenario 2 with added capacity of water reservoir, we found that this new added capacity is enough to carry runoff water. Negative value of inundation height can be described as no inundation. So, Scenario 2 (after via ducting) can be described as improved situation.

Table 4 illustrates inundation heights in reservoir after different return periods of rainfall. This table validates the preliminary hypothesis of this research and local stakeholders' observation on that waterlogging solution can be improved by via ducting the Ononto closure. This research team conduct physical survey to find the exact extent of reservoir and validated the calculated height with local stakeholders' observation.

4   Conclusion

This study shows that via ducting will enhance the scenario of both upstream and downstream area of Ononto closure. As Ichamoti River is serving as a connecting path of two mighty rivers (the Ganges and the Jamuna) via ducting will provide

Table 4 Inundation heights for different magnitudes for different return periods

Return period of 1 h rainfall	Scenario 1 (current situation)		Scenario 2 (after via ducting)	
	Inundation height (m)	Inundation situation	Inundation height (m)	Inundation situation
2	1.25	Inundation	−1.24	No inundation
5	1.91	Inundation	−1.02	No inundation
10	2.35	Inundation	−0.87	No inundation
25	2.9	Inundation	−0.68	No inundation
50	3.31	Inundation	−0.55	No inundation

connectivity and as a result, continuous flow in this channel which will be the life-line of the river. Consequently, appropriate implementation of IWRM approach such as removal of water logging, improvement of water quality, increase in fish diversity with quantity, irrigation water improvement, etc., could be executed. We are concluding this study with some recommendations. Waste water that is dumped in the upstream of Ononto closure should be rerouted to a facility for treatment. Solid waste from city that is dumped on the riverside should be relocated elsewhere. People who are living in the floodplain should be rehabilitated before opening the closure. Ramchandrapur regulator should be monitored closely so that no inundation of floodplain lasts for entire monsoon period. Illegal usurpation of land should be prohibited further so that encroachment comes to a halt.

References

1. Bangladesh Post (2019) Bangladesh Post. Retrieved from www.bangladeshpost.net/save-ich amati-river
2. Gunawardena ERN Operationalizing IWRM through river basin planning
3. Freire Diogo A, do Carmo JA (2019) Peak flows and stormwater networks design—current and future management of urban surface watersheds. Water 11:759
4. Khan DMSA (2015) Guidelines for flood risk assessment and storm water drainage plan. Urban Development Directorate, Mymensingh
5. Khan D (2015) Guidelines for flood risk assessment and storm water drainage plan. Urban Development Directorate, Mymensingh

6. State Water Resources Control Board (2011) The clean water team guidance compendium for watershed monitoring and assessment for state water resources control board, sl.: State Water Resources Control Board
7. Bright Hub PM (2020) Rational method runoff coefficient tables for storm water runoff calculation. Retrieved from https://www.brighthubengineering.com/hydraulics-civil-engineering/93173-runoff-coefficients-for-use-in-rational-method-calculations/

Road Crash in Bangladesh: Where We Were, Where We Are, and Where We Will Be

Shahrior Pervaz, S M Sohel Mahmud, Md Asif Raihan, and Md Imran Uddin

1 Introduction

Road safety has become a rising concern around the world recently. More than a million people are dying, and many more are becoming injured and permanently disabled in road crashes each year globally. In developing countries like Bangladesh, this problem is disproportionately higher and more complex. Although the official statistics (police reported crash data) reveal 2500 crashes and 3000 deaths each year in Bangladesh, the actual scenario is quite contrasting; the actual numbers could well be at least four times more than the reported figures [1]. It is estimated that the annual road traffic fatalities in Bangladesh could be around 20,000 [2]. Various government and non-government organizations are worried regarding the persistent problem and have contemplated various actions to ensure safer transport in the country. Efforts have also been made to conduct research and develop effective countermeasures to overcome the safety challenges. However, studies with updated data, recent trends of the magnitude, and characteristics of the problem are rarely found in recent research. Additionally, identification of the risk factors and associated issues based on updated data is very crucial in the crash mitigation process. Thus, this study intends to provide an insight on recent crash scenario of Bangladesh.

2 Global Burdens of Traffic Crashes

Traffic crashes are being treated as a serious man-made epidemic globally. It is underlined that the annual fatalities from this epidemic have climbed up to 1.35 million [3]. In addition, these crashes have been evaluated as the eighth prominent

S. Pervaz (✉) · S. M. S. Mahmud · Md A. Raihan · Md I. Uddin
Accident Research Institute (ARI), Bangladesh University of Engineering and Technology (BUET), Dhaka 1000, Bangladesh

source of death which implies that they are taking more lives than AIDS [3]. It is also projected that this impact is close to the many contagious diseases, such as malaria [4]. This is also the prominent reason for the deaths of the population between the ages of 15–29 years, and the problem is acute in developing countries. The crash rates are persistently increasing in these countries, while there is a significant decrease in the rates in many developed countries. These developing countries are the realms of nearly 90% of road fatalities of the world; around 70% of the fatalities occurred particularly in low-income countries, although having 82% population and 54% registered vehicles of the world [2, 3]. Besides, the Asia–Pacific region contributes to more than half of the total road deaths with only one-fifth of the registered motor vehicles of the world [5]. Additionally, low-income countries with 27.5 fatalities per 100,000 populations are more than three times vulnerable compared to high-income countries with 8.3 fatalities per 100,000 populations [3]. The costs of these road crashes are often found collectively 1–3% of GDP. Unfortunately, this percentage is projected up to 5% of the GDP in low to middle-income countries [2].

3   Traffic Crashes in Context of Bangladesh

Being the major mode of transport in Bangladesh, road transport has now been characterized as a source of the hidden epidemic through traffic crashes. Every year, thousands of road users are losing their lives and getting injured on the roads of Bangladesh. Though official records exclaim annual 2500 road deaths and 3000 injuries, the accurate scale of this problem is still unknown. Few studies evaluated the annual road deaths ranging from 12,000 to 20,000 [2, 6–9]. The most recent WHO report estimates that the annual road traffic fatalities in Bangladesh could be more than 24,000 [3]. The discrepancy between the reported and WHO estimated rate is further illustrated by plotting fatality rates against GDP per capita in Fig. 1.

Figure 1 shows road fatalities per 100,000 populations with respect to GDP per capita income of 172 countries. According to the WHO estimation, fatality rate per 100,000 populations of Bangladesh is 13.6 (indicated with the red diamond shape in Fig. 1). The rate is in the mid-range of the low-income countries. However, considering the reported fatalities, this rate is at the lower range of the low-income countries (indicated with the red circle, 1.28 fatalities per 100,000 population). Taking into consideration of fatalities per 100,000 vehicles, these values were found at the upper and lower ranges (1020.6 and 98.77 fatalities per 100,000 vehicles, respectively) which indicate reporting discrepancy of the crash data.

An interesting point is that road safety research with updated trends is hardly found in Bangladesh. But, the crash characteristics might have changed in recent years in the country. Therefore, the safety situations considering the recent data are needed to be analyzed. Again, to develop effective road safety strategies, introduce modern and smart technologies, and prioritize these strategies, up-to-date road safety research is essential. That is why this study intends to provide a prevailing road safety scenario considering the latest data in Bangladesh.
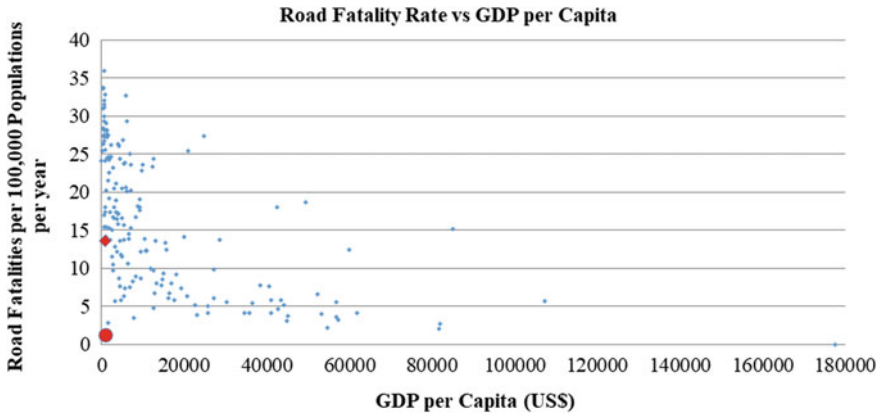
Fig. 1 Road fatalities per 100,000 populations in 172 countries. Bangladesh is represented by red mark (diamond shape for WHO estimation and circle for reported fatalities) [2, 10]

4 Data Collection and Methodology

In Bangladesh, police officially collect information of each road crash after site investigation and fill up the first information report (FIR). Then, they transfer FIR data into Accident Report Form (ARF) which is the prescribed form of road crash data. The ARFs are sent to the Accident Research Institute (ARI) from police range and metropolitan offices. After necessary corrections and editing with road user movement (RUM) code, the data are stored in Micro-computer Accident Analysis Package 5 (MAAP5) software. Besides the police, some non-government organizations collect crash data from newspapers and media reports. Sometimes, hospitals can provide crash data though they are not sufficient for in-depth crash research. In this study, crash data were collected from police reported FIR, MAAP5 records based on ARF, media reports, i.e., newspapers, and other electronic sources. The MAAP5 database of ARI was used for the characteristic analysis. For detailed analysis, the study used 6-year MAAP5 data from 2010 to 2015. Though the data is 6-year old, it is the only database that is compatible for detail characteristics analysis as it contains almost 67 parameters for each crash. FIR or any other available database does not provide detailed information on different attributes of crashes. The onward latest ARF data is still under processing. However, for magnitude, global comparison, trend, and rate analysis, the study used data up to 2019 collected from other available sources such as newspapers, media reports, surveys, and estimations by different organizations.

5　Analyses and Discussions on Results

5.1　Trends of Crashes and Fatalities

As reported in the ARFs, total road fatalities have climbed from 187 to 4138 during 1972–2019 (an increase by 44% per year in 48 years after the liberation of Bangladesh), while in the last two decades, this percentage is different (3314 in 1999 to 4138 in 2019, 13% per year). The trends are shown in Fig. 2.

However, it is also seen that there is a decreasing trend in the numbers from 1998 to 2014 with some fluctuations, and from 2008 to 2017, it is quite significant. This might be attributed to the introduction of the newly developed crash reporting form in 1998, and the organization of successive training programs for police officials with particular aims for capacity building regarding proper ways of reporting and filling up different attributes of the crash in the ARF. This is also attributable partly to the geometric improvement of the existing roads (such as curve straightening, carriageway widening, and black spot treatment), construction of new highways and bridges encompassing safety audit approaches, growing the number of high standard vehicles (like Volvo and Hino), improvement of road users' education and awareness level, police enforcement, and also to the augmentation of the coordination among different agencies. However, a reverse trend is observed during the last two years, particularly a significant increase in 2019. This fluctuation again might be attributed to the increasing of informal vehicles, unskilled drivers, reporting inconsistency, and traffic diversions due to the huge development work particularly construction works on most of the major highways in the last couple of years. Overall, the crashes and fatalities trend line showing a rising trend which is very alarming for the country.
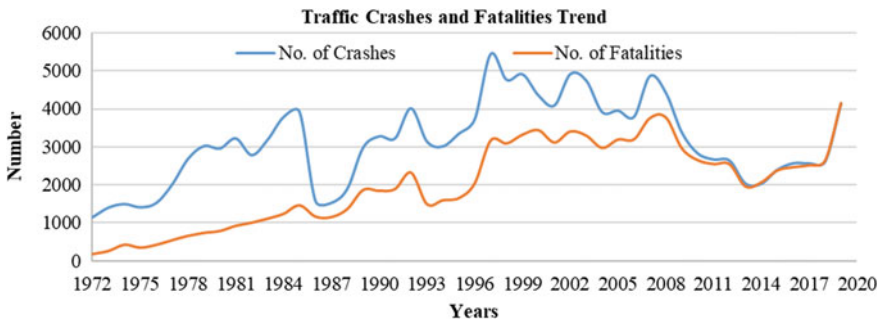
Fig. 2　Traffic crashes and fatalities in Bangladesh (1972–2019) [11, 12]

5.2 Trends by Fatality Rates

Analysis revealed that the fatality rate per 100,000 registered motor vehicles has decreased by more than eight times in the last two decades (594 to 69 during 1998–2018) despite increasing mobility demand (Table 1). Additionally, the fatality rate per capita GDP has decreased by around five times from 1998 to 2018 (7.57 to 1.55 as shown in Table 1). The road fatalities per 100,000 populations and fatalities per 100 km of Roads and Highways Department (RHD) roads also show a gradually decreasing trend except for the last three years, 2017 to 2019. It is seen that the fatality rates have decreased from 2.51 to 1.56 per 100,000 population and 14.79 to

Table 1 Traffic fatalities per 100,000 vehicles, populations, per capita GDP and 100 km roads [11, 14, 15]

Year	Fatalities per 100,000 on-road motor vehicles	Fatalities per 100,000 registered motor vehicles	Fatalities per 100,000 populations	Fatalities per capita GDP) (USD)	Fatalities per 100 km RHD roads
1998	782.36	593.84	2.51	7.57	14.79
1999	795.98	600.36	2.65	8.09	15.81
2000	780.86	588.23	2.69	8.20	16.49
2001	663.89	498.82	2.39	7.49	14.95
2002	671.85	501.07	2.56	8.23	16.34
2003	602.10	446.03	2.44	7.37	15.81
2004	506.07	377.32	2.17	6.24	14.27
2005	528.65	373.85	2.29	6.38	15.34
2006	504.42	342.31	2.27	6.27	15.36
2007	564.05	355.67	2.63	6.72	17.90
2008	432.57	314.15	2.61	5.93	17.83
2009	303.12	220.14	2.03	4.21	13.90
2010	243.18	176.61	1.79	3.39	12.33
2011	208.22	151.22	1.71	2.95	11.77
2012	189.48	137.61	1.68	2.87	11.73
2013	136.00	98.77	1.28	1.99	9.04
2014	132.87	96.49	1.34	1.85	9.48
2015	132.82	96.46	1.52	1.90	10.81
2016	117.77	85.53	1.56	1.76	11.11
2017	104.85	76.15	1.57	1.61	11.27
2018	95.55	69.40	1.63	1.55	11.82
2019	–	–	2.54	–	18.41

Note: Traffic fatality rates were calculated considering the FIR data as there are more reported number of fatalities

11.11 per 100 km of RHD roads during 1998 to 2016, while in the last four years (2016–2019), it has increased a modest amount (1.56 to 2.54, and 11.11 to 18.41, respectively), as shown in Table 1. Both the facts show the same fluctuation in the same period which might be attributed to the same reason.

It is to be noted that due to lack of recent data on vehicle kilometers, crash or fatality rates per 100 million vehicle kilometers could not be driven. However, using the vehicle operation survey carried out by RHD in 1999–2004, this study assessed crash and fatality rates with respect to vehicle kilometers [13]. The study found that while total annual vehicle kilometers driven by motor vehicles have risen by 57%, the corresponding crash and fatality rates have reduced by 49% and 43%, respectively, per 100 million vehicle kilometers of vehicles plying on road during the five years of span. A significant reduction in crash and fatality rates per 100 million vehicle kilometers also indicates a positive approach toward traffic safety improvements in the country. Thus, it can also be concluded that as the extent of exposure in the form of trip numbers, vehicles, road users, and road networks are increasing, these trends show a positive and hopeful sign. This might be due to various positive responses by government and non-government organizations for improving the overall transport system including safety as discussed earlier.

5.3 Vehicle Statistics: Trend and Their Involvement Rates

Table 2 shows the average yearly vehicular involvement by specific vehicle types in the crashes and rates per 100,000 respective vehicles. It also shows the yearly pedestrian fatality rates per 100,000 vehicles of those categories. It is found that the involvement of buses including minibuses is disproportionately higher; with over 700 crashes per year and 1100 crashes per 100,000 buses, this is followed by trucks (around 650 crashes per year, and 387 crashes per 100,000 trucks). In the case of pedestrian fatality rates by vehicle type, buses and trucks are also found as the main contributors.

5.4 Crash Characteristics Analysis

As mentioned earlier, this study analyzed crash characteristics based on the data extracted from the MAAP5 database. The results of the analyses are briefly discussed in the following sections.

- *Crash severity*: Out of 11,427 crashes, 9020 were fatal, 1695 were grievous, 439 were simple, and 273 were motor collision crashes during 2010–2015 in the country. The fatal crashes were found to be 79% of total crashes during this period, and the ratio of the fatal and injury crashes is around 4:1. This high proportion of fatal crashes indicates that mainly the fatal crashes are being recorded, and other

Table 2 Statistics of registered vehicles, traffic crashes and fatalities [12, 14]

Vehicle types	Number of vehicles (registered)[1]	Crash involvement per year[2]	Pedestrian fatalities per year[3]	Crashes per 100,000 vehicles[4]	Pedestrian fatalities per 100,000 vehicles
Motor car	288,237	100	20	35	7
Jeep/microbus	128,322	121	30	94	23
Taxi/pickup	121,829	103	24	84	20
Bus	62,860	705	391	1121	623
Truck	163,802	634	188	387	115
Auto rickshaw/tempo	243,382	182	27	75	11
Motorcycle	1,392,312	315	61	23	4
Rickshaw	–	80	4	–	–
Bicycle	–	66	2	–	–
Others	62,158	313	132	503	212
All	2,462,902	2618	730	106	30

Note: 1. Total number of vehicles registered is 2,462,902 up to 2015; 2. Average number of vehicle involvement in crashes per year (from 2010 to 2015, based on the MAAP5 database); 3. Average pedestrian fatalities by different vehicle types; 4. Crashes per 100,000 respective vehicles

crashes are ignored. According to world statistics, injury crashes are 10–15 times higher than fatal crashes [16]. This again entails that reporting of injury crashes is a neglected issue in Bangladesh.

- *Collision types*: Hit pedestrian with 44% of the total fatal crashes and 48% of the total crashes was the dominant collision type in Bangladesh during 2010–2015. Other common collision types were head-on (20%), rear-end (14%), sideswipe (6%), and overturning (6%). These five types of collision incorporated nearly 90% of the total crashes with 91% of total fatal crashes in the country. In the case of crash severity by crash type, hit pedestrian, overturn, and head-on crash types showed higher severity (0.87, 0.80 and 0.77 fatal crashes per total crashes, respectively). The crashes associated with hit pedestrians, head-on collisions, run-off-roads, and losing control of the vehicles were significant in rural parts of the country. In addition, severe consequences of overloaded buses, hitting bridge rails, and plunged into deep ditches appeared to be of considerable concern of these areas. The analysis has also shown that, among the total crashes, 60% were single-vehicle crashes, and the other 40% were multi-vehicle crashes. The crashes resulting in hit pedestrians, lost control, and hitting objects on the road and off the road are noteworthy crash categories of the single-vehicle crashes.

- *Temporal distribution of crashes*: Nearly, 63% of the total crashes occurred during daytime (6:00 to 18:00) and 37% at night-time (18:00 to 6:00). Again, crashes and fatalities showed nearly uniform distribution during daylight hours (10.33% per hour) with a slight peak during 10:00–11:00 (12%). The lowest number of

crashes happened from midnight to late night, 12:00 to 4:00 (2.4% per hour). Crashes tend to occur to some extent more on weekends (Friday and Saturday, 15% per day) and fairly distributed among the weekdays with an average of 14%. While the highest crashes were seen in March and May (with 10% in each month), the lowest number of crashes were found in the winter season, especially in November (7%) and December (7%).

- *Vehicles involved in crashes*: Heavy vehicles, such as trucks and buses/minibuses, were mostly involved vehicles in the road crashes (buses/minibuses 27%, trucks 24%) of the country, and in fatal crashes, their shares were 28% and 26%, respectively. This group of vehicles was associated with 60% of the pedestrian deaths (shares were buses/minibuses 33%, and trucks 26%). Apart from the heavy vehicles, motorcycles were the third single most contributor to road traffic crashes and fatalities, and with the rising of motorcycle ridership, their share in road crashes is also increasing alarmingly.

- *Urban and rural crashes*: During 2010–2015, a total of 4799 crashes (42% of total reported crashes) took place in urban areas of Bangladesh that resulted in 4062 fatalities (35% of total fatalities). The rural areas with 58% of crashes were responsible for 65% of all fatalities. This implies that the crash severity rate is higher in rural areas than in urban areas. It is quite logical as most of the rural crashes are vehicle-vehicle crashes and occur with higher speed on rural sections of highways. On the other hand, single-vehicle crashes such as pedestrian crashes are predominant in urban streets where speed is comparatively lower.

- *Road crashes by road geometry*: In Bangladesh, around 90% of the crashes occurred on the straight sections of the road followed by 9% on the curve sections, 2% on the curves with vertical or downward slope, and 2% on the slope sections only. Though theoretically, the curve sections are more vulnerable than straight; however, it is quite interesting that the crashes in straight sections are around nine times higher than the curves. This point could be taken for further study. However, it might be due to the over speeding and frequent risky overtaking attitude without considering sufficient gaps between vehicles particularly with oncoming vehicles on undivided two-lane two-way highways. The crash distribution according to the link and junction shows that around 63% of the crashes occurred at the links of the road. Among the other 37% of the crashes, 9% occurred at the T-junctions and 7% at the cross junctions.

- *Road crashes by road class*: All national highways combined 47% of road crashes which were followed by the city roads (20%), regional roads (15%), village roads (9%), and feeder roads (8%) during 2010–2015. Thus, it is clear that crashes on the national highways and city roads are of primary concern to improve the road safety situation in Bangladesh. Several investigations revealed that improper road design and construction along with inadequate road safety features, significant road environmental and traffic operation hazards, and high concentration of roadside local activities are the major causes of concern for road safety in the national highways of Bangladesh [6, 7, 17, 18]. These studies also suggested site-specific treatments. On the other hand, low crash counts on regional, feeder, or rural roads might be due to the reporting and recording problems.

- *Crash distribution by districts*: The highest concentration of crashes per 100,000 populations was in the Dhaka district (3.8 crashes per 100,000 inhabitants per year) followed by Manikganj district (3.2 crashes per 100,000 inhabitants per year). A significant number of crashes occurred in Barguna, Habiganj, and Khagrachari districts, accounting for 2.3 crashes per 100,000 inhabitants per year, which could be ranked at third position simultaneously. Barishal, Sylhet, Rajbari, Chattogram, Kushtia, and Rajshahi districts have also witnessed a notable rate of crashes (2, 2, 1.9, 1.8, 1.8, and 1.8 per 100,000 inhabitants per year, respectively). Apart from the mentioned districts, some districts like Bandarban and Lalmonirhat showed a noticeable rate of crashes (1.7 per 100,000 inhabitants per year in each district), whereas most of those districts have a very less proportion of major national highways and have small city areas, fewer road networks, and less traffic demand. These districts should be brought into further investigation.

5.5 Fatality Class Analysis

- *Fatalities by user classes*: The vulnerable road users, such as pedestrians, bicyclists, motorized 2-wheelers, and non-motorized 3-wheelers, shared nearly 61% of road fatalities in Bangladesh during 2010–2015. Among them, pedestrians alone were the victims of 46% of the fatalities (Fig. 3). Following the pedestrian fatalities, the occupants of 4-wheelers heavy vehicles (17%), occupants of 4-wheelers light vehicles (11%), and 2-wheeler riders (8%) constituted the lion share of the road-user fatalities during the analysis period. In addition, informal para-transits (such as nosimon and korimon), and other non-motorized transports (NMT) shared up to 6% and 4% of the road fatalities, respectively.
- *Fatalities by age distribution*: The population with age between 21 to 40 years was the main victims of the road fatalities in comparison with the proportion of the population belonging to this group (48% vs. 34%). Besides, the age group of 41 to 50 years was also significantly involved in traffic fatalities, representing
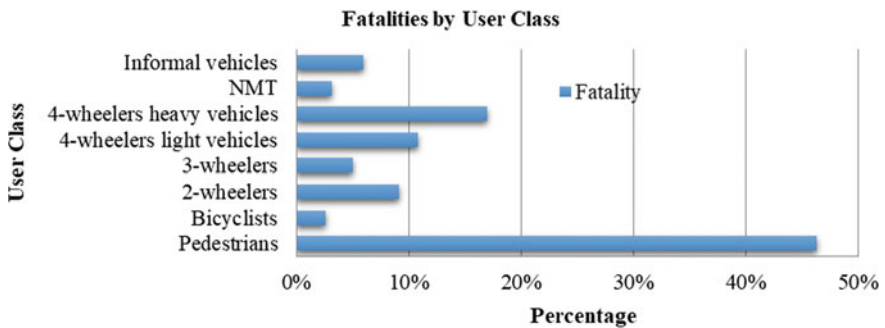
Fig. 3 Road fatalities by user class

15% of the total fatalities with only 12% share in the total population. It is also found that among the total motorcyclist fatalities, 86% were within the age group 16 to 45 years which are the most economically productive young people. The loss of these young people causes serious pains and sufferings to the family and society as well as to the entire nation.

- *Fatalities by gender*: It is evident that males are the predominant victim of road crashes in Bangladesh with 83% share on road fatalities. On the other hand, females share 17% of total road deaths. This could be attributed to the exposure of males and females. Normally, males are more exposed on the road than their female counterparts in Bangladesh. The risk-taking attitude of males also might be higher than females. However, further investigation is needed in favor of this argument.

- *Vulnerable road user fatalities*: Around half of the road fatalities are pedestrians alone. In urban areas, this share is much higher. In Dhaka city, pedestrians shared 74% of all traffic fatalities during 2010–2015. Most of these pedestrian fatalities occurred during crossing the roads (41%) and walking along/on the roads (39%). In addition, the age distribution of pedestrian fatalities revealed that the 21 to 45 years age group is the most involved group in pedestrian fatalities (around 40%). The children who are aged below 15 years represented nearly 19% of the pedestrian fatalities [17]. These statistics demand safe pedestrian facilities, especially for school-going children.

- *Motorcyclist fatalities*: The percentage of motorcycle crashes, fatalities, and injuries have increased more than the increase of motorcycles share in total vehicles. The share of motorcycles rose from 42% in 1998 to 57% in 2015. On the other hand, the share of motorcycle crashes and fatalities was only 5% and 3%, respectively, in 1998, and it climbed up to 15% and 9%, respectively, in 2015. More alarmingly, most of the victims were working-class people of age 21 to 35 (contributed to 56% of motorcycle fatalities). The setting of the speed limit for motorcyclists, enforcement of laws, use of standard helmets, and public awareness regarding the importance of helmet uses are highly needed since the death rate of unaware and non-helmeted motorcyclists is found higher in the study [19].

6   Conclusions

Bangladesh needs a holistic approach to improve the road safety situation. Data are the cornerstone to step forward. The country is lagging in crash data repository; but, the safety interventions and policy decisions should be based on up-to-date data driven. However, available studies on Bangladesh are mostly based on old crash data; thus, pragmatic decisions cannot be expected. This study attempts to analyze the country's road safety status incorporating the latest available MAAP5 database, police reported FIR, newspaper data, and data from accessible electronic sources to bring forth trends, rates, magnitudes, and characteristics of road crashes and resulting casualties. Crashes and fatalities were found to be on a rising trend. Prominent crash

types were hit pedestrian, head-on, and rear-end. National highways and city roads were found contributing to the major percentage of road crashes in the country. The study also sheds light on crash locations, districts with significant crash rate, and vehicles involved in the crashes. Fatalities by different road-user groups were identified clearly. Furthermore, the study pointed out the reporting discrepancy of crash data in Bangladesh. Future potential research scopes were identified in this study as well. The findings of this study will help concerned authorities to prioritize road safety problems and, thus, will assist decision-making processes for reducing road fatalities as well as social and economic losses from traffic crashes in Bangladesh.

References

1. Hoque MM, Hossain MS, Rahman MA, Islam SMA (2014) Safer motorcycling and safer roads: the context of Bangladesh. In: Proceedings of South East Asia Road Safety Summit (SEARSS), Bali, Indonesia
2. World Health Organization (2015) Global status report on road safety 2015 (ISBN 978-92-4-156506-6). Geneva, Switzerland: https://www.who.int/violence_injury_prevention/road_safety_status/2015/en/. Accessed Jul 2020
3. World Health Organization (2018) Global status report on road safety 2018. Geneva, Switzerland: http://www.who.int/violence_injury_prevention/road_traffic/en/. Accessed Jul 2020
4. Bhalla K, Shotten M, Cohen A, Brauer M, Shahraz S, Burnett R, Leach-Kemon K, Freedman G, Murray CJL (2014) Transport for health: the global burden of disease from motorized road transport. Washington, DC, USA
5. Peden M (2004) World report on road traffic injury prevention. Geneva, Switzerland: https://www.who.int/violence_injury_prevention/publications/road_traffic/world_report/en/. Accessed Jul 2020
6. Hoque MM, Mahmud SMS (2009) Road safety engineering challenges in Bangladesh. Paper presented at the 13th road engineering association of Asia and Australasia (REAAA) Conference, Korea, 23–26 September 2009
7. Mahmud SMS, Ahmed I, Hoque MS (2014) Road safety problems in Bangladesh: achievable target and tangible sustainable actions. Jurnal Teknologi 70(4):43–49
8. World Bank (2020) Delivering road safety in Bangladesh: leadership priorities and initiatives to 2030. Washington DC, USA
9. World Health Organization (2013) Global status report on road safety 2013: supporting a decade of action (9241564563). Geneva, Switzerland: http://apps.who.int/iris/handle/10665/83789. Accessed Jul 2020
10. World Bank (2020) World development indicators. Available at: https://data.worldbank.org/indicator Accessed Jul 2020
11. Bangladesh Police (2020) First Information Report (FIR). Police Head Quarter, Bangladesh
12. Accident Research Institute (2020) Road accident facts. MAAP5 Database, Bangladesh
13. Mahmud SMS, Hoque MS (2008) Deficiencies of existing road network in Dhaka metropolitan city. Paper presented at the 10th Pacific regional science conference organization (PRSCO) summer institute, hosted by Bangladesh Regional Science Association (BRSA), Dhaka, Bangladesh, 2008

14. Bangladesh Road Transport Authority (2020) Vehicle statistics data, Bangladesh. Available at: https://brta.portal.gov.bd/. Accessed Jul 2020
15. Roads and Highways Department (2020) Online road network, Bangladesh. Available at: https://www.rhd.gov.bd/OnlineRoadNetwork/Default.asp. Accessed Jul 2020
16. Mahmud SMS, Ferreira L, Hoque S, Tavassoli A (2017) Application of traffic conflict techniques as surrogate safety measures: a sustainable solution for developing countries. In: Proceedings of the 1st GeoMEast international congress and exhibition, Egypt 2017 on sustainable civil infrastructures
17. Mahmud SMS, Hoque MS, Qazi AS (2009) Road safety problems in Bangladesh: some major initiatives, constraints and requirements. In: Transport and communications bulletin (TCB) for Asia and the Pacific, vol 79 (road safety), pp 47–67
18. Hoque MM, Pervaz S, Ashek AAN (2020) Overview of the highway crashes in Bangladesh. In: Proceedings of the 5th International conference on civil engineering for sustainable development (ICCESD 2020), KUET, Khulna, Bangladesh, 7–9 February 2020. ISBN: 978-984-34-8764-3
19. Pervaz S, Rahman MM, Hasanat-E-Rabbi S, Uddin MI, Rahman M (2020) A review of motorcycle safety situation in Bangladesh. In: Proceedings of the 5th International conference on civil engineering for sustainable development (ICCESD 2020), KUET, Khulna, Bangladesh, 7–9 February 2020. ISBN: 978-984-34-8764-3

A Study on Traffic Characteristics and Overtaking Behaviour of Drivers on Bangabandhu Bridge Approach Road

S. Hashi and M. Rana

1 Introduction

In Bangladeshi roads, traffic is mostly seen in mixed types and non-lane based that are vastly seen in local to highway roads. The traffic compositions are mainly comprised of motorized vehicles such as two wheelers that includes motorcycles, three wheelers (auto rickshaw), cars of different speed types and size, trucks of different size, capacity and wheel configuration, buses, and non-motorized vehicles like bicycles, rickshaws, manual vans, etc. Characteristics like the dimensions of the vehicle, speed, acceleration, deceleration, clearances and manoeuvres ability of these vehicles vary enormously, and again, the traffic speed is the most important factor that affects the safe movement of vehicles and human [1]. The speed variation and problems related to these are creating real-time difficulties to the road users. By coping with these difficulties, drivers as well as road users are affected by accidents that likely to happen. Under mixed traffic conditions, vehicles use the space on the road more effectively, and their movement greatly depends on lateral and longitudinal gaps available on the road. Overtaking and lane-changing manoeuvres on a road traffic facility occur when the vehicles do not run at the design speed [2]. Moreover, overtaking is one of the most complicated and important manoeuvres on undivided roads conditions were vehicles that intend to overtake use the opposing lane to overtake [1, 3].

The North-Bengal is one of the most visited zones of our country. The only connecting route to the northern part with the capital city of Bangladesh is through Bangabandhu bridge which is situated on Jamuna River. This bridge connects Tangail

S. Hashi (✉)
Department of Civil Engineering, Bangladesh Army University of Engineering and Technology (BAUET), Natore, Bangladesh

M. Rana
Department of Civil Engineering, Ahsanullah University of Science and Technology(AUST), Dhaka, Bangladesh

and Sirajgong districts with the bridge which is a must to cross if anyone wants to travel from North to the capital and vice versa. Elenga is the meeting point of four directions. Vehicles from Dhaka, Mymensingh, Vuapur, and internal parts of Tangail meet on this point and they play on the Elenga to Bangabandhu Bridge approach road. The zone selected for data collection is in between Elenga to Bangabandhu Setu east railway station, which has a combination of local and highway traffic, the selected area has a high volume of traffic flow. And it is also considered as one of the major highways (NH-405) in our country. This paper aims to study and understand the overtaking characteristics of various vehicles on undivided roads in mixed traffic and non-lane discipline traffic conditions.

2 Methodology

2.1 Study Location and Test Vehicles Selection

For executing the study, a location was selected on basis of the busy and high volume of traffic flow of a two-lane two-way national highway (NH-405). Elenga to Banga-bandhu Setu east railway station (Fig. 1) on Bangabandhu bridge approach road was eventually selected for the study. Most of the drivers tend to speed up in this area

Fig. 1 a Elenga to Bangabandhu Setu east railway station in Google map. *Source* Google map, **b** Real-time pictures during data collection

after losing their framed time in Dhaka city due to congestion. Two specific methods (moving car observer method and registration number plate method) were followed for the collection of different parameters in this study. In the moving car method, the total area was analysed. On the other hand, for the registration number plate method, the study area was divided into three sections with distances of 2.5–3.5 km.

The needed data for this study were screened from a total of 12.5 km road section at Elenga to Bangabandhu Setu east railway station approach road on four different days. Those days are categorized by the weekend, normal day, peak day and holiday.

To identify the physical and operational actions of overtaking manoeuvres, a field survey was conducted in the study area. From the survey data, physical observations such as overtaking characteristics of vehicles, types of overtaking (O) and overtaken (T) vehicles, vehicle registration plate number, the flow rate of vehicles and operational observations such as overtaking manoeuvre of vehicles (i.e. flying overtaking or accelerative overtaking), etc. were identified.

2.2 Moving Car Observer Method

The moving car observer method is commonly used to estimate both speed and traffic flow by collecting data of a moving vehicle [4]. The field survey was carried out to collect data on the major road starting from Elenga towards Bangabandhu bridge east railway station with a length of 12.5 km. In this observation, a test car (T) was driven with a uniform speed of 40 km/h so that the approaching vehicle can overtake it. The acceleration as well as overtaking characteristics of various vehicles such as passenger cars, heavy vehicles (HV), buses, two wheelers (TW) and light commercial vehicles (LCV) were observed in this selected road segment. Five events were involved in the entire overtaking process [5], and a stopwatch was used to record the time taken for each event [5].

> **Event 1**: When the overtaking vehicle (O) approaches to the counteracting lane for initiating the manoeuvre.
> **Event 2**: When the front tyre of the overtaking vehicle (O) and the rear tyre of the test vehicle (T) are in a line.
> **Event 3**: When the front tyres of the overtaking vehicle (O) and the test vehicle (T) are in a line.
> **Event 4**: When the rear tyre of the overtaking vehicle (O) and the front tyre of the test vehicle (T) are in a line.
> **Event 5**: When the overtaking vehicle (O) either comes back to the previous lane or continues to travel in the counteracting lane after overtaking the test vehicle (T).

The schematic picture of the overtaking manoeuvre observed in this study was shown in Fig. 2. Three persons worked as a team and collected the data for this study in the specified segment of the road.
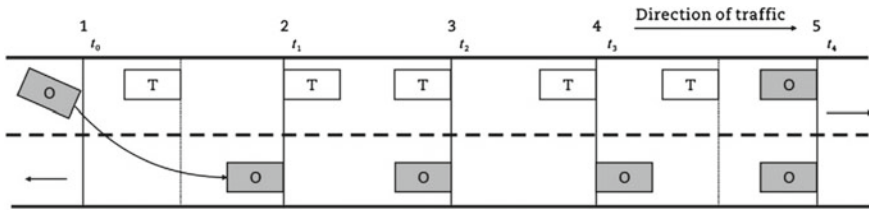
Fig. 2 Events during overtaking process [3]
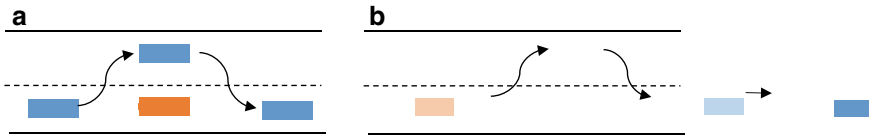
Fig. 3 **a** Schematic picture of flying overtaking, **b** Schematic picture of accelerative overtaking

The overtaking parameters of different types of overtaking vehicles were determined from the collected data. The persons observed two types of overtaking techniques in the study area.

2.2.1 Flying Overtaking

When a faster vehicle moves towards a slow moving vehicle in a free flow stream, it does not follow the slow moving vehicle [6]. When there is no vehicle in the opposing lane, the faster vehicle changes its lane from a longer distance without any slowdown and overtakes the slow moving vehicle. After completing the overtaking operation, it may come back to the previous lane at a larger distance or may continue its movement in the adjacent lane. The schematic picture of flying overtaking is shown in Fig. 3a [6].

2.2.2 Accelerative Overtaking

Accelerative overtaking occurs when a vehicle does not find sufficient space in the adjacent lane to overtake the slow moving vehicle [6]. In such condition, the following vehicle reduces its speed equal to that of the slow moving vehicle for some times depending on the available space in the adjacent lane. Once the following vehicle gets sufficient space in the adjacent lane, it initiates to change the lane and accelerates to complete the overtaking manoeuvre [6]. The schematic picture of accelerative overtaking is shown in Fig. 3b.
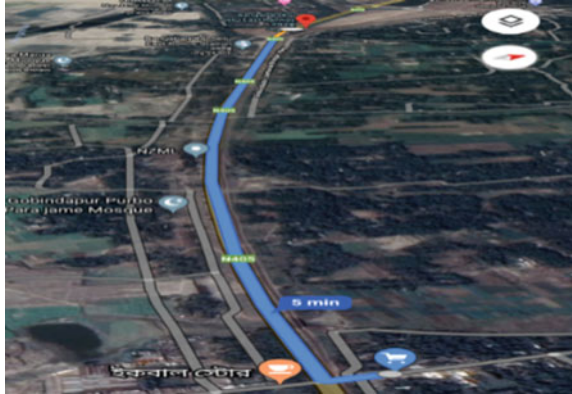
2.3 Registration Number Plate Method

The registration number plate method is considered to be one of the most efficient methods to find out about the state of traffic flow, vehicular characteristics, the number of the overtaking vehicle and overtaken vehicles for both lanes of selected locations. The data for this study were screened from the 2 km road section form the NH-405 Road. In this study, observers were placed on the roadside at each end of the study section.

Each of the persons had a video camera with a tripod. The tripod was placed in such a distance that the cross section of the road was captured and covered. The two persons placed at the end of the section were operating the video camera to capture the vehicle and the registration numbers. Types of the vehicle as well as vehicle registration numbers were observed simultaneously for every 5 min. After every 5 min, the video was stopped and saved for further analysis. The videos were replayed and were analysed thoroughly to get the desired data. When the gross data was collected, the vehicles were divided into various classes. After that the numbers and classes of the vehicles that were frequently overtaking other classes of vehicles or amongst their own class were figured out (Figs. 4, 5 and 6).

3 Results and Discussions

3.1 State of Traffic Flows

This following pie chart contains the percentage of vehicles that were observed on the study section during the study period. Figure 7 gives the general idea of the vehicles during the study period.
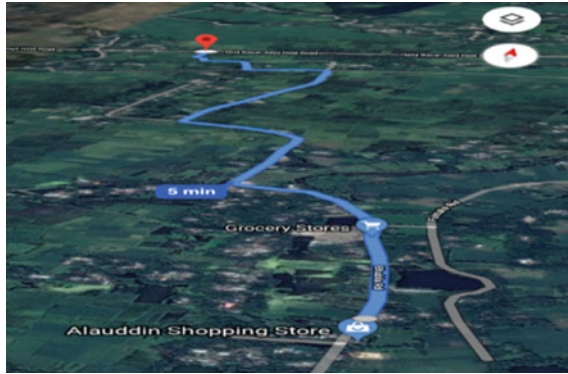
Fig. 5 Bhabla-Hatia bazar in Google Earth Map
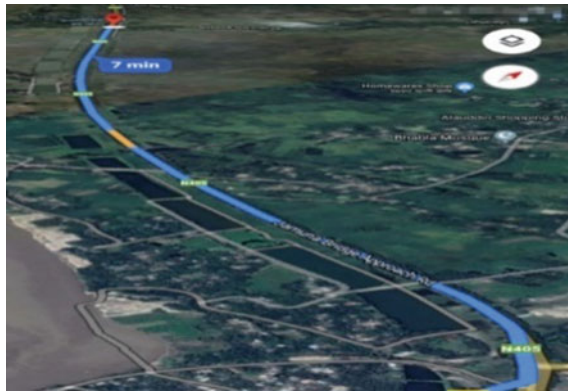
Fig. 6 Elenga-Analiyabari in Google Earth Map
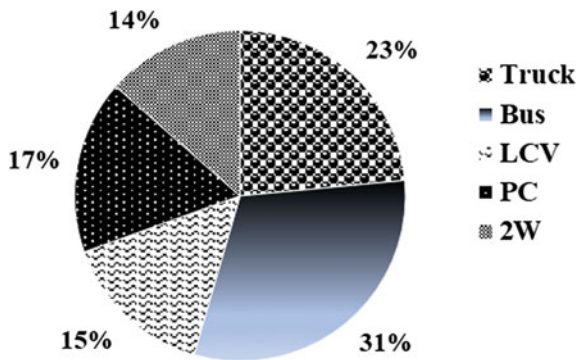
Fig. 7 Distribution of States of traffic flows in Jamuna Bridge approach road
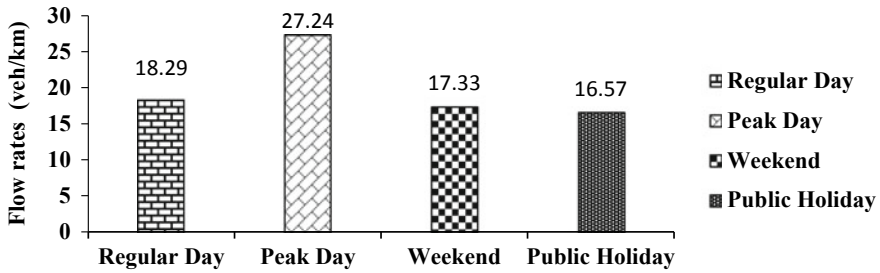
Fig. 8 Flow rates of vehicles on Jamuna Bridge approach road

Whilst the data collection total amount of 200 nos. vehicles were observed. Amongst these 200 vehicles, there were 47 Trucks, 62 Buses, 30 LCVs, 34 PCs, 27 two wheelers. So, the percentage stands like this Bus–31%, Truck–23%, LCV–15%, PC–17% and 2W–14%. As it was a highway (NH-405), it naturally should contain bus and truck more than any other vehicles as most of the heavy vehicles travel through the highways. Less two wheelers on the road and small amount of PC were observed.

3.2 Observation of Flow Rate in Different Days

Figure 8 illustrates the flow rate of the vehicles in the vertical axis and categories of observation days on the horizontal axis. Actual flow rate of the day in a kilometre of road is shown with four types of days that considered to work on. Such as regular day, peak day, weekend, public holiday. The formula that used in here to find the flow rate of vehicles is given below,

Flow Rate of Vehicles = Total Number of Vehicles/Distance Covered by Vehicles

From Fig. 8, it is easily understandable that peak days have the most flow rate that is vehicles per kilometres. Public holidays have the lowest number of vehicles as it is visible by the study. Regular day has a regular flow rate which is the second most vehicles per kilometres. On the other hand, weekend holds the second position from the lowest.

3.3 Overtaking Behaviours of Vehicles by Moving Car Method

There were two types of overtaking behaviours that induced by the drivers were observed for taking the data of moving car method. Percentages of flying (Fig. 9) and accelerative overtaking (Fig. 10) are plotted below:
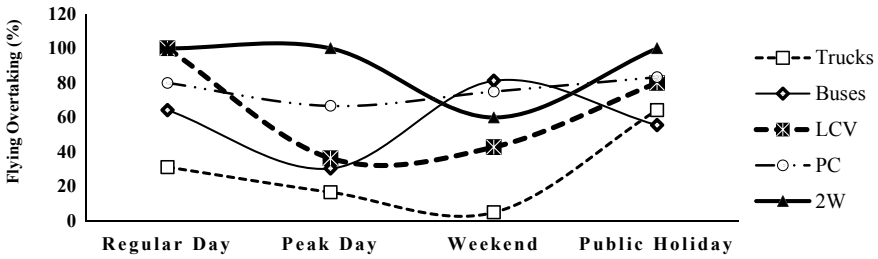
Fig. 9 Percentage study of flying overtaking vehicles
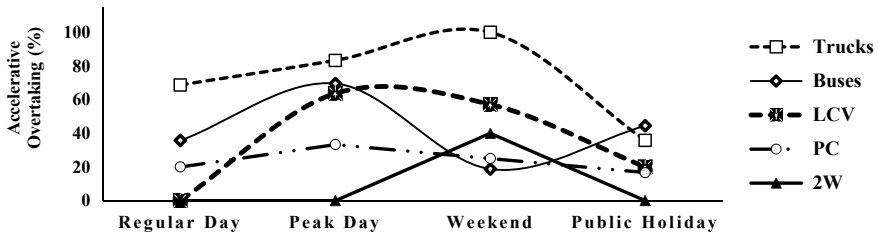
Fig. 10 Percentage of accelerative overtaking vehicles

3.3.1 Percentages of Flying Overtaking Vehicles

Following (Fig. 9) contains trucks, buses, LCV, PC, 2W (two wheelers) and types of days (regular day, peak day, weekend, public holiday) that considered to work on. As the flow rate and the urgency varies with the change of day the overtaking number and the type of overtaking changes along with it.

In the chart, it is clear that regular day shows the highest percentage of flying overtaking are performed by 2W and LCV. This can be attributed due to their fast movability and their relatively smaller sizes. It is seen that trucks perform the least flying overtakes in a regular day. 2W and LCV are more aggressive and on a rush in a regular day, and trucks are not that much aggressive and slower that other vehicles also. In a peak day, it seen that 2W are at the top of the chart, followed by PC, LCV, buses and trucks. So, from this we can understand, still the two wheelers are the most aggressive and trucks are the least.

In a weekend, the amount of the flying overtake is totally different as the buses tops the percentage chart, followed by PC, 2W, LCV, trucks. In a public holiday, the 2W takes the top place again, and it is being, followed by PC, LCV, trucks and buses. There are more two wheelers and passenger cars. There are many buses seen which takes passengers but the duty vehicles are not seen that much.

3.3.2 Percentage of Accelerative Overtaking

Figure 10 demonstrates that in a regular day the highest percentage of accelerative overtaking is performed by trucks, followed by Bus, PC, 2W, LCV. This can be attributed due to their slow movability and their relatively larger sizes.

It is seen that 2W and LCV perform the least accelerative overtakes in a regular day. In a peak day, trucks are at the top of the chart, followed by buses, LCV, PC, 2W. So, from this it can be understand, still the two wheelers are the most aggressive and trucks are the least.

In a weekend, the scenery of the accelerative overtaking is totally different as the trucks tops the percentage chart than LCV, 2W, PC, bus. It changes all the results from the previous charts. In a public holiday, bus takes the top place again. In a public holiday, there are more two wheelers and passenger cars. There are many buses seen which takes passengers but the duty vehicles are not seen that much.

3.4 Overtaking Behaviours of Vehicles by Registration Number Plate Method

There are two types of overtaking manoeuvres. Taking the data of by registration number plate method percentages of overtaking (O) and overtaken (T) that happened by the vehicles were found. They are as follows:

3.4.1 Percentages of Overtaking (O) Vehicles

Figure 11 shows the state of flow of overtaking vehicles (trucks, buses, LCV and PC) by registration number plate method on regular, peak, weekend, public holiday. As the flow rate and the urgency varies with the change of day, the overtaking and overtaken vehicles amount and the type of overtaking changes along with it.
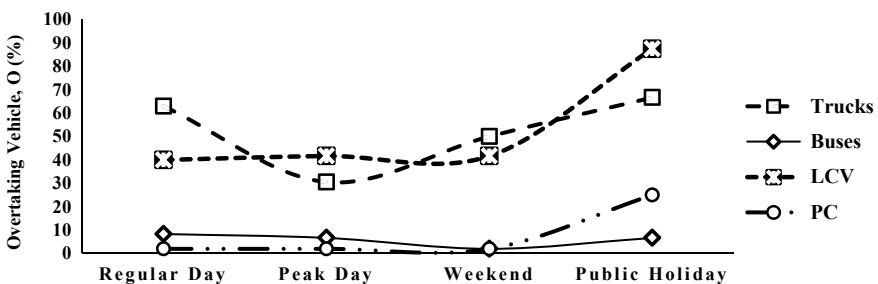
Fig. 11 Percentage of overtaking (O) vehicles on a specific day

In the chart, it appeared that in a regular day the highest percentage of overtaking is performed by PC. Followed by bus, LCV and truck. It is clearly seen that trucks overtakes a least in a regular day and take some time to move to the opposing direction. In a peak day, still the PC and bus were the most aggressive and trucks were the least in case of overtaking. Bus took the top place of overtaking, followed by LCV during public holiday.

There are many buses seen which takes passengers but the duty vehicles are not seen that much. Percentages of overtaking (O) behaviour of vehicles that undergone because of the drivers for a specific vehicle for studied busy road section and installing speed breaker where overtaking behaviour seems very often can be reduced the accident rate.

3.4.2 Percentages of Overtaken (T) Vehicles

As the flow rate and the urgency varies with the change of day the overtaking and overtaken vehicles amount and the type of overtaking changes along with it. From the line graph (Fig. 12), the highest percentage of being overtaken is held by trucks in a regular day, followed by LCV, bus and PC. PC showed a tendency to overtake other vehicles as a result it showed a lowest value in case of overtaken. It is seen that trucks perform the least overtakes in a regular day. It is seen that PC are more aggressive and on a rush in a regular day.

The result of this chart is pretty much the opposite of the immediate previous chart. Heavy vehicles overtaking and overtaken percentage are as 45.13% and 54.87%, respectively. For buses, the overtaking and overtaken percentage are as 88.46% and 11.54%, respectively. The percentage of overtaking and overtaken for LCV remains same (50%). The percentage of overtaking and overtaken for four wheeler is as 93.33% and 6.67%, respectively. The overtaking vehicles usually do not want to follow the larger size vehicles and they often try to overtake but most of the time they do it by accelerative overtaking due to lack of sight. They can't look through the large obstacle so most of the drivers try to overtake after a slight deceleration.
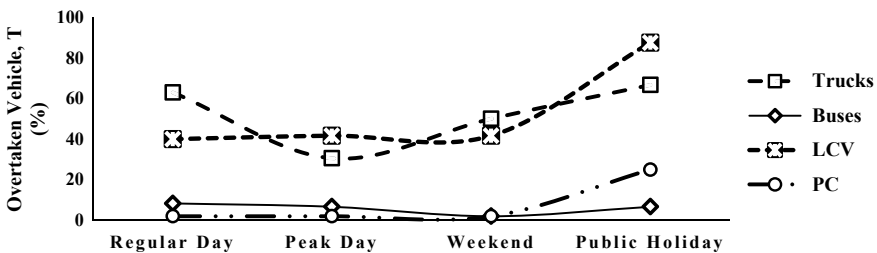
Fig.12 Percentages of overtaken vehicle (T) on a specific day

3.5 Flow Characteristics of Traffic

3.5.1 Time Mean Speed

The rate of speed achieved by all categories of vehicles (HV, BUS, LCV and PC) during overtaking was estimated. The following curve (Fig. 13) which shows the relation between speeds of the vehicles with respect to travelling time as they travelled an average of 3.2-km distance.

A linear relationship trend is drawn between the speed and time showing higher overtaking speed associated with lower rate of time for all types of vehicle separately. This might be attributed due to the fact that the drivers desire to travel at higher speed and often they overtake the leader vehicle to achieve higher speed to cover up their scheduled time frame. It is shown that bus speed often recorded to a highest speed of about 120 kmph in the selected zone comparatively trucks and other vehicle. Over speeding is a major motive that tends to develop a tendency to a driver to step up the vehicle speed.
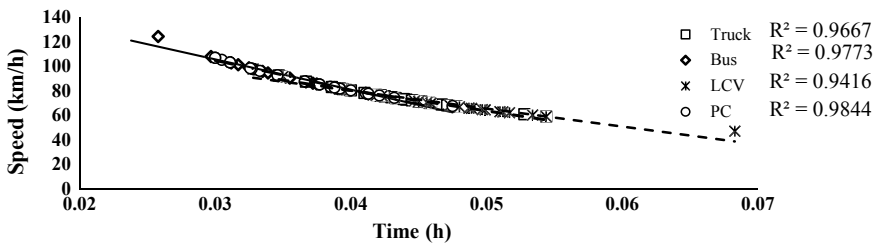
Fig. 13 Time-Speed behaviour pattern
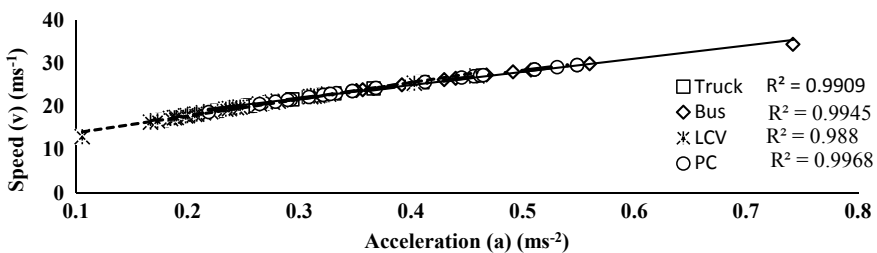
Fig. 14 Speed-Acceleration Pattern at the studied road netwrok

3.5.2 Effect of Speed on Acceleration

The rate of speed achieved by all categories of vehicles (HV, BUS, LCV and PC) during overtaking was estimated. This is a curve (Fig. 14) which shows the relation between speeds of the vehicles with respect to its own individual acceleration.

A best fit relationship is observed between the speed and acceleration showing higher overtaking speed associated with higher rate of acceleration. This deviation from standard relationship may be happen due to the fact that the drivers accelerate the vehicles and often they overtake the leader vehicle to achieve higher speed that causes the rushing tendency. These acceleration depends on brake efficiency that is directly related to sight distance that may affect accident rate in the selected study zone.

4   Conclusions

This study attempts to point out the image of the overtaking behaviour of drivers at the undivided lane road on the Bangabandhu bridge approach road. From the traffic flow, it is vibrant that this road is fully occupied by buses and trucks. Thus it can say, heavy vehicles have a priority on this highway, and the overtaking manoeuvres are highly performed for the sake of adjusting the journey time pre-fixed by the company. Most of the passenger cars are using the flying overtaking method along with buses. On the other hand, trucks maintain their highest percentages of overtaking manoeuvers by mainly accelerative overtaking methods on almost every day. Heavy vehicles overtaking and overtaken percentages are 45.13 and 54.87%. For buses, the overtaking and overtaken percentages are 88.46% and 11.54%, respectively. The percentage of overtaking and overtaken for LCV remains the same (50%). The percentage of overtaking and overtaken for four wheeler is as 93.33% and 6.67%, respectively. From the discussed data, it is clearly visible that the responsibility of rush overtaking is mostly dependent on buses. Mainly, these buses coming from Dhaka has a tendency to rush over the section due to cover up the framed journey time after suffering from the traffic congestion in Dhaka metropolitan city because this is the most suitable section of this highway to cover up the loss of time and speed up towards the Bangabandhu bridge for minimizing the journey time as much as possible and a better way the keep the service level good to the passenger as promised. For mitigating any accidents and loss of lives, the probable concern should be taken by providing traffic control elements such as overtaking lane, traffic calming devices. Though the road has enough overtaking sight distance but for the popularity of overtaking tendency over that section overtaking zone should uphold the safety of the road users including the passengers and drivers. These data can be a help for further development of this road and ensure public safety.

References

1. Balal (2014) Analysis of discretionary lane changing parameters on freeways. Elsevier, pp 277–296
2. Caleb (2018) Modelling behavioural interactions of drivers' in mixed traffic conditions. Elsevier, pp 284–295
3. Chen (2010) Influences of overtaking on two-lane traffic with signals. Elsevier, pp 141–148
4. DeLucia (2015) Effects of oncoming vehicle size on overtaking judgments. Elsevier, pp 163–170
5. Geetimukta Mahapatra AKM (2013) Study of vehicles lateral movement in non-lane discipline traffic stream on a straight road. Elsevier, pp 352–359
6. George (2017) Modeling the effect of traffic regimes on safety of urban arterials: the case study of Athens. Elsevier, pp 240–251
7. Gugulothu G (2017) Overtaking behaviour of vehicles on undivided roads in non-lane based mixed traffic conditions. Elsevier, pp 252–261
8. Gowri Asaithambi GS (2017) Overtaking behaviour of vehicles on undivided roads in non-lane based mixed traffic conditions. Elsevier, pp 252–261
9. Helman (2015) An experimental study of factors associated with driver frustration and overtaking intentions. Elsevier, pp 221–230
10. Hunt (1994) Modelling dual carriageway lane changing using neural networks. Elsevier, pp 231–245
11. Kamel (2014) Modeling and simulation of overtaking behavior involving environment. Elsevier, pp 10–21
12. Satish Chandraa SS (2012) Overtaking behavior on divided highways under mixed. Elsevier, pp 313–322
13. Suzuki (2014) Predicting driver's lane-changing decisions using a neural network model. Simul Model Pract Theory 73–83
14. Tang TQ (2007) A new overtaking model and numerical tests. Physica A 649–657
15. Farah H, Toledo T (2010) Passing behavior on two-lane highways. Transp Res Part F Traffic Psychol Behav 355–364
16. Vlahogianni (2013) Modeling duration of overtaking in two lane highways. Transp Res Part F Traffic Psychol Behav 135–146
17. Yukselen Aksoy R (2010) Effect of soil composition on electrokinetically enhanced persulfate oxidation of polychlorobiphenyls. Electrochim 164–169
18. Zheng Z et al. (2013) The effects of lane-changing on the immediate follower: anticipation, relaxation, and change in driver characteristics. Transp Res Part C Emerg Technol 367–379
19. Solanki MJ et al (2016) Application of moving car observer method for measuring travel time, delay & vehicle flow under heterogeneous traffic condition of C.B.D. area. Int J Current Eng Technol 3(6):799–803
20. Day PP, Chandra S, Gangopadhyay S (2008) Overtaking process on two lane rural. Australian Road Research Board (ARRB), Adelaide Australia

Private Vehicle Ownership Prediction Using Regression and Time Series Analysis

M. M. H. Galib, F. I. Rahman, and A. Hasnat

1 Introduction

Understanding how and why travel occurs is one of the most important tasks of transportation planning. Urban travel and trip patterns influenced by numerous factors. Declining household size and increasing vehicle ownership or private car had, perhaps, the greatest impacts on travel activity. According to AASHTO [1], "The number of household with one vehicle remained roughly constant for 30 years, but after 1990, it began to increase, perhaps attributable to the influx of immigrant populations and growth in single-adult households, note that, for the most part, the great change was in the two-and three-vehicle household." Many researchers have found out that private vehicle ownership is one of the major reasons for traffic congestion. As the number of private vehicles in the developing and developed countries is increasing day by day, traffic congestion is turning into an uncontrollable form. For instance, in Thailand, the ratio of the two-wheeled vehicle was raised from 74 per 1000 persons in 1989 to 215 per 1000 persons in 1999. And, for four-wheeled vehicle ownership, it became 43 vehicles per 1000 persons from 18 vehicles per 1000 persons [2].

There are a lot of factors affecting the private vehicle ownership in the developing and developed countries such as residential location, work location, activity patterns, quality of public transport, independence of mode choice, and much more. But, thriving GDP is irradiated as one of the main factors of increasing private vehicle in the developing and developed countries [3]. Hook and Replogle [4] proposed that the increasing gross domestic product (GDP) and incomes cause the growth of four-wheeled vehicle ownership. Nagai and Fukuda [2] have concluded that in the

M. M. H. Galib (✉) · A. Hasnat
Department of Civil Engineering, Rajshahi University of Engineering and Technology, Rajshahi, Bangladesh

F. I. Rahman
Department of Civil Engineering, University of Yamanashi, Yamanashi 400-8511, Japan

Asian region, the increasing pattern in the number of two-wheeled and four-wheeled vehicles chase the GDP levels growth curve.

Scholars also brought modernization forward as one of the primary reasons for increasing private vehicle [5]. Before modernization, people's activities were confined in their local region. But, due to modernization, activities got a larger form. And, not only activities but also distance got larger. Now, people always find their best whether it is for education, work, or entertainment.

For the low quality of public transport, the limitations of root choosing people are turning away from it day by day. Scholars have inculpated the poor quality of transit systems and inadequate service of public transportation as the reason for people choosing taxi and private car over public transportation. Therefore, people are choosing private vehicle for their easy and comfortable journey. For instance, in Yangon city, Myanmar, bus services have been steadily losing customers at a rate of 10% a year so that volumes as of 2015 are only half of those in 2007 [6]. As a result, where a public bus can carry 30–40 people on average at a time, a private car is used to carry only 2–4 people. Hence, scholars pay more attention on good quality public transport to reduce the increasing vehicle ownership problem [7].

If the traffic problems are wanted to be reduced for long term, adequate planning is required [8]. Road infrastructure and public transport systems and monitoring their usage can be the possible measures to reduce private vehicle ownership. Therefore, it is perspicuous that to solve the traffic-related problems in the developing and developed countries, we need some future plans as well as policies so that the rate of the growth will not be increased as before. And, if the numbers of the private vehicles of the upcoming years can be predicted, it will be easier to choose the policy which one will be more accurate for that condition.

Faysal Ibna Rahman [9] also emphasized the significance of prediction in the field of transportation to reduce the traffic congestion effectively. He also suggested advanced traffic management systems (ATMS) and intelligent transportation systems (ITS) in this regard. Nowadays, the developed countries have already started working with machine learning and deep learning to improve their ATMS and ITS.

In this study, linear regression, one of the most used algorithms of machine learning has been applied along with log regression and log–log regression to predict the number of private vehicle for the upcoming years. Time series analysis was also carried out to predict. The number of the private vehicle of the upcoming years is predicted using population and GDP as the explanatory variables as many of the researchers have found out that these two factors are directly related to the growth of private vehicle in the developing countries.

2 Methodology

There are numerous factors which directly influence the number of private vehicle such as population, GDP, bus routes, and facilities of public transport. In this study, population and GDP have been chosen as explanatory variables and the number of

private vehicle as response variable. Through the correlation test, the explanatory variables were checked whether they have significant dependencies with number or private vehicle or not. As the correlation coefficient of GDP and population were very close to 1, they have been selected for the models. Then, the data of population, GDP, and number of private vehicle of Bangladesh (a developing country) from 2000 to 2018 were collected and analyzed.

The general form of the linear regression model is

$$y = c + ax_1 + bx_2 \tag{1}$$

Here, x_1 and x_2 are the explanatory variables, c is the intercept, and a and b are the coefficients of x_1 and x_2, respectively. And, y is the response variable.

The general equations of the rest of the regression models using in this study are almost same as the general form mentioned above. A little bit of change will be required only for log and log–log regression models. For log regression model, the explanatory variables (x_1 and x_2) will be converted into log value, and for log–log regression model, the response variable (y) will also be converted into log value during analyzing.

In linear regression, the data from 2000 to 2014 were used to train the model. And, the data from 2015 to 2018 were used to examine how much error could be occurred through this model. Then, log regression and log–log regression were consecutively carried out to find the variation in prediction. But, to examine if the error can be reduced more, time series analysis was also done.

In time series analysis, autoregression and the moving average models were carried out to predict the number of private vehicle. In autoregression, the number of private vehicles was considered as a response variable, and different numbers of lagged values were tested as explanatory variables. The backward elimination method with p-value criteria was followed here. As the p-values of the last three variables were larger compared to the first one, variables were eliminated with the response to their significance. Autocorrelation function (ACF) and partial autocorrelation function (PACF) were also plotted to find the best significant order of autoregression and moving average model to get a satisfactory p-value for each explanatory variables along with a satisfactory adjusted R^2 value.

From Fig. 1, it is seen that for the higher lagged value, the ACF curve is going down as expected. And, as they are approaching toward zero, the first lagged value (except for 0, as it is always 1) was found to be significant as an explanatory variable.

In moving average model, the explanatory variable as well as the lagged value will be the average of the previous value of the response variable. Four lagged variables as explanatory variables were analyzed individually. The second lagged value of the moving average model produced the most reduced error among the rest of the models. As this model has higher predicting power with less explanatory variable, this model can be called as parsimonious model and can be considered as our desired model for predicting the number of private vehicles.
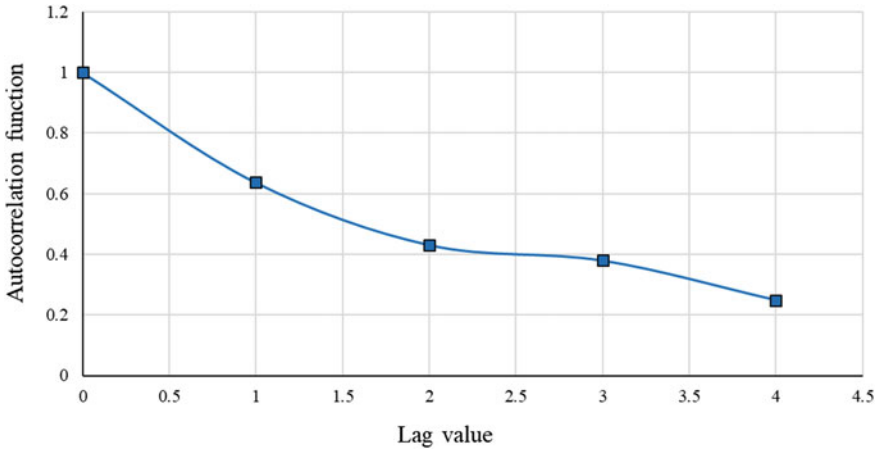
Fig. 1 Autocorrelation function plot for autoregression

2.1 Performance Measurement of the Models

There are a lot of measurement techniques to evaluate the performance of a prediction model. This measurements convey whether the model is good or bad and how accurately it can predict. For regression models, mean absolute percentage error (MAPE) is one of the most used and popular measurement techniques. In this study, MAPE was used to evaluate the model performance along with R-squared value. MAPE was only applied on the test data which were kept aside while training the model.

Formula of MAPE:

$$M = \frac{1}{n} \sum_{t=1}^{n} \left| \frac{A_t - F_t}{A_t} \right| \tag{2}$$

Here,
M = mean absolute percentage error.
A_t = actual value.
F_t = forecasted value.
n = number of observations.
Formula of R^2:

$$R^2 = 1 - \frac{SS_{res}}{SS_{tot}} \tag{3}$$

Here,
SS_{res} = residuals sum of squares.
SS_{tot} = total sum of squares.
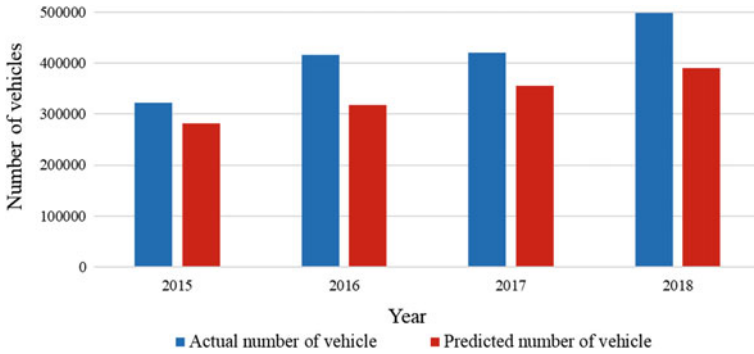
Fig. 2 Number of vehicles with respect to year

3   Result and Discussion

3.1   Linear Regression

In the linear regression model, population and GDP were used as explanatory variables and the number of private vehicles as a response variable. The R-squared value of this model has been found 0.9096 and the adjusted R-squared value 0.8916. Though those values looked fine, the p-values of each of the explanatory variables were greater than 0.05 which were not as expected. And, T-statistic values for GDP and population were 2.10 and 1.42, respectively. The average error of the prediction using this model has been found 18.38%.

The equation of linear regression model:

$$\text{Predicted Number of motor vehicle} = -416859 + 13.732 \times \text{GDP} \\ + 2920.992 \times \text{Population}$$

In Fig. 2, the actual number of private vehicle and the predicted number of private vehicle using the linear regression are represented, whereas R-squared value in Fig. 3.

3.2   Log Regression

In the log regression model, the explanatory variables which were used in linear regression were converted into log values. But, the response variable was the same as in linear regression model. The R-squared and adjusted R-squared values have been found 0.8218 and 0.7921, respectively. T-statistic values for GDP and population have been found 0.75 and 1.08, respectively, in this model. And, the *p*-values were 0.47 and 0.30 which were not expected and beckon that the model could be more
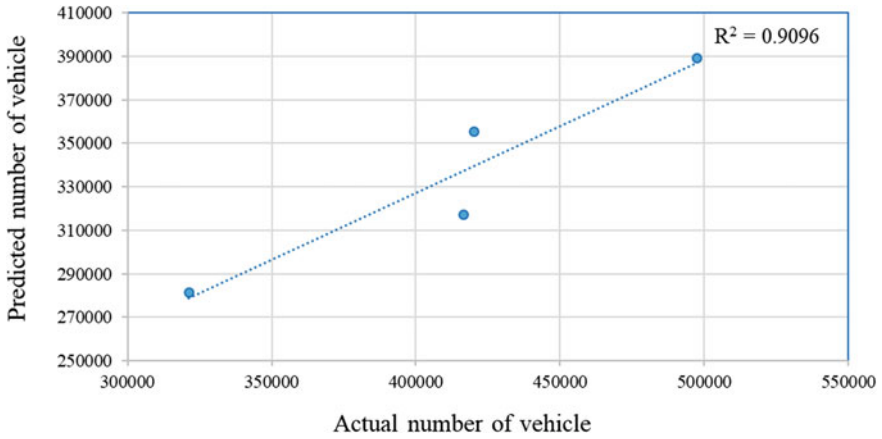
Fig. 3 R-square value for linear regression

accurate. However, the average error of this model was 46.40% (Actual vs Prediction in Fig. 4 and R-squared value in Fig. 5).

The equation of log regression model:

$$\text{Predicted Number of Motor Vehicle} = -2887619 + 121274.2 \times \text{Log GDP} + 1167297 \times \text{Log Population}$$
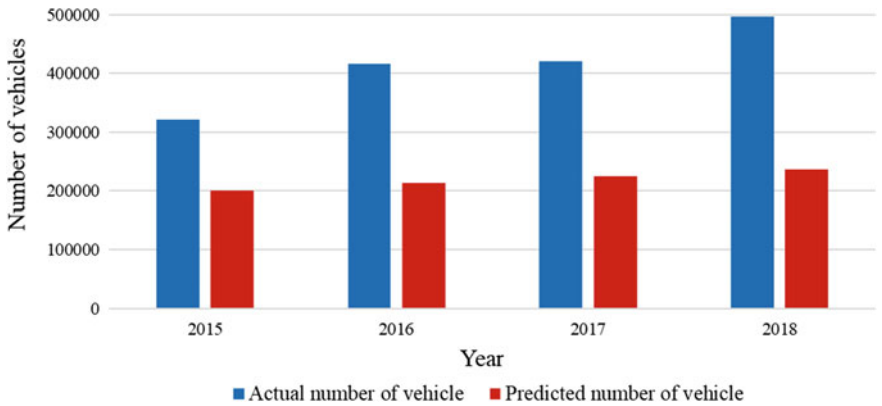
Fig. 4 Number of vehicles with respect to year
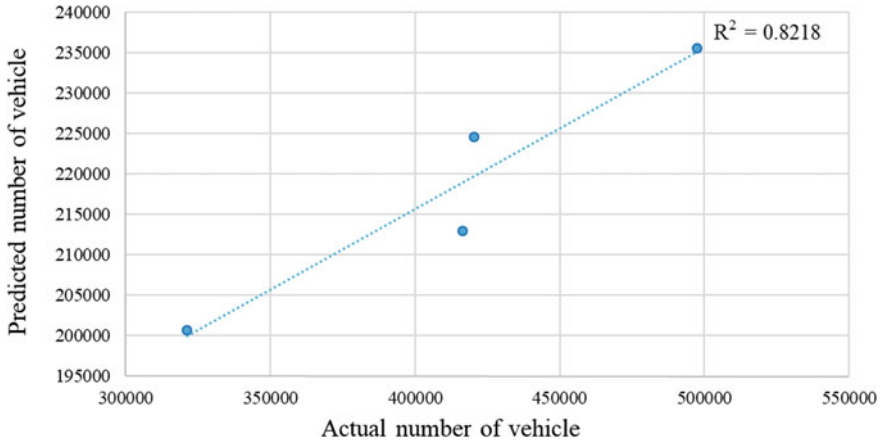
Fig. 5 R-square value for log regression

3.3 Log–Log Regression

As the p-values of the previous explanatory variables of the two models were not that satisfying, another linear regression model was built to observe if the residuals remain close to the trend line. Here, both the explanatory and response variables were converted into log value. Then, the data were analyzed through regression, and a model was built.

The equation of log–log regression model:

$$\text{Predicted Number of motor vehicle(log)} = -13.745 + 0.434 \times \text{Log GDP} \\ + 7.875 \times \text{Log Population}$$

In this model, the R-squared and adjusted R-squared values have been found 0.9271 and 0.9180, respectively. T-statistic values have been found 0.91 and 2.15 for log GDP and log population, respectively. Though the p-value of log GDP was also greater than 0.05 in this model, the p-value of the log population was quite satisfactory and was 0.01. The average error of the prediction using this model has been found 11.21%. Here, one thing should be remembered that the value which was got through this model is a log value, and it is required to be converted to normal during operation (Actual vs Prediction in Fig. 6 and R-squared value in Fig. 7).

From Fig. 6, it is seen that the difference between the actual number of private vehicle and the predicted number of private vehicle using the log–log regression is very less and can easily be neglected. It is a very good sign of a prediction model which indicates that the prediction result is very close to the actual value.
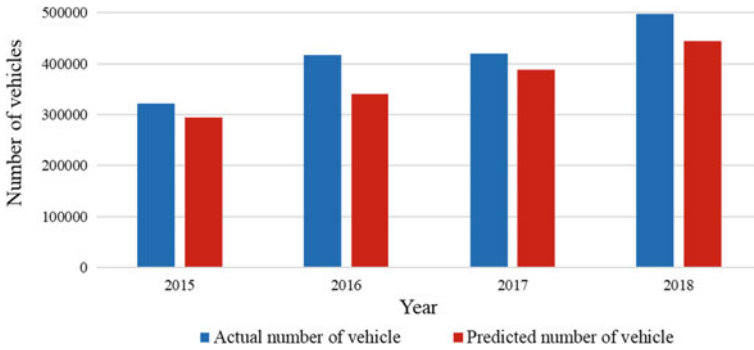
Fig. 6 Number of vehicles with respect to year
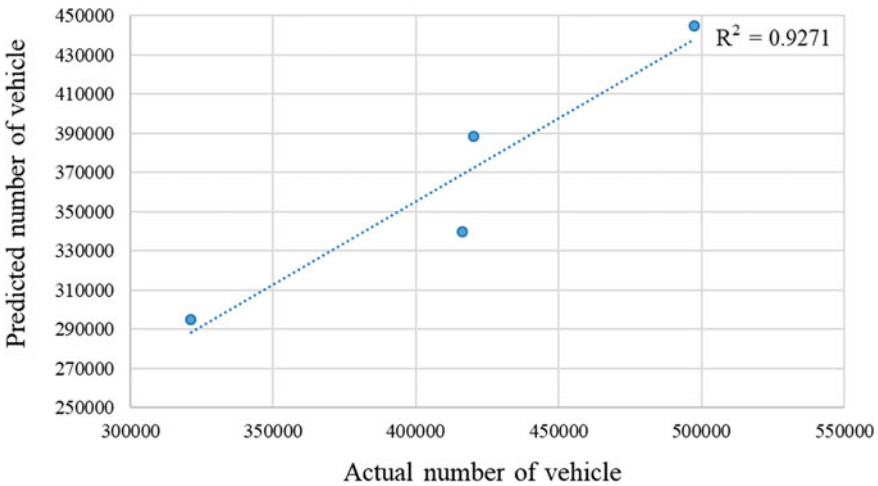
Fig. 7 R-square value for log–log regression

3.4 Auto Regression Model

For a checking purpose, if any other model could perform a better prediction, the data were analyzed through time series analysis, and an autoregression model was built. In this model, the number of private vehicle was considered as a response variable, and the different number of lagged values of the number of private vehicle were considered as explanatory variables.

In this model, the R-squared value and the adjusted R-squared value have been found 0.7855 and 0.7586, respectively. The T-statistic value and p-value for the first lagged variable were 5.41 and 0.00064, respectively. Though the p-value was so satisfying, the overall model cannot perform that accurate prediction. Therefore, the
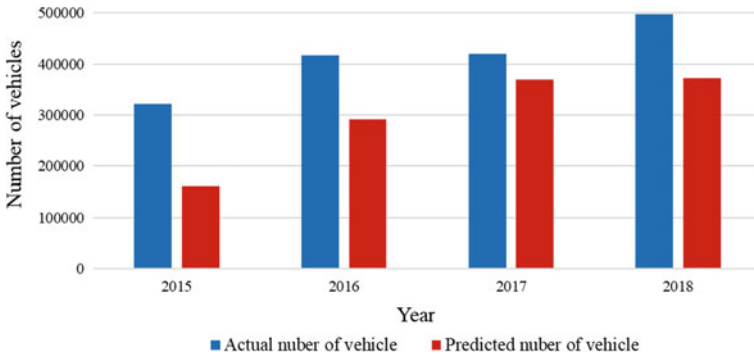
Fig. 8 Number of vehicles with respect to year
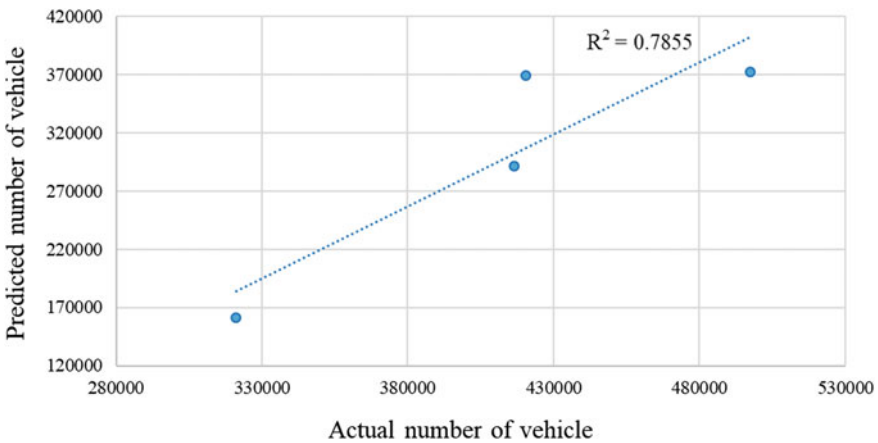
Fig. 9 R-square value for autoregression model

average error of this model has been found 29.34% (Actual vs Predicted in Fig. 8 and R-squared value in Fig. 9).

3.5 Moving Average Model

Moving average model is another type of time series analysis. For this model, a series of averages of different subsets of the raw dataset was formed. Then, auto correlation function (ACF) with respect to lagged value was plotted through a graph. ACF indicates the relationship between raw data with respect to each subset of raw data. From the graph attached below, it is seen that for the higher lagged value, the
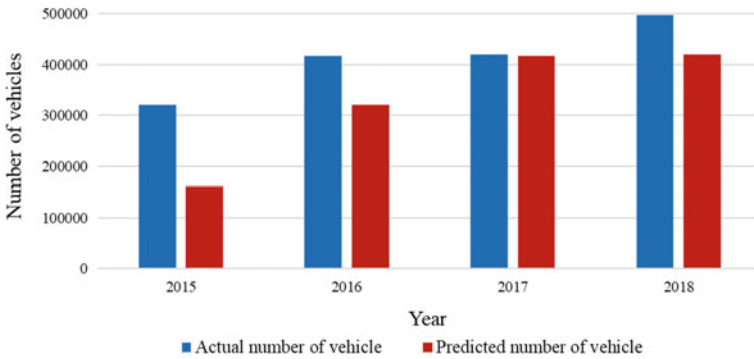
Fig. 10 Number of vehicles with respect to year
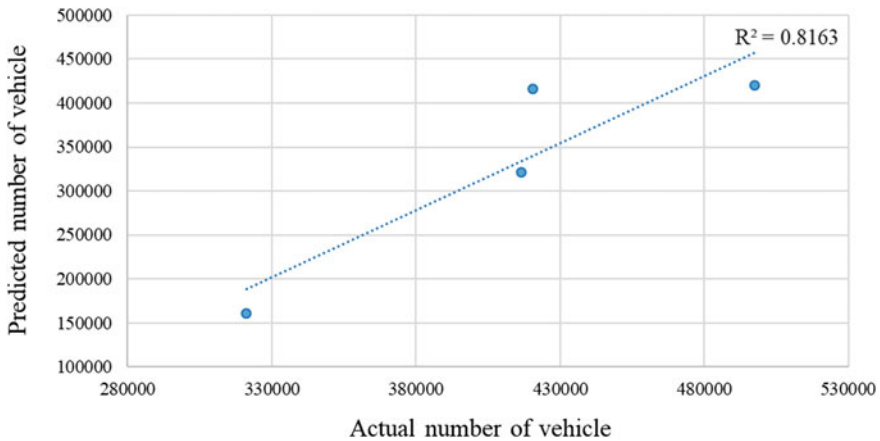
Fig. 11 R-square value for moving average model

ACF is going down as expected. And, as they are approaching toward zero, the first four lagged values (except for 0, as it always is 1) were considered for analysis.

The average errors of this model were 22.32, 30.98, 38.51, and 43.81% for lagged value 1, 2, 3, and 4, respectively. As the average error for lagged value 1 was less than the others, it has been considered as our desired moving average model, which is called MA (1) (Actual vs Predicted in Fig. 10 and R-squared value in Fig. 11).

3.6 Comparison of the Results of Different Models

From Table 1, it is seen that log–log regression model has got the best R-squared value among all of the models, which is 0.9271. Therefore, this model has the average error

Table 1 Comparison of different model accuracy and performance

Model	R^2 value	MAPE	Average error (%)
Linear regression model	0.9096	0.183	18.38
Log regression model	0.8218	0.464	46.40
Log–log regression model	0.9271	0.112	11.21
Autoregression model	0.7855	0.293	29.34
Moving average model	0.8163	0.22	22.32

of 11.21% which is the minimum error compared to the other models. Afterward, linear regression model can be considered as the second best prediction model. Its R-squared value and average error are 0.9096 and 18.38%, respectively.

4 Conclusion

In this study, number of private vehicle, GDP, and population collected from 2000 to 2014 were analyzed, and data collected from 2014 to 2018 were used to ascertain the best model for predicting the number of vehicles. ACF and PACF were plotted to find the best explanatory variable. The p-value criteria were also followed in the selection of explanatory variables. Linear, log, log–log regression, and time series analysis (autoregression and moving average) were carried out to build up the models for predicting the number of vehicles. Among all of the models, log–log regression model has performed with good prediction accuracy. The R2 value and average error of this model have been found 0.9271 and 11.21%, respectively.

From the nature of the trend line found in log–log regression, it is seen that there is no possibility to reduce the number of private vehicle in the upcoming years as the trend line is ascending. It will turn the traffic congestion and other traffic-related problem into a horrendous form in this overpopulated country. So, it is high time to frame new policies as well as monitor the existing policies strictly. Road infrastructure, transportation system, vehicle ownership limitations, and facility of public transportation should be upgraded according to the number of private vehicle for the upcoming years and also regulated in a strict manner. Otherwise, it will not take much time to make this densely country uninhabitable.

Though the log–log regression model has performed quite well, there are still some scopes to work on in the near future. As it has been discussed earlier, some other factors can also be used to train the model along with population and GDP. And, to make the model more generalize and robust, dataset with more observations can be used.

References

1. AASHTO (1997) Standard specification for transportation materials and method of sampling and testing Part 3 edition
2. Nagai Y, Fukuda A, Okada Y, Hashino Y (2003) Two-wheeled vehicle ownership trends and issues in the Asian region. J East Asia Soc Transp Stud 5:135–146
3. Hao L, Guo X (2019) Study on the influencing factors of private car ownership in china under the background of aging, vol. 106, pp. 81–84. https://doi.org/10.2991/febm-19.2019.18
4. Hook W, Replogle M (1996) Motorization and non-motorized transport in Asia: transport system evolution in China, Japan and Indonesia. Land Use Policy 13:69–84. https://doi.org/10.1016/0264-8377(95)00025-9
5. Vasconcellos EA (1997) The demand for cars in developing countries. Transp Res Part A Policy Pract 31:245–258. https://doi.org/10.1016/S0965-8564(96)00021-3
6. Aung T, Kyaing, Lwin KK, Sekimoto Y (2020) An investigation of socioeconomic and land use influence on car ownership in Yangon city. J Disaster Res 15:416–425. https://doi.org/10.20965/jdr.2020.p0416
7. Cullinane S (2002) The relationship between car ownership and public transport provision: a case study of Hong Kong. Transp Policy 9:29–39. https://doi.org/10.1016/S0967-070X(01)00028-2
8. Sanko N, Dissanayake D, Kurauchi S, Maesoba H, Yamamoto T, Morikawa T (2014) Household car and motorcycle ownership in Bangkok and Kuala Lumpur in comparison with Nagoya
9. Rahman FI (2020) Short term traffic flow prediction using machine learning—short term traffic flow prediction using machine learning—KNN, SVM and ANN with weather information. https://doi.org/10.7708/ijtte.2020.10)

Assessing Bus Service Quality in Dhaka City from the Perspective of Female Passengers

S. K. Subah, R. Tasnim, M. I. Jahan, and M. R. Islam

1 Introduction

The role of a smooth and coordinated transport system is the prime key in the continuous development of a rapidly emerging megacity like Dhaka. As the majority of the city-folks comprising women, rely on public buses for daily or occasional traveling, public buses can be addressed as the lifeblood of the national economy [1]. Though present situations state awareness about women's rights among the male passengers to a remarkable level, deficiencies still plague the scenario. Recent research on roads free from sexual harassment features that- in Dhaka city 35% of female fall victim to harassment, while traveling in the public bus by males within the age group of 19–35 (years). About 59% gets distraught by the males of age 26–40 years old [2]. In Dhaka city, women feel the persistent threat of being harassed or abused in the public bus which affects their daily travel patterns and choices like travel mode, travel time and travel companion. Moreover, different service and maintenance lacking prevail and fail to provide boarding comfort, seat availability, friendly staff treatment and comfortable ambience. In reality scarcity of available seats reserved for women would be a common scenario, which is often occupied by male passengers in spite of the existing government law of designating nine seats for children, women and disabled people. As a result, female passengers would have to continue the journey standing. Given this appalling reality, more women-friendly buses need to be brought into regular service prioritizing factors like women safety, comfort and mobility. But to the researchers' knowledge extent female comfort and safety factors are seldom emphasized, and therefore, overall SQ is only judged neglecting female perception and specific requirements, particularly in a heavily populated city such as Dhaka.

S. K. Subah · R. Tasnim · M. R. Islam (✉)
Department of Civil Engineering, MIST, Dhaka, Bangladesh
e-mail: russed@ce.mist.ac.bd

M. I. Jahan
Stamford University, Dhaka, Bangladesh

In the context of customers are the sole judges of service quality [3], to determine customer satisfaction with the provided services mostly adopted methodologies include questionnaire survey. In the sector of perception-based public transit assessment, the commonly approved derived importance methods are: regression analysis, e.g., [3–6] and factor analysis which is consisted of particular methods as confirmatory factor analysis (CFA), e.g., [7, 8], principal component analysis (PCA), e.g., [7, 9–11] or structural equation models (SEM), e.g., [12–15]. Data analyses using SEM can integrate both observed and unobserved variables unlike the former methods which only incorporate observed values. Moreover, there is an absence of supplementary methods for estimating point or interval indirect effects and for modeling multivariate relations other than SEM; given these important features, SEM has gained higher popularity for non-experimental studies as those studies exclude well developed procedures for testing theories and experimental design becomes impractical in the case of ethical concerns [16]. SEM is proven to be a fruitful approach to resolve various research problems comprehending non-experimental research [17]. A few research was undertaken concerning the bus service quality attributes, gap analysis and level of service (LOS) [18–21]. However, a complete perception model focusing primarily on the female passengers of the city buses is found absent in the literature.

The utmost motive of the undertaken study is to distinguish the significant factors prompting overall bus SQ prioritizing female passengers' safety and comfort issues. These factors can be effectively used as a touchstone for the improvement of the existing condition and barriers; leading to a favorable and affordable transportation choice for women. This will surely add new dimensions to the public transportation system of Dhaka, acknowledging the limited resources of the country and attracting more female passengers consequently.

2 Methodology

SEM method has been adopted for the study because other substitute approaches (e.g., regression or the general linear model) may lead to serious inaccuracies by vanishing the substantial errors in the predictor (i.e., independent) variables. The principal step in the model analyzing process would be to regulate the goodness-of-fit between the hypothesized figure and the sample data. Therefore, model-fitting practice can be summed up as: Data = Model + Residual [17].

Different methods have been introduced for the structural equation system including path analysis, ML (maximum likelihood) method, OLS (ordinary least squares), GLS (generalized least squares), and WLS (weighted least squares) [22]. The highest recognized method is ML. Several postulations about probability density function, the complexity of the model, parameter scale characteristics and the size of the statistical sample are to be considered in choosing a suitable method for estimation [23]. STATA 13 software is used in this research work by following the ML method.

Fig. 1 User perception
about overall SQ
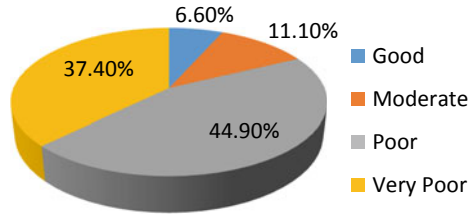
In the SEM analysis, RMR (root mean square) and SRMR (standardized root mean square) measurements can be utilized to judge how well-fitting the analyzed model is. Fit indices have been introduced as a fruitful prospect to the evaluation procedure. The average or mean residual measures extracted from the fitting of the variance–covariance matrix for the prescribed model to that of the sample data can be denoted as RMR. The SRMR then denotes the average or mean value over all standardized residuals, and the value generally varies from 0 to 1 or a smaller value (0.5 or less) in a well-fitting model [16]. However, proper guidelines are available guidelines for standard values of fit indices [24].

2.1 Sample Collection

In general, greater than 200 sample size is an essential for SEM [25]. The sample size depends on some factors like the estimation method followed, complexity of model and the apportioning features of observed variables. There exists a general rule that "The ratio of sample size to the number of free parameters can be as high as 20 to 1 or as low as 5 to 1." [16, 26] Around 250 samples were collected to conduct the study. The bus routes considered under the study mostly covered the central area and the periphery, the planned and unplanned area, and the high- and-low income residential areas. Figure 1 represents user perceptions on overall SQ of the bus.

The questionnaire was divided into two segments. The first segment contained demographic characteristics of the participants including age, occupation, car owner-ship, travel frequency of the respondents were collected (Fig. 2). And the second one was comprised of SQ measurement parameters which were further rated quantitatively in a scale of 1–5. To be mentioned, only female passengers participated in the survey.

2.2 Service Quality Variables

Total 19 SQ variables have been considered in order to develop the SE model. 16 observed variables (Table 1) are chosen from widespread literature work on local bus SQ interpretation and with FGD (focus group discussion), expert advice from
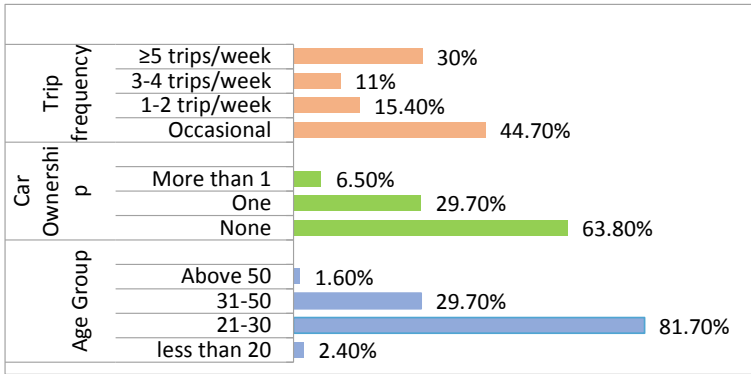
Fig. 2 Demographic characteristics of respondents

practitioners and concerning authorities. Rest of the 3 are unobserved latent variables found from factor analysis. Each observed variable has been rated on scale of one to five depending on their qualitative rating.

2.3 Proposed SE Model

In order to construct the model at first, 16 endogenous observed variables have been clustered among three latent variables and also the latent variables share interrelationships with one another. Figure 3 represents the structure of the model.

The equations derived from the model are as follows:

$$Z = \gamma \eta + \rho + \xi \tag{1}$$

Since the latent variable η stimulates both the endogenous observed variables as well as other latent variables,

$$\eta = \frac{Y - \varepsilon}{\alpha} \tag{2}$$

And $\eta = \beta \eta + \mu$

$$\eta = \frac{\mu}{1 - \beta} \tag{3}$$

Adding (2) and (3)

$$\eta = \frac{Y - \varepsilon}{\alpha} + \frac{\mu}{1 - \beta} \tag{4}$$

Table 1 Description of observed variable

Variable Name	Variable descriptions	Scale	Qualitative rating
Female harassment	Verbal transgressions or range of sexual actions like abuse or assault toward female passengers	1–5	Very often experienced to very less experienced
Daytime security	Ensuring environment which provides protection of life and property and free of harassments during day	1–5	Very low security to very high security
Nighttime security	Ensuring environment which provides protection of life and property and free of harassments during night time	1–5	Very low security to very high security
Waiting time security	No occurrence harassments or crime while waiting for the bus	1–5	Very low security to very high security
Cleanliness	Abstract state of being clean and free from dirt, trash, or waste	1–5	Very poor to very good state
Friendly treatment	Feeling of safety and cooperation from driver, conductor and co-passengers as well	1–5	Very poor to very good
Secured driving	Driving skills include adequate awareness of traffic laws, maneuver and proper control over the vehicle	1–5	Very rough to very skilled
Convenient waiting-time	Acceptable interval time between bus arrivals	1–5	Very poor convenience to highly convenient
Bus-fare	Amount of price charged for the bus ride	1–5	Very high to very low
Bus route arrangement	Bus route selection fulfilling passengers' requirement	1–5	Very poorly planned to well planned
Bus stop distribution	Proper distribution of bus stops within short distances	1–5	Very poorly planned to well planned
Boarding discomfort	Entrance and exit without any occupying obstacles	1–5	Very discomforting to well comforting
Passenger congestion	Overloaded bus carrying passengers beyond usual capacity	1–5	Very highly congested to very less congested
Unavailability of reserved seats	Availability of reserved seats for female passengers	1–5	Very less availability to very high availability
Standing-discomfort	Adequate spaces and grabbing handle for the standing passengers while seats are occupied	1–5	Very discomforting to well comforting

(continued)

Table 1 (continued)

Variable Name	Variable descriptions	Scale	Qualitative rating
Access difficulties	Availability of different transport modes for easy transit from or to the bus stops	1–5	Very poor to very good
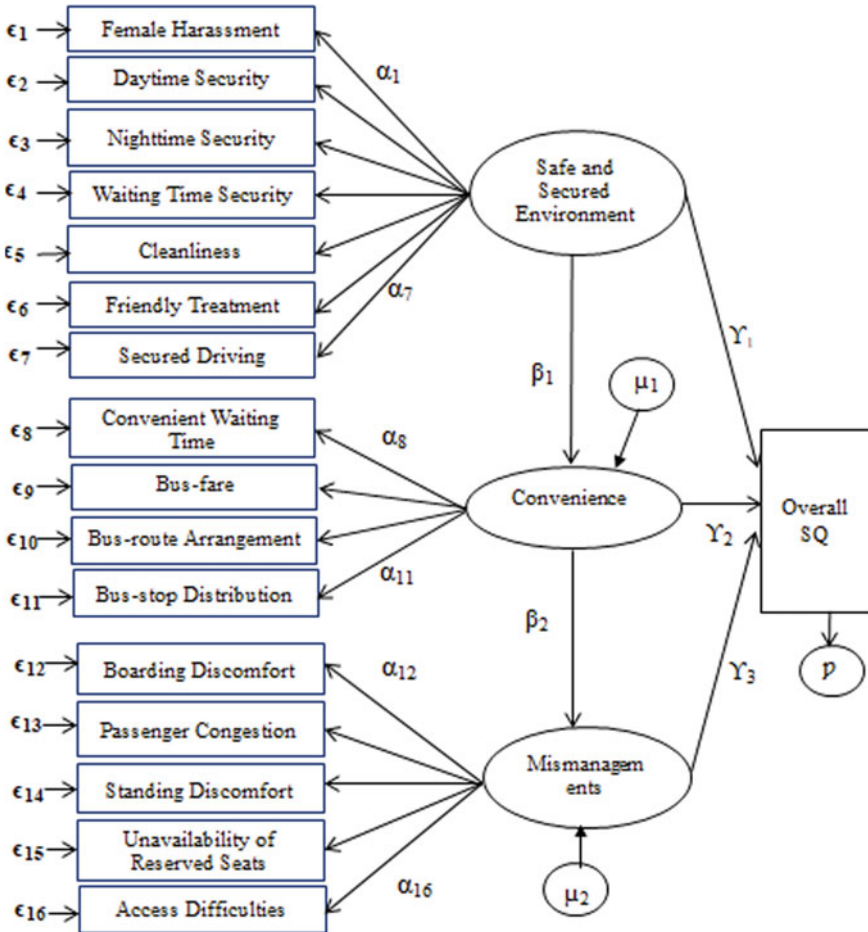
Fig. 3 Proposed structural equation model

where

Y designates endogenous observed variable;

η designates latent variable;

Z designates overall SQ;

ε designates measurement error in Y;

μ designates measurement error in η;

ρ designates measurement error in Z;

α coefficient of η variable, while influencing Y variable;

β coefficient of η variable, while influencing one another;

γ coefficient of η variable, while influencing Z;

ξ designates constant value;

3   Results and Discussions

The study was carried out to reveal the most influencing factors on the overall SQ. Prior to the model development factor analysis was adopted to extract 3 latent variables. In total 16 observed variables were utilized to describe the latent variables. The model was estimated to obtain path coefficient indicating the contribution of factors on the overall evaluation of SQ. At 90% confidence level, a critical value of 1.64 has been standardized for conducting two tailed t-test where values less than 1.64 could be declared as non-significant. Parameters with z value below 1.64 could be considerable for bigger data set. According to Hopper (26), fit indices can be categorized into three classes (absolute, incremental and parsimony indices), and their threshold values have also been guided by the author as shown in Table 2. Guidelines are available for acceptable values of the root mean square residual (RMR), the root mean square error of approximation (RMSEA) and the standardized root mean square residual (SRMR) (Table 2). The CFI value recorded from the proposed model is 0.806 which is close to the prescribed value as referred in Table 2. Other obtained values of RMR, RMSEA and SRMR show significant relationships among the variables as shown in Table 2.

From Table 3, it can be interpreted that among three latent variables L1 has the highest path coefficient 1.463 which means safe and secured environment has the highest influence on overall SQ. Convenience has lesser impact with a coefficient 1

Table 2 Fit index values of the proposed SE model and allowable marginal limit for the fit statistic

Fit statistic	Model value	Allowable marginal limit
Absolute fit indexes		
RMSEA	0.082	0.05–0.1
SRMR	0.069	As high as 0.08
Incremental fit indexes		
Comparative fit index (CFI)	0.806	CFI ≥ 0.95
TLI	0.770	–
	10,256.636	–
	10,450.096	–

Table 3 Parameter measurements of the estimated SE model

Variable category	Variable name	Path coefficient	z value	p value
Observed variables	Female harassment	1	–	–
	Daytime security	1.220	**4.76**	0
	Nighttime security	0.890	**4.92**	0
	Waiting time	1.315	**5.01**	0
	Security cleanliness	1.366	**5.10**	0
	Friendly treatment	*1.531*	**5.28**	0
	Secured driving	1.279	**5.05**	0
	Convenient waiting time	0.975	0.64	0.525
	Bus fare	0.806	0.63	0.531
	Bus route arrangement	1.107	0.63	0.526
	Bus Stop distribution	1.161	0.63	0.527
	Boarding discomfort	1	–	–
	Passenger congestion	0.966	**6.28**	0
	Unavailability of reserved seats	0.722	**5.53**	0
	Standing discomfort	0.793	**5.73**	0
	Access Difficulties	0.988	**4.97**	0
Latent variables	Safe and Secured Environment (L1)	*1.463*	**1.68**	0.093
		1.34^p	0.65	0.517
	L1→L2	1	-	-
	Convenience(L2)	0.828^p	0.65	0.518
	L2→L3	-0.967	-0.59	0.554
	Mismanagement(L3)			

Bold numbers indicate z value greater than 1.64;

Italic numbers indicate highest coefficient values;

P = coefficient of latent variable influencing other latent variable

on the SQ compared to safe and secured environment. Finally, L3 has the least impact with a coefficient of −0.968 which indicates that it inversely affects the overall SQ.

The result emphasizes on the fact that women mostly seek for a safe and secured environment in case of choosing bus ride; given that in context of a developing country concerning authority often fails to ensure a secured environment for a woman. Secured environment comprises of good functional performance, well-instructed transit employees, better understanding among co-passengers combined with a zero tolerance attitude toward any kind of assault or harassment. Friendly treatment, cleanliness, waiting time security, secured driving—these observed variables (coefficient 1.53, 1.367, 1.316, 1.279; Table 3) have the most significant influence over L1. Friendly treatment emphasizes L1 the most due to the utmost need and the absence of well-behaved mannerism from stuff and others. From the expectation to be treated well, and to receive cooperation from co-passengers, it can be of a big issue that inappropriate behavior could lead to discouragement of choosing public buses as a travel mode. Different kind of abusive attitudes toward women is often practiced, while traveling and the culprits include both bus staff and aberrant passengers. From point of view of cleanliness, it is mentionable that lakhs of people from different places travel on a bus every day. As a result, germ transmission is very common here caused by exchange of currency notes, tickets, grabbing same handles, from

sit covers, etc. Also people spit, litter making an uninviting situation for passengers hence affecting overall SQ. Public bus can be unsafe at odd times of the day, at night due to improper lighting facilities at stops and in isolated area as women may face harassment or robbery, while waiting in or walking through unsafe area for bus access. In Dhaka city, buses hardly stop at the bus stop for a convenient time, creating difficulties for women and children in the process of getting on–off from bus and thus accidents often occurs. Considerate driving skill could be a solution to this fact. To be mentioned that all these factors interpreted from result significantly reflect the real scenario.

As per the proposed model, convenience is the second most preferred attribute (coefficient 1; Table 3). A well convenient system offers minimum waiting time, adequate bus stops and more user oriented route linkage with a reasonable ticket pricing. The mobility of travelers is greatly affected by route characteristics as route configuration, bus stop distribution, and station location planning usually regulate bus transit accessibility [27]. Which is why these two service dimensions significantly influences L2 (coefficient 1.108, 1.161; Table 3). It can be recognized from the model that L3 effects SQ inversely (coefficient−0.968; Table 3) which means the growth of this factor reduces SQ. Rapid population, unplanned urbanization and low investment in public transportation sectors lead to mismanagement resulting in service deficiencies. Thus, giving place to many discomforting issues. Boarding discomfort, access difficulties, passenger congestion—these three variables have the highest significance over L3 (coefficients, respectively—1, 0.988, 0.966; Table 3). Public bus authorities allow way greater number of passengers creating passenger congestion which eventually blocks entrance and exit way. This is followed by unavailability of reserved seats and female passengers end up continuing the journey by standing. This can be quite uncomfortable as there being not enough space, and there is always higher possibility of harassments in this situation. Also bus stops are not well facilitated for example—There are no exact information of the bus arrival timetables which increases out of vehicle travel time and unwanted crimes, absence of digital ticketing system leading to the greater possibilities for any kind of deceit or bribing and lastly not having adequate para transit modes for easy transferring. Without these, facilities access difficulties sustain.

The proposed model also manifest the inter relationship among the latent variables. While discussing the interrelationship between L1 and L2, it can be stated that a female traveler would find a service more convenient if a safe journey is ensured as this is a prime issue for her. As a result, this would combined and multiply the overall SQ. This indicates a linear relationship between secured environment and convenience (coefficient 1.34; Table 3). Similarly, convenience has some influence on Mismanagement (coefficient 0.828; Table 3) given that appraising the socio-economic context of our country, people often find public bus affordable and convenient as there are no alternatives reaching out to the commoners. This leads to the mindset of accepting and encouraging mismanagements to some extent.

4   Conclusion

Prevailing socio-economic barriers and different mobility patterns dominates the idea of designing public transportation modes according to the different needs of both men and women. Thriving motility barriers are needed to be recognized for the sake of uprighting women's freedom of travel choices [28]. Looking at the current scenario of the city, women are more encouraged to choose private and other safer but costly modes than public buses unless there are no bound situations and economic issues. The goal of the study was to focus on the prime factors that could be utilized to develop a more inviting and reliable public bus service for all classes of women folk in the city. SEM approach has been taken up to carry out the study purpose. Prior to the analysis, an evaluation survey was conducted including questions related to women's socio-demographics, perception of safety, while traveling, complaints about the service system. The attained responses were further used for constructing an empirical model which could demonstrate the interdependence between the observed and latent variables. Finally, the significant factors regulating the SQ were determined from the estimated model.

The outcome of the analysis imposes that a safe and secured environment is the most preferred SQ attribute in female perception. The second most significant attribute is convenience and contrarily, mismanagement affect the SQ inversely. Moreover, friendly treatment, cleanliness, secured driving have indirect influence over the transit service. The result distinctly is relatable with the current framework of the public transport sector and also it indicates the passenger expectation from the transit service. However, all the findings could be utilized, while planning public transport; hence, woman only buses in a large row can be a way out. Eliminating mismanagement would proportionate the LOS, while making it more accessible for women of all economic class. Operating authority's necessary investments and attention is a prerequisite in this matter.

Though this study represents the summarized scenario of the SQ of bus service observed from female passengers' perspective of Dhaka city, some limitations could still remain, as it was not possible to reach out to all the commuting regions and bus operating systems of the city. Also, small sample size could create some heterogeneity in the model. So there prevails more study scopes covering more areas of the city occupying a wide range of female responses.

References

1. Sham R, Omar N, Amat DW (2012) Hot spot urban crime area for woman travellers. Procedia Soc Behav Sci 68:417–426. https://doi.org/10.1016/j.sbspro.2012.12.238
2. Safe Roads for Women Reducing sexual harassment and road crash in Bangladesh | Request PDF n.d. https://www.researchgate.net/publication/324645024_Safe_Roads_for_Women_Reducing_Sexual_Harassment_and_Road_Crash_in_Bangladesh. Accessed 2 Oct 2020

3. Zeithaml VA, Parasuraman A, Berry LL, Google Books n.d. Delivering quality service: balancing customer perceptions and expectations. https://books.google.com.bd/books/about/Delivering_Quality_Service.html?id=RWPMYP7-sN8C&redir_esc=y. Accessed 29 Sept 2020

4. Morfoulaki M, Tyrinopoulos Y, Aifadopoulou G (2010) Estimation of satisfied customers in public transport systems: a new methodological approach. J Transp Res Forum. https://doi.org/10.5399/osu/jtrf.46.1.981

5. Tyrinopoulos Y, Antoniou C (2008) Public transit user satisfaction: Variability and policy implications. Transp Policy 15:260–272. https://doi.org/10.1016/j.tranpol.2008.06.002

6. Weinstein A (2000) Customer satisfaction among transit riders: how customers rank the relative importance of various service attributes. Transp Res Rec 123–132. https://doi.org/10.3141/1735-15

7. Chen CF, Chen FS (2010) Experience quality, perceived value, satisfaction and behavioral intentions for heritage tourists. Tour Manag 31:29–35. https://doi.org/10.1016/j.tourman.2009.02.008

8. Kim YK, Lee HR (2011) Customer satisfaction using low cost carriers. Tour Manag 32:235–243. https://doi.org/10.1016/j.tourman.2009.12.008

9. Yang CC, Lu CS (2012) Factors influencing the use intention of port logistics information system by ocean carriers. Int J Shipp Transp Logist 4:29–48. https://doi.org/10.1504/IJSTL.2012.044134

10. Kolanović I, Skenderović J, Zenzerović Z (2008) Defining the port service quality model by using the factor analysis. Undefined

11. Pantouvakis A, Lymperopoulos K (2008) Customer satisfaction and loyalty in the eyes of new and repeat customers: evidence from the transport sector. Manag Serv Qual 18:623–643. https://doi.org/10.1108/09604520810920103

12. Eboli L, Mazzulla G (2012) Structural equation modelling for analysing passengers' perceptions about railway services. Procedia Soc Behav Sci 54:96–106. https://doi.org/10.1016/j.sbspro.2012.09.729

13. Karlaftis M, Golias J, Papadimitriou E (2001) Transit quality as an integrated traffic management strategy: measuring perceived service. J Public Transp 4:27–44. https://doi.org/10.5038/2375-0901.4.1.2

14. Jahan MI, Mazumdar AAB, Hadiuzzaman M, Mashrur SM, Murshed MN (2020) Analyzing service quality of pedestrian sidewalks under mixed traffic condition considering latent variables. J Urban Plan Dev 146:04020011. https://doi.org/10.1061/(ASCE)UP.1943-5444.0000563

15. Rahman F, Das T, Hadiuzzaman M, Hossain S (2016) Perceived service quality of paratransit in developing countries: a structural equation approach. Transp Res Part A Policy Pract 93:23–38. https://doi.org/10.1016/j.tra.2016.08.008

16. Bentler PM, Chou CP (1987) Practical issues in structural modeling. Soc Methods Res 16:78–117. https://doi.org/10.1177/0049124187016001004

17. Byrne BM, Google Books Structural equation modeling with EQS: basic concepts, applications, and ... https://books.google.com.bd/books?hl=en&lr=&id=ukFX5boNAhYC&oi=fnd&pg=PP1&dq=Structural+equation+modeling+with+EQS+:+basic+concepts,+applications,+and+programming+/+Barbara+M.+Byrne.+—+2nd+ed.%5D+(Byrne)&ots=UfM_jqOAwP&sig=cJOaaVXN-fgtLSXytZtoIqF_D2o&redir_esc=y#v=onepage&q=StructuralequationmodelingwithEQS%3Abasicconcepts%2Capplications%2Candprogramming%2FBarbaraM.Byrne.—2nded.%5D(Byrne)&f=false. Accessed 30 Sept 2020

18. Das T, Apu N, Hoque MS, Hadiuzzaman M, Xu W (2017) Parameters affecting the overall performance of bus network system at different operating conditions: a structural equation approach. Transp Res Procedia 25:5059–5071. https://doi.org/10.1016/j.trpro.2017.05.206

19. Verma M, Manoj M, Rodeja N, Verma A (2017) Service gap analysis of public buses in Bangalore with respect to women safety. Transp Res Procedia 25:4322–4329. https://doi.org/10.1016/j.trpro.2017.05.283

20. Ponrahono Z, Bachok S, Ibrahim M, Osman MM (2016) Assessing passengers' satisfaction level on bus services in selected urban and rural centres of Peninsular Malaysia. Procedia Soc Behav Sci 222:837–844. https://doi.org/10.1016/j.sbspro.2016.05.183
21. Hadiuzzman M, Das T, Hasnat MM, Hossain S, Rafee MS (2017) Structural equation modeling of user satisfaction of bus transit service quality based on stated preferences and latent variables. Transp Plan Technol 40:257–277. https://doi.org/10.1080/03081060.2017.1283155
22. Bentler PM (1988) Causal modeling via structural equation systems. Handb Multivar Exp Psychol 317–335. https://doi.org/10.1007/978-1-4613-0893-5_9
23. Golob TF (2003) Structural equation modeling for travel behavior research. Transp Res Part B Methodol 37:1–25. https://doi.org/10.1016/S0191-2615(01)00046-7
24. Structural equation modeling: Guidelines for determining model fit | Request PDF n.d. https://www.researchgate.net/publication/312630391_Structural_equation_modeling_G uidelines_for_determining_model_fit. Accessed 30 Sept 2020
25. Lei PW, Wu Q (2007) An NCME instructional module on: introduction to structural equation modeling: issues and practical considerations. Educ Meas Issues Pract 26:33–43. https://doi.org/10.1111/j.1745-3992.2007.00099.x
26. Tanaka JS (1987) "How big is big enough?" Sample size and goodness of fit in structural equation models with latent variables. Child Dev 58:134. https://doi.org/10.2307/1130296
27. Alsnih R, Hensher DA (2003) The mobility and accessibility expectations of seniors in an aging population. Transp Res Part A Policy Pract 37:903–916. https://doi.org/10.1016/S0965-8564(03)00073-9
28. Nicolle C, Peters B (1999) Elderly and disabled travelers: intelligent transport systems designed for the 3rd millennium. Transp Hum Factors 1:121–134. https://doi.org/10.1207/sthf0102_1

Impact of Slag Percentages on Soil CBR for Sub-surface Layers of Flexible Pavement

T. A. Tapu, S. K. Palit, and M. H. Sabbir

1 Introduction

An efficient road network is necessary for any kind of development work in any sector of a country, and hence, the emphasis on road construction and maintenance is increasing day by day. For road construction, a huge amount of construction materials are required for which a significant amount of money is involved. On the other hand, with the infrastructural development of the world, the use of steel is also increasing nowadays. According to the World Steel Association in 2019, the total amount of world crude steel production was about 1869.9 million tons (Mt). As a result, a large volume of slag was also produced as a by-product that year. According to a survey conducted by the European Slag Association (EUROSLAG) among its member every two years since 2000, it is known that 45.6 Mt of ferrous slag was generated in 2008. In addition, more than 400 Mt of iron and steel slag is being produced each year in the world [1]. Slag is classified as waste material, and its disposal often involves substantial land area and, hence, limits the amount of cultivable land [2].

It is beneficial to reuse and recycle industrial wastes instead of disposing of them. The use of steel slag in geotechnical engineering schemes such as stabilizing subgrade is beneficial because of the significant amount of slag can be used in this process. As a result, this will be helpful in reducing the usage of natural aggregates and will foster the usage of recycled materials as alternative aggregates. Additionally, the product used does not cause any unintended detrimental effect on the environment during the construction of the road pavement or throughout the entire lifetime of the road pavement [3].

The use of slag in roadway pavement started from the ancient time. According to the National Slag Association, 2000 years ago, during the regime of the Roman emperors, broken slag from crude iron making was used as a base course. In 1813,

T. A. Tapu (✉) · S. K. Palit · M. H. Sabbir
Department of Civil Engineering, Chittagong University of Engineering and Technology, Chattogram 4349, Bangladesh

the first road using slag was introduced in England. The first slag road in the USA was built in 1830. Within 1880, block casts of slag were being used in both Europe and the USA for street paving [4]. Later on, many kinds of research were undertaken using slag in different ways and applying them in different layers of the roadway. Pamukcu and Tuncan in 1993 conducted their study on evaluation of the properties of slag stabilized with cement, lime, and fly ash in various proportions. They concluded that if iron-rich slag was stabilized with cement and cementitious compounds, this could be a suitable aggregate for reuse in the construction of road bases [5]. In 2003, Rohde et al. studied the usage of weathered electric arc furnace slag as a base material for roads with low volume and found that after correcting the gradation of the slag, the resilient modulus of electric arc furnace slag was higher than that of natural aggregates, and its use in the base course of low volume road could reduce the construction cost [6]. Li et al. in 2010 conducted the test on the performance of the base course and sub-base course using steel slag and fly ash and came out with the fact that it was very efficient in minimizing road base crack. Also, it had good resistance shrinking and temperature shrinking ability. Thus, using it in the base course could extend road life [7]. In 2015, Hainin et al. used steel slag as a road construction material and found that the use of slag improved the performance of the pavement. Also, the rough-textured steel slag surface had strong skid resistance and high specific gravity. Owing to the angularity of steel slag, it provided good interlocking and resulted in the improvement of stability and resistance to rutting [8]. Hence, the use of slag together with soil in various layers of flexible pavement saves environmental hazards as well as government revenue. Moreover, it gives more sub-surface strength than other costly construction materials. In this part, a study was carried out to utilize slag in different sub-surface layers of flexible pavement in order to assess their CBR values and to correlate them with slag content in the soil-slag mix. Therefore, the main objectives of this investigation are stated below:

- To find the physical properties of slag and soil.
- To determine the OMC and MDD for various mix proportion of slag and soil for both standard proctor and modified proctor compaction.
- To establish a design CBR curve for various mix proportion of slag and soil.

2   Materials and Method

Construction of road using slag alone is not feasible because of the cohesion-less nature of the slag, and such a road will be highly erodible in nature [9]. On the other hand, weak soil alone is not suitable for roadway construction. So, the soil used here is blended with slag in the proportion of 0, 10, 20, 30, 40, and 50% to assess its strength. The workflow diagram for completing this investigation has been presented in Fig. 1.
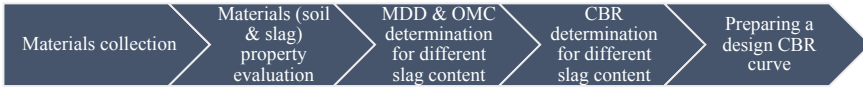
Fig. 1 Workflow diagram of the investigation

2.1 Material Used

The soil sample used in this study has been collected from sand dunes of the teacher's dormitory at the Chittagong University of Engineering and Technology (CUET) campus. The studied slag (37.5 mm down) sample has been collected from Bangladesh Steel Re-Rolling Mills Ltd (BSRM), Chattogram. The grain size distribution of soil and slag has been conducted as per ASTM C136/C136M that are shown in Fig. 2 and Fig. 3, respectively. Pictorial views of collected soil and slag samples are presented in Fig. 4 and Fig. 5, respectively.

Fig. 2 Particle size distribution of soil
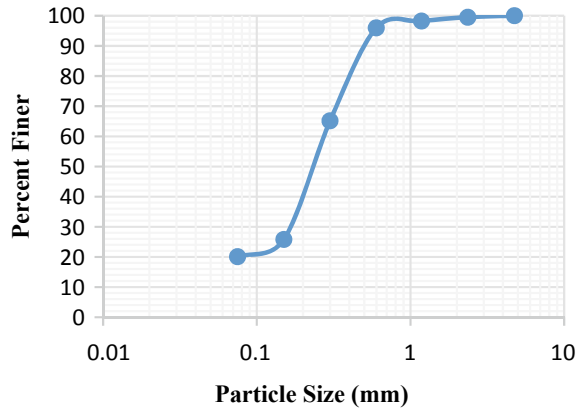
Fig. 3 Particle size distribution of slag
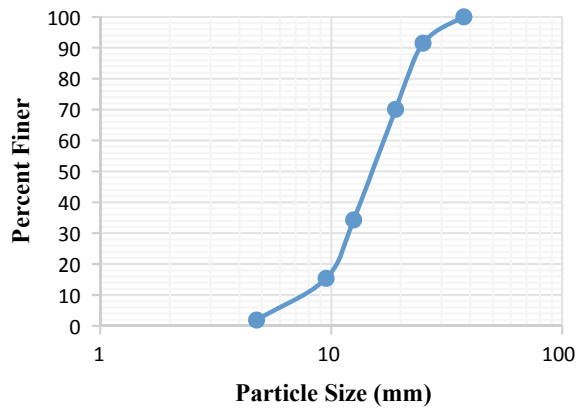
Fig. 4 Collected soil sample

Fig. 5 Collected slag sample

2.2 Physical Properties of Material

Physical properties of soil and slag are evaluated before finding the OMC and CBR values. The specific gravity of soil as per ASTM D 854-06, specific gravity of slag as per ASTM C 127, bulk density of aggregates as per ASTM C 29, the aggregate impact value (AIV) test of slag as per BS 812, aggregate crushing value (ACV) test of slag as per BS 812, Los Angeles abrasion value (LAAV) test of slag as per ASTM C 131, and the elongation and flakiness indexe test of slag as per IS 2386 part 1 have been used for evaluating various properties of the materials during the study.

Fig. 6 CBR test under progress

2.3 OMC and CBR Determination

After evaluating the physical properties of soil and slag, the soil is mixed with 0, 10, 20, 30, 40, and 50% slag content. The OMC of the mixtures has been found as per ASTM D 698—standard test methods for laboratory compaction characteristics of soil using standard effort and ASTM D 1557—standard test methods for laboratory compaction characteristics of soil using modified effort. After that, the CBR tests of these soil-slag mixtures have been conducted as per ASTM D 1883-07 in both soaked and unsoaked conditions using heavy compaction and light compaction methods. An illustrative view of the ongoing CBR test at the laboratory is presented in Fig. 6.

2.4 Preparation of Design Curve

Upon completion of all the above-mentioned procedures, the design CBR curve is produced using linear regression modeling. The slag contents are plotted along the X-axis, and corresponding CBR values are plotted along the Y-axis. Then, the trend line provides the best suitable curve for the plotted values. Two separate design curves will be produced to show the variation of the best-plotted design curve for

both soaked and unsoaked conditions using heavy compaction and light compaction methods.

3 Experimental Investigation

Various tests have been conducted for collected soil, slag, and soil-slag mix in the laboratory of civil engineering, CUET. The results of the experimental investigation are presented in the subsequent sections.

3.1 Material Properties

The physical properties of soil and slag have been conducted and are presented in Table 1.

From Table 1, as the FM value of the collected soil is very low, it is unsuitable for roadway flexible pavement layer construction and, hence, needs to be stabilized.

In this study, slag has been used to stabilize the weak soil. Moreover, while analyzing the properties of slag, it is found that slag is highly porous and has a high absorption capacity. According to BS 812 Part 109: 1990, the water absorption value of a stronger aggregate is less than 1% and is good enough for road pavement construction [10]. Since slag does not fulfill this requirement, it cannot be used on the pavement surface but can be used in the base or sub-base course. Aggregates with aggregate impact value below 10% are considered as tough, and the ones above 35% are normally considered too weak to use in the road surface. According to ASTM C33 (ASTM 1994) and BS 812-112: 1990, the aggregate impact value of

Table 1 Physical properties of tested materials

Soil		Slag	
Physical property	Value	Physical property	Value
Fineness modulus	1.15	Aggregate impact value (AIV)	13.60%
Specific gravity	2.65	Aggregate crushing value (ACV)	32.41%
OMC (standard proctor test)	15.75%	Los Angeles abrasion value (LAAV)	41.38%
OMC (modified proctor test)	11.11%	Elongation index	4.37%
Bulk density (gm/cc)	1.63	Flakiness index	11.50%
		Bulk density (gm/cc)	1.44
		Apparent specific gravity	2.57
		Bulk specific gravity (oven-dry basis)	2.39
		Bulk specific gravity (SSD basis)	2.46
		Absorption capacity	2.96%

the aggregates used in base and sub-base course should be less than 30% [10]. In this case, the collected slag sample fulfills the requirement. According to RHD material specification clause 3.2.2 and 3.3.2, the aggregate crushing value for sub-base should not be greater than 38%. For base type-i, this value should be less than 30%, and for base type-ii, this value should be less than 35% [11]. In that case, the tested slag is not suitable for roadway surface construction but can be used in base or sub-base course to improve the strength of the respective layers. According to BS 812 section 105.2–1990, the elongation index should be less than 35%, and according to BS 812 section 105.1–1989, the flakiness index should be less than 25% [10]. The collected slag sample is not elongated nor is it flaky material as per the mentioned code. The recommended Los Angeles abrasion value for the aggregates used in coating and surface operation is less than 30% [12]. According to RHD material specification clause 3.3.2 and AASHTHO T96, the recommended Los Angeles abrasion value for base type-i is less than 35%, and for base type-ii, it is less than 40% [11]. The collected slag sample is a bit higher than this requirement and is not suitable to be used as an aggregate in the road surface.

3.2   OMC and MDD Values

In the investigation, various percentages of slag are mixed with soil as mentioned earlier. The tested sample undergoes both standard proctor and modified proctor compaction methods. The findings of the conducted experiments by these two methods are presented in Table 2. The variations in OMC and MDD values for different slag content are presented graphically in Fig. 7 and Fig. 8, respectively.

From Table 2 and Fig. 7, it is observed that OMC values decrease slowly with the increase of slag content in the soil-slag mix for both types of compactions. But, modified compaction has lower OMC values compared to standard compaction. Again from Table 2 and Fig. 8, the opposite scenario has been observed for various MDD values. But, modified compaction has higher MDD values compared to standard compaction.

Table 2   OMC and MDD values for different slag content

Slag content (%)	OMC (%)		MDD (gm/cc)	
	Standard proctor test	Modified proctor test	Standard proctor test	Modified proctor test
0	15.75	11.11	1.72	1.84
10	15	11.51	1.83	1.92
20	14.55	12	1.85	1.98
30	14	10.62	1.89	1.99
40	13.25	10.25	1.91	2.04
50	13	10.12	1.94	2.06

Fig. 7 Variation of OMC values with slag content
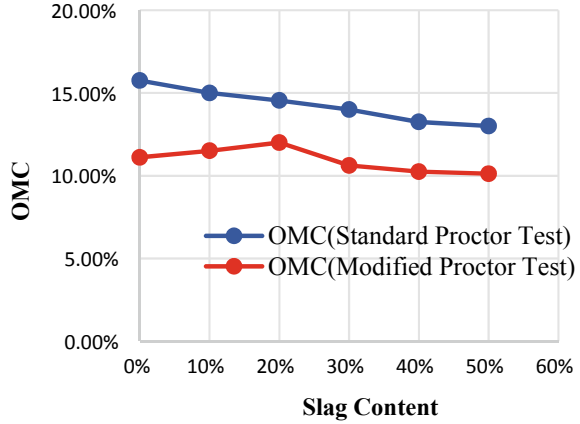
Fig. 8 MDD values for different slag content
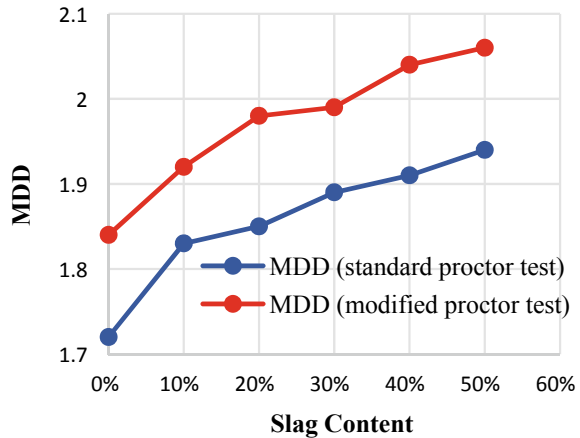
3.3 CBR Test

This investigation emphasized more on finding the CBR values to establish the design CBR curve. In the conducted research work, the CBR values for various slag contents with soil have been found out for both soaked and unsoaked conditions using heavy compaction and light compaction methods as per the above-mentioned code. Three samples have been conducted to determine the average CBR values in each case. The findings of the conducted investigation are presented in Table 3.

From the obtained CBR values in Table 3, it is found that the mean deviation and the standard deviation of unsoaked CBR (light compaction) are 20.22 and 22.73, respectively. In the case of soaked CBR (light compaction), the mean deviation and the standard deviation are 19.94 and 22.05, respectively. For unsoaked CBR (heavy compaction), the mean deviation and the standard deviation are calculated as 20.01

Table 3 CBR values for different slag content

Slag content (%)	CBR (light compaction)		CBR (heavy compaction)	
	Unsoaked	Soaked	Unsoaked	Soaked
0	16.64	16.25	18.93	20.88
10	32.90	27.88	37.42	41.27
20	41.8	37.86	51.76	57.81
30	58.39	55.47	62.72	71.97
40	70.56	66.37	76.89	84.67
50	83.7	79.81	88.56	98.78

and 23.38, respectively. The mean deviation and the standard deviation of soaked CBR (heavy compaction) are found as 22.58 and 26.15, respectively. A larger mean deviation and standard deviation show that the CBR values are scattered over a large range which indicates that with a change in slag content, the CBR values vary greatly in each case.

In the case of light compaction, the CBR in unsoaked condition provides a better result, and the highest CBR value for the light compaction method in the unsoaked condition is 83.7. In the case of heavy compaction, the CBR in soaked condition provides a higher CBR value. The highest CBR value for the heavy compaction method in the soaked condition is 98.78. The required CBR in different layers of flexible pavement is different. According to RHD material specification clause 3.2.2, the 4 days soaked CBR value determined by STP 4.5 (vibrating hammer) when compacted to 98% of maximum dry density should not be less than 25% for the sub-base layer [11]. The soil used in this investigation has 4 days soaked CBR value of 20.88. So, the collected soil sample is not suitable to be used in the road sub-base layer. As per RHD material specification clause 3.3.2, the 4 days soaked CBR value determined by STP 4.5 (vibrating hammer) when compacted to 98% of maximum dry density for base type-i should not be less than 80%, and for base type-ii, this should not be less than 50% [11]. As per this requirement, the collected soil is not favorable to be used as a base course layer since it does not fulfill the requirement of the code. Highway engineers can choose the appropriate soil-slag mix proportion from Table 3 as per their requirement for different layers of flexible pavement.

3.4 Design CBR Curves

The design CBR curves of the conducted investigation are derived from the obtained CBR values presented in Table 3. The desired design CBR curves for both the soaked and unsoaked conditions using heavy compaction as well as light compaction methods have been shown in Fig. 9 and Fig. 10, respectively, that are obtained from the CBR values.

Fig. 9 Design CBR curve
for soaked condition

$y = 1.5253x + 24.43$
$R^2 = 0.9925$

$y = 1.2882x + 15.068$
$R^2 = 0.9954$

- ● CBR Soaked (Heavy compaction)
- ■ CBR Soaked (Light Compaction)
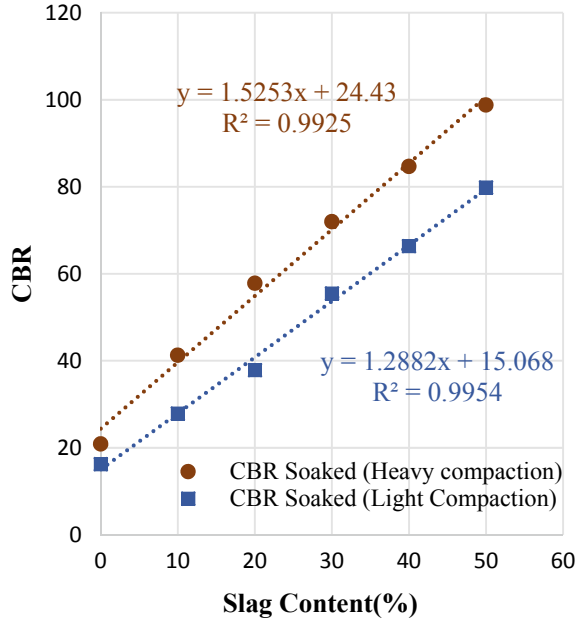
Slag Content(%)

Fig. 10 Design CBR curve
for unsoaked condition

$y = 1.3643x + 21.938$
$R^2 = 0.9934$

$y = 1.3282x + 17.46$
$R^2 = 0.9963$

- ● CBR Unsoaked (heavy compaction)
- ■ CBR Unsoaked (Light compaction)
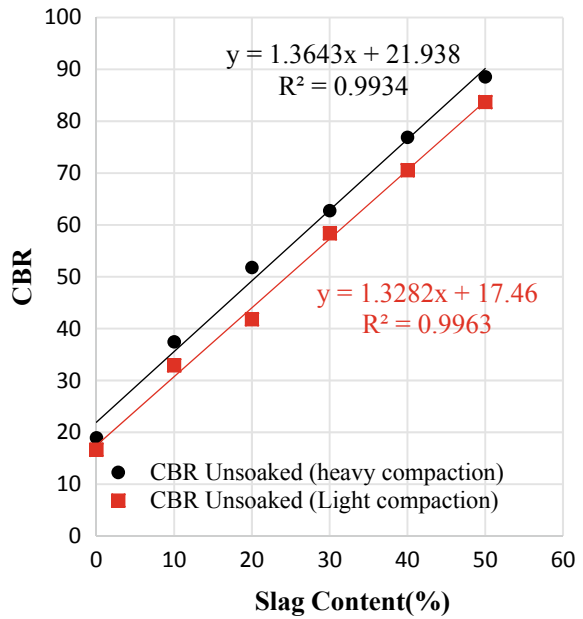
Slag Content(%)

The curves are showing the variation of CBR values for both soaked and unsoaked conditions, respectively, using heavy compaction and light compaction methods for different slag content with soil. From these curves, the amount of slag content for the desired CBR value can be obtained easily. Also, the required amount of slag content for respective CBR values can be found using the trend line equation. The y value is the desired CBR value to be obtained and by solving the equation to find the value of x which gives us the required amount of slag content. The equations of the design curves for both the soaked and unsoaked conditions using the heavy compaction as well as light compaction methods of the conducted investigation are provided below:

i. Soaked CBR (heavy compaction): $y = 1.5253x + 24.43$; $R^2 = 0.9925$
ii. Soaked CBR (light compaction): $y = 1.2882x + 15.068$; $R^2 = 0.9954$
iii. Unsoaked CBR (heavy compaction): $y = 1.3643x + 21.938$; $R^2 = 0.9934$
iv. Unsoaked CBR (light compaction): $y = 1.3282x + 17.46$; $R^2 = 0.9963$.

4 Discussion

The study has been conducted to investigate the property of slag, to improve the CBR of weak soil using slag, and to prepare a design CBR curve for different slag content. From the result of the investigation, it is seen that when slag is blended with weak soil, it provides good results in terms of strength. With the increasing amount of slag content, the CBR value of the mixes also increases. Slag as a coarse aggregate fulfills different standard specifications as per code to be used in the road base and sub-base layer of flexible pavement. So, it is suitable to use slag in these respective layers. But, slag as coarse aggregate is not suitable to be used in the roadway surface since it does not fulfill the requirement as per code. But, it can be used in the roadway surface as a coarse aggregate in the case of a low volume road.

5 Conclusion

From the evaluation of soil and slag properties, it has been found that the soil used in the investigation is weak. Although the slag is porous, other properties of slag to be used in road sub-surface layers of flexible pavement fulfill the requirement as per code. Also, the CBR values of the soil-slag mixes have an increasing trend with the increase of slag content. On the contrary, the amount of slag produced as a by-product during the production of steel in different steel industries increases with time. So, it will be difficult to handle this huge amount of slag in near future. This investigation concluded that the benefits of using slag as coarse aggregate in roadway base and sub-base layer of flexible pavement serve the following threefold purposes: (i) reduction of the government revenue, i.e., use of slag in the roadway sub-surface layers reduces the construction cost significantly, (ii) slag is being considered as a third-class environmental hazard because it requires a large volume of space for dumping and, so,

by utilization of slag in the roadway sub-surface layers provides an environment-friendly feasible solution to solve this problem, and (iii) more importantly, using of slag in the sub-surface layers of flexible pavement increases the strength of the respective layers. Also, from the design curve, professional engineers can estimate the required amount of slag content for the desired CBR value and researchers can use it to their research work.

References

1. Qurishee MA, Iqbal IT, Islam MS, Islam MM (2017) Use of slag as coarse aggregate and its effect on mechanical properties of concrete, pp 1–7
2. Günay E, Kara M, Kavakli B, Tayfur S, Eren K, Yildirim SA (2004) Steel slag and waste management. Key Eng Mater 264–268:2481–2484. https://doi.org/10.4028/www.scientific.net/kem.264-268.2481
3. Maghool F, Arulrajah A, Du YJ, Horpibulsuk S, Chinkulkijniwat A (2017) Environmental impacts of utilizing waste steel slag aggregates as recycled road construction materials. Clean Technol Environ Policy 19:949–958. https://doi.org/10.1007/s10098-016-1289-6
4. National Slag Association (2015) Slag a green product
5. TRANSPORTATION RESEARCH BOARD (1993) Transportation Research Record No. 1424—Environmental issues related to materials and stabilization
6. Rohde L, Núñez WP, Ceratti JAP (2003) Electric arc furnace steel slag: base material for low-volume roads. Transp Res Rec II:201–207. https://doi.org/10.3141/1819b-26
7. Yan Z, Shu Y, Bu J, Li X (2011) Test on the performance of road base-course made of steel slag and fly ash. In: Advanced materials research
8. Hainin MR, Aziz MA, Ali Z, Jaya RP, El-Sergany MM, Yaacoba H (2015) Steel slag as a road construction material. J Teknol 73:33–38. https://doi.org/10.11113/jt.v73.4282
9. Sinha A, Havanagi V, Mathur S (2013) Steel slag waste material for the construction of road. Indian Highw 41:15–22
10. Adanikin A (2018) Mechanical strength determination of crushed stone aggregate fraction for road pavement construction (case study: selected quarries in Western Nigeria)
11. RHD material specification 2016 June.pdf
12. Teymen A (2019) Estimation of Los Angeles abrasion resistance of igneous rocks from mechanical aggregate properties. Bull Eng Geol Environ 78:837–846. https://doi.org/10.1007/s10064-017-1134-0

Pavement Management System Using Deflection Prediction Model of Flexible Pavements in Bangladesh

K. A. Momin and O. F. Hamim

1 Introduction

Insufficient maintenance and rehabilitation of the road network of Bangladesh are mainly responsible for expensive and unreliable transport services, which in turn constrain movements of labor, goods, services and reduce the comfort of road journeys. In addition, an increasing number of vehicles, inadequate road safety measures, and poor roadway surface cause chronic congestion. Flexible pavement surface bears the majority of traffic load; hence, the utmost importance is given while making this surface durable and serviceable. Existing knowledge on constructing roads is abundant, but evaluating road conditions using simple yet convenient methods and maintaining roads to comply with serviceability standards is very challenging [1]. Pavement performance includes both functional performance and structural performance representing the effectiveness or adaptability of pavement conditions to meet various driving requirements [2]. The full functional benefit of roadways is difficult to avail if due consideration is not given to proper maintenance of roadways, so pavement evaluation should be performed to know the nature, severity, and extent of road deterioration. Evaluation of existing flexible pavement conditions is a prerequisite for selecting appropriate improvement techniques to enhance pavement quality.

IRI has been used by highway professionals all over the world as a standard to quantify pavement roughness. Pavement roughness expresses the irregularities in the pavement surface, which causes adverse effects on riding quality; the importance of the roughness index lies in the fact that in addition to affecting ride quality, and it has an impact on other factors, e.g., fuel consumption, vehicle delay costs, and maintenance costs [2]. In contrast, pavement surface deflection measurement

K. A. Momin (✉)
Department of Civil Engineering, Daffodil International University, Dhaka, Bangladesh

O. F. Hamim
Department of Civil Engineering, Bangladesh University of Engineering & Technology, Dhaka, Bangladesh

is used to evaluate the structural strength of flexible pavements. Surface deflection is an important pavement evaluation method. Pavement deflection, an important method for pavement evaluation, is a function of traffic, pavement structural section, temperature, and moisture affecting the pavement structure. Measuring deflection in the field is difficult compared to measuring IRI; hence, a model correlating IRI and deflection can be useful.

Pavement researchers prefer non-destructive testing methods for evaluating existing pavements [3]. Several indicators, such as pavement distress, roughness, rutting, anti-skid resistance, structure strength, etc., are used to assess pavement quality in terms of functional and structural performance [4]. In Ontario, several Key Performance Index (KPIs) are used for taking managerial decisions regarding highway management, such as the Pavement Condition Index (PCI), Distress Manifestation Index (DMI), International Roughness Index (IRI), Riding Comfort Index (RCI), etc. Jannat and Tighe [5] used Seemingly Unrelated Regression (SUR) method to estimate KPI models considering all available models affecting pavement performance, and it has been found that the PCI model is highly correlated with DMI and RCI model. However, the IRI model was found not to be strongly correlated to other models. Rahman et al. [6] found that precipitation is a significant predictor of the Pavement Serviceability Index (PSI) for both asphalt concrete (AC) pavements and jointed plain concrete pavements (JPCP). The Illinois Department of Transportation generated pavement performance models based on historical performance data, route, pavement type, age, and presence of certain distresses [7]. Lin et al. [8] have developed a neural network model to establish a correlation between pavement distresses and IRI. A correlation coefficient of 0.944 between pavement distresses and IRI showed that IRI is capable of reflecting on pavement distress conditions; thus, IRI can be used as a pavement performance index. Mubaraki [9] has developed a pavement roughness and pavement condition model based on rutting, raveling, cracking, and IRI data of Saudi highway pavements using the regression method. The R^2 value was found to be 83.9% and 95%, respectively, for Pavement Condition Rating (PCR) and IRI-based models, respectively.

Developing an empirical model to predict the deflection of flexible pavements using IRI values, annual average daily traffic (AADT), road width, and time since the last overlay on selected flexible pavement sections is the objective of this research. The data used for this study have been collected from the database of the Road Maintenance Management System (RMMS) of Roads and Highways Department (RHD), Bangladesh. The outcome of this research work will help in improving the pavement management system in Bangladesh by using easily collectible IRI values, annual average daily traffic (AADT), road width, and time since the last overlay to predict the deflection of pavements and take adequate rehabilitation measures at regular intervals.

2 Methodology

Multiple linear regression analysis methodology has been used to develop a pavement performance evaluation model for flexible pavements under the traffic loading and geographic condition of Bangladesh.

2.1 Data Collection

At first, a reconnaissance survey was carried out within the RHD road network comprising of different road types to figure out the suitable road sections for collecting relevant data to evaluate the performance of flexible pavement. Selection of the pavement sections depended on: (i) data availability regarding the time since the last overlay performed on that road section, (ii) representative samples covering different types of road sections, and (iii) reliability of collected data. Even though the RHD database included a large number of road sections, the overlay history could be found for only a few pavement sections during the piloting survey. Thus, based on the criteria stated earlier, seven road sections covering about two hundred fifty-two kilometers and six hundred meters (252.6 km) were selected for the final survey. These pavement sections included four national highways and two regional highways.

2.2 Multiple Regression Analysis

In [10], it has been propounded that determining the relationship between several independent or predictor variables and a dependent or criterion variable is the general purpose of multiple regression. In this study, the predictor variables are IRI, AADT, road width, and time since the last overlay. The dependent or criterion variable has been selected as the deflection of flexible pavement. The general multiple linear regression model is given by:

$$Y = \varepsilon_0 + \varepsilon_1 1 X_{i1} + \varepsilon_2 X_{i2} + \varepsilon_3 X_{i3} + \varepsilon_4 X_{i4} \tag{1}$$

where X_i = predictor variables, respectively, IRI, AADT, road width, and time since the last overlay found from the database of RHD, Bangladesh; Y = response variable, deflection of flexible pavement. For developing the multiple linear regression model, the statistical package software, SPSS (v.25), has been used.

3 Results and Discussions

3.1 Site Description

Five road sections from four national highways of RHD, i.e., N3, N5, N501, N504, and two road sections from two regional highways, i.e., R110 and R370 of RHD, were selected to develop a pavement performance model. A brief description of the selected road sections is presented in Table 1.

In Figs. 1 and 2, the histograms represent the variation of deflection and IRI data pertaining to the selected pavement sections, respectively. The deflection values are found to be within the range of 0.5 to 2.0 mm, and the IRI values varied between 2 to 12. From Fig. 1, it can be observed that the deflection value mostly varied from 0.5 to 1.25 mm, whereas Fig. 2 reveals that the majority of the pavement sections had an IRI value ranging from 2 to 6.

The results of correlation analysis between the variables used are presented in Table 2. The correlation between pavement deflection and predictor variables ranges

Table 1 Description of selected road sections

Road name	Road section taken for analysis		Width (m)	AADT	Age (years since the last overlay)
	Chainage from (km)	Chainage to (km)			
N3	0.000	21.008	8.19	18,755	5
N5	0.000	78.155	7.17	8913	1
	100.616	209.365	7.17	8913	3
N501	0.000	5.986	7.33	11,346	5
N504	0.000	5.668	7.32	6489	3
R110	0.000	12.000	8.60	15,309	5
R370	21.087	42.121	4.92	8726	1

Fig. 1 Classification of deflection data
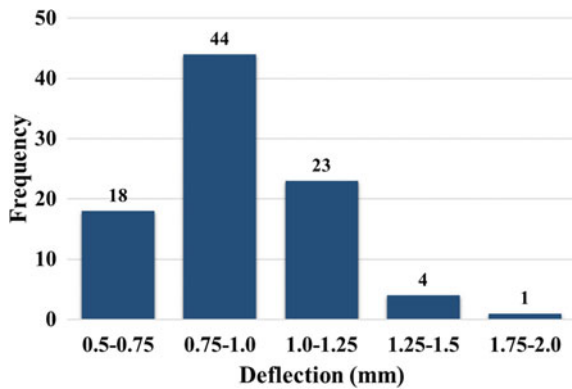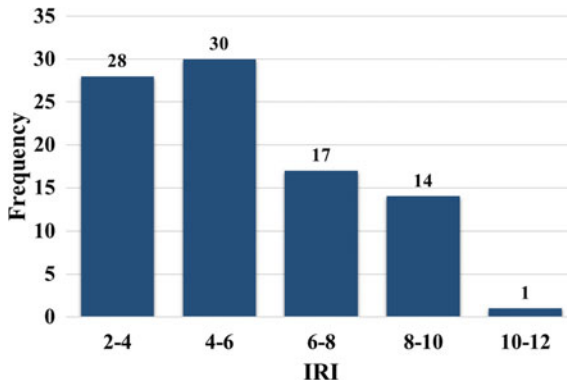
Fig. 2 Classification of IRI data

Table 2 Correlation analysis outcomes among different derivatives

	Deflection	IRI	AADT	Width	Age
Deflection	1				
IRI	0.775***	1			
AADT	0.304**	0.379***	1		
Width	0.062	0.033	0.576***	1	
Age	0.302**	0.221*	0.549***	0.587***	1

Note ***$p < 0.001$, **$p < 0.01$, *$p < 0.05$

from high to low, with the Pearson correlation values (r) ranging from 0.033 to 0.775. IRI has the strongest correlation with the deflection ($r = 0.775$, $p < 0.001$). Table 2 shows that some of the predictor variables have strong correlations with each other. For instance, AADT is strongly correlated with roadway width ($r = 0.576$, $p < 0.001$), which is due to the fact that with the increase in road width, AADT will increase. On the contrary, the correlation between IRI and roadway width is found to be very low and insignificant ($r = 0.033$, $p = 0.378$). However, all of the predictor variables are positively correlated with the dependent variable, which means that with the increase in every predictor variable, pavement deflection will increase.

Multiple linear regression model using IRI, AADT, width, and age as independent variables revealed that IRI and age has a significant positive effect in predicting deflection, while AADT and width have no significant effect in predicting deflection; hence, a modified regression model has been developed using only IRI and AADT as predictor variables. Table 3 presents the constant or intercept term and the regression coefficients (B) for each explanatory variable used in the regression model where the dependent variable was deflection. For a constant value of 0.438, IRI and age have a significant positive effect on deflection, indicating that deflection increases with increasing IRI and age. With every unit increase in IRI, the model predicts an increase of 0.076 in deflection, and for every unit increase in age, the model predicts

Table 3 Model coefficients used to develop model

Model		Unstandardized coefficients		Standardized coefficients	t	Sig
		B	Std. error	Beta		
1	(Constant)	0.438	0.045		9.816	0.000
	IRI	0.076	0.007	0.744	10.956	0.000
	Age	0.020	0.010	0.138	2.024	0.046

an increase of 0.020 in deflection. So, an increase in IRI value and age corresponds to increased deflection indicating loss of riding quality associated with structural deficiency of pavements as the pavement ages. Also, the standardized coefficient for IRI is greater than age, so IRI has a better ability to predict deflection compared to age.

The multiple R and coefficient of determination (R^2) values for the developed regression model are given in Table 4. The R^2 value of 0.618 indicates that 61.8% of the variances in deflection can be explained by this regression model comprising of predictor variables, i.e., IRI and age. If other relevant factors are included, the model will be able to predict the deflection better, which can be a scope of future study. From Table 5, it can be seen that the F value is 70.439, which is significant at $p < 0.001$. Therefore, we can conclude that our regression model results in significantly better prediction of deflection than if we used the mean value of deflection. In other words, the regression model overall predicts pavement deflection significantly well. So, this model can be used as a pavement performance model for flexible pavements in Bangladesh. The regression model can be presented as:

$$\text{Deflection} = 0.438 + 0.076 \times \text{IRI} + 0.02 \times \text{Age} \qquad (2)$$

Table 4 Model summary statistics

Model	R	R^2	Adjusted R^2	Std. error of the estimate
1	0.786[a,b]	0.618	0.609	0.14247

[a]Predictors: (constant), age, IRI
[b]Dependent variable: deflection

Table 5 Fitness of model evaluation

Model		Sum of squares	df	Mean square	F	Sig
	Regression	2.859	2	1.430	70.439	0.000
1	Residual	1.766	87	0.020		
	Total	4.625	89			

Figure 3 presents the normal probability plot where the straight line represents a normal distribution, and the points represent the observed residuals. The observed residuals are closely placed to the straight line; hence, it can be said that the dataset is roughly normally distributed. Also, the histogram presented in Fig. 4 shows a bell-shaped curve indicating that the distribution is roughly normal.

Fig. 3 Normal P-P plot of residuals

Normal P-P Plot of Regression Standardized Residual
Dependent Variable: Deflection
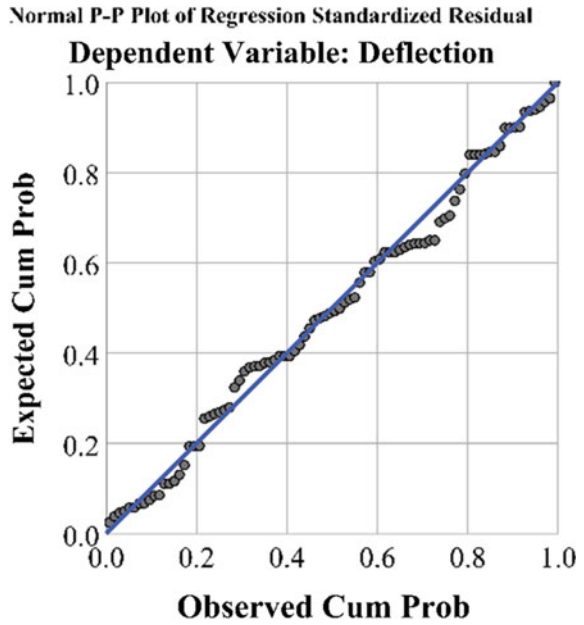
Fig. 4 Histogram of residuals

Histogram
Dependent Variable: Deflection

Mean = 1.92E-15
Std. Dev. = 0.989
N = 90
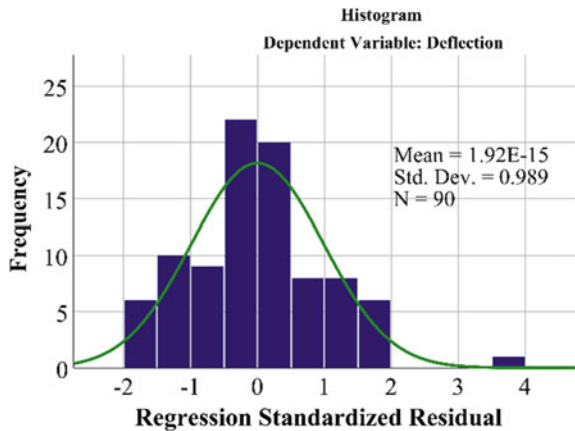
4   Conclusions

Pavement monitoring plays an important role in ensuring the functional and structural performance of flexible pavements. In this study, a pavement performance model has been developed using a multiple linear regression model based on deflection, IRI, and pavement age data of flexible pavements constructed and maintained by RHD, Bangladesh. The influence of pavement width and AADT of the road sections have been found to be insignificant in predicting the deflection of pavement. IRI and age of pavement, i.e., time since the last overlay, have been recognized as significant predictor variables for determining the pavement deflection. Both IRI and age are positively correlated with deflection, indicating that an increase in IRI and age will increase the deflection of pavement. This regression model will help decision-makers to decide on appropriate pavement rehabilitation or maintenance approach using deflection value predicted by IRI and age of pavement sections.

References

1. Andrén P (2006) Development and Results of the Swedish Road Deflection Tester. Royal Institute of Technology
2. Bo L, Kundwa MJ, Jiao CY, Wei ZX (2019) Pavement performance evaluation and maintenance decision-making in Rwanda. Int J Pavement Res Technol 12:443–447. https://doi.org/10.1007/s42947-019-0053-9
3. Aghera HV, Mandhani J, Solanki RV (2017) A Review on Performance Evaluation of Flexible Pavement. Int J Adv Eng Res Dev 4:37–41
4. Qiang L, Gang L, Yuli P (2011) Study on Life-Cycle Cost Analysis Based Pavement. In 8th International Conference on Managing Pavement Assets, November 15–19, 2011, Santiago, Chile: "Fulfilling the Social, Economic and Environmental Responsibility for Sustainable, Well Managed, Better Roads."
5. Jannat G-E-, Tighe SL (2015) Performance Based Evaluation of Overall Pavement Condition Indices for Ontario Highway Systems. In TAC 2015: Getting You There Safely - 2015 Conference and Exhibition of the Transportation Association of Canada
6. Rahman MM, Uddin MM, Gassman SL (2017) Pavement performance evaluation models for South Carolina. KSCE J Civ Eng 21:2695–2706. https://doi.org/10.1007/s12205-017-0544-7
7. Hicks G, Groeger J (2011) Pavement Management Practices in State Highway Agencies: Newington, Connecticut Peer Exchange Results
8. Lin J, Yau J-T, Hsiao L-H (2003) Correlation Analysis Between International Roughness Index (IRI) By. Transp Res Board 82th Annu Meet 1–21
9. Mubaraki M (2013) Development of pavement condition rating model and pavement roughness model for Saudi highways. Adv Mater Res 723:820–828. https://doi.org/10.4028/www.scientific.net/AMR.723.820
10. Nathans LL, Oswald FL, Nimon K (2012) Interpreting multiple linear regression: A guidebook of variable importance. Pract Assessment, Res Eval 17:1–19

Mode Choice Behavior Analysis in N1 Highway: A Case Study from Cumilla to Dhaka

S. I. Feroz, F. H. Chowdhury, N. A. Alam, Y. R. Momo, and M. M. Rahman

1 Introduction

One of the most important activities to promote mobility is urban transportation planning [1] which is an inevitable part of the national growth process. Mode choice analysis is one of the most important and challenging components of transportation planning because it is a part of the conventional four-step travel demand modeling process. The main transportation artery of Bangladesh is the N1 highway which is 250 km in length [2], but here, study area is from Cumilla to Dhaka (97 km). 16.5 km accident-prone length with 38 accident spots [3] N1 highway became the most critical highway of Bangladesh. So exploring the mode choice behavior in this route (only Cumilla to Dhaka) is very important to control the accidents and further planning. Very few studies were conducted on mode choice behavior in Bangladesh but only in Dhaka city [4, 5], and some studies conducted on comparison of accident data analysis in different national highways [6]. But no study is found on mode choice behavior analysis on N1 highway. To know the attributes of travel that influence individual choices of mode in N1 highway, it is important to develop and use models [7]. Multinomial logistics regression model is widely used to analyze the mood choice behavior since the formula for the choice probabilities takes a closed-form and easy to illustrate [8].

In this study, the aim is to find out commuters' preference and use of various existing modes in Cumilla to Dhaka route. For that, a questionnaire survey is conducted in three different locations of this route. After that, the focus is on

S. I. Feroz (✉) · F. H. Chowdhury · N. A. Alam · Y. R. Momo
Department of Civil Engineering, Bangladesh Army International University of Science and Technology (BAIUST), Cumilla, Bangladesh

M. M. Rahman
Department of Civil Engineering, Bangladesh University of Engineering and Technology (BUET), Dhaka, Bangladesh
e-mail: mizanur@ce.buet.ac.bd

the factors that are responsible for the current mode choice. The choice of travel mode is affected by a great many factors which factors are classified in many ways by Olsson [9]. Like hard (traveling time, waiting time, and ticket price) and soft (comfort, service and information) factors, internal (attitudes, socio-economic and demographic factors, habits) and external (traveling time and the cost of the journey) factors, etc. To analyze the factors and predict mode choice behavior a multinomial logistics regression model is developed. To establish the model, seven factors are considered. There are four categorical socio-economic variables (commuters' age, income, gender, and occupation) and three travel-related continuous variables (travel time, travel cost, and waiting time).

2 Materials and Methods

2.1 Selection of Study Area

Here, data collection is done for mode choice behavior analysis in Cumilla to Dhaka route which is a part of N1 highway. Data collection is done in three different locations (i.e., Shashongacha Bus Terminal, Jangalia Bus Terminal, and Cumilla Cantonment Bus Stop) of this route.

2.2 Questionnaire Survey

A questionnaire survey (400 respondents) is conducted at the study areas to know the socio-economic characteristics like commuters age, occupation, income, educational status, occupation, travel-related information like purpose of the trip, frequency of the trip, travel cost, waiting time, travel time, condition of the road, main obstacles of the journey, need of any alternative mood, private vehicle ownership, etc.

2.3 Multinomial Logistic Regression Model

To know the mode choice behavior of the road users and predict the factors behind this preference, a multinomial logistics regression model is established. Logistic probability unit or the logit model [8] which was first introduced in the context of binary choice based on the logistic distribution, its generalization to more than two alternatives are referred to as the multinomial logit (MNL) model. With multiple explicative variables, the logistic regression can be extending to models.

$$Logit[P(Y = 1)] = \alpha + \beta_1 x_1 + \beta_2 x_2 + ... + \beta_k x_k \tag{1}$$

Here, k denotes the number of independent factors for a binary response Y and $x_1, x_2, \ldots, x_k$ are the explanatory variables. We can use alternative formula which directly specifying $\pi(x)$, is:

$$\pi(x) = \frac{\exp(\alpha + \beta_1 x_1 + \beta_2 x_2 + \ldots + \beta_k x_k)}{1 + \exp(\alpha + \beta_1 x_1 + \beta_2 x_2 + \ldots + \beta_k x_k)} \tag{2}$$

To establish the logits in the multinomial case, one of the categories must be considered the base level and all the logits are constructed relative to it. If we have n independent observations with p explanatory variables, and the qualitative response variable has k categories, any category can be taken as the base level, so we will take category k as the base level. Any category may be labelled k since there is no ordering. Let $\pi(j)$ denote the multinomial probability of an observation falling in the jth category, to find the relationship between this probability and the p explanatory variables, $x_1, x_2, \ldots x_p$ the multiple logistic regression model then is:

$$\log\left[\frac{\pi_j(x_i)}{\pi_k(x_i)}\right] = \left(\alpha_{0i} + \beta_{1j} x_{1i} + \beta_{2j} x_{2i} + \ldots \beta_{pj} x_{pi}\right) \tag{3}$$

where $j = 1, 2, \ldots (k-1)$ and $i = 1, 2, \ldots n$. As all the $\pi's$ add to unity, this reduces to:

$$\log\left[\pi_j(x_i)\right] = \frac{\exp\left(\alpha_{0i} + \beta_{1j} x_{1i} + \beta_{2j} x_{2i} + \ldots \beta_{pj} x_{pi}\right)}{1 + \sum_{j=1}^{k=1} \exp\left(\alpha_{0i} + \beta_{1j} x_{1i} + \beta_{2j} x_{2i} + \ldots \beta_{pj} x_{pi}\right)} \tag{4}$$

Equations (1), (2), (3) and (4) are taken from El-Habil [10]. For $j = 1, 2, \ldots (k-1)$. The model parameters are calculated by the method of ML. To do this fitting, usually statistical software is used [11]. When an independent variable is continuous, such statistics are still valid for comparing models differing by relatively few terms [12].

3 Results and Discussions

3.1 Findings from the Field Survey

Figure 1 illustrates the comparison of mode choice preferred by the male and female road users where AC bus is the most preferable mode and microbus (local) is the least preferable mood in both cases. Notable portion of male users use non-AC bus (26.13%) whereas very few local and microbus female user with no motorcycle female road user. For a journey with family and tour purpose, people use private car or rent a car.
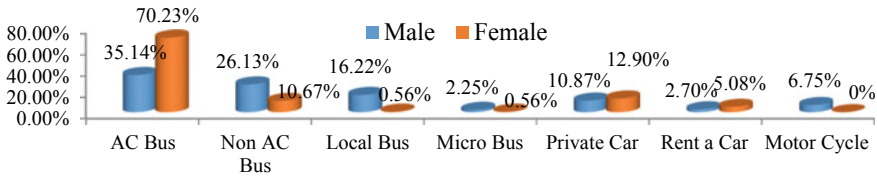
Fig. 1 Comparison of mode choice between male and female road users
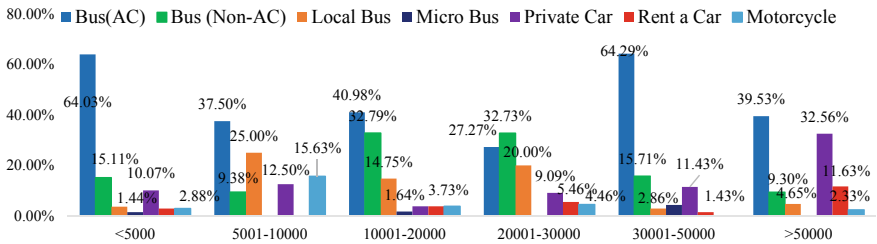
Fig. 2 Comparison of mode choice between different income groups

Figure 2 shows that people with low income (<10,000 BDT) are mostly students, housewives, and retired persons who largely depends on others income. They are the vulnerable road users and mostly use AC bus. On the contrary, people with medium-range income (10,000–30,000 BDT) prefer non-AC bus. Use of private car and rent a car is maximum for people with higher income (>30,000 BDT).

From Fig. 3, it can be seen that people with all ages mostly use AC bus. Old people with age greater than 60 find it comfortable to use AC bus. Respondents with middle age (25–40 years) use non-AC bus. Some middle age local businessman and students use local bus. Private car users are mainly ages greater than 40 years.

From Fig. 4, the respondents who are service holder usually choose AC bus. Most of the local business men are using non-AC bus. Students mostly prefer AC bus because of comfort. Some students have their own motorcycle. Retired person mostly prefers comfortable service like AC bus, microbus, private car, and rent a car. Others are mostly freelancers and housewives. They mostly use buses.
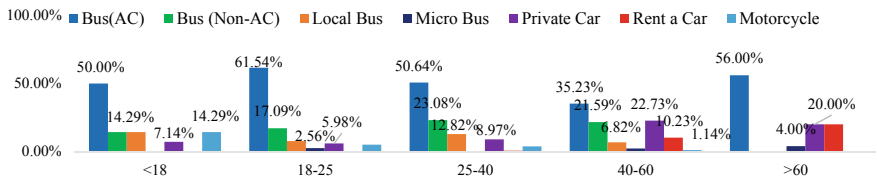
Fig. 3 Comparison of mode choice between different age groups
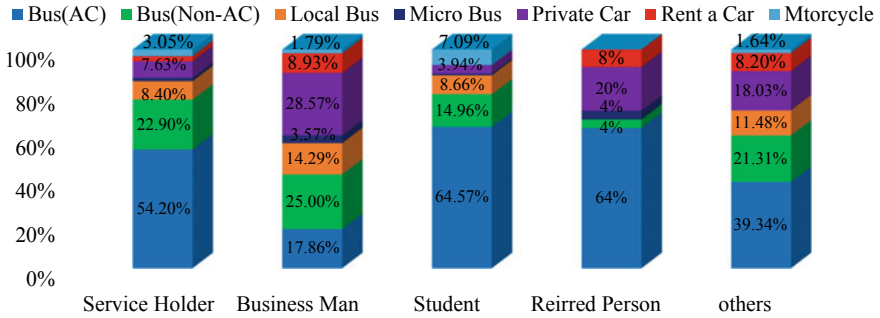
Fig. 4 Comparison of mode choice between different occupations
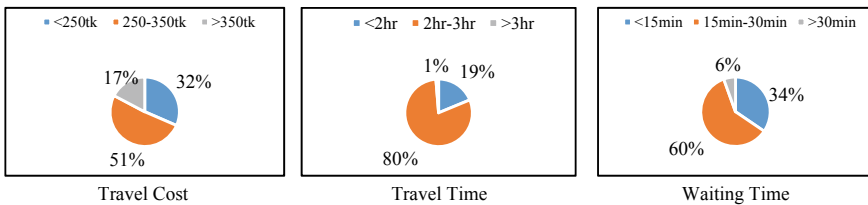
Fig. 5 Travel cost, travel time, and waiting time

Figure 5 shows the travel cost, travel time, and waiting time for the desired vehicle. Cost of local bus is about 150–200 BDT, whereas cost of non-AC bus is about 200–250 BDT. For using AC bus, people have to pay 250–350 BDT. For using private car, rent a car, microbus, and motor bike, 17% respondent has to pay cost fluctuating from 1000 to 5000 BDT. Sometime congestion in three major bridges in this route (Magna Bridge, Gomti Bridge, and Kachpur Bridge) causes long trip length. Average trip length in this route without any congestion is 2–3 h. Rent a car, motorcycle, and private car user's trip length is generally less than average time. Most of the respondents who use bus have to wait for the desired vehicle. In this route, average waiting time is 15 min to 30 min for passengers. 60% respondents have to wait 15 min–30 min for the desired vehicle.

The respondents were asked to mention the reasons they feel important for choosing the mode they were using for that particular trip. A significant difference is observed among different mode users while mentioning the reason in Fig. 6. For example, about 39% and 43% respondents use AC bus for safe travel and comfort, respectively. For non-AC bus users, less fare (26%) and less time (40%) is mostly chosen as reason. On the contrary, local bus users chose less fare (62%) for their reason to select this mode. For microbus user, most important reason is less fare (36%) and less time (29%). Private car owners choose safe travel (31%) and comfort (49%) as their main reason of choosing. Rent a car users also choose comfort (50%) and less time (35%) as their reason. And most of the motorcycle users mostly chose less time (60%).
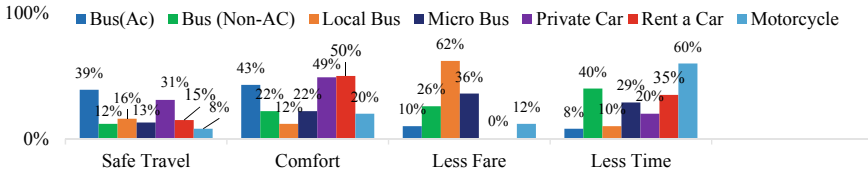
Fig. 6 Reason behind choosing different modes
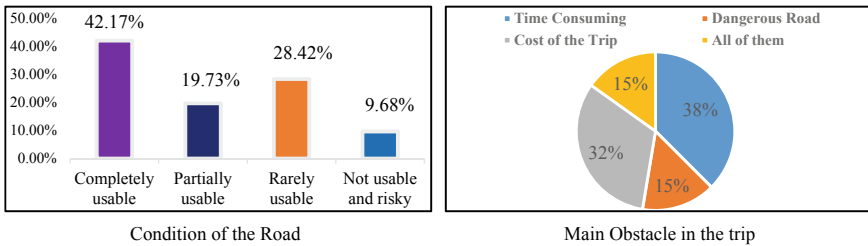
Fig. 7 Condition of the road and main obstacle in the trip

The respondents were asked to mention the condition of the road (N1 highway). From Fig. 7, about 42.17% respondents think road is completely usable. On the contrary, most of the private car owners and motorcycle users find the road rarely useable or not useable and risky. Their main problem is reckless driving and violation of traffic law by bus and truck drivers. Some of the respondents think the road is partially useable. Their main problem is traffic jam. From Fig. 7, most of the respondents think that the trip is time consuming (38%) and costly (32%), respectively. Overtaking mentality of the driver, teenager driver, old public bus, too much passengers in the bus are the main reasons make the road risky.

3.2 Establishment of Multinomial Logistics Regression Model

Here, seven explanatory variables are considered which might had an influence on mode choice behavior of N1 highway road users. SPSS software version 23 is used to find the effects of these variables on mode choice and establish a MLR model to predict the mode choice of commuters. Table 1 shows the details of the explanatory variables.

Footnote in Table 1 indicates that the number of combinations in the data collected and that is 316 overall whereas 308 combinations have the same response variable.

It can be seen from the Table 2 "Sig" column that $p = 0.000 < 0.05$, which means that there is a significance relation between dependent variable and explanatory

Table 1 Case processing summary

Response variable (with dummy code)		Frequency N	Marginal percentage (%)	Cumulative percentage (%)
Mode choice	AC bus (1)	203	50.7	50.7
	non-AC Bus (2)	77	19.3	70
	local bus (3)	37	9.3	79.3
	microbus (4)	6	1.5	80.8
	private car (5)	47	11.8	92.6
	rent a car (6)	15	3.8	96.4
	motorcycle (7)	15	3.8	100
Categorical variables (with dummy code)				
Gender	Male (1)	222	55.5	55.5
	Female (2)	178	44.5	100
Occupation	Service holder (1)	131	32.8	32.8
	Student (2)	127	31.8	64.6
	Business (3)	56	14.0	78.6
	retired person (4)	25	6.3	84.9
	Others-5	61	15.3	100
Age	<18 (1)	14	3.5	3.5
	18–25 (2)	117	29.3	32.8
	25–40 (3)	156	39.0	71.8
	40–60 (4)	88	22.0	93.8
	>60 (5)	25	6.3	100
Income	<5000 BDT (1)	139	34.8	34.8
	5000–10000BDT (2)	32	8.0	42.8
	10,000–20,000 BDT (3)	61	15.3	58.1
	20,000–30,000 BDT (4)	55	13.8	71.9
	30,000–50,000 BDT (5)	70	17.5	89.4
	>50,000 BDT (6)	43	10.8	100
Continuous variables				
Travel cost (BDT)		400	100	100
Travel time (hour)		400	100	100
Waiting time (minute)		400	100	100
Valid		400	100.0	
Missing		0		
Total		400		

Table 1 (continued)

Response variable (with dummy code)	Frequency N	Marginal percentage (%)	Cumulative percentage (%)
Subpopulation	316[a]		

[a]The dependent variable has only one value observed in 308 (97.5%) subpopulations

Table 2 Model fitting information

Model	Model fitting criteria			Likelihood ratio tests		
	AIC	BIC	−2 Log likelihood	χ^2	df	Sig
Intercept only	1153.246	1177.195	1141.246			
Final	503.188	742.676	383.188	758.058	54	0.000

variables. So, it can be summarized that the data is fit for final model, and dependent variable mode choice is dependent on the factors considered here.

Pseudo R^2 values represent the variation of dependent value with independent variable. Generally, we go with Negelkerke value which should be near 1 for a perfect variation. From Table 3, the value is 0.90 which implies that the data set has a good variation between dependent and independent variables.

Table 4 illustrates which of the explanatory variables are statistically significant. From Table 4, it can be seen that gender, income, waiting time, travel time, and travel cost are statistically significant which means there is a direct relation between mode choices with these variables.

Table 5 presents the parameter estimates which are also called the coefficients of the model (B). As there were seven categories of the dependent variable, there are six sets of logistic regression coefficients (sometimes called six logits). Here, only statistically significant values ($p \leq 0.05$ or marginally significant $p \leq 0.1$) are considered. If any variables had some significant effect on mode choice with low statistical significance (i.e., $p \leq 0.1$) might also be retained [13]. Any category of the response variable can be chosen as reference category or baseline with same likelihood and fitted values but with different interpretation [14]. In the model response variable with highest frequency, AC bus is considered as reference category. Here, B is the expected amount of change in the logit for each one unit change in the significant predictor. If B is closer to zero, the less influence the predict or has in predicting the logit. Odd ratio > 1 will increase the logit whereas odd ratio < 1 will decrease the logit. Those predictors which do not have an effect on the logit will display an odd ratio of 1.0.

Table 3 Pseudo R^2

Cox and snell	0.850
Nagelkerke	0.900
McFadden	0.657

Table 4 Likelihood ratio tests

Effect	Model fitting criteria			Likelihood ratio tests		
	AIC of reduced model	BIC of reduced model	−2Log likelihood of reduced model	χ^2	df	Sig
Intercept	503.188	742.676	383.188[a]	0.000	0	
Gender	552.382	767.921	444.382	61.194	6	0.000
Income	519.185	638.929	459.185	75.997	30	0.000
Waiting_Time_min	561.227	776.766	453.227	70.039	6	0.000
Travel_Time_hr	515.422	730.961	407.422	24.234	6	0.000
Cost_BDT	874.384	1089.923	766.384	383.196	6	0.000

[a]This reduced model is equivalent to the final model because omitting the effect does not increase the degrees of freedom

The chi-square statistic is the difference in -2 log-likelihoods between the final model and a reduced model. The reduced model is formed by omitting an effect from the final model. The null hypothesis is that all parameters of that effect are 0

Equation (5) represents the logit for non-AC bus. The likelihood of choosing non-AC bus over AC bus is decreasing if the cost and waiting time is increasing. Males are 5.432 times more likely to choose non-AC bus over AC bus with respect to female. People with middle income range (10–30 k BDT) are more likely to choose non-AC bus over AC bus with respect to people with higher income (>50 k BDT). Equation (6) is the logit for local bus which indicates if cost is decreasing people will choose local bus rather than AC bus and with the increase of waiting time; people will still choose local bus over AC bus due to less fare. Males and middle range income groups are more likely to choose local bus rather than AC bus. In case of microbus Eq. (7) is the logit. If the cost of using microbus is increasing, people will still use microbus. From the field survey, it is found that female road users are less likely to use microbus as their preferable mood which is reflected in the equation. When the travel time is increasing, people are less likely to choose microbus than AC bus. From Eq. (8), if the cost is increasing, people will still use it rather than AC bus due to comfort and safety. Male road users choose private car more than female road users. Odd ratio is negative for waiting time and income. Equation (9) is for rent a car where with the increase of travel time and cost, likelihood of using rent a car over AC bus will increase. Equation (10) is for motorcycle which indicates that the likelihood of choosing motorcycle over AC bus is decreasing if the waiting time and travel time is increasing.

Table 7 explains how well the final model can classify cases. The proportional by chance accuracy rate can be computed by squaring and summing the proportion of cases for each response variables (Shown in Table 1) multiple by 25% improvement [11]. So the proportional by chance accuracy criteria are: $(0.507^2 + 0.193^2 + 0.093^2 + 0.015^2 + 0.118^2 + 0.038^2 + 0.038^2 = 0.319984) * 1.25 = 40\%$. This proportion will be compared with the overall percentage of the final model shown in Table 7. The classification overall percentage computed by model was 85% which is greater

Table 5 Parameter estimates (only statistically significant variables) using statistical analysis

Mode choice[a]	Variables	Denotation	B	Std. error	p-value	Odds ratio
Non-AC Bus	Intercept		5.114	1.743	0.003	
	Travel cost	x_1	-0.032	0.005	0.000	0.968
	Waiting time (min)	x_2	-0.083	0.033	0.012	0.921
	Gender (relative to female)					
	Male	x_3	1.692	0.418	0.000	5.432
	Income (relative to > 50 k BDT)					
	10 –20 k BDT	x_4	1.337	0.828	0.100	3.807
	20 –30 k BDT	x_5	2.428	0.891	0.006	11.331
Local bus	Travel cost	x_1	−0.061	0.009	0.000	0.941
	Waiting time (min)	x_2	0.126	0.048	0.008	1.134
	Gender (relative to female)					
	Male	x_3	4.075	1.546	0.008	58.827
	Income (relative to income >50 k BDT)					
	5 k–10 k BDT	x_6	4.485	1.589	0.005	88.674
	20 k–30 k BDT	x_5	2.821	1.305	0.031	16.792
Microbus(local)	Travel cost	x_1	0.12	0.003	0.000	1.12
	Travel time (hr.)	x_7	−4.970	1.594	0.002	0.007
	Gender (relative to female)					
	Male	x_3	6.780	2.195	0.002	879.848
Private car	Travel cost	x_1	0.011	0.003	0.000	1.011
	Waiting TIME (min)	x_2	−0.256	0.102	0.012	0.774
	Gender (relative to female)					
	Male	x_3	3.311	1.437	0.021	27.401
	Income (relative to income > 50 k BDT)					
	10–20 k BDT	x_4	−4.699	1.880	0.012	0.009
Rent a car	Intercept		−34.480	13.832	0.013	
	Waiting time (min)	x_2	0.454	0.245	0.063	1.575
	Travel cost	x_1	0.016	0.003	0.000	1.016
Motorcycle	Travel time (hr.)	x_7	−4.291	1.673	0.010	0.014
	Waiting time (min)	x_2	−0.685	0.242	0.005	0.504

[a]The reference category is: AC Bus

Table 6 Logit equations

Mode choice	equations
Non-AC bus	$y_1 = 5.114 - .032x_1 - .083x_2 + 1.692x_3 + 1.337x_4 + 2.428x_5$ (5)
Local bus	$y_2 = -.061x_1 + .126x_2 + 4.075x_3 + 2.821x_5 + 4.485x_6$ (6)
Microbus	$y_3 = .12x_1 + 6.780x_3 - 4.970x_7$ (7)
Private car	$y_4 = .011x_1 - .256x_2 + 3.331x_3 - 4.699x_4$ (8)
Rent a car	$y_5 = -34.480 + .016x_1 + .454x_2$ (9)
Motorcycle	$y_6 = -.685x_2 - .4.291x_7$ (10)

Table 7 Classification of transport modes predicted

Observed	Predicted							
	AC bus	non-AC	local bus	microbus	private car	rent a car	motorcycle	Percent correct (%)
AC bus	191	7	2	0	0	0	3	94.1
non-AC bus	22	52	3	0	0	0	0	67.5
local bus	0	7	28	0	0	0	2	75.7
microbus	1	1	2	1	1	0	0	16.7
private car	2	0	0	1	42	1	1	89.4
rent a car	0	0	0	0	1	14	0	93.3
motorcycle	2	0	0	0	1	0	12	80.0
Overall Percentage (%)	54.5	16.8	8.8	0.5	11.3	3.8	4.5	85.0

than the proportional by chance accuracy criterion of 40%. So the overall prediction is satisfactory.

The study is conducted on Cumilla to Dhaka route which is only a portion of N1 highway. A research should be conducted in the entire N1 highway to understand the overall scenario. To increase the effectiveness of the model, more data with more variables (road characteristics, frequency of the trip) are recommended. Vehicle ownership factor can be added to find more accurate outcomes. In that case, nested logit model is suggested.

4   Conclusion

a.   In this study, with the help of a questionnaire survey, the mode that is used by the road users was identified and initial factors that might affect the mode choice preference of the road users on the N1 highway. AC bus was found to be the most preferable mood with 50.7% user because of safe travel (39%) and comfort (43%). Non-AC bus users chose mostly less fare and less time. Less fare also the most preferred reason among local bus users. Microbus, private car, and rent a car user mostly chose comfort and less time, and motorcycle user preferred less time for their current mode choice. Responders who chose to rent a car or private car generally travelled with their families. The motorcycle is mainly popular with the young generation.

b.   From this study, it is also found that the average time of the trip is 2-3 h. In some cases, trip length changed because of congestion. The average cost of the trip is between 250–350 BDT with an average waiting time of 15–30 min.

c.   Here, seven socio-economic and travel-related factors were considered from the primary survey. A multinomial logistic regression model was applied to the disaggregate set of primary preference data to find the factors that contributed significantly to the mode choice behavior of the road users in the N1 highway. Commuter's gender, income, travel cost, travel length, and waiting time were found to be the critical factors.

d.   As most of the responders are middle (18–40) aged (around 68.3%) and students (31.8%), the variation of age was less, so age and occupation were not significant here.

e.   As there were seven categories of mood, AC bus was considered as the reference category and constructed six logits to find the likelihood of choosing any mood with respect to AC bus. From the logits, the probability of choosing any mood for any individual case can be calculated.

f.   Here, the model is 85% classified, whereas it was supposed to predict only 40% from the initial field survey.

References

1. Hasan S (2007) Development of A Travel Demand Model for Dhaka City. M.Sc. Thesis, Department of Civil Engineering, Bangladesh University of Engineering and Technology, Dhaka
2. https://en.wikipedia.org/wiki/N1_(Bangladesh). Accessed 28 September 2020
3. A PPRC report (2014) "Road Safety in Bangladesh Ground Realities and Action Imperatives"
4. Enam A (2011) Methodological Issues in Developing Mode choice models for Dhaka city. M.Sc. Thesis, Department of Civil Engineering, Bangladesh University of Engineering and Technology, Dhaka
5. Hossain M (2004) Shaping up of urban transport system of a developing metropolis in absence of proper management setup: the case of Dhaka, Journal of Civil Engineering (IEB), 32(1)

6. Rahman M M , Ahsan M S , Hadiuzzaman M (2012) Comparative Accident Study on some selected National Highways of Bangladesh, International Journal of Civil Engineering (IJCE) ISSN 2278–9987 Vol. 1, Issue 2 Nov 2012 7–14 © IASET

7. Ortúzar JD, Willumsen LG (2001) Modelling transport, 3rd edn. John Wiley & Sons Ltd., New York

8. Train KE (2003) Discrete choice methods with simulation. Cambridge University Press

9. Olsson A L (2003), Factors that influence choice of travel mode in major urban areas: The attractiveness of Park & Ride, Division of Transportation and Logistics, Department of Infrastructure, Royal Institute of Technology, Sweden. ISBN 91–7323–048–0

10. El-Habil A M (2012) An application on multinomial logistics regression model. Pakistan J. statistics and operation research 8(2):271–291. 10.18187pjsor.v8i2.234

11. Chatterjee S, Hadi A (2006) Regression analysis by example. John Wiley & Sons Ltd., New York

12. Agresti A (2002) Categorical data analysis. Wiley

13. Kockelman K, Kweon Y (2002) Driver injury severity: an application of Ordered Probit model. Accid Anal Prev 34(3):313–321

14. Schafer JL (2006) Multinomial logistic regression models. STAT 544–Lecture 19

Development Progress of Railway Services in Bangladesh

H. M. Ahsan and M. M. Rahman

1 Introduction

Railway is one of the most common and important transportation systems in our country. It represented a major improvement in land transport technology and has introduced important changes in the movement of freight and passengers. Rail transport systems dramatically improved travel time as well as the possibility to offer reliable and consistent schedules. Railway is recognized as the most reliable, time-efficient, energy-efficient, comfortable, cheapest, environment-friendly and safest mode of transport in all over the world. A train needs 50–70% less energy to transport a given tonnage of freight or to transport a given number of passengers than by road [1].

Bangladesh Railway (BR) has a very vast history of 158 years starting as "Eastern Bengal Railway". After the liberation war in 1971, Pakistan Eastern Railway was renamed as "Bangladesh Railway" after emergence of Bangladesh as sovereign state and continued to function under a Railway Board. Although the first passenger train in the Indian subcontinent started running between Bombay and Thane on April 16, 1953, the first railway was launched in Bangladesh territory on November 15, 1962 with a distance of 53.11 km broad gauge line from Darshan to Jagati [2, 3]. Bangladesh Railway is divided into two zones—East zone and West zone, each under control of a general manager who is accountable to the director general of Bangladesh Railway with a 2955.53 km route length, 466 stations, 348 trains and 3143 bridges which connects 43 districts at the end of year 2017–2018 [4]. 90.05 million passengers were transported by Bangladesh Railway in 2017–2018 year, of which 41.70% were transported by intercity trains which were first introduced in Bangladesh in 1985 [4].

H. M. Ahsan (✉) · M. M. Rahman
Department of Civil Engineering, Bangladesh University of Engineering and Technology (BUET), Dhaka, Bangladesh
e-mail: hmahsan@ce.buet.ac.bd

2 Expansion of Railway in Bangladesh (Formerly East Bengal)

Railway expansion in East Bengal was mainly done by five companies. There were also some small railway lines which were established by different companies, but they were also operated by the above five railways in their respective areas. Brief details of five companies are below.

Eastern Bengal Railway (EBR): the idea of building a railway line in East Bengal was initially considered more political than business. The Eastern Bengal Railway Company was established in 1855 and had proposed the introduction of railway transport through East Bengal (now Bangladesh) and into Burma (now Myanmar). In 1857, the company contracted with the Indian government to build and maintain a railway line starting in Kolkata (formerly Calcutta), running to Kushtia (formerly Kooshtee) and then on to Dhaka (formerly Dacca) [5]. After the completion of the construction of the first line, the railway line started from Kolkata to Ranaghat (present-day West Bengal) on 29 September, 1862 and subsequently for the first time, the line was opened for passenger movement from Ranaghat to Jagati on the 15th of November 1862. The railway was extended to Kushtia station in East Bengal on 16 February, 1864 [2]. Thus, we entered into the present Bangladesh Railway through the establishment of a railway between Kolkata and Kushtia in the 1860s. Later, EBR played an important role in the expansion of railways in East Bengal by constructing railway lines at various places of Kushtia, Jessore, Rajshahi and Faridpur districts.

Northern Bengal State Railway (NBR): the Government of Bengal formally requested the Government of India to construct the Northern Bengal State Railway in the year 1872–1873 financial year. Considering the overall situation, the government of India approved the construction of the proposed NBR on November 29, 1873 [6]. The construction of the railway started from Shiliguri to Sara from that year. After the completion of other ancillary activities, including the installation of a rail line, "Lieutenant Governor Ashley Eden" inaugurated the first line of the Northern Bengal railway officially on the 18th of January, 1878, from the Jalpaiguri station to Sara [6]. The line branched off from parbatipur to kaunia on the east and from Parbatipur to dinajpur on the west [2]. In addition to the main line in the northern region, the NBR established many branch line from the main line. Thus, by establishing branch lines, NBR expanded the railway between Pabna, Bogra, Rangpur and Dinajpur districts. The NBR started a new chapter in the economic field of North Bengal by connecting rail lines with places in regional trade. Note that NBR contributes a lot to the export of tea from Jalpaiguri and Siliguri regions.

Bengal Central Railway (BCR): BCR was originally planned to connect Khulna with Kolkata and North Bengal by direct rail. Moreover, one of the reasons was the port of Mongla in Khulna. Between 1882 and 84, the construction of a 127-mile broad gauge line from Dumdum Junction in Kolkata to Khulna in East Bengal and from Ranaghat to Bhanga was completed [6].

Dhaka-Mymensingh State Railway: in 1881, the Government of India approved the Dhaka-Mymensingh State Railway which allows construction of Dhaka-Narayanganj, Dhaka-Mymensingh and Aricha-Dhaka lines under this line. At last, towards the end of 1882, work of the first phase of the Dhaka-Narayanganj line began. When the construction work was finally completed, the historic journey of Dhaka-Mymensingh State Railway started on January 4, 1855 with a 10.25 mile train journey from Narayanganj to Dhaka which has become a memorable chapter in the life of the people of East Bengal [6]. The construction of Dhaka-Mymensingh State Railway was completed between 1885 and 86 and was gradually opened for the transport of passengers and goods. As a result, the line was officially inaugurated by "Sir Augustus Rivers Thompson", the then Lieutenant Governor of the Province of Bengal, on 18 February 1886 [6]. Later, the railway line was extended from Mymensingh to Jamalpur. Then, the railway line was extended from Jamalpur to Jagannathganj Ghat on one side and Bahadurabad on the other side.

Assam Bengal Railway (ABR): the ABR Company was formed in 1892. It was railway built to connect the highlands of Assam with the port of Chittagong. For its construction, the line was divided into three sections: one from Chittagong to Badarpur with branches to Silchar and laksham; the other from Badarpur to Lumding; and the third, from Gauhati to Lumding and further to Makum. The first of these, the Chittagong-Cachhar section, was ready for traffic by 1898. The second, called the hill section, took nearly eleven years to be completed [7].

3 The War of Liberation and Bangladesh Railway

After realizing about the certain defeat during the liberation war in 1971, Pakistani army systematically carried out their plan of destruction and damage of Railway's plants, equipment, permanent way. After the end of liberation war, an assessment shows that the damages are very severe which includes (a) 300 bridges including the major ones namely, the Hardinge, the Bhairab, the old Brahmaputra and Tista bridges, (b) 71 miles of railway track (c) 348 stations, (d) 140 locomotives (of which 12 diesel locomotives irreparably damaged), 367 passenger carriages, 1484 freight wagons, (e) 10,300 units of service and residential buildings and so on [8].

But immediately after liberation of the country on 16th December, 1971, due to the guidance of the Father of the Nation, Prime Minister, Bangabandhu Sheikh Mujibur Rahman, the inspiring Minister for Communications, Mr. M. Mansoor and with the help of patriotic and hardworking railway men, damages were repaired within the shortest possible time. By 30th June, 1973, 296 out of 300 were repaired and made operational. Only one major bridge, i.e. the Bhairab Bridge remained to be recommissioned [8]. 65 miles of railway track have also been relaid. 74 locomotives, 282 passenger carriages, all the 1484 wagons, 5 tugs, 6 wagon ferry barges, 1 pontoon and 3 flats have been repaired and recommissioned for service [8].

4 Railway Length and Connectivity

Bangladesh Railway developed 2858.23 km railway route length in 1969–1970 and increased to 2955.53 km at the end of the year 2017–2018 as explained in Fig. 1. At present, there are three types of gauge available in Bangladesh, i.e. broad gauge (BG), metre gauge (MG) and dual gauge (DG) in two zones (East and West). Dual gauge was introduced in Bangladesh railway in the year 2002–2003 after the completion of the Jamuna Multi-purpose Bridge (Present—Banghabandhu Bridge). Narrow gauge line was also available in Bangladesh (East Pakistan) until 1969–1970 [9].

During the war of liberation in 1971, some lines of Bangladesh Railway were destroyed by Pakistani troops. Bangladesh Railway worked hard gradually to increase the railway route length after the liberation war. Railway network has expanded a lot over the years within the country (see Fig. 2).
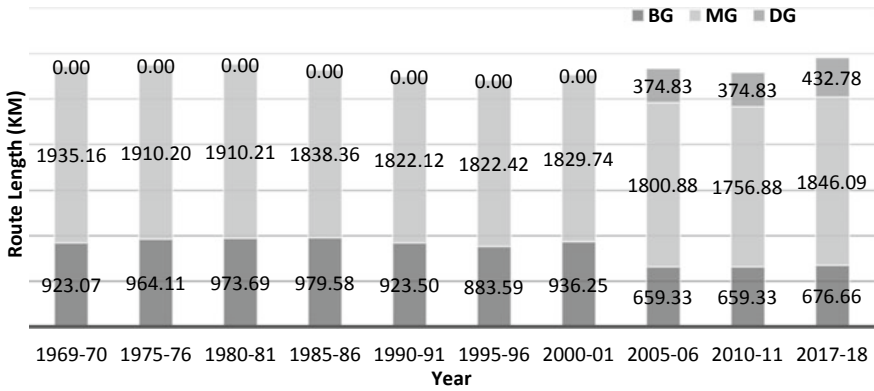
Fig. 1 Rail route length (km) year wise
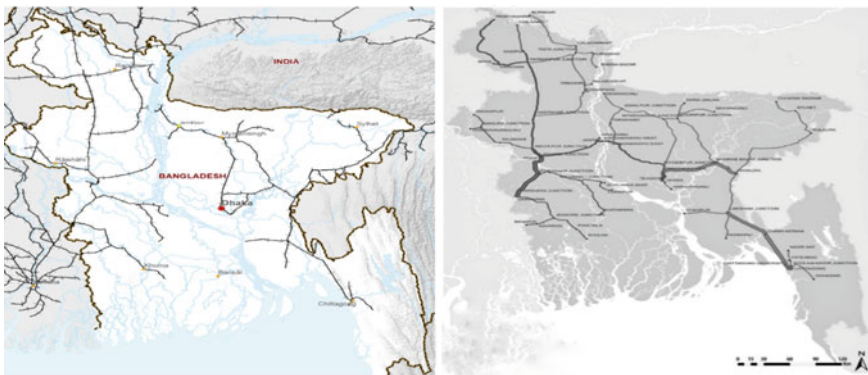
Fig. 2 Map of Bangladesh railway—past and present

West Zone involved works in Rangpur division, Rajshahi division, Khulna division on the other hand East Zone involved works in Dhaka division, Chittagong Division, Mymensingh Division and Sylhet Division. East Zone has 1299.04 kms of metre gauge and 34.89 kms of dual gauge track. There is no broad gauge track in east zone.

West Zone has 547.05 kms of metre gauge, 676.66 kms of broad gauge and 397.89 kms of dual gauge track [4].

At the end of 2018, only 43 civil districts out of 64 districts are connected by railway services as shown in Table 1. Although Bangladesh Railway has been connecting 43 districts since the war of liberation in 1971, Tangail district has come under the purview of Bangladesh Railway since the construction of the Jamuna Multi-purpose Bridge (Present—Banghabandhu Bridge) [9]. But in 2016, Bangladesh Railway cuts its connectivity with Bagerhat district. So, for some year, Bangladesh railway had connectivity with 44 districts.

Bangladesh Railway has taken the initiative of the unification of gauge in whole country. As Bangladesh signed the Trans-Asian Railway (TAR) agreement in 2007, it is now essential to convert its track gauge from existing metre gauge to broad gauge on specified international freight corridor to promote international movement of goods by rail. Apart from that, more efficient use of rolling stock, increased seamless reach of railway, more efficient passenger and freight real operation and more efficient rolling stock maintenance are the causes for the unification of railway track. According to the railway master plan, BR has planned to convert the entire network into broad gauge line by 2040 [10].

Connectivity with other country: historically, there are eight interchange points between Indian Railway (IR) and Bangladesh Railway. Four of these eight inter-change points are currently in operation. Darshana (BR)–Gede (IR), Benepole (BR)–Petrapole (IR), Rohanpur (BR)–Singabad (IR), Birol (BR)–Radhikapur (IR) are the four interchange of these 8 are currently in operation. But Shahbazpur (BR)–Mohishashan (IR) (closed since 07.07.2002), Chilahati (BR)–Holdibari (IR) (closed since 1965), Burimari (BR)–Chengrabandha (IR) (closed since 1971), Moghalhat (BR)–Gitaldah (IR) (closed since 1976) are the other four line which are currently inactive. Akhaura (BR)–Agartala (IR), Chilahati (BR)–Holdibari (IR), Burimari (BR)–Chengrabandha (IR), Dohazari (BR)–Cox's Bazar (BR)–Gundum (IR) are the new proposed railway link between these two countries [11].

There are also new proposed connectivity with Nepal and India through Rohanpur (BR)–Singabad (IR), Birol (BR)–Radhikapur (IR) (By conversion MG into DG) and with Bhutan and India through Chilahati (BR)–Holdibari (IR) (by constructing 7 km missing link in Bangladesh side and signing a new MOU) and Burimari (BR)–Chengrabandha (IR) (transshipment facilities at Burimari and signing a new MOU). Also, according to TAR deal, 3 TAR route will pass through Bangladesh and connect India and Mayanmar. BR also working to establish SAARC, BIMSET, SASEC, etc. regional railway corridors through Bangladesh [11].

Table 1 Railway route length (km) district wise

District	1987 (km)	2001 (km)	2010 (km)	2018 (km)	District	1987 (km)	2001 (km)	2010 (km)	2018 (km)
Bagerhat	21.32	21.32	40.53	–	Rangpur	70.41	70.71	69.40	68.33
Khulna	32.19	32.19	27.24	23.24	Gaibandha	88.55	98.97	80.50	85.65
Jessore	89.72	89.58	56.42	55.92	Bogra	84.89	84.89	84.00	85.75
Jhenaidaha	35.80	35.80	43.40	47.40	Jamalpur	121.91	99.00	102.90	109.55
Chuadanga	43.45	43.45	44.25	46.71	Netrokona	72.02	70.30	65.00	65.00
Faridpur	82.70	46.43	42.80	87.51	Kishorganj	57.13	78.75	73.75	73.75
Gopalgonj	12.99	12.99	32.13	79.23	Mymensingh	133.17	132.00	128.33	128.33
Rajbari	88.84	88.84	92.13	88.72	Tangail	– –	5.00	68.00	95.20
Khustia	92.94	78.00	58.35	57.89	Gazipur	64.78	64.15	73.80	91.00
Serajgonj	40.25	52.30	49.00	43.00	Dhaka	34.20	27.50	30.00	30.00
Pabna	48.25	48.25	61.00	89.08	Narayanganj	46.64	9.50	9.50	9.50
Chapainewabanj	48.48	48.48	69.00	66.15	Narsingdhi	12.86	46.58	38.97	38.97
Rajshahi	69.75	69.75	63.00	63.00	Sunamganj	15.29	13.90	13.90	13.90
Natore	61.16	61.16	37.00	37.00	Brahmanbaria	71.37	72.07	74.64	74.64
Naogaon	19.55	19.55	29.00	27.00	Habiganj	85.87	85.87	72.92	72.92
Jaypurhat	43.85	43.85	54.00	54.00	Moulvi Bazar	100.35	125.33	125.33	125.33
Thakrugaon	42.65	42.65	50.00	47.10	Sylhet	67.19	50.64	50.64	50.63
Panchagar	22.53	22.53	22.00	21.18	Noakhali	28.96	28.44	29.40	39.40
Nilphamari	59.55	59.55	65.68	61.79	Chandpur	41.44	40.69	40.66	40.66
Kurigram	42.65	42.65	51.00	42.56	Cumilla	109.03	109.36	106.40	106.40
Dinajpur	159.39	159.39	152.00	167.96	Feni	53.10	50.69	51.73	51.73
Lalmonirhat	110.97	110.97	110.00	114.00	Chittagong	163.75	174.32	178.45	178.45
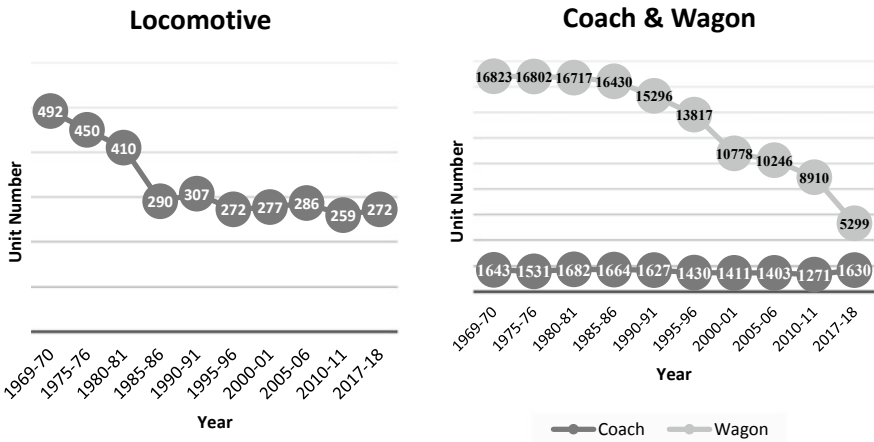
Fig. 3 Year wise locomotives, coaches and wagons

5 Rolling Stock

At present, Bangladesh Railway operates only diesel locomotive. But in past, before there were two kind of locomotives available in Bangladesh, i.e. diesel locomotive and steam locomotive. Currently, no steam locomotives are in service since 1883–1884 [9]. But BR has preserved some steam locomotive. The unit number of locomotive has decreased along the year as shown in Fig. 3. The unit number of wagon has decreased drastically over the years but coach remains almost same (see Fig. 3).

Again, a very high percentage of BR rolling stock is over industry standard economic life. They need frequent maintenance. Almost 33% BG and 35% MG locomotive, 29% BG and 50% MG coaches, 42% BG and 80% MG wagon are overage [10]. Considering all these, BR has taken the initiative to procure 474 locomotives, 5143 coaches and 6493 wagons in six phase within year 2045 [10]. BR also thinking about the construction of new locomotive workshop at Narayanganj as all the three available locomotive workshops (Dhaka, Parbatipur and Pahartali) have very low loco berthing capacity, poor support shop facilities, inadequate space to attend components and sub-assemblies [10].

6 Development Plans

Over the years, BR has worked on many development plans (7 Five-Year Plan, 2 Two-year Plan, 2 Three-Year Rolling Investment Program, Railway Master Plan, Updated Railway Master Plan) for different plan periods [4]. In the First Five-Year Plan (1973–1978) of Bangladesh, there are schemes for consolidation and improvement of the

Railway system and its operating efficiency. In addition to procurement of rolling stock, i.e. new locomotives, passenger carriages and wagons, there are schemes for establishment of an integrated training institute for all railway employees, setting up of a diesel back shop, one workshop complex for manufacture of rolling stock, construction of a bridge over the river Jamuna, Khulna-Mongla railway line with a bridge over the river Bhairab, introduction of modern telecommunication and radio wireless network for increasing operating efficiency, introduction of electric traction between Chittagong and Dhaka, modernization and expansion of workshops, remodelling of yards [8]. Then, first two-year plan (1978–1980) was aimed at completing the incomplete projects taken during the First Five-Year Plan. The main objectives of Second Five-Year Plan (1080–1085) were to achieve a reasonable level of efficiency for utilization of locomotives, wagons and coaches compared to their total numbers, average kilometrage of locomotive, coach and wagon per day and unit cost of operation [9]. Rehabilitation and modernization of the signalling and telecommunication system, improvement of existing repairs and maintenance facilities, training of officers and staff for maintenance, operation and traffic management, etc. were the objective of Third Five-Year Plan (1085–1090) [9]. Rehabilitation of track and bridges, procurement/repair/rehabilitation of Rolling Stock, inland container depot, improvement of the signalling and telecommunication system, etc. were the concern of Fourth Five-Year Plan (1089–1095). Second Two-Year Plan (1995–1997) was aimed at completing the incomplete projects taken during the Fourth Five-Year Plan. Fifth Five-Year Plan (1997–2002) proposes to raise the average growth rate to 7%, domestic savings to about 12% and investment to about 22% of GDP by establishment of a direct railway link between East and West zone through cross Jamuna rail connection, opening up avenues for private sector participation in BR activities, etc. [9]. Procurement of new carriages and locomotive for improvement of passenger services and wagon was the motive of Three-Year Rolling Investment Program. Construction of new railway, conversion of MG track into BG & DG track, rehabilitation of Dhaka-Narayaganj section, rehabilitation of 725 km of existing rail track, procure new locomotives and coaches, increase railway revenue & efficiency, etc. were the motive for Sixth Five-Year Plan (2011–2015) and Seventh Five-Year Plan (2016–2020) [9]. With the railway master plan, the plan is expected to guide the overall development of Bangladesh Railway in foreseeable future [9].

7 Underwhelming Growth of Railway

Though number of passenger and revenue per passenger in increasing day by day in rail transport as explained in Fig. 4, railway is losing its race with roadway both in freight and passenger transport. BR freight traffic has been declining since 1969–1970 as it carried 4.2 million tonnes freight in 1969–1910, but only 2.5 million tonnes freight in 2014–2015, thus the railway witnessed a negative growth rate of (-) 1.5% per annum in those 44 years [10]. This is due to the tough competition from road and water transport sector as they have higher revenue and also decreasing number
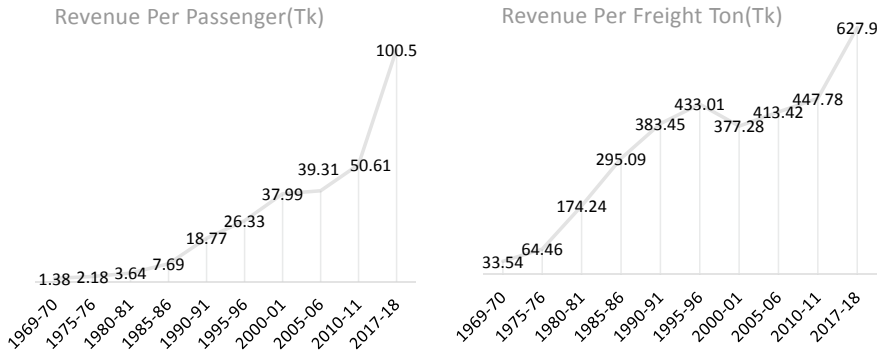
Fig. 4 Revenues per passenger (Tk) and per freight ton (Tk)

of wagon, more time-consuming journey, less investment from government, etc. in rail freight transportation.

In 1975, the long-distance passenger market was 17 billion passenger-km. Rail share was 30% or 5.1 billion passenger-km. By 2006, the rail market had grown more than ten times to 178 billion passenger-km of which rail share had fallen more than tenfold to 2.8%. This implies that since 1975, rail passenger market (passenger-km) has remained roughly static [10].

8 Development Project

Bangladesh Railway is trying to expand rail line all over the country. For wider spread of railway, Railway Master Plan and Updated Railway Master Plan has been approved by the government. The Railway Master Plan (July 2010–June 2030) was approved by the Government on 30 June, 2013 having total 235 projects at BDT 2,33,944 crores (US$30 billion) to be implemented over a period of 20 years spanning from FY 2010–2011 to FY 2029–2030 [4]. The 20 years Railway Master Plane was approved on 30.6.2013. The Master Plan includes 235 development projects in four phases [4]. The 30 years updated Railway Master Plan was approved on 29.01.2018. The Master Plan includes 230 development projects in 6 phases. The Revised Railway Master Plan (July 2016–June 2045) was approved by the government having total 230 projects at BDT 5,53,662 crores to be implemented over a period of 30 years spanning from FY 2016 to FY 2045 [4]. The railway system has been the beneficiary of extensive investment in fixed infrastructure accompanied by purchase of some rolling stock.

Conversion of the Akhaura-Laksam single-line MG section to double-line DG, construction of single-line dual-gauge railway track from Dohazari to Cox's Bazar via Ramu and Ramu to Gundum near Myanmar Border, construction work on the Dhaka –Narayanganj section to add a DG line to the existing single MG line, construction of the Ishurdi-Dhalarchar line, construction of Padma Bridge Rail Link Project (Dhaka-Mawa-Bhanga- Jessore), construction of double track standard gauge railway line from Dhaka to Chittagong via Comilla/Laksam (expressway), construction of double line (DG) railway track between Joydebpur-Iswardi (Ishurdi) sections, construction of Bangabandhu Railway Bridge (2nd) over the River Jamuna, construction of railway line from Khulna to Mongla Port with feasibility study, construction of dual gauge double rail line and conversion of existing rail line into DG between Akhaura and Laksam are the some recent remarkable projects to be implemented in recent years by BR [10].

9   Discussion and Way Forward

Railway as a transport system has a great future for a dense populated, developing country like Bangladesh as train produce only 11–27% of the CO_2 produced by car in per passenger-km [10]. Rail's share in the passenger market is restrained by train frequency, so it can be increased largely in future only if government allow fund on more rolling stock purchases. If the Revised Railway Master Plan (Fig. 5) can be improvised, then it is possible that Bangladesh Railway's freight traffic could increase to 18 million tonnes from a mere 2 million tonnes by 2045 [10]. Also, there is a possibility that Bangladesh Railway container traffic will range to 1.7 million TEU from 262,000 TEU under realistic scenario [10]. Railway link with Myanmar and North-Eastern states of India to Nepal may be implemented in recent future by Bangladesh Railway. In future, a much better rail connection from Dhaka and Eastern Bangladesh to Southwest Bangladesh will be established by the Padma Bridge Rail Link Project. So if the necessary measures are taken, railway has the potential to be the best transport system in the country which will save time, money and also life. Development of railway should be a high priority for Bangladesh government as it could connect the whole country into an integrated transport system.

Fig. 5 Bangladesh railway network by 2045

References

1. Railway Budget India, 2009–2010
2. "National Encyclopaedia of Bangladesh—Railways". http://en.banglapedia.org/index.php?title=Railway. Accessed on 21 August
3. https://en.wikipedia.org/wiki/Rail_transport_in_India#1832%E2%80%931852:_Industrial_railways. Accessed on 21 August 2020
4. Railway Information Book, 2018
5. Indian Railway History—British Law. https://www.irfca.org/docs/history/ir-uklaw-ebr.html. Accessed on 21 August 2020

6. পূর্ব বাংলার রেলওয়ে ইতিহাস 1862-1947, দিনাক সোহানী কবির

7. https://wiki.fibis.org/w/Assam-Bengal_Railway. Accessed on 22 August 2020

8. Railway Information Book, 1974

9. Railway Information Book, (1987, 1997, 2001, 2005, 2010)

10. https://drive.google.com/drive/u/0/folders/17fnhw7DGXYseXgupTFlVV_xg2wqHoO2p
    Final. Report on Updating Railway Project

11. https://www.unescap.org/sites/default/files/Bangladesh_17.pdf. Position Paper on Bangladesh
    Railway. Accessed on 25 August 2020

Effective Width of Sidewalks in Dhaka Metropolitan Area

H. M. Ahsan and M. R. Siddique

1 Introduction

Dhaka is the capital of Bangladesh which plays a great role in an era of regional and sub-regional cooperation. Walking is one of the most used traffic modes in Dhaka city because of the socio-economic conditions. In Dhaka city, about 37.2% trips are making on foot, but the pedestrians are facing many problems while using the sidewalks [1]. Sidewalks are used for avoiding the conflict between the pedestrians and motorized vehicles. Allocation of sidewalks ensures safety of pedestrians by separating the pedestrian movement and vehicular movement. Around 40% of footpath of Dhaka metropolitan city is occupied with street vendors, garbage bins or construction materials [2]. Most of the city sidewalks have problems in their designs and positioning. Different types of obstructions are found in these sidewalks. So, pedestrians are not able to use those parts of sidewalks which are occupied by these obstructions. That is why most of the sidewalks of Dhaka metropolitan area are not effectively used.

Around 43% of the people who die in road accidents are pedestrians, according to Accident Research Institute of BUET. A large number of people who die in accidents were walking on the roads instead of sidewalks. This is because the sidewalk is occupied by different obstruction types. Again, discontinuation of the sidewalk alignment provides inconvenience for the older walkers, and lack of separation of the sidewalks from the road-space offers threat to accident for the school going children, disabled persons. The number of road accidents would have lessened if the footpaths were made pedestrian-friendly.

H. M. Ahsan (✉) · M. R. Siddique
Department of Civil Engineering, Bangladesh University of Engineering and Technology (BUET), Dhaka, Bangladesh
e-mail: hmahsan@ce.buet.ac.bd

For this reason, knowing the *Pedestrian Level of service (PLOS)* is a key factor for the decision makers or the transport planners to understand the extent of problems that the pedestrians are facing in their daily life.

This study is an attempt for emphasizing the effective use of sidewalk width, obstruction types, occupied obstruction width in four areas of Dhaka North City Corporation and fourth areas of Dhaka South City Corporation as well as quantifying the PLOS of the sidewalks.

2   Study Area

The area of study is shown in the Dhaka metropolitan area map. It is selected as four areas of DSCC and four areas of DNCC according to commercial, residential and mixed land use pattern. In Fig. 1, the study area is shown:

3   Concept of Level of Service and Effective Sidewalk Width

3.1   Level of Service

Level of service is a qualitative value which describes operational context of a traffic stream. It is depended on service measures such as speed and travel time, freedom to move, traffic interventions, comfort, and convenience [3]. The level of service (LOS) concept is used to show the level of facility one can receive from a road under different operating features and traffic volume. Level of service ratings are from A to F commonly used to assess travel conditions and point out the problem areas. The criteria for pedestrian level of service (LOS) evaluation are mainly space among the pedestrians, flow rate, pedestrian walking speed, and volume to capacity ratio (V/C) [4, 5]. The pedestrian flow LOS criteria and their relevant evaluation standards are shown in Table 1.

The number of pedestrians per unit area of a sidewalk, which is expressed as pedestrians per square meter is called pedestrian density. Pedestrian space is the provided area for pedestrians in a moving pedestrian stream or queue, in square meters per pedestrian. Pedestrian walking speed is defined by the average walking speed of pedestrians, in meter per second. $Q_{ped} = V_{ped} * D_{ped}$, here Q_{ped} = flow rate (p/min/m), V_{ped} = pedestrian speed (m/min) and D_{ped} = pedestrian density (p/m^2).
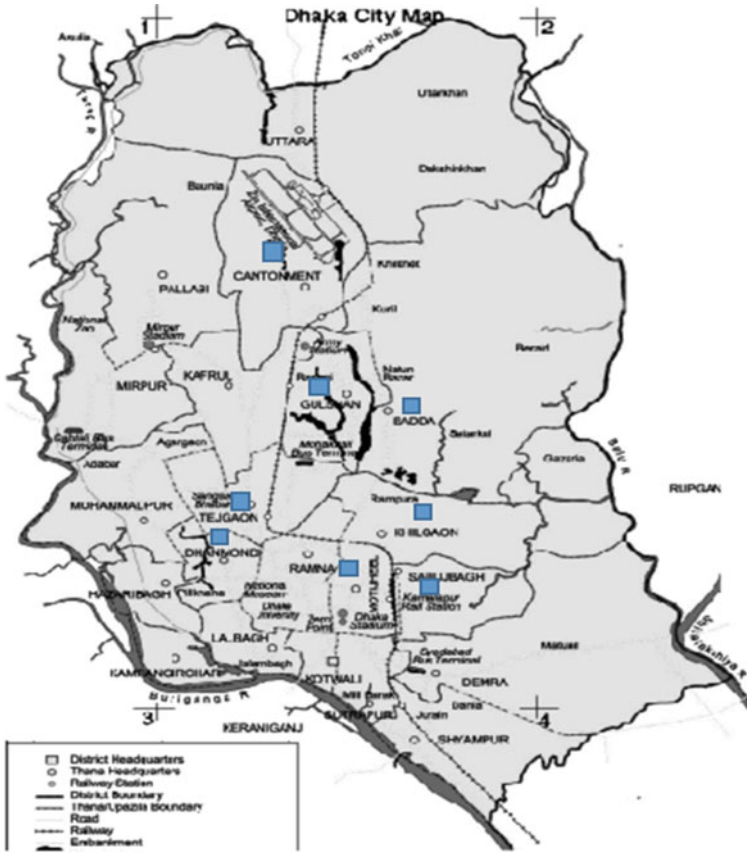
Fig. 1 Study area

Table 1 Average pedestrian flow LOS criteria for walkways and sidewalks

LOS	Ped.space (m2/p)	Flow rate (p/min/m)	Ped.speed (m/s)	V/C ratio
A	>5.6	≤16	>1.30	≤0.21
B	3.7–5.6	16–23	1.27–1.30	0.21–0.31
C	2.2–3.7	23–33	1.22–1.27	0.31–0.44
D	1.4–2.2	33–49	1.14–1.22	0.44–0.65
E	0.75–1.4	49–75	0.75–1.14	0.65–1.0
F	≤0.75	Variable	≤0.75	Variable
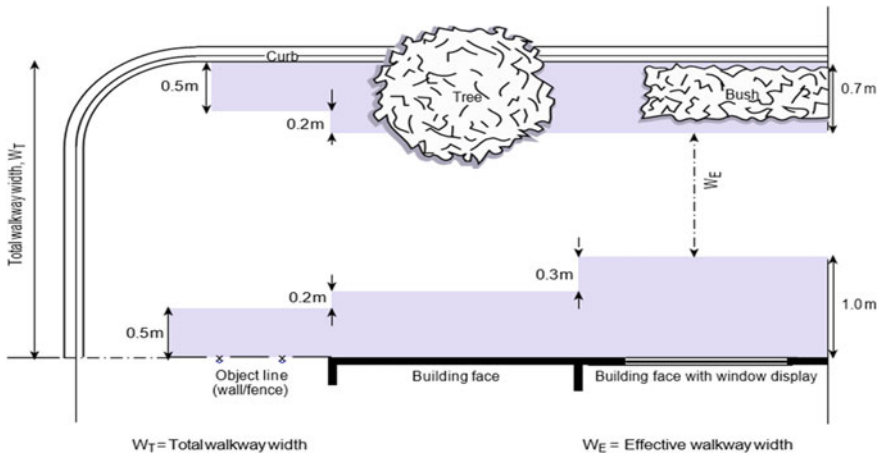
Fig. 2 Effective sidewalk width

3.2 Effective Sidewalk Width

Effective sidewalk width is the part of a sidewalk that can be used effectively by pedestrians. Effective sidewalk width is shown in Fig. 2.

4 Methodology

Sidewalk width, effective width and for pedestrian level of service pedestrian density and speed were measured in four areas of DNCC and four areas of DSCC. These places were of commercial, residential and mixed land use. Data was taken at peak hour for 1 h at each sidewalk.

Sidewalk was separated by five lines or four sub-sections of equal area. Arrival time and the departure time of 20 pedestrian were collected. An instant area (A) of sample pedestrian (w x l).Number of pedestrian in instant area of sample pedestrian on line (n) is (N). An instant density of sample pedestrian on line (n) is K. Both of arrival time and departure time were calculated for calculating the individual velocities v. The instant density of sample pedestrian on line (n) was calculated by N/A.

These steps were followed for calculating pedestrian density and pedestrian walking speed.

(a) Notice the arrival time (t_1) of a sample pedestrian
(b) At the sample pedestrian's foot on the line (n), count a number of pedestrian (N) in an instant area (A).

(c)   Dividing a number of pedestrian by an instant area (*A*) then give an instant density K.
(d)   Repeat the processes b and c until a sample pedestrian arrives on every line (1–5).
(e)   Mark the departure time of a sample pedestrian on line 5.
(f)   The walking time of a sample pedestrian in influential length is subtract of (t_1) from departure time (t_2).
(g)   A sample pedestrian walking velocity is then dividing the length by the walking time.

Then, the average pedestrian density and pedestrian walking speed were calculated for calculating LOS. At the same time sidewalk width, obstructed width were measured using measuring tape.

5   Result and Discussion

Level of service calculation according to Highway Capacity Manual of 8, sidewalks is shown in Table 2. It is found that according to Reference 5, 1 sidewalk offers level of service B, 5 sidewalks offer level of service C, and 2 sidewalks offer level of service D. The table also shows the presence of guardrails on those eight studied sidewalks. In case of LOS B, there is enough area for pedestrians to choose walking speeds according to their wish, to bypass other pedestrians, to avoid conflicts. In this level, pedestrians tend to be aware of other pedestrians, and to respond to their presence in time of selecting a walking way. One sidewalk (Gulshan) in the study area is found having this level of service. At LOS C, sidewalk is spacious enough for normal walking speeds and for bypassing other pedestrians in unidirectional streams. Five sidewalks (Tejgaon, Cantonment, Motijheel, Kamalapur, Dhanmondi) in the study area are found having this kind of sidewalks. At LOS D, pedestrians cannot select individual walking speed and cannot bypass other pedestrians. Crossing movements require frequent changes in speed and position. So they face conflicts very often. Two sidewalks (Badda,Khilaon) in the study area are having LOS D.

Total width of sidewalk depends on the land use pattern of the area. In the commercial area, the width is higher and in residential area the width is lower. The sidewalk width of eight sidewalks and presence of guardrails is shown in Table 3.

In the studied area, mainly eight types of obstructions were found blocking the walking space for pedestrians in the studies sidewalks. They are namely makeshift-shops, telephone box, electric polls, roadside restaurants, footbridge stair, parked vehicles, trees, and manhole cap. On average, 0.8 m of sidewalk is blocked by these obstructions. For this reason, the effective sidewalk width is reduced and on average 60% sidewalk width is effective. The occupied width of different obstruction type and effective sidewalk width percentage at eight sidewalks are shown in Fig. 3.

Average occupied width by different obstruction type is found by the measurement of eight sidewalks. The effective sidewalk percentage shows how much sidewalk

Table 2 LOS Calculation

Place	Selected area of sidewalk (WxL)	Pedestrian density At 5 Lines(p/ m²)	Avg ped den (p/ m²)	Space (m²/p)	Avg speed (m/s)	Flow rate (p/min/m)	Level of service
Link Road,Badda	2.15 * 10 = 21.5	0.23,0.42,0.55,0.70,0.80	0.54	1.85	1.17	37.90	D
North Avenue,Gulshan	1.95 * 10 = 19.5	0.15,0.20,0.26,0.30,0.30	0.24	4.13	1.43	20.77	B
Shahid Tajuddin Sarani,Tejgaon	2.25 * 10 = 22.5	0.27,0.31,0.36,0.44,0.49	0.37	2.70	1.22	27.11	C
Dhaka Cantonment	2.25 * 10 = 22.5	0.27,0.31,0.31,0.36,0.4	0.33	3.03	1.24	24.55	C
Motijheel Commercial Area	2.25 * 10 = 22.5	0.22,0.27,0.31,0.36,0.36	0.30	3.33	1.27	23.06	C
Kamalapur Station Road	2.4 * 10 = 24	0.25,0.29,0.33,0.38,0.38	0.33	3.03	1.24	24.55	C
Taltola Road, Khilgaon	2.15 * 10 = 21.5	0.23,0.55,0.70,0.74,0.80	0.60	1.67	1.16	41.67	D
9/A, Dhanmondi	2.25 * 10 = 22.5	0.27,0.22,0.31,0.36,0.36	0.30	3.33	1.28	23.10	C

Table 3 Total sidewalk width and presence of guardrails

Place	Total sidewalk width (in m)	Presence of guardrails
Link Road, Badda	2.15	No
North Avenue, Gulshan	1.95	No
Shahid Tajuddin Sarani, Tejgaon	2.25	No
Dhaka Cantonment	2.25	Yes
Motijheel Commercial Area	2.25	Yes
Kamalapur Station Road	2.4	Yes
Taltola Road, Khilgaon	2.15	No
9/A, Dhanmondi	2.25	No
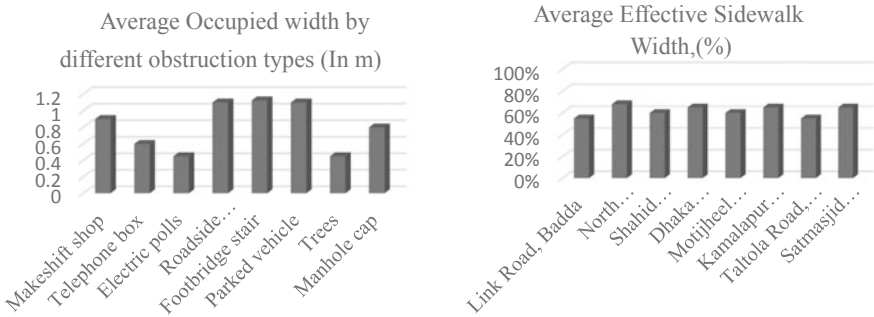
Fig. 3 Average occupied width by different obstruction types and average effective sidewalk width

width is effective in those eight sidewalks. Due to these obstructions, pedestrians tend to walk on the road and take risks which increased the number of accidents. Pedestrians are responsible for 49% of all reported casualties in the accident database. In urban areas of Bangladesh, pedestrians are the reason of 62% of road accident fatalities [6]. Among the accidents on average, 12% accident occur because pedestrians walk along the roadway as they are more willing to walk along the roadway than the sidewalk [7].

There are various reasons behind the ineffectiveness of footpath of the study area. Sometimes various types of street shops are on the sidewalk; they occupied almost half space of the footpath, for that pedestrian force to walk on the main road. There are some garbage also found on the footpath, pedestrians tend to avoid this part of sidewalk. So available walkable width for pedestrian is reduced. Sometimes construction materials, telephone box, footbridge stairs are also on footpath, for that pedestrian cannot walk smoothly here. Effective width available in four different

Fig. 4 Present situation of some sidewalks in Dhaka

locations (Motijheel, Kamalapur, Arambag, Khilgaon in clockwise order) is shown in Fig. 4.

6 Conclusion

In this paper, the authors tried to focus on the present condition of sidewalks in Dhaka Metropolitan Area. It is done by measuring pedestrian level of service. Sidewalk obstructions, occupied width and their effects are also shown in the paper. The study findings portrays that pedestrian traffic movement, and its other related topics are not yet being properly considered as a part of transportation policy and planning in the Dhaka City. Effective width of sidewalks should be according to area-wise demand preferably 2.5 m in case of larger roads and 2.25 m in case of smaller roads. The obstructions found on the sidewalks should be removed for future effective use. All these recommendations are given so that the pedestrian experience in Dhaka's public spaces can be improved. So the government and transportation policy makers should be more concerned about the provided sidewalk facilities and sidewalk conditions which will reduce accidents to a greater extent and ensure safety and comfort for pedestrians.

References

1. Preparatory Survey Report on Dhaka Urban Transport Network Development Study (DHUTS) in Bangladesh Final Report (Appendix Volume). JICA, March 2010. https://openjicareport.jica.go.jp/pdf/11996782_01.pdf
2. Transport Planning of Dhaka City: Some Contemporary Observations. https://www.academia.edu/5393835/Transport_Planning_of_Dhaka_City_Some_Contemporary_Observations
3. Transportation Research Board (2000). Highway capacity manual (Chapter 5–8). https://sjnavarro.files.wordpress.com/2008/08/highway_capacital_manual.pdf
4. Quality Level of Service Handbook. http://www.fltod.com/research/fdot/quality_level_of_service_handbook.pdf
5. Transportation Research Board (2000) Highway capacity manual. https://sjnavarro.files.wordpress.com/2008/08/highway_capacital_manual.pdf
6. Road Safety in Bangladesh: Key issues and counter measures. https://archive.thedailystar.net/forum/2012/July/road.htm
7. Pedestrian Accidents and Awareness: A study of Dhaka city Bangladesh. https://www.researchgate.net/publication/329427504_PEDESTRIAN%27S_ACCIDENTS_AND_AWARENESS_A_STUDY_OF_DHAKA_CITY_BANGLADESH

A Study on Riverbank Erosion-Accretion and Bar Dynamics of Dharla River Using Multi-temporal Satellite Images

S. T. Khan, S. Alam, N. Azam, M. Debnath, A. K. Mojlish, A. Rahman, F. M. Alvee, and M. Maliha

1 Introduction

Riverbank erosion is an alarming issue of high priority concern. It affects human livelihood adversely. Meandering rivers undergo erosion more than any other river type [1]. River channel migration is the recurring method for the proper assembly of a meandering river, which is the lateral movement of an alluvial river channel [2]. The geographic positioning of Bangladesh is the reason why most of the rivers in Bangladesh are alluvial rivers [3]. The rivers of Bangladesh keep altering sediment erosion and deposition to carry the sediments of the alluvial river as a part of the natural process [4]. These characteristics make the catchment of Bangladesh a sporadic example of devastating erosions. For erosion accretion analysis, temporal satellite remote sensing data of a river can be probed in GIS to determine the river banks' erosion accretion. Estimating bank line shifting, change in river widths, and the rivers' sinuosity using satellite images is a convenient procedure. Baki [5] studied river bank migration and island dynamics of braided Jamuna River using LANDSAT images. Takagi [6] analyzed the spatial and temporal changes in the channels of Brahmaputra.

Being a major transboundary river of Bangladesh, the Dharla River carries all the adverse effects of being a meandering river, among which, bank erosion is the most harmful of all. Dharla River has been dealing with excessive bank erosion for the last

S. T. Khan (✉) · S. Alam · N. Azam · M. Debnath · A. K. Mojlish · A. Rahman · F. M. Alvee · M. Maliha
Department of Water Resources Engineering, BUET, Dhaka, Bangladesh

A. Rahman
e-mail: afeefa@wre.buet.ac.bd

F. M. Alvee
e-mail: faisal_wre10@wre.buet.ac.bd

M. Maliha
e-mail: maliha@wre.buet.ac.bd

15 years, causing excessive damage to the lives and livelihood of the surrounding. Erosion by the Dharla River has raised havoc upon four villages in two upazillas of Lalmonirhat and Kurigram, washing away homesteads and croplands for a series of days. The water level at Kurigram attained a peak of 26.74 m PWD on 29th June, which was 24 cm above the danger level, then fell and again rose to 26.68 m (18 cm above the Danger Level) in the 3rd week of July in 2012 [7]. Aforementioned the histories, further analysis of riverbank erosion scrutinizing the river lines of the river for an elongated time will help understand the consistent occurrence of bank erosion leading to a conclusive solution. This analysis can be achieved by investigating the satellite images which is being attained by using Arc-GIS software since it is convenient to delineate and process the data using this software. The objective of this study includes the specific points: (i) measuring the bank line shifting, (ii) evaluating the short-term and long-term erosion and deposition using Arc-GIS, (iii) illustrating the deviation of the river width over time, (iv) showing the variation of sinuosity over time, (v) discerning the characteristics of bar dynamic of Dharla River.

2 Materials and Methods

2.1 Study Area

Dharla River has originated from the Himalayans as Jalakadh River and flows through the Jalpaiguri and Cooch Bihar districts of West Bengal, India. Here, river enters Bangladesh through the Lalmonirhat district and joins with the Jaldhaka River and flows as the Dharla River until it empties into the Brahmaputra River near the Kurigram district. Near Patgram upazilla, it again flows easterly back into India. It then moves south and enters Bangladesh again through Phulbari upazilla of Kurigram district and continues a slow meandering course. The average bed slope of the Dharla River is 0.00018 [8]. A reach length of 52 km of the river is the study area, as shown in Fig. 1.

2.2 Methodology

For the retrospective analysis, bank lines of the Dharla River were illustrated on Google Earth from the year 1989–2019. The riverbanks were delineated from the LANDSAT images of the dry period (from December to March) of corresponding years. Twenty-six cross-sections were drawn in the study area at a 1.5 km interval. The intersecting points of the cross-sections and riverbank lines were segregated, and coordinates of those points were calculated in ArcGIS to determine river bank shifting and river width variation. Calculation of the coordinates' shifting at every cross-section led to the conclusion of riverbank shifting, whereas scheming the distance
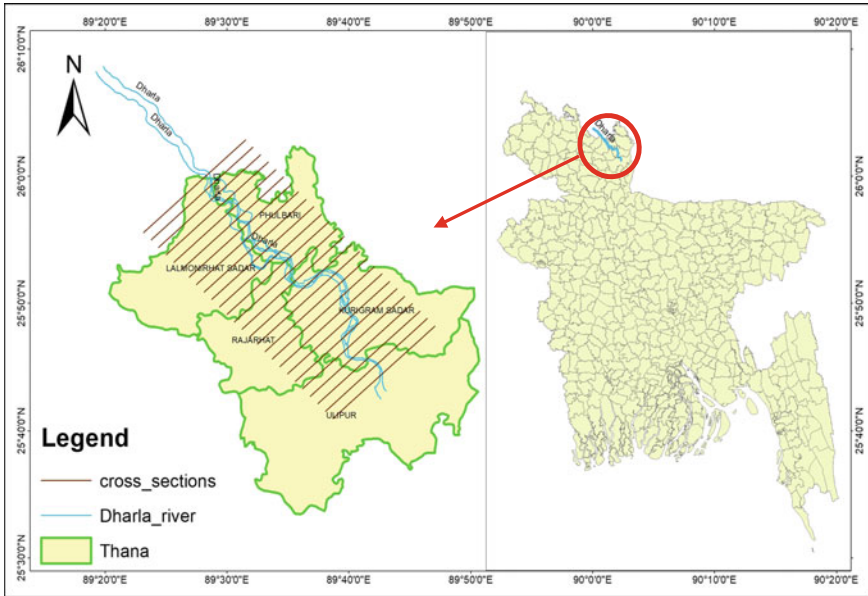
Fig. 1 Study Area Map

of the points from the left bank to the right bank on the same cross-section was the basic technique to govern the change in river width. Short-time erosion–deposition of the bank lines was established by simply superposing each bank line on the bank line of the succeeding year and determining the area of the interstice spaces wedged between the bank lines. By close observation of the course of development of these areas, appearances of these spaces (erosion or accretion) were chosen. However, for analyzing the bar dynamics, the bars of the river were outlined on Google Earth and projected in ArcGIS. Computing the areas on ArcGIS, bar dynamics were studied. The sinuosity index was calculated by taking continuous points along the river channel's entire length using the formula channel length/valley length measuring the individual distances using ArcGIS (Fig. 2).

3 Result and Discussions

The erosion and accretion observed in the satellite images were assessed using the Arc-GIS software which has been shown below through comprehensible representation.
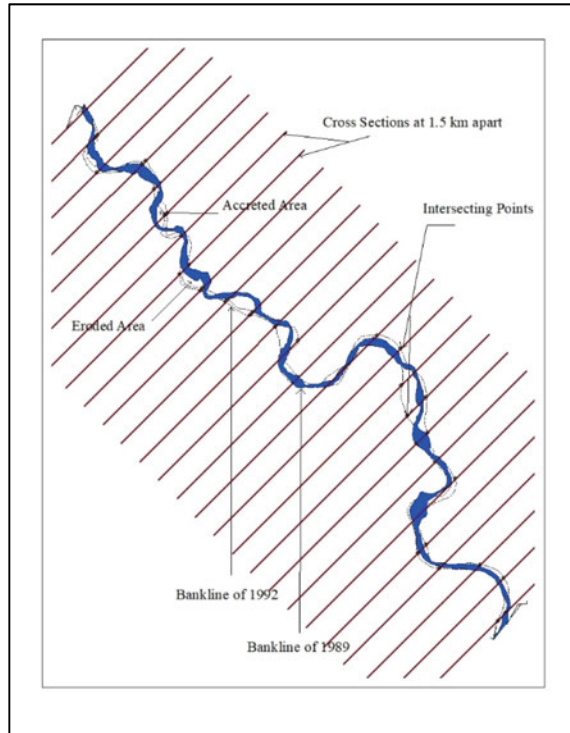
3.1 Bank Shifting of Dharla River and Short Term Changes of Bank Lines

Analysis of bank shifting of Dharla River has been done, showing the shifting of river banks every three years. Two bar charts have been developed showing erosion and accretion of both banks, which are included here. From the bar charts, it is manifested that highest erosion rate at the left bank is 86 m/yr which is 109 m/yr at the right bank. The minimum erosion rate at the left bank is 17 m/yr, and at the right bank, the value is 14 m/yr. The maximum accretion rate at the left bank is 90 m/yr, and the maximum accretion rate for the right bank is 92 m/yr which is the highest accretion rate of the two banks in all the years.

The minimum accretion rate of the left bank for the left bank is 16 m/yr and for the right bank, the value is 12 m/yr. Further, scrutinization of this bar chart demonstrates that the average erosion rate at the right bank (47 m/yr) is more than the average erosion rate at the left bank (44 m/yr) whereas accretion at the left bank (52 m/yr) is more than accretion rate at the right bank (41 m/yr). In Fig. 3, the trendline shows the linear movement of the erosion and accretion values, which represents the changing pattern over the years.
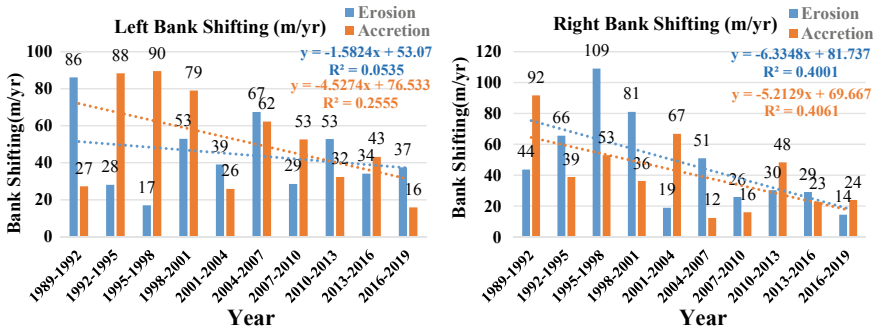
Fig. 3 Left and right bank line shifting of Dharla River from 1989 to 2019

For having a grasp on the bank movement over the years, bank shifting of 1989–1992, 1995–1998, 2016–2019 of both banks were calculated and plotted against X—sectional length and shown in Fig. 4. Erosion is shown downward and accretion is shown upward for both graphs. It is evident that the highest rate of erosion was found in the left bank within 1989–1992 (877.35 m/yr) and in the right bank within 1995–1998 (346.70 m/yr) whereas the highest rate of accretion was observed in the left bank within 1995–98 (322.36 m/yr) and in the right bank within 1989–92 (921.13 m/yr).

3.2 Long-Term Changes to River Banks

The long-term bank erosion and accretion rates of Dharla River for its left and right banks are calculated for 7, 14, 21 and 30 years gap. Maps were created by superimposing the rendered bank lines of the respective years which are comprised below in Fig. 5 with proper legends showing the eroded and accreted areas of each bank line. The eroded and accreted areas within these timelines have been represented in Table 1. From that table, the following information was collected. At the left bank highest erosion was found within 1989–2019 (19.71 km^2) and the highest accretion rate was found during the calculation of the bank shifting from 1989–2017 (18.82 km^2). At the right bank highest erosion was also found calculating the changes for 30 years (21.37 km^2), and the highest accretion rate was found at the same time interval (20 km^2).

3.3 Sinuosity of Dharla River

The sinuosity index of the Dharla River was calculated every 3 years and shown in the graph included. The value ranges from 1.24 to 1.51 proving the fact that it is a
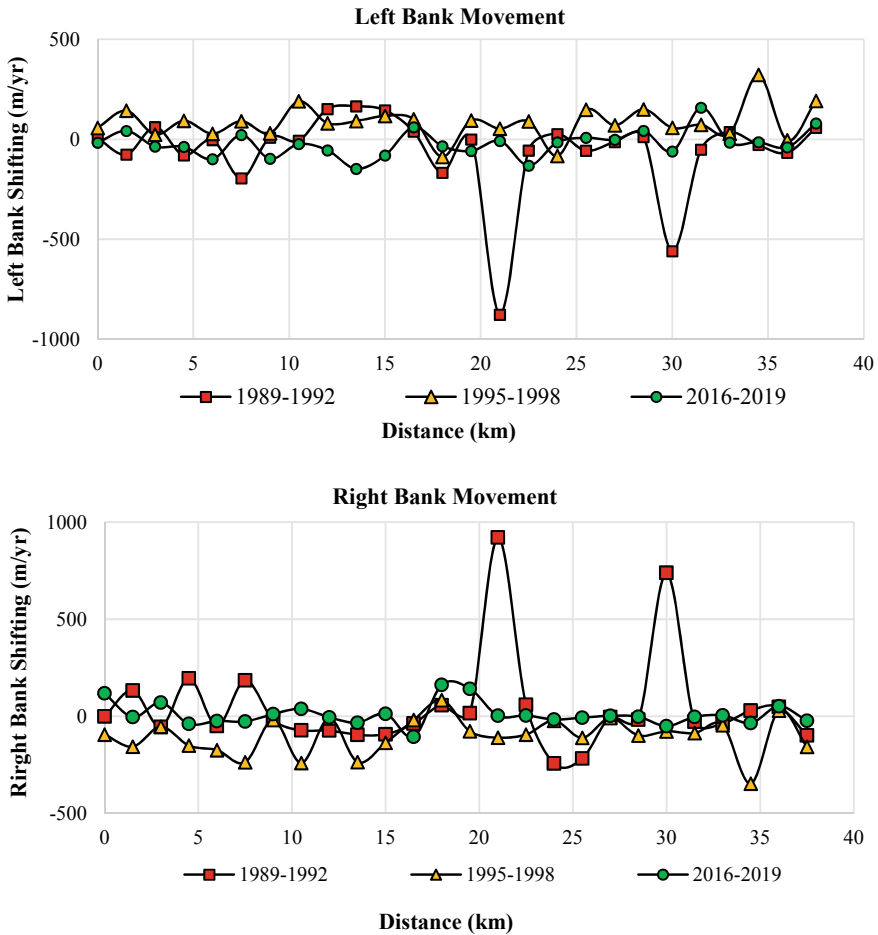
Fig. 4 Left and right bank movement vs. the X—sectional (1.5 km each) length of the river

meandering river. The highest value of sinuosity was 1.51 in 2013, and the lowest value was 1.24 in 1998 (Fig. 6).

3.4 Width Variation of Dharla River

Maximum width, minimum width, the average width of the Dharla River after every three years were calculated within the study duration. Maximum width was found to be highest in 2001 (2964.8 m). The minimum width was lowest in 2013 (47.34 m) and the highest average width was in 2007 (489.65 m) (Fig. 7).
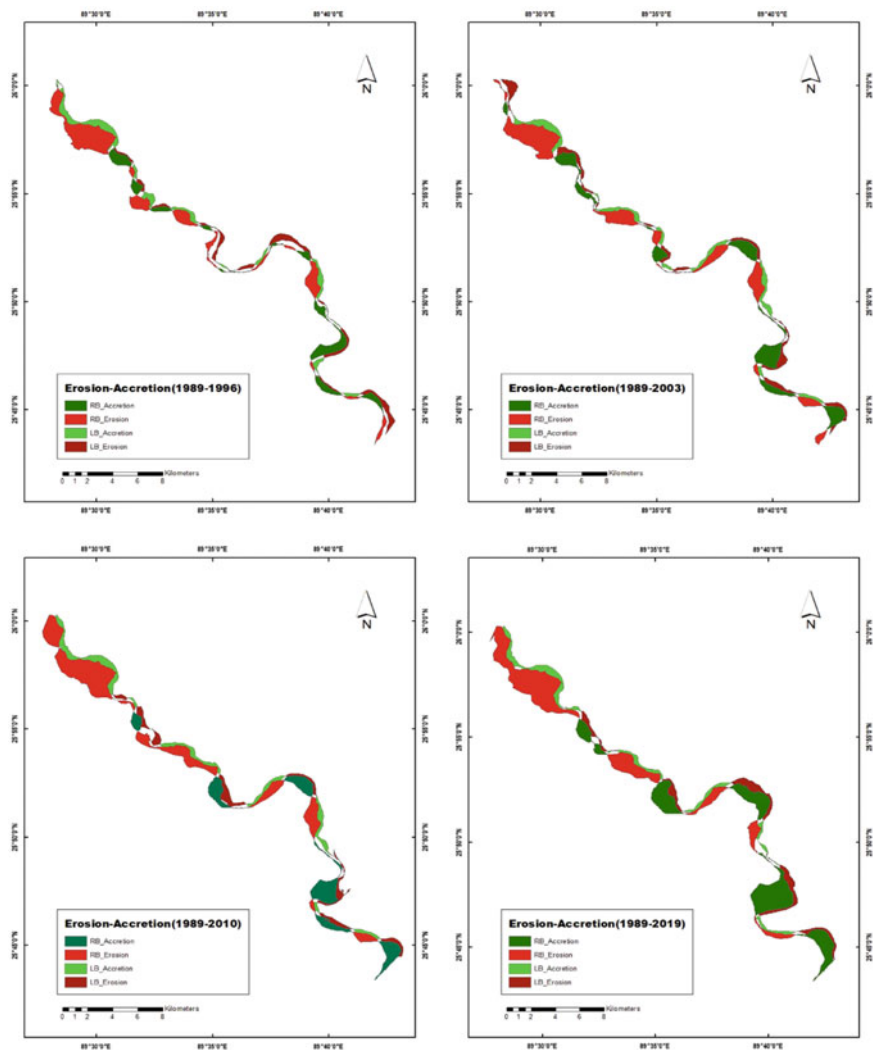
Fig. 5 Riverbank shifting along the Dharla River for long period ranges

Table 1 The long-term riverbank migration rates (erosion and accretion) of the banks of the Dharla River

Bank	Left bank		Right bank	
Year	Erosion (km^2)	Accretion (km^2)	Erosion (km^2)	Accretion (km^2)
1989–1995	8.32	15.71	14.72	8.08
1989–2003	12.29	15.86	16.15	11.83
1989–2017	11.5	18.82	20.65	11.60
1989–2019	19.71	16.51	21.37	20.00
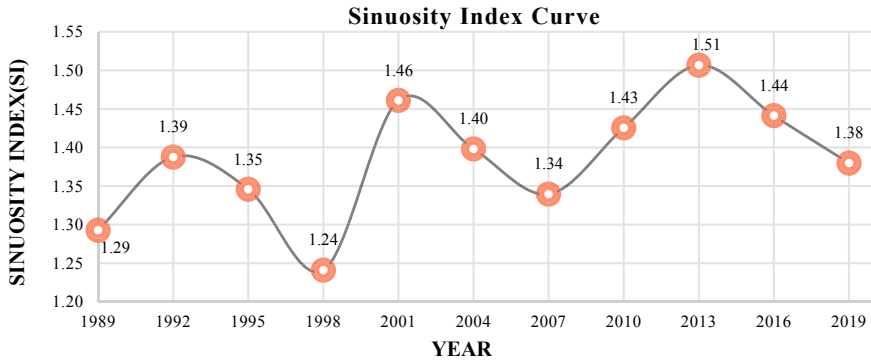
Fig. 6 Sinuosity index vs. years (using the frequency of 3 years)
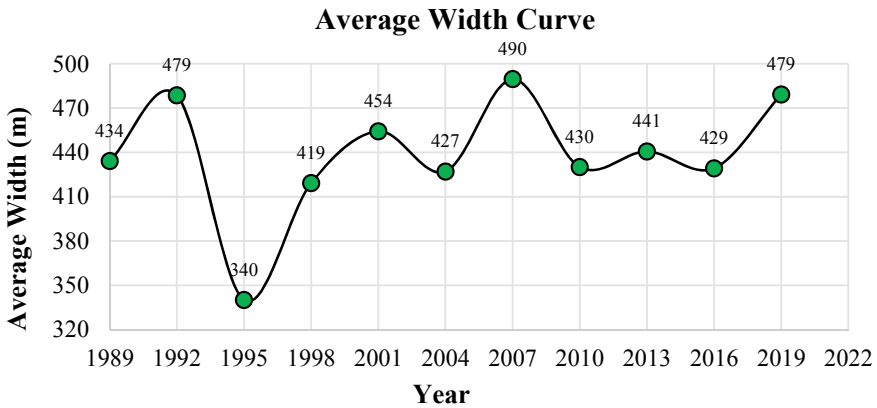
Fig. 7 Average width variation over the years (using the frequency of three years)

3.5 Bar Dynamics

The bar area was calculated and shown in the following table after every three years. This table represents the bar area changes after every three years. The bar area appears to be increasing over the years on average.

The maximum bar area was found in 2013 (731 ha) and the minimum bar area was found in 1989 (182 ha). The average bar area between 1989 and 1999 is 338 ha, 2000–2009 are 481 ha and 2010–2019 are 576 ha suggesting the increasing pattern. In Fig. 8, the trendline shows the linear movement of bar areas, which represents the increasing pattern of bar area over the years.

A map has been included showing the bar areas every six years and the transfer of those bar areas over time. The map below is implying that the bar relocation of the Dharla River is very dynamic (Fig. 9).
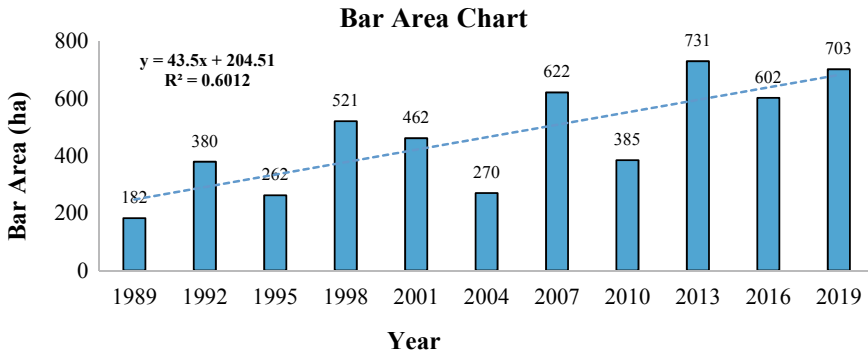
Fig. 8 Bar area calculation every three years

4 Conclusion

Analysis of 31 years of riverbank characteristics of the Dharla River leads to an understanding of the reason behind the previous history of excessive riverbank erosions. Riverbank shifting analysis as well as short-term erosion accretion analysis shows that the average erosion rate has come across higher in the right bank than the accretion rate, whereas the average accretion rate has been observed to be higher in the left bank, which authenticates the right bank line erosions of Kurigram, Lalmonirhat districts. A pattern was perceived while scrutinizing the erosion and accretion over the years. A higher rate of erosion taking place at one side of the bank triggers a higher accretion rate at the opposite side of the bank. This occurrence is the affirmation of the river being dynamic and meandering. This sequential change is also the reason for which variation of river width has not been of much significance. The absence of river width variation may also be the consequence of the analysis during the dry period. Sinuosity index analysis of the river seems to be increasing over the years. The bar area for both the three and six years interval have been calculated for the study area. From 1989 to 1995 a rise of 0.79 km^2, from 1995 to 2001 a rise of 2 km^2, from 2001 to 2007 a rise of 1.6 km^2, from 2007 to 2013 a rise of 1.09 km^2. But from 2013 to 2019, a fall of 0.28 km^2 was observed. First, 24 years had always an increasing rate except for the last six years leading to an average increasing pattern, which agrees with the arid nature of Dharla River banks during dry periods since the images used for analysis were captured during the dry period.
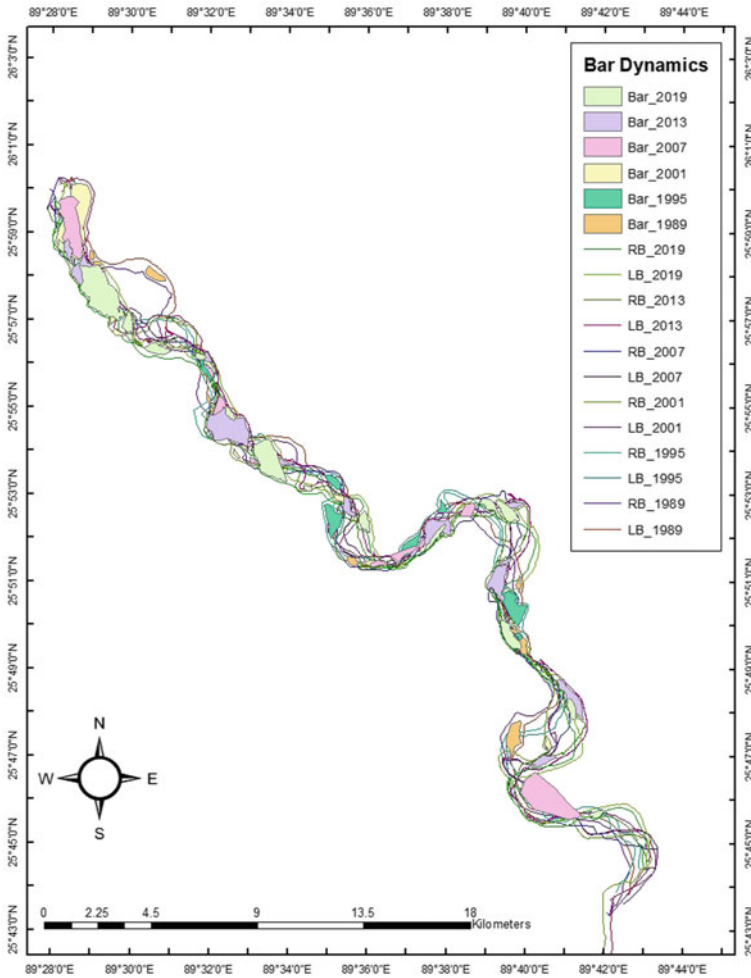
Fig. 9 Change of location of bars for every 6 years

References

1. Nagata T, Watanabe Y, Yasuda H, Ito A (2014) Development of a meandering channel caused by the planform shape of the river bank, pp. 255–270. https://doi.org/10.5194/esurf-2-255-2014
2. Camporeale C, Perona P, Porporato A, Ridolfi L (2005) On the long-term behavior of meandering rivers. Water Resour Res 41:1–13. https://doi.org/10.1029/2005WR004109
3. Kamruzzaman M, Beecham S, Zuppi GM (2012) A model for water sharing in the Ganges River Basin. Water Environ J 26:308–318. https://doi.org/10.1111/j.1747-6593.2011.00290.x
4. Best JL, Ashworth PJ, Sarker MH, Roden JE (2007) The Brahmaputra-Jamuna River. Bangladesh
5. Kumar Pal P, Rahman A, Yunus A (2017) Analysis on river Bank erosion-accretion and bar dynamics using multi-temporal satellite images. Am J Water Resour 5:132–141. https://doi.org/10.12691/ajwr-5-4-6

6. Azuma R, Sekiguchi H, Ono T (2007) Studies of high-resolution morphodynamics with special reference to river bank erosion, 199–209
7. Bose I (2019) Analysis of erosion and accretion of Dharla River (Bangladesh) using Multi-analysis on river bank Erosion-Accretion of Dharla River (Bangladesh) using Multi-Temporal Satellite Images
8. Rahman MM, Arya DS, Goel NK, Dhamy AP (2010) Design flow and stage computations in the Teesta River, Bangladesh, using frequency analysis and MIKE 11 modeling. J Hydrol Eng 16:176–186. https://doi.org/10.1061/(ASCE)HE.1943-5584.0000299

Estimation of Erosion–Accretion Using Remote Sensing Approach: A Case Analysis on Teknaf Coastline

F. I. Mou, N. T. Bhuiyan, F. M. Alvee, A. Rahman, and M. Maliha

1 Introduction

1.1 *Background of the Study*

The coastline is a boundary between land and ocean [1] that is subjected to the dynamic interaction between the ocean and the land [2]. Coastal erosion is the removal or displacement of soil, sediment, and rock fragments along a coastline by the movement of wind, water, and other transporting agents [3]. These eroded materials often settle on the surface by wave action [3]. This process is known as deposition and plays an important role in shaping the coastline by forming unique shoreline features [3]. Owing to be a low-lying delta and vulnerable to erosion, Bangladesh is highly exposed to the impacts of tropical cyclones, coastal floods, coastal erosion, salinity intrusion, climate change, and sea-level rise [4, 5].

Sarwar and Woodroffe [6] reported a systematic assessment of rates of shoreline change using the endpoint rate (EPR) method in the digital shoreline analysis system

F. I. Mou (✉)
Department of Environmental, Water Resources, and Coastal Engineering, Military Institute of Science and Technology, Dhaka, Bangladesh

N. T. Bhuiyan
Institute of Water and Flood Management, Dhaka, Bangladesh

F. M. Alvee · A. Rahman · M. Maliha
Department of Water Resources Engineering, Bangladesh University of Engineering and Technology, Dhaka, Bangladesh
e-mail: faisal_wre10@wre.buet.ac.bd

A. Rahman
e-mail: afeefa@wre.buet.ac.bd

M. Maliha
e-mail: maliha@wre.buet.ac.bd

(DSAS) extension in ArcGIS [6]. Their study revealed that even though accretion has occurred in some places along the Teknaf coastline due to abundant sediment supply, other places are experiencing rapid erosion [6]. A series of dynamic natural processes, including coastal erosion, sediment transport, longshore currents, tide, sea-level rise, and coastal geomorphology, is accountable for changes in the shoreline [7]. Hoque et al. [8] developed a coastal vulnerability index (CVI) of multi-hazardous events for the eastern coastal region of Bangladesh where eight parameters were considered [8]. In this study, various thematic layers were prepared for each parameter using spatial techniques, and all parameters were assigned a vulnerability ranking [8]. Khan et al. [9] conducted a study by the delineation of the changes in the coastal land areas of Chittagong in Bangladesh through the shifting of coastline [9]. The digital shoreline analysis (DSA) using ArcGIS 10.1, and image rectification, atmospheric correction, edge separation techniques between earth surface and water surface using ENVI software were used in this analysis [9]. Bangladesh has the longest natural sea beach in the world located between tertiary hills and the open sea, upholding the country's most important places for tourism, shipping and inland navigations, spectacular wildlife, wide biodiversity, fisheries, and mineral resources [10]. Monitoring coastline migration of Teknaf Upazila is an important task for environmental protection as this can help in the process of integrated planning and in addressing the complex management issues in the Teknaf coastal area to prevent future coastal problems and reduce poverty of this region, and also contributing to the overall economic development of Bangladesh.

1.2 Study Area

Teknaf is an Upazila of Cox's Bazar District in the *Chattogram* Division. Teknaf Peninsula is located at the southernmost point of Bangladesh mainland and is one of the world's most extended sandy beach ecosystems (80 km). Ahsan and Rashid [10] reported that "The Ganges, Brahmaputra, and Meghna River systems provide a minimal amount of sediments in the study area due to its position. Naf River, Moheskhali Channel, Raju khal, and other hilly torrents in this area are the main source of sediments" [10]. Due to its geographical position, Teknaf had always been vulnerable to several extreme climatological events, like cyclones, sea-level rise, and high waves during storm surges, leading to coastal erosion. A map of the study area, Teknaf Upazila, is shown in Fig. 1.
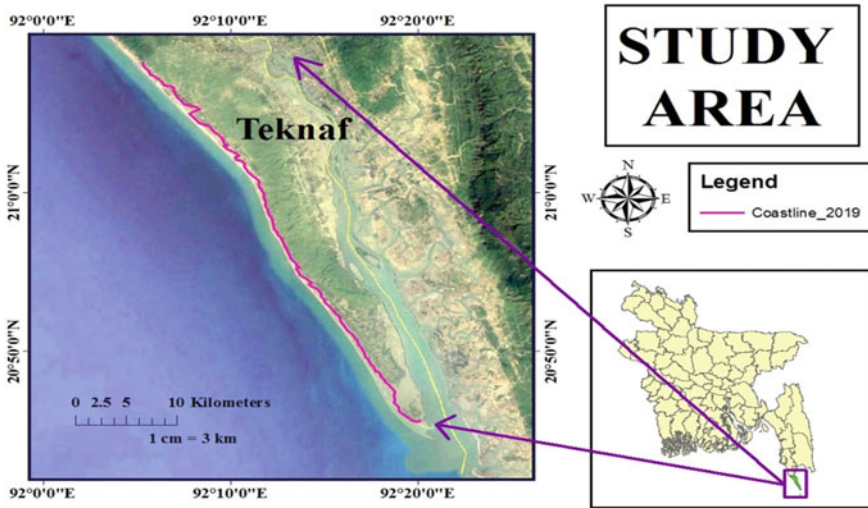
Fig. 1 Map of the study area, Teknaf Upazila

1.3   Objective of the Study

(a)   Coastline migration: Assessment of erosion–accretion rate over a 30-year historical time frame ranging from 1989 to 2019.
(b)   Long-term and short-term coastline migration: Assessment of erosion–accretion at an interval of 5 years for short-term analysis and at an interval of 30 years for long-term analysis.
(c)   Possible impact assessment of major cyclones (1991 Cyclone, SIDR, and AILA) on coastal erosion–accretion.

2   Methodology

2.1   Data Collection Source and Data Set

Multi-temporal Landsat images with a pixel resolution of 30 m were collected from United States Geological Survey (USGS) earth explorer over a 30-year historical time frame ranging from 1989 to 2019 to conduct a systematic assessment of shoreline shifting of the Teknaf coastline. Landsat 4–5 TM (Thematic Mapper) C1 (Collection 1) Level-1 images were acquired for years ranging from 1989 to 2001, and Landsat 7 ETM+ (Enhanced Thematic Mapper Plus) C1 (Collection 1) Level-1 images were acquired for years ranging from 2002 to 2019. The Landsat images were collected during the dry season (January to February) as images from dry season have minimum

cloud cover. Besides, ground conditions, like the water level and vegetation cover, are reasonably consistent during the dry season, which is essential for identifying the coastline and assessing erosion and accretion. In addition, the atmosphere is also comparatively calm and cloud-free during this period. The shapefile of Teknaf was obtained from the Bangladesh administrative level 2 (district) boundaries shapefile, which was downloaded from the website of Bangladesh-Subnational Administrative Boundaries.

2.2 Satellite Image Analysis and Coastline Migration Analysis

Remote sensing and Geographic Information System (GIS) techniques were applied over a 30-year historical time frame ranging from 1989 to 2019 to conduct a systematic assessment of the Teknaf coastline's shoreline shifting. The shapefile of Teknaf obtained from the website of Bangladesh-Subnational Administrative Boundaries was used as a reference for identifying the borderline of Teknaf Upazila. Shorelines were digitized carefully in the Geographic Coordinate System GCS_WGS_1984 from the Landsat images using ArcGIS. Afterward, all the features were transformed from the Geographic Coordinate System GCS_WGS_1984 into a Projected Coordinate System named BTM (Bangladesh Transverse Mercator). The eroded and accreted zones were identified and separated, and the shoreline shifting between two consecutive years was precisely determined by calculating the eroded and accreted areas. Finally, the calculated areas were used to assess shoreline shifting and the detailed analysis of the inter-year change of erosion and accretion. Statistical analysis was conducted using the eroded and accreted areas at an interval of 30 years (for long-term analysis) and at an interval of 5 years (for short-term analysis). From the coastline migration analysis conducted by the ArcGIS, statistical analysis for the impact of major cyclones (1991 Cyclone, SIDR, and AILA) was also conducted. For visualizing coastal erosion–accretion on the Teknaf coast between the years 1989 and 1994, coastline migration is shown in Fig. 2.

3   Results and Discussions

3.1 Erosion–Accretion Rate Analysis Over a Period of 30 years

Erosion–accretion rate over a 30-year historical time frame ranging from 1989 to 2019 has been calculated, and the graphical representation of coastline migration analysis for 30 years is shown in Fig. 3. The maximum erosion is found to be 5.654
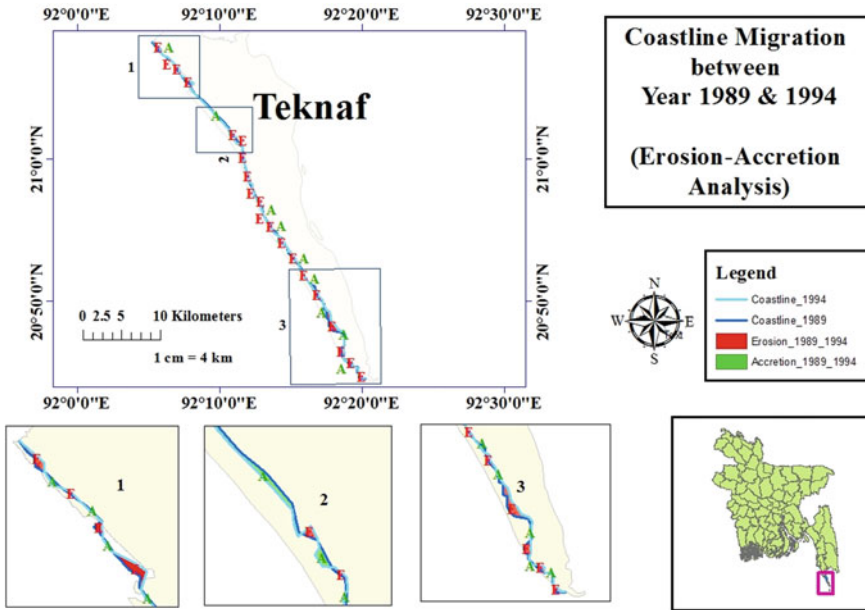
Fig. 2 Coastline migration between years 1989 and 1994 (Erosion–Accretion analysis)
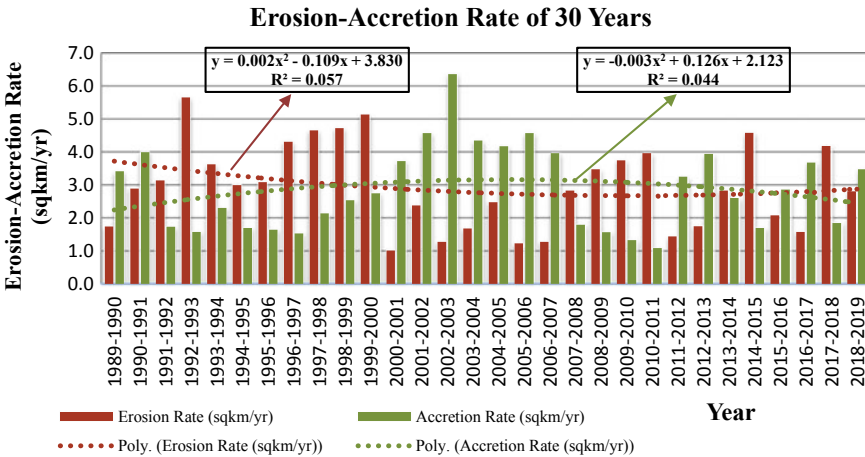
Fig. 3 Erosion–accretion rate (sq. km./year) of last three decades in the studied reach

sq. km./year, and the maximum accretion is found to be 6.366 sq. km./year between the years 1989 and 2019.
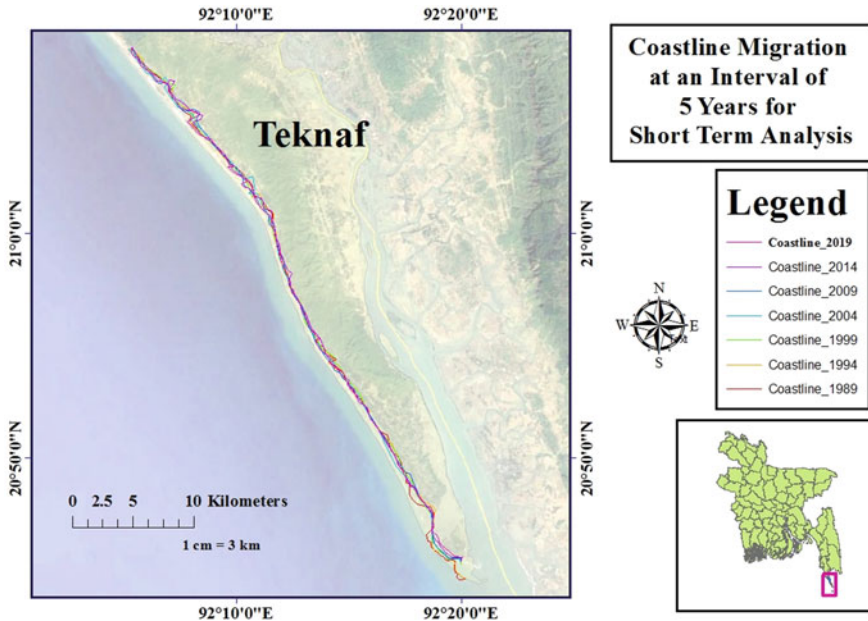
Fig. 4 Map of coastline migration at an interval of 5 years for short-term analysis

3.2 Short-Term Analysis

Short-term analysis has been conducted by analyzing erosion–accretion at an interval of 5 years. A map depicting the coastline migration at an interval of 5 years is shown in Figure 4. In this map, 7 coastlines were digitized at 5 years interval for further analysis.

Figure 5 is the graphical representation with the calculated result at an interval of 5 years. This analysis shows that erosion governed for 10 years between the years 1989 and 1999, and then accretion governed for 5 years (1999–2004) as during this period, tropical cyclones did not hit the Teknaf coastline. After 2004, erosion started to increase again and continued to govern for next 10 years (2004 to 2014). Again, after 2014, the accretion started to increase.

3.3 Long-Term Analysis

Long-term analysis has been conducted by analyzing erosion–accretion at an interval of 30 years. A map depicting the coastline migration at an interval of 30 years is shown in Fig. 6. In this map, 2 coastlines were digitized at 30 years interval for further analysis.

Erosion-Accretion at an Interval of 5 Years for Short Term Analysis

	1989-1994	1994-1999	1999-2004	2004-2009	2009-2014	2014-2019
Erosion (sqkm)	4.479	3.137	1.978	3.773	4.906	1.827
Accretion (sqkm)	1.707	2.451	5.363	2.304	1.955	4.781
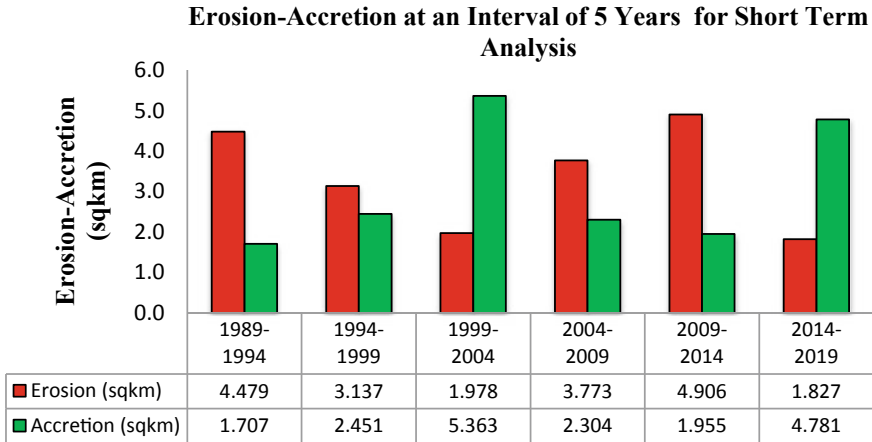
Fig. 5 Erosion–accretion (sq. km.) at an interval of 5 years for short-term analysis
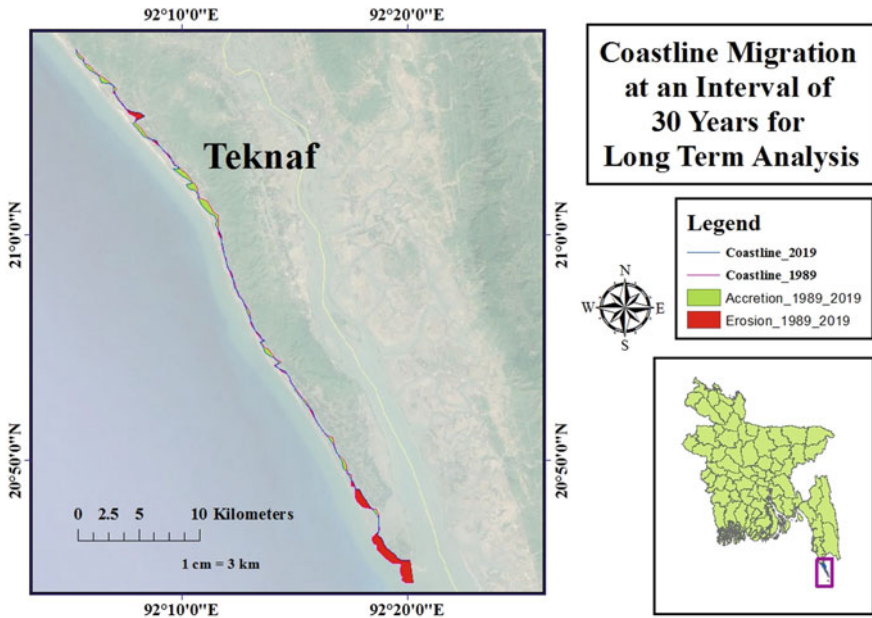
Fig. 6 Map of coastline migration at an interval of 30 years for long-term analysis

From Figure 6, it can be observed that a significant amount of erosion occurred in the southernmost part of Teknaf coastline. This may have occurred as there is not much vegetation in this particular region to reduce the devastating effect of cyclone, storm surge, tide, and coastal erosion.
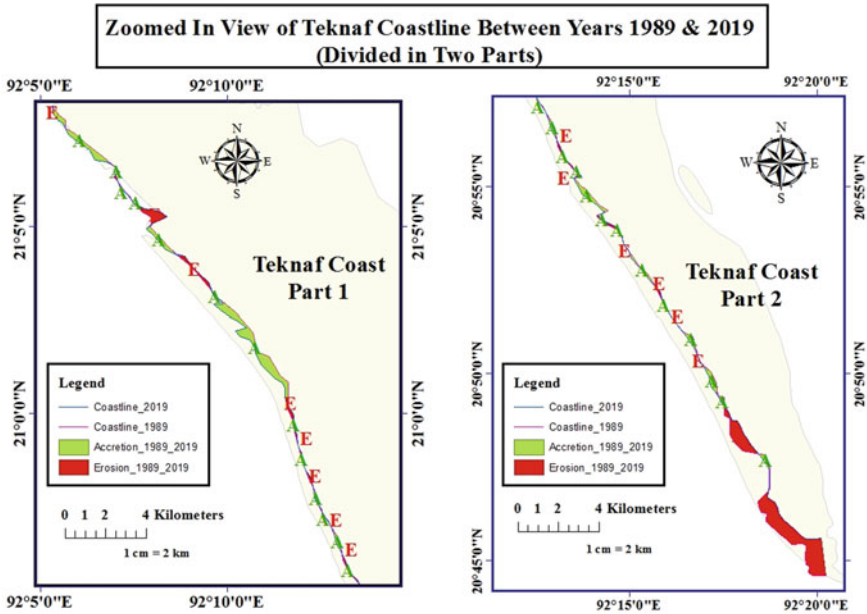
Fig. 7 Zoomed in view of Teknaf coastline between years 1989 and 2019 (divided into two parts)

Figure 7 portrays zoomed in view of Teknaf coastline between years 1989 and 2019 where the coast was divided into two parts for better visualization of eroded and accreted areas. In the upper part of Teknaf coastline (Part 1), the amount of erosion was less than the amount of accretion. However, in the lower part of this coastline (Part 2), the amount of eroded area exceeded the amount of accreted area.

Figure 8 is the graphical representation with the calculated result at an interval of 30 years. This representation depicts that the Teknaf coastline has been governed by
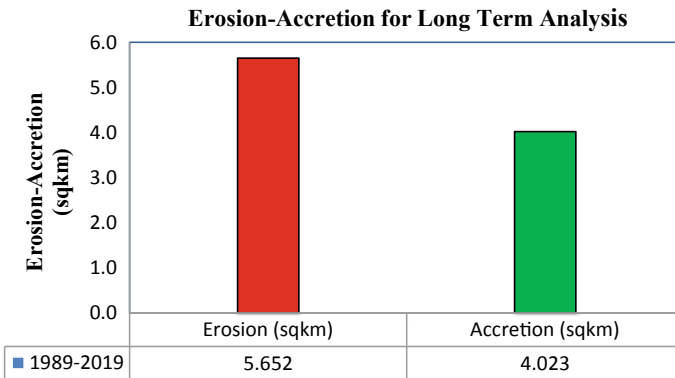
Fig. 8 Erosion–accretion (sq. km.) at an interval of 30 years for long-term analysis

erosion between the years 1989 and 2019. The results of long-term analysis show that the Teknaf coastline is suffering from the impact of coastal erosion and lost land as a result of recurring cyclones, storm surges, tide, and sea-level rise.

3.4 Impact of Major Cyclones (1991 Cyclone, SIDR, and AILA) on Coastal Erosion–Accretion

The before and after scenarios of the 1991 cyclone (April 1991), SIDR (November 2007), and AILA (May 2009) have been analyzed, and the graphical representations are shown in Figs. 9, 10, and 11, respectively. The analysis shows that generally, after every cyclone, the erosion rate becomes high on the Teknaf coast.
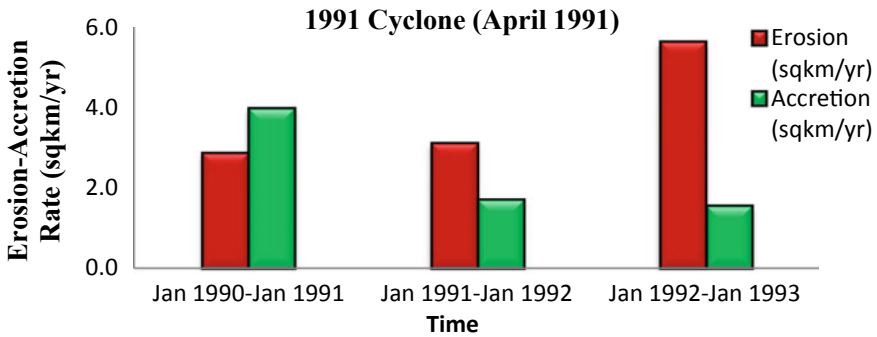
Fig. 9 Impact analysis of 1991 cyclone on coastal erosion–accretion rate (sq.km.)
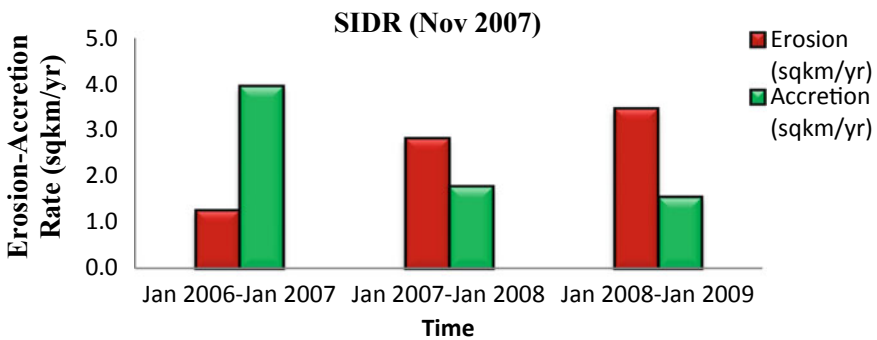
Fig. 10 Impact analysis of cyclone SIDR on coastal erosion–accretion rate (sq.km.)
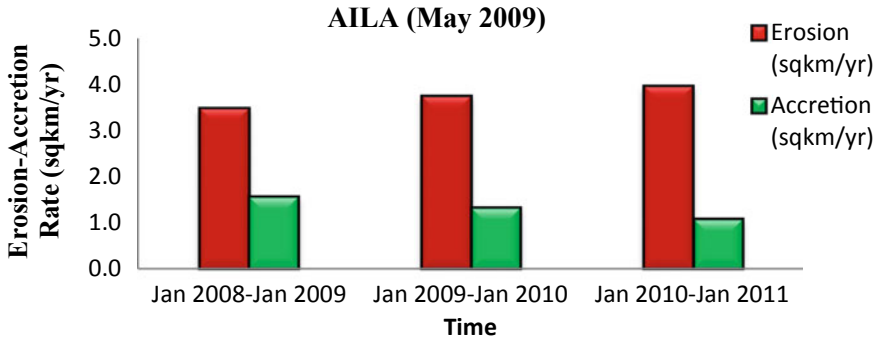
Fig. 11 Impact analysis of cyclone AILA on coastal erosion–accretion rate (sq.km.)

3.4.1 Cyclone

Figure 9 shows that after the 1991 Cyclone, the erosion rate has increased significantly as this was one of the deadliest tropical cyclones on record which struck the southeastern coast of Bangladesh in the Chattogram region on April 29 and caused severe damage to the people, property, and livestock of the coastal area.

3.4.2 SIDR

The cyclone SIDR struck the southwest coast of Bangladesh on 15 November 2007 and then moved inland and destroyed infrastructure and caused numerous deaths. Figure 10 shows that as the cyclone SIDR did not hit the Chattogram region directly, the erosion rate increased moderately on the Teknaf coast.

3.4.3 AILA

Tropical cyclone AILA struck the southwestern part of Bangladesh on 27 May 2009 and caused severe damage in the coastal region. Figure 11 shows that as the cyclone AILA did not directly hit the Chattogram region, the erosion rate increased moderately on the Teknaf coast.

Among these three major cyclones, the 1991 cyclone caused severe damage to the Teknaf coast as this coast was hit directly by the cyclone. Even, the erosion rate was recorded to be 5.654 sq. km. / year after this cyclone which is also highest in the historical period of 30 years between 1989 and 2019.

In this study, the shorelines were digitized manually using satellite images, and high-resolution Landsat images could not be used due to unavailability of data. Adopting automated shoreline extraction procedures and using Landsat images with

higher resolution can produce a better result as these can ensure more accurate delineation of the shorelines. Nevertheless, this study offers a clear idea about the coastline migration of Teknaf Upazila.

4   Conclusions

Using the multi-temporal satellite image analysis, this study has concluded that erosion governed in the historical period of 30 years between the years 1989 and 2019. Particularly, the southernmost part of Teknaf coastline suffered the highest amount of erosion. The erosion–accretion quantity of short-term analysis exhibited a periodic pattern. During the 30 years of the historical period (1989–2019), the first 10 years were governed by erosion, next 5 years were governed by accretion, later 10 years were by governed by erosion, and finally last 5 years were governed by accretion once again. The recurring cyclones, storm surges, tides, and sea-level rise have been contributing to the erosion process in the Teknaf coast. The analysis of the results also revealed that Teknaf coastline suffered more erosion when cyclones hit this coast directly compared to the times when cyclones did not hit Chattogram region directly. The 1991 cyclone (April 1991) hit the Teknaf coast directly and predominately caused erosion of this coastline. Besides, the maximum erosion rate (5.654 sq. km./year) was recorded in this coast after this devastating cyclone. During the time of no major recurring cyclones, the rate of accretion increased which became more prominent during the year 2002–2003 (6.366 sq. km./year). However, after 2004, owing to the persistent tropical cyclones hitting the coastline of Bangladesh, especially SIDR (Nov 2007) and AILA (May 2009), the rate of erosion increased. Nevertheless, the accretion rate has started to increase again after 2014. If steps are not taken immediately, coastline shifting may cause a major problem for the coastal zone people. Integrated Coastal Zone Management (ICZM) should be adopted to minimize shoreline shifting, protect and conserving coastal ecosystems, and provide the best long-term sustainable utilization of coastal natural resources, resulting in the overall economic development of the country. This study will play a vital role for the development of infrastructure and tourism in this area, for providing a survival strategy for millions living in the coastal area at the mercy of nature, for the formulation of an integrated plan to protect this coast from coastal erosion and also for the adoption of mitigation measures owing to the reduction of vulnerabilities caused by coastal hazards.

References

1. Merriam-Webster (n.d.) Coastline. Merriam-Webster.com dictionary. Retrieved September 27, 2020, from https://www.merriam-webster.com/dictionary/coastline
2. Nelson SA (2007) Coastal Zones. Tulane University, Department Earth & Environmental Sciences, Natural Disasters. Date Viewed September 27, 2020, from http://www.tulane.edu/~sanelson/geol204/coastalzones.htm
3. Pidwirny M (2006) Erosion and deposition. In Fundamentals of Physical Geography, 2nd edn. Date Viewed September 27, 2020, from http://www.physicalgeography.net/fundamentals/10w.html
4. Dasgupta S, Huq M, Khan ZH, Murshed A, Mukherjee N, Khan M, Pandey K (2014) Cyclones in a changing climate: the case of Bangladesh. Climate Develop 6. https://doi.org/10.1080/17565529.2013.868335
5. Mullick MRA, Tanim AH, Islam SMS (2019) Coastal vulnerability analysis of Bangladesh coast using fuzzy logic based geospatial techniques. Ocean Coast Manag 174:154–169. https://doi.org/10.1016/j.ocecoaman.2019.03.010
6. Sarwar G, Woodroffe C (2013) Rates of shoreline change along the coast of Bangladesh. J Coastal Conserv 17. https://doi.org/10.1007/s11852-013-0251-6
7. Prasad DH, Kumar ND (2013) Coastal erosion studies—A review. Int J Geosci 5. https://doi.org/10.4236/ijg.2014.53033
8. Hoque MAA, Ahmed N, Pradhan B, Roy S (2019) Assessment of coastal vulnerability to multi-hazardous events using geospatial techniques along the eastern coast of Bangladesh. Ocean Coast Manag. https://doi.org/10.1016/j.ocecoaman.2019.104898
9. Khan MS, Das J, Kabir MH (2019) Monitoring coastline changes in the coastal belt of chittagong in Bangladesh Using GIS and remote sensing. Asian J Geographical Res. https://doi.org/10.9734/ajgr/2019/v2i330087
10. Ahsan K, Rashid MB (2016). Coastal process in the Cox's Bazar-Teknaf area of the Eastern Coast of Bangladesh. In Book of abstracts (IX PIANC-COPEDEC-2016 Ninth International Conference on Coastal and Port Engineering in Developing Countries), Chapter: Coastal Zone and Coastal Risk Management, PIANC COPEDEC IX 2016. https://www.researchgate.net/publication/323943790

Estimation of Crop Water Requirement and Irrigation Scheduling of Rice in Southeastern Region of Bangladesh Using FAO-CROPWAT 8.0

R. A. Amin, M. B. Hossain, and A. Yunus

1 Introduction

With the rapid population growth, cereal food demand will also be increasing and providing freshwater for the world population has also become a major challenge. So water management and irrigation have to be optimized fully to gain maximum yield without water loss. Improvement in water use efficiency will also help in achieving the full benefit of other production inputs, like fertilizers, high-quality seeds, tillage, labor, energy, and machinery [1]. Water management can be done efficiently by CROPWAT [2]-aided irrigation scheduling which ensures the application of the desired amount of water at the right time to conserve water resources. For design and management of irrigation schemes, CROPWAT is a Food and Agricultural Organization (FAO) recommended model, designed by Smith [2] which assesses reference evapotranspiration (ET_o), crop evapotranspiration (ET_c) and irrigation water requirements by integrating climate, crop and soil data [3]. This model was developed by Land and Water Development Division of (FAO). Evaluation of irrigation practices of farmers and estimating the performance of crops under irrigated and non-irrigated conditions can also be done with this program in addition to irrigation scheduling [4]. Presently, the largest amount of water is consumed by agriculture and most of it is lost through evapotranspiration [5]. Rice is a staple food in the tropical region of the world. In Asia, more than 90% of the world's rice (*Oryza sativa L.*) is produced and consumed [6]. For a water-loving crop like rice, standing water is essential in

R. A. Amin (✉) · A. Yunus
Department of Water Resources Engineering, Bangladesh University of Engineering and Technology, Dhaka, Bangladesh

A. Yunus
e-mail: anikayunus@wre.buet.ac.bd

M. B. Hossain
Irrigation and Water Management Division, Bangladesh Rice Research Institute, Gazipur, Bangladesh

the initial stages for supple plant growth and yield maximization. Evapotranspiration loss in this process is very high, and the cost of over irrigation results in higher production prices. Standing water also creates a salinity problem causing the land to become unsuitable for cultivation. Proper scheduling can minimize water logging problems by reducing the drainage requirements and lower fertilization costs by holding surface runoff and deep percolation (leaching) to a minimum.

Constructing dam and reservoirs upstream of transboundary rivers have been causing a shortage of flow in the dry season in Bangladesh, resulting in freshwater scarcity and salinity intrusion in the southern region of Bangladesh. The construction and maintenance of irrigation canal system are not cost-effective. Percolation during the canal flow raises the groundwater level creating marshlands and salinity in the soil along canals. The productivity of the irrigated rice ecosystem is threatened by decreasing water availability since 50% of freshwater is used for rice production in Asia [7] and irrigated rice culture fulfills 75% of the global demand of rice [8]. Water use efficiency may be improved through genetic engineering and biotechnology. But being a complex trait, scientists are skeptical about it [9].

Bangladesh is a riverine country with an average rainfall of 2000 mm. But the temporal and spatial distribution of rainfall is highly uneven and resulting in a dry spell of 5–6 months. Boro season varieties are mainly cultivated during the dry season for its higher yield and better rice quality. Irrigation is mandatory in this season, and water management must be done to minimize the cost. Production of Aus and Aman season can also be increased through irrigation if scheduling is done effectively. Hence, in this paper, an attempt has been made to estimate the irrigation requirement and time of irrigation for rice in the southeastern region of Bangladesh for all three seasons using CROPWAT 8.0.

2   Materials and Methods

2.1   Site Selection

The study area was in the southeastern region of Bangladesh (23.96–23.01°N and 90.66–91.39°E, altitude 5–15 m above mean sea level). Four districts, namely Cumilla, Feni, Chandpur, Brahmanbaria, were selected for the study. The total area of the selected study area is almost 7705.81 sq. km, and the total irrigated area is 3619.253 sq. km [10]. Therefore, almost 46.92% of the total area is irrigated in dry (Boro) season. The study area mainly belongs to agroecological zone (AEZ)-19 (Old Meghna Estuarine Floodplain), AEZ-16 (Middle Meghna River floodplain), AEZ-17(Lower Meghna River floodplain), and AEZ-23 (Chittagong Coastal Plains) [10]. Among these zones, AEZ-19 covers most of the land area [10] and the soil type of study area is mostly silt loam [11].

2.2 Data Collection

The CROPWAT model simulates crop water requirement and scheduling under various types of climatic, crop, and soil conditions. It calculates ET_o by using minimum and maximum temperature (°C), relative humidity (in %), wind speed (km/h), and sunshine hours (hours). The monthly values of these parameters were collected from the Bangladesh Meteorological Department (BMD) from 1981 to 2010 timespan.

From these, the model calculated radiation ($MJ\,m^{-2}\,day^{-1}$) and used it to calculate ET_o for every 10 days (defined as "decade" by FAO) and then accumulated it to generate monthly data.

Climatic data were not available for the Brahmanbaria District. So, climatic data of the Cumilla District were also used for calculating radiation and reference evapotranspiration (ET_o) for the Brahmanbaria District.

Rainfall data of Cumilla, Chandpur and Feni districts were collected from Bangladesh Meteorological Department (BMD) and the same from Bangladesh Water Development Board (BWDB) for Brahmanbaria District.

Rice is cultivated in three seasons (Aus, Aman, and Boro) in Bangladesh. For this research work, all three seasons were considered. BRRI dhan48 (110 days duration), BRRI dhan71 (114 days duration), and BRRI dhan89 (158 days duration) were taken for Aus, T. Aman, and Boro varieties, respectively. 10th May, 30th July, and 10th January were taken as the transplanting date for the selected varieties, respectively. Rice growing period was divided as:

I. Nursery/land preparation (seedling stage 20 days in Aus, 25 days in T. Aman, and 40 days in Boro season).
II. Initial stage (transplanting to seedling establishment, usually 10 days in all season).
III. Crop development stage (tillering to panicle initiation, 20 days in Aus, 19 days in T. Aman, and 48 days in Boro season).
IV. Mid-stage (panicle initiation to 100% flowering, 30 days for all three varieties]).
V. Late stage (flowering to maturity, 30 days for all three varieties).

Maximum rooting depth and puddling depth were considered 40 cm and 15 cm, respectively. The default values were taken from the model for crop coefficient ($K_{c_{dry}}$ and $K_{c_{wet}}$), critical depletion fraction, yield response factor (Ky). 1.05 m, 1.08 m, and 1.06 m were taken as the crop height for the varieties, respectively [12].

Hossain [13] reported the moisture content of silt loam soil at field capacity and wilting point were 26.8% and 12.9%, respectively, whereas drainable porosity was approximately 18% [12]. The bulk density of silt loam soil was 1.5 g cm-3 [13]. The maximum infiltration rate of the soil was considered 40 mm day^{-1}.

2.3 Calculation of Reference Evapotranspiration (ETo)

CROPWAT model calculated reference evapotranspiration using the FAO Penman–Monteith method [14]. The Penman–Monteith equation can be written as

$$ET_o = \frac{0.408\Delta(R_n - G) + \gamma\frac{900}{T+273}u_2(e_s - e_a)}{\Delta + \gamma(1 + 0.34u_2)}$$

(1)

where ET_o = reference evapotranspiration [mm day^{-1}], R_n = net radiation at the crop surface [MJ m^{-2} day^{-1}], G = soil heat flux density [MJ m^{-2} day^{-1}], T = mean daily air temperature at 2 m height [°C], u_2 = wind speed at 2 m height [m s^{-1}], e_s = saturation vapor pressure [kPa], e_a = actual vapor pressure [kPa], $e_s - e_a$ = saturation vapor pressure deficit [kPa], Δ = slope vapor pressure curve [kPa °C], γ = psychrometric constant [kPa °C^{-1}], and 900 is a conversion factor.

2.4 Calculation of Effective Rainfall

CROPWAT model considers four methods for effective rainfall calculation. These are fixed percentage, FAO/AGLW formula, empirical formula, and USDA soil conservation service method. In this study, the USDA soil conservation service method [15] was used.

$$P_{eff(dec)} = P_{dec} * \frac{(125 - 0.6 * P_{dec})}{125} \text{ for } P_{dec} \leq \frac{250}{3} \text{ mm}$$

(2)

$$P_{eff(dec)} = \frac{125}{3} + (0.1 * P_{dec}) \text{for } P_{dec} > \frac{250}{3} \text{ mm}$$

(3)

where $P_{effective}$ = effective monthly rainfall (mm), P_{dec} = total decade rainfall (mm).

2.5 Estimation of irrigation water requirement and time of application

The amount of water that is supplied to meet the water requirement of the crop is called crop water requirement. It is determined by subtracting efficient rainfall from crop evapotranspiration (ET_c). ET_c denotes the amount of water that is lost through evapotranspiration and is found by multiplying crop coefficient (K_c) with reference evapotranspiration. Since default values were taken for K_c, the model estimated Kc dry value was 0.70, 1.05, and 0.7 in nursery, development, and late stages, respectively. Whereas K_c wet value was 1.20, 1.20, and 1.05 in the nursery,

development, and late stages, respectively. The crop water requirement was estimated by using [16].

$$\mathrm{CWR}_i = \sum_{t=0}^{T} \left(k_{c_i} \cdot \mathrm{ET_o} - P_{\mathrm{eff}} \right) \tag{4}$$

where Kc_i = crop coefficient of the given crop during the growth stage t and T is the final growth stage. The crop evapotranspiration $\mathrm{ET_c} = K_c \times \mathrm{ET_o}$ where K_c is crop coefficient and $\mathrm{ET_o}$ = reference crop evapotranspiration (mm day -1).

For irrigation scheduling, it was considered that irrigation will be done at 0 mm standing water depth and water will be refilled up to 50 mm water depth. Irrigation efficiency was considered 80%. Irrigation scheduling was done for all three seasons (Aus, T. Aman, and Boro) in all four districts in the study area.

3 Results and Discussions

3.1 Reference Evapotranspiration

Reference evapotranspiration ($\mathrm{ET_o}$) for three districts was estimated and shown in Fig. 1. The mean annual $\mathrm{ET_o}$ of rice crop was 1398 mm year^{-1} for four selected districts in the southeastern region of Bangladesh. For Chandpur and Feni, observed $\mathrm{ET_o}$ values were higher (more than average value of 118 mm and 114 mm, respectively) from March to June and lower from July to February. For Cumilla District, observed $\mathrm{ET_o}$ values were higher (more than average value of 116 mm) from March to September and lower from October to February. In all three districts, the highest (155–168 mm) $\mathrm{ET_o}$ was observed in May and the lowest (77–85 mm) in January. In March to May, low relative humidity and high temperatures resulted in increased
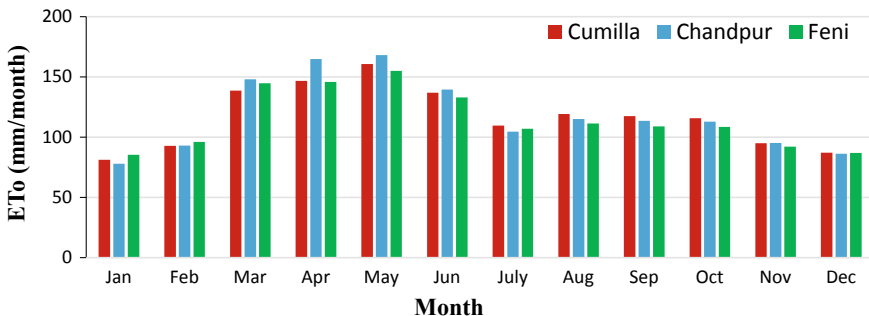
Fig. 1 Spatiotemporal distribution of monthly normal evapotranspiration in Cumilla, Chandpur, and Feni districts

ET_o. In March to May, low relative humidity and high temperatures resulted in increased ET_o. On the other hand, high humidity along with low temperature and sunshine hours reduced ET_o in the rainy season. Lower ET_o observed in the winter (November–February) was caused by lower values of temperature, sunshine, and wind speed.

3.2   Rainfall vs Crop Evapotranspiration

Rainfall, effective rainfall, evapotranspiration, and crop evapotranspiration requirement are shown in Fig. 2. Rainfall data analysis provides an approximate average of 2100 mm rainfall in Cumilla, Chandpur, Brahmanbaria districts with an average effective rainfall of 1085 mm $year^{-1}$. For the Feni District, the observed rainfall is approximately 3100 mm with an effective rainfall of 1203 mm $year^{-1}$. Maximum rainfall was observed in July, and almost 80% of the total rainfall occurs between April and September. From May to October, rainfall is almost enough to meet the evapotranspiration requirement. However, imbalanced spatial and temporal distribution may account for supplemental irrigation in some areas. For the other six months of the year, irrigation is necessary to avoid yield reduction.
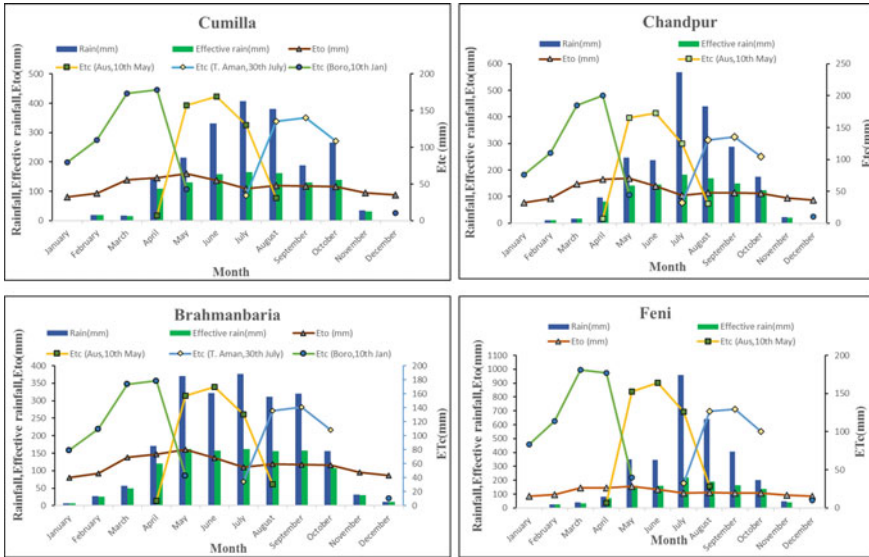
Fig. 2 District-wise distribution of average rainfall, effective rainfall, reference evapotranspiration over the months and rice crop evapotranspiration in three seasons (Aus, T. Aman & Boro)

3.3   Rice evapotranspiration and Irrigation requirement

Tables 1, 2, and 3 show the crop water requirements for all three seasons in four districts inside the study area. For all four districts of the study region, the CROPWAT model estimated crop water requirement and irrigation requirement during its growing period. BRRI dhan48, BRRI dhan71, and BRRI dhan89 were selected for Aus, Aman, and Boro season. For T.Aus rice transplanted on 10th May accounted crop evapotranspiration (ET_c) of a range of 478–500 mm. For seedling and initial stages, effective rainfall was enough to fulfill the water requirement. But for development and mid-stages, supplemental irrigation is necessary. In late stages, monsoon season rainfall was enough to satiate the water requirement as shown in Table 1. Transplanting date for Aman is assumed 30th July with a lifespan of 114 days. Almost no irrigation is required for this season and crops are considered rainfed in this season as shown in Table 2. But uneven spatial distribution may require a little irrigation to gain maximum yield. For Boro season, 10th January is taken as the transplanting date. Since it is dry season, heavy irrigation requirement is observed as shown in Table 3. Boro season rice yields the highest amount of rice, and so irrigation requirements must be met. The crop coefficient (K_c) values are shown for Cumilla District only.

3.4   Irrigation Scheduling

Irrigation scheduling for Cumilla and Chandpur districts for all three seasons is shown in Tables 4 and 5, respectively. In Cumilla District, 7 split applications of irrigation were required during T. Aus season with a gross irrigation of 503 mm. Though T. Aman is considered as rainfed crop, the model showed that it requires 340 mm water to avoid yield reduction. Boro season crop is highly irrigation-dependent, and 969 mm irrigation with 14 split application was necessary to fulfill the need. In Chandpur District, the gross irrigation in T. Aus and T. Aman season is 513 mm and 271 mm with 7 and 4 split applications, respectively. But in Boro season, 16 split applications of total 1109 mm water were required to avoid water stress as shown in Table 5.

Irrigation scheduling for Brahmanbaria and Feni districts for all three seasons is shown in Tables 6 and 7, respectively. In Brahmanbaria District, irrigation requirement remains more or less consistent with Cumilla and Chandpur districts with 505 mm (7 split applications) in T. Aus season. In Aman season, 268 mm (with 4 split applications) irrigation is required which is more or less consistent with Chandpur district. In Boro season, 980 mm irrigation (with 14 split applications) was necessary which is more or less consistent with Cumilla District. Feni District has higher rainfall than the rest of the study area. So lesser irrigation requirement was observed in the district with gross irrigation of 436 mm (6 split application) in T. Aus, 269 mm (4 split application) in Aman, and 1037 mm (15 split application) in Boro season.

Table 1 Normal crop water requirement for T. Aus rice at different locations of southeastern region

Stage	Duration	K_c	Cumilla			Chandpur			B. Baria			Feni		
			ΣEt_c (mm)	Eff. rainfall (mm)	IR (mm)	ΣEt_c (mm)	Eff. rainfall (mm)	IR (mm)	ΣEt_c (mm)	Eff. rainfall (mm)	IR (mm)	ΣEt_c (mm)	Eff. rainfall (mm)	IR (mm)
Seedling/land prep	0–20	1.2	6.6	29.9	0	7.2	25.1	0	6.6	52.6	0	6.5	18.6	0
Initial	21–30	1.12	37.1	38.7	0	38.2	39.4	0	37.1	52.1	0	34.8	50.8	0
Development	31–50	1.13 ± 0.02	120.2	92.2	28	126.9	102.8	24.1	120.3	110	10.3	117.6	109.4	8.2
Mid	51–80	1.25	169.6	158.1	11.5	172.8	144.8	28	169.6	157.1	12.5	163.8	159.2	4.6
Late	81–110	1.16 ± 0.09	161.3	202.2	0	155.1	217.6	0	161.3	199.5	0	154.6	258.9	0
Total			494.8	521.1	39.5	500.2	529.7	52.1	494.9	571.3	22.8	477.3	596.9	12.8

Table 2 Normal crop water requirement for T. Aman rice at different locations of southeastern region

Stage	Duration	K_c	Cumilla			Chandpur			B. Baria			Feni		
			ΣEt_c (mm)	Eff. rainfall (mm)	IR (mm)	ΣEt_c (mm)	Eff. rainfall (mm)	IR (mm)	ΣEt_c (mm)	Eff. rainfall (mm)	IR (mm)	ΣEt_c (mm)	Eff. rainfall (mm)	IR (mm)
Seedling/land prep	0–25	1.2	6.8	89.8	0	6.7	96.3	0	6.8	85.7	0	6.8	117.2	0
Initial	26–35	1.12	27.4	53.1	0	25.3	59.3	0	27.4	54.5	0	25.6	73.5	0
Development	36–54	1.12 ± 0.02	89	101.5	0	86.9	104.7	0	89	103.2	0	82.1	123.9	0
Mid	55–84	1.2	145.7	145.1	0.6	137.2	157.9	0	145.7	158.4	0	135.7	170.9	0
Late	84–114	1.125 ± 0.075	150	162.3	0	146.1	158.4	0	150	149.2	0.8	138.3	171.9	0
Total			418.9	551.8	0.6	402.2	576.6	0	418.9	551	0.8	388.5	657.4	0

Table 3 Normal crop water requirements for Boro rice at different locations of southeastern region

BORO

Stage	Duration	K_c	Cumilla			Chandpur			B. Baria			Feni		
			ΣEt_c (mm)	Eff. rainfall (mm)	IR (mm)	ΣEt_c (mm)	Eff. rainfall (mm)	IR (mm)	ΣEt_c (mm)	Eff. rainfall (mm)	IR (mm)	ΣEt_c (mm)	Eff. rainfall (mm)	IR (mm)
Seedling/land prep	0–40	1.2	10.3	0.3	10	10.4	0	10.4	10.3	10.4	0	10.4	0.3	10.1
Initial	41–50	1.12	17.9	0	17.9	17.3	0	17.3	17.9	2.3	15.6	18.5	0	18.5
Development	51–98	1.16 ± 0.06	171.2	20.8	150.4	168.7	11.8	156.9	171.2	30.2	141	178.8	27.8	151
Mid	59–128	1.26	173.6	16.2	157.4	185.1	16.9	168.2	173.6	50	123.6	180.9	34.5	146.4
Late	129–158	1.195 ± 0.055	221.5	135.9	85.6	244.7	108.7	136	221.5	156.2	65.3	217	104.9	112.1
Total			594.5	173.2	421.3	626.2	137.4	488.8	594.5	249.1	345.4	605.6	167.5	438.1

Table 4 Irrigation scheduling of rice (Cumilla District)

Date of Irrigation	Days to irrigate	Stage	Net irrigation (mm)	Gross irrigation (mm)
10th May transplanting (Aus)				
5 May	-4	Puddling	77	96
9 May	0	Puddling	53	66
22 May	13	Dev	54	68
31 May	22	Dev	55	69
12 June	34	Mid	54	68
22 June	44	Mid	54	68
2 July	54	Mid	51	64
Total			402	502
30 July transplanting (T. Aman)				
31 July	2	Init	54	68
2 September	35	Mid	55	69
12 September	45	Mid	56	70
22 September	55	Mid	50	63
16 October	79	End	54	68
Total			272	340
10 January transplanting (Boro)				
5 January	-4	Puddling	77	96
8 January	-1	Puddling	57	72
16 January	7	Init	51	64
24 January	15	Dev	50	62
1 February	23	Dev	51	64
10 February	32	Dev	54	68
17 February	39	Dev	50	63
25 February	47	Dev	55	69
4 March	54	Dev	50	63
11 March	61	Mid	58	73
18 March	68	Mid	54	67
24 March	74	Mid	54	67
30 March	80	Mid	54	68
11 April	92	End	54	67
Total			775	968

Table 5 Irrigation scheduling of rice (Chandpur District)

Date of Irrigation	Days to irrigate	Stage	Net irrigation (mm)	Gross Irrigation (mm)
10th May transplanting (Aus)				
5 May	-4	Puddling	77	96
9 May	0	Puddling	53	66
22 May	13	Dev	56	70
1 June	23	Dev	57	71
12 June	34	Mid	57	71
22 June	44	Mid	57	71
2 July	54	Mid	51	64
Total			410	513
30 July transplanting (T. Aman)				
31 July	2	Init	53	66
2 September	35	Mid	53	66
21 September	54	Mid	57	71
6 October	69	End	52	65
Total			217	271
10 January transplanting (Boro)				
5 January	-4	Puddling	77	96
8 January	-1	Puddling	57	71
16 January	7	Init	51	63
25 January	16	Dev	55	69
2 February	24	Dev	52	65
10 February	32	Dev	55	69
17 February	39	Dev	50	63
25 February	47	Dev	56	71
4 March	54	Dev	55	68
10 March	60	Mid	54	67
16 March	66	Mid	50	63
22 March	72	Mid	56	70
28 March	78	Mid	55	69
4 April	85	Mid	51	64
11 April	92	End	54	67
19 April	100	End	53	66
Total			887	1109

Table 6 Irrigation scheduling of rice (Brahmanbaria District)

Date of Irrigation	Days to irrigate	Stage	Net irrigation (mm)	Gross Irrigation (mm)
10th May transplanting (Aus)				
5 May	-4	Puddling	77	96
10 May	1	Init	55	69
22 May	13	Dev	54	68
1 June	23	Dev	54	68
12 June	34	Mid	54	68
22 June	44	Mid	54	68
2 July	54	Mid	51	64
Total			404	505
30 July transplanting (T.Aman)				
31 July	2	Init	54	68
2 September	35	Mid	55	69
12 September	45	Mid	50	63
16 October	79	End	53	67
Total			215	268
10 January transplanting (Boro)				
5 January	-4	Puddling	77	96
8 January	-1	Puddling	56	70
16 January	7	Init	51	64
25 January	16	Dev	55	69
2 February	24	Dev	51	64
10 February	32	Dev	53	66
18 February	40	Dev	50	63
26 February	48	Dev	54	67
5 March	55	Dev	56	71
11 March	61	Mid	50	63
19 March	69	Mid	54	67
29 March	79	Mid	57	71
6 April	87	Mid	57	72
12 April	93	End	56	70
Total			784	980

Since Boro season is the dry season (December–March) of Bangladesh, irrigation requirement for this season is maximum among all seasons.

Table 7 Irrigation scheduling of rice (Feni District)

Date of Irrigation	Days to irrigate	Stage	Net irrigation (mm)	Gross Irrigation (mm)
10th May transplanting (Aus)				
5 May	-4	Puddling	77	96
10 May	1	Init	54	68
22 May	13	Dev	53	67
1 June	23	Dev	55	68
12 June	34	Mid	54	68
22 June	44	Mid	53	66
Total			348	436
30 July transplanting (T. Aman)				
31 July	2	Init	53	67
2 September	35	Mid	53	66
22 September	55	Mid	53	66
11 October	74	End	54	67
Total			215	269
10 January transplanting (Boro)				
5 January	-4	Puddling	77	96
8 January	-1	Puddling	58	72
16 January	7	Init	52	65
24 January	15	Dev	51	64
1 February	23	Dev	53	66
11 February	33	Dev	56	71
19 February	41	Dev	57	71
26 February	48	Dev	50	63
4 March	54	Dev	52	65
10 March	60	Mid	55	69
17 March	67	Mid	54	67
24 March	74	Mid	50	63
31 March	81	Mid	51	63
10 April	91	End	52	65
18 April	99	End	56	71
Total			829	1037

4 Conclusion

The CROPWAT model estimates evapotranspiration, effective rainfall, and crop water requirement and does irrigation scheduling in the study with precision and assurance. Boro season rice requires maximum 1109 mm supplementary irrigation

in Chandpur and overall more irrigation than other seasons. T. Aman requires a minimum of 268 mm irrigation in Brahmanbaria which denotes that without irrigation yield reduction might occur. T. Aus requires 489 mm supplementary irrigation an average. These results can be used for further research in the study area. Proper scheduling of irrigation can alleviate yield stress in crop and increase yield to maximum. Lessening cultivation costs will help to ensure food safety for the rapidly growing population of Bangladesh.

References

1. Sharma B, Molden D, Cook S (2015) Water use efficiency in agriculture: measurement, current situation and trends. Manag water Fertil Sustain Agric Intensif 39–64
2. Smith M (1991) CROPWAT: Manual and guidelines. FAO UN, Rome
3. Karuppanan S (2018) Determination of Water Requirements of Main crops in the Tank Irrigation Command area using CROPWAT 8 . 0 Determination of Water Requirements of Main crops in the Tank Irrigation Command area using
4. Surendran U, Sushanth CM, Mammen G, Joseph EJ (2015) Modelling the Crop Water Requirement Using FAO-CROPWAT and Assessment of Water Resources for Sustainable Water Resource Management: A Case Study in Palakkad District of Humid Tropical Kerala, India. Aquat Procedia 4:1211–1219. https://doi.org/10.1016/j.aqpro.2015.02.154
5. Barrow CJ (2016) Water resources and agricultural development in the tropics. Routledge
6. International Rice Research Institute (IRRI): Annual Report 2012,International Rice Research Institute (IRRI) (2012). DAPO Box 7777, Metro Manila, Philippines
7. Guerra LC (1998) Producing more rice with less water from irrigated systems. IWMI
8. Dawe DC, Hardy B, Hettel GP (2002) Rice Almanac: source book for the most important economic activity on earth. Rice Alm source B Most important Econ Act earth. https://doi.org/10.1079/9780851996363.0000
9. Boutraa T (2010) Improvement of water use efficiency in irrigated agriculture: a review. J Agron 9:1–8
10. Bangladesh Bureau of Statistics (BBS) (2017) Yearbook of Agricultural Statistics. People's Republic Bangladesh, Stat Informatics Div Ministry of Planning, Govt, p 360
11. Bridges M (2014) Soil Texture. Encycl. Environ. Chang. 1028–1030
12. Bangladesh Rice Knowledge Bank (BRK), Bangladesh Rice Research Institute (BRRI), Gazipur
13. Hossain M, Yesmin S, Maniruzzaman M, Biswas J (2017) Irrigation Scheduling of Rice (*Oryza sativa* L.) Using CROPWAT Model in the Western Region of Bangladesh. Agric 15:19–27. https://doi.org/10.3329/agric.v15i1.33425
14. Allen RG, Pereira LS, Raes D, Smith M (1998) Crop evapotranspiration-Guidelines for computing crop water requirements-FAO Irrigation and drainage paper 56. Fao, Rome 300:D05109
15. Pongpinyopap S, Mungcharoen T (2012) Comparative Study of Green Water Footprint Estimation Methods for Thailand: A Case Study of Cassava-based Ethanol. Environ Nat Resour 10:66–72
16. Land, FAO (1997) Irrigation potential in Africa; A basin approach. 4

Application of Numerical Model Coupled with Field Sampling to Investigate Increased Salinity in a Coastal Aquifer at Aveiro, Portugal

M. S. Rahman and M. T. Condesso de Melo

1 Introduction

Groundwater being one of the prime sources of public water supply in Europe can complement surface water supplies and reduce the vulnerability of water supply systems to climate change [1]. Present groundwater configuration in deep coastal aquifers of Europe is mainly governed by sea-level fluctuations and tectonic movements over a geological timescale. These deep coastal aquifers are mainly composed of formations from Quaternary to Mesozoic age where fresh groundwater has been found at greater depths that are not consistent with present-day hydraulic gradients and recharge inputs [2, 3]. The Aveiro Cretaceous aquifer in the north-west of Portugal belongs to one of those coastal aquifers that hold groundwater between formations of Quaternary and Jurassic/ Triassic age. This multilayered confined aquifer has pristine water with residence times in excess of 18 ka [4–8].

Overexploitation of slowly renewed aquifers can have severe environmental and economic consequences [9]. Comparably, excessive groundwater abstraction from the Aveiro Cretaceous aquifer from the 1960s to 2000s resulted in rapid groundwater depletion below the sea level [5, 6, 8]. Despite the continuous groundwater depletion in the aquifer, limited signs of seawater intrusion or salt mobilization were observed in studies conducted till the early 2000s. In recent years, the local water supply company of the Aveiro region (ADRA) has observed high chloride concentration (300–750 mg/L) in some boreholes at the northern and central parts of the aquifer.

M. S. Rahman (✉) · M. T. C. de Melo
CERIS, Instituto Superior Técnico, Lisboa, Portugal
e-mail: srr@iwmbd.org

M. T. C. de Melo
e-mail: teresa.melo@tecnico.ulisboa.pt

Present Address:
M. S. Rahman
Institute of Water Modelling, Dhaka, Bangladesh

Climate change all over Europe may lead to limited rainfall, temperature extremes and severe water stress during the summer period [10]. This has made the Cretaceous aquifer one of the key strategic resources for the Aveiro region. To ensure sustainable supply from the aquifer in future, determining the origin of recently recorded high salinity was amongst the top priorities of ADRA, and thus, this investigation was initiated. The investigation was devised to develop a groundwater flow model of the aquifer to have an understanding of the flow regime; to assess the then (2018) extent of salinization; and identify the origin of the excessive salinity in the aquifer.

2 Study Area

The Aveiro Cretaceous aquifer is located in the north-west of Portugal (Fig. 1). Shallow Quaternary aquifer and Cretaceous aquifer form an integrated system which covers about 1800 km^2 area in lower Vouga sedimentary basin including mainland and adjacent continental shelf. The north and north-eastern boundary of the aquifer is defined by the geological contact between the Cretaceous formation and the Paleozoic–Proterozoic basement rocks. Tocha–Febres–Mogofores anticlinal structure forms the southern boundary while the south-eastern part is bounded by the Vouga and Certima rivers. Upper Cretaceous formations outcrop sporadically on the south-eastern part and act like a recharge area. There is existence of fault structures in the south-eastern part. The Atlantic Ocean forms the western boundary on the mainland; however, the extension of the Cretaceous formations is not known. A deep-see borehole drilled in the past at about 21 km from the coast indicates possible extension of the aquifer until the edge of the continental shelf [4–6, 8].

3 Materials and Methods

A multidisciplinary approach was followed for the study including field data collection and numerical modelling. A field campaign was conducted in 33 active boreholes. The distribution of the borehole locations reasonably covered the whole aquifer. Essential field parameters such as temperature (T), pH, electrical conductivity (EC), dissolved oxygen (DO) and oxidation–reduction potential (ORP) were measured. A three-dimensional steady-state groundwater flow model was developed and calibrated for the predevelopment condition of 1980. The calibrated model was used to simulate the high pumping scenario of 1996 and the reduced pumping scenario of 2018.

Numerical codes of USGS MODFLOW in the interface of 3D simulation tool groundwater modelling system (GMS) were used to develop the groundwater flow model. With a flexible modular structure and covering of all the hydrogeological processes, MODFLOW has become the standard in the art of groundwater modelling since its release in 1988 [11]. A three-dimensional geological model for the whole
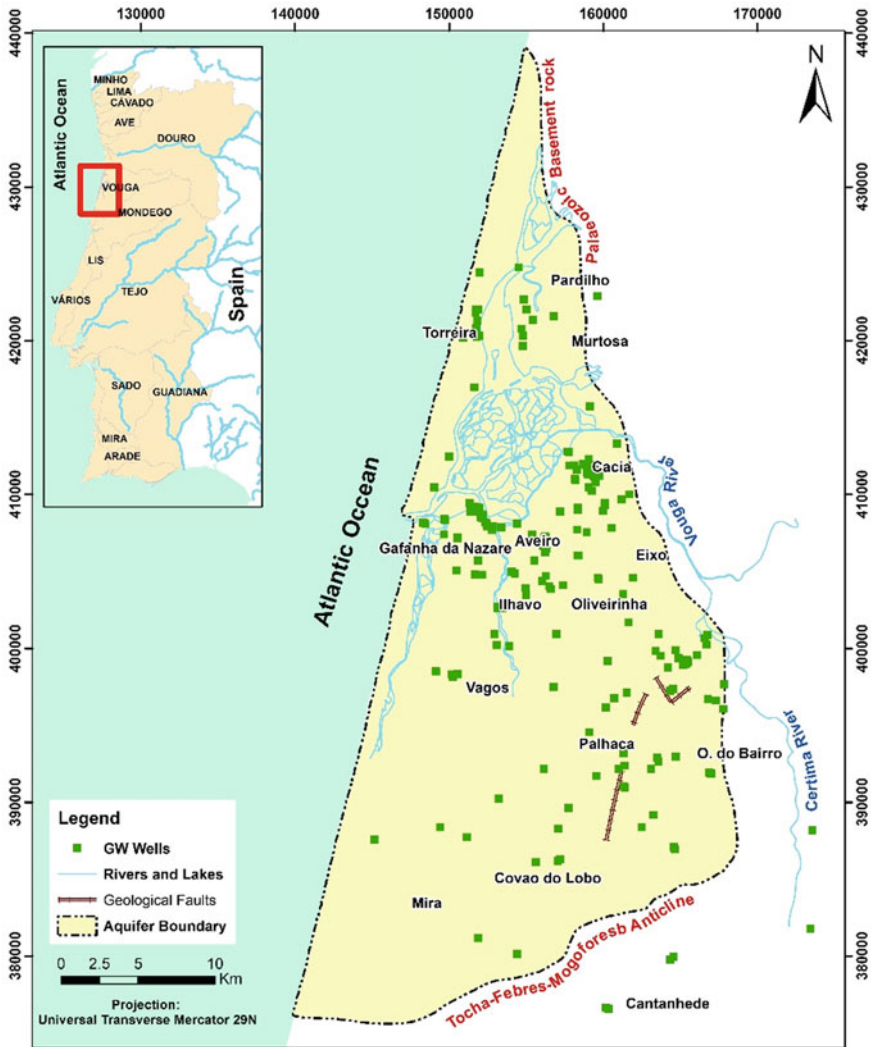
Fig. 1 Physical setting of the Aveiro Cretaceous aquifer

aquifer system was developed at first. Description of lithology for 170 boreholes was classified into eight hydrogeological units. Later the 3D geological model was converted into MODFLOW grids in GMS. The eight-layer model was simplified to four layers to assign values of hydraulic conductivities more realistically.

The model domain was divided into three-dimensional finite-difference grids consisting of four layers, 261 rows and 121 columns (Fig. 2). Uniform square grids (250 m on side) were used for discretization in the horizontal direction. In the vertical direction, the model was discretized with non-uniform grids. A minimum
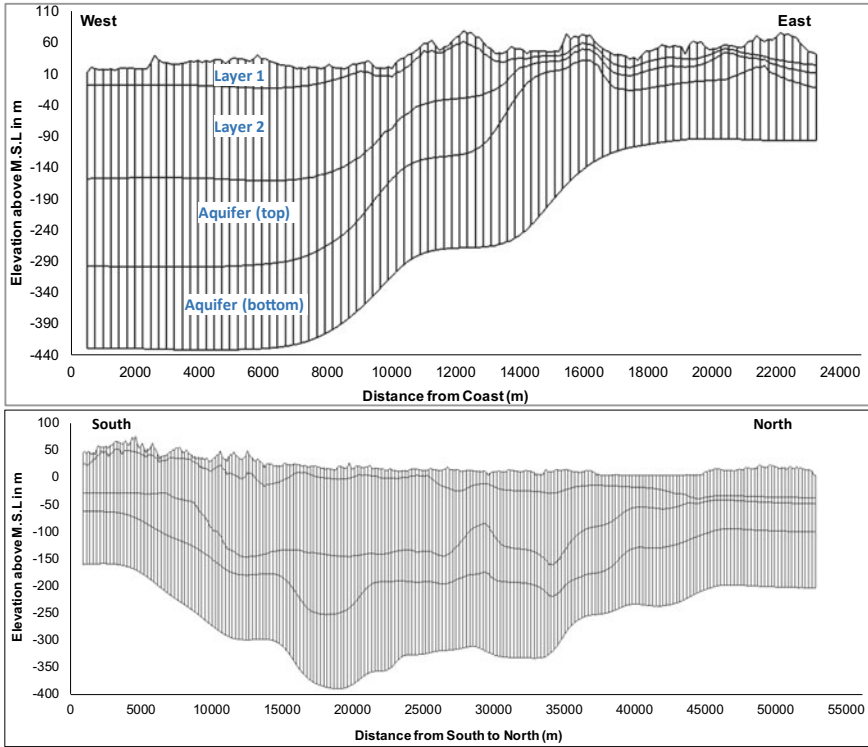
Fig. 2 Vertical discretization of the aquifer into four layers

thickness of 10 m was assigned for each layer to prevent discontinuities between cells.

Layer 1 of the model represents the Quaternary aquifer formation while layer 2 consists of Aveiro clay and upper Cretaceous formations corresponding to low permeability confining layer. Hydrogeological units 3–8 which belong to the Cretaceous formation were divided into two aquifer layers. Units 3 and 4 consisting of Verba and Oiã sandstone formation have comparatively lower hydraulic conductivities than units 5–8. Thus, units 3 and 4 were merged together which represents the top of the Cretaceous aquifer. Units 5–8 altogether represent the bottom of the aquifer which is most productive in terms of hydraulic properties.

Initially, layer 1 was defined as unconfined and layers 2–4 were defined as confined in the model. But during trial simulation unexpectedly very high head was observed for some of the cells in layer 2, having properties of Aveiro clay and located below the dry cells in layer 1. This was might be due to model nonlinearity caused by the change of computed hydraulic head during simulation due to the change of saturated thickness. To avoid such nonlinearity of the model and allied very high computed heads, all four layers were simulated by adopting the specified thickness approach [12].

A constant head boundary of 0 m M.S.L was assigned at the western boundary. A constant head boundary was also assigned at the southern/south-eastern boundary using hydrostatic surface contour values. Rivers and lagoons were considered as specified head boundaries. No flow boundary was assigned on the north-eastern part. Recharge from precipitation and abstraction from boreholes were assigned as specified flux boundary.

The steady-state model was calibrated for the predeveloped condition of 1980 by optimizing mainly hydraulic conductivities of different formations and recharge amounts. Calibration was done initially by changing the hydraulic conductivities globally and later automated parameter estimation (PEST) technique was adopted. Automatic optimization was done for ranges of hydraulic conductivities of different formations obtained from Condesso de Melo [8]. Evaluation of calibration was done through graphical and statistical approaches.

Coefficient of determination (R^2) and Nash–Sutcliffe efficiency (NSE) are two widely used statistical indicators which were used to evaluate the model calibration. The scatter plot of the observed head against the computed head under predevelopment condition of 1980 showed values of R^2 and NSE as 0.7 and 0.67, respectively (Fig. 3). From the statistical point of view, both the indicators are satisfactory. Based on the NSE values, the performance of the model can be rated as "good" [13].

To evaluate the calibration efficiency at spatial scale, the concept of reduced deviation based on the z-score concept was applied. The calibration deviation corresponds to 95% confidence interval under the assumption of Gaussian error if its value falls within the range of ± 2 times the standard deviation of estimated error [14]. Computation of reduced deviation was done using computed heads from the flow model,

Fig. 3 Scatter plot of computed head vs observed head (steady state in 1980)
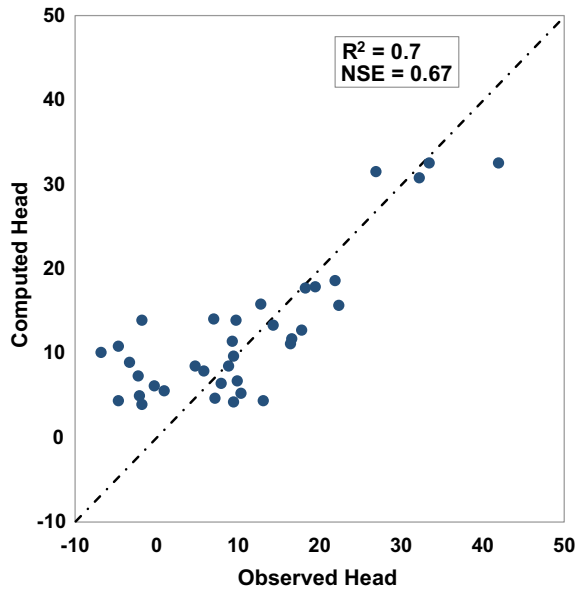
interpolated observed data and kriging standard error of estimation. Reduced deviation for most of the model domain was below 2 which corresponds to 95% confidence interval including most of the places where high EC values were observed during the field campaign.

4 Results and Discussions

4.1 Water Budget and Flow from Boundaries

Total inflow and outflow budget for the aquifer (Fig. 4) showed recharge as the main source of inflow that accounts for about 92% of the flow budget in predevelopment condition (1980). In this condition, the contribution from constant head boundaries to the inflow budget is around 8%. However, it increases up to 14% under the high abstraction scenario. Under predevelopment state, 82% of the outflow is due to natural discharge through western and south-eastern boundaries. The natural discharge decreases to 57% under high abstraction scenario.

While groundwater abstraction was about 18% under the predevelopment condition, it accounted for 43% of the outflow budget under the high abstraction condition (Fig. 4). The bottom part of the aquifer (layer 4) provides most of the extracted water, about 84% under the high abstraction condition (Fig. 5). This is reasonable since the bottom part of the aquifer is consists of the most productive geological formations. Specified head boundary at south accounted for 3% of the inflow water budget in the predevelopment scenario. It increases to 6% under the worst pumping scenario. Such low contribution from the southern boundary complies with the presence of Tocha–Febres–Mogofores anticlinal structure with Jurassic formation at the core. Both the Cértima River and Pateira lagoon, which represent the south-eastern boundary, contribute insignificantly to the overall inflow budget. However, a significant amount of discharge occurs through this boundary. Discharge through this boundary accounts for 12% of the overall discharge in the predevelopment condition (Fig. 5). However, it reduces to 5% under the high pumping scenario.
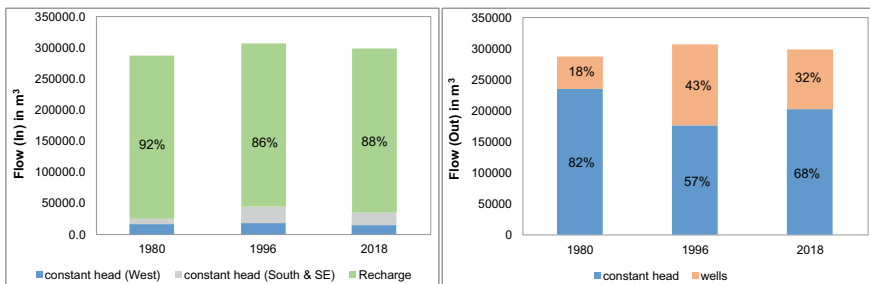
Fig. 4 Total water budget of the aquifer
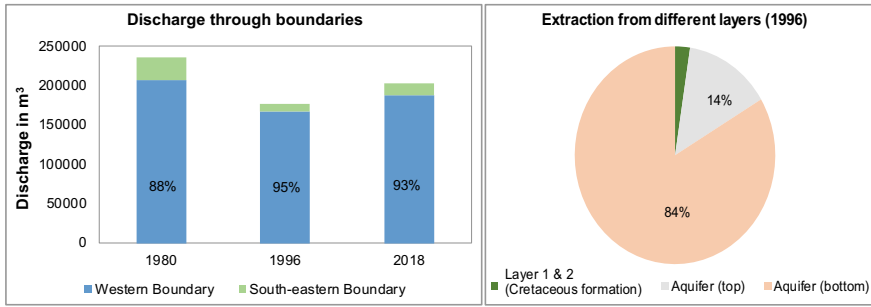
Fig. 5 Discharge through boundaries and abstraction from different layers

4.2 Groundwater Flow Direction

Groundwater flow paths in the Quaternary aquifer (layer 1) are mainly governed by the topography. Flow directions in layer 2 are quite identical to the Quaternary aquifer except for the areas where Aveiro clay formation is present (Fig. 6). The clay layer boundary in layer 2 along the south-north direction plays a crucial role in governing flow paths. Three distinctive regional flow paths can be recognized. The first one represents groundwater flow from south-east to north-west and finally discharging to the Atlantic Ocean. On the extreme south, groundwater flow is mainly from east to west resulted due to topographic relief. This flow path is the dominant one for layer 1, whereas it is not at all significant in layer 2 due to Aveiro clay formation. The second flow path represents groundwater flow from the south towards the open water bodies on the south-eastern part. The third flow path represents groundwater flow from the central-east part of the aquifer towards the extreme north of the aquifer and discharging to the ocean (Fig. 6).

Groundwater flows through the Cretaceous aquifer layers (layers 3 and 4) exhibit a similar pattern. Groundwater flows predominantly from the south-east to the north-west direction and finally discharges to the coast. Flow paths get contracted in the central-east part induced by water abstraction. Groundwater discharges from the southern boundary towards the open water bodies on the south-eastern boundary also exist.

4.3 Impact of Water Abstraction

Model computations showed that the groundwater table under the predevelopment condition of 1980 did not go below sea level. It is an underestimation by the model (mainly due to coarse grids around the well location) as the piezometric observations of 1980 showed local depletion up to −6.0 m below sea level. Analysis of model results showed high depletion of piezometric head up to −25 m below
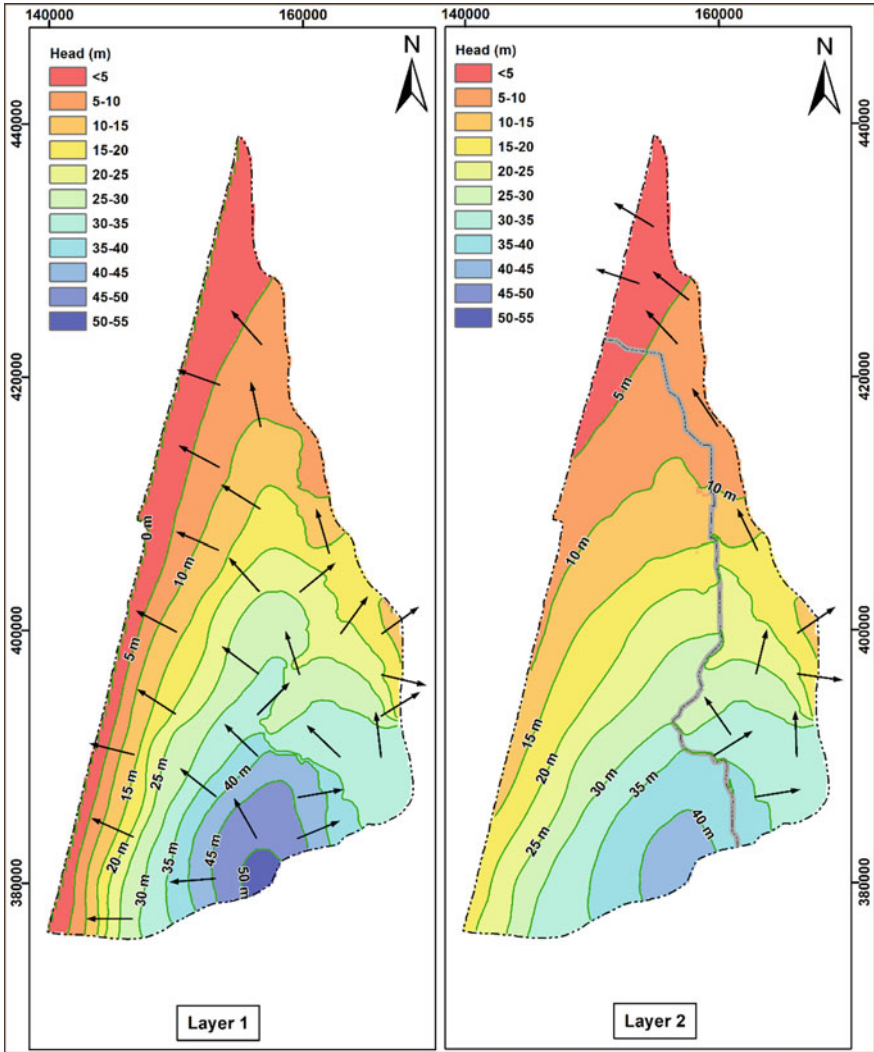
Fig. 6 Groundwater contours (layers 1 and 2) and flow direction for predevelopment state in 1980

the mean sea level under high abstraction scenario of 1996 (Fig. 7). Under the reduced pumping scenario of 2018, the piezometric level recovered significantly with maximum depletion of −9 m below sea level.

Flow direction from the southern boundary under the high abstraction scenario was similar to the predevelopment condition but is mostly concentrated towards the abstraction locations. Flow direction changed significantly in the northern part compared to the predevelopment scenario. Groundwater flow got concentrated to the high abstraction locations resulting in reversed flow direction and reduced natural
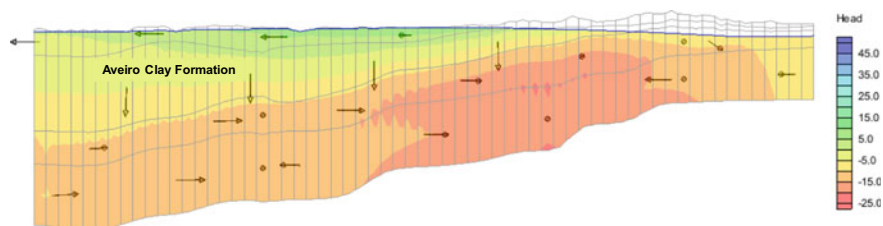
Fig. 7 Piezometric head depletion under high pumping scenario of 1996

discharge through the north-western boundary (Fig. 7). Interaction of the Aveiro clay formation with the Quaternary and Cretaceous aquifer increased under the high pumping scenario though is not a drastic change in terms of outflow volume.

4.4   Spatial Extent of Salinity and DO in 2018

The spatial extent of groundwater salinity in 2018 (Fig. 8) showed that most of the aquifer has groundwater with reasonably low EC from 250 to 1000 µS/cm with a median of 456 µS/cm. Waters with EC higher than 1000 µS/cm were found in four boreholes. The distribution of salinized boreholes was discrete and did not show any global trend along the coast. DO in groundwater was present only in the unconfined part of the aquifer which is obviously due to the influence of modern recharge. DO was absent in the salinized boreholes (Fig. 8).

4.5   Probable Sources of Salinity

Evidence of high depletion in the piezometric heads in the past gave an initial hypothesis of saline intrusion in the aquifer along the coastline. Findings from the numerical modelling approach are supportive of this hypothesis. Flow direction got reversed from the ocean to the inland under the high pumping scenario (Fig. 7). This indicates a potential movement of the freshwater–seawater interface to the inland which could be the reason for increased salinity. However, if this was the case, the salinity would have been first detected at the boreholes located close to the coastline and the distribution of salinity should show a consistent decrease from coast to inland.

Contrarily, boreholes affected with high salinity in the northern and central parts showed a discrete distribution. Some of the boreholes closer to the coast showed remarkably low salinity (<50 mg/L) compared to some boreholes located further inland (Fig. 8). Screen depths of the highly salinized boreholes near the coast are quite similar to the boreholes showing low salinity. Such discrete distribution of
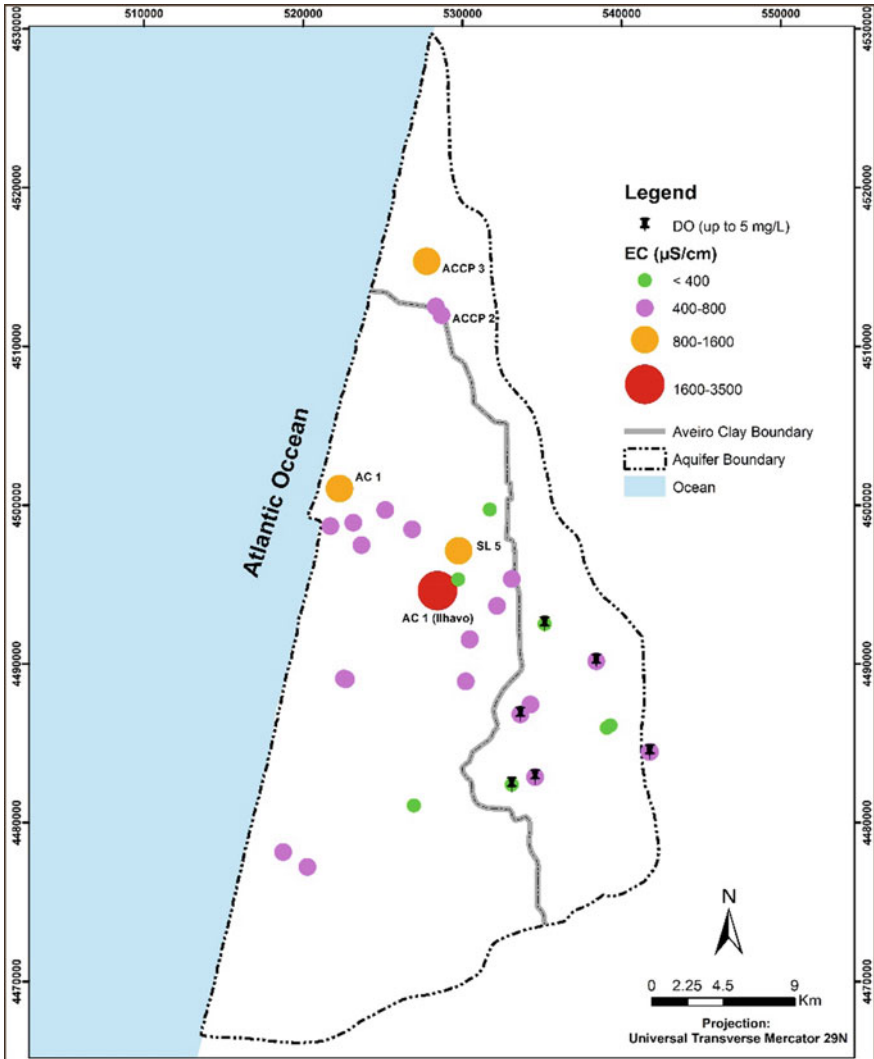
Fig. 8 Extent of groundwater salinity in 2018 along with DO observations

salinity cannot be explained by the movement of freshwater–seawater interface from offshore.

Besides, a flowing artesian well was found in the discharge zone during the field camping of 2018 which did not exist in the early 2000s. This represents a considerable recovery of piezometric head and is a contradiction to the basic saline intrusion mechanism. This was also evident from model results under the reduced pumping condition of 2018. This indicates the freshwater–seawater interface is localized far away from the present coastline and complies with the study of Vandenbohede and

Condesso de Melo [15] which concluded that water quality in the offshore part is quite fresh and the salinity front is limited to the areas close to the continental shelf.

Disruption of borehole screens and not sealing them immediately would result in leakage of saline water from the bottom of the Quaternary aquifer and can be considered as a reason for high salinity. But DO observations taken during the field campaign do not support this hypothesis. DO was absent in the salinized boreholes which limits the possibility of saline water leakage from the Quaternary aquifer since water of the shallow aquifer is highly enriched with DO.

Proved insignificance of saline intrusion and contradictory evidences for the saline water leakage from shallow aquifer leads to the hypothesis that geochemical processes may contribute to the recently observed increased salinity in the aquifer. However, geochemical processes are relatively slow and cannot be the only reason for increased salinity in the aquifer over the last two decades. Rather it is possible that high depletion of piezometric head induced by excessive groundwater abstraction has facilitated grabbing high salinity water from deeper formations of the aquifer, and this phenomenon probably has also contributed to the salinity problem.

5 Conclusion

The Cretaceous aquifer has satisfied the water demand of the Aveiro region for more than 40 years, and if properly managed can be a precious asset to tackle future water stress. Heavy exploitation of the aquifer for decades resulted in very low piezometric head in the central part. Thus, being a coastal aquifer there was a high risk of salinity intrusion. This investigation provides substantial evidences that the recently observed high salinity in the aquifer is not due to saline intrusion from the ocean. High salinity in the aquifer is governed probably by geochemical processes and the mixing of high salinity water from deeper aquifer formations. Improved management and monitoring are required to keep the salinity extent within control so that water quality in the aquifer is preserved.

Like all technical studies, this research also had some limitations. Calibration of the model was reasonably within the acceptable range; however, depletion of the piezometric head was underestimated. Besides, geochemical analysis of the ground-water samples would have provided more evidences to have a precise conclusion about the salinization source. Despite these limitations, this project has high significance for future research regarding this aquifer. The model developed in this study can represent groundwater flow dynamics of the Cretaceous aquifer with reasonable accuracy. It can be updated and calibrated for transient conditions, which will provide opportunities for studying sustainable operation of the boreholes and advective transport of salinity in the aquifer.

References

1. Taylor R G, Scanlon B, Doll P, Rodell M, van Beek R, Wada Y, Longuevergne L, Leblanc M, Famiglietti JS, Edmunds M, Konikow L (2013) Ground water and climate change. Nature Climate Change 3(4):322–329. https://doi.org/10.1038/nclimate1744

2. Edmunds WM (2001) Palaeowaters in European coastal aquifers—the goals and main conclusions of the PALAEAUX project. Geol Soc Spec Pub 189:1–16. https://doi.org/10.1144/gsl.sp.2001.189.01.02

3. Custodio E (2010) Coastal aquifers of Europe: an overview. Hydrogeol J 18(1):269–280. https://doi.org/10.1007/s10040-009-0496-1

4. Marques da Silva M A (1990) Hidrogeologia del sistema multiacuifero cretdcico del Bajo Vouga - Aveiro (Portugal). PhD Thesis, Universitat de Barcelona, Barcelona, Spain.

5. Condesso de Melo MT, Marques da Silva MA (2009) The Aveiro quaternary and cretaceous aquifers Blackwell Publishing Portugal. Natural Groundwater Qual, 233–262 https://doi.org/10.1002/9781444300345.ch11

6. Condesso de Melo MT, Carreira Paquete PMM, Marques da Silva MA (2001) Evolution of the Aveiro cretaceous aquifer (NW Portugal) during the late pleistocene and present day: evidence from chemical and isotopic data. In: Edmunds W M & Milne C J (eds). Palaeowaters in Coastal Europe: evolution of groundwater since the Late Pleistocene; Geological Society, London, Special Publications, 189, pp 139–154. https://doi.org/10.1144/gsl.sp.2001.189.01.09

7. Carreira PMM, Soares AMM, Marques da Silva MA, Araguás LA, Rozanski K (1996) Application of environmental isotope methods in assessing groundwater dynamics of an intensively exploited coastal aquifer in Portugal. Isotopes in Water Resources Management 2:45–58

8. Condesso de Melo MT (2002) Flow and hydro-geochemical mass transport model of the Aveiro cretaceous multilayer aquifer (Portugal). PhD thesis, Universidade de Aveiro, Aveiro, Portugal.

9. Gleeson T, Vander Steen J, Sophocleous MA, Taniguchi M, Alley WM, Allen DM, Zhou Y (2010) Groundwater sustainability strategies. Nat Geosci 3(6):378. https://doi.org/10.1038/ngeo881

10. Kovats RS, Valentini R, Bouwer LM, Georgopoulou E, Jacob D, Martin E, Rounsevell M, Soussana JF (2014) Europe. In: Barros VR, Field CB, Dokken DJ, Mastrandrea MD, Mach KJ, Bilir TE, Chatterjee M, Ebi KL, Estrada YO, Genova RC, Girma B, Kissel ES, Levy AN, MacCracken S, Mastrandrea PR, White LL (eds) Climate change 2014: impacts, adaptation and vulnerability, part B: Regional aspects, Contribution of working group ii to the fifth assessment report of the intergovernmental panel on climate change (pp 1267–1326). Cambridge University Press.

11. Zhou Y, Li W (2011) A review of regional groundwater flow modeling. Geosci Front 2(2):205–214. https://doi.org/10.1016/j.gsf.2011.03.003

12. Condesso de Melo MT (2002) Flow and hydro-geochemical mass transport model of the Aveiro cretaceous multilayer aquifer (Portugal). PhD thesis, Universidade de Aveiro, Aveiro, Portugal

13. Moriasi DN, Arnold JG, Van Liew MW, Bingner RL, Harmel RD, Veith TL (2007) Model evaluation guidelines for systematic quantification of accuracy in watershed simulations. Watershed Simul 50(3):885–900. https://doi.org/10.13031/2013.23153

14. Zammouri M, Ribeiro L (2017) Analyzing the effect of transmissivity uncertainty on the reliability of a model of the northwestern Sahara aquifer system. J Afr Earth Sc 129:910–922. https://doi.org/10.1016/j.jafrearsci.2017.02.034
15. Vandenbohede C, de Melo MT (2020) Estimating the offshore salinity distribution from onshore data in the Aveiro cretaceous aquifer Submitted to Hydrogeology. J Portugal. In press

Assessment of Agricultural Water Demand of Arial Khan River Catchment Using Cropwat 8.0 Model

Md Abul Kalam Azad, Umme Kulsum Navera, and Sabrina Rashid Sheonty

1 Introduction

The water demand of Bangladesh has been growing rapidly due to population growth and socio-economic development of the country. Due to its very fertile land and favorable weather, various types of crops grow abundantly in the country. The agriculture sector contributes about 17% gross domestic product (GDP) and employs more than 45% of the total labor force of the country [1]. The performance of the agriculture sector has a great impact on employment generation, human resources development, poverty alleviation and food security. Though Bangladesh is a land of rivers, irrigation plays an important role for half of the year, especially during dry periods from November to May/June. The irrigation water requirement (IWR) and crop water requirement (CWR) for some selected crops in Rangpur and Dinajpur districts haves been estimated, and it is found that the water requirements for Rice and Wheat are more than the other crops [2]. It is also found that the agriculture water demand (AWD) is likely to increase by 13% (by 2035) to 25% (by 2060) if available agricultural land is optimally utilized [3]. Bhuiyan [4] has studied on meteorological data and consumptive irrigation requirement for four upazillas of Rajshahi districts. They found that the consumptive irrigation water requirement is maximum in March and April due to less rainfall while no additional water is required during June and July due to excessive rainfall.

This study is initiated to estimate AWD in the catchment of Arial Khan River for the dry season. The need of an accurate and standard method to estimate ET_0

M. A. K. Azad (✉) · S. R. Sheonty
Department of Civil Engineering, Military Institute of Science and Technology, Dhaka,
Bangladesh

U. K. Navera
Department of Water Resources Engineering, Bangladesh University of Engineering and
Technology, Dhaka, Bangladesh
e-mail: uknavera@wre.buet.ac.bd

to predict crop water requirements has been stated by several authors [5–7]. The Penman–Monteith equation is accepted as the most precise one for its good results when compared with the other equations in various regions of the world [6]. Penman–Monteith equation has been used in CROPWAT 8.0 model for estimating the crop water requirement including irrigation water requirement. Arial Khan River catchment is located in the southern part of the Ganges Basin in Bangladesh. The catchment area lies within the districts of Shariatpur, Madaripur, Faridpur and Barishal districts. The main occupation of the people living in the area is agriculture. The country grows a wide variety of crops which are broadly classified as Kharif and Rabi crops. Rabi season crops need irrigation while occasional irrigation may be required for Kharif crops due to delayed rain which is also common for the Arial Khan River catchment.

2 Methodology

2.1 Data Collection

Generally, the estimation of water demand for crops is followed with the help of meteorological parameters [8]. Various climatological data such as monthly maximum and minimum temperature, monthly average humidity, monthly average sunshine hours, daily average wind speed, monthly total rainfall, rainfall stations and its altitude, latitude and longitude are collected from Bangladesh Meteorological Department (BMD) for three stations at Faridpur, Mdaripur and Barishal. Delineation of the catchment area of Arial Khan River by Digital Elevation Model (DEM) is collected from WARPO. Total cultivable areas and coverage of different crops are collected from the Bangladesh Bureau of Statistics (BBS). Meteorological and crop data are collected from 2006 to 2015. Cropping pattern, stages of growth, planting date, harvesting date, rooting depth, etc., are collected from Bangladesh Rice Research Institute (BRRI), Bangladesh Agricultural Research Institute (BARI), Bangladesh Agricultural Research Council (BARC) and Department of Agricultural Extension (DAE). The other data such as crop coefficient for Wheat and Potato is taken from IWMD of BARI while crop efficient value for Boro Rice is taken from FAO table and then adjusted according to the local climatic condition as suggested by Allen [5]. Soil classification of the study area is taken from the Soil Resources Development Institute (SRDI). Field capacity, permanent wilting point, total available soil moisture, rate of infiltration are taken from the physical properties of soils in the Ganges River flood plain of Bangladesh [9]. The above data are used as input to the CROPWAT 8.0 software to determine the irrigation water requirement of different crops of the Arial Khan River catchment.
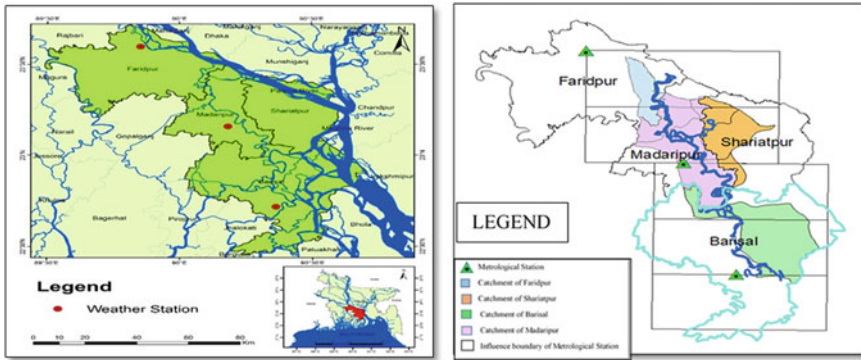
Fig. 1 Location map of study area (left), locations of metrological station (right)

2.2 Reference Crop Evapotranspiration (ET_o)

To determine the reference crop evapotranspiration (ET$_o$), the metrological data of nearby stations were collected. To make the data most representative, by using GIS the catchment area is divided into three metrological stations at Faridpur, Madaripur and Shariatpur district as shown in (Fig. 1). ET$_o$ represents the potential evapotranspiration of a well-watered grass crop. Penman–Monteith equation as suggested by FAO (1998) for determining ET$_o$ is given below:

$$ET_0 = \frac{0.408\Delta(R_n - G) + \gamma \frac{900}{T+273}u_2(e_s - e_a)}{\Delta + \gamma(1 + 0.34u_2)} \tag{1}$$

where R_n = net radiation at the crop surface (MJ/m^2 per day); G = soil heat flux density (MJ/m^2 per day); T = mean daily air temperature at 2 m height (°C); u_2 = wind speed at 2 m height (m/sec); e_s = Saturation vapor pressure (kPa); e_a = Actual vapor pressure (kPa); e_s–e_a = saturation vapor pressure deficit (kPa); Δ = slope of saturation vapor pressure curve at temperature T (kPa/°C); γ = psychrometric constant (kPa/°C).

2.3 Rainfall

Part of the crop water use comes from the water through rainfall while during dry season major supply of water comes from irrigation. Again, not all the water through rainfall can be used because of losses due to surface runoff or deep percolation below the root zone. CROPWAT 8.0 suggests different methods to calculate effective rainfall. However, in this paper, the United States Department of Agriculture (USDA) Soil Conservation Service (SCS) method is used as recommended by Smith [10].

This method calculates effective rainfall (P_{eff}) with the help of actual rainfall per month (P_{month}) with the following formulae:

$$P_{\text{eff}} = \frac{P_{\text{month}\,(125-0.2P_{\text{month}})}}{125} \text{ for } P_{\text{month}} \leq 250 \text{ mm} \tag{2}$$

$$P_{\text{eff}} = 125 + 0.1P_{\text{month}} \text{ for } P_{\text{month}} > 250 \text{ mm} \tag{3}$$

2.4 Crop Characteristics

The CROPWAT 8.0 model requires the characteristics of crops to calculate the crop water requirements. There are three overlapping crop seasons: Rabi (November–April), Aus (March–July) and Aman (July–December). Full irrigation is always required for Rabi crops while supplementary irrigation is required for Aus and Aman during drought years. Tables 1 and 2 show the crop schedules of the different crops.

For rice, land preparation and nursing time are also required to be given as input to the CROPWAT. Though land preparation and nursing may go on simultaneously, at least 35 days of nursing is required for Boro Rice [11]. Humphereys [12] suggested 200 mm water for land preparation in clay soil while Smith [10] used 180 mm water for land preparation. Mainuddin [13] used 200 mm water for nursery and land preparation for clay loam soil. In this study, 200 mm water is being considered for nursery and land preparation of Boro Rice. A staggered seed sowing (30% area for first seed sowing and 40% area for second seed sowing and 30% for third seed sowing) is considered for Boro Rice. In case of Wheat, Potato and Jute, 50% of the area covered during the first sowing and 50% during the last sowing is considered.

Table 1 Crop schedule for non-rice crops

Crop	Stages					Planting date	Harvesting date	Rooting depth
	Initial	Dev	Mid-season	Late-season	Total			
Wheat	15	25	40	30	110	November to December	March to April	90–100 cm
Potato	15	20	35	27	97	Mid-September to November	Mid-January to March	40–50 cm
Jute	25	31	39	20	115	Early March to May	July to September	70–85 cm

Table 2 Crop schedule for Boro Rice

Crop	Stages					Planting date	Harvesting date	Rooting depth	Plant height
	Initial	Dev	Mid-season	Late-season	Total				
Boro rice	50	45	35	30	160	Mid November to Mid February	April to June	95 cm	90–95 cm

2.5 Crop Coefficient

The concept of crop coefficient (K_c) introduced by Jensen [14] and further developed by the other researchers [15, 16]. The value of K_c for most crops increases from a minimum value at planting until maximum K_c is reached at full canopy cover. For rice irrigation in Bangladesh, where the average relative humidity is greater than 70% and wind condition is moderate during the dry season, K_c values of 1.1, 1.05 and 0.95 are reasonable for the first and second months, mid-season and last four weeks, respectively, [16]. Again, in the assessment of state water resources, K_c values of 1.10, 1.25 and 1.00 are considered for initial, mid-season and late-season, respectively, for Boro Rice [3]. The values of K_c for initial, mid-season and late-season for rice is given as 1.05, 1.20 and 0.90–0.60, respectively. However, these values are to be adjusted with local climatological conditions. Accordingly, the crop coefficient, K_c of rice is taken as 1.05 for initial stage [5] and K_c of the mid-season stage is adjusted by using the following formula:

$$K_{cmid} = 1.20 + [0.04(u_2 - 2) - 0.004(RH_{min} - 45)]\left(\frac{h}{3}\right)^{0.3} \tag{4}$$

where K_{cmid} is crop coefficient of the mid-season stage, u_2 is the mean daily wind speed at 2 m height over grass (ms^{-1}), RH_{min} is mean daily minimum relative humidity (%) and h is the plant height (m).

Similarly, for the late-season stage, crop efficient is given by

$$K_{cend} = 0.90 + [0.04(u_2 - 2) - 0.004(RH_{min} - 45)]\left(\frac{h}{3}\right)^{0.3} \tag{5}$$

CROPWAT 8.0 uses two crop coefficients such as K_c wet and K_c dry for rice. The first one K_c wet is used when there is ponding water on the soil surface, while K_c dry is used when there is no water standing on top of the soil, which is a common situation toward the end of the late-season during the drying out of the soil profile. The dry crop coefficient for nursery, land preparation, initial, growth stage and late-season is considered as 0.70, 0.30, 0.50, 1.05 and 0.70, respectively. Crop coefficient values of non-rice crops in semi-arid climates of Bangladesh [17] are given below (Table 3):

Table 3 K_c values for non-rice crops

Crop	K_c values for different crop growth stages			
	Initial	Development	Mid-season	Late-season
Wheat	0.42	0.78	1.13	0.48
Potato	0.25	0.62	0.79	0.18
Jute	0.72	1.39	1.26	0.46

2.6 Soil Characteristics

Soil textures referred to the relative properties of sand, silt and clay occurring on the soil. Major textural classes of soil of Bangladesh as defined by are sand, sandy loam, loam, clay loam and clay (SRDI). Types of soil for the districts of Barishal, Faridpur, Shariatpur and Madaripur and are given below (Fig. 2).

For estimation of crop water requirement, CROPWAT 8.0 needs soil information like total available soil moisture (TAM), maximum rain infiltration rate (MRIR), initial soil moisture depletion (as % of TAM) and initial available soil moisture. Physical properties of soils in the Ganges River flood plain [9] are given below (Table 4).

The initial soil moisture depletion is expressed as a percentage of the total available soil moisture (TAM). The value of 0% represents a fully wetted soil profile at field capacity while 100% is soil at wilting point (WP). Drainage porosity for clay, clay loam and silty clay is taken as 3–11%, well-structured loam 10-15% and sand 18–35%. The crop evapotranspiration (ET_c) is a key factor in determining proper irrigation schedule and to improve water use efficiency in irrigated agriculture. The values of ET_c and crop water requirements (CWR) are identical, whereby ET_c refers to the amount of water lost through evapotranspiration and CWR refers to the amount of water that is needed to compensate for the loss. ET_c can be calculated from climatic data by directly integrating the effect of crop characteristics into ET_o. The CWR or crop evapotranspiration is computed by multiplying the reference crop evapotranspiration (ET_o) with crop coefficient (K_c) at different growth stages. Thus

$$ET_c = K_c * ET_0 \qquad (6)$$
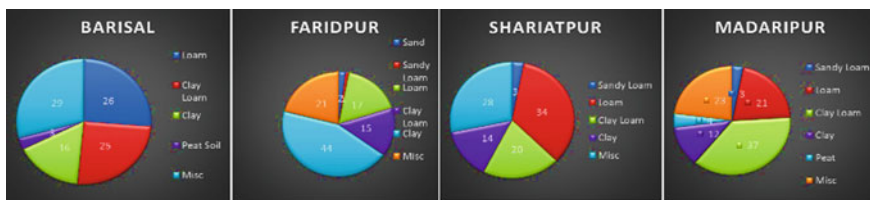
Fig. 2 Textural classification of soil for different districts of Arial Khan River catchment

Table 4 Soil information for different types of soil

Ser	Soil Information	Types of Soil		
		Silt loam	Silty clay loam	Silty clay/clay
1	TAM	282 mm	205 mm	160 mm
2	MRIR	48–240 mm/day	48–240 mm/day	240–2400 mm/day

where ET_c = Crop evapotranspiration (mm/day) and ET_o = Reference crop evapotranspiration (mm/day).

2.7 Irrigation Water Demand

Irrigation water demand is the difference between crop water evapotranspiration (ET_c) and effective rainfall. Crop water requirement module of CROPWAT includes calculations, producing the irrigation water requirement of the crop on a daily/ monthly/ decadal basis and over the total growing season. This irrigation water requirement when multiplied by the command area of each crop will give the total irrigation water demand of that crop.

2.8 Irrigation Efficiency

The ratio of the quantity of water that is diverted from a source for irrigation to that used in actual crop consumptive use is called irrigation efficiency. In Bangladesh, the ratio is low, usually 40–60%. Mondal [18] used an irrigation efficiency of 70% for estimating dry season water demand in Ganges delta within Bangladesh. In this study, an irrigation efficiency of 70% has also been used for determining the AWD of the crops.

3 Results and Discussions

3.1 Reference Crop Evapotranspiration (ET_o)

The FAO-Penman equation is used to determine the ET_o utilizing 10 years data for the study area. The results showed that ET_o is maximum during April and May which is the peak of the dry season. In Table 5, it is shown that the ET_o is comparatively less during December and January. It implies that Rice, Wheat, Potato and Jute which cultivate during this season need more irrigation during April and May while less irrigation is needed during December and January.

The average yearly ET_o for 10 years showed a decreasing tendency from 2006 to 2015. It indicates that a change in climate will cause a slight reduction in irrigation water (Fig. 3).

Table 5 Monthly average ET$_o$ for 10 years (2006–2015) for BMD station at Faridpur, Madaripur and Barishal

District/Month	10 Year Average ETo (mm/month)											
	January	February	March	April	May	June	July	August	September	October	November	December
Faridpur	58.8	82.1	117.6	147.3	139.1	121.4	114.4	113.6	109.6	103.3	83.1	58.2
Madaripur	57.0	78.9	107.5	131.8	129.6	111.7	106.8	106.5	101.7	96.9	80.1	57.2
Barisal	62.1	84.2	116.7	139.4	136.1	112.5	103.5	103.9	101.3	101.1	84.2	61.6
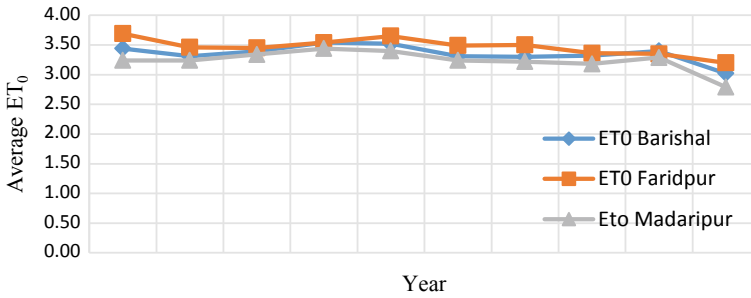
Fig. 3 Yearly variation of reference crop evaporation (ET_o) for different study locations

3.2 Crop Coefficient (K_c)

Crop coefficient (K_c) for rice is determined by using Eqs. (4) and (5) based on relative humidity and wind speed of the study area. District wise K_c values for rice are shown in Table 6.

3.3 Crop Water Requirement (ET_c)

The crop water requirement (ET_c) is computed by multiplying the crop coefficient (K_c) with ET_0 at different growth stages. The irrigation requirement is then calculated by deducting the effective rainfall (Eqs. 2 and 3) from the crop water requirement. From the analysis, it is found that for Boro Rice, ET_c varies from 0.19 mm/day to 4.48 mm/day while irrigation requirement from 0.00 mm/dec to 467.80 mm/dec for Clayey Soil. It is observed that there is a significant difference in irrigation water requirement of rice-based on type of soil. For Wheat, ET_c varies from 0.65 to 3.56 mm/day while irrigation water requirement from 0.00 to 35.30 mm/dec. For Potato, ET_c varies from 0.66 to 1.42 mm/day while irrigation water requirement from 0.00 to 12.80 mm/dec. Finally, for Jute, ET_c varies from 1.50 to 4.54 mm/day while irrigation requirement from 0.00 to 5.50 mm/dec. From the value of ET_c and irrigation requirement, it is evident that the water requirement for rice is much higher than non-rice crops.

3.4 Total Crop Area

Jute is the major crop cultivated in Faridpur district, and there is an increasing trend in the cultivation of Jute. Boro Rice and Wheat coverage are almost similar while Boro Rice coverage is showing decreasing trend, but Wheat is in increasing coverage. The cultivation of Potato is not very significant in Faridpur district. Boro Rice is the

Table 6 District wise K_c values for rice

Year	Madaripur			Faridpur			Barisal		
	K_c Value for Boro Rice			K_c value for Boro Rice			K_c Value for Boro Rice		
	Initial	Mid	End	Initial	Mid	End	Initial	Mid	End
2006	1.05	1.13	0.83	1.05	1.17	0.87	1.05	1.14	0.84
2007	1.05	1.13	0.83	1.05	1.16	0.86	1.05	1.14	0.84
2008	1.05	1.14	0.84	1.05	1.15	0.85	1.05	1.14	0.84
2009	1.05	1.13	0.83	1.05	1.16	0.86	1.05	1.14	0.84
2010	1.05	1.13	0.83	1.05	1.16	0.86	1.05	1.15	0.85
2011	1.05	1.13	0.83	1.05	1.16	0.86	1.05	1.14	0.84
2012	1.05	1.12	0.82	1.05	1.16	0.86	1.05	1.14	0.84
2013	1.05	1.13	0.83	1.05	1.16	0.86	1.05	1.14	0.84
2014	1.05	1.13	0.83	1.05	1.16	0.86	1.05	1.15	0.85
2015	1.05	1.12	0.82	1.05	1.15	0.85	1.05	1.13	0.83
2016	1.05	1.12	0.82	1.05	1.15	0.85	1.05	1.13	0.83

(a)

(b)
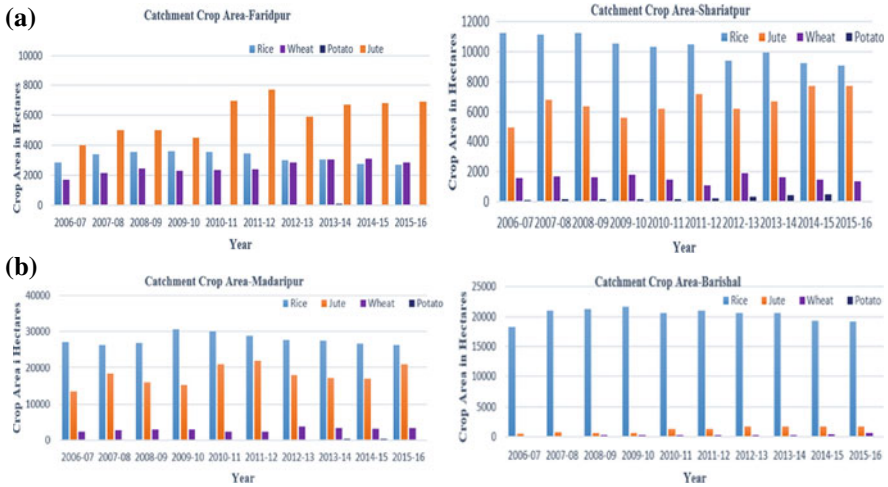
Fig. 4 **a** Catchment crop area-Boro Rice, Wheat, Potato and Jute for Faridpur and Shariatpur **b** Catchment crop area-Boro Rice, Wheat, Potato and Jute for Madaridpur and Barishal

major cultivated crop in Shariatpur district while Jute is the second largest produced crop. Boro Rice shows a decreasing trend while Jute is in an increasing trend of coverage. Compare to Boro Rice and Jute, Wheat and Potato cultivation are not that significant. Boro Rice is again a major cultivated crop in Madaripur district while Jute is the second largest crop. Though Boro Rice shows a decreasing trend in cultivation, Jute cultivation shows almost a static pattern of coverage. Wheat and Potato coverage are not significant compare to Rice and Jute. Boro Rice is the single most dominant crop cultivated in Barishal district while coverage of Jute, Wheat and Potato is not significant compare to the Boro Rice cultivation (Fig. 4).

3.5 Agricultural Water Demand (AWD) of the Catchment for Various Crops

Total AWD of Arial Khan River catchment for Boro Rice, Jute, Potato and Wheat are given in (Fig. 5) is for Faridpur, Madaripur, Shariatpur and Barishal districts. This water demand is based on the irrigation requirement and the total crop area of each district within the catchment. Total AWD of Fardipur, Madaripur and Shariatpur districts shows decreasing trend while increasing trend is found in Barishal districts. This is because of increasing area of Boro Rice cultivation in Barishal districts than that of other districts.

Total water demand for Boro Rice, Wheat, Potato and Jute is also shown in Table 7. It is seen that maximum average water demand is 347 mm^3/year and minimum is 055 mm^3/year for Potato.

(a)

(b)
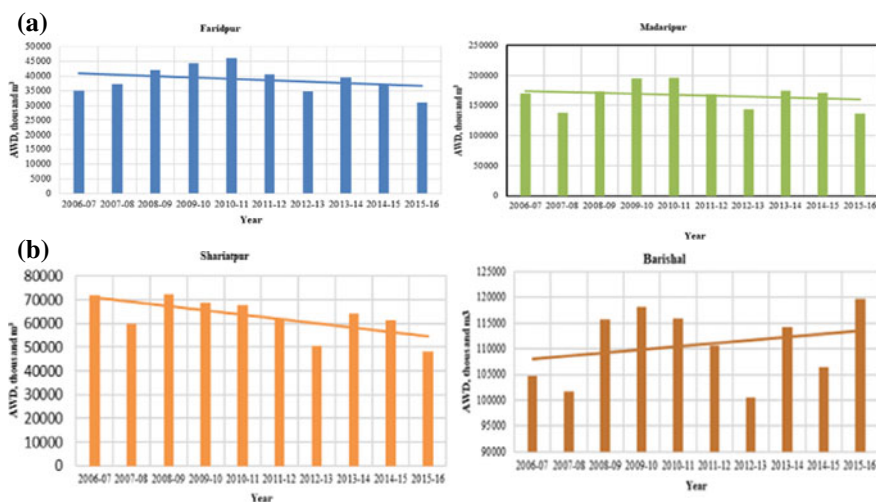
Fig. 5 **a** Total AWD of Faridpur & Madaripur **b** Total AWD of for Shariatpur and Barishal

Table 7 Total AWD for Boro rice, Wheat, Potato and Jute

Crop	10 year average of AWD (mm3)				Total AWD
	Barisal	Faridpur	Madaripur	Shariatpur	
Boro rice	110	30	151	56	347
Wheat	0.55	5	6	3	14.55
Potato	0.1	0.05	0.22	0.18	0.55
Jute	0.41	4.1	9.65	3.56	17.72

4 Conclusion

AWD of Boro Rice is largely influenced by the type of soil, whereas in other crops, influence of soil is not significant. CROPWAT 8.0 model used modified Penman–Monteith equation to calculate the irrigation water requirement depends mostly on climatic data, cropping pattern, crop coefficient and type of soil. From the 10-years period of climatic data, it is seen that the average reference crop evapotranspiration is in decreasing trend which indicates AWD of crop will also be in decreasing trend. Variations of AWD of all four crops of the catchment are due to the maximum water demand for Boro Rice and also due to the crop coverage of individual crops. Again, crop coefficient of Boro Rice is more compare to other crops. This indicates that Boro Rice has higher crop water demand than that of other crops. As regards to the crop area coverage, Jute is the leading crops in Faridpur district while in other districts Boro Rice cultivation is more than Jute, Wheat and Potato. AWD as well as the water demand of other sectors will help assist in water balance study which will ultimately contribute in planning the water security of the particular catchment.

References

1. BBS, Bangladesh Bureau of Statistics (2007, 2008, 2009, 2010, 2011, 2012, 2013, 2014, 215 and 2016) Yearbook of Agricultural Statistics. Statistics and Informatics Division (SID), Ministry of Planning, Government of Bangladesh
2. Islam MR, Mizan MH, Akter M, Zakaria G (2017) Assesment of Crop and Irrigation Water Requirements for Some Selected Crops in Northwestern Bangladesh. Global J Science Frontier Res: Agriculture and Veterinary. Global J Inc. (USA) 17(3):15–22
3. WARPO, Water Resources Planning Organization (2016) Assessment of state water resources. WARPO, Dhaka 2:83–88
4. Bhuyian MK, Ahmed B, Imran MAA (2014) Study on meteorological data and consumptive irrigation requirement for four upazillas of Rajshahi. International J Adv Structures Geotechnical Eng 3:202–206
5. Allen RG (1996) Assessing integrity of weather data for reference crop evapotranspiration estimation. J Irrigation Drainage Engineering-ASCE 122(2):97–106. https://doi.org/10.1061/(ASCE)0733-9437(1996)122:2(97)
6. Chiew FHS, Kamaladasa NN, Malano HM, McMahon TA (1995) Penman-Monteith FAO-24 reference crop evapotranspiration and class-A pan data in Australia. Agric Water Manag 28(1):9–21
7. Martinez-Cob A, Tejero-Juste M (2004) A wind based qualitative calibration of the Hargreaves ET_0 estimation equation in semiarid regions. Agric Water Manag 64:251–264
8. Daniel I, Elliott RL, Allen RG, Walter IA (2003) Comparison of reference crop evapotranspiration calculations as part of the ASCE standardization efforts. J Irrig Drain Eng 129(6):440–448
9. Joshua WD, Rahman M (1983) Physical properties of soils in the Ganges river floodplain of Bangladesh. Strengthening of Soil Resources and Development Institute, FAO/UNDP Project BGD/81/023, Department of Soil Survey, Dhaka, pp 62–67
10. Smith M (1992) CROPWAT: A computer program for irrigation planning and management. FAO Irrigation and Drainage Paper 46, Rome, Italy
11. BRRI, Bangladesh Rice Research Institute (2015) Modern cultivation of rice. 18th edition, May 2015, Gazipur
12. Humphreys H (1986) Sukhothai Ground water Development Project: Aquifer Modelling Studies. Appendix IV, Howard Humphreys, Surry, UK
13. Mainuddin M (1994) Groundwater Irrigation Planning under Multiple Objectives: Sukhothai Project Zone I, Thailand. Maters Thesis, Asian Institute of Technology, Bangkok, Thailand, p 151
14. Jensen ME (1968) Water consumption by agricultural plants. Kozlowski, T.T. (Ed.), Water deficits and plants growth, Vol. II. Academic Press, Inc., New York, NY, pp 1–22
15. Burman RD, Wright JJ, Nixon PR, Hill RW (1980) Irrigation management-water requirements and water balance. Irrigation, Challenges of the 80's of the Second National Irrigation Symposium, American Society of Agricultural Engineer, St Joseph, MI, pp 141–153
16. Doorenbos J, Pritt WO (1975) Guidelines for predicting crop water requirements. Irrigation and Drainage Paper no. 24, FAO-ONU, Rome, Italy. p 168
17. IWMD, BARI, Irrigation and Water Management Division, Bangladesh Agricultural Research Institute, 2017. Crop coefficient values of different crops in Bangladesh condition. pp 26–31
18. Mondol MH, Wasimi SA (2005) Estimation of dry season water demand and availability for Ganges delta within Bangladesh up to the year 2050. Bangladesh Journal of Water Resources Research. Water Resources Engineering Department. Bangladesh University of Engineering and Technology (BUET), Dhaka 20:1–20

Numerical Modeling of Contaminant Transformation in a Permeable Reactive Barrier

A. Rahman and Anurag

1 Introduction

Groundwater is mostly being polluted by anthropogenic activities like decentralized wastewater treatment systems, acid rain, landfill leachate, and mine tailings [1]. The pollutants can also migrate horizontally as a dilute solution, causing the pollution of surface water [2]. The conventional approach to treat the groundwater contaminants is the pump and treat (P&T) technology in which groundwater is abstracted first and then treated as necessary [3], where the incurred expense is relatively high. The permeable reactive barriers (PRB) technique appears as a preferable alternative to treat groundwater due to its low energy requirement and lower operation and servicing costs [4]. The best part of the PRB is it treats the contaminants within the groundwater by hindering the lateral transition of the contaminant plume before pumping [5–8]. The specific advantages of the PRB technique over the traditional remedies motivated several experimental studies on the removal of both the organic and inorganic contaminants from groundwater using PRBs [9].

Metal contamination of water means exposure to heavy metals like mercury, chromium, lead, and arsenic [10]. Because of its noxious nature, particularly concerning arsenide, drinking water guidelines allow an incredibly low arsenic concentration [1]. Arsenic contamination of natural drinking water has affected millions of people globally, increasing the urge to invent technologies to improve

A. Rahman (✉) · Anurag
Department of Civil and Environment Engineering, University of Illinois At Urbana-Champaign, Urbana, IL, USA
e-mail: afeefar2@illinois.edu

Anurag
e-mail: aanurag2@illinois.edu

A. Rahman
Department of Water Resources Engineering, Bangladesh University of Engineering and Technology, Dhaka, Bangladesh

existing arsenic removal remedies. In this regard, PRBs represent a verified environmental remedial technology for arsenic treatment from groundwater [11]. Materials such as activated carbon, zeolite, zero-valent iron (ZVI), and sludge have been used as reactive media of PRBs to explore their contaminant removal performance. Among the available iron-based options, zero-valent iron (ZVI) is an effective reactive reagent for the removal of contaminants due to its high reduction potential of 440 mV [12, 13]. The effectiveness of ZVI as a PRB media is defined by the rate of contaminant reduction generally, which relies upon the grain size and explicit surface region of the iron and the geochemical states of the aquifer [14, 15].

Even with each passing moment, we are losing freshwater supplies due to some sort of contamination. In the future, there will be limitations on water supply and people will suffer from various crises to health issues due to unreasonable water supplies. So, there is dire need to develop and research into ways and technology for remediation of groundwater and prevent its contamination. This effort aims to develop a one-dimensional numerical model of the contaminant flow through the PRB by using the advection–dispersion equation of solute transport along with the reaction terms representing adsorption of the contaminant by reagent considered. We will be using the column experiment done with the reagent material as secondary data for calibration and validation of the numerical simulation. Simulation of the validated numerical model for the variable time domain would allow checking how long the PRB material takes to preserve the contaminant concentration downgradient less than the maximum allowable contaminant level (MCL) that could be present in drinking water. The finding of the study will depict the efficiency and longevity of the material pumice-nZVI as a reactive media in a PRB.

2 Methodology

2.1 Material Preparation and Column Experiment Design

As the initial step of the fabrication process, pumice was grounded and sieved to particle size with a range of 0.5–1 mm. The pumice sample was acid-activated in 1 M HCl for 24 h. After 24 h, pumice was rinsed with deionized water until the pH reached neutral levels. Acid-activated pumice samples were dried at 700 ℃ in the oven before the nZVI coating. The pumice-supported nanoscale zero-valent iron (P-nZVI) was developed according to the conventional liquid phase method in which the pumice was used as a support layer and borohydride (NaBH4) used as a reduction agent for iron ions (FeCl3). In the iron solution (0.81 gm ferric chloride in ethanol–water solution (100 mL, 8:1 v/v)), 3.36 gm of pumice samples were added in a three-neck flask and stirred for an hour. A freshly prepared NaBH4 solution (0.95 gm in 100 ml) was added dropwise with a flow rate of one drop/second after being stirred. The nanoparticles were separated from the solution by centrifuging at 8000 rpm for 10 min. The particles then dried in a vacuum dryer at 650 ℃ all

night long. All processes for synthesis were carried out in the nitrogen atmosphere. Tests were conducted on the formed reactive media to determine its properties like hydraulic conductivity, porosity, etc. Material porosity has been calculated by the formula shown in Eq. 1.

$$n = 100 \times \frac{\text{Volume of voids}}{\text{Total Volume}} \tag{1}$$

The tracer test is performed to estimate the longitudinal dispersion coefficients of the material. A mixture of tap water and sodium chloride with an initial concentration of 1000 mg/l is utilized as a tracer material. Firstly, a 20 cm long glass column with an inner diameter of 4.5 cm is filled with the reactive material (pumice-ZVI). Then water is allowed to pass through the column at the groundwater flow rate (3.14 cm/hr) using a peristaltic pump for 24 h to make the material in the column completely saturated. We started injecting the NaCl solution through the column after 24 h and let it run at the groundwater flow rate for 12 h. The tracer solution is allowed to run through the column using the injections at a 1-h interval until 12 h. The conductivity of the samples collected is calculated, which thereby gives the concentration of the samples. A plot of the ratio of obtained concentration and original concentration vs. time is prepared to get the value of the dispersion coefficient using Eq. 2.

$$Dx = \frac{1}{2} x_v \left[\frac{t_{84} - t_{16}}{2 t_{50}} \right]^2 \tag{2}$$

Once the properties are known, we performed the Column test to calculate the efficiency of pumice-ZVI as the reactive media in removing arsenic contamination. The arsenic solution was injected into the saturated column of pumice-ZVI at a rate of 50 ml/hr from a peristaltic pump using the falling head method and a nitrogenous head for five days. A beaker was used to collect the effluent from the column end, and syringes were used to collect samples from the examination port. Firstly the samples were taken at an interval of one hour, then at an interval of four hours, and then at an interval of eight hours. The conductivity of all the samples for all duration is converted to concentration. We formulated concentration curves that depict the effectiveness of the pumice-ZVI material. Figure 1 shows the laboratory setup for the tests.

2.2 Numerical Modeling of Advective–dispersive Contaminant Transport

A one-dimensional numerical model for the contaminant flow through the reactive medium was developed with boundary conditions as of our column experiments. The 1D partial differential equation for advective–dispersive solute transport of arsenic is
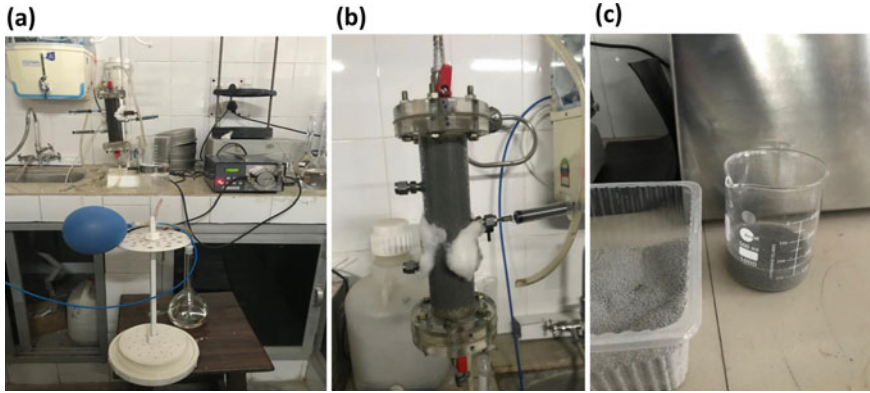
Fig. 1 a Ongoing column experiment; **b** tracer test; and **c** porosity test

shown in Eq. 3 [11]. The first and second term of the right-hand side are the advection–dispersion term respectively, and the third is the reaction term representing the arsenic reduction rate by chemical reaction. The oxidation and adsorption process is slow. Therefore, these reactions are modeled using a first-order loss reaction.

$$\frac{\partial C}{\partial t} = D_x \frac{\partial^2 C}{\partial x^2} - u_x \frac{\partial C}{\partial x} - kC \tag{3}$$

where C = arsenic concentration, D_x = dispersive coefficient, u_x = average pore velocity, and k = reaction rate coefficient. To simulate the 1D partial differential equation for advective–dispersive solute transport of arsenic, fully implicit, fully explicit, and Crank–Nicolson schemes of upwind and central finite difference scheme have been used as shown from Eqs. 4, 5, 6, 7, 8, 9, and 10.

2.2.1 Fully Implicit Method

The discretized form of fully implicit and upwind scheme is expressed by the following equation:

$$\frac{C_p^{k+1} - C_p^k}{\Delta t} = D_x \frac{C_{p+1}^{k+1} - 2C_p^{k+1} + C_{p-1}^{k+1}}{\Delta x^2} - u_x \frac{C_p^{k+1} - C_{p-1}^{k+1}}{\Delta x} - kC_p^{k+1} \tag{4}$$

The fully implicit and central scheme can be expressed by the following equation:

$$\frac{C_p^{k+1} - C_p^k}{\Delta t} = D_x \frac{C_{p+1}^{k+1} - 2C_p^{k+1} + C_{p-1}^{k+1}}{\Delta x^2} - u_x \frac{C_{p+1}^{k+1} - C_{p-1}^{k+1}}{2\Delta x} - kC_p^{k+1} \tag{5}$$

2.2.2 Fully Explicit Method

The fully explicit and upwind scheme can be expressed by the following equation:

$$\frac{C_p^{k+1} - C_p^k}{\Delta t} = D_x \frac{C_{p+1}^k - 2C_p^k + C_{p-1}^k}{\Delta x^2} - u_x \frac{C_p^k - C_{p-1}^k}{\Delta x} - kC_p^k \quad (6)$$

The fully explicit and central scheme can be expressed by the following equation:

$$\frac{C_p^{k+1} - C_p^k}{\Delta t} = D_x \frac{C_{p+1}^k - 2C_p^k + C_{p-1}^k}{\Delta x^2} - u_x \frac{C_{p+1}^k - C_{p-1}^k}{2\Delta x} - kC_p^k \quad (7)$$

2.2.3 Crank–Nicolson Method

The Crank–Nicolson and upwind scheme can be expressed by the following equation:

$$\frac{C_p^{k+1} - C_p^k}{\Delta t} = D_x \frac{(C_{p+1}^{k+1} - 2C_p^{k+1} + C_{p-1}^{k+1} + C_{p+1}^k - 2C_p^k + C_{p-1}^k)}{2\Delta x^2}$$
$$- u_x \frac{\left(C_p^{k+1} - C_{p-1}^{k+1} + C_p^k - C_{p-1}^k\right)}{2\Delta x} - \frac{k}{2}\left(C_p^{k+1} + C_p^k\right) \quad (8)$$

The Crank–Nicolson and central scheme can be expressed by the following equation:

$$\frac{C_p^{k+1} - C_p^k}{\Delta t} = D_x \frac{(C_{p+1}^{k+1} - 2C_p^{k+1} + C_{p-1}^{k+1} + C_{p+1}^k - 2C_p^k + C_{p-1}^k)}{2\Delta x^2}$$
$$- u_x \frac{\left(C_{p+1}^{k+1} - C_{p-1}^{k+1} + C_{p+1}^k - C_{p-1}^k\right)}{4\Delta x} - \frac{k}{2}\left(C_p^{k+1} + C_p^k\right) \quad (9)$$

For the numerical simulations of all the schemes, the Dirichlet boundary condition is considered with a fixed concentration of arsenic at the upstream boundary and zero concentration at the downstream boundary. As an initial condition, the concentration of arsenic at all the intermediate nodes is considered as zero. Equation 10 is the initial and boundary conditions for the 1D numerical model.

$$C(0, t) = C_0$$
$$C(x, 0) = 0 \text{ and } \frac{\delta C}{\delta X} = 0 \text{ for } x = \infty \quad (10)$$

Fig. 2 Methodological
framework of the project
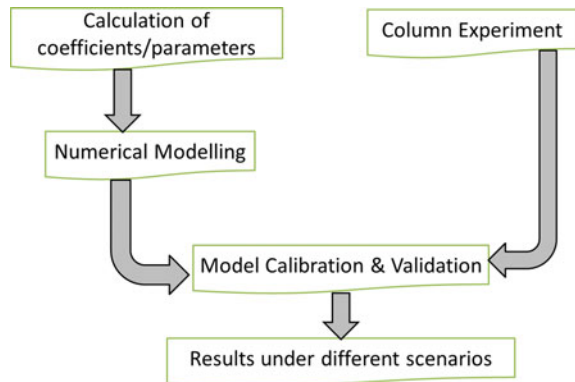
Both the numerical and experimental outputs were compared to attain an approximate value of efficiency of the fabricated ZVI. The steps of this study methodology can be simplified in the following flowchart as shown in Fig. 2.

3 Results and Discussion

3.1 Results of the Conducted Experiment

From the tracer test and column experiment, we got the material properties and boundary conditions to develop the numerical model. Table 1 shows the specifications values of the major variables.

3.2 Temporal Trend of Arsenic Removal from Numerical Modeling

Calibration of the 1D numerical model of advection–dispersion reaction of arsenic for different schemes has been done by tuning mass transfer loss coefficient, k from $0.02\,\text{day}^{-1}$ to $0.2\,\text{day}^{-1}$. $k = 0.165\,\text{day}^{-1}$ was the finally suggested value of the linear mass transfer coefficient. Figure 3 shows the trend of the adsorbed arsenic at 4 cm of the PRB column for the numerical solution from six different numerical schemes, and the experimentally observed adsorbed concentration of arsenic.

The trend achieved in all the numerical schemes is similar in shape but varied in magnitude depicting the variable amount of arsenic removal at an instance in the numerical schemes. The trend shows a higher rate of the removal of arsenic initially, which slows down after some days and finally reaches the equilibrium condition representing the saturation condition of the PRB medium. The decrease in the arsenic

Table 1 Description of the materials and setup used for the experiments and modeling

Contaminant	Arsenic
Reactive material for the barrier	Pumice (0.5–1 mm)—zero-valent iron (ZVI)
Column length and dia	16 cm, 4.5 cm
Water flow (rate)	0.00038 m/day
Tracer element used	NaCl
The concentration of tracer element	1000 ppm
Concentration of arsenic solution	5 ppm (0.005 kg/m^3)
Porosity	0.595
Bulk density	0.25
Dispersion coefficient	9×10^{-6}
Mass transfer loss Coefficient	Calibration parameter (0.02 day^{-1} to 0.2 day^{-1})

removal rate can be attributed to the decrease in concentration difference between the solution and the surface on ZVI, which adsorbs As (V). The arsenic removal rate is proportional to the initial concentration injected into the column. The results show that all the schemes can simulate the arsenic removal process by the PRB.

3.3 The Efficiency of Pumice Stone-NZVI as PRB Medium

This study also attempted to estimate the efficiency of the pumice stone-nZVI reactive medium in removing the arsenic centration from contaminated groundwater from the 1D numerical modeling of solute transport represented by advection, dispersion, and reaction terms. From the simulated results of fully implicit upwind, implicit central, fully explicit upwind, explicit central, Crank–Nicolson-upwind, and Crank–Nicolson central scheme, the maximum adsorbed concentration of arsenic was obtained as 0.0209 ppm, 0.0054 ppm, 0.0119 ppm, 0.003 ppm, 0.0167 ppm, and 0.0043 ppm, respectively. The point of the maximum adsorption of the contaminant is represented by the horizontal part of the concentration profile as shown in Fig. 4 that potentially means that the rate of removal of arsenic is zero onward. The maximum removal was obtained for the fully implicit upwind scheme, and the lowest was observed in the case of a fully explicit central scheme. For all the schemes, the time elapsed before the pumice stone nZVI reaches its capacity varied from 70 to 80 days. The observation depicts the fact that for the continued removal of the highly polluted groundwater, the PRB medium might be needed to be maintained and replaced couple of times a year.
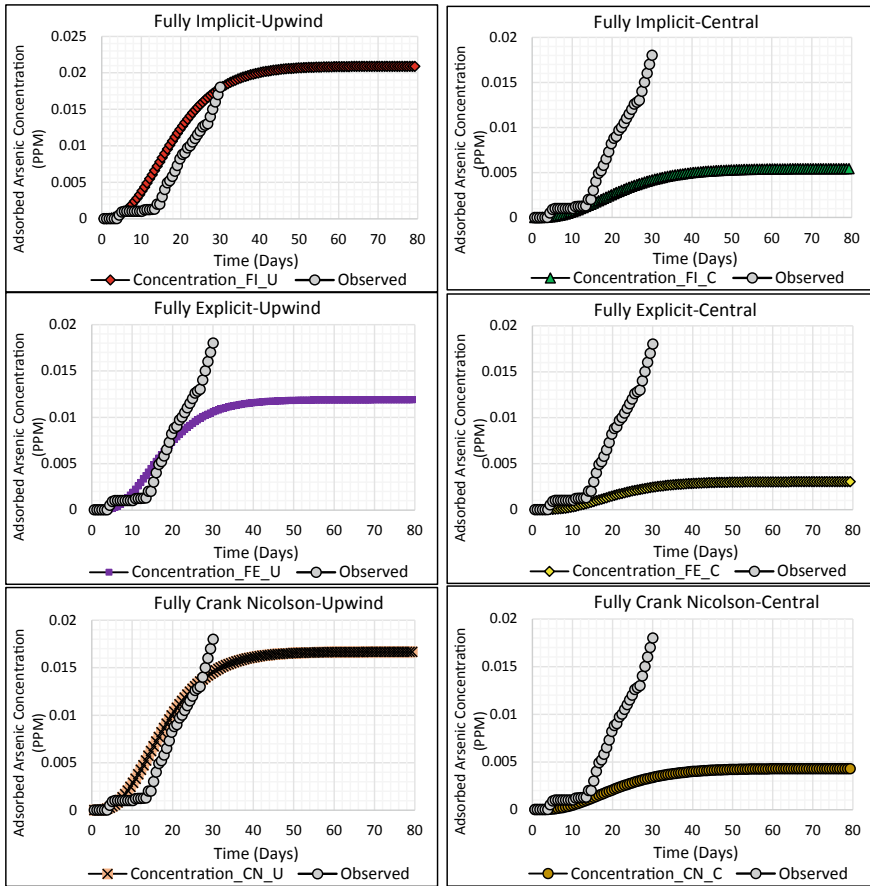
Fig. 3 Adsorbed arsenic for 1D numerical simulation and experimental observation

3.4 Adapting the Most Optimum Numerical Scheme

To compare the simulated adsorbed concentration and the experimentally removed arsenic concentration by PRB, these two have been plotted, and the trend is observed. The trend line for the fully implicit and upwind scheme has been shown in Fig. 4. It has been observed from the trend lines that the coefficient of determination for the fully implicit upwind, implicit central, fully explicit upwind, explicit central, Crank–Nicolson-upwind, and Crank–Nicolson central scheme are 0.9086, 0.9477, 0.9098, 0.954, 0.9096, and 0.9512, respectively, depicting a good alignment between the simulated and observed results. We know the coefficient of determination cannot say much about model performance. Therefore, we calculated the root means square error (RMSE), Nash–Sutcliffe efficiency (NSE), and the mean absolute deviation (MAD) for all the six numerical schemes as represented in Table 2. Table 2 shows that
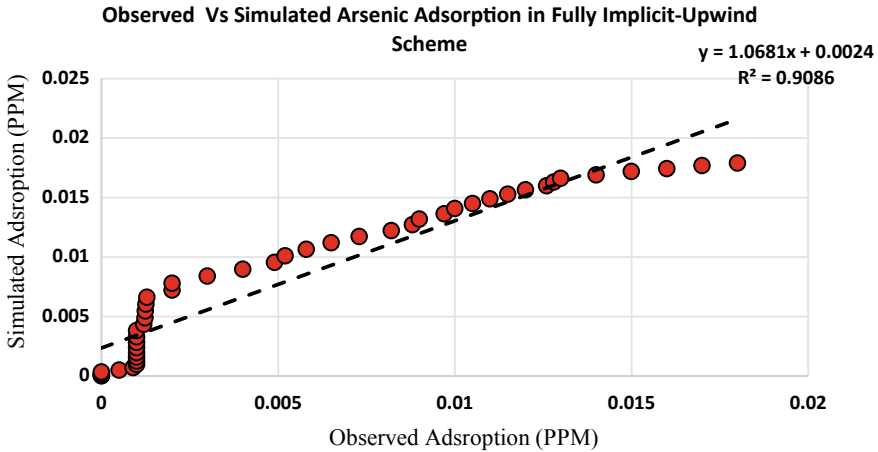
Fig. 4 Observed vs simulated arsenic adsorption in fully implicit-upwind scheme

	Scheme type	RMSE	NSE	MAD
Table 2 Comparative assessment of finite differences schemes for modeling arsenic removal by PRB	Fully implicit and upwind	0.00335	0.99220	0.00276
	Fully implicit and central	0.00568	0.97756	0.00387
	Fully explicit and upwind	0.00236	0.99611	0.00163
	Fully explicit and central	0.00661	0.96957	0.00464
	Crank–Nicolson and upwind	0.00201	0.99718	0.00156
	Crank–Nicolson and central	0.00611	0.97402	0.00423

the upwind approach of all three numerical schemes provided better matching of the simulated and the observed arsenic removal than the central approaches of the numerical schemes. This fact is understandable from the analysis of the amplification factor, phase change, amplitude ratio (AR), and phase error (PE) of the upwind and central of the explicit and Crank–Nicolson schemes. Both the upwind and central methods give similar phase errors except for a small deviation for small wavelengths. Central schemes have amplification ratios larger than unity, implying overall amplification of error that might lead to oscillation in solution. On the other hand, the upstream schemes of the explicit and Crank–Nicolson numerical approaches have amplification less than unity, meaning that they are more diffusive and cause less oscillation. In the case of the Crank–Nicolson upwind scheme, the NSE is the maximum, and the RMSE and the MAD are the minimum. The visual comparison presented in Fig. 3 shows the most optimum matching of the simulated and observed adsorbed arsenic for the Crank–Nicolson upwind scheme. The fully explicit central scheme caused the maximum RMSE and MAD value among the six chosen options. Therefore, from the perspective of the model performance matrices, the Crank–Nicolson upwind scheme

can be suggested as the most optimum numerical scheme for designing the PRB and modeling the solute transport through the groundwater.

4   Conclusion and Recommendations

This study investigated the performance of synthesized ZVI with pumice stone from an experimental and numerical modeling perspective. A 1D numerical model of the contaminant flow through the PRB consisting of pumice stone ZVI is developed using the advection–dispersion and a reaction term representing solute transport and adsorption of the contaminant, respectively. Two distinct approaches of fully explicit, fully implicit, and Crank–Nicolson have been implemented. The temporal profile of the adsorbed arsenic from the numerical model has been compared with the experimental adsorption of arsenic in a column test conducted in the laboratory to calibrate the model. The performance of the numerical schemes depicts the superiority of the Crank–Nicolson upwind scheme above others. Simulation of the calibrated numerical model allowed us to check how long the PRB material takes to preserve the contaminant concentration downgradient less than a certain level, highlighting the medium's efficiency. Here in this study, we selected only arsenic as the pollutant of groundwater and the finite difference approach of the numerical scheme. The performance of pumice-nZVI in the removal of other pollutants is worthwhile to explore. Here in this study, the column has been tested for one concentration level of arsenic that is five ppm. Variable initial concentration level might lead us to the slightly variable capacity of the permeable reactive barrier medium. Moreover, the study has been conducted using 1D only where reactivity is ignored, and the flow is expressed by the advection–diffusion process only. Inclusion of the reactivity numerically would provide us a better approximation of the capacity of the PRB medium. Besides, the finite element method to simulate the rate of the removal of arsenic and other contaminants by PRB can also be explored following a similar approach presented in this study. The comparison of the simulated adsorbed concentration obtained from the finite difference scheme and finite element scheme is indeed an interesting topic of study. For the simplicity of the calculation, here, the Dirichlet type of boundary condition has been used. Other boundary conditions, such as the flux-type boundary, can also be used to portrait the trend of the removal of arsenic by PRB.

References

1. Viraraghavan et al (1999) Arsenic in drinking water problems and solutions. Water Sci Technol 40(2):69–76
2. Mieles J, Zhan H (2012) Analytical solutions of one-dimensional multispecies reactive transport in a permeable reactive barrier-aquifer system. J Contam Hydrol 135:54–68
3. Hashim et al (2017) Reaction mechanism of zerovalent iron coupling with microbe to degrade tetracycline in permeable reactive barrier (PRB). Chem Eng J 316:525–533

4. National Research Council (1994) Alternatives for groundwater cleanup. National Academy Press, Washington D.C., p 315
5. Carey et al (2002). Guidance on the Use of Permeable Reactive Barriers for Remediating Contaminated Groundwater. National Groundwater and Contaminated Land Centre Report NC/01/51, UK Environment Agency,140–150
6. Puls RW (2006) Long-term performance of permeable reactive barriers: lessons learned on design, contaminant treatment, longevity, performance monitoring and cost—an overview. Protection and Remediation, Springer, pp 221–229
7. Skinner SJ, Schutte CF (2006) The feasibility of a permeable reactive barrier to treat acidic sulphate- and nitrate-contaminated groundwater. Water SA 32(2):129–136
8. Chen et al. (2011a) Interactions between BTEX, TPH, and TCE during their bio-removal from the artificially contaminated water. The Second International Conference on Bioenvironment, Biodiversity and Renewable Energies, Venice, Italy, 33–37.
9. Faisal AH, Abd Ali ZT (2017) Remediation of groundwater contaminated with the lead–phenol binary system by granular dead anaerobic sludge-permeable reactive barrier. Environ Technol 38:2534–2542
10. Jarup L (2003) Hazards of heavy metal contamination. Br Med Bull 68:167–182
11. Eljamal et al (2011) Numerical simulation for reactive solute transport of arsenic in permeable reactive barrier column including zero-valent iron. Appl Math Model 35:5198–5207
12. Korte NE (2001) Zero-valent iron permeable reactive barriers: A review of performance. Environmental Sciences Division Publication No. 5056, U.S. Department of Energy
13. Henderson AD, Demond AH (2007) Long-term performance of zero-valent iron permeable reactive barriers: a critical review. Environ Eng Sci 24(4):401–423.
14. Gallinati et al (1995) Design and evaluation of an in situ ground water treatment wall composed of zero-valent iron. Ground Water 33(5):834–835
15. O'Hannesin SF, Gillham RW (1998) Long-term performance of an in situ '"Iron Wall"' for remediation of VOCs. Ground Water 36(1):164–170

Application of Information Theoretic Approach in Characterizing a Hydroclimatic Process Network During Climatic Event

A. Rahman and M. Xie

1 Introduction

Natural systems in earth science can be considered as a complex process network of information flow consisting of the variables representative of the system, and the flow of information among the different variables helps to sense the identifiable patterns of the system [1]. It is necessary to characterize the interactions such as forcing and feedback in a complex system to form the process network. Information theory-based analysis approach, such as transfer entropy [2], has very recently been introduced in the domain of earth, geosciences, and climate studies [1]. The information-theoretic approach can characterize the information flow between pairs of coupled variables. In any complex system, source and target variables are the block of the system components which are connected by the system flow from the source to target and vice versa. A term named as "Mutual information" quantifies the information overlap (the common portion of both the source and target variable). However, mutual information does not contain dynamical and directional information. Thereafter comes the role of transfer entropy. It quantifies the information flow between pairs of variables within the system taking a variable as a source and another one as the target variable as well as the directionality of the information flow and coupling between the components (variables) comprising the system [2].

A. Rahman (✉) · M. Xie
Department of Civil and Environment Engineering, University of Illinois At Urbana-Champaign, Urbana, IL, USA
e-mail: afeefar2@illinois.edu

M. Xie
e-mail: mchie@illinois.edu

A. Rahman
Department of Water Resources Engineering, Bangladesh University of Engineering and Technology, Dhaka, Bangladesh

Analysis on the spatially extended systems with multivariate time series data is one of the prominent applications of transfer entropy. For example, transfer entropy can identify the causal relationship of any of the dynamic events which does not get reflected by the correlation analysis. This is why, transfer entropy has been widely used to identify direct couplings in complex systems. For example, Bhaskar et al. [3] applied transfer entropy in the identifying the primary drivers of recent climate variability with a quantification of the influence [3]. As a contribution to earth science, Goodwell and Kumar [4] introduced an information theory-based framework named–temporal information partitioning networks (TIPNets) to analyze the process connectivity in a multivariate complex system and facilitate the inference of behavior shifts in ecohydrological system [4]. Information theory could prove to be a powerful tool to facilitate us to identify the dominant processes in the hydroclimatic process network. In the USA, flooding and drought can be considered as recurring and extreme events over the historical time series. Climatic extreme events always lead to extensive socioeconomic effects, including loss of life, infrastructural damage, and food scarcity. Climate studies say that the change in climatic variables like temperature and precipitation would result in more frequent occurrences of extreme climate events. Therefore, it is imperative and meaningful to explore the mechanism which controls the pattern underlying the natural dynamics during hydroclimatic events like floods and droughts. In this study, we aim to apply information theory-based modeling framework—TIPNet for detecting interactions between different components (variables) of the selected complex network; we characterize the hydroclimate process network and identify the trend of couplings and feedback during climatic events. Then, we use information measures to investigate the predominant indicators of the discharge pattern.

2 Materials and Methods

2.1 Model Overview

Entropy-based information measures deals with the transfer entropy and mutual information [1]. By definition, mutual information measures the degree of reduction in uncertainty of the target variable, given the knowledge of the source variable. It is a symmetric idea and can be formulated as expressed in Eq. 1. However, transfer entropy is a non-symmetric measure of information transfer from a source variable X to a target variable Y, lagged in time by an amount τ, at time t when we ignore the target variable Y's dependence on its own history. Mathematically, information transfer is defined as a reduction in uncertainty of the target variable when we know about the source variable [2] and can be obtained from Eq. 2.

$$I\left(X_t, Y_t\right) = \sum_{x_t, y_t} p(x_t, y_t) \log \frac{p(x_t, y_t)}{p(x_t)\mathrm{p}(y_t)} \tag{1}$$

$$T_{x_{t-\tau} \to y_t} = \sum_{y_t y_t^k x_t^k} p\left(y_t, y_{t-\tau}^k x_{t-\tau}^l\right) \cdot \log \frac{p\left(y_t |, y_{t-\tau}^k, x_{t-\tau}^l\right)}{p\left(y_t |, y_{t-\tau}^k\right)} \tag{2}$$

Here, y_t and $x_{t-\tau}$ are the target, Y and source, X at times t and $t - \tau$, respectively, and l and k are the block lengths used in the definition of the probability distributions [1]. Here in this study, Eq. 2 is evaluated over a range of lags (τ) to determine which timescales provides highest amounts of information transfer. Information partitioning networks (TIPNet), a developed framework by [5], is used in this study to create the information process networks for no-lag and lagged time series of the hydroclimatic variables. Variables are hypothesized as nodes in the complex network, and the information flow represents the links among the node variables in the system. The basic structural unit of the model TIPNet comprises of two source variables and one target variable [4]. The mutual information of the target source system is then partitioned into unique, redundant, and synergic components [4]. Equations 3, 4, and 5 are the formulations for the partitioning of the mutual information into three components, where the X_1, X_2, and X_t are the source 1, source 2, and target variable and the U_1, U_2, S, and R are the unique information shared from the source 1, unique information shared from source 2, redundant and synergic information from the sources to the target.

$$I(X_1, X_2; X_t) = \sum_{x_t, y_t} p(x_1, x_2; x_t) \log \frac{p(x_1, x_2; x_t)}{p(x_1, x_2) p(x_t)} \tag{3}$$

$$I(X_1, X_2; X_t) = U_1(X_1; X_t) + U_2(X_2; X_t) + R(X_1, X_2; X_t) + S(X_1, X_2; X_t) \tag{4}$$

$$I(X_1; X_t) = U_1(X_1; X_t) + R(X_1, X_2; X_t) \tag{5}$$

$$I(X_2; X_t) = U_2(X_2; X_t) + R(X_1, X_2; X_t) \tag{6}$$

2.2 Selection of Study Area and Data Collection

In this study, we aim to analyze and compare the coupling nature of the hydroclimatic network for several years as the flood or drought event approaches. This regard, an area prone to both the flooding and drought, would be a reasonable choice. Midwest of the USA, more particularly Illinois, experienced several flooding events in spring or late winter in the historical time frame. March of 2006, August of 2007, June of 2008, August of 2009, and April of 2013 are few of the notable flood events that occurred in Illinois. In 2008, precipitation in the range of 2.39–10.51 inches throughout 51 h caused the flood in Illinois. Besides, the state experienced several

Table 1 Data types and location

Variable	Site name	Latitude	Longitude
Temperature of air (TA)	US-IB1	41.8593	−88.22273
Relative humidity (RH)			
Wind speed (WS)			
Wind direction (WD)			
Air pressure (PA)			
Soil temperature of soil (TS)			
Soil moisture (water) content (SWC)			
Ground heat flux (G)			
Discharge (D)	DuPage river (ID: 05,540,095)	41.8175	−88.17138

drought seasons in history. It experienced one of the most severe droughts in recent decades in the year 2012. In this study, a subwatershed in the western part of the DuPage river basin in northwestern Illinois has been proposed as the study location due to its exposure to flood and drought. 2005–2014 has been chosen as the time window of the variables considered. To form the complex network of the hydro-climatic system of the subwatershed of the DuPage river in Illinois, nine climatic and hydrogeologic variables and one hydrologic parameter are selected as represented in Table 1. Data on the variables except discharge have been obtained from the Ameriflux site, and the discharge data is obtained from the USGS surface water data portal for 2005–2014. The raw dataset comes up with different time intervals for the climatic, hydrogeologic, and hydrologic parameters. We computed the hourly averages for all the variables that ended up with a total of 78,840 data points for each variable. Figure 1 shows a map of the study area, including the site location of the measurement of the variables. The distance of the data stations is 6 km.

2.3 Methodology

Firstly, the datasets are normalized to eliminate the impact of the variable dimensions of the different variables and bring them to a common scale to compare after removing outliers and calculating 5-day anomalies. For the construction of probability density functions (pdf) in the TIPNet model, a fixed bin method with 25 number of bins has been selected. Data of nine variables for ten selected years are then fed into TIPNet and simulated for monthly segments having 720 data points. After simulation, the matrices of mutual information at zero-time lag, transfer entropy at dominant time lag, dominant lag, unique information, redundant information, and synergic information have been exported from the model. The specific question to be answered in this study includes how the coupling within the complex network constituting ten hydroclimatic variables varies as the flood and drought event approaches the
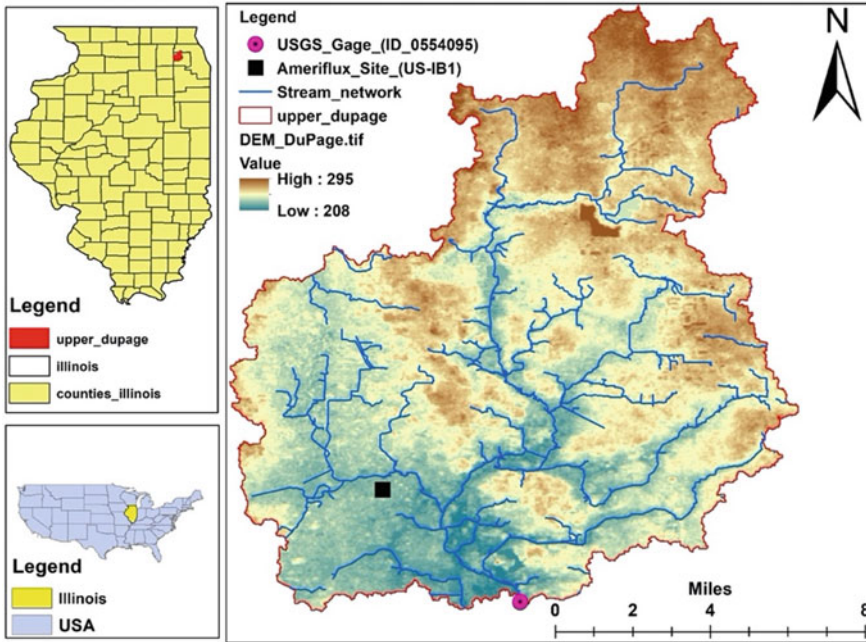
Fig. 1 Map of study area

study area from the information metric more particularly the mutual information and transfer entropy. A ratio named "synchronization ratio" (T_z) is computed using the transfer entropy (TE) and mutual information at zero lag (I_0), as presented in Eq. 6. Based on the value of synchronization ratio and values of the transfer entropy and mutual information, coupling type of each of the node couples is defined in one of the four available types. The four types of coupling considered are synchronization-dominated, feedback-dominated, forcing-dominated, and uncoupled. Node pair that has the synchronization ratio greater than unity is defined as feedback dominated. Pairs having synchronization ratio as zero are considered as synchronized in nature. The zero value of the synchronization ratio says that the node couple got at least some shared information but do not have the transfer of the information. Pairs with more I than T are considered forcing-dominated, and in this case, the synchronization ratio is less than one but greater than zero. Pairs without significant I or T are considered uncoupled [1].

$$T_z = \frac{\text{TE}}{I_0} \tag{7}$$

The second task of this study is to identify the dominant sources for the variables taken as a target by information measures. This regard, the matrices of the mutual information, transfer entropy at dominant time lag, unique, redundant, and synergic

information are exported from TIPNet. When one variable is fixed as the target variable, all other eight variables are going to play the role of source variables. Based on the ascending/descending order of the magnitude of the information measure (mutual information, transfer entropy, unique information, redundant information, and synergic information), the source variables are assigned to ranks ranging from 1 to 8. The higher value of the transfer entropy means a greater decrease in uncertainty of the target variable when the information of the source variable is known. Thus, the higher the value of the transfer entropy, the greater the rank will be. Similar thinking is applicable in mutual, unique, and synergic information. A higher magnitude of unique information indicates the greater influence of the source on the target variable. In the case of redundancy, the trend is the opposite. Since the redundancy is a measure of the overlapped information contribution from the source to the target, the higher redundant information would get the lower rank and vice versa. Afterward, the rank assigning the total rank of each of the source variables is computed by summing the ranks obtained from different information matrices. Here in this study, all the information matrices, including mutual information, transfer entropy, unique information, redundant information, and synergic information, are equally weighted. From the total ranks of the source variables, the top two sources are declared as the most dominant sources for the target variable. By applying this approach, dominant sources have been identified for each of the variables of the hydroclimatic complex network.

3   Analysis and Results

3.1   Characterizing the Complex Network

Complex networks have been formed with the time series data of the selected climatic, hydrologic, and hydrogeologic variables of each month of the years ranging from 2005 to 2014. Time series data of the variables constituting the complex network for each of the months are then simulated in TIPNet. The information measures like transfer entropy at dominant lag and zero-time lagged mutual information have been exported from TIPNet for each of the months from the year 2005–2014. An excel containing the information of transfer entropy and mutual information is then fed into the code developed in Python for the calculation of synchronization ratio and characterization of each node pair. Characterization of the node pairs within the hydroclimatic complex network is based on the approach suggested by Ruddell and Kumar in their article [1]. The Python code gives the output containing the total number of the feedback, forced, synchronized, and decoupled node pairs. The types of coupling between links can reveal behaviors and interactions between variables within the system and depict the nature of the system as a single entity. Here for analyzing the coupling of the links within the hydroclimatic network, we first divided

the years into three categories (drought years, flood years, and non-drought–non-flood years). The years 2005 and 2012 are considered as the drought years. In the year 2005, during the mid of May, the study area of DuPage river basin in Illinois becomes abnormally dry, and then moderate drought (D1 Drought) occurred in mid-May. To visualize the temporal change in the coupling types of the links within the complex network, the fraction of the four types of the coupling types (feedback, forced synchronized, and decoupled) with respect to the total number of links is plotted for each month of the year 2005 and 2012 in four different figures as shown in Fig. 2.

To compare the couplings of the links during drought and the same month of a non-drought year, the coupling types of the complex network for all the months of 2009 have also been included in the plots. The year 2009 has been considered as the normal ecosystem without any drought and flood experience. Coupling type trends are displayed over time for each month of the three selected years, including two droughts and one non-drought year. Figure 2a shows that the feedback coupling within the links of the complex network in the month of April, May, June, and July of the year 2005 is well below the same months of the year 2009 depicting the D2 and D3 drought period of the year. Comparison of the feedback coupling for the months of May, June, and July of the year 2012 with the same months of the year 2009 shows a similar trend. Plots of the two drought years show the same patterns in
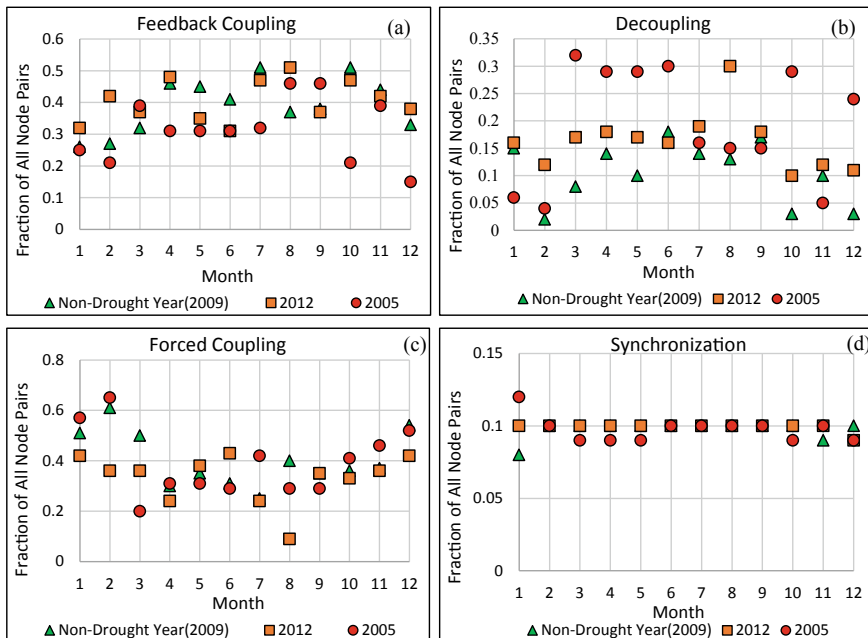

Fig. 2 Coupling types for all the node pairs for the drought years (2005 and 2012) and non-drought year (2009): **a** feedback coupling; **b** decoupling; **c** forced coupling; and **d** synchronized coupling

feedback coupling as the severity of the drought develops. This observation supports the finding by Ruddell and Kumar, highlighting the fact that during the drought, the feedback among the variables comprising the ecohydrological/hydroclimatic system decreases significantly.

Figure 2b displays the fraction of the uncoupled nodes for each month of the year 2005, 2009, and 2012, respectively. This plot shows that during the drought months for both the years 2005 and 2012, the uncoupled node pairs increase considerably compared with the same months of a non-drought year, 2009. This increased uncoupling can be attributed to significant loss of mutual information between the node pairs throughout the system. Forcing-dominated coupling showed an increase in meaning that the mutual information is larger than the information flow during drought. Comparison of the forcing dominated node pairs for the drought and non-drought years could not come up with a definite trend. The trends of the synchronized coupled links did not depict much sensitivity when the trend of the drought year 2012 was compared with the drought-free year 2009. In the year 2005, when the study area experienced extreme drought, the synchronization showed a decrease during the drought months when compared with the same months of the drought-free year 2009.

The fraction of total node pairs classified by each coupling type has also been compared among the flood years, including 2008, 2010, and 2013 and no-flooding year 2009, as shown in Fig. 3. In general, in all the three flooding years selected, the flood occurred due to heavy precipitation and propagation of snowmelt conveyed from upstream of the connecting basins. The month of June, July, and April can be selected as the flooding months for the years 2008, 2010, and 2013, respectively. In 2008, heavy precipitation in late March and April showed higher feedback. During second shift of heavy precipitation in May and June and inundation occurred in June and July, feedback increased. In August and September of 2010, the feedback was also higher compared with the same months in 2009. In 2013, the flood occurred in April due to heavy precipitation in March, showing higher feedback in the month of March. Decoupling increased during the inundation period of 2008 (July, August, and September), 2013, and 2010 (August). Forced coupling decreased during heavy precipitation and inundated period. The monthly variation of the coupling types in different years is difficult to categorize by a definite system state. This regard, seasonality impacts greatly on the coupling interaction between variables and makes the coupling pattern difficult to comprehend. But in the flooding and drought years synchronization dominated fractions remain mostly unchanged.

3.2   Identification of Dominant Indicators of Discharge

To identify the predominant indicators of discharge, we run the TIPNet model for each month from 2005 to 2014 and generate information matrices, including mutual information, transfer entropy at dominant time lag, unique, redundant, and synergic information. Information matrices can measure the actual information flow between

variables based on their definition. In this project, ten variables are fixed as the target variable, respectively. For each target variable, the other nine variables are considered as source variables of it, which can reduce the uncertainty of the target variable. Based on the ascending/descending order of magnitude of information measure, source variables are ranked from 1 to 9. The higher value of TE, U, and I contributes to obtaining a higher ranking. The role of R is the opposite. The total rank of each source variable is then calculated by summing the ranks obtained from different information matrices. Here, source variables ranking in the top two are considered as the most dominant variables.

Then, the dominant variables are collected over 120 months, and we calculate the number of times each source appears as the most dominant variable for each target. The total ranking is calculated as shown in Table 2. The ranking indicates the relative influence of different hydrologic and meteorological variables in reducing uncertainty in determining discharge that is the target variable here in this study. From the table, we see that wind speed and direction, relative humidity, and atmospheric temperature play predominant roles for almost all the variables when taken as target variable. However, soil temperature, soil moisture content, and ground heat flux are weaker drivers for most of the variables in this area. The underlying mechanisms that
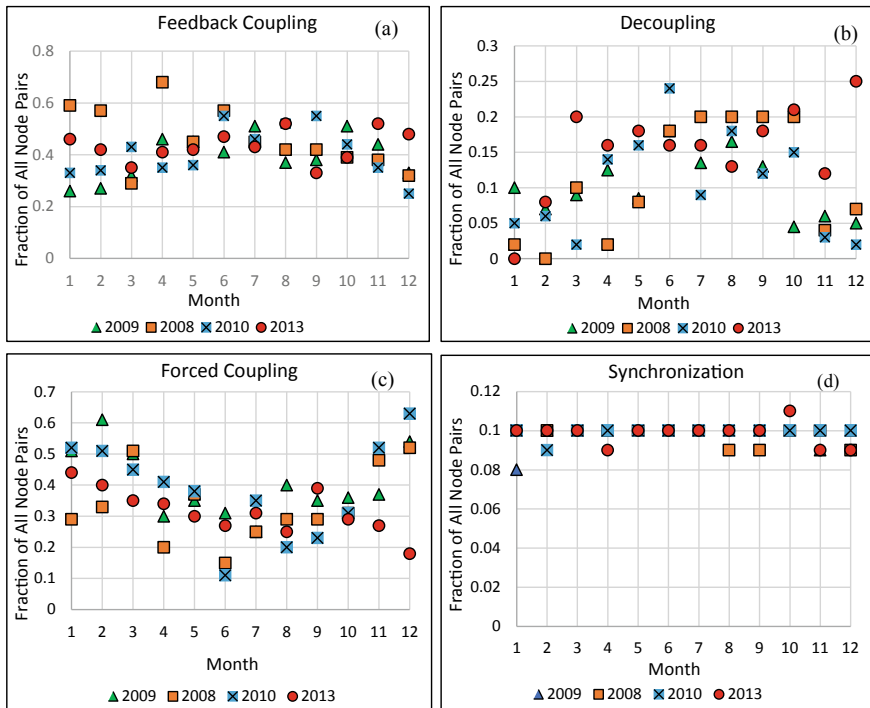

Fig. 3 Coupling types for all the node pairs for the flood years (2008 and 2012) and non-flood year (2009): **a** feedback coupling; **b** decoupling; **c** forced coupling; and **d** synchronized coupling

Table 2 Number of times source Y appears as the most dominant variable of target X (The full form of the variables is available in Table 1; for instance, TA means the air temperature)

	TA	RH	WS	WD	PA	P	G	TS	SWC	D
TA	0	34	35	51	31	33	42	9	25	24
RH	53	0	86	64	68	26	72	70	54	52
WS	75	77	0	35	60	30	39	54	48	56
WD	56	49	54	0	59	31	26	64	68	57
PA	37	47	37	39	0	48	26	27	20	12
P	37	47	37	39	1	1	26	27	20	12
G	4	6	4	3	7	16	0	3	9	18
TS	1	13	11	28	11	14	21	0	12	13
SWC	10	12	10	16	4	27	12	9	0	8
D	4	2	3	3	0	15	2	4	4	0

can help to understand the results are: The watershed is in north Illinois and near Lake Michigan. Lake Michigan is the major factor that affects the hydroclimate within the watershed we are focusing on. Lake Michigan play a significant role in enhancing the impact of wind speed and wind direction in the considered hydroclimatic system. The wind that blows across Lake Michigan can carry moisture onto the watershed and changes the temperature and relative humidity of atmosphere. Therefore, wind speed and direction are important contributors of atmospheric temperature and humidity level. The weather system is another major factor that controls the mechanism of the climate system. It can create variable weather conditions due to varying air mass and passing storms within the study area. The polar jet stream is located over Illinois and is the focal point for the creation of low-pressure storms driven by wind and cloud formation. The settled weather associated with high-pressure systems is always ended by the passage of low-pressure systems. Therefore, air pressure and air temperature are dominant drivers of precipitation (Table 3).

Table 3 Ranking of dominance of source variables for each target variable

	TA	RH	WS	WD	PA	P	G	TS	SWC	D
1	WS	WS	RH	RH	RH	PA	RH	RH	WD	WD
2	WD	WD	WD	TA	WS	TA	TA	WD	RH	WS
3	RH	PA	PA	PA	WD	WD	WS	WS	WS	RH
4	PA	TA	TA	WS	TA	WS	WD	PA	TA	TA
5	SWC	TS	TS	TS	TS	SWC	PA	TA	PA	G
6	G	SWC	SWC	SWC	G	RH	TS	SWC	TS	TS
7	D	G	G	G	SWC	G	SWC	D	G	PA
8	TS	D	D	D	P	D	D	G	D	SWC
9	P	P	P	P	D	TS	P	P	P	P

When the discharge is the target variable, results show that wind direction/speed and relative humidity possess the greatest likelihood to influence the discharge variable and reduce uncertainty in discharge at the catchment outlet. Thus, these three variables qualify to be the predominant drivers of the observed discharge. The results are basically consistent with the climatic mechanism and previous studies in north Illinois. Based on the historical data in the study area, from December to the following April, the snow depth is four to eight times of precipitation. Therefore, northern Illinois is a snowmelt-driven system. Snowmelt contributes to streamflow via multiple pathways and is the dominant driver of spring flooding. There are two processes that determine the dominant drivers of discharge: (1) When the wind blows from the lake in winter, the climatic system will be affected by lake. Lake-effect snow gets shaped during the cooler atmospheric conditions when the cold air mass glides over the warmer lake surface. In the study area, winds allow air to pass over the relatively warm Lake Michigan, boosting storm system energy and water content, and leading to increased snowfall. In this process, wind, air temperature, and relative humidity are important factors. For example, the higher the humidity, the more heat can be transferred to the snow to dissolve it. (2) Based on the physical mechanism of snowmelting, wind, air temperature, and relative humidity are considered as major indicators that control the snowmelting process. The rate of the snowmelt will highly influence the magnitude of discharge in spring. As a result, wind direction and wind speed rank the top two in Table 2 and can reduce the most uncertainty of discharge. Relative humidity and air temperature are also important drivers of discharge. However, observed from the results, the precipitation and soil water content play relatively marginal roles comparing with other source variables. This finding further verifies the snowmelt-driven mechanism in the watershed. In the previous study, McNamara et al. [6] illustrate the mechanisms explaining the generation of streamflow form the snowmelt. Meltwater infiltrates downward to the shallow bedrock as the snowmelt progresses. Antecedent dry conditions may initially constrain the gravity drainage to the deepest soil layers resulting initial disconnection between the streamflow and the shallow soil moisture dynamics. Therefore, SWC ranks last when discharge is the target variable in the results, which means SWC does not contribute to subtracting from the level of uncertainty in discharge through the snowmelt mechanism substantially.

4 Discussion and Conclusion

The major goals of this endeavor include the characterization of a hydroclimate network under different hydrological events and the identification of predominant drivers of discharge among nine climate variables considered in the study. Firstly, an attempt has been undertaken to characterize the hydroclimatic complex network using information measures. The synchronization ratio of each of the node couples is the main measurement parameter. Uncoupled pairs showed a clear increase, and feedback gets reduced in the drought event. Forcing-dominated coupling showed

an increase depicting that the mutual information is higher compared to the information flow during drought. In the case of flooding period in the selected flood years, feedback and uncoupling showed an increase. In the second task, dominant driver indicators of different target variables are identified based on the information-theoretic approach. Information measures, including transfer entropy, U, I, R, and S, are used to detect the information exchanged or transferred between coupled components in the hydroclimate system. Based on the magnitude of information measures, the ranking of the dominance of source variables for each target variable is obtained. As shown in the result, in this snowmelt-driven system, wind speed, wind direction, and relative humidity are predominant indicators of discharge variables. This finding is basically consistent with the hydroclimate mechanism in the study area. In this study, the flux tower data for the climatic variables have been used, and the discharge data at a downstream location has been taken for the formation of a complex network. Indeed, a comprehensive view of entropy, mutual information, and coupling types can provide insights into the functions and interactions within ecosystems. The study approach followed in this study can be helpful to analyze the feedback and coupling within a natural system from the information theory perspective. More particularly, this technique can be utilized to understand and predict oncoming droughts based on the interaction and characteristics of climatic variables for basins that deserve a focus.

References

1. Ruddell BL, Kumar P (2009) Ecohydrologic process networks:1. identification. Water Resour Res 45(3)
2. Sun et al (2014) Identifying the coupling structure in complex systems through the optimal causation entropy principle. Entropy 16(6):3416–3433
3. Bhaskar et al (2017) Assessment of drivers of recent global temperature variability: an information theoretic approach. Clim Dyn 49:3877–3886
4. Goodwell AE, Kumar P (2017) Temporal information partitioning: Characterizing synergy, uniqueness, and redundancy in interacting environmental variables. Water Resources Res 53(7):5920–5942
5. Goodwell A, Kumar P (2015) Information theoretic measures to infer feedback dynamics in coupled logistic networks. Entropy 17(11):7468
6. McNamara et al (2005) Soil moisture states, lateral flow, and streamflow generation in a semi-arid, snowmelt-driven catchment. Hydrological Processes: An Int J 19(20):4023–4038

Jamuna–Brahmaputra River Natural Channel Design for Flood Control, Bank Erosion Protection, Navigation Improvement, and Land Reclamation

S. M. Bahar, K. W. Shushmi, M. A. Rafy, and Q. A. Mowla

1 Introduction

The Brahmaputra–Jamuna River system is one of the world's largest, highly dynamic, sophisticated, and unpredictable braided rivers. The river is braided with metastable islands and nodal reaches, mobile sandbars, shifting anabranches, and severe bank erosion [1]. Systematic analysis of time series of dry season satellite images and with the supplement of available historical maps and aerial photographs, Center for Environmental and Geographic Information Services (CEGIS) reported that the Jamuna River shows a persistent trend of westward migration [2–5]. Analysis indicates that the centerline of the river has moved an average of 4.3 km toward west since 1830 with a maximum westward movement of 13 km at its northern end. In recent years, the Jamuna River is migrating westward at an average of 75 m per year [6]. Sarker and Thorne [7] proposed a hypothesis in their study that morphological changes in the Jamuna–Padma–Lower Meghna system have occurred in response to the sediment wave triggered by the Assam earthquake of 1950. Jamuna transformed into a multibraided channel from a less braided index channel by several bifurcation and minor channel development. Since the early 1970s, the Jamuna River has widened from 8.3 to 11.8 km in the mid-1990s. The Lower Jamuna River has undergone a similar transformation process, from reach-averaged width of 6 km in the 1970s to the increase to 10 km in the early 1990s [8]. Also, during the major flood of 1988, a

S. M. Bahar (✉) · K. W. Shushmi · M. A. Rafy · Q. A. Mowla
Ahydtech Water Resources (BD) Ltd, Dhaka, Bangladesh
e-mail: bahar@ahydtech.ca

K. W. Shushmi
e-mail: shushmi@ahydtech.com

M. A. Rafy
e-mail: rafy@ahydtech.com

Q. A. Mowla
e-mail: ashique@ahydtech.com

huge amount of sedimentation took place in the floodplain of Jamuna River which caused the development of two major channels in the lower reach of the river. These two channels are the main reason behind this unusual widening of the river along with insufficient sediment management. Due to this Great Assam Earthquake, sedimentation rate has increased in the Jamuna River. As a result, big islands like Char Alexander, Char Jobbar, etc., have been created. But recently the sediment wave has reached the Lower Meghna and its effect is diminishing [7]. This means that the channel patterns of the Jamuna tend to be more pronounced with fewer, deeper, and stable channels. As the widening phenomenon of Jamuna is decreasing, the Government of Bangladesh (GoB) is planning to reclaim thousands of acres of land lost into the riverbed. GoB has implemented some riverbank protection and flood control projects in Jamuna River funded by Asian Development Bank (ADB), World Bank, and other donor agencies for managing this heavily unpredictable and complex river system. Recently adapted "Flood and Riverbank Erosion Risk Management Investment Program (FRERMIP) Project-1" is a short-term ongoing riverbank protection and flood control project. Institute of Water Modeling (IWM) has conducted a study named "Jamuna River Economic Corridor Development Program" funded by the World Bank, that shows how land reclamation in Jamuna River can be done to transform the reclaimed area into an economic hub. Recently, IWFM and Bangladesh Water Development Board (BWDB) has developed a concept paper that proposes building a braided corridor to allow Jamuna River to move according to its own morphology. But all these studies focus on short-term solutions to the management of this complex river system including temporary river protection structure and dredging, which is not sustainable in the long run. In the year 2015, World Bank, under the River Management Improvement Program (RMIP), developed a long-term plan to narrow down Jamuna River to align it along a single corridor. Focusing on the flood remediation, river training, natural stabilizing, land reclamation, and sediment control of the Jamuna River, this study proposes a design of creating a 264 km long Natural Channel Design (NCD) of Jamuna River from Kurigram to Padma.

1.1 Objective of This Study

The main objective of this study is to-

1. Investigate the effect of narrowing down Jamuna River to develop a green, deeper corridor where the river will flow through different major and minor channels.
2. Develop an efficient sediment management program to eradicate navigation and flooding issues.

2 Methodology

As a part of the Jamuna River natural channel design, this study has reviewed available previous reports and studies on the Jamuna–Brahmaputra River. This study has collected secondary topography, bathymetry, flow, and water level data including aerial photograph from various sources. Digital elevation model (DEM) was created from aerial photographs. Using these data and information from the previous reports/studies, two 2D hydraulic models and a 2D sediment transport model have been developed with completed meander belt analysis and conceptual natural channel design of the Jamuna River.

2.1 2D Hydraulic Model

The Jamuna River in the study area causes severe flooding and erosion every year. To understand the existing Jamuna River flow conditions and to develop a conceptual natural channel design, two different 2D hydraulic models are developed using SMS SRH-2D software. One of the 2D hydraulic models uses 2011 bathymetry data to estimate the existing water level and flooding in the Jamuna River for low, bankfull, annual maximum and 100 year flow conditions. This model domain ranges from the Bangladesh–India border to the Padma River confluence. The model uses implicit finite difference methods with grid size varying from 220 to 450 m. At the upstream boundary of the model, flows from Bahadurabad gauge station (BWDB) are applied as inflow. A discharge vs water surface elevation rating curve is created and used at the downstream boundary. The model simulated results are analyzed to understand the existing flooding and flow conditions of the Jamuna River. A second 2D hydraulic model is developed from Gaibandha to the Ganges confluence for the analysis of an Initial Natural Channel Design (INCD). This INCD has a 2 km wide main river and 1.5 km wide floodplains on both sides of the main river. Topography and bathymetry of the INCD were created by a Geomorphic Innovative Technique (GeoITECH) software. GeoITECH used the existing Jamuna River upstream and downstream river invert elevations, and slope (0.0001). The main river of the INCD has meandering longitudinal profile with 1:3 bank slope and 12.0 m of depth. There are high embankments at the end of 1.5 km wide floodplains to contain the 100 year flood flow. Both left and right floodplains have a 0.2% ground slope from the embankment to the main river. It is assumed that the floodplains will be covered by vegetation, grass and plants, and the riverbanks with river protection measures to provide non-erodible surface in the model. This study has analyzed cross section, slope, and longitudinal profile to determine the main river bankfull cross section and combined cross-sectional area of the main river and floodplains. The model has applied low, bankfull, annual maximum and 100 year flows to perform hydraulic assessment of the INCD and to determine the main river and floodplain cross section.

2.2   2D Sediment Transport Model

The Jamuna–Brahmaputra River is one of the biggest braided rivers in the world, which has many bifurcations, islands, Chars, and settlements in Bangladesh. Based on available estimates, the river carries 260–720 Mt/year sediment load at its Bahadurabad gauge station. This high sediment load with a very mild river slope made it a highly dynamic braided river with significant sediment erosion and deposition. This study has developed a 2D sediment transport model using SMS and SRH-2D software. The model is about 46 km long from Gaibandha Sadar to Sariakandi. First 10.0 km of the model upstream has the existing Jamuna River shape and bathymetry of 2011. The remaining 36.0 km of the model has the INCD with main river and floodplains design. There is a transition reach of 3.0 km length from the existing Jamuna River to the INCD. GeoITECH software was used to create topography and bathymetry of the INCD reach. The main river and floodplain slopes and cross sections were similar to the second 2D hydraulic model except for the 3.0 km transition reach. In the INCD reach, the floodplains are covered by vegetation and grass, and the riverbanks have protection measures. It is assumed that the floodplains, river banks, and embankments have non-erodible surfaces in the sediment transport model. The 2.0 km wide main river of the 36 km INCD reach and the 10.0 km long existing Jamuna River have erodible river bed. The model's governing equations are discretized using the finite-volume method. Its mesh containing both structured and unstructured elements is created using SMS Map Module. Element size is about 18 m in the banks and 45–50 m in the main river. In the floodplains, element size varies from 45 to 195 m. The model sediment transport parameters include sediment specific gravity, particle diameter, transport equation coefficient for suspended load (deposition and erosion), adaptation length for bedload transport (Philips-Sutherland Saltation length formula), and active layer thickness specification. It uses a total of eight sediment size bins with D_{50} of 0.26 mm to define sediment particle size distribution. This study used the Engelund–Hansen (1972) sediment transport equation for the mobile bed simulation. The river bed material was assigned through sediment material coverage. The model has two sediment materials: river and non-erodible. The river sediment material has two layers of sediment. Top layer is 0.5 m thick, and the second layer is 15 m. The top layer acts as an active layer for sediment that interacts in the water column. Both the layers need sediment particle size distribution through a gradation curve and sediment density (kg/m^3). At the downstream boundary, a flow vs water surface elevation rating curve was applied, and a steady-state flow was used at the upstream boundary. Similar to the 2D hydraulic model, the sediment transport model has also analyzed low, bankfull, annual maximum, and 100-year flows for sediment movement in the Jamuna River and in the INCD reach.

2.3 Meander Belt Analysis

Meander belt delineation is a tool for assigning a corridor in which meander migration may occur, with the ultimate goal of restraining development encroachment, minimizing the loss or damage of property, and protecting natural areas or sensitive habitats along river systems [9, 10]. Following this theory, this study has performed meander belt delineation of the 264 km long Jamuna River from the Bangladesh–India border to the Padma River confluence in order to determine the alignment of the natural channel. Initially, bathymetry data of 2008, 2011, 2017, and 2018 have been analyzed, and the meandering channel as well as the thalweg for each year was determined from the four years bathymetry data. Thalweg is defined as the line following the lowest elevation point along the riverbed. From the thalweg analysis, it was observed that, about 45 km upstream of the Padma–Jamuna confluence, the active channel of Jamuna River follows two major paths.

This study has defined and divided the Jamuna River into several reaches considering regional variation and sinuosity of the river. For each of the reaches, limits of the meander belt are defined by drawing parallel lines tangential to outside meanders of the reach. Meander axis is defined by determining the centerline of the meander belt. Meander amplitude and belt width determine the lateral extent of a river's occupation in the floodplain. Leopold [11] has defined meander amplitude as the lateral distance between tangential lines drawn to the center channel or meandering axis of two successive meander bends. On the other hand, meander wavelength is defined as the distance between two successive meander crest/trough.

Table 1 shows estimated values of meander wavelength and amplitude of each of the reaches. It is observed that maximum wavelength and amplitude of the Jamuna meandering channel have been found to be 32 km and 3.1 km, respectively, whereas minimum wavelength is 7.6 km and minimum amplitude is 0.35 km, approximately. The average wavelength and amplitude of the meandering channel are 15.6 km and 1.7 km, respectively.

Although the meandering channel represents the most active path of the river flow, alignment for the proposed natural channel had to be adjusted considering several indispensable factors which include: settlement near the river banks and existing chars, existing bank protection structures and other infrastructures, probable increase of flow velocity inside extreme bends, etc. These adjustments have been made by maintaining the maximum, minimum, and average limits of the wavelength and amplitude of the meandering channel as analyzed in Table 1. After adjusting the full meandering line, 2 km channel width has been provided along with 1.5 km flood plain on each side as shown in Fig. 1.

Table 1 Meander wavelength and amplitude analysis

Reach no.	Crest/trough	Meander amplitude(m)	Max meander amplitude (m)	Min meander amplitude (m)	Avg. meander amplitude (m)	Meander length (m)	Max meander length (m)	Min meander length (m)	Avg. meander length (m)
A	1	2945.51	2945.51	1366.24	2155.88	20,519.3	20,519.3	20,519.3	20,519.3
	2	1366.24							
B	1	1912.68	1912.68	899.63	1196.10	9324.38	9324.38	9010.27	9167.33
	2	899.63							
	3	944.20				9010.27			
	4	1027.9							
C	1	2326.22	2326.22	1536.87	1967.77	14,692	18,705.78	14,692	16,698.89
	2	1536.87							
	3	2040.22				18,705.78			
D	1	2922.92	3015.23	2922.92	2969.075	13,379.3	13,379.3	13,379.3	13,379.3
	2	3015.23							
E	1	1685.54	1906.74	**354.90**	1386.63	18,083.2	24,254.1	18,083.2	21,168.65
	2	354.90							
	3	1906.74				24,254.1			
	4	1599.33							
F	1	1891.68	2284.8	1340.88	1839.12	14,265.8	16,605.08	14,265.8	15,435.44
	2	2284.8							
	3	1340.88				16,605.08			
G(i)	1	3101	**3101**	2310	2705.5	31,702.1	**31,702.1**	31,702.1	31,702.1
	2	2310							
G(ii)	1	1062.54	1086	1062.54	1074.27	11,249.8	11,249.8	11,249.8	11,249.8

(continued)

Table 1 (continued)

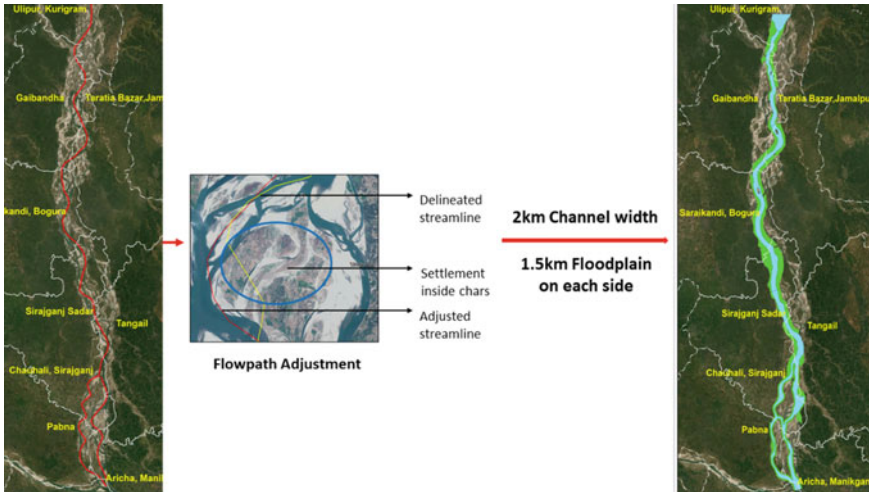| Reach no.	Crest/trough	Meander amplitude(m)	Max meander amplitude (m)	Min meander amplitude (m)	Avg. meander amplitude (m)	Meander length (m)	Max meander length (m)	Min meander length (m)	Avg. meander length (m)
	2	1086							
H	1	1322	1322	1322	–	16,829.66	16,829.66	16,829.66	16,829.66
I	1	1436.8	1520	1067.94	1286.19	10,326.2	12,214.1	10,326.2	11,384.71
	2	1067.94							
	3	1120				12,214.1			
	4	1520							
	5	520	520	520	–	11,613.82			
J	1	1427	2915	1427	2171	20,516.5	20,516.5	20,516.5	20,516.5
	2	2915							
K	1	381.18	2138.83	381.18	1260.01	7638.45	7638.45	**7638.45**	7638.45
	2	2138.83							

Fig. 1 Finalizing the alignment of the natural channel

2.4 *Jamuna Natural Channel Design*

This study attempts to propose a conceptual plan for flood protection, bank erosion control, navigation improvement, intake/offtake management, irrigation water supply, and land reclamation after incorporating results from the 2D hydraulic model, 2D sediment transport model, and meander belt analysis. The plan comprises four zones within the Jamuna River with different design criteria including sediment management, soft natural channel design, and comprehensive natural channel design using building with nature river training works.

Figure 2 below illustrates the conceptual plan and extents of the proposed four zones:

Detail components of the conceptual plan within the four zones are briefly described below:

Zone 1

"Do nothing" is proposed for the first 20 km reach of Jamuna River from the Bangladesh border. The plan proposes no intervention and channelization for this reach. Within this zone, Jamuna River will be untouched and kept as braided as it is.

Zone 2

This zone is about 45-50 km long from Kurigram to Gaibandha, which will gradually transit from the existing Jamuna River to the proposed natural channel design section of the conceptual plan. About 2.0 km wide main river and floodplain of 1.5 km on each side of the main river will be created with few minor channels through comprehensive
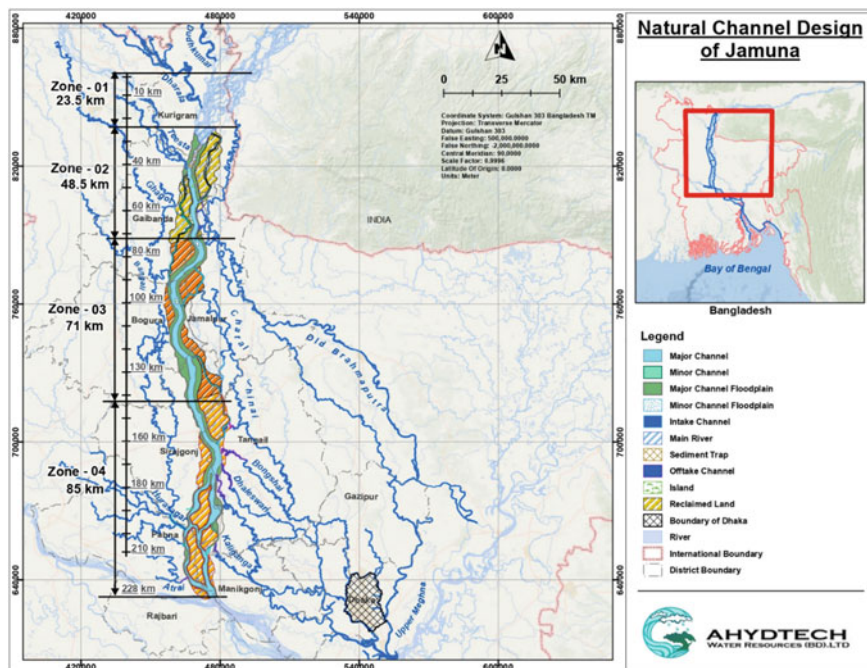
Fig. 2 Proposed four zones in Jamuna River

intervention and river training measures. A sediment trap will be constructed along the first 10–15 km of this zone for efficient sediment management.

Zone 3

In Zone 3, this study proposes a soft natural channel design along the 70 km stretch of Jamuna River starting from Sariakandi, Bagura to Sirajganj Sadar. The main river will be wide and deep enough to contain the bankfull flow. The main river will follow the existing Jamuna River thalweg and meandering, and the existing other bifurcation channels will be closed through connecting islands and chars except a few minor channels. This design will include soft natural channel design criteria, which will allow the river to move through erosion and deposition of sediment without creating bifurcations and braided channels.

Zone 4

In Zone 4, the conceptual plan has comprehensive natural channel design with main river, floodplains, embankment, and land reclamation. The conceptual plan in Zone 4 has two phases. These two phases are explained below:

Phase 1: The Phase 1 of Zone 4 is about 34 km long, which starts from Sirajganj Sadar to 12 km downstream of Bangabandhu Bridge. Similar to the design of Zone 2, this phase of Zone 4 will have comprehensive sediment management and natural

channel design with compound channel cross section including the main river and floodplains.

Phase 2: The conceptual plan of Phase 2 starts from Chauhali, Sirajganj to Padma Confluence at Aricha, Manikganj. As shown in Fig. 2, there will be a large area of land reclaimed on both sides of this 5 km Jamuna River. The reclaimed land will be used for multimodal development purposes.

3   Results and Discussions

The Jamuna–Brahmaputra River in Bangladesh is one of the largest braided and dynamic rivers in the world, which carries a huge amount of sediment load every year causing erosion and deposition. The hydraulic analysis of the Jamuna River using 2011 bathymetry data and wide range of discharge indicates lateral extent of the river for different flow conditions. During the low flow, the river shows braided multiple channels, diversions, and bifurcations. These flow multiple channels and diversions have made the main channel inaccessible and unnavigable during dry periods due to sedimentation and lower flow. The river becomes 8–14 km wide during a bankfull flow of 48,000 m3/s and causes flooding and bank erosion every year. The hydraulic modeling of the 100-year flow shows further devastating flooding, which extends to over 55 km width of flooding.

The INCD and its hydraulic analysis indicate that it is possible to reduce the width of the Jamuna River to contain the flooding within the 5 km wide river with the 2 km of main channel and 1.5 km of floodplain on both sides of the main river. This INCD closes the minor channels, and then divert these to the main channel, which will make the main channel deeper with higher flow. This will eventually provide enough navigability even during low flow. The hydraulic model shows with low flow of 3000 cms, and the main channel provides a water depth of 2.2 m. The minor channels will be filled up naturally with sedimentation after 2–3 flood seasons. The floodplain will be designed to contain flood water during an extreme event. Results from the hydraulic modeling show that bankfull flow of 48,000 m^3/s will be entirely contained within the main river, and flow as high as 100-year flow (123,000 m^3/s) will be contained within the INCD, and thus prevent large areas from flooding.

The 2D sediment transport model was run for 10 days for a wide range of flows. Objectives of the model are to understand sediment transport rate and load in the existing Jamuna River and to manage sediment in the INCD. As excessive sediment load in the river is causing instability, dynamic and braided nature of the river, sediment management, and reduction of the sediment load are important components for successful implementation of the Jamuna natural channel design. The 46 km long model simulates sediment concentration, transport rate, and sediment load in the Jamuna River and INCD. This study analyzes the model simulated results at different cross sections of the model to compare sediment transport rate and load in the Jamuna River and INCD.

A total of nine cross sections (LN-1 to LN-9) was installed in the model to monitor/observe sediment erosion and deposition phenomenon. LN-1 and LN-2 are situated in the existing Jamuna River, whereas, from LN-3 to Line9 were in the INCD reach. Figure 3 represents the comparison of maximum sediment load that is observed in different locations of the channel for various flow conditions. This figure shows maximum sediment load (kg/m/s) vs discharge (m3/s) of five cross sections in the model of which LN-1 is located in the existing Jamuna River, and LN-6, LN-7, and LN-8 cross sections are in the INCD reach. The model simulated sediment load is highest in each cross section for bankfull flow (48000cms). Moreover, sediment load is extremely high in the existing Jamuna (LN-1). The sediment flow decreases when it enters in the INCD and subsequently reduces up to 50% in the downstream (Fig. 3). For 15,000 cms flow, sediment deposition occurs in the first 4–5 km of the INCD. The INCD bed's disturbance, erosion, and deposition are very less in the downstream cross sections (LN-7 & LN-8). The sediment model for the bankfull flow (48,000cms) indicates sediment deposition is in the first 7–8 km of the INCD reach. Similarly, for this case, the INCD bed's disturbance, erosion, and deposition are very less in the downstream cross sections (LN-7 & LN-8).

For the 65,000 cms overbank flow case, a significant portion of the flow is transferred through floodplain, and the bed disturbance is less compared to that of the bankfull case. The bed disturbance of the overbank flow propagates up to 5–6 km of the INCD reach. The INCD shows erosion instead of deposition in the first 7 km of the reach for the 100-year flow (103,000 cms) case.

The sediment model has run two simulations of flow (44,000cms), which is less than the bankfull flow. First simulation runs for 10 days, and second one for 20 days simulation. Results of the two simulations show that sediment deposition in the INCD further increases and propagates in the downstream if the simulation continues from
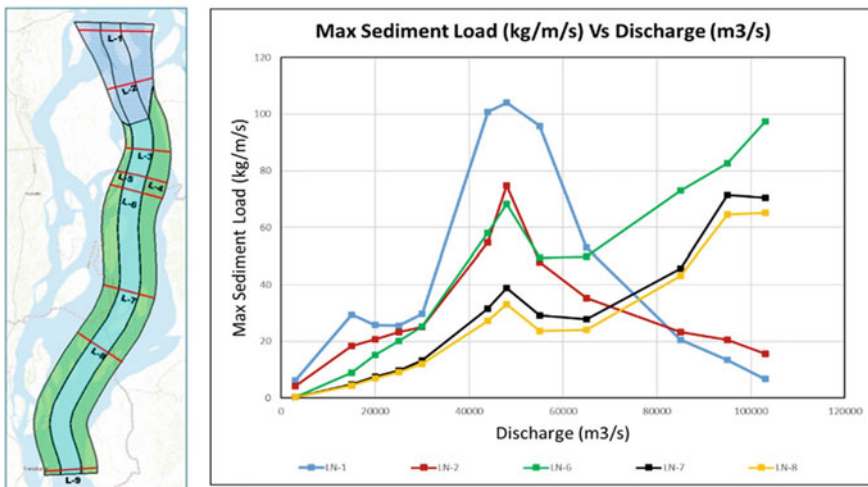

Fig. 3 Maximum sediment load (kg/m/s) vs discharge (m^3/s)

10 to 20 days. After the 10 days simulation, sediment deposition occurred in the first 7 km of the reach. The sediment deposition length increased to 12–14 km after the 20 days simulation. Even after the 20 days simulation, the downstream cross sections still have very less bed disturbance. This analysis and result indicate that if the upstream section of INCD (about 7–10 km) is dredged every year, then the downstream INCD section will remain more stable river without exhibiting any significant erosion and deposition. The annual dredging of the upstream INCD will be helpful for proper sediment management in the Jamuna NCD.

It is evident that sediment load is the highest for bankfull flow (48000cms) at each of the cross sections. Moreover, sediment load is extremely high in the existing Jamuna. The sediment flow decreases when it enters the INCD and subsequently reduces up to 50% in the downstream (Fig. 3).

Figure 4 represents the cross-sectional bed elevation in the monitoring cross sections. The cross-sectional LN-1 shows river instabilities and bed elevation changes in the existing Jamuna River for different flow conditions. In the INCD, instabilities and bed elevation changes are limited in the main river. Cross-sectional LN-3 is in the upstream section of the INCD reach. This cross section shows deposition for flows at or below bankfull. For the overbank flows, especially during the 100-year flow, this section shows significant erosion. Further downstream, the natural channel bed remains almost undisturbed. For instance, in LN-3, the amount of deposition is significant. This deposited material must be dredged every year, and the natural channel has to be brought back to its original design condition for sediment management in the river. This will reduce the sediment disturbance downstream. In LN-7
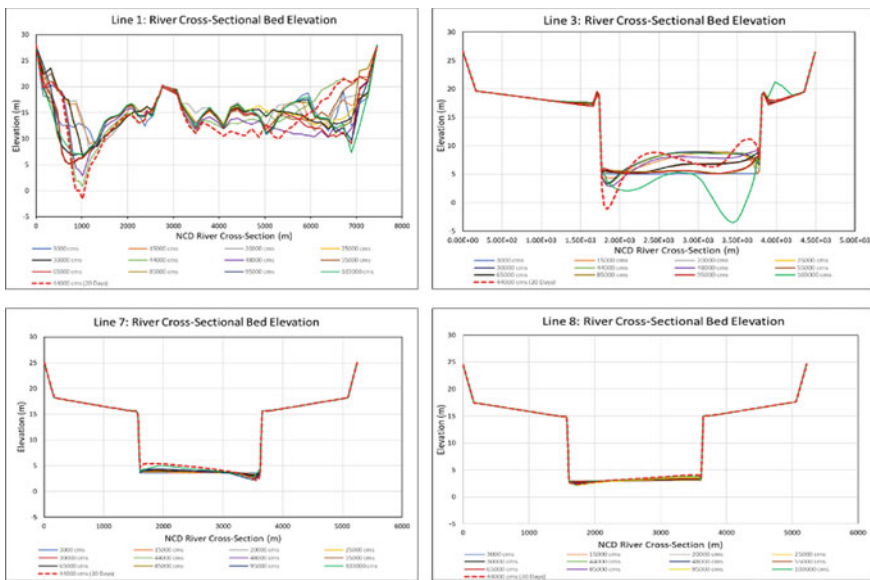

Fig. 4 Cross-sectional bed elevation of line 1, 3, 7, and 8

and LN-8, the INCD remains more stable than that of LN-3. It is evident that the rate of erosion and deposition is comparatively less in the INCD.

Analysis of sediment transport rate and load in Zone 1 will help to understand how the downstream river system can be managed including the proposed natural channel design, river morphology, sediment transport, bank erosion, and flooding. The results from 2D sediment transport modeling show that a large amount of sediment deposits in the upstream section (within the first 10–15 km) of the NCD of Zone 2. It is possible to create a sediment control basin within the section for sediment harvesting and dredging and eventually be controlled within this zone. Every year, deposited sediment will be harvested through dredging up to the level of original channel bed elevations created for the NCD and to maintain morphological balance. The dredged material can be used to fill and reclaim floodplain and construction of embankments. The present study indicates that if the upstream deposited sediment is dredged annually, the remaining section of the INCD will be almost stable and in equilibrium sediment transport conditions.

4   Conclusion

This study has collected and reviewed available reports, studies, and data on the Jamuna–Brahmaputra River. Based on the available information and data, and examples of NCD in the world, the study has prepared an INCD and conceptual plan for the Jamuna River Natural Channel Design. The plan and design consisting of four zones can provide multidimensional facilities such as land reclamation of 2018 sq. km which opens the door of immense possibilities like industrial zones, transportation, and newly developed cities. However, it needs further study and assessment on how much sediment load control is required for the sediment management in the Jamuna NCD. This INCD needs further study and analysis to improve the channel design and to accommodate and address environmental, ecological, social, and other issues and concerns. This study proposes different components and facilities within each zone to stabilize the course of Jamuna River for flood control and bank erosion protection. These components will collectively eliminate flooding, reduce lateral erosion, and stabilize the river by efficient natural channel design, river training, and sediment management. The conceptual plan will be confirmed by further hydraulic and sediment transport analysis to prepare the detailed design of the Jamuna Natural Channel. The analysis will provide information on what kind of measures will be required for the long-term stability of the proposed plan. The main river alignment will be derived from the meander belt analysis and the simulation results of the sediment transport model. From the simulation results, the study will observe how this natural channel will be moving within this zone. Though flow estimation from measured stages at Bahadurabad bears a lot of uncertainty, it will have influences on the result of the simulation. This is a limitation which requires further study and has a future study scope to simulate the natural channel movement more precisely.

References

1. Thorne CR, Russell APG, Alam MK (1993) Planform pattern and channel evolution of the Brahmaputra River, Bangladesh. Geol Soc Spec Publ 75:257–276. https://doi.org/10.1144/GSL.SP.1993.075.01.16
2. CEGIS (Center for Environmental and Geographic Information Services) (2004) Monitoring and prediction of Bank Erosion and Morphological Changes of the Jamuna and Padma Rivers Series
3. CEGIS (Center for Environmental and Geographic Information Services) (2005) Monitoring and prediction of Bank Erosion and Morphological Changes of the Jamuna and Padma Rivers Series
4. CEGIS (Center for Environmental and Geographic Information Services) (2006) Monitoring and prediction of Bank Erosion and Morphological Changes of the Jamuna and Padma Rivers Series
5. CEGIS (Center for Environmental and Geographic Information Services) (2007) Monitoring and prediction of Bank Erosion and Morphological Changes of the Jamuna and Padma Rivers Series
6. Nakagawa H, Zhang H, Baba Y, Kawaike K, Teraguchi H (2013) Hydraulic characteristics of typical bank-protection works along the Brahmaputra/Jamuna River, Bangladesh. J Flood Risk Manag 6:345–359. https://doi.org/10.1111/jfr3.12021
7. Sarker MH, Thorne CR (2009) Morphological response of the Brahmaputra–Padma–Lower Meghna River system to the Assam earthquake of 1950. Braided Rivers 289–310.https://doi.org/10.1002/9781444304374.ch14
8. ADB (2013) Main river flood and bank erosion risk management program final report, Annex E River and Charland Morphology and River Engineering. 292
9. Geomorphic P (2004) Belt width delineation procedures. Submitted to the Toronto and Region Conservation Authority
10. Kline M, Cahoon B (2010) Protecting river corridors in vermont. J Am Water Resour Assoc 46:227–236. https://doi.org/10.1111/j.1752-1688.2010.00417.x
11. Leopold LB, Wolman MG and JPM (1964) Fluvial processes in geomorphology. Dover Publications Inc., New York

Trend Analysis of Water Quality Parameters in a Selected Distribution System

K. Chowdhury and A. Akter

1 Introduction

Increased urbanization not only suffers the drinking water supply but also poses a threat to public health. Many as 500 million urban residents have inappropriate access to water services or experience water scarcity [1]. Chattogram city, the commercial capital of Bangladesh, is one of the densely populated urban areas struggling to meet the drinking water supply within acceptable water quality. The primary sources of the Chattogram city water supply are surface water (Halda and Karnafuli Rivers) [2, 3] and groundwater. Then, the treated water from the treatment plant travels through a distribution system. During the transfer, a range of physical, chemical, and microbiological transformations might affect the quality while reached to the consumer. Despite seasonal variation to the source water, pipe material, pipe size, pipe age, and decay of a disinfectant agent can influence the distributed water quality [4, 5]. The present citywide water distribution was established in 1963 to meet the city water demand of 30 million liters per day (MLD). In 2005, CWASA supplied only 110 MLD when the demand was about 230 MLD. So, there was a shortfall of 120 MLD, and presently, after 40 years, the demand has increased to about 402.6 MLD (Table 1). Available supply suppose to meet about 48% of the total the city dwellers' demand (Table 1).

Surface water extracted from both the Karnafuli [3] and Halda Rivers [2] is often polluted despite significant seasonal water fluctuation [6]. The source water already showed higher turbidity [7] and heavy metals [8]. Due to tropical nature, higher water temperature persists and possibly increases both corrosion rate and bacterial activity.

K. Chowdhury
Procurement Division, Chattogram WASA, Chattogram, Bangladesh

A. Akter (✉)
Department of Civil Engineering, Chittagong University of Engineering & Technology (CUET), Chittagong, Bangladesh
e-mail: aysha_akter@cuet.ac.bd

Table 1 Water supply and demand in Chittagong [10]

Year	Demand (MLD)	Supply of water (MLD)	Demand met (% of total)
1963	30	20.5	68
1970	60	25	42
1980	140	30	21
1990	200	50	25
2000	210	70	33
2005	230	110	48
2010	296	127	43
2015	344.7	127	37
2017	367.3	270	74
2020	402.6	360	89

During water treatment, coagulation is greatly dependent on weather. Unstandardized water distribution systems, intermittent water supply often lead to fecal contamination in supply water at the users' end. Regrowth of fecal coliform organisms in the distribution system is usually absent; however, researchers found exceptions with BOD_5 is greater than 10 mg/l, or, the water temperature is above 15 °C, and if there is no free chlorine residual [9]. Due to the proximity of the Bay of Bengal, the water source faces salinity problems during the dry period (November–January).

Higher chloride in water is proportionally related to the electrical conductivity of water. Chloride reacts with metal ions in metal pipes to form soluble salts and increase the pitting corrosion of metal pipes. Presently the city water supply mode is intermittent and experiences frequent pressure drops as well as negative pressure. The negative pressure creates a suction effect inside the pipe and causes the pipeline to leak, and the contaminant (microbial contaminants, i.e., bacteria from faces) can intrude in the pipeline. The treated water quality can be deteriorated after leaving the treatment plant through a pipe network. Responsible factors for water quality variations during the travel from the treatment plant to consumers tap, i.e., source water quality (i.e., biological and chemical) are: efficiency and effectiveness of the treatment process, the connection of the distribution system with the storage, treatment plant, and disinfection facilities, type, age, design, and maintenance of the distribution network, water pressure, treated water quality, water traveling duration; water mixing within hydraulic conditions from different sources and a distribution network [11, 12]. Water age is the duration of water travels from source to consumer, also responsible for the water quality deterioration. Thus, water quality trends could play a vital role in the decision support system.

2   Materials and Methods

The Chattogram city was divided by the service provider into four zones based on the network system (i.e., Zone-1, Zone-2, Zone-3, and Zone-4). In this study, sampling locations were selected by applying the Analytic Hierarchy Process (AHP) (Fig. 1). There were some criteria for identifying the sample locations, i.e., the number of pipe leakage, pipe age, source of water, and pipe materials.

The primary data were collected from twenty locations in Chattogram city, and secondary data were also collected from Chittagong water supply and sewerage authority (CWASA). Then, the data have been processed and analyzed to conduct the supply water quality analysis. The weighted linear combination (WLC) method is widely applied as a GIS-based decision rule. Due to simplicity, this is often used in resource evaluation problems, site selection, and also suitability analysis [13], 14. In ArcGIS, an integrated analysis was provided by the weighted sum analysis based on multiple combined inputs and their assigned weights that were generated from AHP. Combines multiple inputs were raster format, representing multiple factors. The WLC analysis was conducted as:

$$s = \Sigma W_i X_i \tag{1}$$

where

s = Sampling locations weightage, W_i = A weighting of factor i, and X_i = The criterion score of factor i.

WHO recommends the minimum sample numbers for verification of the microbial quality of drinking water. In distribution systems for a population > 500,000, the
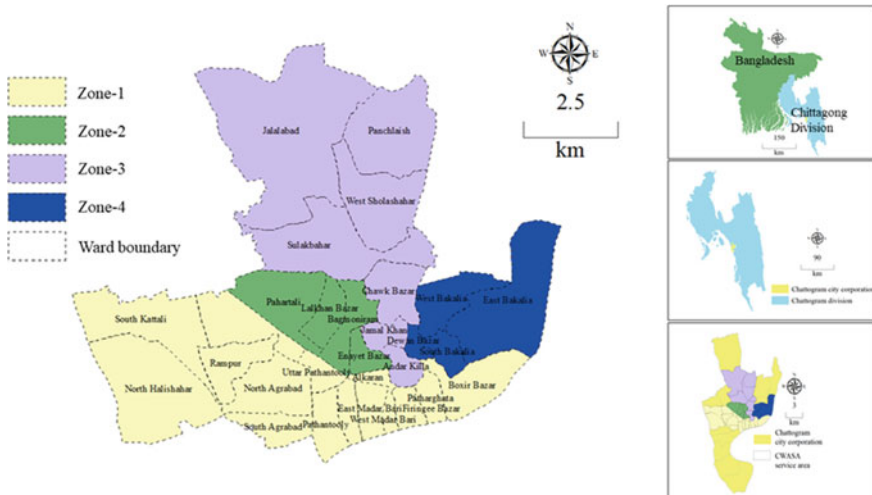

Fig. 1 Zone wise ward map of the water distribution system

sample number is 12 per 100,000 head of population plus an additional 180 samples per year (WHO, 2008). Several options were provided by this method for selecting appropriate locations for sample collections (Figs. 2 and 3). The final output of this method offered a map containing weightage values for sampling locations. Individual weights were assigned to this map to express their relative importance. The study is based on secondary data for the year 2011–2020 that was collected from CWASA. Secondary data (5-year data 2016–2020 among the available ten years) was verified with primary data collecting water quality parameter data from October 2017 to December 2017 with 15 days intervals. Primary data collection was done by collecting mainly water sample data for the eight parameters, i.e., pH, temperature, turbidity, BOD_5, Total coliforms (TC), Fecal Coliforms (FC), residual chlorine, and
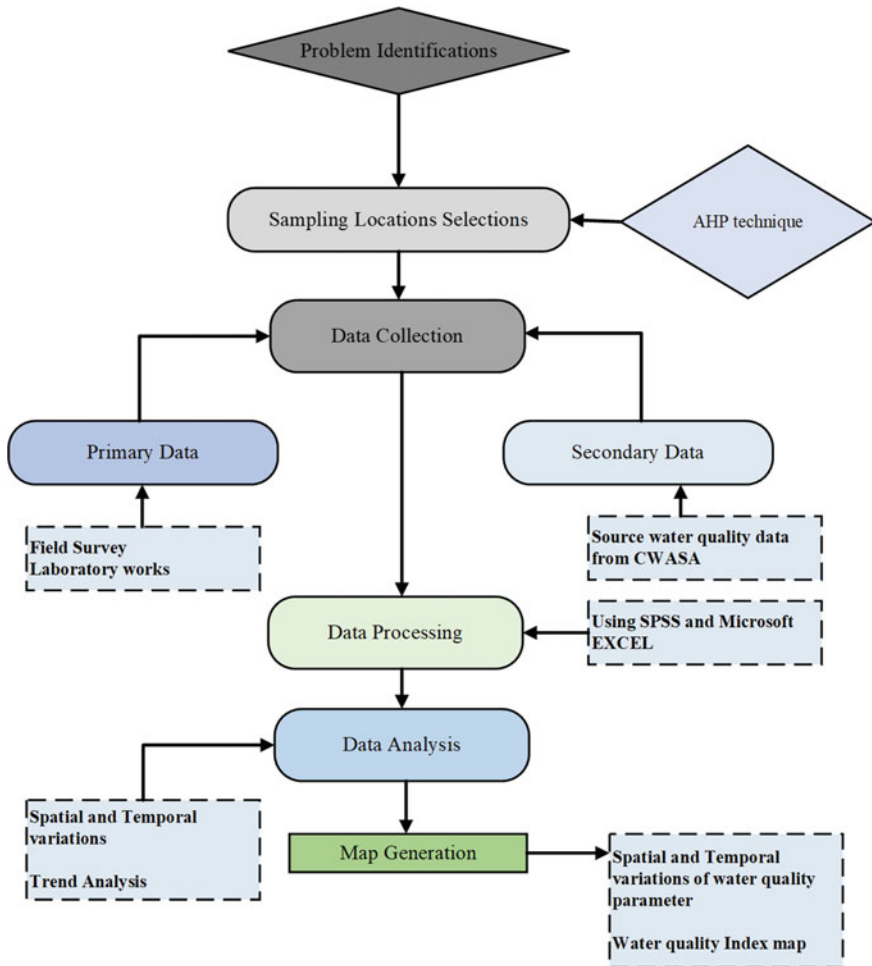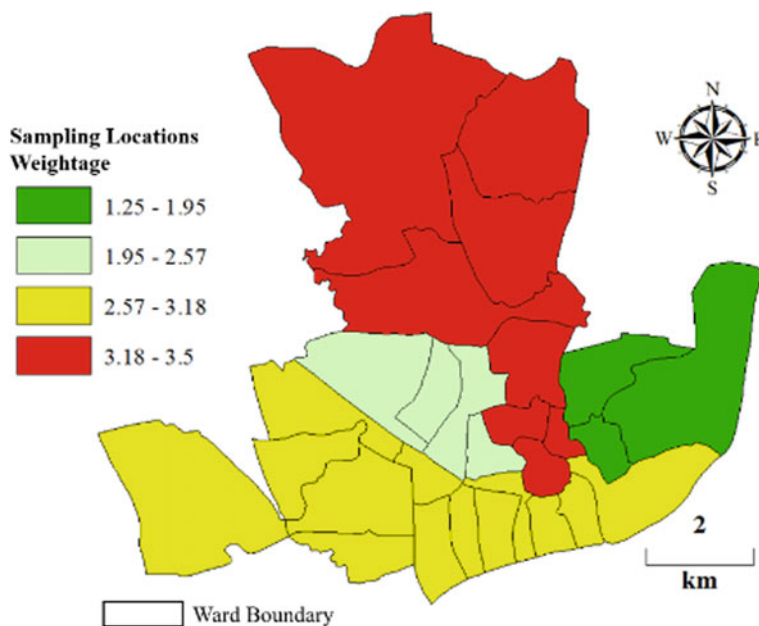

Fig. 2 Methodological flow chart

Fig. 3 Weightage value for the different zones

chloride from selected twenty locations (Fig. 4) within the study area for October 2017 to December 2017.

Moreover, observation and interviews with key personal of CWASA were also done for primary data collection. Turbidity ($R^2 = 0.9664$) and BOD$_5$ ($R^2 = 0.9461$) concentration in the field dataset were strongly correlated with CWASA provided data. Slightly variations were observed in pH ($R^2 = 0.8117$) and temperature ($R^2 = 0.7781$) (October–November) (Fig. 5). Chloride ($R^2 = 0.969$), TC ($R^2 = 0.957$) and residual chlorine ($R^2 = 0.958$) concentration in field data were strongly correlated with CWASA provided data (Fig. 6). On the contrary, slight variations were observed in FC ($R^2 = 0.8468$) concentration value in field data with CWASA provided data.

In this study, water samples were collected from twenty different places from October to December 2017, and other water quality parameters were collected from CWASA for 2016–2020. Water sample collection locations were selected by adopting the AHP technique. Sites having pipe leakage conditions were given more priority than other criteria. Selection criteria were discussed in the previous section. The analysis was done for three divisions, i.e., pre-monsoon (March to May), monsoon (June to October), and a post-monsoon period (November to February) following Ahmed and Kim [15].

Statistical analyses were carried out using SPSS and Microsoft excel 2016 software. Water quality index (WQI) was applied to get a comprehensive idea of overall water quality in the distribution system. WQI is determined as a rating reflecting the
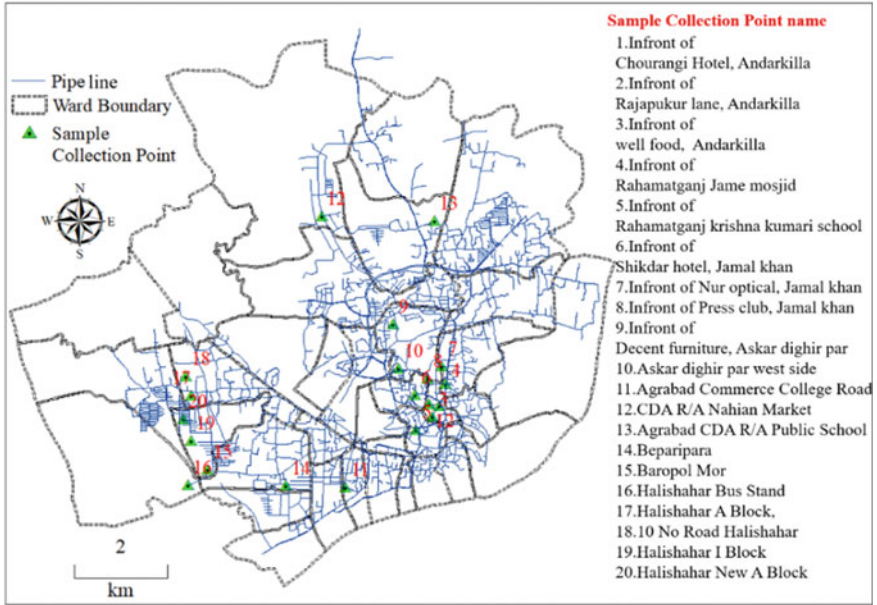
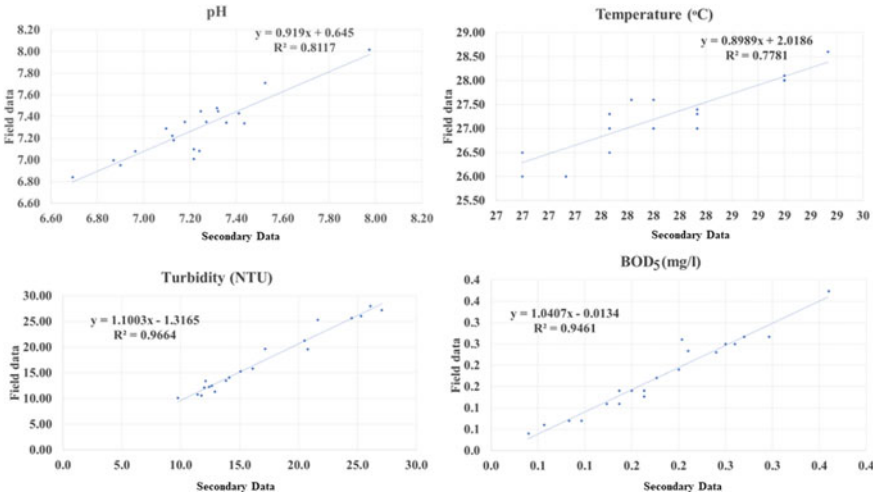**Fig. 4** Water sample collection point

Fig. 5 Variation of average pH, turbidity, chloride, and temperature value between field and secondary data (October 2017–December 2017)
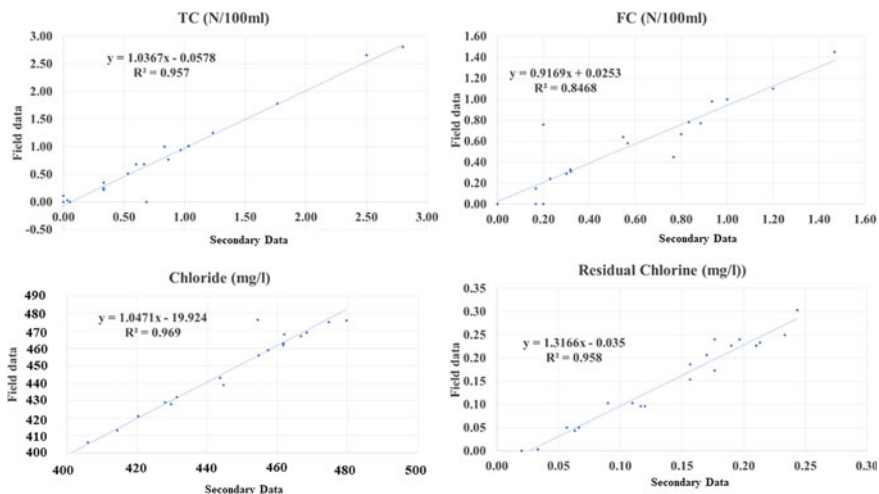
Fig. 6 Variation of average BOD_5, TC, FC, and residual chlorine value between field and secondary data (October 2017–December 2017)

composite impact of different water quality parameters in the distribution system on the overall water quality.

The WQI values were categorized into five class, i.e., water unsuitable for drinking (WQI > 300), very poor water (WQI = 200–300), poor water (WQI = 100–200), good water (WQI = 50–100), and excellent water (WQI < 50) [13].

A map was generated using GIS that includes water quality and its distribution over the study area based on the water quality index (Fig. 7). Spatial analysis was carried out by adopting the interpolation technique, i.e., inverse distance weighted (IDW) method, to generate a WQI value map in a GIS environment using ArcGIS software. SPSS was an effective tool to monitor the water quality parameter that could handle monthly and yearly average water quality data in time series. The graphical presentation analyzed the spatial and temporal trends of water quality parameters.

3   Results and Discussions

As part of the historical time series (i.e., 2011–2015) are subject to discontinuity, and water sampling locations are different than the study location. Most of the time, the p^H value was more significant than 7, and more alkaline water was found in the post-monsoon period than in another season. No significant variation of temperature was found in the distribution line. The turbidity level was significantly varied over the period in respect to different seasons. Biological parameters, i.e., most of the time, nonstandard BOD_5 levels were found over the period, varied with season.

Fig. 7 Zone wise water quality index map during the study period

Among the samples, maximum samples were found to have TC within 1/100 ml–3/100 ml and FC within 1/100 ml–8/100 ml over the period. Chemical parameters, i.e., seasonal variation of chloride concentration was significantly observed over the period and varied with the season—all these results in a lower residual disinfectant in the network. Maximum locations showed standard pH levels from 2016 to 2020 at the pre-monsoon period except for four areas, i.e., #4, #5, #7, and #12. Higher, alkaline, and acidic water was found in pre-monsoon (#6, #9, #10, #11, and #12) and monsoon periods (#7, #9, and #10), respectively. The temperature was revealed to be of high importance due to the tendency to affect other parameters. Here, the temperature at different distribution sites was 20–30 °C, acceptable according to the WHO and BECR'97. At the water distribution line, maximum locations were found in nonstandard turbidity levels at the pre-monsoon period from 2016 to June 2020.

Nine locations in Zone 1 and three locations in zone 3 were found in nonstandard turbidity levels at the pre-monsoon period. The number of locations in Zone 3 with nonstandard turbidity levels was increased at the post-monsoon period compared to the pre-monsoon period. On the contrary, the number of locations in Zone 1 with a standard turbidity level was increased after the pre-monsoon period. At the pre-monsoon period, the maximum average turbidity was found in a water sample collected from Halishahar A Block, i.e., #17 in Zone 3, and the value was 38 NTU. The minimum average turbidity, 0.2 NTU, was also found in a water sample collected

from Agrabad CDA, i.e., #12, Zone 3. In the whole distribution line, around 75% of water samples showed BOD_5 concentration within the range of 0–0.2 mg/l, 25% of water samples showed BOD_5 concentration greater than 0.2 mg/l. In Zone-1, around 26% of water samples were found with nonstandard BOD_5 concentration, i.e., greater than 0.2 mg/l. On the contrary, 23% of water samples were found in Zone-3 with nonstandard BOD_5 concentration, i.e., greater than 0.2 mg/l. Among the samples collected from the whole distribution network, TC was within 1/100 ml–3/100 ml at the monsoon period except for locations #4 and #7. At the pre-monsoon, maximum locations were found to have TC in Zone-3 (location#11, #12, #17, #18, #19, and #20) and three locations in Zone-1 (i.e., #4, #5 and #6). The maximum TC count of 8/100 ml was found in location#4 during the monsoon period. Among the samples collected from the whole distribution network, maximum samples were found to have FC within the range of 1/100 ml–8/100 ml during the monsoon period. At pre-monsoon period, six locations were found to have zero FC (i.e., location #4, #5, #6, #7, #8, and #10) in Zone-1 and five locations in Zone-3 (i.e., location #11, #12, #15, #19, and #20). On the contrary, four locations were found to have FC in Zone-1 (i.e., location #1, #2, #3, and #10) and five locations in Zone-3 (i.e., location #13, #14, #16, #17, and #18). At the monsoon period, four locations were found to have zero FC (i.e., location #4, #7, #8, and #9) in Zone-1 and two locations in Zone-3 (i.e., location #14 and #19). On the contrary, six locations were found to have FC in Zone-1 (i.e., location #1, #2, #3, #5, #6, and #10) and eight locations in Zone-3 (i.e., location #11, #12, #13, #15, #16, #17, #18, and #20). Nevertheless, with the absence and frequent failure of the power supply for pumping, water remains stagnant in the net, and the chlorine concentration gets reduced. Loss of disinfectant residual can also result in reactions between disinfectant and nutrients or ammonia nitrogen. No locations were found to have standard residual chlorine in the post-monsoon period over period. At the pre-monsoon period, three locations were found to have residual standard chlorine (i.e., location #4, #5, and #7) in Zone-1 and two locations in Zone-3 (i.e., location #12 and #13). On the contrary, seven locations were found to have nonstandard residual chlorine in Zone-1 (i.e., location #1, #2, #3, #6, #8, #9, and #10) and eight locations in Zone-3 (i.e., location #11, #14, #15, #16, #17, #18, #19, and #20). At the monsoon period, four locations were found to have standard residual chlorine (i.e., location #7, #8, #9, and #10) in Zone-1 and three locations in Zone-3 (i.e., location #13, #14, and #18). Maximum chloride concentration values in collected water samples were found at the pre-monsoon and post-monsoon. High chloride concentration values may be due to saline water intrusion problems frequent in the supply source nowadays. At concentrations above 250, mg/l chloride-rich water gives a salty test, causes various diseases, but this also depends on individual adaptability (Sawyer and McCarty, 1978). During the study period, all samples were within the standard chloride level.

The spatial variation of the water quality was obtained to prepare a water quality index map for the distribution line's water quality according to the pre-monsoon, monsoon, and post-monsoon periods from 2016 to 2020 (Fig. 7). The result shows that the majority of samples showed reasonably good for drinking purposes. In the pre-monsoon period, one location was found with poor water quality in the distribution

line in Zone-1, i.e., location #10, and four areas in Zone-3, i.e., location #11, #12, #14, and #16. During monsoon, one site showed poor water quality in Zone-1.

3.1 The Trend of pH, Temperature, Turbidity, and BOD$_5$ at the Distribution Site

The time series of average pH, temperature, turbidity, and BOD$_5$ in each year for the whole distribution site shows that the pH concentration is almost the same over the period, and the lowest pH was found in 2017. The concentration of BOD$_5$ and pH value similar trends over the period, but the temperature and turbidity value have fluctuated. The maximum temperature was found in 2016 and 2020. The maximum turbidity was discovered in 2020; thus, there is a relationship between temperature and turbidity concentrations. In Zone 1, the concentration of p^H value is almost the same over the period. BOD$_5$ and pH value concentration continue parallel over the period, but the temperature and turbidity value has fluctuated. The maximum temperature was recorded in 2018, and the maximum turbidity was discovered in 2017 (Fig. 8).
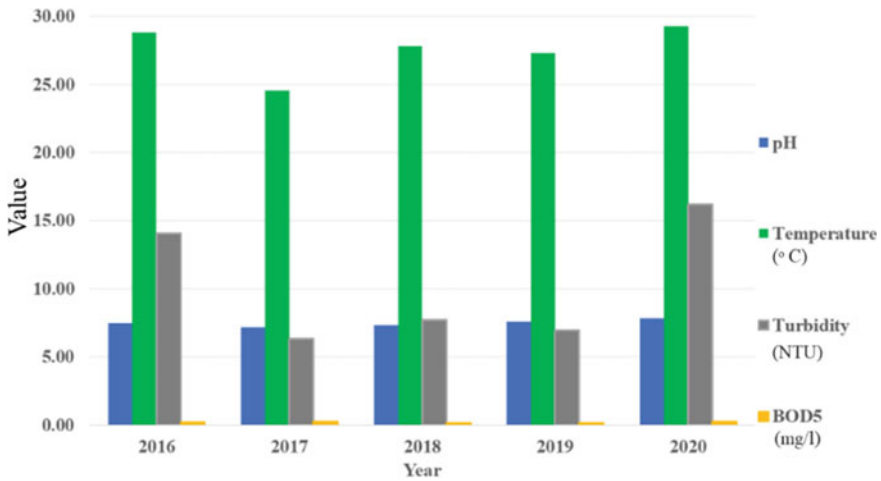

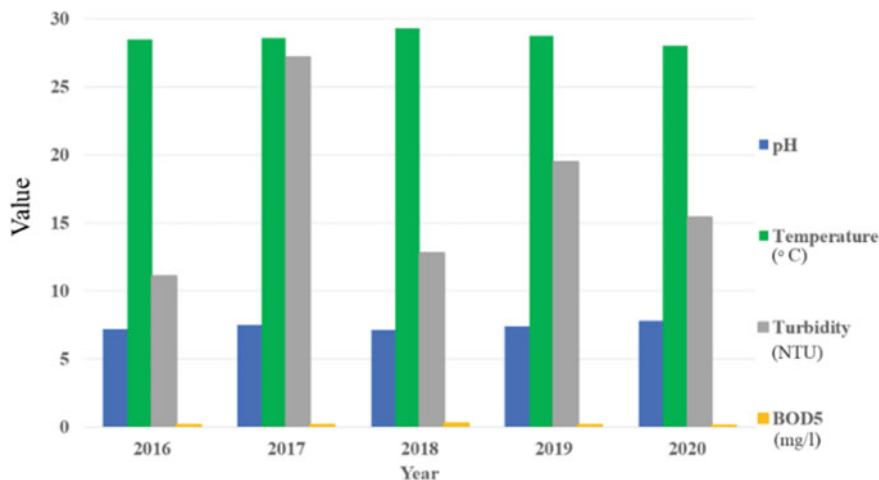**Fig. 8** Trend of pH, temperature, turbidity, and BOD$_5$ at the distribution site

Fig. 9 Trend of TC and residual chlorine at the distribution site

3.2 The Trend of TC, FC, and Residual Chlorine at the Distribution Site

The concentration of TC and FC values was changing very rapidly compared to the residual chlorine. Residual chlorine value has remained almost the same over the period. Maximum TC was found in 2020 and FC in 2019. Low concentrations of TC were found in 2018 and FC in 2020. After 2017, the TC and FC value was started increasing. More than 90% of the household have an underground reservoir in the city as water availability is too uncertain [14].

Along with the underground reservoir, also use small plastic tanks or other concrete reservoirs over the roof. Water from the underground reservoir is pumped to these small reservoirs for the required pressure in the supply tap. As the water supply is intermittent in Chattogram and the water has to be stored for significant periods in the home, even more than a week. This causes the loss of residual chlorine in the reservoir (Fig. 9).

3.3 The Trend of Water Quality at the Distribution Lines

The result indicates that the majority of samples fall in the class of suitable water type for drinking. The poor water quality areas were increasing from 2018, covering 17% of the whole distribution lines. After this, about 21% of the entire distribution lines receive relatively poor water quality. In 2020, the percentage of poor increases to 26% of the whole distribution lines. Thus, a deteriorating water quality trend was observed.

3.4 Reasons for Water Quality Deterioration

- Analyzing the water quality parameter, samples became contaminated in the network from any nearby contamination source. All the treated water parameters just before entering the distribution network were within the permissible limit, and the contamination of water was influenced by high turbidity or low residual chlorine.
- Most of the pipe network in the city passes over the open drains or very near to the septic tanks, pit latrines, or other contamination sources. As the city does not have a sewer system, these open drains carry the wastewater, and most of the time, the household waste.
- The presence of the FC provides evidence of recent fecal contamination.
- One of the excellent means of water getting contaminated in the distribution network is leakage and damage.

4 Conclusion

This study has focused on trend analysis of water quality parameters in Chattogram city using statistical analysis and GIS mapping. This study discusses the secondary water quality parameter and the effectiveness of SPSS as an innovative tool to operate and interpret the collected data to produce useful water quality information with GIS mapping of the Chattogram city.

- In this study, water quality data interpretation was made by adopting the IDW technique in the ArcGIS environment. WQI, i.e., assembling different parameters into one single number, provides a proper understanding of the index in this study, thus providing an important tool to identify water quality in a different location and as a guiding tool for management purposes.
- A decision support system would be benefited with easy identifications of the location where WQI classifications found excellent or poor water quality, i.e., excellent water (WQI < 50), good water (WQI 50–100), poor water (100–200), very poor water (200–300) and unsuitable for drinking (>300).
- In 2020, the percentage of insufficient class water stood at 26% of the whole distribution lines. The number of locations with good water quality was less in the post-monsoon period than others (2016–2020).
- The water quality status for the selected twenty locations of Chattogram city has deteriorated more in recent years. For all the locations around the city, high fluctuation of turbidity, TC, FC, Chloride, and residual chlorine was observed in pre-monsoon, monsoon, and post-monsoon seasons. Selected twenty locations were found with significantly lower residual chlorine and higher turbidity, TC, FC, and chloride concentration.
- In terms of other parameters considered in this study, i.e., temperature and BOD_5 were found the excellent and acceptable range. Seasonal variation in the number

of measured water quality parameters was significant. However, in this study, water quality variations were examined at the source and distribution site, and changes were also identified.

Thus, this study reveals the spatial and temporal water quality conditions for the Chattogram city. The acquired spatial maps are expected to provide spatial information to support both existing and future city dwellers.

References

1. USAID (2006) Making cities work: Urban water supply and distribution. Urban Themes
2. The Daily Star (2019) Halda River pollution getting worse. *The Daily Star*
3. The Daily Star (2020) Dredging of Karnaphuli hampered by polythene!; Strictly Strictly enforce the ban on plastics. *The Daily Star*
4. World Bank (2010) Project Appraisal Document on a Proposed Credit in the Amount of SDR 112.5 Million (US $ 170 Million Equivalent) to the People's Republic of Bangladesh for a Chittagong Water Supply Improvement and Sanitation Project. Sustainable Development Department
5. Osman Amin M (2006) Status of water & sanitation services in Chittagong water supply and sewerage authority, Bangladesh
6. Shahid S, Wang XJ, Moshiur Rahman M, Hasan R, Bin Harun S, Shamsudin S (2015) Spatial assessment of groundwater over-exploitation in northwestern districts of Bangladesh. J Geol Soc India 85(4):463–470
7. Rahman M, Al Bakri D (2010) A study on selected water quality parameters along the River Buriganga, Bangladesh. Iran J Energy Environ 1(2):81–92
8. Ali MM, Ali ML, Islam MS, Rahman MZ (2016) Preliminary assessment of heavy metals in water and sediment of Karnaphuli River, Bangladesh. Environ Nanotechnology Monit Manag 5:27–35
9. Tropfke H (1992) The importance of biochemical oxygen demand (BOD) in the water analysis sector, in The Biology of Effluents, 2nd edn. Werner-Verlag
10. CWASA DPP (2020) Appendix-140
11. Rossman LA (2000) EPANET user's manual. Cincinnati (OH): United States Environmental Protection Agency, Risk Reduction Engineering Laboratory
12. WHO (2014) Water sanitation health: Water safety in distribution systems
13. Kawo NS, Karuppannan S (2018) Groundwater quality assessment using water quality index and GIS technique in Modjo River Basin, central Ethiopia. J African Earth Sci 147(June):300–311
14. Chowdhury F (2010) Assessment of microbial quality of supply water in Chittagong city
15. Ahmed R, Kim IK (2003) Patterns of daily rainfall in Bangladesh during the summer monsoon season: Case studies at three stations. Phys Geogr 24(4):295–318